stellar populations in early-type coma cluster galaxies

Moore, Stephen Anthony William

Stellar Populations in Early-Type Coma Cluster Galaxies

Stephen Anthony William Moore

A thesis submitted to the University of Durham
in accordance with the regulations for admission to the
Degree of Doctor of Philosophy.

Department of Physics
University of Durham
2001

Abstract

A detailed modelling and statistical analysis is conducted of the stellar populations (which act as fossil records of galaxy formation and evolution) and the spectro-photometric relations of a sample of 87 bright early-type galaxies within the core of the rich Coma cluster (a diameter of 1 degree $\equiv 1.26\,h^{-1}$ Mpc) using a high quality, homogeneous data set with well characterised errors together with published Gunn r CCD surface photometry. The sample data set allows for the first time a new unbiased assessment of the Coma clusters' bright early-type galaxies' intrinsic properties and of the factors affecting their spectro-photometric relations, without any need to combine multiple data sets with the inherent systematic error problem that ensues. This work acts as an important baseline at $z \sim 0$ for studies of distant high redshift clusters, utilising the rich Coma cluster as a laboratory to explore hypotheses. It also expands the existing knowledge base of galaxy formation and evolution in rich clusters and provides further evidence for the usefulness of the fundamental plane as a distance indicator.

The stellar populations show that the bright early-type galaxies within the Coma cluster core have a large metallicity distribution (with $-0.55 \leq$ [Fe/H] $\leq +0.92$). Whilst it is more likely that there is also a small distribution in age, a single age of stellar population formation for the dominant group of galaxies is supportable. The bright early-type galaxies are found to have a luminosity-weighted mean age of 8 Gyrs. There are in addition real differences between the elliptical and lenticular galaxy populations, with the elliptical stellar populations (mean age of 9 Gyrs) on average 2 Gyrs *older* than those within the lenticulars (mean age of 7 Gyrs). Modelling of the age distributions of the early-type galaxies shows that an age model of 8 Gyrs with a scatter of 0.300 dex is likely, with the ellipticals having a smaller age scatter of 9 Gyrs $\pm$ 0.275 dex rather than the 7 Gyrs $\pm$ 0.325 dex of the lenticulars.

The fundamental plane (FP) analysis shows that the FP relation is in general well behaved and common for ellipticals and lenticulars. The early-type galaxy sample is well fit by a fundamental plane of the form $\log_{10} r_e = 1.36(\pm 0.07) \log_{10} \sigma - 0.78(\pm 0.03) \log_{10}\langle I \rangle_e - 0.64(\pm 0.16)$ for galaxies with velocity dispersions, σ greater than $100\,\mathrm{km\,s^{-1}}$. This FP has a significant intrinsic rms thickness of 0.044 ± 0.005, implying that the scatter in the FP relation is not simply due to measurement errors. A detailed FP residual correlation analysis concludes that there are no additional terms for the existing FP relation and that previously suggested mechanisms are *not* responsible for the presence of an intrinsic scatter, suggesting that the real source lies in the underlying physics of the kinematics and dark matter structures.

The evidence for real intrinsic differences between ellipticals and lenticulars is overwhelming, leading to the conclusion that they have differing: kinematics; dark matter fractions; formation mechanisms; and/or evolution histories. It is therefore important to no longer analyse conglomerate samples of early-type galaxies, and instead to consider separately elliptical and lenticular galaxies in rich galaxy clusters.

Contents

List of Figures

List of Tables

Preface

The work described in this thesis was undertaken between 1997 and 2001 whilst the author was a research student supported by PPARC within the Extragalactic Astronomy Group in the Department of Physics at the University of Durham under the supervision of Dr. J. R. Lucey. This work has not been submitted for any other degree, either at the University of Durham or at any other University.

Acknowledgements

Grateful thanks go first and foremost to my parents who have supported me throughout my life and have always given me the drive and encouragement to succeed in anything I do. For this I owe them endless thanks.

I am indebted to my supervisor throughout this work, Dr. John Lucey and to Dr. Harald Kuntschner who provided much guidance. I am also indebted to my fencing coach, Professor László Jakab who has taught me so much and has led me to excel in my international fencing career.

My friends at the Durham University Fencing Club and the Durham University Athletic Union also deserve thanks. Throughout my time in Durham I have fenced for the University, leading them to victory in the British Universities Sports Association (BUSA) Team Championships in 1999/2000 whilst I was President of the club, and was awarded a Full Palatinate in 1999 (this is the University Colours, which is the highest award possible for sport at the University). Fencing has kept me sane and remains a huge and important part of my life.

I acknowledge financial support from the Particle Physics and Astronomy Research Council (PPARC). I also acknowledge additional financial support from the University of Durham, who funded me during my PhD under their Elite Sportsman Bursary Scheme. Additional thanks go to the Graduate Society at the University of Durham, who also contributed to my fencing costs throughout.

A final thanks goes to all my friends who have always been there with help and drink. You have all been important to me.

This work is based on observations made with the 4.2m William Herschel Telescope operated on the island of La Palma by the Isaac Newton Group in the Spanish Observatorio del Roque de los Muchachos of the Instituto de Astrofisica de Canarias.

"Education is an admirable thing, but it is well to remember from time to time that nothing worth knowing can be taught."

Oscar Wilde

Chapter 1

Introduction

1.1 Background

Rich clusters provide a large sample of galaxies at a common distance, making them ideal laboratories for studying the global correlations between the dynamical, structural and stellar population properties of galaxies. The dominant cluster population of early-type galaxies, elliptical and lenticular (or "S0") galaxies, are observed to have several important correlations: the colour-magnitude relation, the Mg_2 line strength versus velocity dispersion relation and the Fundamental Plane. Spiral and other late-type galaxies are considerably rarer than early-type galaxies in the hostile environment of rich clusters. These early-type galaxy relations provide a rich source of constraints for galaxy formation scenarios (Bower, Lucey & Ellis 1992; Bender, Burstein & Faber 1992, 1993; Guzmán, Lucey & Bower 1993; Ciotti, Lanzoni & Renzini 1996).

A complicated picture has emerged from studies of the stellar populations of cluster early-type galaxies, with measurements of their stellar populations hampered by low quality data and by the age/metallicity degeneracy present in broad-band colours. In the core of the Coma cluster, Caldwell et al. (1993) found evidence of a small dispersion in the ages of the large majority of early-type galaxies (with only 3 out of 68 (4%) younger than $\sim$ 1 Gyr), whilst Jørgensen (1999) found evidence of a large spread in age (5.25 Gyr $\pm$ 0.166 dex) and a small spread in metallicity ([Fe/H] of $+0.08 \pm 0.194$). In the Fornax Cluster, a small age spread (ellipticals coeval at $\sim$8 Gyrs) and a large metallicity spread (-0.25 to $+0.30$ in [Fe/H]) was found (Kuntschner & Davies 1998; Kuntschner 2000). These differing results highlight an uncertain understanding of cluster early-type galaxy populations. This has important ramifications on studies of the evolutionary processes of galaxies in clusters, making it difficult to test the two competing theories of the formation of elliptical galaxies: hierarchical merging or early monolithic collapse.

The hierarchical model is of the formation of galaxies from the merger of smaller objects and is favoured by cold dark matter models (Kauffmann, White & Guiderdoni 1993; Baugh et al. 1996; Kauffmann 1996; Cole et al. 2000). These small objects form first within a given dark matter halo and gradually merge to form larger and larger objects. The smallest objects may

form via the monolithic collapse scenario, but typically merge before any supernova blow-out event occurs. When gaseous object mergers occur they trigger star-formation events, the scale of which depends on the structure and mass of the interacting objects. Since the objects are merging over time, star formation within the galaxy can be spread over many billions of years. In this way elliptical galaxies can span a wide range of properties: young cores, disky or boxy isophotes, kinematically decoupled cores, inner dust lanes, stellar disks plus other variations that are observed.

The monolithic dissipative collapse model forms large galaxies first by the collapse of material before smaller objects are formed (Larson 1974a,b, Larson & Tinsley 1974, Bressan, Chiosi & Fagotto 1994). This latter model is favoured by hot dark matter models. The model is of a collapse from the outside inwards, forming stars and funnelling metal-enriched gas towards the centre. Once supernovae provide enough energy to the inter-stellar medium (ISM) to blow out the gas, star formation ceases. This is generally a rapid process, taking only a few billion years. Elliptical galaxies formed in this way would exhibit colour and line strength gradients originating from a metallicity gradient in the galaxy (Arimoto & Yoshii 1987; Kodama & Arimoto 1997). Also smaller and less massive ellipticals would have smaller nuclei and an overall lower mean and nuclear metallicity than large ellipticals.

It is uncertain at present which models match best the observations of early-type galaxies. Recent evidence from stellar population modelling, kinematics, and isophotal shapes support elliptical formation by hierarchical merging. However the colour–magnitude and Mg–σ relations and the presence of colour and line-strength gradients support monolithic collapse. The evidence from studies of the ages and metallicities of cluster early-type galaxies is at present unclear.

1.2 Environmental effects

Current evidence on the effect of environment on stellar populations and on scaling relations is unclear.

Evidence of differences between field and cluster early-type galaxies is mixed. Sandage & Visvanathan (1978) found no evidence of any environmental dependence for the colour–magnitude (CM) relations of early-type galaxies. However when this same data was re-analysed by Larson, Tinsley & Caldwell (1980) they found evidence for increased scatter in the CM relations of field early-type galaxies over cluster early-type galaxies. This same variation in

scatter around the FP for field and cluster early-type galaxies was see by Dressler et al. (1987) and Lucey, Bower & Ellis (1991). de Carvalho & Djorgovski (1992) found systematic differences between field ellipticals in several scaling relations (including the fundamental plane). However their result depends on the sample used: for the Faber et al. (1989) sample there exists no significant difference between the scaling relations of cluster and field early-type galaxies.

Evidence of homogeneity between clusters has come from Bower, Lucey & Ellis (1992) who showed the remarkable similarity of the Virgo and Coma CM relations. Also Dressler et al. (1987) found similar Mg_2–σ relations in a number of rich clusters, though Jørgensen, Franx & Kjaergaard (1996) found evidence for zero point variations but similar slopes. Burstein, Faber & Dressler (1990) examined the Mark II peculiar velocity catalogue and found no evidence for any environmental dependence of the D_n–σ slope (with slopes of 1.16 ± 0.27, 1.37 ± 0.12 and 1.24 ± 0.11 for the Fornax, Virgo and Coma clusters which span a large range of cluster richness). The strongest evidence for environmental effects comes from studies of individual clusters. Guzmán et al. (1992) found an offset in the zero point of the Mg_2–σ relation of 0.017 ± 0.005 mag between the halo (more than 1 degree from the core) and inner core samples in Coma.

The main conclusion on the effect of environment on the scaling relations and stellar populations of early-type galaxies is that its effect is still unknown. However the overall tightness of the scaling relations does restrict the range of variation in contributing stellar population and structural factors. Any variations in the range of stellar population ages and metallicities both within clusters and between clusters have yet to be studied in any detail. This caveat of the possible presence of environmental effects should be born in mind before applying any conclusions about the early-type galaxies in the central 1 degree of the Coma cluster to other clusters and indeed to other parts further out from the core of the Coma cluster.

1.3 Butcher–Oemler effect

Butcher & Oemler (1978) conducted an observing campaign to search for the progenitors of todays lenticular galaxies. They found an excess of blue galaxies in distant clusters over that found in nearby clusters. Blue galaxies were defined to be galaxies more than 0.2 mag bluer (Butcher & Oemler 1984) than the ridge line of red galaxies in the cluster (presumably consisting of elliptical and lenticular galaxies); such galaxies are nearly absent in nearby clusters. The

observed over-abundance of blue galaxies in more distant clusters seems to grow with redshift (Butcher & Oemler 1984; Rakos & Schombert 1995; Lubin 1996) and is now known as the "Butcher–Oemler effect". This effect was initially questioned and attributed to contamination from foreground field galaxies or due to local supercluster structure. However Dressler & Gunn (1982,1983,1992) conducted a spectroscopic survey of several clusters at $z < 0.5$ and found that the blue galaxies were indeed members of these intermediate redshift clusters, and that a substantial fraction ($\sim$30% at $z \sim 0.4$) of the cluster galaxies were spectroscopically active having either AGN spectra, emission-line spectra or post-starburst spectra indicative of very recent bursts of star formation (called "E+A" galaxies). Couch & Sharples (1987) examined the Hδ strengths of cluster galaxies as a function of $B - R$ colour in three rich clusters at $z \sim 0.3$. Using the evolutionary synthesis models of Bruzual (1983) they suggested that post-starburst galaxies occupied just a single stage in an evolutionary "cycle" of star-formation events in the lives of cluster galaxies. Recent work by Barger et al. (1996) predicts the fraction of cluster galaxies at each stage along this star-formation "cycle" and agrees with their $z \sim 0.3$ findings.

A picture has emerged over the past 20 years of a sizeable fraction of galaxies in intermediate-redshift clusters undergoing or having recently undergone star formation events. At nearby redshifts, local rich clusters contain a small fraction of star-forming galaxies and large numbers of early-type galaxies which are therefore hypothesised to have old stellar populations. Since the Coma cluster is a nearby rich cluster we expect it to have little current star formation, with the majority of the star-formation having occurred at intermediate redshifts.

1.4 Surface photometry and kinematics of early-type galaxies

One of the earliest results of elliptical galaxy surface photometry was that the surface brightness as a function of radius was remarkably uniform from galaxy to galaxy (de Vaucouleurs 1948) and followed a $r^{1/4}$ law:

$$I(r) = I_e \exp\left(-c_n\left[\left(\frac{r}{r_e}\right)^{1/4} - 1\right]\right) \tag{1.1}$$

where I_e is the mean surface brightness ($\langle I \rangle_e$) in $L_\odot/pc^2$ and r_e is the effective (half-light) radius of a model profile in kpc. The constant c_n is chosen such that one-half of the total light of the system is emitted interior to r_e (for a circularly symmetric galaxy $c_n = 7.67$).

In the 1980's CCDs revolutionised the field of surface photometry (see Kormendy & Djorgovski 1989 for a review). Lauer (1983, 1985a,b,c) was the first to apply these detectors to the surface brightness distributions of elliptical galaxies. He found that the elliptical galaxy isophotes (contours of constant luminosity) were not perfectly elliptical. Isophotes were found to span a range between boxy and disky shapes, with several showing stellar disks and others showing dust lanes — evidence of merger or accretion events.

CCD surface photometry questioned the universality the de Vaucouleurs $r^{1/4}$ law. Caon et al. (1993) and d'Onofrio et al. (1994) showed that the more general $r^{1/n}$ law, first proposed by Sérsic (1968), was more appropriate for the total elliptical galaxy population:

$$I(r) = I_e \exp\left(-c_n\left[\left(\frac{r}{r_e}\right)^{1/n} - 1\right]\right) \tag{1.2}$$

The parameter n broadly follows galaxy luminosity, with bright ellipticals having $n \simeq 4$ (the standard de Vaucouleurs $r^{1/4}$ law) whilst lower luminosity dwarf elliptical galaxies have lower values of n.

In contrast, the surface brightness profiles of the disks in spiral and lenticular galaxies have long been described by the exponential law (Freeman 1970):

$$I(r) = I_0 \exp\left(-\frac{r}{\lambda}\right) \tag{1.3}$$

where I_0 is the central intensity and λ is the disk scale length. This law can be thought of a special case of the $r^{1/n}$ law with $n = 1$.

The late 1970's and 1980's also saw an explosion of information on the kinematics of elliptical galaxies. Illingworth (1977) showed that luminous ellipticals rotate slowly, and Davies et al. (1983) showed that intrinsically faint ellipticals rotate quickly. This implies that bright ellipticals are supported by velocity anisotropies, and faint ellipticals are supported by and flattened by rotation. Many groups (see Kormendy & Djorgovski 1989) have found evidence for kinematically-decoupled substructures in ellipticals, cores that have completely separate kinematics from the main body of the galaxy. Around 25% of ellipticals (de Zeeuw & Franx 1991) show evidence for kinematically-decoupled cores. Kormendy (1984) was the first to suggest that

such cores may be the results of a (mostly gas-free) merger of a low-luminosity system with a high-luminosity elliptical.

The conclusion is that more recent observational evidence has shown the early-type galaxy population to be far less straightforward and uniform than previously thought. The more the galaxies are studied in detail, the more differences are found.

1.5 Spectro-photometric properties of early-type galaxies

The global parameters of elliptical and lenticular galaxies have been found to follow a number of tight scaling relations. With the work on elliptical galaxies by Djorgovski & Davis (1987) and by Dressler et al. (1987) it became clear that a relation exists between the effective radius (r_e in kpc, the radius encompassing half the light), the mean surface brightness within this radius ($\langle\mu\rangle_e$ in mag arcsec^{-2}, $\langle I\rangle_e$ in $L_\odot/pc^2$) and the central velocity dispersion (σ in km s^{-1}) — defining a three-dimensional plane in that parameter space. This relation is linear in logarithmic space* and is known as the Fundamental Plane (FP):

$$\log_{10} r_e = \alpha \log_{10} \sigma + \beta \log_{10} \langle I\rangle_e + \gamma \tag{1.4}$$

Within the effective radius, the mean surface brightness ($\langle\mu\rangle_e$) in mag arcsec^{-2} is related to the mean surface brightness ($\langle I\rangle_e$) in $L_\odot/pc^2$ by the following equation:

$$\log_{10}\langle I\rangle_e = -0.4(\langle\mu\rangle_e - \text{constant}) \tag{1.5}$$

At a rudimentary level, the FP relation may be understood as arising from the virial theorem and reflects the formation and evolution processes of the galaxies. The actual observed plane is tilted with respect to the natural coordinate system. This tilt may arise from either:

- a relation between the mass-to-light ratios and the masses of the galaxies (Faber et al. 1987; Bender, Burstein & Faber 1992), implying that significant star formation must have occurred after the dark matter potential is in place. If the luminosity profiles as well as

*unless specifically indicated, logarithms in this dissertation refer to a logarithm to the base 10

the dynamical structure of the galaxies are similar (i.e. are homologous), then the virial theorem implies that the mass-to-light (M/L) ratio is a function of r_e, $\langle I \rangle_e$ and σ (from which the masses can be derived). If this function is unique and a power law, then a relation like the FP is to be expected (see also Faber et al. 1987; Djorgovski, de Carvalho & Han 1988); or

- a structural/dynamical effect where the dark-to-stellar matter scale-length depends on mass (Guzmán et al. 1993; Ciotti et al. 1996; Mobasher et al. 1999).

Importantly for distance determination, the FP relation has a low scatter. The intrinsic scatter about the FP is also an extremely important constraint for all theories of the FP's origin. The dominant sources of uncertainty for the value of the FP's tilt and intrinsic scatter are:

- the selection biases in the existing samples;
- the precise treatment of the outliers in the distribution; and
- the measurement errors, both random and systematic, in the σ values.

For the FP relation to be applied universally as a distance indicator it is important that the relation itself be universal, with no hidden dependence on other factors. With the large homogeneous and high quality dataset of this study, the three uncertainties listed above can be dramatically reduced, allowing a powerful test of model predictions and a determination of whether there are any other factors that need to be included to make the relation truly universal. For instance, the line indices Mg_2 and $H\beta$ are strongly correlated with the velocity dispersions of the galaxies (e.g. Burstein et al. 1988; Fisher, Franx & Illingworth 1995; Jørgensen 1997; Trager et al. 1998), while the $\langle Fe \rangle$ index shows a rather weak correlation with the velocity dispersion (Jørgensen 1997; Trager et al. 1998). Could there be an additional stellar population term in the FP relation (and hence a dependence on stellar population derived age and/or metallicity)? This study will be able to answer this question. The intrinsic scatter will also be used to place limits on the allowed variations of ages and metallicities among early-type galaxies.

While elliptical and S0 galaxies appear to follow the same FP relation, zero-point differences of $\pm 5\%$ have been reported. The proposed dataset will allow such differences to investigated at the level of $\sim 3\%$.

1.6 Stellar populations of early-type galaxies

The resolution of M32, NGC205 and the outer nucleus of M31 by Baade (1944) and his determination of two distinct stellar population types (Populations I and II) mark the beginning of the study of stellar populations of early-type galaxies. His concept came from the morphologies of the colour-magnitude diagrams of the two stellar populations. It was not until the early 1950's, when stellar evolutionary models fully including the red giant branch (RGB) were beginning to be developed, that the concept of age became a crucial part of Baade's thinking, although Gamow, Russell and Spitzer had all suggested it privately or in print by the end of the 1940's (Osterbrock 1995). Differences in chemical composition were not included until the work of Roman and others in the mid-1950's (Roman 1995). Baade's resultant canonical view of the stellar populations of elliptical galaxies was that the integrated spectra of giant elliptical galaxies are dominated by stars of spectral types G and K of higher metallicity than that the Milky Way halo Population II stars. In other words, the stellar populations of elliptical galaxies are old and metal-rich.

Stellar population synthesis began when Whipple (1935) attempted to reproduce the colours of galaxies by using arbitrary combinations of colours of nearby stars. His work showed what Baade later discovered from investigations of integrated spectra, namely that the colours of elliptical galaxies are dominated by the light from G and K stars. Modern stellar population synthesis relies upon libraries of stellar spectra and computed stellar evolutionary isochrones (contours of constant age), including detailed treatment of the red giant branch (RGB), the early asymptotic giant branch (AGB) and the evolution to the thermally pulsing asymptotic giant branch (TPAGB). Parameters such as the cluster initial mass function (IMF), initial element abundances, age, metallicity or star formation history can be changed and observational properties of a galaxy predicted (Spinrad & Taylor 1971; Faber 1972; O'Connell 1976,1980; Pickles 1985; Tinsley & Gunn 1976; Gunn, Stryker & Tinsley 1981; Bruzual 1983; Charlot & Bruzual 1991; Bruzual & Charlot 1993; Worthey 1994).

1.6.1 Current state of stellar population synthesis models

Enormous amount of effort in last few years to develop evolutionary stellar population synthesis models (Bruzual & Charlot 1993; Worthey 1994,1997; Weiss, Peletier & Matteucci 1995; Vazdekis et al. 1996a; Kodama & Arimoto 1997) in order to analyse the integrated light of

galaxies and derive estimates of their mean ages, metal abundances, stellar formation histories and overall evolutionary history. The most widely used stellar evolutionary population synthesis model over the past 6 years has been the model of Worthey (1994) with a Salpeter initial mass function (IMF) and a single star burst scenario. This is the model that is adopted herein to main commonality between this and other studies of stellar populations. Currently the field is in a state of transition from the universally accepted Worthey (1994) model to the next set of universally accepted models which promise better handling of the crucial red giant branch of the stellar isochrones as well as other stellar effects (e.g. differential stellar rotation). In the course of the next few years it is anticipated that we will have ironed out the problems with these new models, but as yet no one model has been widely accepted, leading to the continued general reliance on the Worthey (1994) models.

1.6.2 Stellar population model parameters

Before embarking on a discussion on the stellar population models, it is best to firstly introduce the basic terminology and parameters used in these models.

Element abundances are referred to by their fractional abundances by weight using three symbols:

X = fractional abundance by weight of hydrogen
Y = fractional abundance by weight of helium
Z = fractional abundance by weight of everything else

The metallicity of an object can then be defined by:

$$\text{metallicity, } Z = \frac{\text{mass of heavy elements}}{\text{mass of gas}} \tag{1.6}$$

i.e. the mass of the heavy elements (elements other than hydrogen and helium) is divided by the mass of the "gaseous" elements (hydrogen and helium). Obviously the caveat that $X+Y+Z=1$ holds. Solar fractional abundance values are shown in Table 1.1.

Rather than expressing the metallicity in models using Z, it is often converted to [Fe/H] which tracks the metallicity relative to solar:

Element		Fractional abundance by weight
hydrogen	$X_\odot$	0.709
helium	$Y_\odot$	0.274†
everything else	$Z_\odot$	0.0169‡

† from Anders & Grevesse 1989.

‡ from Vandenberg 1985

Table 1.1: Solar fractional element abundances.

$$[\mathrm{Fe/H}] = \log_{10}\left(\frac{Z}{Z_\odot}\right) \tag{1.7}$$

This use of [Fe/H] rather than Z decreases any discrepancies in models due to stellar lifetimes differences from the use of sets of isochrones from various contributors (see Worthey 1994).

1.6.3 Age/metallicity degeneracy

Worthey (1994) pointed out that the determination of the ages and metallicities (Z) of old stellar populations is complicated by the similar effects that age and metallicity have on the integrated spectral energy distributions. Broad band colours and most of the line strength indices are degenerate along the locus of:

$$\Delta\mathrm{age} \simeq -3/2\,\Delta\mathrm{Z} \tag{1.8}$$

A doubling in age together with a reduction in the total metallicity by a factor of three can result in an identical stellar population indicator.

In the optical wavelength range only a few narrow band absorption line strength indices have so far been identified which can break this degeneracy. In terms of age, the Balmer lines Hβ, Hγ and Hδ are the most promising features and are clearly more sensitive to age than metallicity. The absorption features Mg_b and $\langle\mathrm{Fe}\rangle$ (and the derived index [MgFe] — see Section 3.7.2) are primarily sensitive to metallicity rather than age. By plotting an age-sensitive index against a metallicity-sensitive index one can break the degeneracy and estimate the luminosity-weighted mean age and metallicity of an integrated stellar population (González 1993; Fisher, Franx

& Illingworth 1996; Mehlert 1998; Jørgensen 1999; Kuntscher 2000; Trager et al. 2000a,b). However the usefulness of the Balmer lines as an age indicator is affected by nebular emission; it is therefore necessary to emission correct these indices before employing them.

1.6.4 Lick/IDS system

To counter the degeneracy present in the use of broad-band colours, more recent efforts have concentrated on the use of absorption features mapped on to the Lick/IDS system (Burstein et al. 1984; Worthey et al. 1994; Trager et al. 1998,2000a,b; Kuntschner 1998,2000) which has been used by many authors (González 1993; Davies, Sadler & Peletier 1993; Fisher, Franx & Illingworth 1995,1996; Ziegler & Bender 1997; Longhetti et al. 1998; Mehlert 1998,2000; Jørgensen 1999). In contrast with high resolution index systems (Rose 1994; Jones & Worthey 1995) which promise a better separation of age and metallicity, the Lick/IDS system allows the investigation of dynamically hot galaxies that have intrinsically broad absorption lines.

By plotting appropriate age sensitive and metal sensitive Lick indices against one another one can combat the age/metallicity degeneracy problem and largely break the degeneracy allowing confident estimates of luminosity weighted ages and metallicities of galaxy stellar populations through model predictions. However this problem is complicated by non-solar abundance ratios present in the stellar populations of observed galaxies which have yet to be successfully integrated in current models (which are based on knowledge of stellar populations gleaned from our local stellar neighbourhood) - see Weiss, Peletier & Matteucci 1995 for an example. In particular the Magnesium/Iron ratio seems to be larger in luminous early-type galaxies (O'Connell 1976; Peletier 1989; Worthey, Faber & González 1992; Davies, Sadler & Peletier 1993; Henry & Worthey 1999; Worthey 1999; Jørgensen 1999; Kuntchsner 2000). This abundance problem hampers the derivation of accurate *absolute* ages and metallicities from integrated light spectroscopy (Worthey 1998). Instead at present only studies of relative trends in ages and abundances are possible. Attempts are under way to solve this problem (Worthey 1998; Peletier et al. 1999).

The Lick/IDS system of stellar population indices is based upon spectra obtained between 1972 and 1984 using the red-sensitive Image Dissector Scanner (IDS) and Cassegrain spectrograph on the 3m Shane Telescope at the Lick Observatory. The spectra cover roughly 4000-6400Å and have a mean resolution of 9Å (higher at the ends of the spectra). The full IDS database contains absorption line strengths of 381 galaxies, 38 globular clusters and 460 stars,

fully establishing a common spectrophotometric index system to study stellar populations.

1.6.5 Worthey (1994) stellar population models

The Worthey (1994) galaxy stellar population models† depend only on metallicity ($-2 <$ [Fe/H] < 0.5), single star-burst age (1<age<18 Gyr), and initial mass function exponent (IMF). Combinations of model parameters allow arbitrarily complex stellar populations to be modelled. The models are based on three major ingredients: isochrones and opacities; a flux library; and absorption line strengths:

Isochrones and opacities: From the bottom of the main sequence to the base of the red-giant branch (RGB), the Worthey (1994) models use the stellar evolutionary isochrones by Vandenberg and collaborators (Vandenberg 1985; Vandenberg & Bell 1985; Vandenberg & Laskarides 1987). These isochrones are mated to the giant branches of the Revised Yale Isochrones (Green, Demarque & King 1987), appropriately shifted in $\Delta \log L$ and $\Delta \log T_{eff}$ to match at the base of the RGB. Extrapolations are made to cover a wide range of (Z, Y, age), assuming $Z_{\odot} = 0.0169$ and $Y = 0.228 + 2.7Z$. Note that the corner of parameter space containing ages less than 8 Gyr and [Fe/H]<-0.225 has been excluded. Evolution beyond the top of the RGB is approximated as a single red clump plus a theoretical prescription for evolution from the early asymptotic giant branch (AGB) to the thermally pulsing asymptotic giant branch (TPAGB).

Flux library: To derive observational properties from these models, a flux library is need for every stellar luminosity, temperature, gravity and composition. As no such observational library of fluxed stellar spectra exists which covers the entire parameter space spanned by these models, Worthey (1994) chose to use model atmospheres of Kurucz (1992) for stars hotter than 3500K, and a combination of model atmospheres of Bessel et al. (1989,1991) and the observed fluxed spectra of Gunn & Stryker (1983) for cooler M giants (blackbody curves were appended in the UV as necessary for these stars).

Absorption line strengths: The novel feature of the Worthey (1994) models at the time was

†herein I refer to using Worthey (1994) models, although I have actually used a slightly modified version of these models provided by Dr. Guy Worthey via private communication. These models are still single burst models with a Salpeter IMF and $Y = 0.228 + 2.7Z$, but with corrections for improvements to the red giant branch treatment within the models.

the inclusion of empirically-calibrated absorption line strengths. Using the IDS stellar data, Worthey et al. (1994) derived polynomial fitting functions for 21 Lick/IDS indices as a function of $1/T_{eff}$, [Fe/H] and surface gravity. Worthey & Ottaviani (1997) extended this analysis to include the higher-order Balmer lines Hδ and Hγ.

In this study I use a Worthey (1994) grid that assumes a single initial star burst to form the stellar population and a standard Salpeter power law initial mass function (Salpeter 1955). Since only low stellar masses ($M < 2M_{\odot}$) are needed for old populations, more recent IMFs that treat massive stars more carefully are unjustified. The IMF gives the relative number of stars as a function of initial stellar mass, and takes the form:

$$dN = CM^{-x}dM \tag{1.9}$$

where C is a constant, N is the number of stars in the population, and M is the stellar mass. The variable x is a parameter which Salpeter (1955) estimated to be 2.35 for local stars. From this equation we derive what the total initial mass is in the stellar system:

$$M_{tot} = \int MdN \equiv \int_{M_l}^{M_u} MCM^{-x}dM \tag{1.10}$$

where M_l is the lower mass cutoff and M_u is the upper mass cutoff. Worthey (1994) adopts $M_l = 0.1M_{\odot}$ and $M_u = 2M_{\odot}$ and fixes $M_{tot} = 10^6 M_{\odot}$. A relation between fractional element abundances by weight is also adopted:

$$\mathrm{Y} = 0.228 + 2.7\mathrm{Z} \tag{1.11}$$

This function for Y is chosen so that the primordial value is 0.228 (Peimbert & Torres-Peimbert 1976; Pagel et al. 1992) and so that $Y_{\odot} = 0.274$ (Anders & Grevesse 1989) at $Z_{\odot}$. The slope of this relation (2.7) may be too step for stars greater than solar metallicity, but the impact of changes in Y on integrated light is mild because perturbations in Y do not seriously affect either RGB temperatures or main-sequence turnoff temperature when population age and Z are held constant. The value of Y impacts chiefly on evolutionary lifetimes (see Worthey 1994).

The stellar population grid is derived from libraries of nearby stars which, because of their proximity, have solar abundance ratios. This introduces complexities when studying extragalactic objects which do not necessarily contain stars with solar abundance ratios.

1.6.6 Overabundance issues

Over the last decade there has been a growing consensus that the stellar populations of luminous elliptical and lenticular galaxies show evidence of non-solar abundance ratios. In particular magnesium, measured by the Mg_2 and Mg_b indices, when plotted against iron, measured by various Fe indices, does not track solar abundance ratio model predictions and implies [Mg/Fe]>0 (O'Connell 1976; Peletier 1989; Worthey, Faber & González 1992; Weiss, Peletier & Matteucci 1995; Tantalo, Chiosi & Bressan 1998; Worthey 1998; Jørgensen 1999; Kuntschner 2000).

Most of the currently available stellar population models cannot predict the strength of indices as a function of [Mg/Fe] since they are built on databases of solar abundance stars (this is because at present it is difficult to build libraries of high-quality stellar spectra from other galaxies). This can lead to seriously flawed age/metallicity estimates if particular, worst case indicators are used. For example, if non-solar abundance ratios are indeed present in a galaxy stellar population then the use of Mg_b as a metallicity indicator (versus $H\beta$) would result in the inferment of mean ages that are younger and mean metallicities that are larger. If the index $\langle Fe \rangle$ is used it would result in the opposite inferment (see e.g. Worthey 1998; Kuntschner 2000). However, if we combine Mg_b and $\langle Fe \rangle$ to the index [MgFe] we can significantly reduce the effects of non-solar abundance ratios (Kuntschner 2000).

1.6.7 Caveats when using stellar population models

Evolutionary stellar population synthesis models are *not* appropriate for comparison on a galaxy-by-galaxy basis: a single model cannot be expected to match a real galaxy in more than a few indices. This is because the models assume exactly one metallicity, Z and one age for the whole population, whereas galaxies are composite in at least Z and probably in age as well (e.g. possessing a combination of Population I and II stars). Comparison of model sequences to galaxy sequences *is* however permissable. Charlot, Worthey & Bressan (1996) also showed that different prescriptions for isochrones and flux libraries in stellar population models can induce systematic uncertainties of approximately 25% in age and metallicity measurements. However *relative* ages and metallicities are little affected.

It should also be noted that the "ages" and "metallicities" that are derived using stellar population models are in fact luminosity-weighted mean ages and metallicities such that younger (brighter) populations are disproportionally important compared with their mass.

Another problem that is not yet fully understood is the impact of a population of primordial binaries. If blue straggler stars arise from primordial binaries, then a large primordial binary fraction ($\sim 50 - 100\%$) evolving into blue stragglers (Leonard 1989, Trager et al. 1998) could significantly increase the Balmer line strengths in stellar population models. If this evolution arises in elliptical galaxies, a young age derived from the models could in fact correspond to an old population with a large population of blue stragglers.

1.7 The Coma cluster

1.7.1 Previous early-type galaxy stellar population studies

A complicated picture has emerged from studies of cluster early-type galaxies, with measurements of their stellar populations hampered by low quality, inhomogeneous data and by the age/metallicity degeneracy present in broad-band colours. Recent work has concentrated on trying to overcome this degeneracy by using line index measurements. The principal studies of recent years are summarised below.

1. Caldwell et al. (1993) obtained multi-fibre spectroscopy for 125 early-type Coma cluster galaxies from two 45′ diameter fields, one centred on the cluster core ($14.3 < B < 18.1$ mag) and one centred 40′ south west (SW) of the cluster centre ($14.3 < B < 19.0$ mag). Data were obtained with the Hydra multi-fibre positioner with 3″ fibres and the bench spectrograph on the Kitt Peak (KPNO) 4 metre telescope with a spectral resolution of 3.8Å FWHM. Caldwell et al. (1993) found that for $B < 17.2$ mag, 11 out of the 28 galaxies (39%) in the SW region are "abnormal", as opposed to only 3 out of 68 (4%) in the central field. They define "abnormal" spectra to be spectra indicative of recent star formation or nuclear activity (with CN/H8< -0.5). Their definition of "abnormal" is analogous to the "E+A" galaxies of Dressler (1987), Gunn & Dressler (1988) and MacLaren et al. (1988). "E+A" galaxies are defined as post-starburst galaxies with significant star-formation ~ 1 Gyr ago (for $z \simeq 0.3 - 0.5$). Caldwell et al. (1993)'s results imply a small dispersion in early-type galaxies in the cluster core (with the overwhelming majority of galaxies having old stellar populations), whilst there is evidence for a wider spread in ages in the SW corner of the

cluster implying that this part of the cluster (centred on NGC 4839) is possibly infalling to the main, older core of galaxies at the centre of the cluster;

2. González (1993) measured Lick/IDS absorption line strengths for a sample of 40 elliptical galaxies, selected to study the kinematics of a relatively "large" sample of normal, non-interacting elliptical galaxies mostly free of dust and gas. Most of the galaxies in the sample are members of small nearby groups. The galaxies cover a considerable range in luminosity, flattening, velocity dispersions and rotation. Observations were undertaken with the CCD Cassegrain Spectrograph initially in grism mode (FWHM resolution of $\sim$ 3.3Å) and later in grating mode (FWHM resolution of $\sim$ 2.7Å) on the 3 metre Shane Telescope at the Lick Observatory from August 1985 to September 1989. A slit width of 2.1″ was used and stellar population analyses were done with co-added spectrum from a $2.1 \times 5''$ region. He found a large variation in the ages of the galaxies of between 4 to 15 Gyrs, whilst he found a small variation in their metallicities, Z with a variation of $\sim$0.3 dex;

3. Kuntschner & Davies (1998) (see also Kuntschner 2000) measured Lick/IDS absorption line strengths for a magnitude-limited sample of early-type galaxies in the nearby Fornax cluster (at $\sim$1380 km s^{-1}) with the 3.9 metre AAT telescope and the RGO spectrograph (with a slit width of 2.3″, giving a spectral resolution of 4.1Å FWHM). Their sample comprises 11 elliptical and 11 lenticular galaxies more luminous than $M_B = -17$ ($B_T = 14.2$), with spectra co-added within a 3.85″ (5 pixel) aperture. With this relatively small data set, they concluded that the elliptical galaxies appear to be roughly coeval at $\sim$8 Gyrs (i.e. a small spread in age) and form a sequence in metallicity varying roughly from –0.25 to +0.30 in [Fe/H] (corresponding to a large spread in metallicity). In contrast they find that the lenticular galaxies have a wide range in ages, but are younger than the ellipticals. The lenticulars also span an even wider range in metallicity from –0.50 to +0.50 in [Fe/H];

4. Jørgensen (1999) constructed a data set of 71 Coma cluster early-type galaxies within the central $64 \times 70''$ region by observing with the McDonald observatory 2.7 metre telescope equipped firstly with a large Cassegrain spectrograph (44 galaxies, slit width 6.35″, resolution 0.97Å) and then with a fibre multi-object spectrograph (38 galaxies, fibre diameter 2.6″, resolution 4.25Å). This data was then combined with literature data to create a data set of 115 early-type galaxies with Mg_2, $H\beta_G$ and $\langle Fe \rangle$ Lick/IDS index measurements

corrected to a 3.4″ diameter aperture (though there were only 68 with all of the indices measured), all with signal-to-noises considerably less than that of the study herein (typically $\sim$ 28 per Å). She concluded that the median age of the Coma cluster early-type galaxies is 5.25 Gyr, with an intrinsic scatter of $\sim$ 0.166 dex (corresponding to a large spread in age), and that the mean metallicity, [Fe/H] was 0.08 with an intrinsic scatter of 0.194 (implying a small spread in metallicity);

5. Kuntschner et al. (2001) re-analysed a spectroscopic run on the 2.5 metre INT telescope with the Intermediate Dispersion Spectrograph (with a 3″ wide slit giving a resolution of $\sim$ 4Å FWHM) from the SMAC fundamental plane (FP) programme (Smith et al. 2000) and measured absorption line indices, correcting them to an equivalent 3.4″ diameter aperture. The SMAC programme data set of FP parameters (but *not* stellar population parameters) has been well calibrated across its many observing runs and with many overlapping published data sets allowing a comprehensive treatment of any systematic errors. Kuntschner et al. (2001) constructed a sample of 72 early-type galaxies (with signal-to-noises greater than 30 per Å and a median S/N of $\sim$40 per Å) drawn mostly from cluster and group environments, 31 of which came from the Coma cluster. They conclude (using some Monte Carlo simulations) that the data is largely consistent with a constant age sequence of $\sim$11 Gyrs, but with a small number ($\sim$ 5) of galaxies with ages of $\leq$ 3 Gyrs. A range in metallicity from −0.50 to +0.50 in [Fe/H] is seen.

As can be seen, a variety of different and contrasting conclusions have been reached by previous stellar population studies. However all of these previous studies have suffered from a number of limitations, including many of the following: low signal-to-noise (Jørgensen 1999 and Kuntschner et al. 2001's SMAC data), small numbers of galaxies (González 1993, Kuntschner & Davies 1998's Fornax data and Kuntschner et al. 2001's SMAC data), poor and uncertain characterisation of errors (all studies), systematic errors introduced through the combination of data sets (Caldwell et al. 1993, González 1993, Jørgensen 1999 and Kuntschner et al. 2001's SMAC data), and finally relatively poor age and metallicity indicators (Caldwell et al. 1993).

These differing results highlight an uncertain understanding of cluster early-type galaxy populations. This has important ramifications on studies of the evolutionary processes of galaxies in clusters. Higher quality, homogeneous data sets with good age and metallicity indicators allow direct testing for the presence or absence of an age distribution, enabling us to distinguish

between hierarchical merging or early monolithic collapse models:

- a significant age distribution in cluster early-type galaxies implies a hierarchical picture for the construction of galaxies in which galaxies form via multiple mergers creating bursts of star formation in the evolving galaxy (Baugh et al. 1996; Kauffmann 1996; Cole et al. 2000);
- no age distribution in cluster early-type galaxies supports the conventional view that all luminous elliptical galaxies are old and coeval. In this picture the global spectrophotometric relations observed for ellipticals (e.g. the colour-magnitude relation – Visvanathan & Sandage 1977; Bower, Lucey & Ellis 1992; Terlevich 1998) are explained by the steady increase in the abundance of heavy elements with increasing galaxy mass. This increase arises naturally in galactic wind models, e.g. Arimoto & Yoshii (1987), Kodama & Arimoto (1997).

1.7.2 Kinematic structure of the Coma cluster

In this section I explore what the kinematic data presented in this dissertation (given in Section 3.9) tells us about the kinematic structure of the Coma cluster core (the "core" of the Coma cluster explored in this dissertation refers to a 1 degree diameter field which is equivalent to $1.257\,h^{-1}\,\mathrm{Mpc}$[‡]).

It is important to note that since this study concentrates on the *bright early-type* galaxy population, little can be said about the kinematic distribution of the faint early-type nor late-type galaxies due to incompleteness effects. However the Coma cluster core (as in most rich clusters) is dominated by the bright early-type galaxies, so this does not bias any conclusions on the kinematic structure made in this section.

Figure 1.1 shows two 1D morphological velocity wedge plots, probing for any heliocentric redshift ($cz_{\odot}$) structure versus the right ascension and declination coordinates. These slices

[‡]if I assume the cluster radial velocity to be $7200\,\mathrm{km\,s^{-1}}$ and that the Coma cluster peculiar velocity relative to the Hubble flow is zero (see for example Jørgensen et al. 1996). Therefore if I parameterise Hubbles constant at this epoch as $H_0 = 100\ h\ \mathrm{km\,s^{-1}\,Mpc^{-1}}$, where h represents the uncertainty with which we know Hubbles constant, I derive a Coma cluster centre distance of $72\,h^{-1}\,\mathrm{Mpc}$ and a relation of $1.257\,h^{-1}\,\mathrm{Mpc}$ per deg (or $0.349\,h^{-1}\,\mathrm{kpc}$ per arcsecond). If I took $h = 0.5$ then this would imply a Hubbles constant of $50\,\mathrm{km\,s^{-1}\,Mpc^{-1}}$, which leads to a relation of 2.514 Mpc per degree. However herein I prefer to use units of $h^{-1}\,\mathrm{kpc}$ as it removes any dependence upon cosmological model assumptions.

show no structure, either for the total early-type galaxy population or for the sub-populations (the ellipticals or the lenticulars). However these figures are merely a 1D method of considering a more complicated picture and are limited in power which means that either sophisticated analysis needs to be undertaken to probe these distributions or a different approach needs to be taken. The latter is the approach that is taken herein.

The simple redshift histogram shown in Figure 1.2 immediately demonstrates that the Coma cluster core is not virialised and indeed has significant kinematic sub-structure (if this were not the case and if the cluster core was virialised then the redshift distribution would be Gaussian). Studies such as Colless & Dunn (1996) have probed this redshift distribution using multiple Gaussian analysis tools and have found evidence for two sub-populations in the process of merging centred around the cD galaxies NGC 4874 and NGC 4889.

Figure 1.3 is a better test for any kinematic structure, since it maps in 2D (and indeed in 3D) the kinematic parameters (heliocentric redshift, $cz_{\odot}$ and central velocity dispersion, σ) around the central dominant galaxy NGC 4874; a plot of any kinematic parameter dependence on radial distance from this galaxy is also shown. The cD galaxies NGC 4874 (located at $0\,h^{-1}$Mpc in the plots) and NGC 4889 are highlighted by a large black circle surrounding their respective data points. In this figure units of h^{-1} Mpc are used for the X and Y coordinates and the radial distance. In the figures on the left (figures (a) and (c)) the symbol size is scaled to represent either the heliocentric redshift, $cz_{\odot}$ or the central velocity dispersion, σ value for that galaxy, with the scaling key for a figure given at its top. The figures on the right (figures (b) and (d)) show the radial dependence of a parameter with respect to a galaxies distance from the central dominant galaxy NGC 4874. I will now discuss each of these kinematic structure plots in turn.

REDSHIFT STRUCTURE: Figures (a) and (b) show that there is no heliocentric redshift ($cz_{\odot}$) structure in the Coma cluster core if we consider the distribution of the redshifts around the *mean* redshift of the cluster (with redshifts *larger* than the mean shown in red and redshifts *smaller* than the mean shown in blue in the figures). The mean heliocentric redshift of the cluster is $6841\,km\,s^{-1}$ and the dispersion of the redshifts is $982\,km\,s^{-1}$. If we consider the redshift distribution around either the cD galaxy NGC 4874 (at $7180\,km\,s^{-1}$) or the cD galaxy NGC 4889 (at $6495\,km\,s^{-1}$) asymmetric redshift distributions are seen, with either too many redshifts *smaller* than the redshift of NGC 4874 or too many redshifts *larger* than the redshift of NGC 4889. This implies that the cD galaxy NGC 4874 has a peculiar velocity of $+339\,km\,s^{-1}$

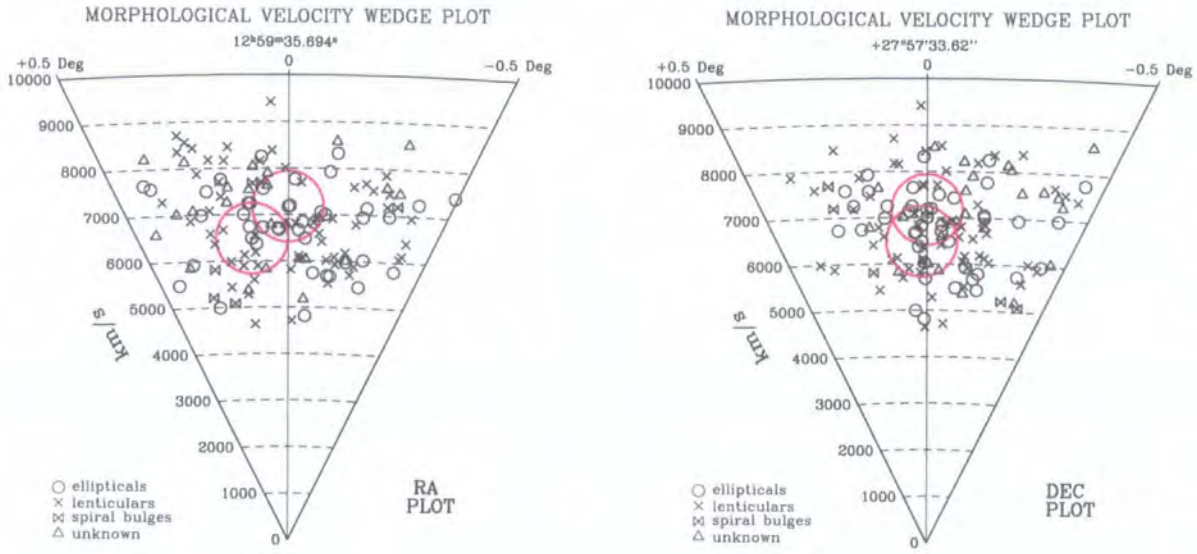

Figure 1.1: 1D morphological velocity wedge plots. The cD galaxy NGC 4874 is located at zero RA and DEC in the plots and is highlighted by a large black circle. The cD galaxy NGC 4889 is also highlighted by a large black circle, but is at a different position in the plots.

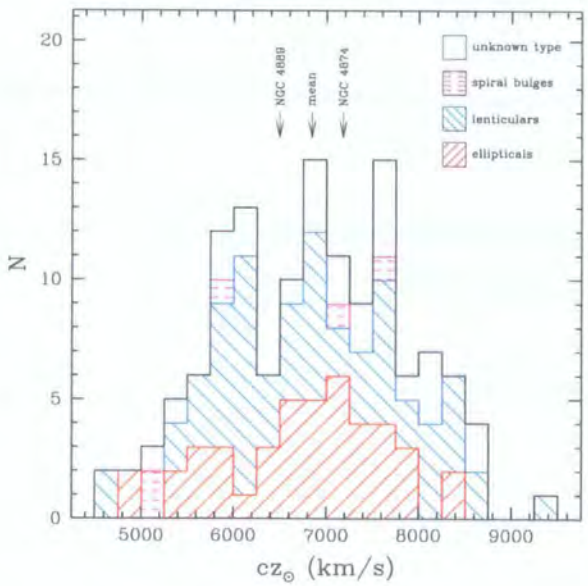

Figure 1.2: Redshift histogram. The different shading indicates the different morphological components that make up the total redshift histogram. Note that this study has concentrated on the *early-type* galaxies and is therefore incomplete in late-type galaxies.

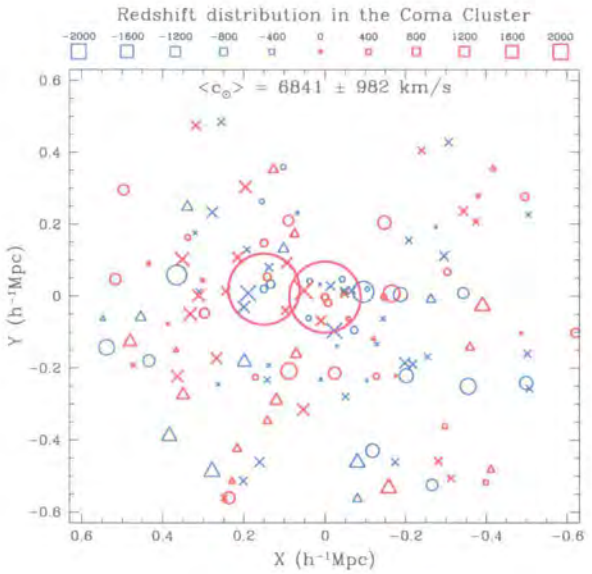

(a) $cz_\odot$ map

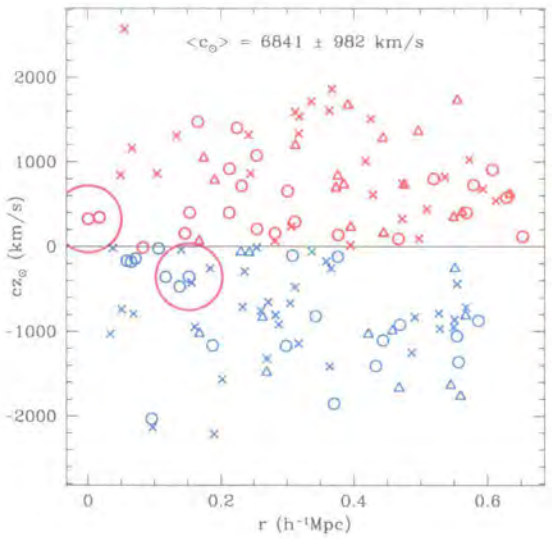

(b) $cz_\odot$ radial dependence

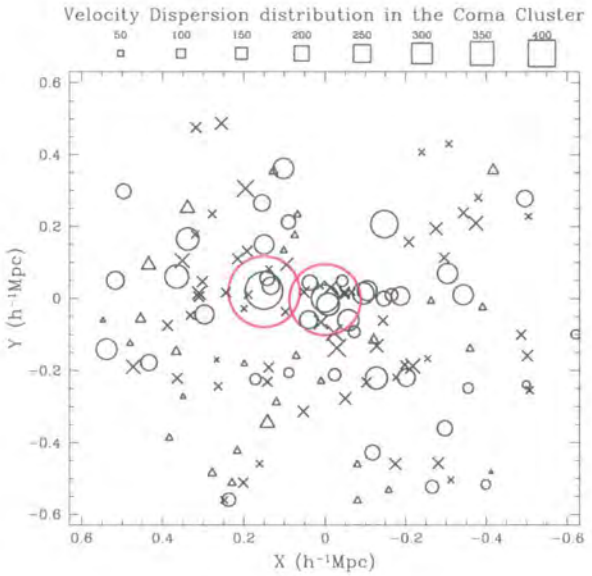

(c) velocity dispersion map

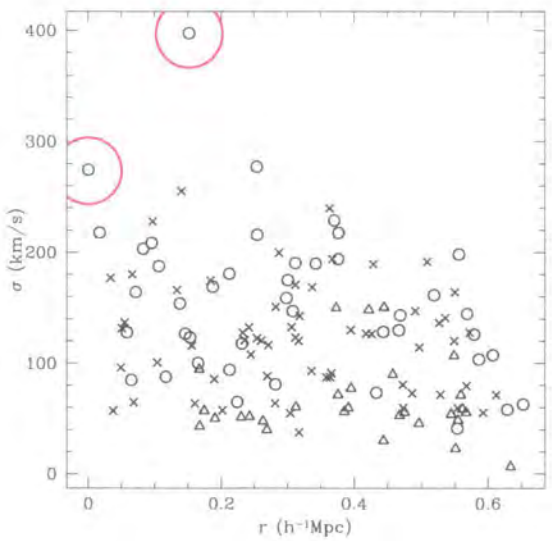

(d) velocity dispersion radial dependence

Figure 1.3: 2D kinematic structure of the Coma cluster. The symbols used in this figure are the same as those used in Figure 1.1. See text for a full description of this figure.

and the cD galaxy NGC 4889 has a peculiar velocity of $-346\,\mathrm{km\,s^{-1}}$, both with respect to the mean cluster redshift. This conclusion means that the Coma cluster core is not yet relaxed, i.e. there is still dynamic structure present. This structure can be interpreted as a "fossil record" of a merger between two groups of galaxies centred around the two cD galaxies we see today, NGC 4874 and NGC 4889.

CENTRAL VELOCITY DISPERSION STRUCTURE: Figures (c) and (d) show that there is no galaxy central velocity dispersion (σ) structure in the Coma cluster core. This means that any dynamical structure present in the redshift distribution "fossil record" represents the last vestiges of the merging history, with the Coma cluster core close to full relaxation (or full mixing).

The picture that emerges from this dynamical analysis is of a cluster core that is almost relaxed and well-mixed, but still contains evidence centred around the cD galaxies NGC 4874 and NGC 4889 of its dynamic merger history. This conclusion agrees well with the findings of e.g. Fitchett & Webster (1987), Biviano et al. (1996), Colless & Dunn (1996), Gambera et al. (1997) and Pagliaro et al. (1999). Using various different techniques including advanced wavelet analysis, maximum likelihood methods and multiple Gaussian distribution analysis they have all shown that rather than following the standard Zwicky (1933) model of a rich cluster core being in equilibrium, there is instead strong kinematical evidence of a multiple hierarchical substructure on scales ranging from a few hundreds of kiloparsecs to about $4\,\mathrm{h^{-1}\,Mpc}$. Thus Coma can no longer be thought of as the archetypal rich, dynamically regular and relaxed galaxy cluster.

1.7.3 X-ray structure of the Coma cluster

The Coma cluster is the nearest very rich cluster of galaxies and as such is probably the best studied cluster at all wavelengths. The observations at different wavelengths allow a complete picture of the cluster structure and variations to be formed.

The distribution of gravitationally heated hot gas in elliptical galaxies and clusters (under the assumption that it is approximately in hydrostatic equilibrium) reflects the distribution of mass, i.e. the shape of the gravitational potential of these systems; the gas temperature is a measure of

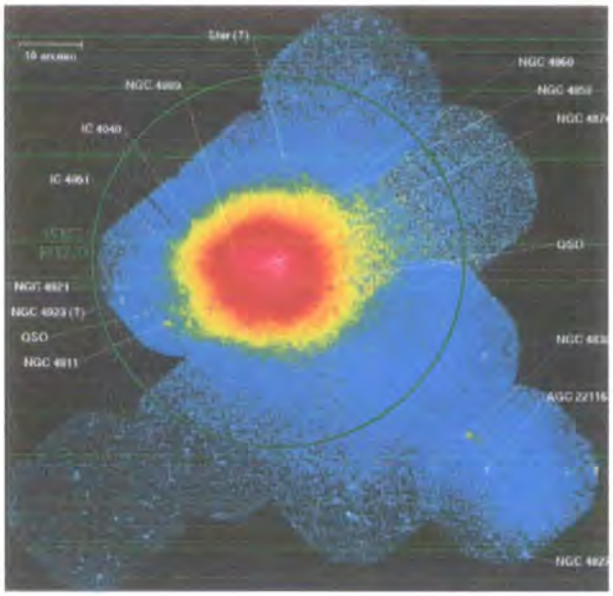

Figure 1.4: XMM–Newton X-ray mosaic of the Coma cluster (source: Briel et al. 2001). This is a merged EPIC-pn image of the Coma cluster of galaxies from 12 pointings in the 0.3 to 2.0 keV energy band. The EPIC camera has a field of view of about 26 arcmin. Indicated are tentative identifications of points sources. The WHT/WYFFOS field observed in the study discussed herein is shown superimposed on the image.

the depth of the potential well in which it is confined (indeed up to 30% of the total mass of galaxy clusters has been identified as X-ray emitting intracluster gas — a significant fraction of the so-called "missing" mass). Typically ellipticals have temperatures $\sim$1 keV (indicating equilibrium temperatures of order 10^7 K), whilst poor clusters have temperatures of 1–2 keV ($1\text{–}2\times10^7$K) and rich clusters have temperatures of 2–10 keV ($2\text{–}10\times10^7$K). X-ray luminosities range from 10^{41} erg/s for individual ellipticals to 10^{45} erg/s for rich clusters, making rich clusters some of the most luminous X-ray sources in the Universe (together with AGNs and QSOs). X-ray studies can also be used to study several key properties of the hot intracluster medium. Spatially resolved spectroscopy allows the determination of the radial variations of the gas density, temperature and metallicity. The knowledge of metallicities is important in the context of the chemical evolution of galaxies and gas in clusters and relates directly to the stellar population work discussed in this study. Also the presence of central cooling flows, with decreasing gas temperatures towards the centres of the clusters, can lead to the accretion of relatively cool gas in the nuclear regions of elliptical galaxies and clusters. Such material can feed the central engine and relates to present-day star formation in these systems.

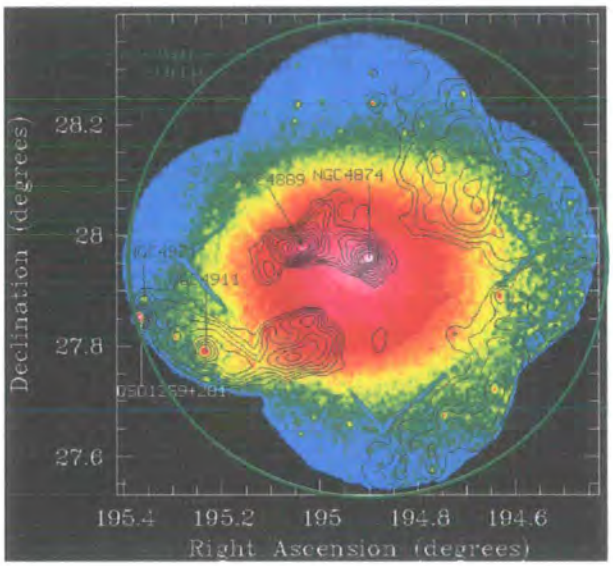

Figure 1.5: XMM–Newton X-ray mosaic of the central region of the Coma cluster (source: Arnaud et al. 2001). This is a merged EPIC-pn image of the Coma cluster of galaxies from 5 pointings in the 0.3 to 2.0 keV energy band. The EPIC camera has a field of view of about 26 arcmin. The iso contours are the residuals (in σ) after subtracting the best fit 2D β model (see Arnaud et al. 2001 for a full description). The step size is 4σ and the lowest isocontour corresponds to 3σ significance. The position of the bright galaxies are marked and the WHT/WYFFOS field observed in the study discussed herein is shown superimposed on the image.

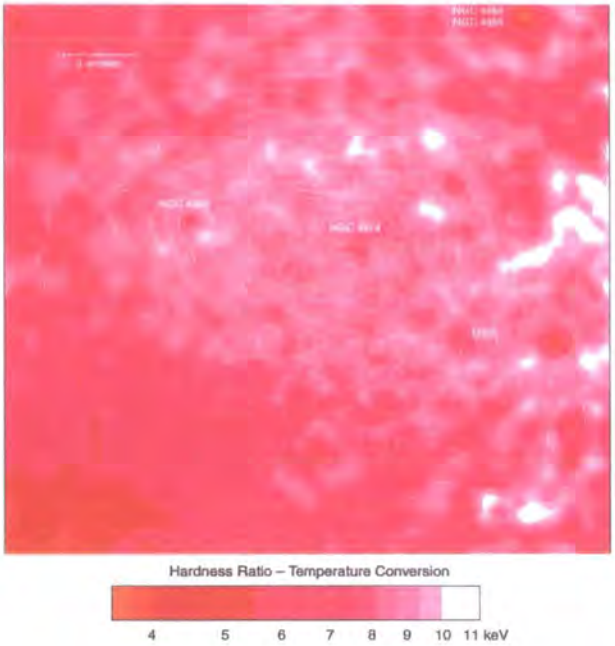

Figure 1.6: XMM–Newton hardness ratio map of the Coma cluster in the energy bands 0.3-2 keV and 2-7.15 keV (source: Briel et al. 2001). The overlaid contours are from the smoothed surface brightness distribution in the energy band from 0.3-2 keV. The image dimensions are $25.5 \times 23.3\,\mathrm{arcmin}^2$.

Recent studies of the Coma cluster with the ASCA satellite (Honda et al. 1996, Briel & Henry 1998, Donnelly et al. 1999, Watanabe et al. 1999) have revealed complex temperature variations, indicative of recent mergers, confirming the earlier evidence based on optical dynamical studies (see Section 1.7.2) and from X-ray morphological analyses with the ROSAT satellite and PSPC instrument (Briel et al. 1992, White et al. 1993, Vikhlinin et al. 1994,1997). These results show that Coma, rather than being the archetypal example of a relaxed cluster of galaxies, has irregular structure on different scales supporting the theory of formation through hierarchical clustering. The ASCA satellite covers a broad energy band (which is essential for precise temperature estimates). However it suffers from a relatively large energy dependent point spread function (which could introduce systematic errors) and a spatial resolution insufficient to resolve precisely the temperature radial profile in the very core of the cluster. The recently launched XMM–Newton X-ray satellite (Jansen et al. 2001) with its EPIC instrument (Turner et al. 2001) now provides a unique capability to study the temperature structure in the central region of Coma. It combines a high sensitivity with good spatial ($\sim$40 arcsecs) and spectral resolution across a wide energy range. The Coma cluster has been observed with XMM–Newton

during its performance verification phase in 12 partially overlapping pointings (camera field of view of 26 arcmin) with $\sim 25\,\mathrm{ksec} \cong 7\,\mathrm{hrs}$ length exposures, making it ~ 8 times deeper than the ROSAT PSPC observations whilst simultaneously extending over a ~ 3 times wider energy range with ~ 4 times better angular resolution (Neumann et al. 2001, Arnaud et al. 2001, Briel et al. 2001). Figure 1.4 shows a merged XMM–Newton EPIC image of the Coma cluster in the 0.3 to 2.0 keV energy band overlaid with tentative point source identications and the position of the field observed in this study (source: Briel et al. 2001). Figure 1.5 is a similar mosaic image of the central region of the Coma cluster (source: Arnaud et al. 2001). To look for spectral variations in the central Coma region a hardness ratio map was constructed by Briel et al. (2001) by comparing images from different energy bands:

$$\text{Hardness ratio} = \frac{\text{image(2-7.15 keV)} - \text{image(0.3-2 keV)}}{\text{image(2-7.15 keV)} + \text{image(0.3-2 keV)}} \tag{1.12}$$

Using simulations, Briel et al. (2001) converted the hardness ratios into "temperatures". Figure 1.6 shows this hardness ratio map with a hardness ratio to temperature conversion key. What these figures tell us is that the Coma cluster is far from being the archetypal relaxed (i.e. virialised) cluster, and instead has significant sub-structure (shown very clearly in the temperature fluctuations of Figure 1.6). A closer examination of the mosaic images in Figures 1.4 and 1.5 reveals the central contours to be *elliptical* and not spherical as would be expected from a relaxed core; this implies again that there is still traces in the X-ray "fossil" map of a merger most likely between two large groups centred around the cD galaxies NGC 4889 and NGC 4874, but that this merger is almost complete (since the contours are not grossly distorted). These findings agree with those discussion in Sections 1.7.2 and 5.11, showing that all the separate results from the different studies discussed together form a cohesive picture of the Coma cluster. Future work of the XMM–Newton team will probe the abundance distribution of the Coma cluster core which should prove to be very interested when compared to this work.

1.8 Dissertation outline

In this dissertation I present for the first time a high quality, high signal-to-noise and homogeneous sample of early-type galaxies within the central 1 degree ($\equiv 1.26\,h^{-1}\,\mathrm{Mpc}$) of the Coma cluster. I analyse this data using the Lick/IDS system and Worthey (1994) models to probe the age and metallicity distributions of the early-type galaxy populations. In this way I can differentiate between the two galaxy formation scenarios in clusters: hierarchical merging or monolithic dissipative collapse. This is done by probing the "noise" of galaxy formation manifested in the age structure of a cluster: a small intrinsic scatter around a single age of stellar population formation would imply that they all formed at the same time, supporting a monolithic dissipative collapse model, whereas a large distribution in ages would support a hierarchical merging model. I extend my data sample by including published photometry and investigate the spectro-photometric relations of the cluster and test the universality of these relations and their usefulness as distance indicators. I test the relations for other contributing factors. I draw conclusions on the applicability of these relations to other clusters.

This dissertation is organised into the following chapters: observations; data reduction; comparison with other data; stellar population analysis; spectro-photometric relations; and finally the conclusions.

Chapter 2

Observations

2.1 Introduction

This dissertation represents a great step forward in the field of early-type galaxy stellar population studies. From the outset the programme plan was to obtain a large, homogeneous, high quality spectroscopic data set that would not suffer the limitations and problems of previous stellar population studies. The primary emphasis was on quality and a true understanding of the errors. With this in mind it was felt that a large number of repeat observations, each with high signal-to-noise, were desirable to fully characterise and tie down the errors. This is the first time such a detailed and in-depth study has been carried out. I will describe in this chapter the sample selection, the instrument selection, the observational strategy and finally give an overview of the observations themselves and their success against the original goals.

2.2 Sample selection

The first step in the sample selection is to choose the cluster to observe. The nearby, rich galaxy cluster Coma (Abell 1656) has been extensively studied over the years and a great deal of data is available for cross-comparison with any data gathered herein and to extend this work above and beyond the programme observations. The Coma cluster has a cluster radial velocity of $7200\,\mathrm{km\,s^{-1}}$, with zero peculiar velocity relative to the Hubble flow (see e.g. Jørgensen et al. 1996). This puts the cluster at a distance of $72\,h^{-1}\,\mathrm{Mpc}$ and a relation of $1.26\,h^{-1}\,\mathrm{Mpc}$ per deg (h represents the uncertainty with which we know Hubbles constant, $h = 0.5$ implies a Hubbles constant of $50\,\mathrm{km\,s^{-1}\,Mpc^{-1}}$). Therefore if we observe a 1 degree field (radius of 30 arcmin) around the centre of the Coma cluster it will correspond to observing out to a radius of $2.51\,h^{-1}\,\mathrm{Mpc}$ around the cluster. This is sufficient to provide a large sample of early-type galaxies within the central portion of the cluster and is well-matched to available instrumentation.

Morphological typing for the galaxies in the Coma cluster was taken from Dressler (1980). These types are supplemented by "E+A" typing from Caldwell et al. (1993). They identified

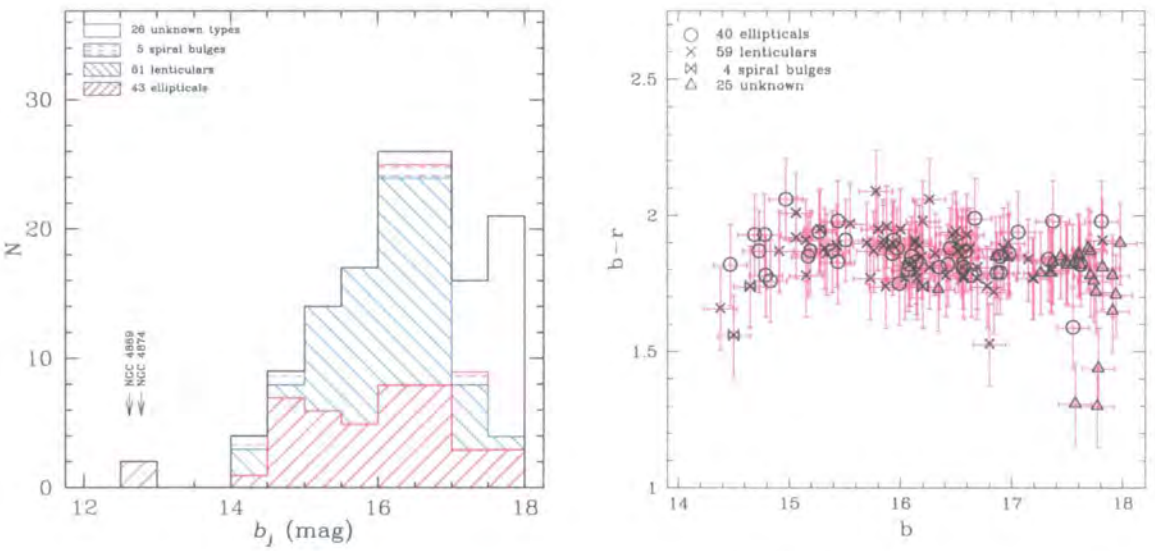

(a) luminosity function

(b) colour–magnitude diagram

Figure 2.1: Coma cluster photometry for the 135 galaxies observed. Figure (a) shows the luminosity function of the observed galaxies. The different shading indicates the different morphological components that make up the total observed luminosity function. Note that this study has concentrated on the *early-type* galaxies and is therefore incomplete in late-type galaxies. Figure (b) shows the colour–magnitude diagram for the observed galaxies. Magnitudes (b_j) and colours ($b - r \simeq \mathrm{B} - \mathrm{R}$) are taken from Godwin, Metcalfe & Peach (1983), whilst morphological types are taken from Dressler (1980).

"abnormal" spectra indicative of recent star formation or nuclear activity (with CN/H8<–0.5). The "abnormal" spectra of Caldwell et al. (1993) are analogous to the "E+A" galaxies of Dressler (1987), Gunn & Dressler (1988) and MacLaren et al. (1988) which were defined as post-starburst galaxies with significant star formation at approximately 1 Gyr ago for galaxies at $z \simeq 0.3 - 0.5$. Caldwell et al. (1993) found that 11 out of 28 galaxies (39%) of galaxies observed in the south western corner of the Coma cluster were "abnormal", whilst only 3 out of 68 galaxies (4%) in the central region were "abnormal".

The next step is to select the early-type galaxies to observe within this 1 degree field. The popular Godwin, Metcalfe & Peach (1983) sample contains 450 galaxies with $b_j < 17.5$ in the central Coma area (their total sample for a $2.63° \times 2.63°$ square area centred on the Coma cluster contains 6724 galaxies with $b_{26.5} < 21.0$); magnitudes (b_j) and colours ($b - r \simeq$ B – R) for the galaxies were taken from this study (see Figure 2.1). In addition to this large, complete data set we also used 800 redshifts in the Coma cluster region kindly provided by Colless (private communication). With these redshifts we can have unambiguous cluster membership assignment.

Using this combined data set we created a desired observational data set of bright early-type galaxies within the central 1 degree of the Coma cluster. The selection criteria employed and the subsequent observational priorities passed to the multi-fibre instrument configuration program are summarised in Table 2.1 (the configuration program uses the assignment priorities to maximise the return on any observations). These selection criteria are designed to obtain the maximum amount of data for early-type galaxies in the Coma cluster, with the emphasis on bright galaxies and on those with previous observations so that the systematics can be explored.

2.3 Astrometry

To determine precise astrometry prior to spectroscopic observations three Schmidt plates were used:

- one 10 min exposure plate (OR17491) taken on 3/4/1997;
- one 30 min exposure plate (OR18041) taken on 18/6/1998; and
- one 85 min exposure plate (OR9945) taken on 25/2/1985.

The shorter exposure plates were specifically requested to measure accurate astrometry for

Priority	Selection Criteria
9	– galaxy has measured redshift (confirmed cluster member)
	– early-type galaxy morphological type
	– galaxy has previously measured velocity dispersion
8	– galaxy has measured redshift (confirmed cluster member)
	– early-type galaxy morphological type
7	– galaxy has measured redshift (confirmed cluster member)
6	– early-type galaxy morphological type
5-2	– galaxies with only magnitude information, split by 0.5 mag bins

Table 2.1: Observation selection criteria and priorities given to multi-fibre configuration program (9 is the highest priority, 1 is the lowest). These selection criteria are applied to a data set of the central 1 degree of the Coma cluster constructed from the Godwin, Metcalfe & Peach (1983) catalogue, the Dressler (1980) study and the recent work of Colless (private communication).

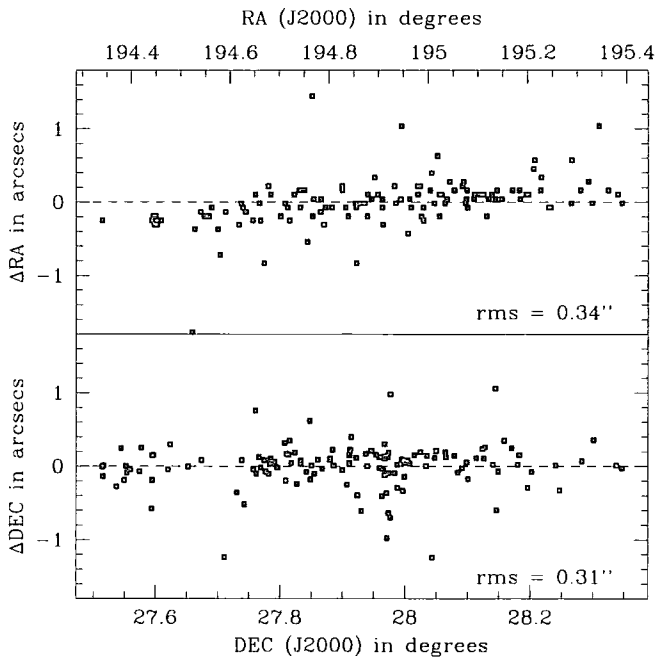

Figure 2.2: Accuracy of Coma cluster astrometry. The astrometry from this study was compared with the astrometry from the ongoing study of Colless (kindly provided by private communication). The astrometry is typically accurate to 0.3″ — sufficient for multi-fibre spectroscopy to be undertaken.

the bright Coma galaxies. The plates were taken at the UK Schmidt Telescope using 3mm glass with emulsion IIIaF and filter OG590. These Schmidt plates were scanned in using the SuperCOSMOS scanner at the Royal Observatory Edinburgh, which digitises plates at a 10μm resolution with 15-bit transmission values. The data was then analysed and positions of all the programme objects determined by matching field star positions to the USNOA2* catalogoue and creating an astrometry solution for the plate. Comparison with published Coma cluster astrometry confirms that the astrometry is accurate to 0.3″ — sufficient for multi-fibre spectroscopy to be undertaken (see Figure 2.2). The astrometry, together with the various names associated with the galaxies, is shown in Table 2.2.

*http://www.nofs.navy.mil/data/FchPix/cfra.html

n1	n2	n3	n4	n5	type		b_j	$b-r$	RA (J2000)			DEC (J2000)		
d112		gmp4945		b40	E	E+A	16.64	1.78	12	57	21.731	+27	52	49.75
d75		gmp4679		b91	S0		16.13	1.91	12	57	46.139	+27	45	25.51
d201		gmp4666			S0		17.35	1.80	12	57	46.697	+28	8	26.77
d93		gmp4664		b39	S0		16.26	2.06	12	57	47.296	+27	50	0.03
d74		gmp4656		b84	E		17.62	1.82	12	57	47.863	+27	46	10.03
d210		gmp4648			E		15.97	1.88	12	57	48.658	+28	10	49.48
d110		gmp4626			S0/E		16.60	1.93	12	57	50.627	+27	52	46.34
d220	ngc4848	gmp4471			Scd		14.50	1.56	12	58	5.598	+28	14	33.31
		gmp4469		b79			17.69	1.88	12	58	6.820	+27	34	37.09
d29		gmp4447		b78	E		17.81	1.98	12	58	9.688	+27	32	57.86
		gmp4420		b75			17.60	1.86	12	58	11.426	+27	56	23.85
d209		gmp4391			S0		16.04	1.77	12	58	13.792	+28	10	57.20
d200		gmp4379		a35	S0		16.08	1.82	12	58	15.032	+28	7	33.25
		gmp4348					17.77	1.30	12	58	18.203	+27	50	54.46
d73		gmp4341	rb183	b24	E	E+A	17.33	1.84	12	58	19.186	+27	45	43.65
d199	ngc4851	gmp4313			S0		16.00	1.95	12	58	21.722	+28	8	56.18
d137	ngc4850	gmp4315		a8	E/S0		15.39	1.87	12	58	21.828	+27	58	4.05
d44		gmp4255		b64	S0	E+A	16.57	1.77	12	58	28.386	+27	33	33.31

Table 2.2: *continued on next page*

continued from previous page

n1	n2	n3	n4	n5	type		b_j	$b-r$	RA (J2000)			DEC (J2000)		
d225		gmp4235			S0		16.80	1.53	12	58	29.503	+28	18	4.60
d161		gmp4230	rb241		E		15.19	1.87	12	58	30.202	+28	0	53.20
d59		gmp4209	rb188		E		16.90	1.85	12	58	31.596	+27	40	24.73
d182		gmp4200	rb243	a15	S0		16.84	1.72	12	58	31.908	+28	2	58.66
d43	ngc4853	gmp4156		b42	S0p	E+A	14.38	1.66	12	58	35.193	+27	35	47.00
d197	ic3943	gmp4130			S0/a		15.55	1.97	12	58	36.343	+28	6	49.46
d28		gmp4117		b83	E/S0		16.67	1.99	12	58	38.405	+27	32	39.09
		gmp4103	rb245				17.74	1.76	12	58	38.931	+27	57	14.11
		gmp4083	rb198	a9/b3	SA0		17.82	1.91	12	58	40.780	+27	49	37.41
		gmp4060	rb199				17.57	1.31	12	58	42.641	+27	45	38.71
d224		gmp4043			S0		17.19	1.77	12	58	43.903	+28	16	57.62
d91	ic3946	gmp3997		a57/b77	S0		15.28	1.95	12	58	48.723	+27	48	37.72
d181		gmp3972	rb252	a2	S0		16.52	1.87	12	58	50.767	+28	5	2.47
d72	ic3947	gmp3958		a74/b61	E		15.94	1.91	12	58	52.102	+27	47	6.45
d90		gmp3943	rb209	a69	S0		16.93	1.88	12	58	53.020	+27	48	48.51
d136		gmp3914	rb257		E		16.57	1.81	12	58	55.254	+27	57	53.02
d71		gmp3882	rb214	a96/b44	S0		16.97	1.85	12	58	57.638	+27	47	7.81
d42		gmp3879		b55	S0		16.31	1.86	12	58	58.103	+27	35	41.06
d135		gmp3851	rb260		E		16.98	1.86	12	59	0.068	+27	58	3.19

Table 2.2: *continued on next page*

continued from previous page

n1	n2	n3	n4	n5	type	b_j	$b-r$	RA (J2000)			DEC (J2000)		
		gmp3829				17.44	1.85	12	59	1.590	+27	32	12.87
d194	ngc4860	gmp3792			E	14.69	1.93	12	59	3.902	+28	7	25.29
d134		gmp3794	rb261		E	17.37	1.98	12	59	4.143	+27	57	33.07
d108		gmp3782	rb262	a76	S0	16.55	1.85	12	59	4.639	+27	54	39.69
d109	ic3960	gmp3733			S0	15.85	1.89	12	59	7.948	+27	51	17.95
d69	ic3959	gmp3730		a19/b86	E	15.27	1.94	12	59	8.211	+27	47	3.10
		gmp3706	rb223			17.61	1.85	12	59	9.626	+27	52	2.71
d53		gmp3697	rb224	a50/b93	E	16.59	1.87	12	59	10.302	+27	37	11.70
d159	ngc4864	gmp3664		a58	E	14.70		12	59	13.176	+27	58	36.55
d68	ic3963	gmp3660			S0	15.76	1.87	12	59	13.493	+27	46	28.73
d133	ngc4867	gmp3639		a82	E	15.44	1.83	12	59	15.227	+27	58	14.88
		gmp3588		b43		17.76	1.72	12	59	18.453	+27	30	48.74
		gmp3585				17.29		12	59	18.541	+27	35	36.67
d107		gmp3557	rb6		E	16.35	1.81	12	59	20.162	+27	53	9.56
d158		gmp3534	rb7		S0	17.20	1.77	12	59	21.393	+27	58	24.96
d105	ngc4869	gmp3510			E	14.97	2.06	12	59	23.356	+27	54	41.89
d67		gmp3493	rb230		S0	16.50	1.94	12	59	24.924	+27	44	19.93
d132		gmp3487	rb13		S0	16.63	1.88	12	59	25.320	+27	58	4.73
d157		gmp3484	rb14		S0	16.26	1.81	12	59	25.479	+27	58	23.72

Table 2.2: *continued on next page*

continued from previous page

n1	n2	n3	n4	n5	type	b_j	$b-r$	RA (J2000)			DEC (J2000)		
d156		gmp3471	rb18	a56	E/S0	16.45		12	59	26.585	+27	59	54.69
d88	ic3976	gmp3423		a21	S0	15.80	1.95	12	59	29.393	+27	51	0.56
d87		gmp3403	rb234		E	16.87	1.79	12	59	30.632	+27	47	29.31
d103	ic3973	gmp3400		a68	S0/a	15.32	1.88	12	59	30.823	+27	53	3.27
d155	ngc4873	gmp3367		a20	S0	15.15	1.91	12	59	32.781	+27	59	1.16
d130	ngc4872	gmp3352		a47	E/S0	14.79	1.78	12	59	34.110	+27	56	48.85
d129	ngc4874	gmp3329			cD	12.78		12	59	35.694	+27	57	33.62
		gmp3298				17.26	1.79	12	59	37.838	+27	46	36.68
d104	ngc4875	gmp3296		a54	S0	15.88	1.96	12	59	37.904	+27	54	26.40
d154		gmp3291	rb38	a7	S0	16.41	1.78	12	59	38.304	+27	59	14.08
d153		gmp3213	rb45		E	16.14	1.83	12	59	43.730	+27	59	40.84
d124	ngc4876	gmp3201		a66	E	15.51	1.91	12	59	44.393	+27	54	44.97
d152	ic3998	gmp3170		a59	SB0	15.70	1.90	12	59	46.770	+27	58	26.13
d57		gmp3165		a4	S0/a	15.15	1.78	12	59	47.138	+27	42	37.32
		gmp3129	rb153			17.94	1.71	12	59	50.271	+28	8	40.61
		gmp3126	rb60			17.55	1.82	12	59	51.000	+27	49	58.78
		gmp3113	rb58			17.82	1.81	12	59	51.750	+28	5	54.80
d85		gmp3092			E	17.55	1.59	12	59	54.870	+27	47	45.63
d193		gmp3084	rb155	a16	E	16.43	1.82	12	59	55.095	+28	7	42.21

Table 2.2: *continued on next page*

continued from previous page

n1	n2	n3	n4	n5	type		b_j	$b-r$	RA (J2000)			DEC (J2000)		
d175	ngc4883	gmp3073		a97	S0		15.43	1.89	12	59	56.012	+28	2	5.09
d123		gmp3068	rb64		SB0		16.47	1.93	12	59	56.685	+27	55	48.45
		gmp3058	rb66				17.71	1.78	12	59	57.600	+28	3	54.47
d217	ngc4881	gmp3055			E		14.73	1.87	12	59	57.738	+28	14	48.02
		gmp3017	rb71				17.91	1.65	13	0	0.936	+27	56	43.95
		gmp3012					17.49	1.83	13	0	1.530	+27	43	50.39
d216		gmp2989	rb160	a65	Sa	E+A	17.05		13	0	2.998	+28	14	25.16
d151	ngc4886	gmp2975		a95	E		14.83	1.76	13	0	4.448	+27	59	15.45
		gmp2960	rb74		SA0		16.78	1.74	13	0	5.396	+28	1	28.24
d84		gmp2956		a51	S0		16.20	1.98	13	0	5.503	+27	48	27.87
		gmp0552					16.34	1.73	13	0	6.263	+27	41	7.01
d65		gmp2945		a11	S0		16.15	1.77	13	0	6.285	+27	46	32.93
d150	ic4011	gmp2940		a86	E		16.08	1.82	13	0	6.383	+28	0	14.94
d174	ic4012	gmp2922			E		15.93	1.86	13	0	7.997	+28	4	42.89
d148	ngc4889	gmp2921			cD		12.62	1.91	13	0	8.125	+27	58	37.22
d207		gmp2912	rb167	a45	E		16.07	1.80	13	0	9.109	+28	10	13.49
d40		gmp2894			S0		17.15	1.84	13	0	10.413	+27	35	42.20
d64		gmp2866		a94	E		16.90	1.79	13	0	12.629	+27	46	54.75
d122	ngc4894	gmp2815		a12	S0		15.87	1.74	13	0	16.510	+27	58	3.16

Table 2.2: *continued on next page*

continued from previous page

n1	n2	n3	n4	n5	type	b_j	$b-r$	RA (J2000)			DEC (J2000)		
d171		gmp2805	rb91	a17	S0	16.57	1.78	13	0	17.024	+28	3	50.24
d206	ngc4895	gmp2795		a24	S0	14.38		13	0	17.915	+28	12	8.57
		gmp2783				17.37	1.83	13	0	18.569	+27	48	56.09
		gmp2778	rb94		SB0/a	16.69	1.81	13	0	18.767	+27	56	13.52
d39		gmp2776			S0/E	16.17	1.89	13	0	19.101	+27	33	13.37
d170	ic4026	gmp2727		a23	SB0	15.73	1.77	13	0	22.123	+28	2	49.26
		gmp2721				17.50	1.82	13	0	22.376	+27	37	24.85
		gmp2688				17.71	1.87	13	0	25.165	+27	33	8.25
d27		gmp2670			E	16.45	1.88	13	0	26.833	+27	30	56.26
d147		gmp2651	rb100	a93	S0	16.19	1.85	13	0	28.376	+27	58	20.77
d26		gmp2640			S0p	16.18		13	0	29.210	+27	30	53.72
d232	ngc4896	gmp2629			S0	15.06	2.01	13	0	30.762	+28	20	47.12
d63		gmp2615			S0/a	16.97	1.90	13	0	32.508	+27	45	58.27
d83		gmp2603			S0	17.36	1.80	13	0	33.357	+27	49	27.44
d192		gmp2584		a61	S0	16.14	1.79	13	0	35.572	+28	8	46.15
d38		gmp2582			Sbc	16.20	1.74	13	0	35.709	+27	34	27.27
d118	ngc4906	gmp2541		a62	E	15.44	1.98	13	0	39.753	+27	55	26.45
d145	ic4041	gmp2535		a42	S0	15.93	1.90	13	0	40.830	+27	59	47.81
d144	ic4042	gmp2516			S0/a	15.34	1.86	13	0	42.761	+27	58	16.87

Table 2.2: *continued on next page*

continued from previous page

n1	n2	n3	n4	n5	type	b_j	$b-r$	RA (J2000)			DEC (J2000)		
d116		gmp2510	rb113	a64	SB0	16.13	1.90	13	0	42.825	+27	57	47.44
d231		gmp2495			S0	15.78	2.09	13	0	44.226	+28	20	14.26
d191		gmp2489	rb116		S0	16.69	1.77	13	0	44.629	+28	6	2.38
d117		gmp2457	rb119	a83	S0/a	16.56	1.88	13	0	47.383	+27	55	19.76
d168	ic4045	gmp2440		a6	E	15.17	1.85	13	0	48.631	+28	5	26.92
d205	ngc4907	gmp2441			Sb	14.65	1.74	13	0	48.804	+28	9	30.30
		gmp2421		a81		17.98	1.90	13	0	51.124	+27	44	34.43
d167	ngc4908	gmp2417			S0/E	14.91	1.87	13	0	51.525	+28	2	35.10
d62		gmp2393		a25	S0	16.51	1.90	13	0	54.217	+27	47	2.60
d143	ic4051	gmp2390			E	14.47	1.82	13	0	54.457	+28	0	27.59
		gmp2385	rb122			17.62	1.82	13	0	54.769	+27	50	31.47
d50		gmp2355			SBa	16.56	1.81	13	0	58.371	+27	39	7.64
d98		gmp2347	rb124	a78	S0/a	15.85	1.91	13	0	59.262	+27	53	59.59
d81		gmp2252			E	16.10	1.85	13	1	9.215	+27	49	6.00
		gmp2251	rb128			17.35	1.79	13	1	9.435	+28	1	59.25
		gmp2201	rb129	a43	unE	16.86	1.85	13	1	13.616	+27	54	51.64
d79	ngc4919	gmp2157		a88	S0	15.06	1.92	13	1	17.595	+27	48	32.95
		gmp2141	rb131			17.78	1.44	13	1	19.317	+27	51	37.94
d204		gmp2091			E	15.99	1.75	13	1	22.767	+28	11	45.86

Table 2.2: *continued on next page*

continued from previous page

n1	n2	n3	n4	n5	type	b_j	$b-r$	RA (J2000)			DEC (J2000)		
d142		gmp2048	rb133	a49	E	17.06	1.94	13	1	27.147	+27	59	57.20
d78	ngc4923	gmp2000		a36	E	14.78	1.93	13	1	31.794	+27	50	51.37
		gmp1986				17.91	1.78	13	1	33.817	+27	54	40.39

"n1" names from Dressler (1980) "n2" names from New General Catalogue or Index Catalogue

"n3" names from Godwin, Metcalfe & Peach (1983) "n4" names from Rood & Baum (1967)

"n5" names from Caldwell et al. (1993). a = Table 1(a), b = Table 1(b). 64 out of 125 galaxies in common

"type" morphological types from Dressler (1980). "E+A" typing from Caldwell et al. (1993)

"b_j" magnitudes from Godwin, Metcalfe & Peach (1983), accurate to ± 0.15

"$b-r$" colours from Godwin, Metcalfe & Peach (1983), accurate to ± 0.15. Note that $b-r \simeq \mathrm{B}-\mathrm{R}$

Table 2.2: Coma cluster astrometry for the 135 galaxies observed. RA and DEC are given in J2000 coordinates. Columns 1–5 give the different names associated with the galaxy. The astrometry is accurate to 0.2″. This accuracy is good enough to undertake multi-fibre spectroscopy.

2.4 Instrument selection

The William Herschel 4.2 metre telescope (WHT) on the island of La Palma in the Canary Islands is well suited to our observational programme. Its wide-field multi-object spectroscopy instrument WYFFOS (Bingham et al. 1994, Worswick et al. 1995, King & Worswick 1998 and Figure 2.3) situated on an optical table on one of the Nasmyth platforms can observe a 1 degree field over a wide wavelength range (3900 $\rightarrow$ 5600 Å) at high resolution (2Å FHWM) using the H1800V grating at two angles and with around 120 2.7 arcsec fibres. Also its latitude facilitates observations of the Coma cluster around the meridian. The multi-fibre positioner AUTOFIB2 (Worswick et al. 1994, Figure 2.4) can configure a field in less than 30 mins using a robotic fibre positioner (Figure 2.5).

2.5 Observing strategy

We were allocated 6 half-nights on the WHT between 13-18 April, 1999. Our observing strategy for this allocation was to obtain a large number of high quality repeat observations, each with high signal-to-noise, to fully characterise and tie down the errors. To do this, three different multi-fibre field configurations were observed at the centre of the Coma cluster with two different wavelength ranges. In this way the sample completeness for the central 1 degree region can be increased. To achieve maximal scientific benefit from the observations, the second field is configured in a similar way to the first except that the objects that had been observed in the first field are included in the desired observation list at a priority two levels lower (see Table 2.1 for a definition of the priorities used). In a similar way the third field is configured with the galaxies observed in the first and second fields included at a priority two levels lower.

Exposure times of typically 6×1650 secs per configuration and wavelength range combination were sufficient for high signal-to-noise linestrength measurements on our programme objects. Each exposure is also long enough to enable high signal-to-noise line strength measurements on the brighter objects. Therefore a large number of repeats both during a night and night-to-night can be gathered to enable proper treatment of the random and systematic errors.

To measure the redshifts, velocity dispersions and to flux calibrate the observed spectra a number of standard stars were observed throughout the course of the run. Also a large body of data was taken to characterise fully the variations across the field and down the slit; this body of data includes standard stars observed down different fibres (and hence different positions in the

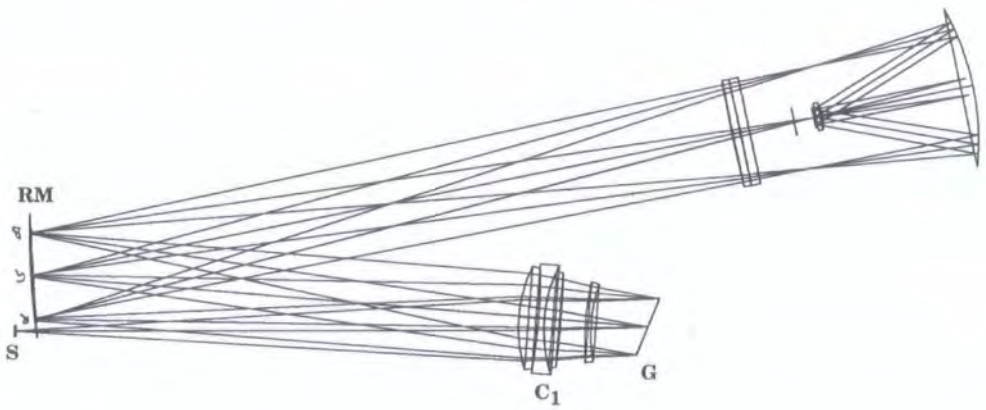

Figure 2.3: The optical path of WYFFOS. S = curved slit of radius 1190 mm, C_1 = dioptric collimator, G = reflection grating. The fibres are arranged and set onto the *curved* slit of radius 1190 mm, directed towards the centre of the first collimator in order to minimise vignetting at the collimator. Light from the fibres emerges at f/2.5 (instead of f/2.8 due to focal-ratio degradation, FRD) and is then slowed to f/8.2 using microlenses which form a real exit pupil at the position to control the FRD. The beam emerging from each fibre is matched to the f/8.2 collimator. The collimated beam then passes onto the grating, back through the collimator at a small angle (7.1 degrees), relative to the incoming beam, towards the relay mirror. An image is formed close to this mirror which then becomes the object for the re-imaging camera. Note that the IDS grating H1800V used is *smaller* than the beam in WYFFOS so it vignettes the fibres at the top and bottom ends of the slit. The Schmidt camera is fed from the relay mirror which images the collimator pupil onto the camera pupil. The camera re-images the spectral image that is formed close to the relay mirror. The TEK6 detector sits in the curved focal plane of the camera on a cold finger protruding from its cryostat.

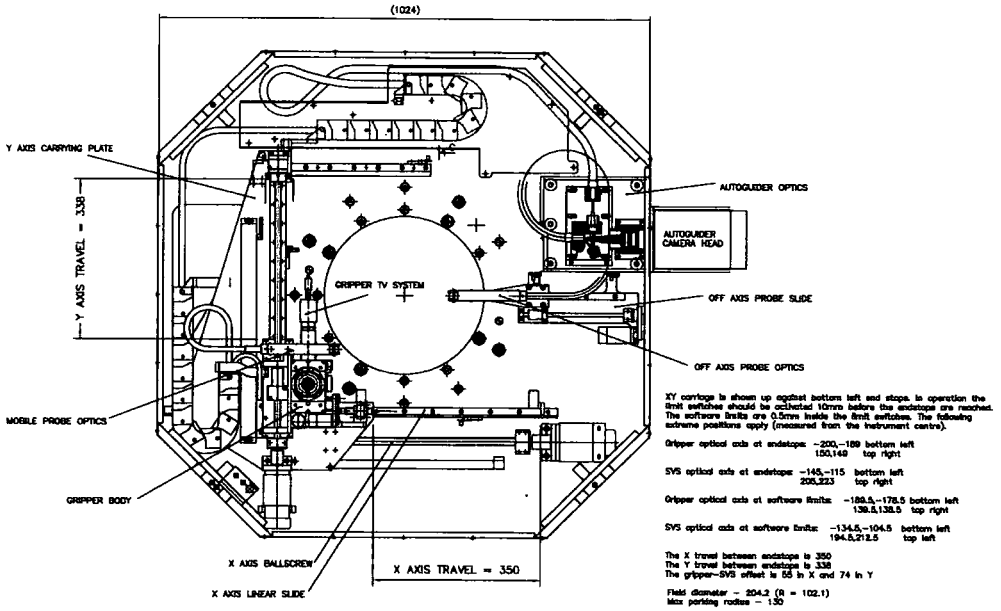

Figure 2.4: AF2 plan. The mobile and fixed (i.e. off-axis) probes look at the sky, and the gripper TV views the back-illuminated fibres.

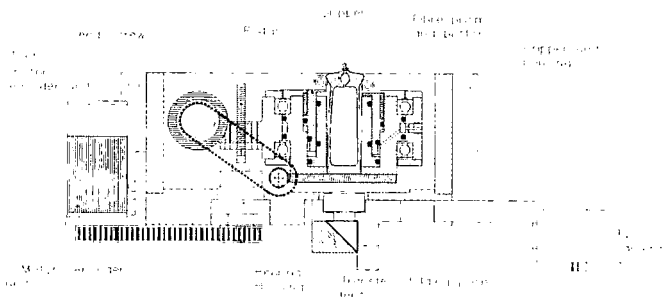

Figure 2.5: AF2 gripper. Gripper cross-section.

field *and* on the slit) and arc lamp data mapping in high resolution the entire field (see Section 3.5 for more details).

2.6 Summary of Coma cluster observations

A summary of the principal observing parameters is given in Table 2.3. The entire observing run went very well and according to plan. The conditions, though not photometric, were good enough to obtain high-quality, high signal-to-noise data on our programme objects.

The completeness of this project is shown in the table at the bottom of Figure 2.6. This is calculated by comparing the numbers of galaxies observed for each priority class (as defined in Table 2.1) to the number of possible galaxies given by our constructed catalogue of the central 1 degree of the Coma cluster based on the Godwin, Metcalfe & Peach (1983) catalogue, the Dressler (1980) study and the recent work of Colless (private communication). The completeness against our highest priority programme objects is 78%. A completeness of 100% is difficult to achieve in the Coma cluster because of the close proximity of the galaxies and the associated difficulties of placing fibres too close to each other to measure the spectra of these galaxies. To achieve a higher completenss it would have been necessary to observe another two fields with different fibre configurations. This would have not improved greatly the scientific content of the data set and would not of been possible given the observing time allocated to the project without deterimentally sacrificing exposure time (and hence signal-to-noise).

In summary, the observations were a complete success. Spectroscopic data of a high-quality, high signal-to-noise and homogeneous nature was collected for 76% of the known Coma cluster early-type galaxies brighter than $b_j < 17.5$. This data set represents the best data available for this cluster and for this area of work and is a great step forward in the field of stellar population analysis.

Telescope	WHT 4.2m at ING, La Palma
Instrument	WYFFOS + AUTOFIB-2
Field diameter	1 degree $\equiv 1.26\,h^{-1}$ Mpc at Coma
Unvignetted field	40 arcmin
Focal ratio	f/2.81
Collimator	f/8.2; $f = 820$ mm
Short camera	f/1.2; $f = 132$ mm
Number of fibres	126
Fibre diameter	$126 \times 153\mu$m ($2.7'' \equiv 0.94\,h^{-1}$ kpc at Coma)
Positioning accuracy	better than $10\,\mu$m (i.e. $0.18''$ rms)
Science fibres length	26.5 m
Camera	thinned Tektronix (TEK6) CCD
Camera size	1024 x 1024 pixels
Pixel size	$24\,\mu m$ square $\equiv$ 0.93Å
Grating used	H1800V
Resolution	~3.2Å FWHM
Gain	1.7e$^-$ per ADU
Readout noise	5.6e$^-$
Wavelength ranges†	4600–5600Å and 3900-4900Å
Number of nights observed	6 half nights
Typical field exposure time	6×1650 secs
Date of observations	13–18 April, 1999
Moon phase	dark grey (0–14% illumination)
Observers	Stephen Moore, John Lucey
Field centre (J2000)	$12^h59^m32.9^s$, $+27°55'49''$

† *the wavelength ranges vary due to the stepping of the fibres on the CCD*

Table 2.3: The principal parameters of the observations.

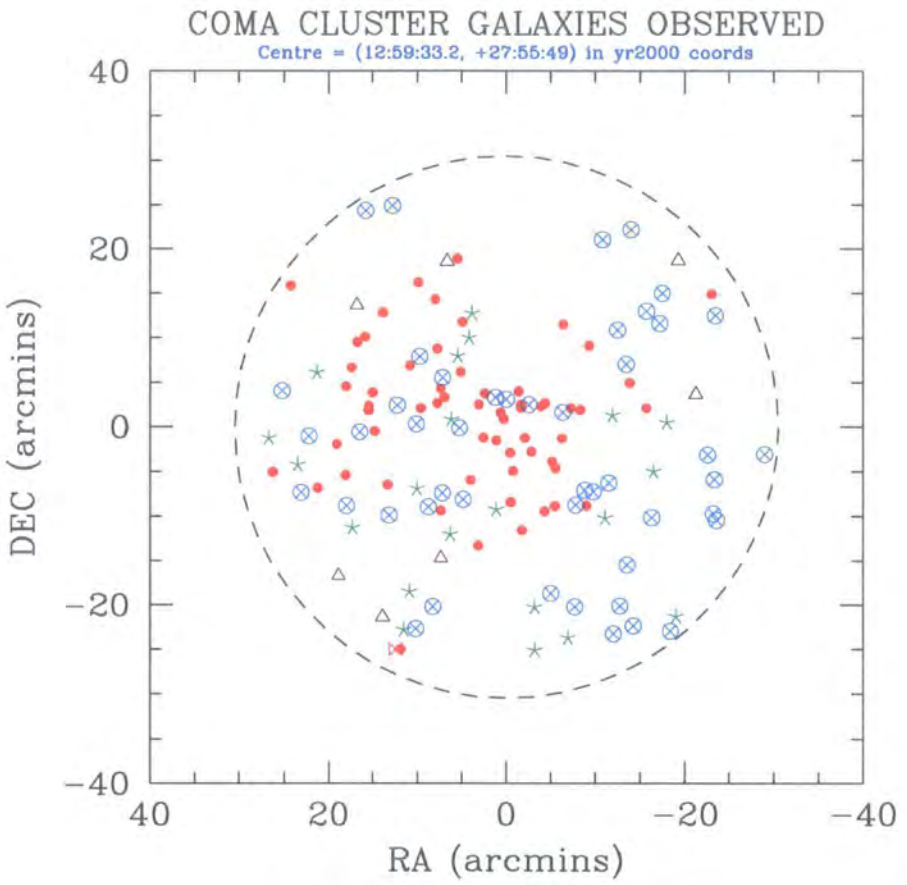

	N_{obs}	DATA PRIOR TO THIS STUDY
•	60/77=77.9%	cluster members, E&S0's, previous dispersions
⊗	47/63=74.6%	cluster members, E&S0's, no previous dispersions
⋆	21/43=48.8%	cluster members, no morphology or dispersions
⋈	1/4=25.0%	E&S0's but no redshifts or dispersions
△	7/29=24.1%	only magnitude info

Figure 2.6: Coma galaxies observed.

Chapter 3

Data reduction

3.1 Introduction

In Chapter 2 I outlined the Coma cluster sample selection, astrometry, observing strategy and summarised the observations made for this dissertation with the WHT at La Palma.

The next step is to carefully analysis and reduce this data set to examine and remove any instrumental variations and to characterise the random and systematic errors in a formal and unambiguous way, resulting in a high-quality, high signal-to-noise, homogeneous spectroscopic data set of the early-type galaxy population within the central 1 degree of the Coma cluster.

This chapter will detail this raw reduction from the 4600–5600Å wavelength range data obtained at the telescope to a status ready for the subsequent kinematic, stellar population and fundamental plane analysis. I will describe the raw reduction with `IRAF`, the wavelength calibration, the cosmic ray removal, the combining of individual spectra, the calculation of signal-to-noise, the measurement of redshifts and velocity dispersions and any subsequent corrections, flux calibration of the spectra, measurement of stellar population indices using the Lick/IDS system and corrections for velocity dispersion broadening and for nebular emission, and finally a treatment of the errors for the index measurements. This data will be studied in subsequent chapters.

3.2 Initial raw reduction of Coma WHT data

This section will describe the raw reduction with `IRAF`* (Tody 1986 and 1993), the wavelength calibration, the cosmic ray removal and the combining of individual spectra.

*IRAF is distributed by the National Optical Astronomy Observatories, which are operated by the Association of Universities for Research in Astronomy, Inc., under cooperative agreement with the National Science Foundation.

3.2.1 IRAF environment setup

The first step in analysing the data is to reduce the raw data. WYFFOS data reduction software exists in the IRAF software environment. The tasks used are those supplied in the rgo package: wyffos, wyf_red, wyfgeom (see the "AUTOFIB2/WYFFOS User Manual" by Pollacco et al. 1999).

Two highly important pre-reduction parameters need to be checked before using the WYFFOS tasks. Firstly because of the extraordinarily large headers associated with the WHT data files, it is very important that the following be set (either in the login.cl file or at the IRAF command prompt):

```
set min_lenuserarea = 300000
```

Secondly the raw data files do not have a parameter correctly which should indicate that large headers are being used. To correct this change to the directory containing the data files and enter the following at the IRAF command prompt:

```
hedit *.imh WYFFEED LARGE verify=no
```

The next step is to use the wyfgeom task to specify the order in which the fibres appear on the output frame (i.e. left to right or vice versa) and whether the redder wavelengths are at the bottom or the top. By examining individual frames the layout of the data on each CCD frame was determined to be:

- fibre numbers increase to the left
- CCD has bluer wavelengths at the top, redder at the bottom

3.2.2 Bias subtraction

A "bias" level is introduced onto a CCD chip in order to ensure that the chip is working in a linear regime. A bias also guards against negative numbers at readout which have a statistical chance of occurring in regions of low emission. This bias level must be determined and subtracted out of an input CCD frame before any further analysis can be carried out. This can be done in one of two ways. The first is to look at the over-scan region of each frame and do a statistical

analysis to find the mean bias and then to subtract this constant off the whole rest of the frame. The second is to average a sample of bias frames (frames taken with zero exposure time) pixel by pixel to produce a mean bias frame. This mean frame is then subtracted (pixel by pixel) from each input image. This is the method that is used here because it can also remove any structure in the bias of the chip.

3.2.3 Aperture identification

One of the most critical things to get right in multi-object spectroscopy is the determination of the aperture information for each spectrum. That is the location of each spectrum, the spread of each spectrum in the spatial direction and the distortion of the spectrum in the dispersion direction. The latter is quite important for instruments such as WYFFOS where, owing to field distortions introduced by the optics of the system, a spectrum won't necessarily line up along the rows/columns in the dispersion direction (in fact usually the spectra can be very distorted, particularly near the edge of a frame). It is also very important so that the spectroscopic data can be matched to the programme object ancillary information (name, coordinates etc.).

This aperture identification is done automatically by the reduction software using a high signal-to-noise aperture reference frame, with lots of counts down each fibre (a tungsten lamp exposure is used here), and is cross-checked manually.

3.2.4 Scattered light correction

All spectrographs have scattered light which is important to get rid of when trying to observe faint objects. Here the reduction software fits a function to the residual scattered light along the lines and columns of the images, ignoring the places where the aperture definition says there should be a part of a spectrum. When the excess light between the spectra has been successfully modelled, it is interpolated to the region where the spectra are located and then subtracted off the frame.

3.2.5 Flat fielding and throughput correction

This is an alias for the removal of the multiplicative effects that originate from the inherent instrumental signature, the variable throughput of the fibres, the spatial vignetting and the pixel-to-pixel variation in the chip response. The instrumental signature and pixel-to-pixel variations are found through flat field exposures (an exposure of a uniform light source through

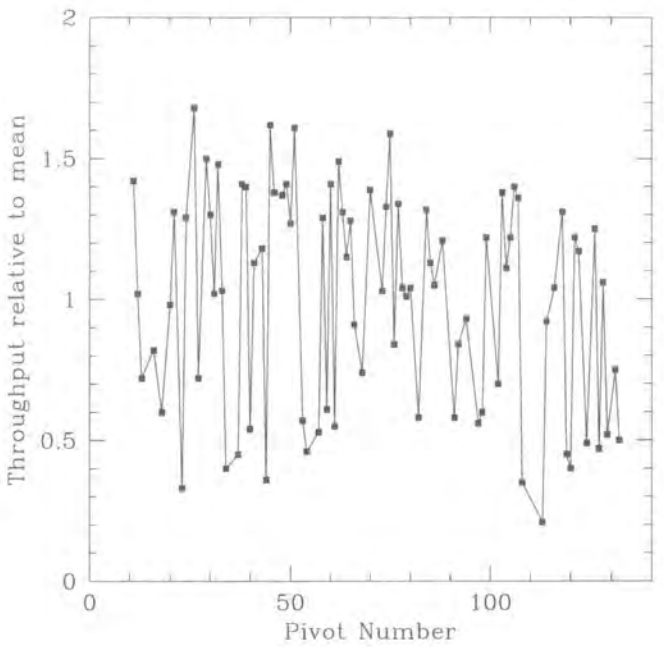

Figure 3.1: Throughput variation of fibres. The throughput is calculated from offset sky exposures and is expressed relative to the average counts received down each fibre.

the fibres). These are very high signal-to-noise frames since the pixel-to-pixel variation is usually only of the order of a few percent. The fibre throughput and vignetting corrections are found through offset sky exposures. These are frames of sky taken very near to the programme region with the fibres in the same configuration as the programme region. The signal-to-noise of these frames isn't very high as only the mean counts per fibre are important. A few different offset sky frames are taken with various field offsets to ensure that light from a bright star does not accidently fall down one or more of the fibres. The fibre-to-fibre throughput of one of the programme fields is shown in Figure 3.1; this figure shows that the fibre-to-fibre throughput varies from 0.2 to 1.7 times the mean throughput of 1.0, with a standard deviation of 0.4.

3.2.6 Fibre extraction

Fibre extraction means the summing up of spectral pixels along the spatial direction into a final one-dimensional spectrum. The WYFFOS reduction package uses a method called "optimal extraction" (or "variance weighted extraction") which gives lower weight to regions of relatively low signal-to-noise than to those with relatively high signal-to-noise (see Horne 1986, Marsh 1989 and Mukai 1990). The net result is that in low signal-to-noise regions where the signal is

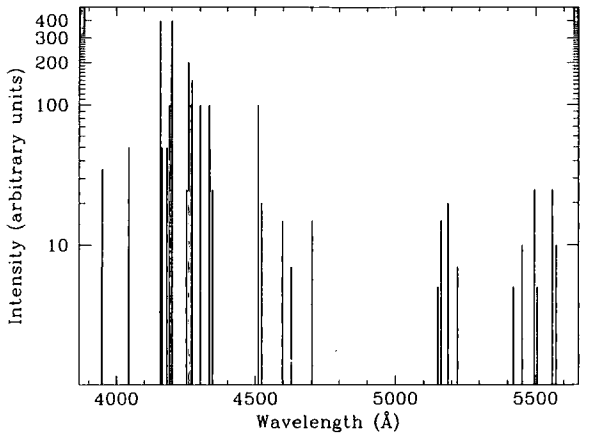

Figure 3.2: Artificially created Argon I spectra used to identify lines in arc lamp exposures to calibrate galaxy spectra.

of the same order as the readout noise of the chip, the lower weights mean that the contribution to the final spectrum of the readout noise is significantly reduced. This method maximises the possible signal-to-noise in the output spectrum.

As part of the extraction process, it predicts roughly the number of counts it expects to find in each pixel of a spectrum (depending upon the wavelength and its position in the point-spread function) and removes pixel values which are significantly higher than the predicted value (likely to be cosmic ray events). This causes the removal of many "spurious" pixels and results in a much cleaner final spectrum.

3.2.7 Wavelength calibration

Following investigation of the `wyf_red` wavelength calibration options, I found that it is best to manual calibrate each fibre (option 3 in the `wyf_red` task). The automatic and semi-automatic calibration options were found to fail randomly with no warning.

The fibres were calibrated against an Argon I lamp, with manual identification of lines performed using an artificially created Argon I spectra from standard atomic data tables (Figure 3.2).

The results of the manual calibration for the two wavelength ranges for all of the nights are shown in Table 3.1. Uncertainties in the wavelength calibration of the order shown in Table 3.1 will have a negligible effect on line strength measurements due to the width of the feature and continuum bandpasses (see Section 3.7).

	Wavelength range	Median rms of calibration residuals
Field config number 1	4600–5600Å	0.050Å
Field config number 2	4600–5600Å	0.083Å
Field config number 3	4600–5600Å	0.062Å

Table 3.1: RMS of wavelength calibration residuals.

One important point to note about the WYFFOS data is that the fibre data on the CCD has a *sawtooth* arrangement. Most fibre optic spectrographs have the fibre ends in a co-linear arrangement at the slit end. This means that (ignoring the distortion of the camera) a given position in the spectral direction will be at roughly the same wavelength for each spectrum. However for WYFFOS, in order to save space at the detector, the fibre ends are placed in three parallel rows, which means that a given point in the spectral direction can have three (approximate) wavelengths. The starting wavelength can typically be shifted by 50Å between spectra. The reduction software takes this sawtooth effect into account.

3.2.8 Sky subtraction

Sky subtraction is done using typically 10 to 20 dedicated fibres in each field configuration to obtain sky spectra at the same time as gathering programme data. These dedicated sky fibres were checked prior to assignment to ensure that no bright objects coincided with their allocated positions. A mean sky spectrum from these fibres is computed and then subtracted from the spectra of the programme objects.

3.2.9 Cosmic ray and night sky line removal

Individual galaxy spectra have any cosmic rays removed and the effect of the night sky line at 5577Å minimised.

Cosmic rays are removed used a straightforward technique: since we have multiple exposures for each night, we can median filter the spectra setting any deviations greater than a specified number of sigma times the Poisson noise ($\sqrt{N}$) from the median value for each wavelength to the median value (typically a greater than 15 sigma deviation rejection criterion is used). During the median filtering a record is kept of modified values to allow accurate setting of the filtering threshold and for later cross-checking with the defined Lick/IDS band wavelengths to determine

whether a particular index has been adversely affected. This process will not affect any emission lines since these are present in all of the separate galaxy exposures.

Any effect of non-perfect removal of the night sky line at 5577Å is minimised by setting the region around the line to a mean value. This is only a minor problem as this night sky line is only at the extremity of one of the wavelength ranges observed and does not affect any Lick/IDS indices nor any velocity dispersion measurements.

3.2.10 Combination of spectra

Individual spectra from a particular night are summed together to produce a spectrum with a higher signal-to-noise.

Where galaxies were observed on multiple nights with the same wavelength range it was decided not to add the combined exposure from each night. This is because of the problem of slight differences in wavelength ranges and pixel scales due to factors such as a slightly different grating angle or a different fibre position.

3.3 Signal-to-noise calculation

Since we know the gain to be 1.7e^- per analogue-to-digital unit (ADU), the readout noise to be 5.6e^- and the mean residual sky counts after sky subtraction (the sky subtraction noise) to be 8.1 counts, we can calculate the signal-to-noise (S/N) per Angstrom, Å straightforwardly:

$$\text{S/N per Å} = \frac{\text{COUNTS} \times 1.7}{\sqrt{5.6^2 + \text{COUNTS} \times 1.7 + 8.1 \times 1.7}} \tag{3.1}$$

This assumes that the noise is Poissonian (i.e. goes as the square root of the counts).

A signal-to-noise is calculated at the central rest wavelength of each spectral line index feature that is investigated herein. This is illustrated in Figures 3.3 and 3.4 which show the example of the line indices Hβ_G and [MgFe] as well as the total results for the data set. The mean signal-to-noise of Hβ_G and [MgFe] for the combined exposures with S/N$\geq$35 is 58.7 and 66.7 respectively.

Where only a single signal-to-noise is quoted subsequently, unless otherwise specified, it refers to the signal-to-noise per Å at the central wavelength of Fe5270 for the wavelength range 4600Å to 5600Å.

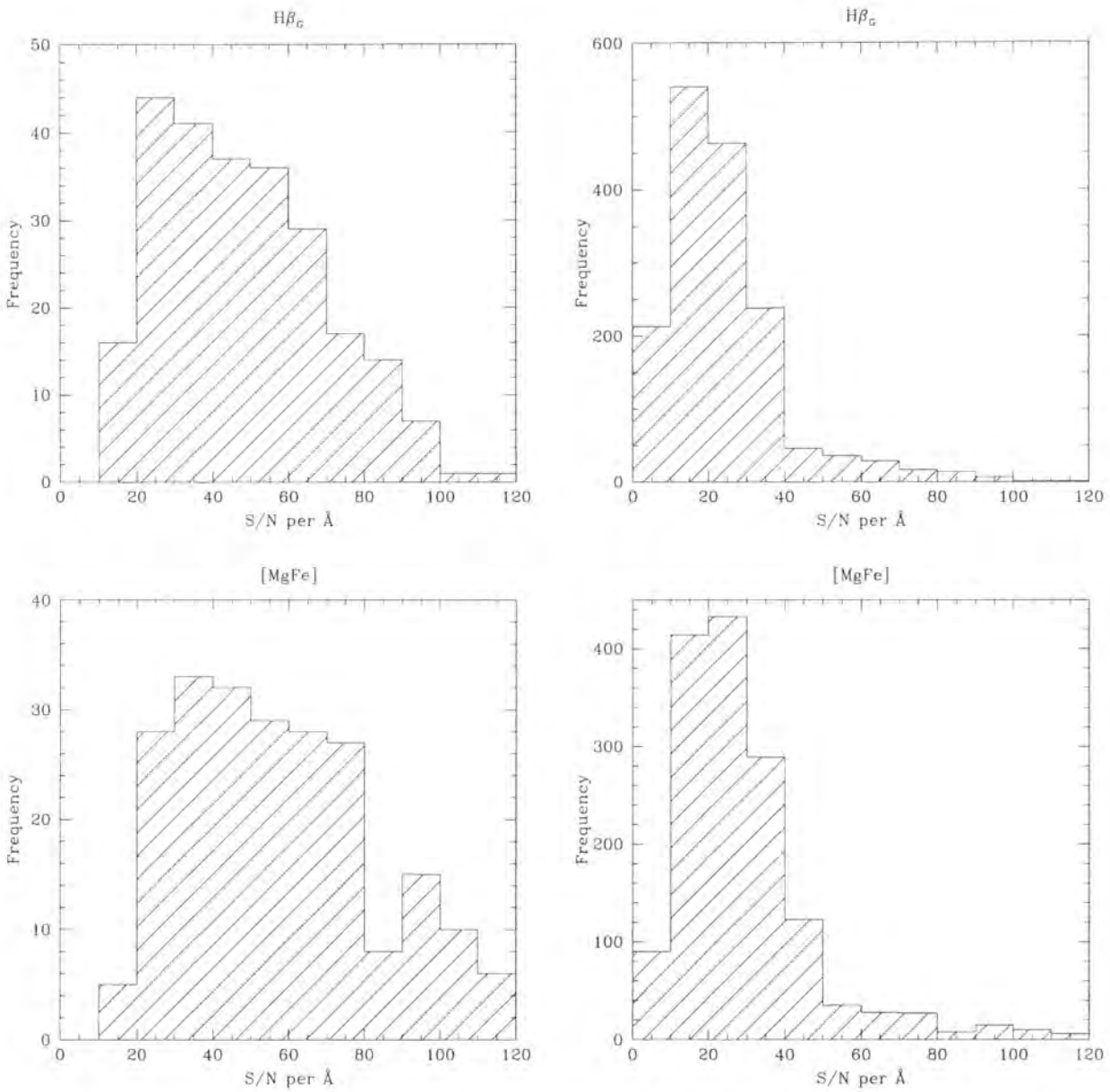

a. combined exposures only

b. individual and combined exposures

Figure 3.3: S/N per Å of line indices $H\beta_G$ and [MgFe].

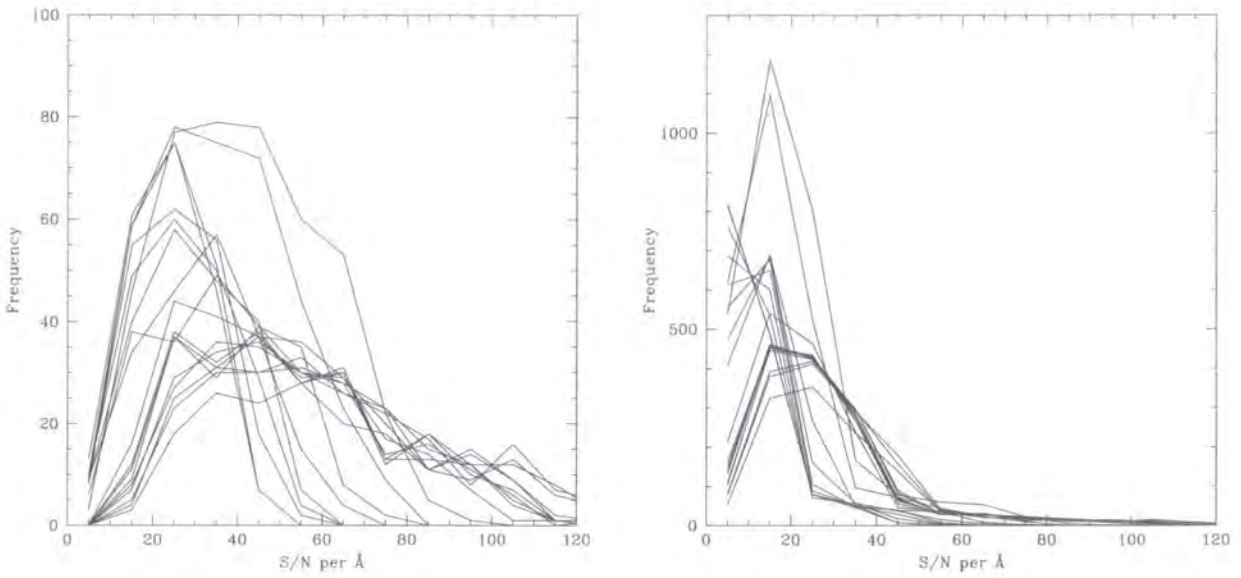

a. combined exposures only

b. individual and combined exposures

Figure 3.4: S/N per Å for all line index measurements. A separate line is plotted for each individual line index.

3.4 Redshift and velocity dispersion measurement

3.4.1 Redshift and velocity dispersion measurement using cross-correlation techniques

Velocity dispersions, σ of the central 2.7″ region of a galaxy (corresponding to $0.94\,h^{-1}\,\mathrm{kpc}$, assuming a cluster radial velocity of $7200\,\mathrm{km\,s^{-1}}$) were measured by use of the well-known Fourier Quotient method of Sargent et al. (1977). In the simplest approximation, the galaxy spectrum $G(n)$ can be considered as the convolution of a representative stellar spectrum $S(n)$, with an appropriate broadening function $B(n)$. Here G, S and B are defined in velocity space, over channels n. The convolution,

$$G(n) = S(n) \star B(n) \tag{3.2}$$

in velocity space becomes in Fourier space:

$$\tilde{G}(s) = \tilde{S}(s).\tilde{B}(s) \tag{3.3}$$

where s is the velocity-frequency variable. Assuming a functional form — in practice a Gaussian — for $\tilde{B}$, we fit the observable quotient:

$$\tilde{B}(s) = \frac{\tilde{G}(s)}{\tilde{S}(s)} \tag{3.4}$$

and transform to normal parameter space to yield the broadening width.

In order for the recovered width to represent only the intrinsic velocity broadening of the galaxy spectrum, it is necessary to ensure that the stellar spectrum has been subject to the same instrumental resolution effects as the galaxy spectrum. This is done by observing well-matched standard stars throughout the observing run (see Table 3.2) and comparing these spectra to the observed galaxy spectra.

Prior to computing $\tilde{G}$ and $\tilde{S}$, continuum fits were subtracted (using a 5th order polynomial) from both the template spectrum and the galaxy spectrum, and modulated by a cosine bell function to fix the ends of the spectrum to zero. The latter step is necessary to avoid unphysical signals appearing at all frequencies in the Fourier transforms.

The spectra require filtering in Fourier space to remove signals arising from from noise, inadequate continuum removal and the application of the cosine bell. A cut is made at high frequencies, to suppress channel-to-channel noise. The resulting σ values are fairly insensitive to the exact value, $k_{\rm high}$, chosen for the high frequency cut. $k_{\rm high} = 200$ has been used throughout. At low frequencies, a filter must be applied to remove residual continuum features, and the effects of the cosine-bell modulation function described above. For the case of the low frequency cut, results are found to exhibit a clear trend: velocity dispersions are measured to be smaller when $k_{\rm low}$ is larger. The cutoff frequency must therefore be chosen with care. It is required that the low frequency filter should remove the signal arising from the cosine bell modulation, whilst preserving intrinsic features in spectra of velocity dispersion $\leq$ 500 km s^{-1}. For the spectra herein, these constraints leave a range of $k_{\rm low} = 6 - 9$.

After discarding a few stellar template spectra which gave consistently discrepant results, the velocity dispersions obtained from each galaxy spectrum were averaged over all available template spectra from the run.

Recession velocities, cz, were obtained simultaneously with velocity dispersions, as a result of the Fourier Quotient fit.

Redshifts and velocity dispersions are measured from each galaxy exposure and from the combined galaxy exposure for each night the galaxy was observed.

3.4.2 Zero redshifting & heliocentric corrections

Before embarking on the line strength measurement of the spectra it is necessary to ensure that we accurately know the redshifts of the galaxies so that they can be zero-redshifted to match the line index bandpasses precisely (note that there is some degree of latitude in the definition of the bandpasses in that they are reasonably wide with respect to the principal features they are attempting to measure).

As discussed in Section 3.4 I have so far measured the redshifts of galaxies with respect to the radial velocity standard stars observed during the run. These standard stars have very small but non-zero radial velocities. It is necessary to correct the previously measured redshifts for these template redshifts to get the true measured galaxy redshift for that night and time. Additional corrections then need to be made to correct the redshift to first a geocentric (Earth centred, $\sim 1\,\mathrm{km\,s^{-1}}$ correction) and then to a heliocentric (Sun centred, $\sim 30\,\mathrm{km\,s^{-1}}$ correction) redshift (these corrections account for the rotation of the Earth and then the motion of the Earth around the Sun).

The first step is to use an independent set of zero-redshifted, high-resolution stars to cross-correlate against our radial velocity templates. I use spectra obtained from Claire Halliday (*private communication*). These are 0.5Å per pixel, high signal-to-noise spectra that have been precisely zero-redshifted by identifying spectral features and shifting them to their laboratory rest frame, removing any innate redshift. These spectra are the same ones that are subsequently used in my modelling of fibre effects (see Section 3.5.2). The radial velocities of the observed radial velocity standard stars are then measured by cross-correlation against these zero-redshifted spectra, giving $z_{meas}(star)$.

It is then necessary to correct measured radial velocities to heliocentric radial velocities. These corrections vary with the coordinates of the observed object and from night to night as the Earth moves around the Sun (there is not a great deal of variation during a night). The corrections also vary with the location of the observer (the observers' position on the Earth). Heliocentric radial velocity corrections are computed using the Starlink program **rv** (short for "radial velocity"). This program takes as input the observers' location, the dates of the observations and the source coordinates. It outputs a list of corrections, $z_{\odot corr}(star)$ throughout the observing run (at various time intervals) that can then be subtracted from the measured radial velocity (**rv** uses a sign convention such that a +ve value means the observer is moving away from the source position).

Star	RA (J2000)	DEC (J2000)	Type	V (mag)	$z_{\odot true}(star)$
HD 132737	14 59 51.2	+27 09 44	K0 III	8.02	-29.1 ± 5.7 km.s^{-1}
SAO 065108	16 08 58.5	+36 29 10	K0 III-IV	4.76	-29.3 ± 5.8 km.s^{-1}
SAO 123140	18 07 18.3	+08 44 01	G8 III	4.64	-13.3 ± 5.7 km.s^{-1}
SAO 124799	19 34 04.6	+07 22 52	K3 IIIb	4.45	-35.0 ± 5.8 km.s^{-1}
SAO 032042	19 50 37.8	+52 59 20	K3 III	5.03	-32.8 ± 5.7 km.s^{-1}

Table 3.2: Radial velocity standard stars observed. Heliocentric radial velocities measured in this study are given in the final column.

The true heliocentric radial velocity of the observed radial velocity standards can be calculated using the following equation:

$$z_{\odot true}(star) = z_{meas}(star) - z_{\odot corr}(star) \tag{3.5}$$

Using this approach I compute the heliocentric radial velocities of the observed radial velocity standard stars. These velocities are then used to adjust the previously measured galaxy redshifts to ensure that there is no template radial velocity component in the measurement:

$$\begin{aligned} \text{galaxy geocentric radial velocity} \quad z_{\oplus}(gal) &= z_{meas}(gal) + z_{meas}(star) \\ &\equiv z_{meas}(gal) + z_{\odot true}(star) + z_{\odot corr}(star) \end{aligned} \tag{3.6}$$

$$\begin{aligned} \text{galaxy heliocentric radial velocity} \quad z_{\odot}(gal) &= z_{\oplus}(gal) - z_{\odot corr}(gal) \\ &\equiv z_{meas}(gal) + z_{\odot true}(star) + z_{\odot corr}(star) - z_{\odot corr}(gal) \end{aligned} \tag{3.7}$$

These galaxy heliocentric radial velocities can then be compared to measurements in previous studies. The geocentric radial velocities are used to zero-redshift spectra prior to stellar population line strength measurement.

3.5 Velocity dispersion corrections

Using any multi-fibre spectroscopy instrument introduces intra-fibre and fibre-to-fibre variations in resolution and throughput that necessarily have to be removed before accurate stellar population analysis can be undertaken. These variations are due to the optical performance of the telescope plus instrumentation setup both across the field and down the slit where the fibres are fed into the spectrograph.

As was noticed at the time the observations were made, these variations are significant in the WHT/WYFFOS configuration. There is sizeable variation in the width of spectral lines both between fibres (seen as a variation in width versus fibre number) and within a fibre (seen as a variation in width versus wavelength), with the widths varying from ~ 4Å at the end of the slit and at the edge of the field to ~ 1.7Å at the centre of the slit and at the centre of the field. This conclusion was reached after careful analysis of arc lamp calibration spectra. This can be explained by referring to Section 2.4 which detailed the layout and optics of the WYFFOS/AUTOFIB2 instrument: it is evident from this that there are various degrees of curvature and mis-matching (principally the problem that the IDS grating H1800V used is *smaller* than the beam in WYFFOS so it vignettes the fibres at the top and bottom ends of the slit) that act to exaggerate any vignetting and results in the observed line width variations. These variations in line width will affect any velocity dispersion measurements (with a maximum error of $12\,\mathrm{km\,s^{-1}}$ for $\sigma = 100\,\mathrm{km\,s^{-1}}$ reducing to a maximum error of $6\,\mathrm{km\,s^{-1}}$ for $\sigma = 200\,\mathrm{km\,s^{-1}}$ — see Figure 3.8), but will not change the redshift measurements (there is no systematic shift introduced by this problem) and will have a minor effect on line strength measurements (negligible if mapped) since the spectrum are broadened to a mean resolution of 9Å (see Section 3.7.3).

The first step in removing this effect is to characterise the problem fully by analysing the calibration spectra taken on each night. It would have been preferable to use twilight sky flats to characterise the performance of the system, since these would place a solar spectrum down each fibre and would follow exactly the same optical path as later galaxy exposures, however these flats were not taken. The arc lamps are instead located at the Cassegrain focus of the WHT and shine their light source onto the tertiary mirror from which it is then relayed to the fibres. These allow accurate mapping of the vignetting caused by the IDS grating H1800V convolved with a function representing the vignetting of the telescope optics from that point onwards. This approach is capable of removing the majority of the overall vignetting, since any effects superimposed by the telescope optics prior to the tertiary mirror are significantly smaller than

the dominant effects subsequent to the tertiary mirror.

3.5.1 Modelling the fibre characteristics

Each calibration spectrum taken during the observation run was reduced and split into individual files for each night and each fibre. The full width half maximum (FWHM) of the Argon I emission lines within each fibre is then measured using the Starlink package `emlt` and a number of other programs written by myself. These arc lines have no appreciable width (at the level that we are interested here) other than that due to instrumental broadening coupled with fibre effects, both of which we want to map. This means that they are an ideal choice for this analysis.

Figure 3.5 shows the dependence of spectral line FWHM on wavelength and fibre number. Six plots are shown, two for each of the three different field configurations. The plots on the left show the dependence on wavelength. In these plots, for each spectral line wavelength there are a number of points shown, each of which corresponds to a different spectral line width measurement of that line for each fibre used (the superimposed lines are fits to the variation - see Section 3.5.2). A clear variation in spectral line width is seen within a fibre, with the ends of a spectrum typically broadened by an additional ~ 0.5Å when compared to the central FWHM. This is manifested in these plots by the FWHM measurements being larger at the lowest and highest wavelengths than for the central wavelength. A clear dependence on fibre number (and hence position in the field and on the slit) is also seen, with a variation of an additional ~ 1.3Å between the best (fibre numbers around 50) and worst fibres (fibre numbers lower than 20 or higher than 100). This is manifested in these plots by the spread of points in the vertical direction for the wavelength of each spectral line analysed. This is more clearly seen in the plots on the right, which show the dependence of Argon I emission FWHM on fibre number. In these plots, for each fibre number there are a number of points shown, each of which corresponds to a different spectral line width measurement within that fibre. A clear variation in spectral line width within a fibre is again seen, with a similar broadening at the ends. This is manifested in these plots by the spread of points in the vertical direction for each fibre number. A clear dependence on fibre number (and hence position in the field and on the slit) is also seen, again at the same level as the dependence on wavelength (shown in the plots on the left).

These plots have been sifted to only include emission lines with a signal-to-noise greater than 5, where signal-to-noise is defined as:

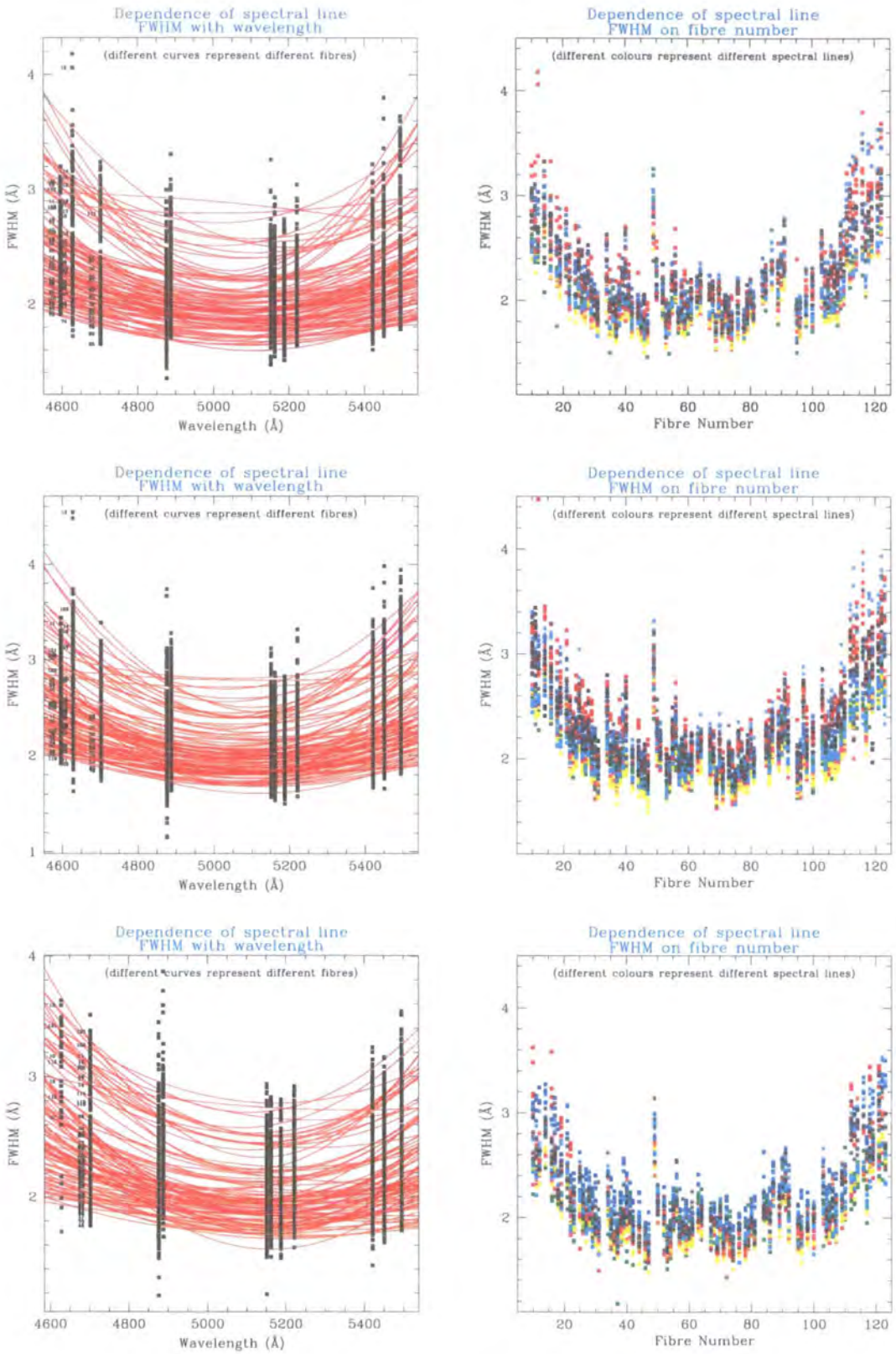

Figure 3.5: Dependence of Argon I emission FWHM on wavelength and fibre number for the 4600–5600Å data. The plots on the left show the dependence on wavelength, whilst the plots on the right show the dependence on fibre number. The plots at the top are for the field configuration number 1, the middle ones for number 2 and the bottom ones for number 3. See text for a more detailed explanation.

$$S/N = \frac{\text{peak line height}}{\sqrt{\text{mean level}}} \tag{3.8}$$

assuming the noise is Poissonian (i.e $\propto \sqrt{N}$).

It is possible that the variable throughput of the fibres might play a role here, with a dependence on FWHM with the strength of an arc line. Note that there could be a further complication in that the tracking of the field centre on the Coma cluster during an exposure is not perfect. Therefore during an exposure and between exposures there could be a drift in fibre position relative to the object that could introduce a time dependence into the mapping of the fibre characteristics. This effect was investigated by comparing the first and last spectra on a night and was found to be negligible compared to the other effects discussed.

In conclusion, there are clear differences and therefore it is necessary to map each of the setups used and to correct the final results.

3.5.2 Modelling the effect of intra-fibre and fibre-fibre variations

The first stage in removing the effect of any intra-fibre and fibre-fibre variations is to fit a function to the FWHM variation within each fibre for each configuration. A 2nd order polynomial is fit to the wavelength range 4600–5600Å. These fits can be seen in Figure 3.5.

We now have functions to map the variation of spectral line FWHM with wavelength for each fibre and each configuration. These functions can then be convolved with an ideal template spectrum and the result used to cross-correlate against that of an observed galaxy to find its dispersion with any intrinsic fibre variation removed. The problem with this method is in having a template spectrum of very high resolution that is not itself suffering from any internal or instrumental variation.

To counter this problem I have devised the following method. I use 0.5Å per pixel, high signal-to-noise spectra obtained from Claire Halliday (*private communication*) which have been precisely zero-redshifted through the identification and then subsequent shifting of spectral features to their laboratory rest frame. These are the same spectra that were previously used to removed any redshift from observed standard stars in Section 3.4.2. These spectra will still suffer from some intrinsic variation (due to e.g. the telescope/instrument setup they were obtained with), but this is unimportant in the proposed method. These spectra are convolved with a particular fibre model, resulting in a "template spectrum". The new template spectra are then

cross-correlated against a mock galaxy created by convolving the original high-resolution spectra with a fibre model (not necessarily the same fibre) and broadening it by a fixed amount (to simulate the Doppler broadening caused by a galaxy). A correction can then be calculated for each fibre configuration and each galaxy dispersion case:

$$\begin{matrix}\text{dispersion} \\ \text{correction}\end{matrix} = \begin{matrix}\text{measured} \\ \text{dispersion}\end{matrix} - \begin{matrix}\text{true} \\ \text{dispersion}\end{matrix} \tag{3.9}$$

These corrections are then used to modify the real calculated dispersions which are calculated using template spectra observed on the night to cross-correlate against the galaxy spectra. This is done by subtracting the calculated correction from the measured value. In this way the "true" (or best estimate) of the dispersion with any modifications due to intra-fibre and fibre-fibre variations removed is derived.

Some results of this method can be seen in Figures 3.6 to 3.8.

Figure 3.6 shows the velocity dispersion measured versus galaxy fibre number for template stars observed down different fibres. Three plots are shown for high-resolution, high signal-to-noise template spectra (provided by Claire Halliday, *private communication*) broadened to 100, 200 and 300 $\mathrm{km\,s^{-1}}$ which have then been convolved with the previously computed broadening function for a given fibre number to simulate a galaxy observed down that fibre and cross-correlated against another template spectra convolved with the broadening function down a separate fibre that matches a fibre that an actual standard star was observed down during the WHT/WYFFOS run. Ideally each plot should be a straight line, however this is not the case because of variations due to the fibre position both within the field and on the spectrograph slit. Consequently a correction needs to be applied to spectra down different fibres when they are cross-correlated against a standard star down this particular fibre to obtain the true velocity dispersion for that galaxy. A different correction needs to be calculated for each fibre that a standard star is observed down and for each field configuration. These plots also show that the size of the correction that needs to be applied decreases with the velocity dispersion of the galaxy. Typically the size of the correction that needs to be applied is anything from a zero to a 20 $\mathrm{km\,s^{-1}}$ correction.

Figure 3.7 shows the velocity dispersion correction versus galaxy fibre number for one template star observed down a particular fibre over a range of different galaxy velocity dispersions. Seven plots are shown for high-resolution, high signal-to-noise template spectra (provided by

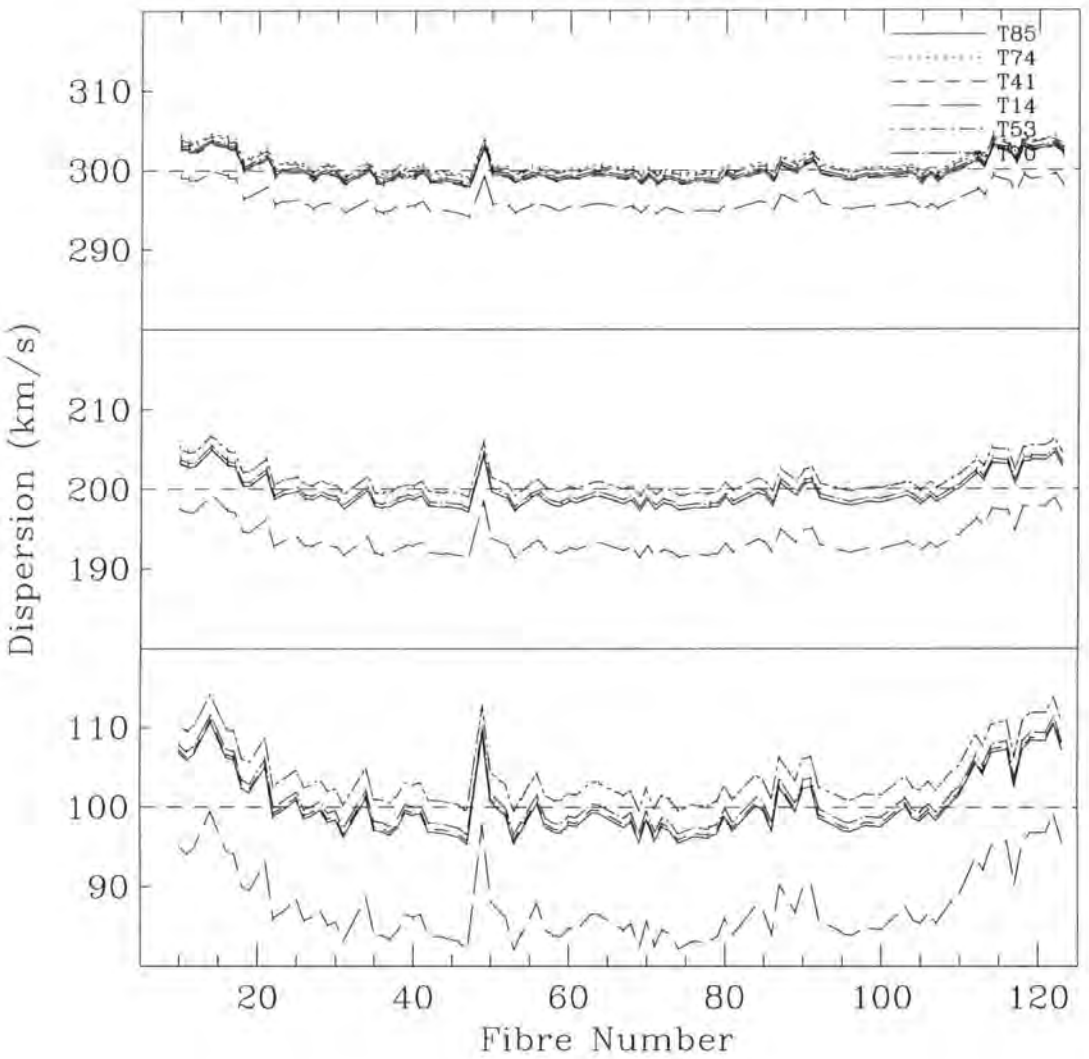

Figure 3.6: Velocity dispersion measured versus galaxy fibre number for template stars observed down different fibres. See text.

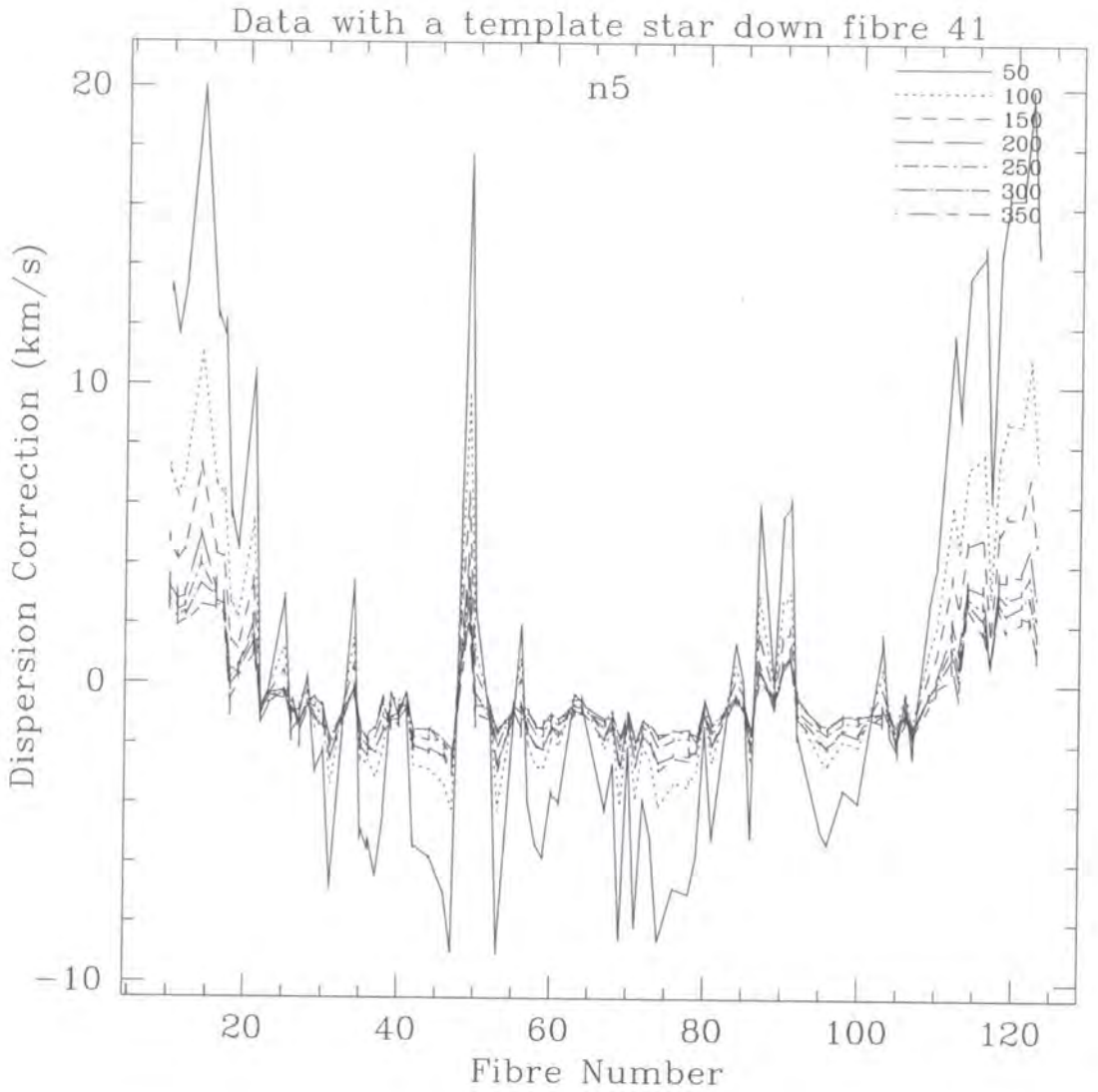

Figure 3.7: Velocity dispersion correction versus galaxy fibre number for one template star observed down a particular fibre cross-correlated against a mock galaxy observed down different fibres with various broadening factors. See text.

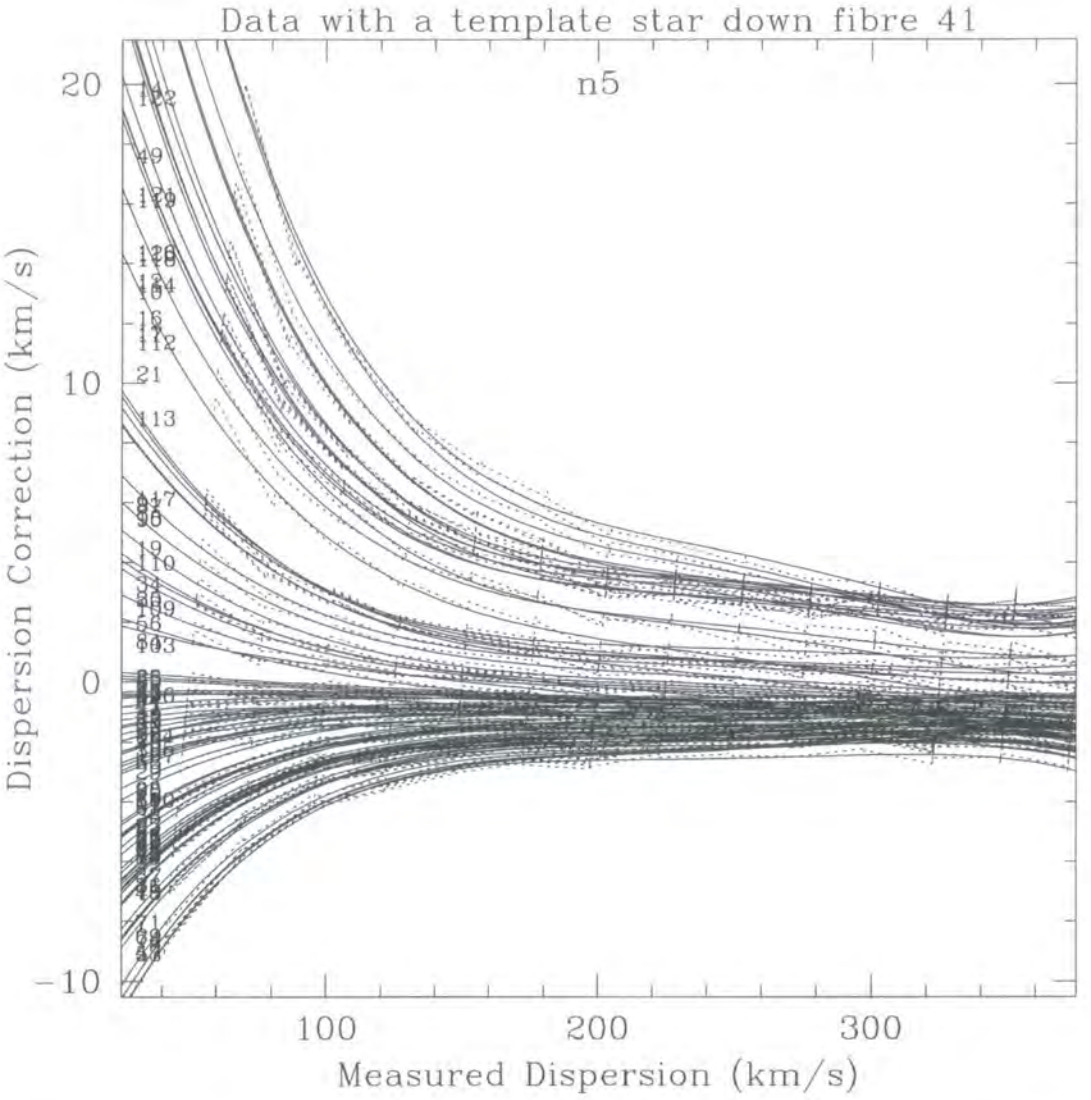

Figure 3.8: Velocity dispersion correction versus measured velocity dispersion for each fibre cross-correlated against a standard star down a particular fibre (in this case fibre number 41). See text.

Claire Halliday, *private communication*) broadened from 50 to 350 km s^{-1} which have then been convolved with the previously computed broadening function for a given fibre number to simulate a galaxy observed down that fibre and cross-correlated against another template spectra convolved with the broadening function down a separate fibre that matches a fibre that an actual standard star was observed down during the WHT/WYFFOS run (in this case fibre number 41). Ideally each plot should be a straight line and equal to zero, however this is not the case because of variations due to the fibre position both within the field and on the spectrograph slit. These plots shown that the corrections that need be applied are typically small, but where an unfavourable pairing between galaxy fibre and standard star fibre occurs the velocity dispersion correction can be as large as 20 km s^{-1} for low velocity dispersion galaxies. Note that a different correction factor needs to be calculated for each pairing of galaxy fibre number and standard star fibre number and for the different field configurations. As expected though, when a galaxy is cross-correlated against a standard star observed in the same field configuration and down the same fibre the velocity dispersion correction is zero.

Finally Figure 3.8 shows the velocity dispersion correction versus measured velocity dispersion for each fibre cross-correlated against a standard star down a particular fibre (in this case fibre number 41). The required velocity dispersion correction is dependent on the fibre number (and hence position within the field and down the slit) of the galaxy, the fibre number of the standard star against which it is been cross-correlated, and the field configuration used (which determines the distribution of all the fibres across the field and the down the slit). This means that all possible combinations need to be analysed and modelled for the appropriate velocity dispersion correction to be computed. This is what is done in my reduction of the WHT/WYFFOS data. This figure shows the resultant correction curves for this particular configuration that are subsequently used to correct real galaxy velocity dispersion measurements for the instrument/configuration imposed variable broadening. The curves are constructed by taking a high-resolution, high signal-to-noise template spectra (provided by Claire Halliday, *private communication*), convolving it with a previously computed broadening function for a given fibre number and then broadening it by a given velocity dispersion from 25 to 350 km s^{-1}. This resultant mock galaxy spectra is then cross-correlated against a similar template spectra which has been convolved with a broadening function for a different fibre (matching a fibre number down which a standard star was observed during the run). The computed velocity dispersion is compared to the true velocity dispersion and a correction computed. A curve is then fit to

the variation of the velocity dispersion correction with measured velocity dispersion. This curve (overlaid on the plot) can then subsequently used to correct an actual galaxy velocity dispersion measurement. Ideally all lines should be straight and coincident with a zero correction. However because of the variations due to the fibre position both within the field and on the spectrograph slit this is not the case. This figure shows that for the typical velocity dispersions of the galaxies that we observe in this project ($\sigma \sim 100\,\mathrm{km\,s^{-1}}$ and greater) the corrections are not large, but significant if high-precision work is required.

This modelling of the effect of intra-fibre and fibre-fibre variations results in accurate velocity dispersions for the galaxies, which are subsequently required during the Lick/IDS stellar population index measurement process (see Section 3.7). Bootstrap tests on the accuracy of this method using the high-resolution, high signal-to-noise template spectra have shown that the errors on the velocity dispersion corrections are $1 - 2\,\mathrm{km\,s^{-1}}$, demonstrating the success of this approach.

3.6 Redshift and velocity dispersion dependence on airmass

Figure 3.9 shows two plots designed to probe for any dependence for redshift or velocity dispersion measurements on airmass. All data for the 4600-5600Å wavelength range exposures are shown. Table 3.3 gives the airmass of each observation at mid-exposure. Since the redshifts and velocity dispersions are calculated through cross-correlation against standard stars (Section 3.4) there are a number of data points in Figure 3.9 at each airmass for each galaxy. The y-axis represents the deviation of each of these cross-correlation derived redshifts or velocity dispersions for a galaxy from the mean for that galaxy (calculated from the total kinematic data set for that galaxy). Note that the redshifts are all corrected to heliocentric redshifts (which should have removed any time dependence) and the velocity dispersions are all corrected as discussed in Section 3.5 (which should removed any vignetting effects). A line connects all the mean deviations at each exposure for a particular galaxy. All results for all galaxies are shown. No trend of redshift nor velocity dispersion versus airmass is seen, re-affirming the quality of the kinematic data presented in this dissertation.

Night	Exposure	UT date	UT time	Barycentric JD	HA	sec(z)
n1	1	14 4 1999	02 04	2451282.590731	1 20 13	1.049
n1	2	14 4 1999	02 33	2451282.610869	1 49 18	1.095
n1	3	14 4 1999	03 02	2451282.631007	2 18 23	1.159
n1	4	14 4 1999	03 42	2451282.658784	2 58 29	1.288
n1	5	14 4 1999	04 11	2451282.678922	3 27 34	1.422
n1	6	14 4 1999	04 41	2451282.699755	3 57 39	1.614
n3	1	16 4 1999	02 12	2451284.596222	1 36 08	1.072
n3	2	16 4 1999	03 14	2451284.639276	2 38 18	1.216
n3	3	16 4 1999	03 44	2451284.660109	3 08 23	1.329
n3	4	16 4 1999	04 12	2451284.679552	3 36 27	1.472
n5	1	18 4 1999	01 48	2451286.579486	1 19 57	1.049
n5	2	18 4 1999	02 15	2451286.598236	1 47 01	1.091
n5	3	18 4 1999	02 44	2451286.618374	2 16 06	1.153
n5	4	18 4 1999	03 12	2451286.637817	2 44 10	1.235
n5	5	18 4 1999	03 41	2451286.657956	3 13 15	1.350
n5	6	18 4 1999	04 09	2451286.677399	3 41 20	1.502
n5	7	18 4 1999	04 39	2451286.698232	4 11 25	1.728

Table 3.3: Airmasses for each of the Coma cluster 4600-5600Å wavelength range observations at mid-exposure.

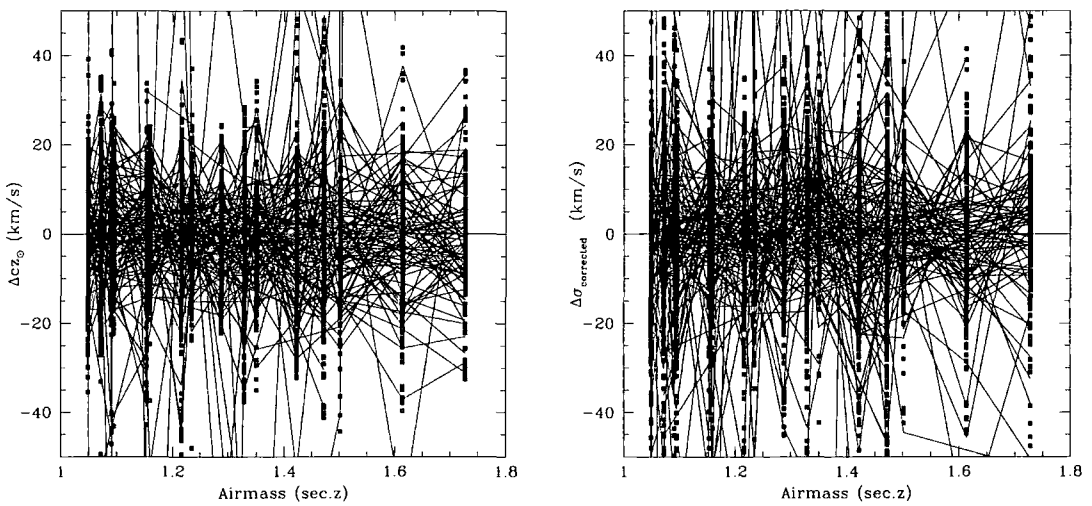

Figure 3.9: Redshift and velocity dispersion dependence on airmass. See text.

Star	RA (J2000)	DEC (J2000)	Stellar Type	$m_{\lambda 5556}$	Resolution (Å per pixel)	Photometric Precision (mag)
Feige 66	12 37 23.6	+25 03 59	O	10.54	2.08	<0.03
HZ 44	13 23 35.5	+36 07 59	O	11.74	1.64	<0.03
HD 192281	20 12 33.2	+40 16 06	Ovf	7.44	2.08	<0.03

Table 3.4: Flux standard stars observed and the source data parameters.

3.7 Absorption line strength measurements

3.7.1 Flux calibration

The next stage in the data reduction is to flux calibrate the spectra. This is necessary to remove the overall instrumental response function from the spectra prior to line strength measurement. Spectra will be affected by:

- response of the optics;
- response of the CCD;
- response of the grating;
- atmospheric conditions;
- airmass.

We remove these effects by observing flux standard stars during an observing run (see Table 3.4). These are stars that have previously been carefully observed and flux calibrated using other systems in photometric conditions. The observations are then compared to the previous standard observations and the instrumental response function computed.

The principal literature source of flux calibrated data was Massey et al. (1988) [†], which had the most readily accessible electronic version of the data tables and which covered the stars I observed. The data in Massey et al. (1988) is given in magnitudes. To convert the data to flux units I use the same relationship used by Massey et al. (1988) based on the work of Hayes & Latham (1975):

[†]They observed stars over the course of 25 nights with the Intensified Reticon Scanner (IRS) on the No.2 0.9 m telescope at the Kitt Peak National Observatory in Arizona, USA (KPNO) and over 8 nights with the Intensified Image Dissector Scanner (IIDS) on the 2.1 m telescope also at KPNO.

$$m = -2.5 \log_{10} f_\nu - 48.59 \tag{3.10}$$

with the flux, f_ν measured in ergs cm^{-2} s^{-1} Hz^{-1}.

Any relation between magnitudes and flux units depends on the adopted absolute calibration. This relation defines the magnitude of Vega to be 0.04 at 5556Å.

To convert my observed spectra from units of ADU to pseudo-flux units prior to flux calibration I use the following equation:

$$\text{flux} \propto \text{photons per sec} = \frac{1.7 \times \text{ADU's}}{\text{exposure time (secs)}} \tag{3.11}$$

where "ADU's" is the counts received in analogue-to-digital units and "1.7" is simply the gain of the CCD in e^- per ADU.

To flux calibrate the data it is necessary to compute the ratio of the observed standard star spectrum to the standard literature spectrum. However, since I'm interested in only fluxing the continuum component of the spectra it is necessary to first smooth the two spectra to minimise the effect of features present in the spectra (due to the high resolution of both spectra). This is done using a moving median window smoothing function of 30Å width for both spectra (not the same as binning). The final smoothed spectra will still have the same number of wavelength points (less half the window size at the beginning and ends of the spectra).

A ratio of the observed flux value to the literature flux value is calculated using Equation 3.12. Mis-matches in pixel scales between the two data sets are corrected through linear interpolation between two pixel values in the standard spectrum to match the pixel wavelength in the observed spectrum.

$$\text{ratio} = \frac{\text{observed flux value}}{\text{literature flux value}} \tag{3.12}$$

The observed spectrum can then be flux calibrated by dividing the spectrum by the computed ratio:

$$\frac{\text{observed flux}}{\text{(calibrated)}} = \frac{\text{photons per sec}}{\text{ratio}} \equiv \text{photons per sec} \times \frac{\text{literature flux}}{\text{photons per sec}} \tag{3.13}$$

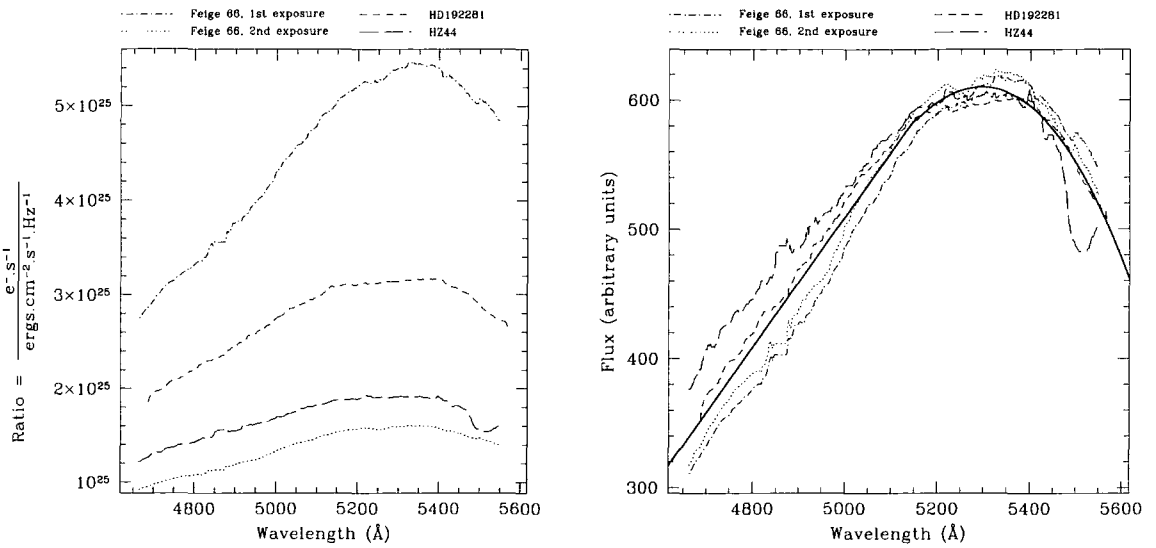

a. before corrections b. after corrections

Figure 3.10: Ratio of observed to literature flux value before and after photometric corrections. A number of stars were observed throughout the WHT/WYFFOS run in a variety of atmospheric conditions and down different fibres for both wavelength ranges. There are scale and systematic differences between the different ratio functions because the spectra were not observed on photometric nights. However this data is good enough to correct for the instrumental response function to some arbitrary units.

It is obvious from this equation how we get to the flux calibrated spectrum in this specific instance for the standard star. If the calculated ratio function is a general fit to all the observed standard stars then this equation will apply in general to all observed galaxies, allowing their spectra to be flux calibrated.

To calculate this total intrinsic flux correction, the ratios of all the flux standard stars are calculated. It is then necessary to correct the ratios for scale and systematic differences so that they are all on the same system (see Figure 3.10a). This is because our observations were not taken on photometric nights. The effect of these corrections is to change the flux units to some arbitrary units; however this is good enough for the purposes of correcting the spectral continuum to remove the instrumental response function.

The scale and systematic corrections are computed by minimising the maximum absolute deviations (MAD) between the first ratio data set and the remaining data sets through iterating the parameter space.

A function is then fit to these re-scaled and shifted ratio functions to compute the general ratio function that will later be applied to our observed galaxies. It is necessary to compute a general function since I wish to smooth out any star, fibre or configuration dependent features in the ratio functions to prevent these being introduced into the galaxy spectra and contaminating any line strength measurements.

A combination of a linear and 4th order polynomial function is fitted to the ratio functions for the wavelength range 4600-5600Å, intersecting at 5150Å (the two functions are matched at the wavelength intersection to prevent any discontinuities). The corrected ratios with the overlaid fitted function are shown in Figure 3.10b.

All of this work results in a function that will be used to flux calibrate any observed spectra to arbitrary flux units, removing any instrumental/system response function.

Figure 3.11 summarises this process. The top part of the figure shows both the observed flux data and the flux data from the literature (Massey et al. 1988), both of which have then been smoothed using a moving median window smoothing function of 30Å width which has then been overlaid on the spectra. The bottom part of the figure shows the ideal ratio function for this particular data set (flux standard star HD192281 observed for 30secs down aperture number 74 for a wavelength range of 4600-5600Å). This is computed by dividing the observed flux by the literature flux for the standard star. The overall ratio function is also shown. This is the function that results from a fit to all the photometrically adjusted ratio functions shown in Figure 3.10. The observed stellar spectra, corrected for the instrumental response function using both the ideal and computed ratio function is also shown. As can be seen the flux calibration process works and removes the instrumental response function.

It should be noted that for multi-fibre work, this is the best method to use without detrimentally affecting the available observing time. A more precise method would be to observe in photometric conditions and observe multiple flux standard stars down each fibre to compute the exact flux calibration function. This is impractical when dealing with hundreds of fibres.

3.7.2 The Lick/IDS system

Absorption line strengths are measured in this work using the Lick/IDS system of "indices", where a central "feature" bandpass is flanked on either side by "pseudo-continuum" bandpasses. The choice of these bandpasses is dictated by three criteria:

1. proximity to the feature intended to be measured;

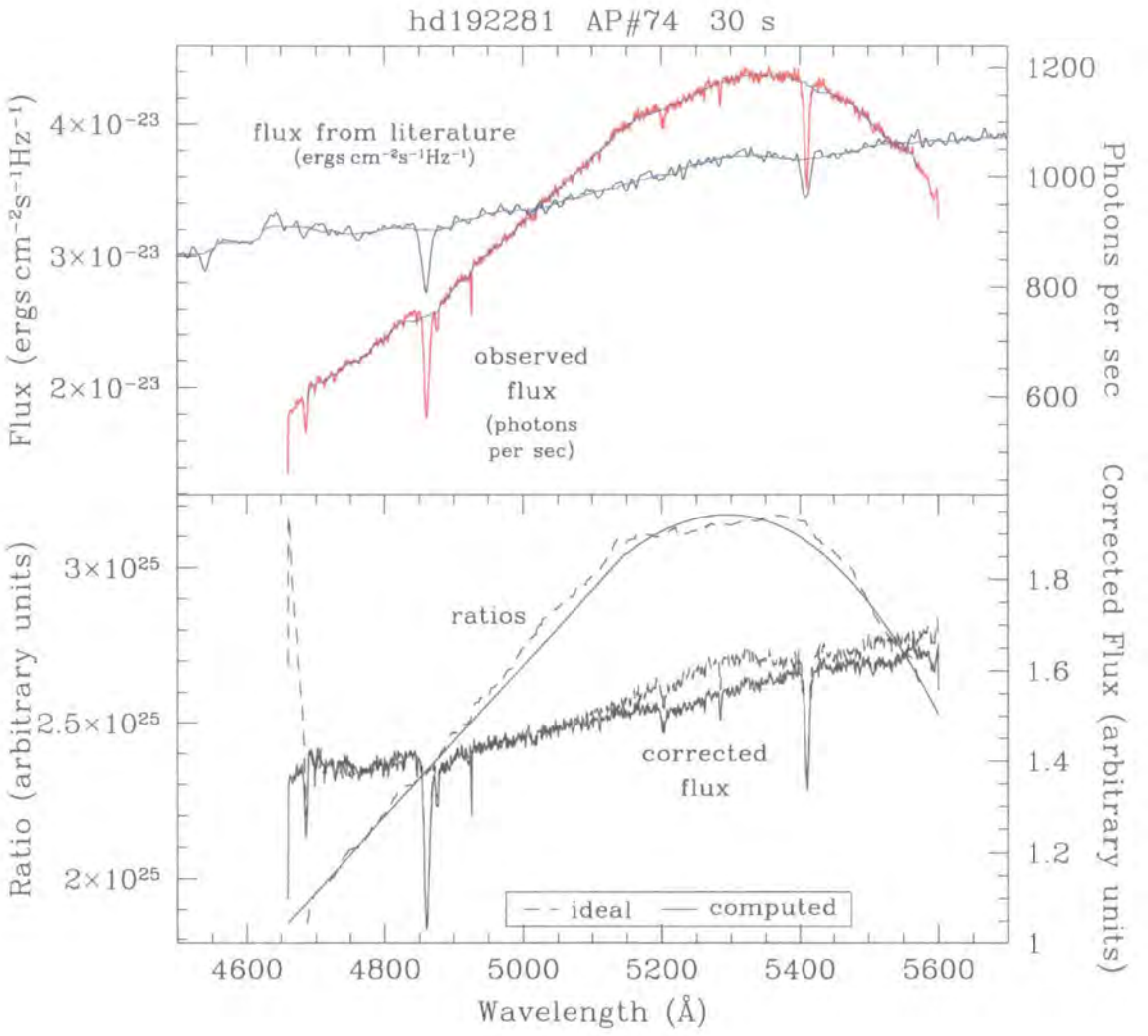

Figure 3.11: Flux calibration summary. The top part of the figure shows both the observed flux data and the flux data from the literature (Massey et al. 1988), both of which have then been smoothed using a moving median window smoothing function of 30Å width which has then been overlaid on the spectra. The bottom part of the figure shows the ideal ratio function for this particular data set (flux standard star HD192281 observed for 30 secs down aperture number 74 for a wavelength range of 4600-5600Å). This is computed by dividing the observed flux by the literature flux for the standard star. The overall ratio function is also shown. This is the function that results from a fit to all the photometrically adjusted ratio functions shown in Figure 3.10. The observed stellar spectra, corrected for the instrumental response function using both the ideal and computed ratio function is also shown.

2. less absorption in the continuum regions than in the central bandpass;

3. maximum insensitivity to velocity-dispersion broadening.

Whilst the last point is unnecessary when measuring stars, in the case of galaxies it is crucial and sets a minimum length for the pseudo-continuum bandpasses.

Table 3.5 presents the bandpasses measured in this work. Column 5 is after the work of Tripicco & Bell (1995), who modelled the Lick/IDS system using stellar spectra. They found that many of the Lick/IDS indices do not in fact measure the abundances of the elements for which they are named.

In addition to the Lick/IDS indices defined in Table 3.5, I also used a number of derived indices to probe the stellar populations of the galaxies. These derived indices are defined below:

$$\langle \mathrm{Fe} \rangle = \frac{\mathrm{Fe5270} + \mathrm{Fe5335}}{2} \tag{3.14}$$

$$\mathrm{Fe3} = \frac{\mathrm{Fe4383} + \mathrm{Fe5270} + \mathrm{Fe5335}}{3} \tag{3.15}$$

$$[\mathrm{MgFe}] = \sqrt{\mathrm{Mg_b} \times \langle \mathrm{Fe} \rangle} \tag{3.16}$$

Over the last decade there has been a growing consensus that the stellar populations of luminous elliptical and lenticular galaxies show evidence of non-solar abundance ratios. In particular magnesium, measured by the Mg_2 and Mg_b indices, when plotted against iron, measured by various Fe indices, does not track solar abundance ratio model predictions and implies [Mg/Fe]>0 (O'Connell 1976; Peletier 1989; Worthey, Faber & González 1992; Weiss, Peletier & Matteucci 1995; Tantalo, Chiosi & Bressan 1998; Worthey 1998; Jørgensen 1999; Kuntschner 2000).

Most of the currently available stellar population models cannot predict the strength of indices as a function of [Mg/Fe] since they are built on databases of solar abundance stars (this is because at present it is difficult to build libraries of high-quality stellar spectra from other galaxies). This can lead to seriously flawed age/metallicity estimates if particular, worst case indicators are used. For example, if non-solar abundance ratios are indeed present in a galaxy stellar population then the use of Mg_b as a metallicity indicator (versus $H\beta$) would result in the

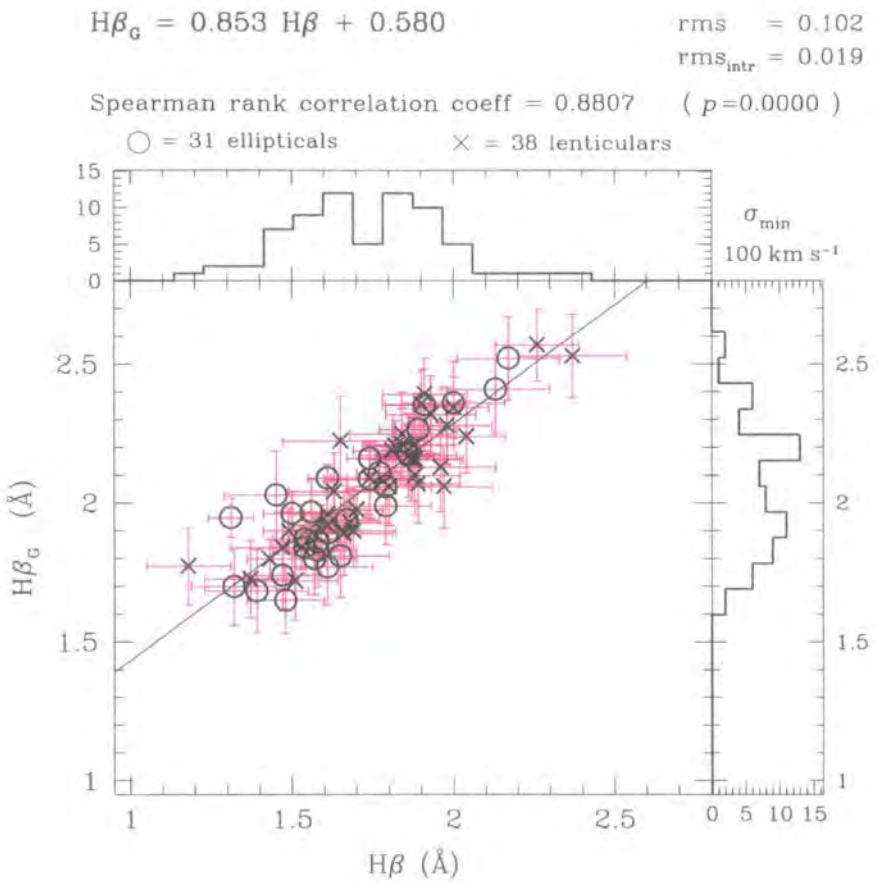

Figure 3.12: Relation between the González (1993) $H\beta_G$ line index and the Lick/IDS $H\beta$ line index. A minimum signal-to-noise of 35 per Å and a lower velocity dispersion cutoff of 100 km s^{-1} have been applied to the early-type galaxy sample presented in this dissertation. A Spearman rank correlation coefficient test confirms the tight correlation between $H\beta_G$ and $H\beta$, with a least squares fit giving $H\beta_G = 0.853\,H\beta + 0.580$ with a rms scatter of 0.102Å.

inferment of mean ages that are younger and mean metallicities that are larger. If the index ⟨Fe⟩ is used it would result in the opposite inferment (see e.g. Worthey 1998; Kuntschner 2000). However, if we combine Mg_b and ⟨Fe⟩ to the index [MgFe] we can significantly reduce the effects of non-solar abundance ratios (see Kuntschner 2000 and Section 5.4).

After González (1993), I use an index $H\beta_G$ to trace the age of galaxy stellar populations, rather than the standard Lick/IDS index $H\beta$. This is because the existing Lick/IDS definition of $H\beta$ has very narrow continuum bands (20Å and 15Å) which results in a high uncertainty on the derived index and a wide central index bandpass (28.75Å) which therefore includes a contribution from an adjacent iron line. The $H\beta_G$ index has a narrower central index bandpass

(20Å) to limit the effect of the iron line and wider continuum bands (30Å and 50Å) to give a better relative measure of the line strength. This index has also been adopted in other recent stellar population studies (see for example Kuntschner 1998 or Jørgensen 1999). There is of course a tight correlation between the $H\beta_G$ and $H\beta$ line indices, as shown in Figure 3.12.

Name	Index Bandpass (Å)	Pseudocontinua (Å)	Units	Measures	Source
(1)	(2)	(3)	(4)	(5)	(6)
C4668†	4634.000–4720.250	4611.500–4630.250	Å	C,(O),(Si)	Lick
		4742.750–4756.500			
Hβ	4847.875–4876.625	4827.875–4847.875	Å	Hβ,(Mg)	Lick
		4876.625–4891.625			
Fe5015	4977.750–5054.000	4946.500–4977.750	Å	(Mg),Ti,Fe	Lick
		5054.000–5065.250			
Mg_1	5069.125–5134.125	4895.125–4957.625	mag	C,Mg,(O),(Fe)	Lick
		5301.125–5366.125			
Mg_2	5154.125–5196.625	4895.125–4957.625	mag	Mg,C,(Fe),(O)	Lick
		5301.125–5366.125			
Mg_b	5160.125–5192.625	5142.625–5161.375	Å	Mg,(C),(Cr)	Lick
		5191.375–5206.375			
Fe5270	5245.650–5285.650	5233.150–5248.150	Å	Fe,C,(Mg)	Lick
		5285.650–5318.150			
Fe5335	5312.125–5352.125	5304.625–5315.875	Å	Fe,(C),(Mg),Cr	Lick
		5353.375–5363.375			

Table 3.5: *continued on next page*

continued from previous page

Name	Index Bandpass (Å)	Pseudocontinua (Å)	Units	Measures	Source
(1)	(2)	(3)	(4)	(5)	(6)
Fe5406	5387.500–5415.000	5376.250–5387.500	Å	Fe	Lick
		5415.000–5425.000			
Hβ_G	4851.320–4871.320	4815.000–4845.000	Å	Hβ,(Mg)	González (1993), pg 116
		4880.000–4930.000			
Fe4930	4903.000–4945.500	4894.500–4907.000	Å	Fe I,Ba II,Fe II	González (1993), pg 34
		4943.750–4954.500			
[OIII]$_1$	4948.920–4978.920	4885.000–4935.000	Å		González (1993), pg 116
		5030.000–5070.000			
[OIII]$_2$	4996.850–5016.850	4885.000–4935.000	Å		González (1993), pg 116
		5030.000–5070.000			
[OIII]$_{hk}$	4998.000–5015.000	4978.000–4998.000	Å		Kuntschner (2000)
		5015.000–5030.000			

† Worthey (1994) called this index Fe4668. In publications after 1995 this index is called C4668 since it turned out to depend more on carbon than on iron.

Table 3.5: Stellar population analysis spectral line index definitions.

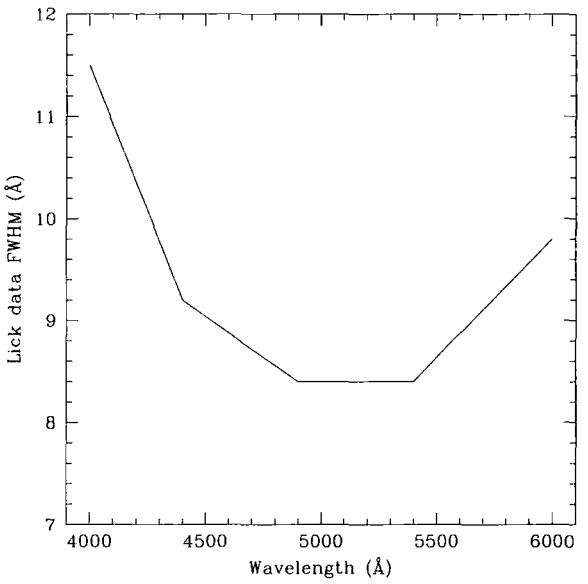

Figure 3.13: Lick/IDS system FWHM. The mean resolution is 9Å which varies to values 30% higher at the ends of the spectra. To measure line strengths on the Lick/IDS system it is necessary to broaden any higher resolution spectra to the same resolution.

3.7.3 Mapping to Lick/IDS system

The Lick/IDS spectra have a mean resolution of 9Å which varies to values 30% higher at the ends of the spectra (Figure 3.13). To ensure my line strength measurements for the Coma cluster are on the Lick/IDS system it is thus necessary to broaden my spectra to the same resolution. This broadening allows safe and comprehensive comparisons between separate data sets without any instrument specific variations affecting the results.

This transformation to the Lick/IDS system is performed by using the known resolution function of a fibre (as discussed in Section 3.5.1) and computing the required transformation function:

$$FWHM_{transformation}(\lambda)^2 = FHWM_{Lick}(\lambda)^2 - FWHM_{fibre}(\lambda)^2 \qquad (3.17)$$

This transformation full width half maximum (FWHM) function, which is a function of wavelength (λ), is then used to broaden the measured spectra to the Lick/IDS resolution. This broadening is done by computing a Gaussian smoothing function with a sigma, σ given by the following standard relationship which matches σ to the required FWHM of the transformation function:

$$\text{sigma, } \sigma = \frac{\text{FWHM}}{2.35482} \tag{3.18}$$

The spectra is then broadened by this Gaussian function to a 3σ limit. Since the transformation function is a function of wavelength, λ this has to be separately computed for each pixel along the spectra.

Figure 3.14 shows the example of galaxy NGC 4889. The fluxed spectrum (after the method of Section 3.7.1) of the galaxy is shown together with the same spectrum broadened to the Lick/IDS system FWHM overlaid on top of it. At the top of the figure is the transformation function used (after Equation 3.17).

3.7.4 Index measurement

Indices are measured by first zero-redshifting galaxy spectra to the laboratory rest frame (or geocentric frame) using the previously measured heliocentric redshifts corrected back to the geocentric rest frame. Then the mean height in each of the two pseudo-continuum regions is determined in either side of the feature bandpass, and a straight line is drawn through the mid-point of each one. The difference in flux between this line and the observed spectrum within the feature bandpass determines the index. For narrow features, the indices are expressed in angstroms (Å) of equivalent width (EW); for broad molecular bands, in magnitudes. Specifically, the average pseudo-continuum flux level is:

$$F_P = \int_{\lambda_1}^{\lambda_2} \frac{F_\lambda}{(\lambda_2 - \lambda_1)} d\lambda \tag{3.19}$$

where λ_1 and λ_2 are the wavelength limits of the pseudo-continuum sideband. If $F_{C\lambda}$ represents the straight line connecting the midpoints of the blue and red pseudo-continuum levels, an equivalent width is then:

$$\text{EW} = \int_{\lambda_1}^{\lambda_2} \left(1 - \frac{F_{I\lambda}}{F_{C\lambda}}\right) d\lambda \tag{3.20}$$

where $F_{I\lambda}$ is the observed flux per unit wavelength and λ_1 and λ_2 are the wavelength limits of the feature passband. Similarly, an index measured in magnitudes is:

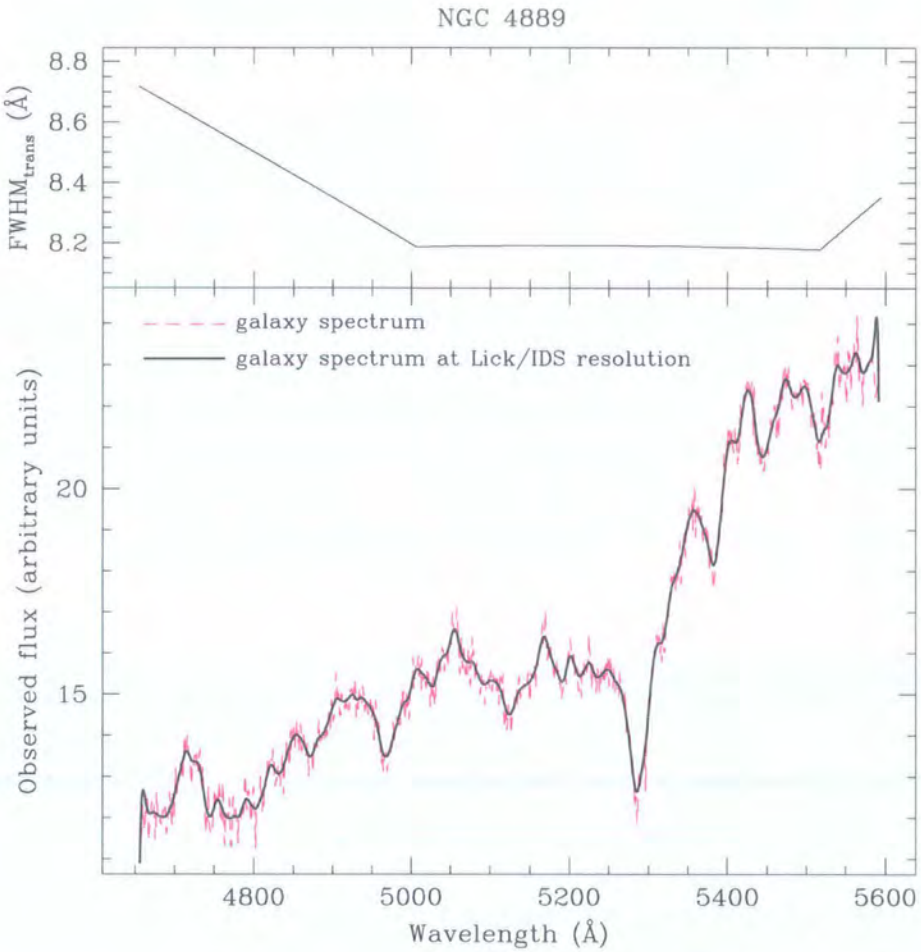

Figure 3.14: NGC 4889 fluxed spectrum overlaid with the spectrum transformed to the Lick/IDS system FWHM (bold line). At the top of the figure, the function to transform the data to the Lick/IDS system FWHM is shown. This function takes into account the variability of the data FWHM down fibres and between fibres as discussed in Section 3.5.1.

$$\mathrm{mag} = -2.5 \log_{10} \left[\left(\frac{1}{\lambda_2 - \lambda_1} \right) \int_{\lambda_1}^{\lambda_2} \frac{F_{I\lambda}}{F_{C\lambda}} d\lambda \right] \tag{3.21}$$

These definitions, after Trager et al. (1998), differ slightly from those used in Burstein et al. (1984) and Faber et al. (1985) for the original 11 IDS indices. In the original scheme, the continuum was taken to be a horizontal line over the feature bandpass at the level $F_{C\lambda}$ taken at the midpoint of the bandpass. This flat rather than sloping continuum would induce erroneous small, systematic shifts in the feature strengths.

An example of the measurement of the $\mathrm{Mg_b}$ index for galaxy NGC 4869, an elliptical galaxy with $b_j = 14.97$ and $\sigma = 203\,\mathrm{km\,s^{-1}}$, is shown in Figure 3.15. All of the Lick indices measured for galaxy NGC 4869 are shown in Figures 3.16 and 3.17.

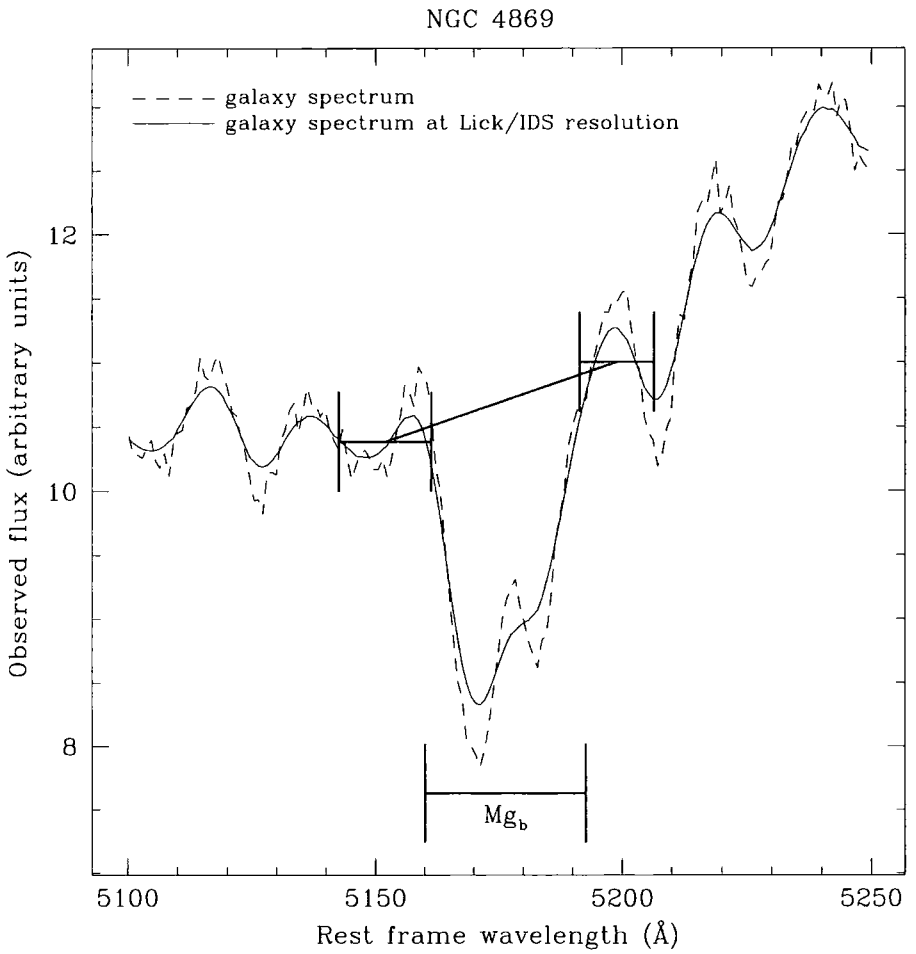

Figure 3.15: Measurement of Mg_b index for galaxy NGC 4869 (an elliptical galaxy with $b_j = 14.97$ and $\sigma = 203\,\mathrm{km\,s^{-1}}$). Fluxed spectrum at rest wavelength is overlaid with the spectrum transformed to the Lick/IDS system FWHM (solid line). The two pseudo-continuum bandpasses are marked either side of the Mg_b feature (also marked); the mean level at the mid-point of the two pseudo-continuum bandpasses are joined by a straight line and the flux in the index feature relative to this line computed. See text in Section 3.7.4 for a more detailed index measurement description.

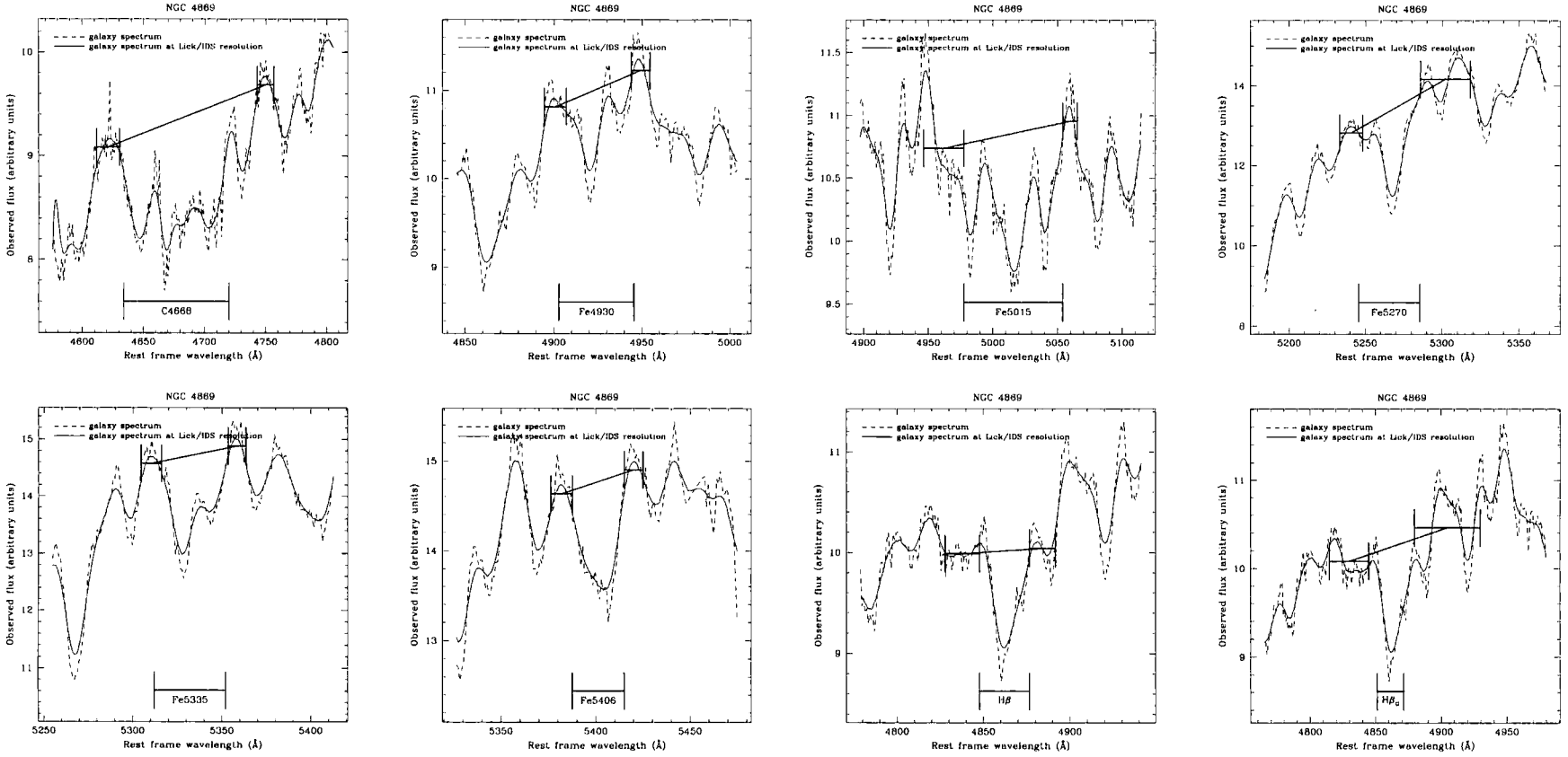

Figure 3.16: Measurement of Lick indices for galaxy NGC 4869 (an elliptical galaxy with $b_j = 14.97$ and $\sigma = 203\,\mathrm{km\,s^{-1}}$). Fluxed spectrum at rest wavelength is overlaid with the spectrum transformed to the Lick/IDS system FWHM (solid line). The two pseudo-continuum bandpasses are marked either side of each Lick index feature (also marked); the mean level at the mid-point of the two pseudo-continuum bandpasses are joined by a straight line and the flux in the index feature relative to this line computed. See text in Section 3.7.4 for a more detailed index measurement description.

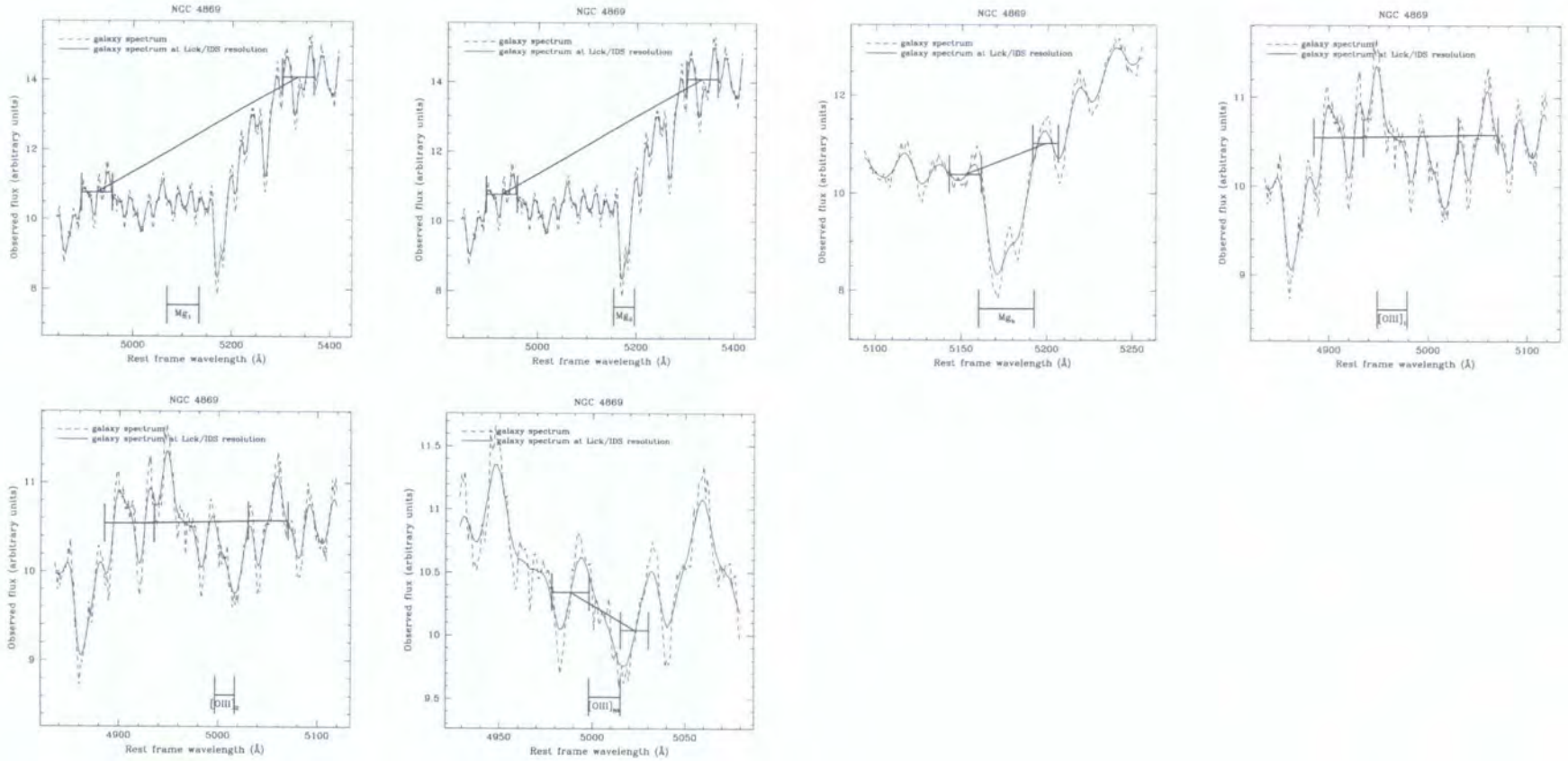

Figure 3.17: Measurement of Lick indices for galaxy NGC 4869 (an elliptical galaxy with $b_j = 14.97$ and $\sigma = 203\,\mathrm{km\,s^{-1}}$). Fluxed spectrum at rest wavelength is overlaid with the spectrum transformed to the Lick/IDS system FWHM (solid line). The two pseudo-continuum bandpasses are marked either side of each Lick index feature (also marked); the mean level at the mid-point of the two pseudo-continuum bandpasses are joined by a straight line and the flux in the index feature relative to this line computed. See text in Section 3.7.4 for a more detailed index measurement description.

3.7.5 Velocity dispersion corrections to absorption line indices

The observed spectrum of a galaxy is the convolution of the integrated spectrum of its stellar population with the instrumental broadening and the distribution of line-of-sight velocities of the stars (parameterised by the velocity dispersion measurement). The instrumental and velocity dispersion broadenings broaden the spectral features which causes the absorption line indices to appear weaker than they intrinsically are.

To successfully probe the stellar population of a galaxy it is necessary to remove the effects of the instrumental and velocity dispersion broadening. This will give an index measurement corrected to zero velocity dispersion. This is done by using the standard stars that were observed during the run. These stars are convolved with a Gaussian function of widths 0–460 $\mathrm{km\,s^{-1}}$ (in steps of 20 $\mathrm{km\,s^{-1}}$). Index strengths are then measured for each convolved spectrum. These values are compared to the zero dispersion values and a correction function computed. For line indices measured in equivalent width this correction function is:

$$\begin{matrix}\text{line index}\\ \text{correction ratio}\end{matrix} = \frac{\text{line index measurement at zero velocity dispersion}}{\text{line index measurement at } \sigma \text{ velocity dispersion}} \tag{3.22}$$

For line indices measured in magnitudes this correction function is:

$$\begin{matrix}\text{line index}\\ \text{correction ratio}\end{matrix} = \begin{matrix}\text{line index measurement at}\\ \text{zero velocity dispersion}\end{matrix} - \begin{matrix}\text{line index measurement at}\\ \sigma \text{ velocity dispersion}\end{matrix} \tag{3.23}$$

A second order polynomial is fit to this ratio function for all the standard stars versus velocity dispersion. This function is then evaluated at the velocity dispersion of the galaxy and the line index corrected to a zero velocity dispersion value. In the case of line indices measured in equivalent width this is done by the following equation:

$$\begin{matrix}\text{velocity dispersion}\\ \text{corrected line index}\end{matrix} = \begin{matrix}\text{line index}\\ \text{measurement}\end{matrix} \times \begin{matrix}\text{line index}\\ \text{correction ratio}\end{matrix} \tag{3.24}$$

and for line indices measured in magnitudes, the corrected line index is calculated using:

$$\begin{matrix}\text{velocity dispersion}\\ \text{corrected line index}\end{matrix} = \begin{matrix}\text{line index}\\ \text{measurement}\end{matrix} + \begin{matrix}\text{line index}\\ \text{correction ratio}\end{matrix} \tag{3.25}$$

		correction $= a0 + a1.\sigma + a2.\sigma^2$			Correction at
Index	Units	a0	a1	a2	$\sigma = 200\,\mathrm{km\,s^{-1}}$
C4668	Å	9.994e–01	–5.779e–06	9.102e–07	× 1.035
Fe4930	Å	9.945e–01	1.087e–04	4.743e–06	× 1.206
Fe5015	Å	9.893e–01	3.144e–04	1.494e–06	× 1.112
Fe5270	Å	9.914e–01	2.538e–04	1.553e–06	× 1.104
Fe5335	Å	1.001e+00	–7.494e–05	5.355e–06	× 1.200
Fe5406	Å	1.007e+00	–2.662e–04	5.744e–06	× 1.184
Hβ	Å	1.003e+00	–6.225e–05	7.326e–07	× 1.020
Hβ_G	Å	9.994e–01	–1.935e–05	1.007e–06	× 1.036
Mg_1	mag	–4.380e–04	1.154e–05	2.233e–08	+ 0.0028
Mg_2	mag	2.811e–05	1.888e–06	3.147e–08	+ 0.0017
Mg_b	Å	9.963e–01	4.038e–05	2.034e–06	× 1.086
$[OIII]_1$	Å	9.941e–01	1.791e–04	2.401e–07	× 1.040
$[OIII]_2$	Å	9.979e–01	5.947e–05	1.373e–06	× 1.065
$[OIII]_{hk}$	Å	1.011e+00	–3.992e–04	1.842e–06	× 1.005

Table 3.6: Velocity dispersion correction polynomial coefficients. The final column also gives the correction for a $\sigma = 200\,\mathrm{km\,s^{-1}}$ galaxy as an example of the scale of the correction necessary. See Section 3.7.5 for more details.

The only additional complication is the exclusion of stars with low Hβ line index values (less than 1.6Å EW) which are unrepresentative of the galaxies I observed and therefore do not give the appropriate zero velocity dispersion transformation function. Hβ is the only index which shows a significant dependence of the correction factor on line strength at a given velocity dispersion (see Kuntschner 2000).

The velocity dispersion correction plots are shown in Figure 3.18 and the correction function polynomial coefficients in Table 3.6.

3.7.6 Lick/IDS offsets

Although the spectral resolution of the Lick/IDS system has been well matched, small systematic offsets in the indices introduced by continuum shape differences are generally present (note that the original Lick/IDS spectra are not flux calibrated). These offsets do not depend on the

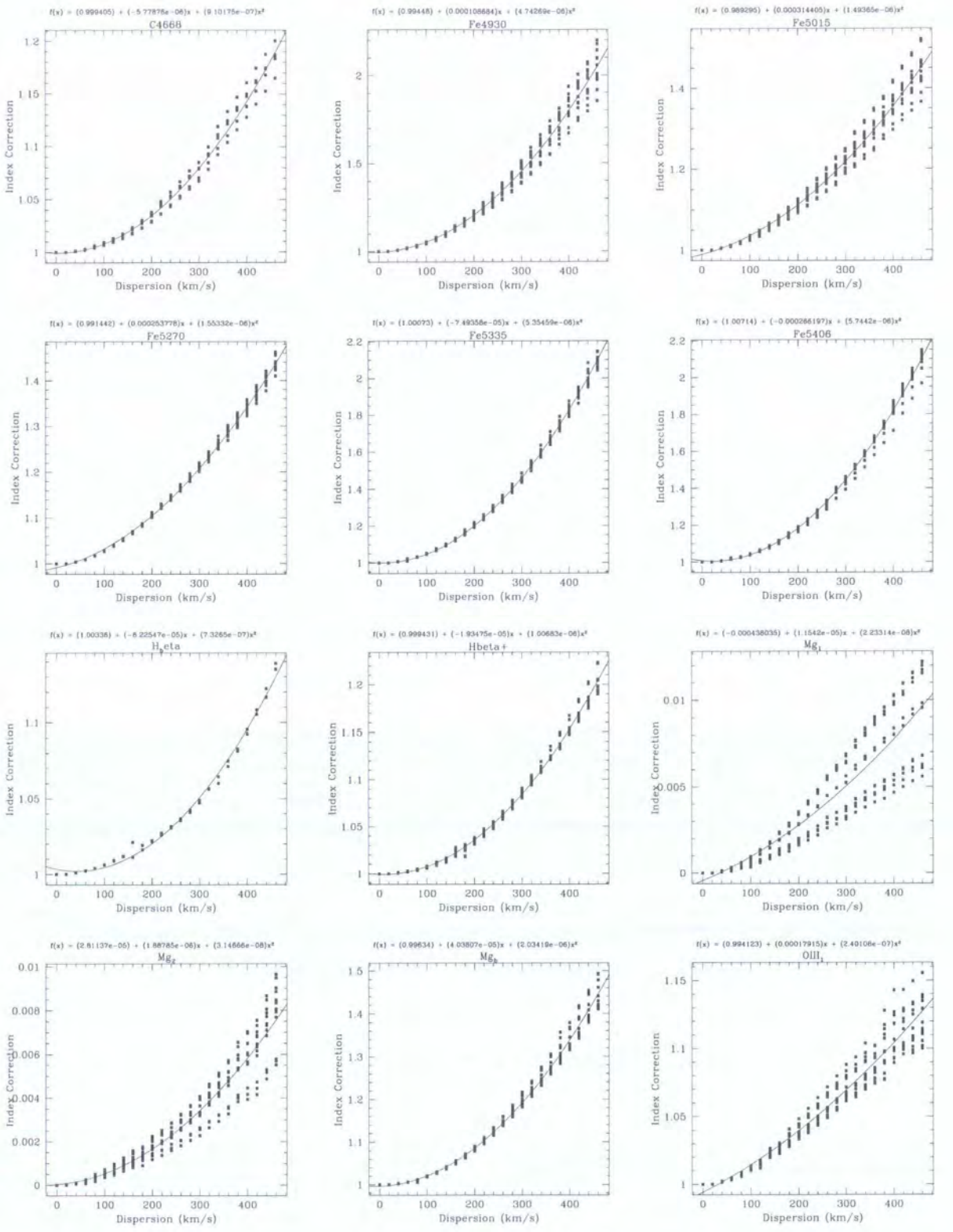

Figure 3.18: Velocity dispersion corrections. Standard stars observed during the run are convolved with a Gaussian function of widths 0–460 km s^{-1} (in steps of 20 km s^{-1}). Index strengths are then measured for each convolved spectrum. These values are compared to the zero dispersion values and a correction function computed. A second order polynomial is fit to this ratio function for all the standard stars versus velocity dispersion. This function can then be evaluated at the velocity dispersion of a galaxy and its line index corrected to a zero velocity dispersion value.

velocity dispersion of the galaxy itself. To establish these offsets I compared my measurements with data from overlapping studies. These comparisons are detailed extensively in Chapter 4. The overall conclusion of Chapter 4 is that there are *no* offsets present in my measurements of the principal indices used in this study, Hβ and [MgFe]. Therefore no correction is made.

3.7.7 Emission correction

An important issue when estimating ages and metallicities from line strength indices is nebular emission. Elliptical galaxies normally contain much less dust and ionized gas than spirals, and were regarded as dust and gas free for a long time. Surveys of large samples of early type galaxies (Phillips et al. 1986; Caldwell 1984; Goudfrooij et al. 1994) have revealed however that 50–60% of the galaxies show weak optical emission lines. The measured emission line strengths of [OII], [Hα] and [NII]λ6584 indicate a presence of only 10^3–$10^5 M_\odot$ of warm ionized gas in the galaxy centre. Additionally, HST images of nearby bright early type galaxies revealed that approximately 70–80% show dust features in the nucleus (van Dokkum & Franx 1995). Stellar absorption line strength measurements can be severely affected if there is emission present in the galaxy (Goudfrooij & Emsellem 1996): nebular Hβ emission on top of the integrated stellar Hβ absorption weakens the Hβ index and leads therefore to incorrectly older age estimates.

In the González 1993 study of the Coma cluster, he noted that [OIII] emission at 4959Å and 5007Å are clearly detectable in about half of the nuclei in his sample and that most of these galaxies also have detectable Hβ emission (see his Fig 4.10). For galaxies in his sample with strong emission, Hβ is fairly tightly correlated with [OIII] such that:

$$\frac{\text{H}\beta \text{ emission}}{[\text{OIII}]} \sim 0.7 \tag{3.26}$$

A statistical correction of:

$$\Delta\text{H}\beta = 0.7\,[\text{OIII}] \qquad \text{after González (1993)} \tag{3.27}$$

was therefore added to Hβ to correct for this residual emission.

Trager et al. (2000a,b) re-examined the accuracy of this correction by studying Hβ/[OIII] among the González 1993 galaxies, supplemented by additional early type galaxies from the emission line catalogue of Ho, Filippenko & Sargent (1997). The sample was restricted to

include only normal, non-AGN Hubble types E through to S0 and well measured objects with Hα > 1.0Å. For 27 galaxies meeting these criteria, they found that Hβ/[OIII] varies from 0.33 to 1.25, with a median value of 0.60. They suggest that a better correction coefficient in Equation 3.27 is 0.6 rather than 0.7, implying that the average galaxy in the González 1993 sample is slightly over-corrected.

$$\Delta \mathrm{H}\beta = 0.6\,[\mathrm{OIII}] \qquad \text{after Trager et al. (2000a,b)} \qquad (3.28)$$

For a median [OIII] strength through the González 1993 $r_e/8$ aperture of 0.17Å, the error due to this correction difference would be 0.02Å or ~3% in age. This systematic error for a typical galaxy is negligible compared to other sources of error.

In this study we adopt the 0.6 multiplicative factor to correct the Hβ index for nebular emission using the [OIII]λ5007Å emission line strength. Whilst there is evidence that this correction factor is uncertain for individual galaxies (Mehlert et al. 2000), it is good in a statistical sense for my sample. After Kuntschner 2000, I adopt a slightly different definition of the [OIII] emission line strength index bandpasses which we have found better measures the true [OIII] emission. After the Lick/IDS system of measuring line indices, I define the feature bandpass to be 4998–5015Å and the continuum side bandpasses to be 4978–4998Å and 5015–5030Å. This new definition does not affect the conclusions of Trager et al. (2000a,b) nor González 1993 on the relationship of [OIII] to Hβ emission. To further improve the measurement of the [OIII] emission line strength in this study, I measure the true emission by first subtracting a zero emission template from a galaxy spectrum and then measuring the residual equivalent width. The zero emission template is simply a standard star. The process is repeated for a set of zero emission templates and an average [OIII] emission line strength calculated. An example of this process is shown in Figure 3.19.

A total of 50 galaxies were found to have 1 sigma evidence of [OIII]λ5007Å emission, with a median emission of 0.228Å giving a median Hβ correction of 0.137Å. The Hβ correction is calculated separately for each galaxy using Equation 3.28 and the true [OIII]λ5007Å emission value for that galaxy. This is summarised in Figure 3.20.

Figure 3.21 shows the environmental dependence of the nebula emission (as traced by [OIII]λ5007Å) surrounding the central dominant galaxy NGC 4874; a plot of this dependence versus radial distance from this galaxy is also shown. The cD galaxies NGC 4874 (located at

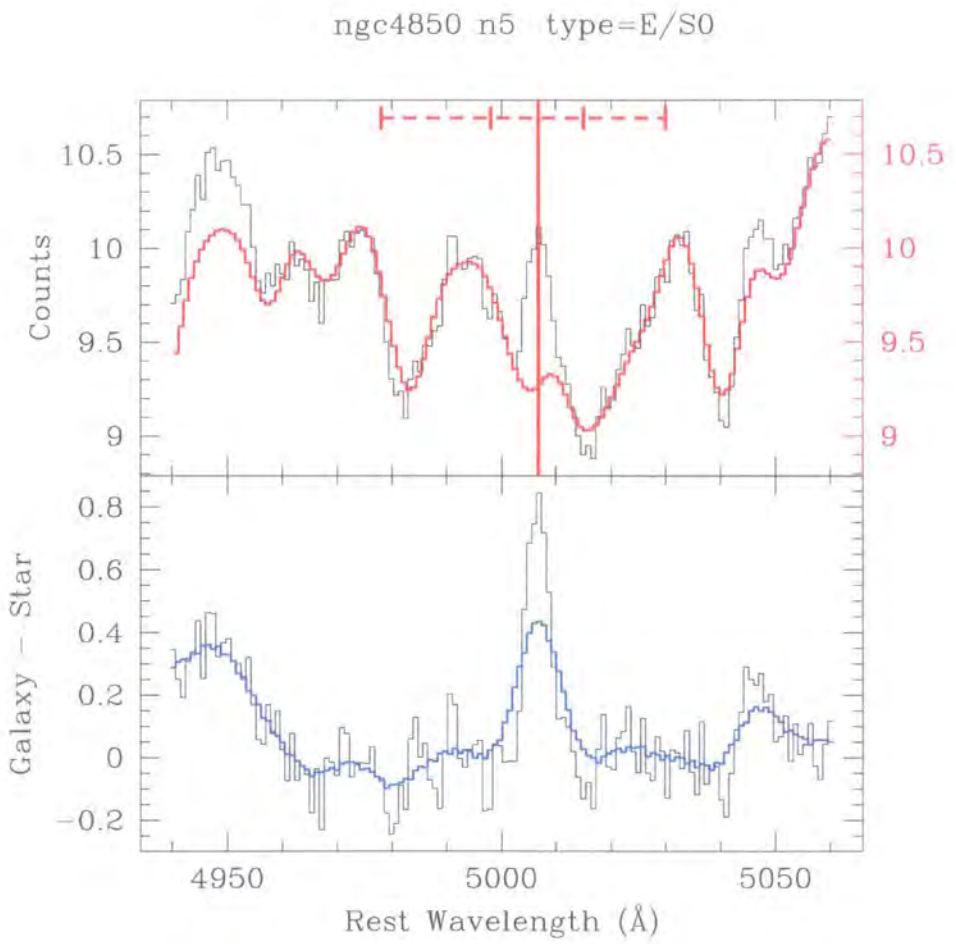

Figure 3.19: Example of [OIII]λ5007Å emission line strength measurement. Galaxy NGC4850, type E/S0, is shown. The top part of the figure shows the fluxed galaxy spectrum (arbitrary units) overlaid with a zero emission template (thick line) whose continuum has been matched to the galaxy by minimising the maximum absolute deviation between the two spectrum. The vertical line marks the centre of the [OIII]λ5007Å feature, whilst the dashed horizontal bar at the very top marks the continuum side bandpasses and width of the feature. The bottom part of the figure shows the difference between the galaxy and the zero emission template (a standard star) overlaid with the difference broadened to the Lick resolution (thick line). The spectrum shows clear [OIII]λ5007Å emission.

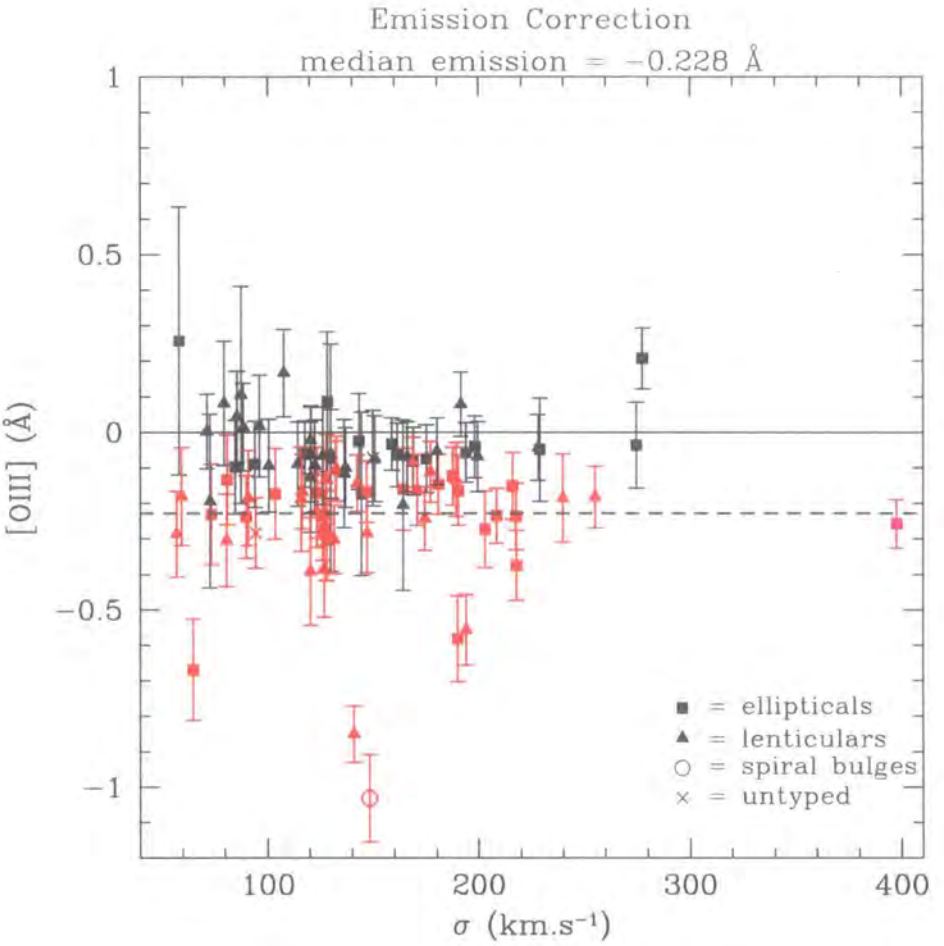

Figure 3.20: Summary of [OIII]λ5007Å emission line strength measurements. A total of 50 galaxies (shown in a lighter shade on the graph) were found to have 1 sigma evidence of [OIII]λ5007Å emission, with a median emission of 0.228Å (marked as a bold dashed line on the graph) giving a median Hβ correction of 0.137Å. The Hβ correction is calculated separately for each galaxy using Equation 3.28 and the true [OIII]λ5007Å emission value for that galaxy.

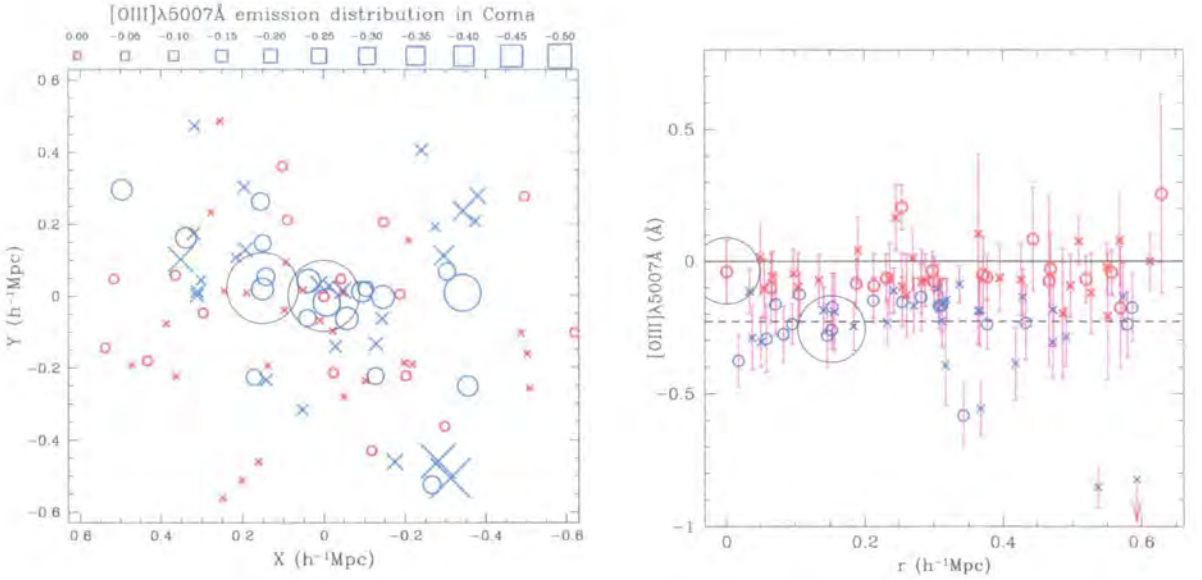

(a) nebula emission map

(b) nebula emission radial dependence

Figure 3.21: Environmental dependence of nebula emission (as measured by [OIII]λ5007Å). Ellipiticals are represented by circles, whilst lenticulars are represented by crosses. See text for a full description of this figure.

$0\,h^{-1}$Mpc in the plots) and NGC 4889 are highlighted by a large black circle surrounding their respective data points. In this figure units of h^{-1} Mpc[‡] are used for the X and Y coordinates and the radial distance. In Figure 3.21(a) the symbol size is scaled to represent the [OIII]λ5007Å value for that galaxy, with the scaling key given at the top. Figure 3.21(b) shows the radial dependence of [OIII]λ5007Å with respect to a galaxies distance from the central dominant galaxy NGC 4874.

Figures 3.21(a) and 3.21(b) show no environmental dependence of nebula emission (as traced by [OIII]λ5007Å). There is a even distribution of galaxies with 1 sigma evidence of emission (blue points) and galaxies with no evidence of emission (red points) across the cluster core. This indicates that there are no large scale dynamic interactions triggering excessive star formation

[‡]These are derived from the angular unit of arcseconds by assuming the cluster radial velocity to be 7200 km s^{-1} and that the Coma cluster peculiar velocity relative to the Hubble flow is zero (Jørgensen et al. 1996). Therefore if I parameterise Hubbles constant at this epoch as $H_0 = 100\ h$ km s^{-1} Mpc^{-1}, where h represents the uncertainty with which we know Hubbles constant, I derive a Coma cluster centre distance of $72\,h^{-1}$ Mpc and a relation of $1.26\,h^{-1}$ Mpc per deg (if I assume $h = 0.5$ this would imply a Hubbles constant of 50 km s^{-1} Mpc^{-1}, giving a relation of 2.51 Mpc per degree).

within the core of the Coma cluster. This implies that any merging event in the cluster cores' history is largely over.

3.8 Errors

The line index measurement errors were calculated by internal comparison during a night and between nights. With the large amount of multiple observations with different fibre configurations and high signal-to-noise data this allows accurate mapping of the random and systematic errors.

The method assumes that the errors have an underlying Gaussian nature and exploits the central limit theorem. Firstly it is necessary to compute the difference between the several line index measurements from the several exposures taken during a night to the "true" line index measurement, taken to be the measurement from the combined exposure for that night (this combined exposure has a much higher signal-to-noise than the separate exposures). To prevent any contaminating systematics, only exposures from a particular night are compared. In this way we can map the random errors as a function of galaxy signal-to-noise (see Section 3.3 for definition of signal-to-noise used) up to a maximum signal-to-noise governed by the individual exposures. To extend this random error mapping to a higher signal-to-noise limit, I use the fact that a number of galaxies were observed every night during the observing run and further compare the line index measurement from the combined exposure for a night to the mean line index measurement from all of the nights, taken here to be the "true" measurement as before. This mapping to higher signal-to-noises is only done for galaxies observed on all nights (often down different fibres due to the different field fibre configurations) to minimise any systematic error contamination of the random error mapping.

Once we have obtained a plot of how the random errors vary with signal-to-noise for a particular line index, we can deduce the error function for that index. The error function is calculated by binning the data by signal-to-noise from 5–35 SN per Å with bin widths of 3 SN per Å (the lower limit is to exclude very low signal-to-noise spectra which would contaminate the derivation of the error function). These bins are then analysed and a standard deviation computed for each bin. For spectra with a signal-to-noise greater than 35 per Å binning is no longer used to prevent contamination by small number statistics. Instead a standard deviation is computed for the differences for all galaxies with a signal-to-noise greater than 35 per Å and

then this lower limit is incremented by the bin width and the standard deviation re-computed. This process is repeated up to a maximum signal-to-noise of 120 per Å. We now have a data set of standard deviation versus signal-to-noise. For the wavelength range 4600–5600Å a 4th order polynomial is fit to the natural log of the variation of standard deviation with signal-to-noise (the function is fit to the natural logarithm of the data to simply fit a smoother function to the data, without any introducing any erroneous high order fluctuations). Figure 3.22 shows the error calculation plots for each line index measured.

To test the correctness of the error determination the central limit theorem is exploited to perform a scale test on the data. If the errors computed are appropriate then the following function will have a standard deviation equal to unity:

$$\text{scale test parameter} = \frac{\text{line index measurement} - \text{true line index value}}{\text{line index error}} \tag{3.29}$$

This scale test is performed on all data with a signal-to-noise greater than 10 per Å to prevent any false contamination by very low signal-to-noise measurements. In our case the true line index value is equal to the mean line index value. It is therefore necessary to include the error on the mean in the line index error.

Figure 3.23 shows the scale test plots for each line index measured. The scale test parameter does indeed have a standard deviation approximately equal to unity, showing that the errors calculated are truly representative.

The computed error function versus signal-to-noise is subsequently used to calculate the errors for all of the line index measurements.

This process is repeated for each line index measured.

An internal systematic error analysis was conducted using the same error calculation data set (shown in Figure 3.22). A mean difference is calculated for data with a S/N$\geq$10 per Å (the same low signal-to-noise cutoff used in the scale test), however only the central 68.3% of this sample (i.e. 1 sigma clipping) are used so that effect of any rogue outliers in the sample distribution is minimised. This conclusion of this analysis is that there are no internal systematic errors either during a night or between nights.

A summary of the results of the error calculation, the scale test and the systematic error analysis is shown in Table 3.7.

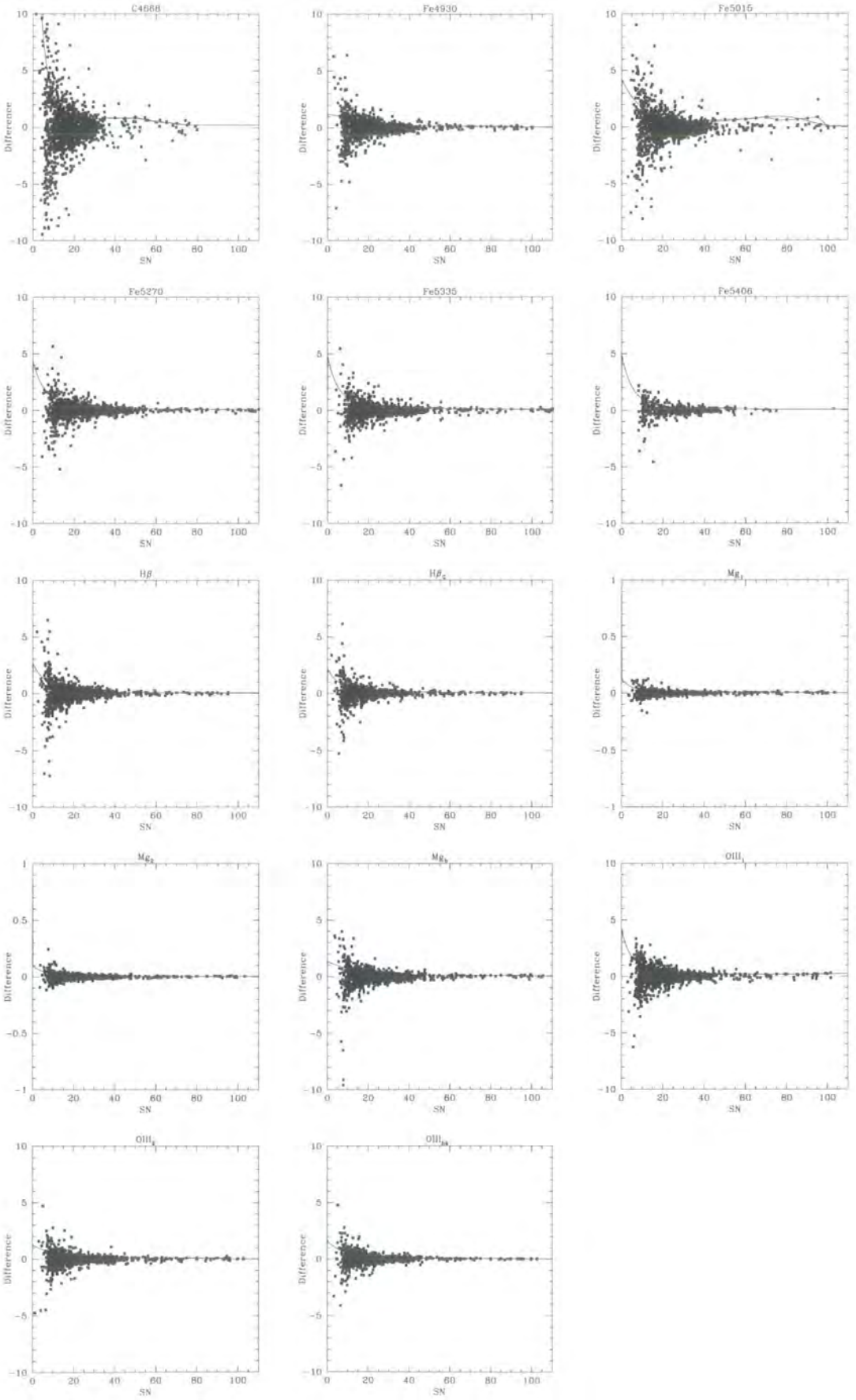

Figure 3.22: Error calculation plots (see text).

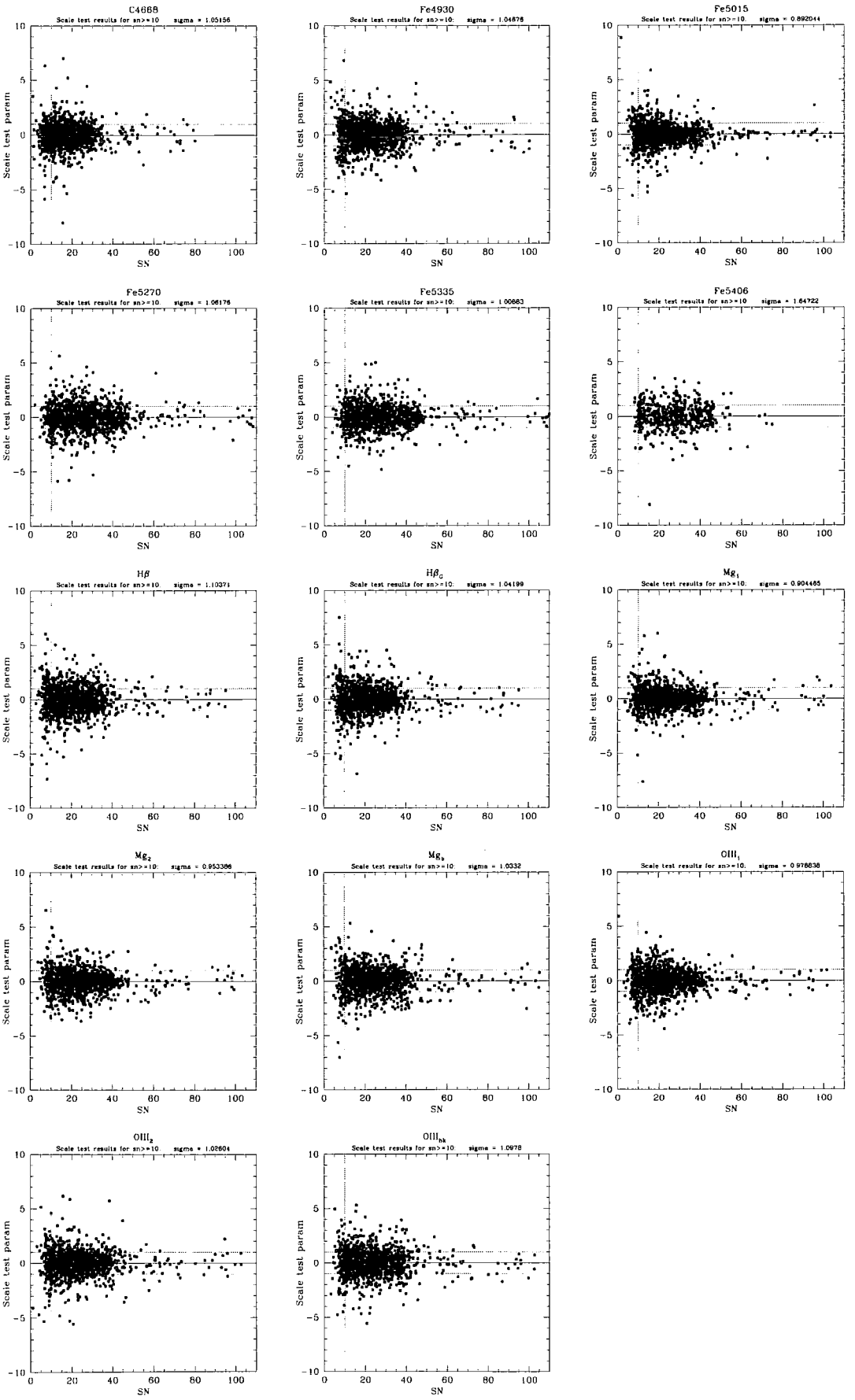

Figure 3.23: Scale test plots (see text).

Index	N_{gals}	Median error		Systematic error	Scale test result
C4668	75	0.638	Å	−0.007 ± 0.019 Å	1.052
Fe4930	97	0.160	Å	−0.002 ± 0.007 Å	1.047
Fe5015	101	0.729	Å	−0.001 ± 0.012 Å	0.892
Fe5270	109	0.136	Å	−0.002 ± 0.005 Å	1.062
Fe5335	109	0.180	Å	0.002 ± 0.006 Å	1.007
Fe5406	54	0.118	Å	−0.000 ± 0.006 Å	1.647
Hβ	95	0.106	Å	−0.002 ± 0.006 Å	1.104
Hβ_G	95	0.103	Å	−0.001 ± 0.004 Å	1.042
⟨Fe⟩	109	0.114	Å	0.002 ± 0.005 Å	1.035
Mg_1	103	0.0090	mag	−0.0002 ± 0.0002 Å	0.904
Mg_2	102	0.0066	mag	−0.0001 ± 0.0002 Å	0.953
Mg_b	103	0.123	Å	0.000 ± 0.005 Å	1.033
[MgFe]	109	0.085	Å	−0.006 ± 0.003 Å	1.034
$[OIII]_1$	99	0.203	Å	0.001 ± 0.006 Å	0.979
$[OIII]_2$	101	0.122	Å	0.003 ± 0.004 Å	1.026
$[OIII]_{hk}$	93	0.075	Å	−0.002 ± 0.004 Å	1.048

Table 3.7: Summary of error calculation results. Median errors for all data with a S/N≥35 per Å are shown. The results of an internal systematic error analysis and of the scale test check are also included (see text). There are no internal systematic errors during a night nor between nights. The only significant scale test result is that for Fe5406; this result implies that the median error should be 0.194Å however since this index is not used in the later stellar population analysis a correction to the error is not applied.

3.9 Final kinematic measurements

Table 3.8 is the final data table listing the heliocentric redshift and velocity dispersion measurements for the galaxies observed in the Coma cluster for this study.

The redshift errors are calculated by combining the error in the wavelength calibration in quadrature with the error resulting from the cross-correlation technique plus the template mis-matching error (calculated through cross-correlating the galaxy spectrum against *different* stellar spectra) and an additional error component factor (calculated from the variance between multiple exposures on a galaxy cross-correlated against a single stellar spectrum).

The velocity dispersion errors are calculated by combining the error resulting from the cross-correlation technique in quadrature with the error resulting from template mis-matching (calculated through cross-correlating the galaxy spectrum against *different* stellar spectra) plus an additional error component factor (calculated from the variance between multiple exposures on a galaxy cross-correlated against a single stellar spectrum).

name	type‡	S/N×	b_j†	$b-r$†	$cz_\odot$ (km/s)	σ (km/s)
d26	S0p	53.5	16.18		7396 ± 12	71.5 ± 9.4
d27	E	41.3	16.45	1.88	7762 ± 12	107.4 ± 3.6
d28	E/S0	57.9	16.67	1.99	5974 ± 12	103.5 ± 4.5
d29	E	33.9	17.81	1.98	6973 ± 16	63.1 ± 8.6
d38	Sbc	38.8	16.20	1.74	5084 ± 12	71.3 ± 14.4
d39	S0/E	76.1	16.17	1.89	5897 ± 12	120.4 ± 3.4
d40	S0	47.0	17.15	1.84	5597 ± 12	72.9 ± 6.2
d42	S0	80.7	16.31	1.86	6016 ± 12	147.1 ± 7.0
d44	S0	55.7	16.57	1.77	7533 ± 12	55.4 ± 11.5

Table 3.8: *continued on next page*

continued from previous page

name	type‡	S/N×	b_j†	$b-r$†	$cz_\odot$ (km/s)	σ (km/s)
d50	SBa	38.4	16.56	1.81	5211 ± 11	54.0 ± 6.3
d53	E	80.2	16.59	1.87	5742 ± 12	128.4 ± 5.4
d57	S0/a	97.4	15.15	1.78	8384 ± 12	142.5 ± 4.7
d59	E	66.0	16.90	1.85	6947 ± 12	129.9 ± 5.0
d62	S0	51.9	16.51	1.90	8359 ± 16	126.2 ± 10.9
d63	S0/a	34.8	16.97	1.90	6675 ± 12	87.3 ± 4.8
d64	E	50.5	16.90	1.79	7010 ± 12	80.9 ± 5.6
d65	S0	65.1	16.15	1.77	6191 ± 12	116.3 ± 3.2
d67	S0	52.3	16.50	1.94	6039 ± 12	150.8 ± 2.0
d71	S0	42.3	16.97	1.85	6919 ± 12	63.9 ± 7.7
d73	E	49.2	17.33	1.84	5440 ± 12	73.5 ± 5.5
d74	E	27.9	17.62	1.82	5793 ± 11	41.1 ± 10.9
d75	S0	48.2	16.13	1.91	6132 ± 13	79.6 ± 5.8
d81	E	48.7	16.10	1.85	5928 ± 12	143.3 ± 2.3
d83	S0	31.3	17.36	1.80	8184 ± 12	37.5 ± 9.8
d84	S0	46.8	16.20	1.98	6553 ± 11	120.6 ± 3.5
d85	E	42.4	17.55	1.59	8251 ± 12	65.0 ± 5.8
d87	E	63.2	16.87	1.79	7770 ± 12	94.0 ± 4.7
d90	S0	52.0	16.93	1.88	5522 ± 12	88.5 ± 4.1
d93	S0	78.4	16.26	2.06	6063 ± 12	136.3 ± 4.9
d98	S0/a	77.7	15.85	1.91	6868 ± 12	130.0 ± 5.4
d107	E	39.3	16.35	1.81	6491 ± 12	87.7 ± 3.7
d108	S0	66.8	16.55	1.85	6424 ± 12	115.9 ± 3.2
d110	S0/E	60.3	16.60	1.93	6948 ± 12	114.4 ± 3.2
d112	E	50.8	16.64	1.78	7433 ± 13	58.3 ± 6.5
d116	SB0	75.7	16.13	1.90	8437 ± 12	123.2 ± 4.2
d117	S0/a	38.2	16.56	1.88	8561 ± 12	93.1 ± 4.8
d123	SB0	50.0	16.47	1.93	7712 ± 12	100.6 ± 3.3

Table 3.8: *continued on next page*

continued from previous page

name	type‡	S/N×	b_j†	$b-r$†	$cz_\odot$ (km/s)	σ (km/s)
d132	S0	46.7	16.63	1.88	7698 ± 12	96.2 ± 3.5
d134	E	63.7	17.37	1.98	7009 ± 12	126.7 ± 2.2
d135	E	36.8	16.98	1.86	8323 ± 12	100.2 ± 3.9
d136	E	82.0	16.57	1.81	5682 ± 11	168.8 ± 2.3
d142	E	79.0	17.06	1.94	7652 ± 12	161.4 ± 2.3
d147	S0	58.9	16.19	1.85	7713 ± 12	107.7 ± 3.9
d153	E	52.7	16.14	1.83	6684 ± 11	127.9 ± 2.7
d154	S0	51.1	16.41	1.78	6833 ± 11	57.1 ± 5.0
d156	E/S0	51.8	16.45		6671 ± 12	84.8 ± 7.9
d157	S0	74.8	16.26	1.81	6107 ± 12	131.5 ± 2.4
d158	S0	28.9	17.20	1.77	6058 ± 12	64.8 ± 6.1
d161	E	86.9	15.19	1.87	7146 ± 12	190.3 ± 4.9
d171	S0	81.0	16.57	1.78	6135 ± 12	127.5 ± 2.9
d181	S0	63.0	16.52	1.87	6090 ± 12	120.3 ± 4.5
d182	S0	44.0	16.84	1.72	5702 ± 12	120.2 ± 2.3
d191	S0	44.4	16.69	1.77	6592 ± 12	90.9 ± 5.2
d192	S0	56.4	16.14	1.79	5435 ± 12	87.5 ± 5.5
d193	E	72.4	16.43	1.82	7567 ± 12	117.6 ± 3.4
d200	S0	104.0	16.08	1.82	7466 ± 12	189.3 ± 4.5
d201	S0	36.5	17.35	1.80	6409 ± 12	59.6 ± 9.4
d204	E	53.1	15.99	1.75	7578 ± 12	126.1 ± 4.0
d207	E	78.1	16.07	1.80	6743 ± 12	146.9 ± 2.8
d209	S0	48.5	16.04	1.77	7182 ± 12	80.7 ± 5.2
d210	E	66.6	15.97	1.88	7252 ± 12	144.6 ± 3.8
d216	Sa	43.5	17.05		7684 ± 12	71.5 ± 13.0
d224	S0	42.2	17.19	1.77	7597 ± 12	59.5 ± 6.2
d225	S0	38.1	16.80	1.53	5879 ± 14	71.7 ± 6.7
d231	S0	62.9	15.78	2.09	7878 ± 13	127.8 ± 5.0

Table 3.8: *continued on next page*

continued from previous page

name	type‡	S/N×	b_j†	$b-r$†	$cz_\odot$ (km/s)			σ (km/s)		
ic3943	S0/a	97.8	15.55	1.97	6789	±	12	168.6	±	1.9
ic3946	S0	73.8	15.28	1.95	5927	±	12	199.6	±	2.6
ic3947	E	93.6	15.94	1.91	5675	±	12	158.8	±	2.1
ic3959	E	95.1	15.27	1.94	7059	±	12	215.9	±	6.0
ic3960	S0	95.5	15.85	1.89	6592	±	12	174.3	±	2.9
ic3963	S0	74.7	15.76	1.87	6839	±	12	122.4	±	3.9
ic3973	S0/a	78.3	15.32	1.88	4716	±	12	228.0	±	3.1
ic3976	S0	105.8	15.80	1.95	6814	±	14	255.2	±	6.4
ic3998	SB0	75.5	15.70	1.90	9420	±	12	136.9	±	4.9
ic4011	E	52.5	16.08	1.82	7253	±	11	123.2	±	3.6
ic4012	E	90.7	15.93	1.86	7251	±	12	180.7	±	3.7
ic4026	SB0	86.3	15.73	1.77	8168	±	12	132.2	±	3.0
ic4041	S0	76.6	15.93	1.90	7088	±	12	132.5	±	2.3
ic4042	S0/a	67.8	15.34	1.86	6371	±	12	170.6	±	3.3
ic4045	E	107.9	15.17	1.85	6992	±	22	217.6	±	3.6
ic4051	E	56.1	14.47	1.82	4994	±	12	228.8	±	2.5
ngc4848	Scd	46.7	14.50	1.56	7199	±	16	106.8	±	7.4
ngc4850	E/S0	105.6	15.39	1.87	6027	±	12	189.8	±	2.5
ngc4851	S0	50.0	16.00	1.95	7861	±	12	126.8	±	3.3
ngc4853	S0p	88.5	14.38	1.66	7676	±	12	140.8	±	4.4
ngc4860	E	76.6	14.69	1.93	7926	±	12	277.3	±	7.2
ngc4864	E	103.4	14.70		6828	±	12	187.6	±	3.2
ngc4867	E	117.3	15.44	1.83	4817	±	12	208.5	±	2.0
ngc4869	E	101.9	14.97	2.06	6844	±	12	203.1	±	4.4
ngc4872	E/S0	80.1	14.79	1.78	7198	±	12	217.8	±	3.4
ngc4873	S0	100.8	15.15	1.91	5818	±	12	176.9	±	1.8
ngc4874	cD	64.4	12.78		7180	±	12	274.5	±	3.3
ngc4875	S0	88.7	15.88	1.96	8014	±	13	180.1	±	4.3

Table 3.8: *continued on next page*

continued from previous page

name	type‡	S/N×	b_j†	$b-r$†	$cz_\odot$ (km/s)	σ (km/s)
ngc4876	E	82.0	15.51	1.91	6710 ± 12	164.1 ± 3.1
ngc4881	E	94.7	14.73	1.87	6730 ± 12	193.9 ± 4.9
ngc4883	S0	85.3	15.43	1.89	8161 ± 12	166.1 ± 2.7
ngc4886	E	41.7	14.83	1.76	6377 ± 12	153.8 ± 2.8
ngc4889	cD	141.6	12.62	1.91	6495 ± 13	397.5 ± 10.1
ngc4894	S0	55.0	15.87	1.74	4640 ± 12	85.6 ± 3.8
ngc4895	S0	106.9	14.38		8458 ± 15	239.8 ± 5.0
ngc4896	S0	67.7	15.06	2.01	5988 ± 18	164.0 ± 2.6
ngc4906	E	91.4	15.44	1.98	7505 ± 12	175.0 ± 4.4
ngc4907	Sb	56.8	14.65	1.74	5812 ± 12	148.2 ± 2.6
ngc4908	S0/E	72.5	14.91	1.87	8710 ± 12	193.9 ± 4.3
ngc4919	S0	121.0	15.06	1.92	7294 ± 12	191.5 ± 3.1
ngc4923	E	109.0	14.78	1.93	5487 ± 12	198.3 ± 3.5
rb58		22.6	17.82	1.81	7634 ± 12	50.1 ± 6.7
rb60		34.7	17.55	1.82	7895 ± 12	57.1 ± 6.8
rb66		30.7	17.71	1.78	5822 ± 11	43.0 ± 6.4
rb71		35.4	17.91	1.65	6839 ± 12	
rb74	SA0	32.2	16.78	1.74	5899 ± 11	63.8 ± 4.8
rb94	SB0/a	28.7	16.69	1.81	5283 ± 12	57.6 ± 6.4
rb122		33.4	17.62	1.82	7082 ± 11	77.3 ± 6.3
rb128		36.0	17.35	1.79	7013 ± 12	150.3 ± 2.4
rb129	unE	58.2	16.86	1.85	5852 ± 12	89.9 ± 4.6
rb131		20.5	17.78	1.44	8209 ± 12	45.7 ± 11.3
rb153		22.9	17.94	1.71	6780 ± 12	51.6 ± 6.9
rb198	SA0	31.1	17.82	1.91	6177 ± 12	54.8 ± 5.7
rb199		21.2	17.57	1.31	8476 ± 46	
rb223		64.0	17.61	1.85	6916 ± 12	94.4 ± 3.6
rb245		25.1	17.74	1.76	6009 ± 11	47.6 ± 6.1

Table 3.8: *continued on next page*

continued from previous page

name	type‡	S/N×	b_j†	$b-r$†	$cz_\odot$ (km/s)	σ (km/s)
gmp0552		47.1	16.34	1.73	7542 ± 12	149.9 ± 2.8
gmp1986		13.3	17.91	1.78	6591 ± 12	22.8 ± 17.8
gmp2421		28.0	17.98	1.90	8132 ± 13	30.0 ± 38.6
gmp2688		30.1	17.71	1.87	7261 ± 12	58.8 ± 4.7
gmp2721		28.7	17.50	1.82	7580 ± 11	55.6 ± 5.4
gmp2783		22.6	17.37	1.83	5360 ± 12	39.8 ± 11.3
gmp3012		25.8	17.49	1.83	8041 ± 12	60.4 ± 8.2
gmp3298		28.5	17.26	1.79	6786 ± 12	51.3 ± 8.3
gmp3585		29.5	17.29		5178 ± 22	52.8 ± 23.1
gmp3588		24.1	17.76	1.72	6033 ± 13	55.5 ± 7.2
gmp3829		18.6	17.44	1.85	8577 ± 12	48.4 ± 5.0
gmp4348		29.2	17.77	1.30	7581 ± 12	56.3 ± 18.8
gmp4420		40.6	17.60	1.86	8520 ± 13	59.6 ± 12.0
gmp4469		15.8	17.69	1.88	7467 ± 12	

× measured at the centre of index Fe5270

† taken from Godwin, Metcalfe & Peach (1983)

‡ taken from Dressler (1980)

Table 3.8: Final kinematic measurements. There are a total of 135 galaxies in this data table.

3.10 Final line strength measurements

Table 3.9 is the final data table listing the line strength measurements for the galaxies observed in the Coma cluster for this study. Only line strengths with a signal-to-noise greater than 35 per Å are included. Where a galaxy was observed on multiple nights with the same wavelength range, the line strength measurements from each night were combined using the square of the signal-to-noise to weight the measurements. The H_β and $H\beta_G$ line strengths given in the table have not been corrected for nebula emission. The [OIII]λ5007Å emission line strength measurement used for this correction is in the column $[OIII]_{sm}$ (see Section 3.7.7).

name	type		C4668	Fe4930	Fe5015	Fe5270	Fe5335	Fe5406	⟨Fe⟩	H_β	$H\beta_G$	Mg_1	Mg_2	Mg_b	[MgFe]	$[OIII]_1$	$[OIII]_2$	$[OIII]_{hk}$	$[OIII]_{sm}$
d26	S0p		0.18	1.38	1.72	1.39	1.22	1.14	1.31	5.16	4.98	0.020	0.088	1.27	1.29	−0.45	0.39	0.15	0.00
			0.83	0.15	0.56	0.15	0.20	0.15	0.12	0.13	0.13	0.009	0.006	0.12	0.09	0.21	0.12	0.10	0.10
d27	E			1.74	5.08	3.02	2.67		2.84			0.112	0.228	3.58	3.19	−0.90	0.91		−0.18
				0.23	0.51	0.19	0.24		0.15			0.008	0.008	0.17	0.11	0.23	0.15		0.15
d28	E/S0		4.55	1.79	4.55	2.66	2.51	1.76	2.58	1.86	2.06	0.124	0.235	3.91	3.18	−0.97	0.75	0.21	−0.17
			0.84	0.15	0.61	0.14	0.18	0.14	0.11	0.12	0.12	0.009	0.006	0.11	0.08	0.21	0.12	0.10	0.13
d29	E					2.36	2.40	1.49	2.38						2.96				−0.55
						0.22	0.25	0.16	0.17						0.13				0.76
d38	Sbc				2.03	1.52	1.51	1.11	1.52			0.082	0.142	1.93	1.71		−0.32		−0.85
					0.51	0.20	0.23	0.16	0.15			0.008	0.007	0.16	0.11		0.15		0.26
d39	S0/E		6.86	1.85	5.01	2.86	2.60	1.69	2.73	1.74	2.08	0.136	0.281	4.08	3.34	−0.70	1.14	0.43	−0.02
			0.80	0.15	0.89	0.11	0.14	0.08	0.09	0.09	0.10	0.010	0.006	0.11	0.07	0.20	0.12	0.06	0.10
d40	S0			1.61	4.10	2.73	2.34	1.50	2.54	2.11	2.31	0.111	0.226	3.78	3.09	−0.69	0.89	0.28	−0.19
				0.18	0.50	0.16	0.21	0.16	0.13	0.15	0.14	0.008	0.007	0.13	0.09	0.21	0.13	0.12	0.24
d42	S0		7.07	1.85	5.75	2.82	2.72	1.81	2.77	1.83	2.08	0.144	0.265	4.43	3.50	−0.69	1.13	0.20	−0.28
			0.78	0.15	0.98	0.10	0.13	0.08	0.08	0.09	0.09	0.010	0.006	0.11	0.07	0.19	0.13	0.06	0.11
d44	S0	E+A	4.01	2.02	2.12	1.85	2.03		1.94	3.23	3.28	0.052	0.122	2.18	2.05	−1.59	−2.55	−3.16	−3.46
			0.83	0.14	0.61	0.14	0.19		0.12	0.12	0.12	0.009	0.006	0.11	0.08	0.20	0.12	0.10	0.31
d50	SBa					2.76	1.87		2.32			0.100	0.224	3.56	2.87				−0.04
						0.20	0.24		0.16			0.008	0.008	0.18	0.12				0.17
d53	E		5.83	1.46	4.85	2.54	2.44	1.49	2.49	1.47	1.74	0.115	0.240	4.17	3.22	−0.13	1.24	0.40	0.09
			0.74	0.15	0.96	0.10	0.13	0.08	0.08	0.08	0.09	0.010	0.006	0.11	0.07	0.20	0.13	0.05	0.20
d57	S0/a		6.00	1.98	5.25	2.84	2.51	1.38	2.68	1.83	2.11	0.114	0.245	3.69	3.14	−0.96	0.98	0.24	−0.14
			0.36	0.11	0.53	0.09	0.12	0.08	0.08	0.07	0.06	0.006	0.006	0.09	0.06	0.19	0.09	0.04	0.08
d59	E		5.69	1.87	5.22	2.43	2.59	1.33	2.51	1.63	1.76	0.122	0.234	3.89	3.12	−0.60	1.03	0.35	−0.07
			0.83	0.15	0.77	0.12	0.17	0.08	0.10	0.10	0.11	0.010	0.006	0.11	0.08	0.20	0.12	0.08	0.32
d62	S0		3.63	1.84	4.25	2.22	1.45	0.23	1.83	1.90	2.19	0.080	0.197	3.41	2.50	−0.76	0.85	0.27	−0.07
			0.82	0.17	0.55	0.15	0.21	0.15	0.13	0.13	0.13	0.009	0.007	0.13	0.09	0.21	0.13	0.11	0.14
d63	S0/a						3.00		2.89						3.29				−0.03
							0.26		0.18						0.14				0.17
d64	E		3.04	1.50	3.81	2.22	1.89	1.32	2.06	1.79	2.05	0.085	0.216	3.34	2.62	−0.30	0.96	0.23	−0.13
			0.81	0.17	0.52	0.16	0.21	0.16	0.13	0.14	0.14	0.008	0.007	0.13	0.09	0.21	0.13	0.11	0.13
d65	S0		6.67	1.89	4.49	2.91	2.54		2.73	1.92	2.22	0.118	0.265	4.07	3.33	−0.71	0.99	0.30	−0.17

Table 3.9: *continued on next page*

continued from previous page

name	type		C4668	Fe4930	Fe5015	Fe5270	Fe5335	Fe5406	⟨Fe⟩	H_β	$H\beta_G$	Mg_1	Mg_2	Mg_b	[MgFe]	$[OIII]_1$	$[OIII]_2$	$[OIII]_{hk}$	$[OIII]_{sm}$
			0.84	0.15	0.69	0.13	0.17		0.11	0.11	0.11	0.010	0.006	0.11	0.08	0.21	0.12	0.08	0.11
d67	S0			1.52	5.73	2.87	2.40	1.44	2.64	1.47	1.84	0.133	0.254	4.47	3.43	−0.81	1.22	0.33	−0.07
				0.18	0.54	0.16	0.22	0.17	0.13	0.14	0.14	0.010	0.007	0.13	0.09	0.21	0.13	0.11	0.12
d71	S0			2.10	4.22	2.69	2.05		2.37	2.25	2.28	0.073	0.178	3.38	2.83	−0.73	0.68		−0.13
				0.19	0.49	0.18	0.22		0.14	0.16	0.15	0.008	0.007	0.14	0.10	0.22	0.14		0.25
d73	E	E+A	4.70	1.82	4.57	2.45	2.20	1.67	2.32	2.04	2.21	0.079	0.180	2.81	2.56	−0.63	0.94	0.16	−0.23
			0.81	0.16	0.52	0.15	0.20	0.15	0.13	0.14	0.13	0.008	0.007	0.12	0.09	0.21	0.13	0.12	0.14
d75	S0		7.63	2.38	5.67	2.99	2.31	1.61	2.65	1.57	1.68	0.091	0.201	2.95	2.79	−1.27	0.99	0.54	0.08
			0.81	0.16	0.53	0.15	0.20	0.14	0.13	0.13	0.13	0.009	0.007	0.12	0.09	0.21	0.13	0.12	0.17
d81	E			1.95	4.98	2.46	2.15		2.30	2.13	2.41	0.140	0.291	4.70	3.29	−0.72	0.98	0.33	−0.03
				0.19	0.52	0.17	0.22		0.14	0.15	0.14	0.009	0.007	0.14	0.10	0.22	0.14	0.11	0.13
d84	S0			2.17	5.33	2.88	2.56	1.77	2.72	1.96	2.13	0.132	0.275	3.97	3.29	−0.54	1.33	0.34	−0.06
				0.20	0.51	0.17	0.22	0.16	0.14	0.16	0.15	0.009	0.007	0.14	0.10	0.22	0.14	0.12	0.13
d85	E			1.65	4.18	2.91	2.14		2.53			0.083	0.205	3.50	2.98	−0.83	0.65	−0.22	−0.67
				0.21	0.50	0.19	0.23		0.15			0.008	0.007	0.16	0.11	0.22	0.14	0.13	0.14
d87	E		5.66	1.74	4.74	2.85	2.84		2.85	1.90	2.10	0.077	0.201	3.51	3.16	−0.25	1.19	0.27	−0.09
			0.84	0.14	0.68	0.13	0.17		0.11	0.11	0.11	0.010	0.006	0.11	0.08	0.20	0.12	0.08	0.12
d90	S0		4.92	2.15	5.63	3.02	2.85	1.58	2.93	1.97	2.19	0.110	0.239	3.74	3.31	−0.85	1.18	0.39	0.01
			0.81	0.16	0.52	0.15	0.20	0.15	0.13	0.14	0.13	0.009	0.007	0.13	0.09	0.21	0.13	0.10	0.12
d93	S0		5.68	1.85	4.31	2.69	2.42	1.51	2.56	1.65	1.84	0.111	0.237	4.16	3.26	−0.53	0.82	0.24	−0.12
			0.68	0.15	1.00	0.10	0.13	0.08	0.08	0.08	0.09	0.010	0.006	0.11	0.07	0.19	0.13	0.06	0.15
d98	S0/a		8.40	1.99	5.79	2.96	3.11		3.04	2.26	2.55	0.115	0.259	4.10	3.53	−1.13	1.26	0.45	−0.06
			0.73	0.15	0.98	0.10	0.13		0.08	0.08	0.09	0.010	0.006	0.11	0.07	0.19	0.13	0.06	0.12
d107	E				4.94	2.71	2.26		2.49			0.084	0.207	3.67	3.02		1.00		−0.05
					0.51	0.20	0.24		0.16			0.008	0.008	0.17	0.12		0.15		0.14
d108	S0		6.06	1.86	4.78	2.76	2.51	1.55	2.63	1.69	1.96	0.121	0.250	4.30	3.36	−0.75	0.94	0.23	−0.19
			0.84	0.14	0.75	0.12	0.16	0.09	0.10	0.10	0.11	0.010	0.006	0.11	0.08	0.20	0.12	0.08	0.15
d110	S0/E		6.67	1.71	5.24	2.69	2.49	1.84	2.59	1.66	1.88	0.107	0.243	4.21	3.30	−0.71	1.14	0.31	−0.09
			0.84	0.15	0.65	0.13	0.18	0.09	0.11	0.11	0.12	0.010	0.006	0.11	0.08	0.21	0.12	0.09	0.12
d112	E	E+A	3.71	2.21	4.09	2.38	2.48		2.43	3.34	3.40	0.032	0.133	2.32	2.37	−0.92	1.02	0.61	0.26
			0.82	0.15	0.55	0.15	0.20		0.12	0.13	0.13	0.008	0.006	0.12	0.09	0.21	0.12	0.11	0.38
d116	SB0		7.42	1.85	5.33	2.72	2.80		2.76	1.90	2.26	0.117	0.251	4.14	3.38	−1.00	1.04	0.22	−0.22
			0.77	0.15	0.92	0.11	0.14		0.09	0.09	0.10	0.010	0.006	0.11	0.07	0.20	0.13	0.06	0.10
d117	S0/a					2.29	2.37		2.33			0.092	0.209	3.86	3.00				−0.31
						0.21	0.25		0.16			0.008	0.008	0.18	0.12				0.15
d123	SB0			2.24	5.04	3.02				2.37	2.53			3.62		−1.00	0.97	0.37	−0.09
				0.17	0.52	0.16				0.14	0.14			0.13		0.21	0.13	0.11	0.13

Table 3.9: *continued on next page*

continued from previous page

name	type	C4668	Fe4930	Fe5015	Fe5270	Fe5335	Fe5406	⟨Fe⟩	H_β	$H\beta_G$	Mg_1	Mg_2	Mg_b	[MgFe]	$[OIII]_1$	$[OIII]_2$	$[OIII]_{hk}$	$[OIII]_{sm}$
d132	S0		1.86	5.03	2.62	2.92		2.77	1.56	1.87	0.132	0.288	4.85	3.66	-0.91	1.18	0.48	0.02
			0.18	0.51	0.17	0.22		0.14	0.15	0.14	0.008	0.007	0.14	0.10	0.21	0.13	0.12	0.14
d134	E	5.71	0.82	4.39	2.60	2.25	1.81	2.43	1.74	1.92	0.114	0.262	4.39	3.26	-0.03	1.07	0.24	-0.28
		0.84	0.15	0.68	0.13	0.18	0.13	0.11	0.11	0.11	0.010	0.006	0.11	0.08	0.21	0.12	0.08	0.12
d135	E				3.22	2.78		3.00			0.070			3.37				-0.39
					0.22	0.26		0.17			0.008			0.13				0.17
d136	E	7.06	3.52	5.33	2.60	2.48	1.78	2.54	1.48	1.65	0.117	0.263	4.51	3.39	-1.25	1.08	0.38	-0.08
		0.72	0.16	1.01	0.10	0.14	0.09	0.09	0.08	0.09	0.010	0.006	0.11	0.07	0.20	0.13	0.05	0.10
d142	E	7.77	2.02	4.95	2.80	2.62	1.54	2.71	1.58	1.83	0.149	0.301	4.70	3.57	-0.76	1.03	0.35	-0.06
		0.76	0.16	0.97	0.11	0.14	0.08	0.09	0.09	0.09	0.011	0.006	0.11	0.07	0.20	0.13	0.05	0.09
d147	S0	7.22	1.91	5.35	2.81	2.62		2.72	1.97	2.06	0.092	0.230	3.56	3.11	-1.11	1.41	0.66	0.17
		0.84	0.15	0.60	0.14	0.19		0.12	0.12	0.12	0.009	0.006	0.12	0.08	0.21	0.12	0.09	0.12
d153	E		1.68	3.06	2.81	2.26		2.54	1.39	1.51	0.146	0.290	4.16	3.25	-0.54	0.64	0.13	-0.29
			0.17	0.53	0.16	0.21		0.13	0.14	0.13	0.009	0.007	0.13	0.09	0.21	0.13	0.11	0.13
d154	S0		1.70	4.09	2.62	2.30		2.46	1.14	1.59	0.096	0.233	3.18	2.80	-0.44	0.71	0.05	-0.29
			0.17	0.51	0.16	0.20		0.13	0.14	0.14	0.008	0.007	0.13	0.09	0.21	0.13	0.11	0.12
d156	E/S0	5.53	1.83	4.18	2.23	2.41		2.32	1.91	2.07	0.104	0.229	3.80	2.97	-0.35	0.98	0.26	-0.10
		0.83	0.15	0.55	0.15	0.20		0.12	0.12	0.13	0.009	0.007	0.12	0.09	0.21	0.12	0.11	0.13
d157	S0	6.23	1.64	5.27	3.02	2.46	1.64	2.74	1.84	2.03	0.129	0.269	4.26	3.42	-0.55	1.11	0.17	-0.30
		0.78	0.15	0.90	0.11	0.15	0.08	0.09	0.09	0.10	0.010	0.006	0.11	0.07	0.20	0.13	0.06	0.10
d161	E	8.48	1.82	4.96	2.82	2.59		2.71	1.53	1.83	0.143	0.297	4.83	3.62	-0.61	1.04	0.25	-0.16
		0.57	0.16	0.98	0.09	0.13		0.08	0.07	0.08	0.009	0.006	0.11	0.07	0.19	0.12	0.05	0.10
d171	S0	7.39	2.19	5.50	2.81	2.62	1.64	2.72	1.91	2.22	0.116	0.270	4.17	3.37	-0.74	1.17	0.26	-0.23
		0.75	0.15	0.97	0.10	0.13	0.08	0.08	0.09	0.09	0.010	0.006	0.11	0.07	0.20	0.13	0.05	0.09
d181	S0	5.91	2.06	5.05	2.92	2.62	1.66	2.77	1.84	2.06	0.106	0.247	3.81	3.25	-0.62	1.03	0.25	-0.13
		0.84	0.15	0.71	0.13	0.17	0.08	0.11	0.10	0.11	0.010	0.006	0.11	0.08	0.21	0.12	0.09	0.16
d182	S0		1.32	3.84	2.19	2.20		2.20	1.65	1.99	0.131	0.256	4.34	3.09	-0.17	0.71	0.03	-0.39
			0.21	0.51	0.18	0.23		0.15	0.17	0.15	0.009	0.008	0.15	0.11	0.22	0.14	0.12	0.15
d191	S0		2.19	4.27	2.62	2.29		2.45	1.88	2.05	0.116	0.228	3.57	2.96	-0.70	0.87	0.13	-0.18
			0.20	0.50	0.18	0.22		0.14	0.17	0.15	0.008	0.007	0.15	0.10	0.22	0.14	0.12	0.13
d192	S0	6.70	2.24	4.43	2.70	2.24	1.67	2.47	2.03	2.18	0.099	0.234	3.55	2.96	-0.60	1.13	0.53	0.11
		0.83	0.15	0.59	0.14	0.18	0.08	0.11	0.12	0.12	0.009	0.006	0.11	0.08	0.21	0.12	0.10	0.30
d193	E	6.62	1.75	5.47	3.03	2.73		2.88	1.57	1.80	0.128	0.268	4.09	3.43	-0.70	1.23	0.32	-0.06
		0.80	0.15	0.86	0.11	0.15		0.09	0.09	0.10	0.010	0.006	0.11	0.07	0.20	0.12	0.07	0.09
d200	S0	8.17	1.95	5.38	2.75	2.86		2.81	1.87	2.10	0.136	0.287	4.36	3.50	-0.78	1.18	0.33	-0.13
		0.26	0.07	0.25	0.09	0.17		0.10	0.07	0.06	0.005	0.007	0.07	0.06	0.20	0.06	0.03	0.10
d201	S0				3.15	2.38	1.74	2.77						2.83				-0.05

Table 3.9: *continued on next page*

continued from previous page

name	type		C4668	Fe4930	Fe5015	Fe5270	Fe5335	Fe5406	⟨Fe⟩	H_β	$H\beta_G$	Mg_1	Mg_2	Mg_b	[MgFe]	$[OIII]_1$	$[OIII]_2$	$[OIII]_{hk}$	$[OIII]_{sm}$
						0.22	0.25	0.17	0.17						0.12				0.17
d204	E		7.39	1.83	4.05	2.56	2.46		2.51	2.00	2.22	0.129	0.244	4.11	3.21	−0.78	0.69	0.17	−0.23
			0.82	0.17	0.54	0.16	0.21		0.13	0.14	0.13	0.009	0.007	0.13	0.09	0.21	0.13	0.11	0.13
d207	E		6.32	2.09	5.85	3.10	3.17		3.13	1.79	1.96	0.120	0.255	4.07	3.57	−1.05	1.16	0.30	−0.17
			0.76	0.15	0.96	0.11	0.14		0.09	0.09	0.09	0.010	0.006	0.11	0.07	0.20	0.13	0.06	0.09
d209	S0			2.03	4.57	2.68	2.99		2.84	2.14	2.25	0.102	0.229	3.61	3.20	−0.82	0.93	0.09	−0.30
				0.17	0.51	0.16	0.21		0.13	0.14	0.14	0.008	0.007	0.13	0.09	0.21	0.13	0.11	0.13
d210	Ep		4.37	2.29	5.35	2.78	2.87	1.41	2.83	1.62	1.88	0.139	0.277	4.20	3.44	−0.53	1.19	0.28	−0.17
			0.85	0.15	0.77	0.12	0.16	0.08	0.10	0.10	0.11	0.011	0.006	0.11	0.08	0.21	0.12	0.09	0.23
d216	Sa	E+A		1.72	4.23	2.49	2.20		2.35	2.82	2.83	0.067	0.158	2.84	2.58	−0.58	1.00		0.06
				0.20	0.50	0.17	0.22		0.14	0.16	0.15	0.008	0.007	0.14	0.10	0.22	0.14		0.20
d224	S0			1.62	4.50	2.58	2.60		2.59	1.85	2.16	0.108	0.203	3.02	2.80	-0.00	1.17	0.18	−0.18
				0.20	0.49	0.19	0.23		0.15	0.16	0.15	0.008	0.007	0.15	0.11	0.22	0.14	0.13	0.14
d225	S0				4.04	1.99	1.88	1.39	1.94			0.087	0.204	3.41	2.57	−0.62	0.90		0.23
					0.51	0.20	0.24	0.16	0.15			0.008	0.007	0.17	0.11	0.23	0.15		0.21
d231	S0		5.82	2.18	5.05	2.94	2.48	1.58	2.71	1.85	2.05	0.104	0.245	4.06	3.32	−0.75	1.04	0.27	−0.13
			0.84	0.15	0.70	0.13	0.18	0.08	0.11	0.11	0.11	0.010	0.006	0.11	0.08	0.21	0.12	0.09	0.13
ic3943	S0/a		7.18	1.76	5.97	3.11	2.82	1.81	2.97	1.53	1.79	0.148	0.284	4.07	3.47	−0.44	1.36	0.31	−0.08
			0.44	0.13	0.73	0.09	0.13	0.09	0.08	0.07	0.07	0.007	0.006	0.10	0.06	0.18	0.10	0.03	0.07
ic3946	S0		7.76	1.61	4.47	2.89	2.58		2.73	1.89	2.07	0.147	0.282	4.52	3.52	−0.33	1.09	0.33	−0.07
			0.82	0.16	0.91	0.12	0.17		0.10	0.09	0.10	0.012	0.007	0.12	0.08	0.20	0.13	0.06	0.10
ic3947	E		5.86	1.94	4.93	2.61	2.47	1.56	2.54	1.58	1.86	0.137	0.272	4.38	3.34	−0.81	1.03	0.37	−0.03
			0.54	0.14	0.91	0.09	0.12	0.08	0.08	0.07	0.07	0.008	0.006	0.11	0.07	0.18	0.11	0.04	0.07
ic3959	E		7.92	1.65	5.66	2.84	2.87	1.80	2.85	1.53	1.79	0.159	0.298	4.94	3.75	−0.64	1.20	0.29	−0.15
			0.47	0.14	0.81	0.09	0.14	0.09	0.08	0.07	0.07	0.009	0.007	0.10	0.07	0.19	0.11	0.04	0.09
ic3960	S0		8.84	1.78	4.73	2.98	2.56		2.77	1.59	1.76	0.172	0.311	4.85	3.66	−0.69	0.90	0.22	−0.24
			0.50	0.14	0.86	0.09	0.12		0.08	0.07	0.07	0.008	0.006	0.11	0.07	0.18	0.11	0.04	0.09
ic3963	S0		4.27	1.80	5.44	2.72	2.65	1.73	2.69	1.54	1.74	0.098	0.227	4.03	3.29	−0.50	1.15	0.27	−0.09
			0.77	0.15	0.93	0.11	0.14	0.08	0.09	0.09	0.09	0.010	0.006	0.11	0.07	0.20	0.13	0.07	0.13
ic3973	S0/a		7.32	1.49	6.22	2.99	2.79	1.64	2.89	2.04	2.24	0.136	0.268	4.42	3.57	−0.59	1.44	0.44	−0.04
			0.80	0.17	0.99	0.11	0.16	0.09	0.10	0.09	0.10	0.012	0.007	0.12	0.08	0.20	0.13	0.06	0.09
ic3976	S0		7.28	1.51	5.36	2.86	2.84	1.82	2.85	1.44	1.70	0.159	0.298	4.94	3.75	−0.66	1.12	0.23	−0.18
			0.37	0.11	0.49	0.10	0.18	0.10	0.10	0.07	0.06	0.008	0.008	0.08	0.07	0.19	0.08	0.03	0.09
ic3998	SB0		7.34	1.97	5.63	2.96	2.71		2.83	1.83	2.08	0.128	0.273	4.16	3.43	−1.03	1.15	0.37	−0.10
			0.74	0.15	0.97	0.11	0.12		0.08	0.08	0.09	0.008	0.006	0.11	0.07	0.20	0.13	0.07	0.11
ic4011	E		8.29	1.64	4.54	2.69	2.37		2.53	2.17	2.42	0.146	0.273	4.30	3.30	−0.82	0.75	0.16	−0.17
			0.81	0.17	0.54	0.16	0.21		0.13	0.14	0.13	0.009	0.007	0.13	0.09	0.21	0.13	0.11	0.13

Table 3.9: *continued on next page*

continued from previous page

name	type		C4668	Fe4930	Fe5015	Fe5270	Fe5335	Fe5406	⟨Fe⟩	H_β	$H\beta_G$	Mg_1	Mg_2	Mg_b	[MgFe]	$[OIII]_1$	$[OIII]_2$	$[OIII]_{hk}$	$[OIII]_{sm}$
ic4012	E		8.55	1.90	5.23	2.79	2.80		2.79	1.86	2.09	0.148	0.286	4.55	3.56	−0.67	1.10	0.27	−0.14
			0.56	0.15	0.97	0.09	0.13		0.08	0.07	0.08	0.009	0.006	0.11	0.07	0.19	0.12	0.04	0.08
ic4026	SB0		8.32	2.13	5.88	3.04	3.10	1.75	3.07	2.00	2.28	0.131	0.271	4.13	3.56	−1.00	1.21	0.32	−0.11
			0.63	0.15	1.00	0.10	0.12	0.08	0.08	0.08	0.08	0.009	0.006	0.11	0.07	0.19	0.12	0.04	0.08
ic4041	S0		8.06	1.93	6.38	2.92	2.80	1.95	2.86	1.88	2.15	0.128	0.285	4.34	3.52	−1.04	1.30	0.36	−0.10
			0.78	0.15	0.90	0.11	0.14	0.08	0.09	0.09	0.10	0.010	0.006	0.11	0.07	0.20	0.13	0.06	0.09
ic4042	S0/a		8.13	1.52	4.43	2.59	2.69		2.64	1.38	1.63	0.135	0.278	4.47	3.43	−0.85	0.90	0.20	−0.16
			0.85	0.16	0.76	0.13	0.18		0.11	0.10	0.11	0.011	0.007	0.12	0.08	0.21	0.13	0.08	0.10
ic4045	E		8.40	2.14	5.39	2.90	2.68	1.73	2.79	1.73	2.00	0.161	0.314	4.77	3.65	−0.89	0.96	0.21	−0.24
			0.29	0.09	0.33	0.10	0.18	0.09	0.10	0.07	0.06	0.006	0.007	0.07	0.06	0.20	0.07	0.03	0.09
ic4051	E			2.05	4.63	3.22	2.50		2.86	1.45	2.03	0.200	0.371	5.71	4.04	−0.50	0.96	0.40	−0.05
				0.20	0.58	0.16	0.23		0.14	0.14	0.14	0.011	0.008	0.14	0.10	0.22	0.14	0.11	0.14
ngc4848	Scd			1.84	2.01	2.08	2.54		2.31	−4.82	−4.39	0.100	0.200	4.05	3.06	−1.89	−2.40	−2.95	−3.26
				0.18	0.52	0.17	0.21		0.14	0.14	0.14	0.009	0.007	0.14	0.10	0.21	0.13	0.12	0.43
ngc4850	E/S0		6.70	1.88	4.92	2.77	2.57	1.74	2.67	1.28	1.57	0.127	0.264	4.40	3.43	−0.93	0.63	−0.14	−0.58
			0.45	0.12	0.52	0.09	0.17	0.09	0.10	0.07	0.07	0.006	0.007	0.08	0.06	0.19	0.09	0.03	0.12
ngc4851	S0			1.65	4.63	2.55	2.68		2.62	1.85	2.02	0.101	0.256	4.10	3.27	−0.50	0.90	0.08	−0.38
				0.17	0.53	0.16	0.22		0.14	0.14	0.13	0.009	0.007	0.13	0.09	0.21	0.13	0.11	0.14
ngc4853	S0p	E+A	5.09	1.45	4.01	2.73	2.04		2.38	1.98	2.11	0.078	0.160	2.95	2.65	−0.98	0.09	−0.44	−0.85
			0.54	0.15	0.94	0.09	0.12		0.08	0.07	0.08	0.008	0.006	0.11	0.07	0.18	0.12	0.04	0.08
ngc4860	E		9.27	1.86	5.46	2.89	3.28		3.08	1.33	1.70	0.174	0.342	5.57	4.14	−0.78	1.31	0.54	0.21
			0.78	0.19	1.05	0.12	0.18		0.11	0.09	0.10	0.013	0.008	0.13	0.08	0.20	0.14	0.06	0.09
ngc4864	E		7.55	1.74	5.25	2.59	2.53		2.56	1.61	1.82	0.150	0.286	4.47	3.38	−0.60	1.19	0.30	−0.12
			0.34	0.10	0.47	0.09	0.14		0.08	0.07	0.06	0.006	0.007	0.09	0.06	0.19	0.08	0.03	0.08
ngc4867	E		7.43	1.45	5.11	2.74	2.57	1.70	2.65	1.61	1.95	0.149	0.297	4.55	3.47	−0.82	0.94	0.20	−0.23
			0.26	0.03	0.14	0.10	0.18	0.09	0.10	0.07	0.06	0.006	0.007	0.07	0.06	0.23	0.04	0.04	0.08
ngc4869	E		8.29	1.85	4.96	2.99	2.84	1.86	2.92	1.52	1.81	0.164	0.311	4.86	3.77	−0.59	0.94	0.18	−0.27
			0.36	0.10	0.48	0.09	0.16	0.09	0.09	0.07	0.06	0.007	0.007	0.09	0.06	0.19	0.08	0.03	0.11
ngc4872	E/S0		8.76	2.00	5.85	2.96	3.05		3.01	1.91	2.13	0.153	0.299	4.90	3.84	−1.04	1.03	0.11	−0.37
			0.82	0.17	1.01	0.11	0.15		0.09	0.09	0.10	0.012	0.007	0.12	0.08	0.20	0.13	0.06	0.10
ngc4873	S0		6.08	1.53	5.65	2.73	2.58	1.73	2.65	1.70	1.91	0.146	0.300	4.52	3.47	−0.70	1.24	0.34	−0.11
			0.47	0.13	0.72	0.09	0.14	0.09	0.08	0.07	0.07	0.007	0.006	0.10	0.06	0.18	0.10	0.03	0.09
ngc4874	cD		8.78	2.24	5.62	3.10	3.10		3.10	1.65	1.81	0.153	0.306	4.86	3.88	−0.76	1.28	0.46	−0.04
			0.89	0.19	0.76	0.15	0.23		0.14	0.11	0.12	0.013	0.009	0.13	0.09	0.22	0.13	0.09	0.12
ngc4875	S0		7.16	1.74	2.45	2.83	2.63		2.73	1.62	1.87	0.163	0.289	4.62	3.55	−1.11	0.73	0.36	−0.05
			0.55	0.15	0.96	0.09	0.13		0.08	0.07	0.08	0.009	0.006	0.11	0.07	0.19	0.12	0.05	0.09
ngc4876	E		6.83	1.88	5.15	2.60	2.70	1.62	2.65	1.92	2.18	0.117	0.262	3.95	3.24	−0.62	1.10	0.27	−0.16

Table 3.9: *continued on next page*

continued from previous page

name	type	C4668	Fe4930	Fe5015	Fe5270	Fe5335	Fe5406	⟨Fe⟩	H_β	$H\beta_G$	Mg_1	Mg_2	Mg_b	[MgFe]	$[OIII]_1$	$[OIII]_2$	$[OIII]_{bk}$	$[OIII]_{sm}$
		0.65	0.16	1.02	0.10	0.13	0.08	0.08	0.08	0.09	0.010	0.006	0.11	0.07	0.19	0.12	0.06	0.12
ngc4881	E	8.30	1.43	5.02	2.86	2.54		2.70	1.67	1.94	0.152	0.291	4.85	3.62	−0.66	1.05	0.38	−0.06
		0.58	0.15	0.94	0.09	0.13		0.08	0.07	0.08	0.009	0.006	0.11	0.07	0.19	0.12	0.04	0.08
ngc4883	S0	6.99	2.03	5.67	3.06	2.77		2.91	1.63	1.97	0.135	0.289	4.39	3.58	−0.58	1.33	0.36	−0.07
		0.61	0.15	1.00	0.09	0.12		0.08	0.08	0.08	0.009	0.006	0.11	0.07	0.19	0.12	0.05	0.10
ngc4886	E			6.06	2.85	3.36		3.11			0.164	0.290	4.76	3.85	−1.53	0.90		−0.04
				0.53	0.20	0.25		0.16			0.009	0.008	0.17	0.12	0.23	0.16		0.16
ngc4889	cD	9.59	1.49	6.10	3.06	3.03	2.31	3.05	1.86	2.03	0.186	0.361	5.39	4.05	−0.74	1.12	0.12	−0.26
		0.29	0.04	0.17	0.12	0.27	0.14	0.15	0.07	0.06	0.010	0.011	0.08	0.08	0.25	0.05	0.05	0.07
ngc4894	S0		1.33	5.02	3.03	3.18		3.11	1.25	1.97	0.096	0.233	3.51	3.30	−0.31	1.39	0.51	0.04
			0.17	0.53	0.15	0.19		0.12	0.14	0.14	0.009	0.007	0.12	0.09	0.21	0.13	0.10	0.13
ngc4895	S0	6.76	1.83	4.96	3.11	2.74		2.93	1.48	1.78	0.142	0.286	4.54	3.65	−0.69	1.04	0.24	−0.18
		0.26	0.06	0.17	0.10	0.19		0.11	0.07	0.06	0.006	0.008	0.07	0.06	0.22	0.05	0.03	0.12
ngc4896	S0	6.38	1.96	5.68	2.87	2.56	1.62	2.71	1.94	2.24	0.149	0.303	4.26	3.40	−0.81	1.09	0.24	−0.20
		0.84	0.15	0.77	0.12	0.17	0.08	0.11	0.10	0.11	0.011	0.007	0.11	0.08	0.21	0.13	0.08	0.24
ngc4906	E	7.63	1.96	4.85	2.78	2.60	1.75	2.69	1.55	1.85	0.154	0.306	4.66	3.54	−0.53	1.07	0.32	−0.07
		0.56	0.15	0.97	0.09	0.12	0.09	0.08	0.07	0.08	0.009	0.006	0.11	0.07	0.19	0.12	0.04	0.10
ngc4907	SBb	8.16	1.86	4.10	3.05	2.90		2.97	1.12	1.55	0.133	0.268	4.21	3.54	−1.06	0.01	−0.58	−1.03
		0.83	0.17	0.58	0.15	0.20		0.13	0.13	0.13	0.010	0.007	0.12	0.09	0.21	0.13	0.10	0.12
ngc4908	S0/E	5.98	1.25	5.24	2.77	2.76		2.76	1.18	1.44	0.141	0.265	4.46	3.51	−1.26	0.48	−0.09	−0.56
		0.83	0.16	0.89	0.12	0.17		0.10	0.10	0.10	0.012	0.007	0.12	0.08	0.20	0.13	0.07	0.10
ngc4919	S0	7.96	1.77	5.49	3.04	2.79	2.20	2.92	1.61	1.92	0.143	0.308	4.49	3.62	−0.78	1.37	0.54	0.08
		0.26	0.03	0.14	0.10	0.17	0.09	0.10	0.07	0.06	0.005	0.007	0.07	0.06	0.23	0.04	0.04	0.09
ngc4923	E	8.56	1.77	5.13	2.79	2.84	1.85	2.82	1.78	2.11	0.155	0.303	4.62	3.61	−0.59	1.19	0.38	−0.04
		0.31	0.09	0.35	0.10	0.18	0.09	0.10	0.07	0.06	0.006	0.007	0.07	0.06	0.20	0.07	0.03	0.09
rb60	-				2.79	2.78	1.52	2.79						2.95				−0.05
					0.22	0.25	0.16	0.17						0.13				0.20
rb71	-				1.60	1.25	2.88	1.42						1.58				−0.65
					0.22	0.25	0.17	0.17						0.13				0.16
rb128	-				2.16	1.77		1.96						2.73				−0.23
					0.23	0.27		0.18						0.14				0.18
rb129	unE	5.27	1.72	4.15	2.41	2.08	1.29	2.24	1.82	2.05	0.117	0.254	3.73	2.89	−0.49	0.74	0.09	−0.24
		0.83	0.15	0.58	0.14	0.19	0.12	0.12	0.12	0.12	0.009	0.006	0.12	0.08	0.21	0.12	0.10	0.12
rb223	-	6.22	1.66	4.51	2.75	2.55	1.66	2.65	2.04	2.14	0.116	0.235	3.99	3.25	−0.91	0.80	0.12	−0.28
		0.84	0.14	0.68	0.13	0.17	0.12	0.11	0.11	0.11	0.010	0.006	0.11	0.08	0.20	0.12	0.08	0.10
gmp0552	-		1.67	4.27	2.40	2.08		2.24	1.49	1.77	0.121	0.257	4.51	3.18	−0.71	0.91	0.28	−0.07
			0.20	0.52	0.18	0.23		0.15	0.15	0.15	0.009	0.008	0.14	0.10	0.22	0.14	0.12	0.13

Table 3.9: *continued on next page*

continued from previous page

name	type	C4668	Fe4930	Fe5015	Fe5270	Fe5335	Fe5406	⟨Fe⟩	H_β	$H\beta_G$	Mg_1	Mg_2	Mg_b	[MgFe]	$[OIII]_1$	$[OIII]_2$	$[OIII]_{hk}$	$[OIII]_{sm}$
gmp4420	-		1.63	4.94	2.00	2.21		2.11	2.31	2.74	0.068	0.179	3.05	2.54	−0.50	1.26		0.21
			0.19	0.49	0.18	0.20		0.13	0.15	0.14	0.008	0.006	0.14	0.10	0.22	0.14		0.29

Table 3.9: Final line strength measurements. Only line strengths with a signal-to-noise of 35 per Å or greater are shown. Errors are given below the line strength measurement. The H_β and $H\beta_G$ line strengths given in the table have not been corrected for nebula emission (this can be done using $[OIII]_{sm}$ and referral to Section 3.7.7). There are a total of 110 galaxies in this data table.

Chapter 4

Comparison with other data

4.1 Introduction

The purpose of this chapter is to determine the quality of the data presented in this dissertation through comparison with data from previous studies of the Coma cluster. Any systematic differences between studies (due to a combination of a systematic error between the comparison data sets plus a systematic offset between either or both of the data sets and the Lick/IDS line index measurement system) can be determined and removed to bring all line index measurements onto the same Lick/IDS system.

4.2 Method of analysis

Offsets throughout this chapter are calculated as follows:

$$\text{offset} = \text{data from this study} - \text{data from comparison study} \tag{4.1}$$

Offsets are only calculated against data from this study with a signal-to-noise of 35 per Å or higher. This offset is plotted versus the data from this study and a mean offset for the sample calculated. Only the central 68.3% of the sample (i.e. 1 sigma clipping) are used to calculate the sample statistics; this minimises the effect of any rogue outliers in the sample distribution. The following statistics are calculated for each sample:

— mean offset to this study;
— root mean squared of sample differences (rms);
— intrinsic root mean squared of sample differences, taking into account the sample errors (rms_{intr});
— a Lilliefors test of the differences distribution against the null hypothesis that the sample data has *no offset* from this study ($p_{\text{zero offset}}$);

— a Lilliefors test of the differences distribution against the null hypothesis that the sample data has an *offset* from this study (p_{offset});
— a Spearman rank correlation coefficient test against the null hypothesis that the sample differences are *not correlated* against the sample value from this study (p_{spearman}).

The intrinsic root mean squared of sample differences is a test of the quality of the data errors: if the errors on the parameters are correct, then the intrinsic rms should be negligible (i.e. close to zero). The Lilliefors test is similar to the standard Kolmogorov-Smirnov (KS) test, except that it uses parameters derived from the sample for its test hypothesis whereas the KS test uses independent parameters. The Spearman rank correlation coefficient tests for any correlation between the sample differences and the parameter from this study; no correlation is expected (any highly significant correlation detected would imply some other problems with one or the other of the data sets). Where a statistical p-value is quoted it should be interpreted according to:

$p < 0.05$	the null hypothesis is strongly inconsistent with the data
$0.05 < p < 0.10$	there is a marginal inconsistency with the null hypothesis
$p > 0.10$	there is little or no evidence against the null hypothesis

The main hypothesis for this analysis is that there could be a mean offset between the data in this dissertation and that in the published data sets used for comparison, but that there should be no offset between each of the comparison data sets since these have already been corrected to a common Lick/IDS system.

4.3 Comparison data sets

The following studies are compared to the results from this study:

- **Seven Samurai comparison:** In the late 1980's a large scale survey of elliptical galaxies was conducted by Alan Dressler, Donald Lynden-Bell, David Burstein, Roger Davies, Sandra Faber, Roberto Terlevich and Gary Wegner (Djorgovski & Davis 1987; Dressler et al. 1987; Faber et al. 1987) — a group collectively known as the "Seven Samurai" (a reference to the great film by Akira Kurosawa telling of seven great samurai out to combat injustice). The group observed 35 galaxies within the Coma cluster using the Lick 3m

telescope with a slit of dimension $1.5'' \times 4''$ and using the Las Campanas Observatory with a $4'' \times 4''$ slit. Out of this total there are 23 galaxies in common, with measurements of $\log \sigma$, $cz_{\odot}$ and Mg_2.

- **Lick/IDS comparison:** The full Lick/IDS database, from which the indices were originally defined, contains absorption line strength measurements of 381 galaxies, 38 globular clusters and 460 stars based upon 7417 spectra observed in the 4000–6400Å region between 1972 and 1984 at the Lick Observatory with the Cassegrain Image Dissector Scanner spectrograph. It was one of the largest homogeneous collections of galaxy spectral line data of its time. Trager et al. (1998) presents the absorption line strength measurements of the 381 galaxies and 38 globular clusters. In this sample there are measurements of 22 galaxies in the Coma cluster, 11 of which are in common with this study. There are measurements of: C4668, Fe5015, Fe5270, Fe5335, Fe5406, Hβ, $\langle$Fe$\rangle$, Mg_1, Mg_2, Mg_b and [MgFe] all corrected to an equivalent long-slit of dimension $1.4'' \times 4''$.

- **Comparison with Jørgensen (1999):** Jørgensen (1999) measured mean ages and metal abundances for the stellar populations in a sample of early-type galaxies in the central 64 arcmin $\times$ 70 arcmin of the Coma cluster. Using two different telescopes (with different instrument setups) she obtained a sample of 71 galaxies with Mg_2, $\langle$Fe$\rangle$ and Hβ_G absorption line index measurements, corrected to a fibre diameter of $3.4''$. This sample is 61 per cent complete to a total magnitude of 15.05 in Gunn r. This data set became the definitive spectroscopic data set for the Coma cluster and as such represents a key test of the data presented in this study. There are 36 galaxies from this sample in common, with measurements of Hβ, Hβ_G, Mg_1, Mg_2, Mg_b, $\langle$Fe$\rangle$, [MgFe] and $\log \sigma$.

- **Comparison with Mehlert et al. (2000):** Mehlert et al. (2000) measured high signal-to-noise long-slit spatially resolved spectra, giving line strength measurements as a function of radius from the galaxy centre, for a sample of 35 early-type Coma cluster galaxies (27 in the inner square degree, 8 at a distance greater than 40 arcmin). The spectra were centred on the 5170Å Mg triplet and were taken along the major axes of the galaxies. The inner sample of 27 galaxies is complete to a Kron-Cousins magnitude R = 12.63 mag and 42% complete in the range 12.63 mag $< R <$ 14.06 mag. The outer sample is complete to R = 13.21 mag. There are 18 galaxies from this sample in common, with measurements of Hβ, Mg_b, $\langle$Fe$\rangle$ and [MgFe]. Following Jørgensen et al. (1995a,b) and Mehlert et al. (2000)

I calculate a "slit-equivalent" radius to match the aperture width used in this study and convert the long-slit absorption line strengths to fibre equivalent values.

- **Comparison with Kuntschner et al. (2001):** Kuntschner et al. (2001) re-analysed a spectroscopic run from the SMAC programme (Smith et al. 2000) to measure line indices to investigate the Mg–σ and $\langle$Fe$\rangle$–σ relations from a sample of 72 early-type galaxies from a selection of cluster and group environments. They published data for 31 galaxies in the Coma cluster, all with S/N$\geq$30 and corrected to a fibre diameter of 3.4″. There are 14 galaxies from this sample in common, with measurements of $\log\sigma$, Hβ, Mg$_2$, Mg$_b$ and $\langle$Fe$\rangle$.

- **Comparison with the SMAC programme:** The SMAC or "Streaming Motions of Abell Clusters" programme constructed a catalogue of fundamental plane data within 12,000 km s^{-1} to analyse streaming motions (Hudson et al. 1999, Smith et al. 2000). They published measurements for 56 Coma cluster galaxies (Hudson et al. 1999), corrected to a fibre diameter of 3.4″. There are 34 galaxies from this sample in common, with measurements of Mg$_2$, $\log\sigma$ and cz$_\odot$.

Appendix A tabulates the common data between these studies and this dissertation. This appendix also details the conversion of the long-slit data of Mehlert et al. (2000) to equivalent fibre data.

4.4 Results of comparisons

Table 4.1 and Figures 4.1 to 4.8 show the results of the comparisons between the data in this study and that published in the studies described in Section 4.3. The mean offset between this data set and the comparison data set is indicated in the figures by the dashed horizontal line. These initial comparisons have no correction for different aperture sizes. This is dealt with in Section 4.5.

The initial hypothesis was that there could be a mean offset between this data and the comparison data sets, but that there should be *no offset* between each of the comparison data sets (since they have been corrected to the Lick/IDS system). Therefore a careful analysis would yield a correction factor to place the data in this study fully into the Lick/IDS system. This is necessary as it is common for small systematic errors to be present in the data. Previous studies

have often used large numbers ($\sim$ 20 or more) of high signal-to-noise Lick standard stars to compute these offsets. However in this study, because of observing time constraints (the observations were performed over 6 *half-nights*), it was not possible to observe large numbers of these standard stars. Therefore it is necessary to compare lower signal-to-noise galaxy observations to compute the corrections. This does however have the benefit of ensuring that the *galaxy* line indices are on a common system, as the other method only ensures that the *stellar* line indices are on the Lick/IDS system.

Considering the primary indices of interest, Hβ and [MgFe], the comparison analysis gives an initial mean offset in Hβ of -0.092 ± 0.026 Å and a mean offset in [MgFe] of 0.004 ± 0.021 Å. This implies that the [MgFe] values in this study require no correction to place them fully on the Lick/IDS system (as the computed correction is not statistically significant), but that the Hβ do require a correction. However a closer examination of the comparison data sets shows that there are systematic offsets between them. For instance, if the Jørgensen (1999) data set (which has the largest offset from this study for the line indices Hβ and [MgFe]) is excluded from the comparative analysis a mean offset in Hβ of -0.002 ± 0.040 Å and a mean offset in [MgFe] of 0.140 ± 0.022 Å is found. This implies the reverse of the previous result, namely that the [MgFe] values in this study *do* require a correction, whilst the Hβ values do not. This analysis highlights problems with the comparison data sets, indicating that either there are underlying problems with their line index measurements or that they have not been fully corrected to the Lick/IDS system (again highlighting the importance of having a large, homogeneous data set to analyse galaxy stellar populations without any inherent systematic errors clouding any results). This leads to the conclusion that any systematic correction to the data set in this dissertation would be uncertain because of the discrepancies between published data sets. However this analysis does not take into account the effect of different aperture sizes. Section 4.5 analyses the impact of these corrections on this comparative analysis of the Hβ and [MgFe] indices using the Mehlert et al. (2000) data. It is necessary to quantify the effect of these corrections before any defintive conclusions can be reached over the presence of any systematic differences between this data set and those published. It will be seen however that the aperture corrections are small and have little effect on the conclusions from this raw comparison analysis.

Parameter	Units	Source	N_{match}	Offset to this study	rms	rms_{intr}	$p_{\text{zero offset}}$	p_{offset}	p_{spearman}
$\log\sigma$		7S	23 (16)	0.0038 ± 0.0055	0.0215	0.0132 ± 0.0033	0.0987	0.5617	0.0208
$\log\sigma$		HK	14 (9)	−0.0034 ± 0.0049	0.0140	0.0059 ± 0.0020	0.3204	0.2010	0.8504
$\log\sigma$		Jørg	18 (13)	−0.0071 ± 0.0065	0.0226	0.0096 ± 0.0027	0.0016	0.1192	0.1186
$\log\sigma$		SMAC	33 (22)	0.0073 ± 0.0034	0.0157	0.0049 ± 0.0010	0.0026	0.6682	0.8542
$\log\sigma$		*ALL*	*88 (61)*	*0.0031 ± 0.0024*	*0.0187*	*0.0027 ± 0.0003*	*0.0200*	*0.3259*	*0.1311*
C4668	Å	Lick	9 (6)	0.679 ± 0.294	0.657	0.492 ± 0.201	0.0000	0.1838	0.8480
Fe5015	Å	Lick	11 (8)	−0.021 ± 0.157	0.416	0.684 ± 0.242	0.2517	0.1670	0.1015
Fe5270	Å	Lick	11 (8)	−0.044 ± 0.089	0.235	0.161 ± 0.057	0.6727	0.7352	0.2568
Fe5335	Å	Lick	10 (7)	0.228 ± 0.107	0.263	0.272 ± 0.103	0.0003	0.9906	0.0662
Fe5406	Å	Lick	5 (4)	−0.002 ± 0.264	0.457	0.075 ± 0.038	0.2327	0.2238	0.0833
⟨Fe⟩	Å	HK	14 (9)	0.092 ± 0.065	0.184	0.035 ± 0.012	0.0012	0.0650	0.0660
⟨Fe⟩	Å	Jørg	36 (25)	−0.162 ± 0.025	0.124	0.127 ± 0.025	0.0000	0.7711	0.7716
⟨Fe⟩	Å	Lick	10 (7)	0.181 ± 0.036	0.087	0.243 ± 0.092	0.0000	0.1043	0.1616
⟨Fe⟩	Å	Mehlert	18 (13)	0.120 ± 0.018	0.064	0.153 ± 0.042	0.0000	0.5475	0.5552
⟨Fe⟩	*Å*	*ALL*	*78 (53)*	*0.026 ± 0.023*	*0.163*	*0.074 ± 0.010*	*0.0830*	*0.8480*	*0.0061*
Mg_1	mag	Jørg	36 (25)	0.0199 ± 0.0015	0.0071	0.0042 ± 0.0008	0.0000	0.2724	0.1785
Mg_1	mag	Lick	11 (7)	0.0144 ± 0.0049	0.0120	0.0024 ± 0.0009	0.0000	0.9462	0.3817
Mg_1	*mag*	*ALL*	*47 (32)*	*0.0190 ± 0.0015*	*0.0083*	*0.0035 ± 0.0006*	*0.0000*	*0.4564*	*0.2972*

Table 4.1: *continued on next page*

continued from previous page

Parameter	Units	Source	N_{match}	Offset to this study	rms	rms_{intr}	$p_{zero\ offset}$	p_{offset}	$p_{spearman}$
Mg_2	mag	7S	23 (16)	−0.0086 ± 0.0020	0.0076	0.0004 ± 0.0001	0.0000	0.8832	0.3351
Mg_2	mag	HK	14 (8)	0.0149 ± 0.0040	0.0105	0.0011 ± 0.0004	0.0000	0.5376	0.5707
Mg_2	mag	Jørg	36 (25)	0.0028 ± 0.0022	0.0109	0.0010 ± 0.0002	0.0039	0.3536	0.0494
Mg_2	mag	Lick	11 (8)	0.0191 ± 0.0052	0.0138	0.0008 ± 0.0003	0.0000	0.6565	0.4884
Mg_2	mag	SMAC	33 (21)	0.0050 ± 0.0015	0.0067	0.0002 ± 0.0001	0.0000	0.6291	0.7989
Mg_2	*mag*	*ALL*	*117 (78)*	*0.0044 ± 0.0012*	*0.0104*	*0.0018 ± 0.0002*	*0.0000*	*0.6321*	*0.0933*
Mg_b	Å	HK	14 (9)	0.128 ± 0.041	0.117	0.118 ± 0.039	0.0000	0.8684	0.6041
Mg_b	Å	Jørg	36 (25)	−0.006 ± 0.038	0.184	0.080 ± 0.016	0.3443	0.3112	0.2794
Mg_b	Å	Lick	11 (8)	−0.078 ± 0.117	0.311	0.102 ± 0.036	0.4056	0.9023	0.4497
Mg_b	Å	Mehlert	18 (13)	0.104 ± 0.036	0.125	0.125 ± 0.035	0.0000	0.2344	0.1142
Mg_b	*Å*	*ALL*	*79 (54)*	*0.065 ± 0.023*	*0.166*	*0.101 ± 0.014*	*0.0000*	*0.0410*	*0.1269*
[MgFe]	Å	HK	14 (9)	0.124 ± 0.055	0.156	0.006 ± 0.002	0.0000	0.6626	0.3458
[MgFe]	Å	Jørg	36 (25)	−0.170 ± 0.022	0.108	0.072 ± 0.014	0.0000	0.9877	0.2480
[MgFe]	Å	Lick	10 (7)	0.102 ± 0.064	0.156	0.115 ± 0.043	0.0007	0.3606	0.5997
[MgFe]	Å	Mehlert	18 (13)	0.129 ± 0.026	0.089	0.073 ± 0.020	0.0000	0.8241	0.9848
[MgFe]	*Å*	*ALL*	*78 (53)*	*0.004 ± 0.021*	*0.151*	*0.033 ± 0.005*	*0.1282*	*0.0802*	*0.0897*
Hβ	Å	HK	13 (8)	0.189 ± 0.092	0.242	0.039 ± 0.014	0.0000	0.2224	0.1658
Hβ	Å	Jørg	35 (24)	−0.197 ± 0.038	0.185	0.058 ± 0.012	0.0000	0.3790	0.4052
Hβ	Å	Lick	10 (7)	−0.106 ± 0.085	0.209	0.153 ± 0.058	0.0001	0.2094	0.6618

Table 4.1: *continued on next page*

continued from previous page

Parameter	Units	Source	N_{match}	Offset to this study	rms	rms_{intr}	$p_{\text{zero offset}}$	p_{offset}	p_{spearman}
Hβ	Å	Mehlert	18 (13)	−0.095 ± 0.044	0.153	0.077 ± 0.021	0.0009	0.1859	0.3609
Hβ	*Å*	*ALL*	*76 (51)*	*−0.092 ± 0.026*	*0.187*	*0.075 ± 0.011*	*0.0000*	*0.2276*	*0.2191*
Hβ_G	Å	Jørg	35 (24)	−0.103 ± 0.026	0.124	0.059 ± 0.012	0.0000	0.1417	0.1222

SOURCE:

7S	Seven Samurai studies (Dressler et al. 1987)
SMAC	Streaming Motions of Abell Clusters (Hudson et al. 1999)
Jørg	Jørgensen (1999)
HK	Kuntschner et al. (2001)
Lick	Lick/IDS database (Trager et al. 1998)
Mehlert	Mehlert et al. (2000)

Table 4.1: Comparison between this study and other studies of the Coma cluster. The number of matching data between the studies is given by N_{match}, where the number in brackets is the sub-sample of the matching data, after 1 sigma clipping, that is used to calculate the comparison statistics.

Index	Mean aperture correction
Hβ	0.019 ± 0.010 Å
$\langle$Fe$\rangle$	0.025 ± 0.010 Å
Mg$_b$	0.042 ± 0.011 Å
[MgFe]	0.033 ± 0.009 Å

Table 4.2: $2.7'' \rightarrow 3.4''$ aperture corrections. Aperture corrections for the line indices Hβ, Mg$_b$, $\langle$Fe$\rangle$ and [MgFe]. All data is calculated from the long slit data of Mehlert et al. (2000). Subtract the mean correction factor from the $2.7''$ line indices presented in this dissertation to convert them to $3.4''$ equivalent line indices.

Table 4.1 and Figures 4.1 to 4.8 also contain comparative analyses of velocity dispersion measurements and of other line indices as well as results of various statistical tests performed. In brief, there is no highly statistically significant evidence for any offsets between any data presented in this dissertation and the comparison data, except for the Mg$_1$ index. This is found to have a mean offset of 0.0190 ± 0.0015 mag. However since this index is not used in this study, this offset is not corrected for and will not affect any of the study conclusions*. The velocity dispersion measurements have a scatter of only 0.0187 dex ($\equiv\sim 1\%$) and no statistically significant offsets. The Lilliefors test always supports the removal of an offset (p_{offset}) — but this is expected. In addition, the Lilliefors often also supports the hypothesis that there is *no* offset present in the data ($p_{\text{zero offset}}$). The Spearman rank correlation test shows that there is no highly statistically significant evidence for any correlations between the sample differences and the parameters from this study, implying that there are no underlying unknown problems or differences either in the parameters or in the measurement processes used.

4.5 Aperture corrections

Because galaxies exhibit a radial dependence for line strength measurements (see e.g. Mehlert et al. 2000) it is necessary to understand the offsets introduced when comparing data from

*It is possible that the presence of an offset in the Mg$_1$ index could be due to an incorrect velocity dispersion correction. Figure 3.18 shows that the observed standard stars give a range of *different* correction curves, however the computed correction at $\sigma = 200\,\mathrm{km\,s^{-1}}$ is $+0.0028^{+0.0012}_{-0.0016}$ mag and is therefore not large enough to explain the presence of an offset

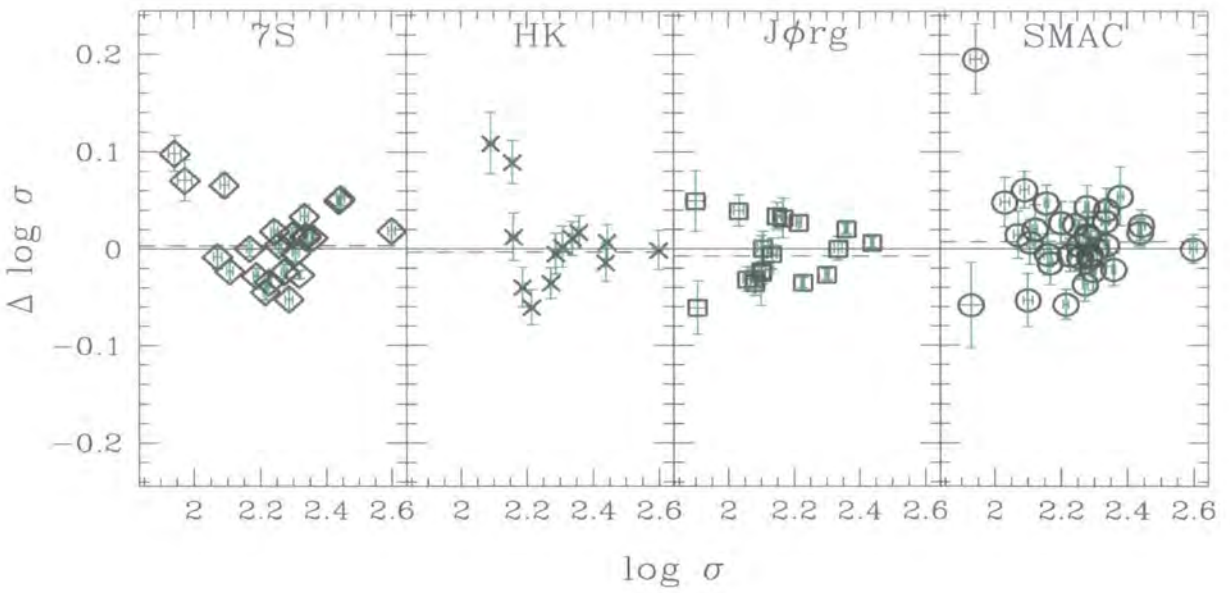

(a) comparison between this study and other studies

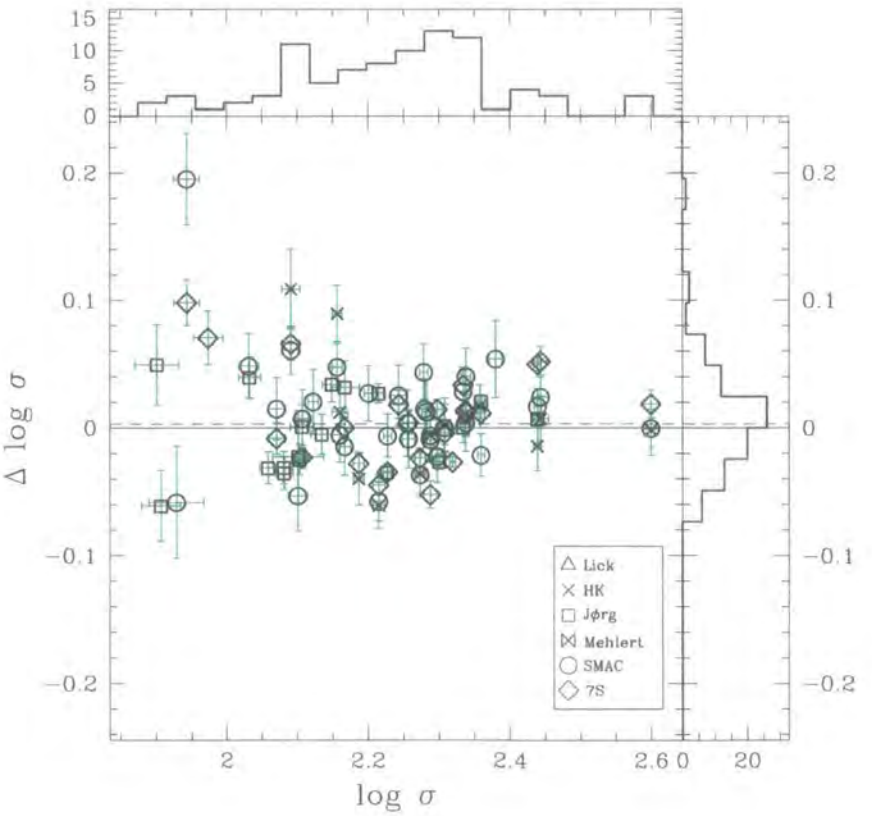

(b) adding comparisons together

Figure 4.1: log σ comparisons between this study other studies of the Coma cluster.

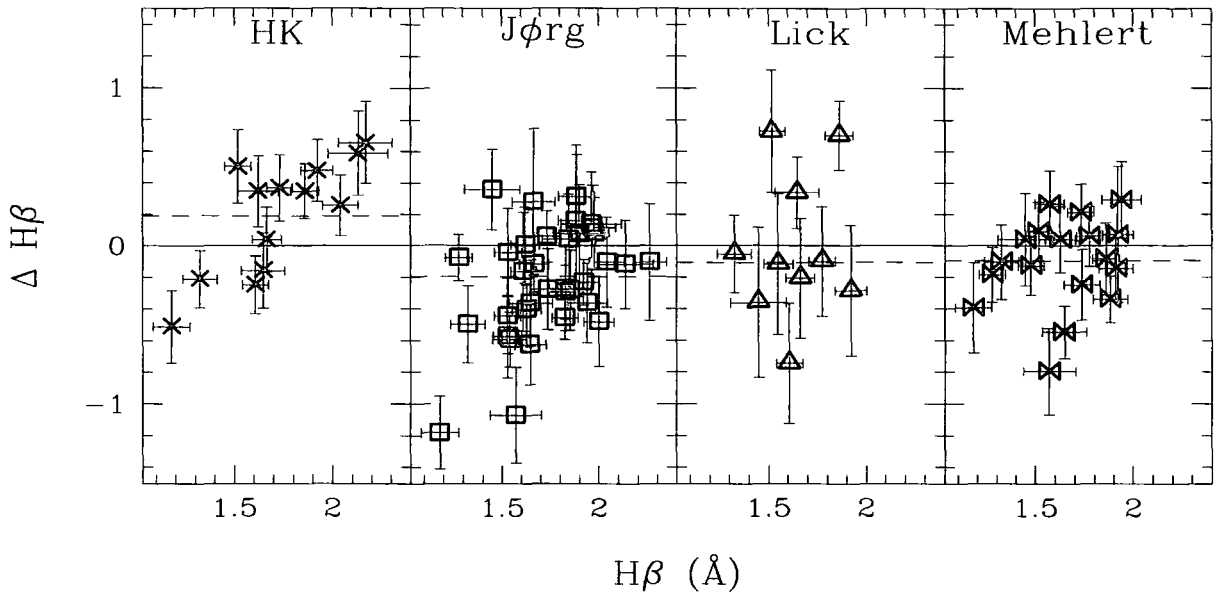

(a) comparison between this study and other studies

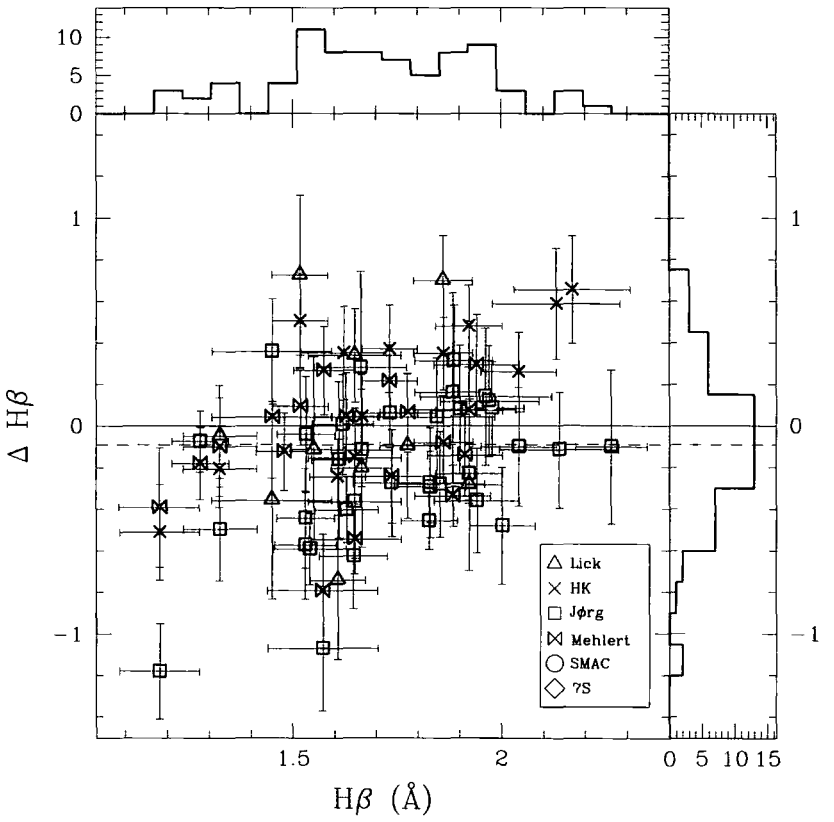

(b) adding comparisons together

Figure 4.2: Hβ comparisons between this study other studies of the Coma cluster.

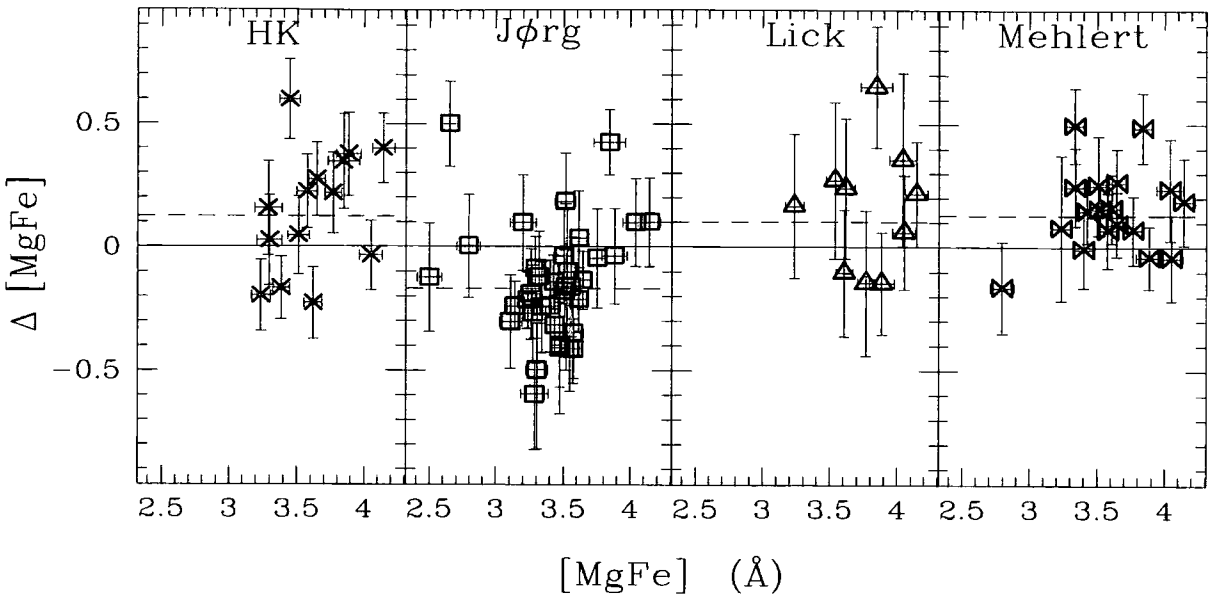

(a) comparison between this study and other studies

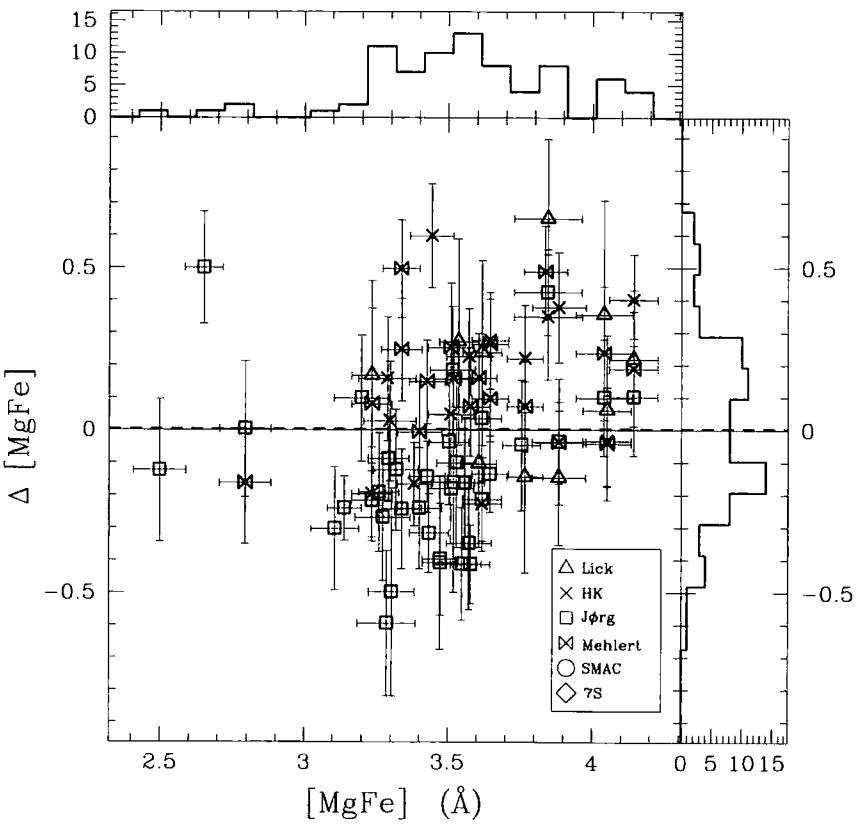

(b) adding comparisons together

Figure 4.3: [MgFe] comparisons between this study other studies of the Coma cluster.

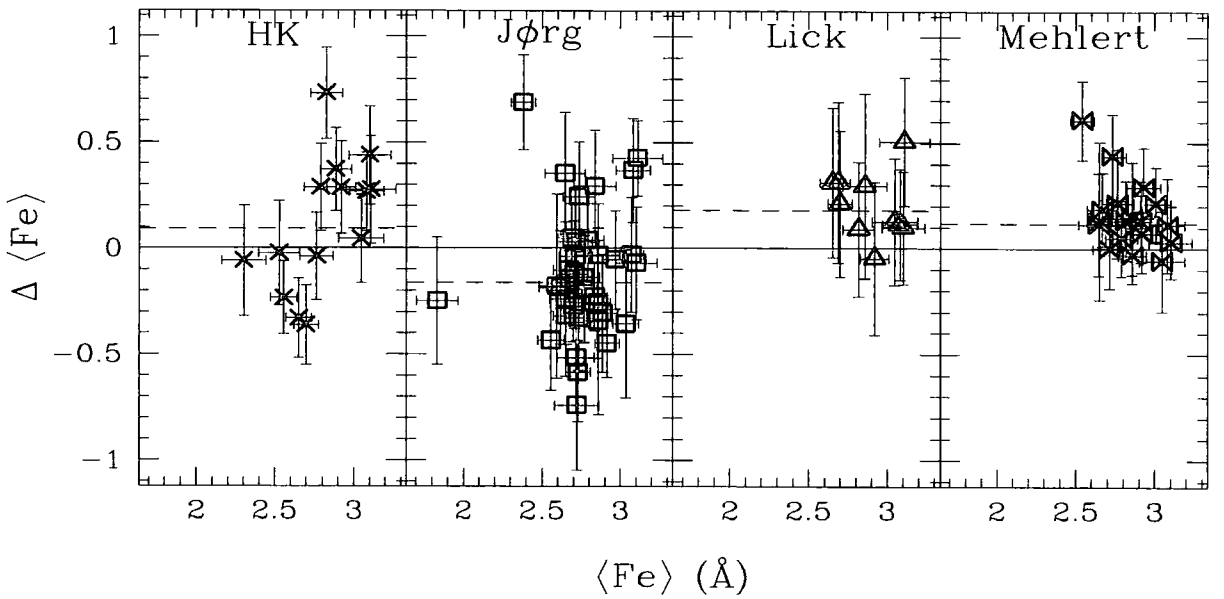

(a) comparison between this study and other studies

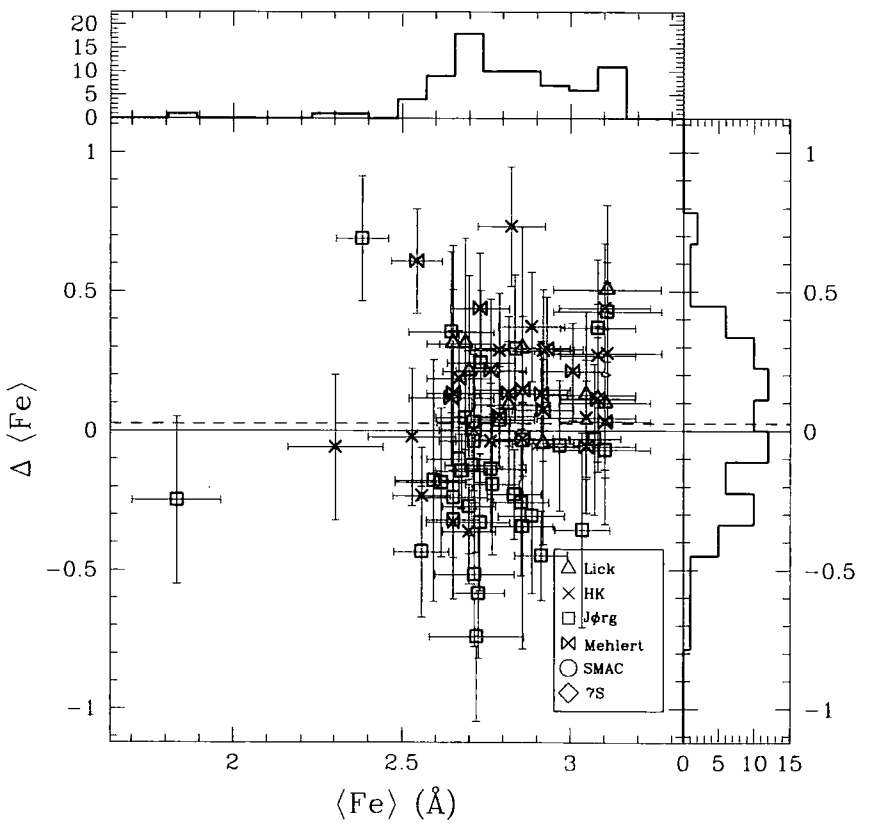

(b) adding comparisons together

Figure 4.4: ⟨Fe⟩ comparisons between this study other studies of the Coma cluster.

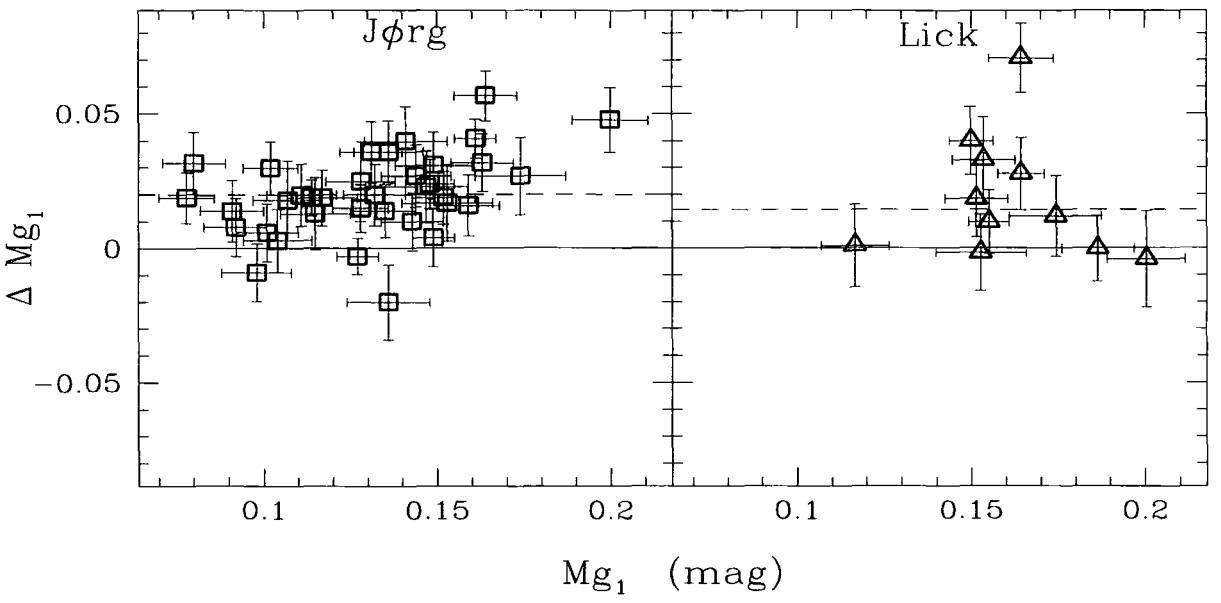

(a) comparison between this study and other studies

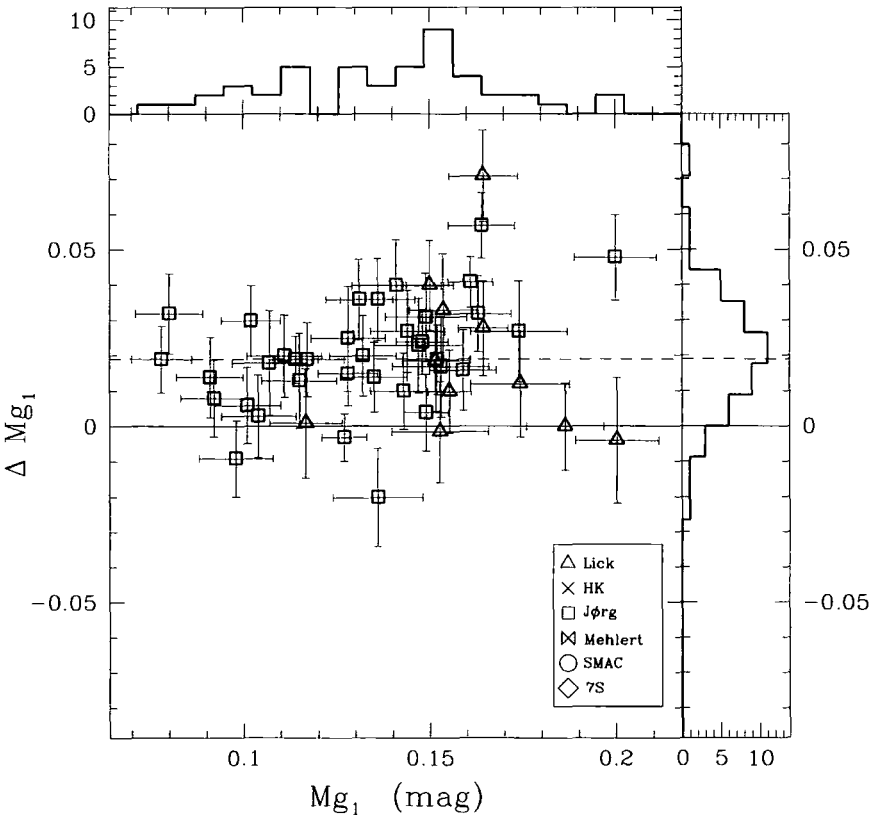

(b) adding comparisons together

Figure 4.5: Mg_1 comparisons between this study other studies of the Coma cluster.

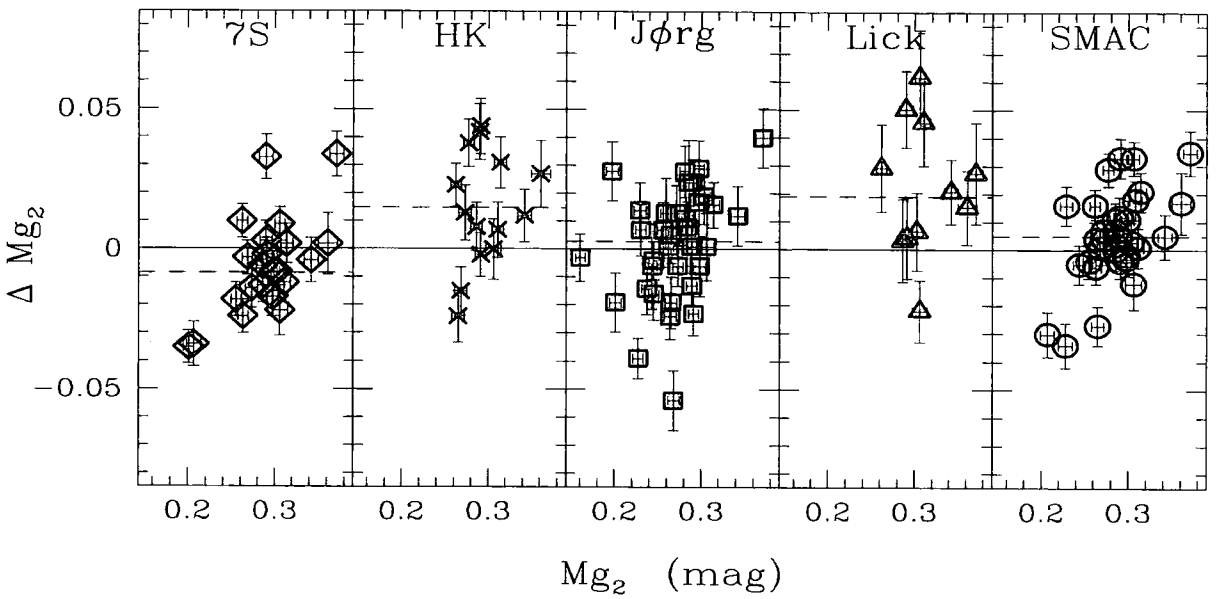

(a) comparison between this study and other studies

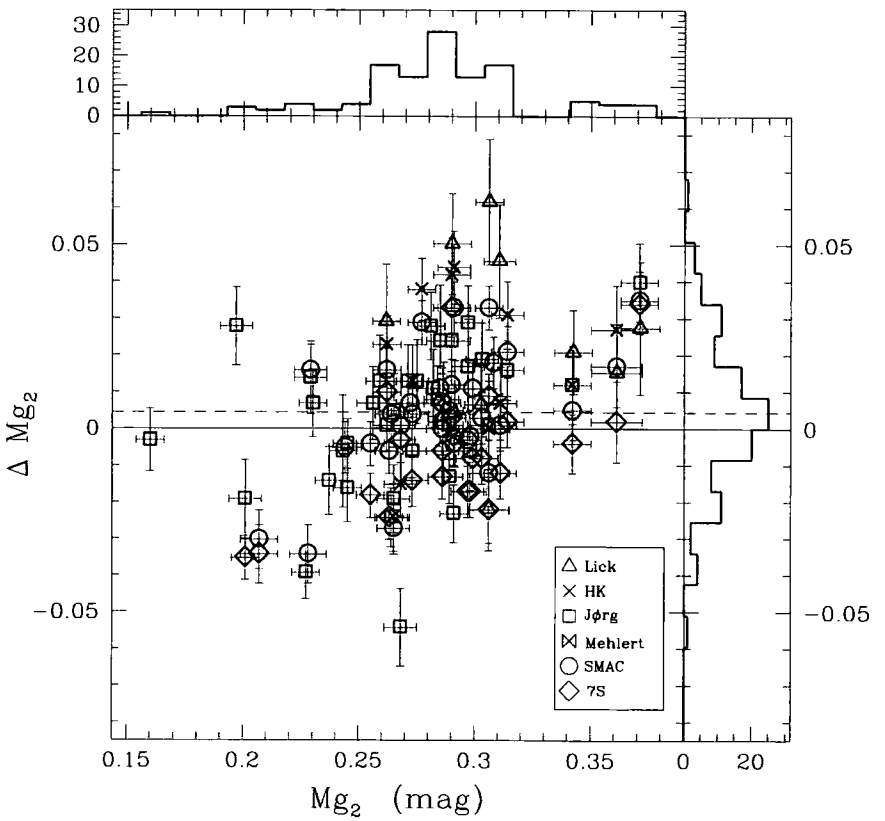

(b) adding comparisons together

Figure 4.6: Mg_2 comparisons between this study other studies of the Coma cluster.

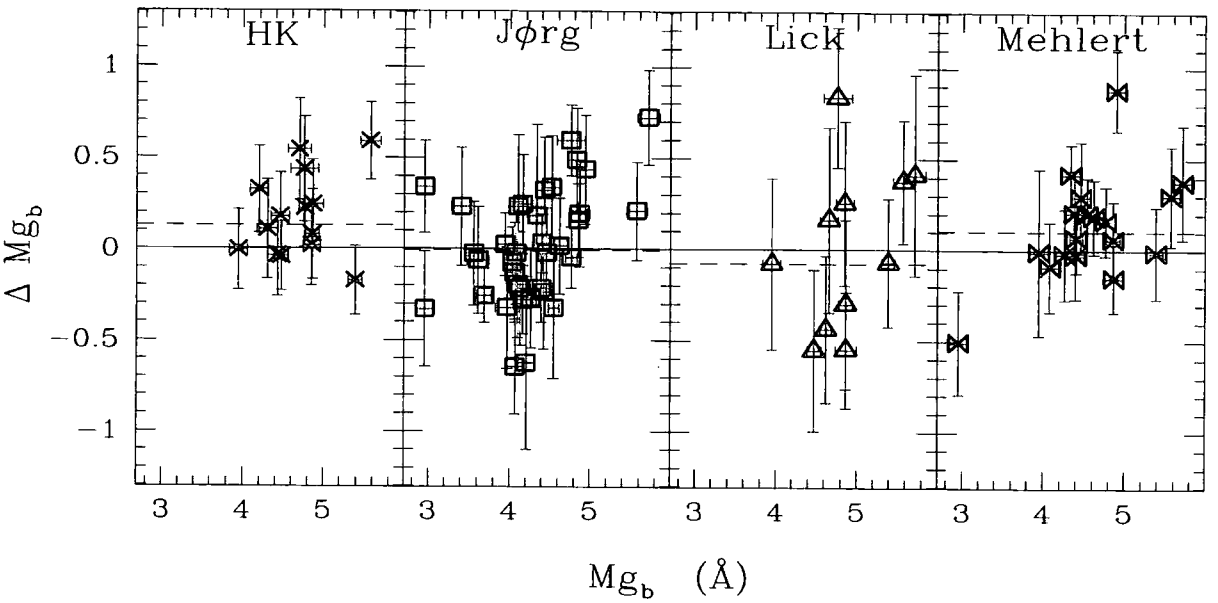

(a) comparison between this study and other studies

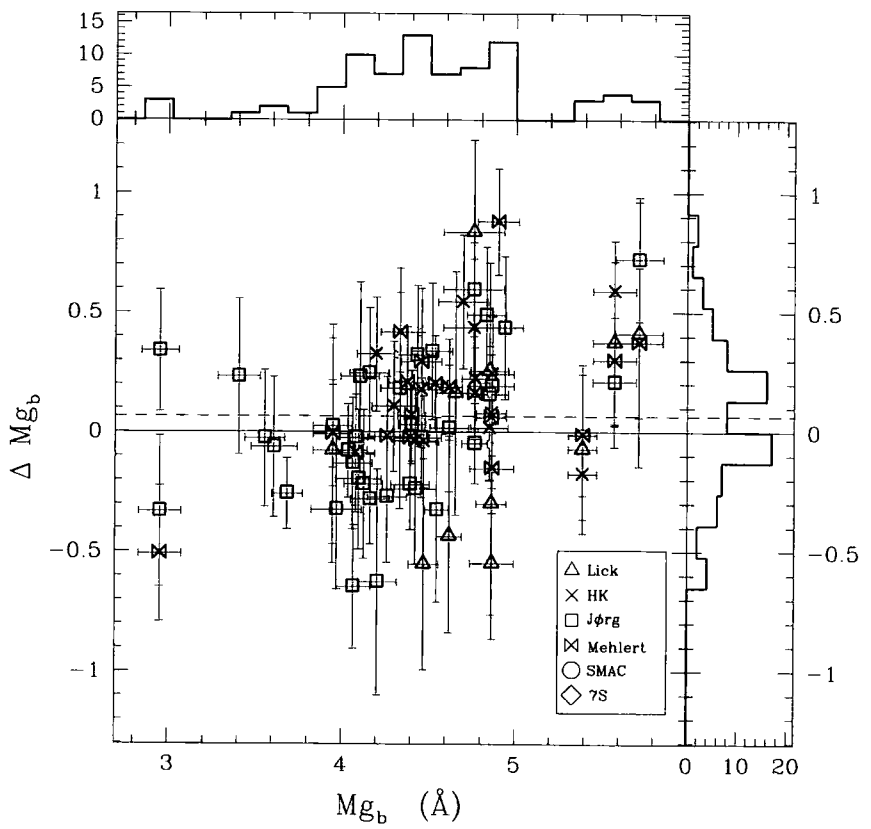

(b) adding comparisons together

Figure 4.7: Mg_b comparisons between this study other studies of the Coma cluster.

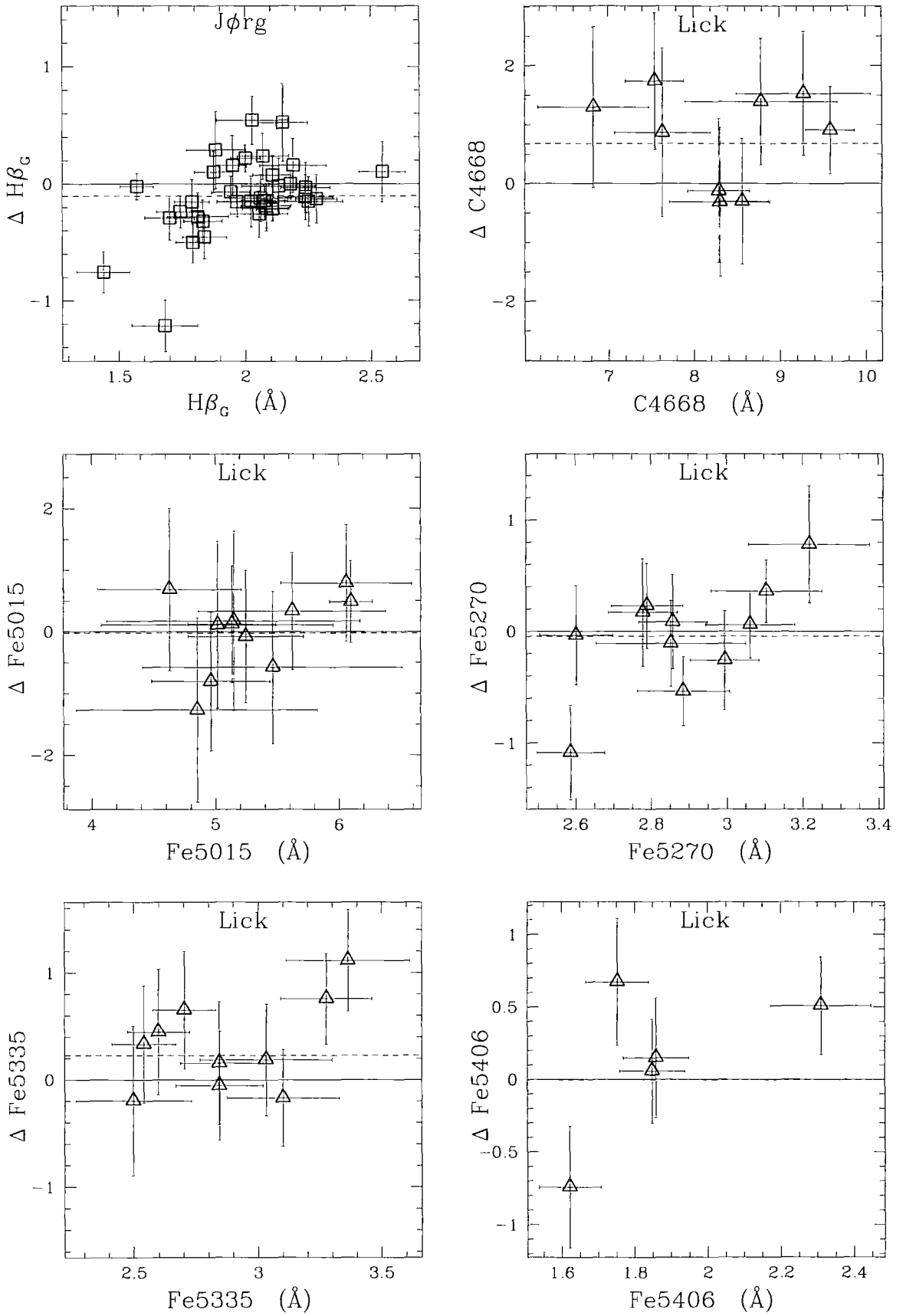

Figure 4.8: Other comparisons between this study other studies of the Coma cluster. Here the comparisons are for the absorption line indices: $H\beta_G$, C4668, Fe5015, Fe5270, Fe5335 and Fe5406 and are shown. In each case there was only one data set to compare these data to.

Index	Mean aperture correction
Hβ	-0.009 ± 0.007 Å
$\langle$Fe$\rangle$	-0.012 ± 0.009 Å
Mg$_b$	-0.026 ± 0.008 Å
[MgFe]	-0.018 ± 0.008 Å

Table 4.3: $2.7'' \rightarrow 1.4'' \times 4''$ aperture corrections. Aperture corrections for the line indices Hβ, Mg$_b$, $\langle$Fe$\rangle$ and [MgFe]. All data is calculated from the long slit data of Mehlert et al. (2000). Subtract the mean correction factor from the $2.7''$ line indices presented in this dissertation to convert them to equivalent line indices for a long-slit of dimension $1.4'' \times 4''$.

studies with different aperture dimensions. Following Jørgensen et al. (1995a,b) and Mehlert et al. (2000) I calculate a "slit-equivalent" radius to match the aperture width of $2.7''$ used in this study and convert the long-slit absorption line strengths of Mehlert et al. (2000) to fibre equivalent values (see Appendix A.4). Since Mehlert et al. (2000) only measured Hβ, Mg$_b$ and $\langle$Fe$\rangle$ (and therefore [MgFe] as well as it is a derived index), this data can only be used to corrected these indices. However as these are the primary indices used in this dissertation, this is not a problem (they do not measure the H$\beta_{\rm G}$ index, but any calculated corrections for the Hβ index will be the same as those for the H$\beta_{\rm G}$ index). To calculate the aperture correction to convert the $2.7''$ data to $3.4''$ equivalent data (thereby matching the aperture width of some of the comparison studies) I re-compute absorption line strengths from the data of Mehlert et al. (2000), this time matched to an aperture with of $3.4''$. A mean offset between the two apertures is then calculated by taking the $2.7''$ data and subtracting the $3.4''$ data and then analysing the results. This analysis can be seen in Table 4.2 and Figure 4.9.

To calculate the mean offset between the data in this dissertation (using a $2.7''$ diameter fibre) to the Lick/IDS long-slit data of Trager et al. (1998) (with a long-slit of dimension $1.4'' \times 4''$) I again use the data of Mehlert et al. (2000) and get the results shown in Table 4.3.

Applying these aperture corrections to the study comparisons detailed in Table 4.1 for the Lick/IDS line indices Hβ and [MgFe] (the principal line indices used in this dissertation) yields Table 4.4 and Figure 4.10. A mean offset in Hβ of -0.103 ± 0.026 Å and a mean offset in [MgFe] of -0.014 ± 0.022 Å are found.

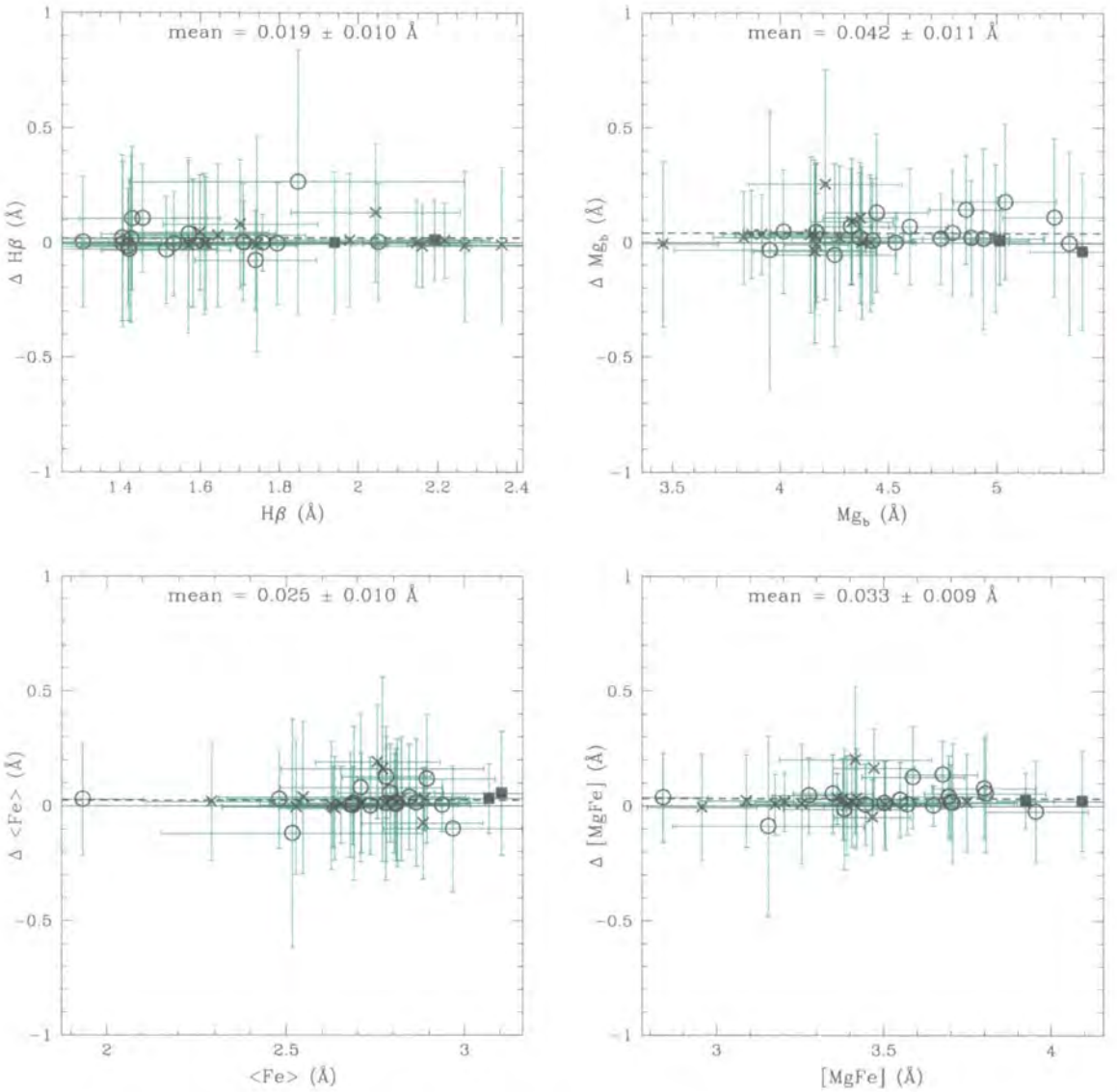

Figure 4.9: $2.7'' \rightarrow 3.4''$ aperture corrections. Aperture corrections for the line indices Hβ, Mg$_b$, $\langle$Fe$\rangle$ and [MgFe]. The y-axis in the figures is equal to the line index measured using $2.7''$ diameter fibres minus the line index measured using $3.4''$ diameter fibres. The x-axis is the $2.7''$ data. All data is calculated from the long slit data of Mehlert et al. (2000). The circle symbols are ellipticals, the crosses are lenticulars and the solid squares are the cD galaxies. There are 35 galaxies in the Mehlert et al. (2000) study. Subtract the mean correction factor (shown at the top of each figure and indicated by the dashed horizontal line) from the $2.7''$ line indices presented in this dissertation to convert them to $3.4''$ equivalent line indices.

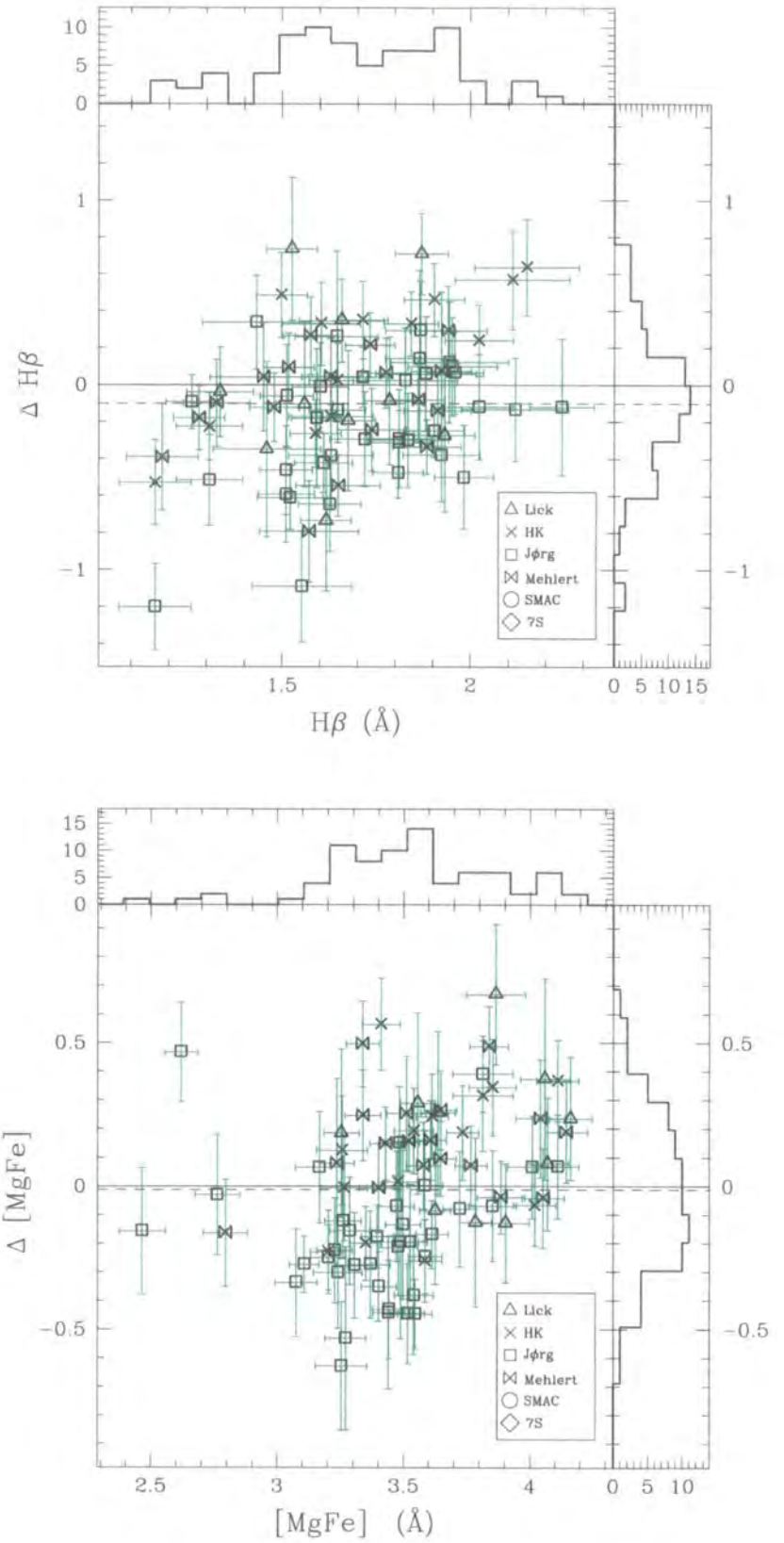

Figure 4.10: Comparison between this study and other studies of the Coma cluster after aperture corrections for the line indices Hβ and [MgFe].

Parameter	Source	Offset to this study		
Hβ	HK	0.170	$\pm$	0.093 Å
Hβ	Jørg	−0.216	$\pm$	0.039 Å
Hβ	Lick	−0.097	$\pm$	0.085 Å
Hβ	Mehlert	−0.095	$\pm$	0.044 Å
Hβ	*ALL*	*−0.103*	$\pm$	*0.026 Å*
[MgFe]	HK	0.091	$\pm$	0.056 Å
[MgFe]	Jørg	−0.203	$\pm$	0.024 Å
[MgFe]	Lick	0.120	$\pm$	0.064 Å
[MgFe]	Mehlert	0.129	$\pm$	0.026 Å
[MgFe]	*ALL*	*−0.014*	$\pm$	*0.022 Å*

Table 4.4: Comparison between this study and other studies of the Coma cluster after aperture corrections for the line indices Hβ and [MgFe].

4.6 Discussion of aperture corrected comparison analysis

The raw comparison analysis gave an initial mean offset in Hβ of -0.092 ± 0.026 Å and a mean offset in [MgFe] of 0.004 ± 0.021 Å. Aperture corrections were then calculated (Section 4.5) to ensure that there are no other systematics introduced into this analysis. These aperture corrections (Tables 4.2 and 4.3) are all small in comparison to the data errors. After aperture correction, a mean offset in Hβ of -0.103 ± 0.026 Å and a mean offset in [MgFe] of -0.014 ± 0.022 Å are found. This again implies that the [MgFe] values in this study require no correction to place them fully on the Lick/IDS system (as the computed correction is not statistically significant), but that the Hβ do require a correction. However, as in Section 4.4, a closer examination of the comparison data sets shows that there are still systematic offsets between them. If the Jørgensen (1999) data set (which has the largest offset from this study for the line indices Hβ and [MgFe]) is again excluded from the comparative analysis a mean offset in Hβ of -0.004 ± 0.039 Å and a mean offset in [MgFe] of 0.134 ± 0.022 Å is found after aperture corrections have been applied. The conclusion is therefore once more the reverse of the previous result in that the [MgFe] values in this study *do* require a correction, whilst the Hβ values do not. This comparison analysis with the effects of different aperture sizes removed confirms that there are problems with the comparison data sets.

4.7 Conclusions

In this chapter I have compared the data in this dissertation to previous studies of the Coma cluster to determine the quality of the data and to test for any systematic differences that need to be removed.

A comparison analysis of the primary indices of interest, Hβ and [MgFe], gives a mean offset in Hβ of -0.103 ± 0.026 Å and a mean offset in [MgFe] of -0.014 ± 0.022 Å after aperture corrections are applied. These aperture corrections are however small.

The initial conclusion is that the [MgFe] values in this dissertation require no correction to place them fully on the Lick/IDS system (as the computed correction is not statistically significant), but that the Hβ do require a correction. A closer analysis of the comparison data sets shows that there are however systematic offsets between them. This means that either there are underlying problems with the line index measurements or that they have not been fully corrected to a common Lick/IDS system. The Jørgensen (1999) data set has the largest offset from this study for the line indices Hβ and [MgFe]. If this data set is excluded from the aperture corrected comparative analysis a mean offset in Hβ of -0.004 ± 0.039 Å and a mean offset in [MgFe] of 0.134 ± 0.022 Å is found. This implies the reverse of the previous result, namely that the [MgFe] values in this study *do* require a correction, whilst the Hβ values do not. Because of this and because of the fact that any correction that would need to be applied is only ~ 0.1 Å (a correction of either ~ 0.05 in [Fe/H] or ~ 2 Gyrs, depending on where the data point is on a Worthey (1994) grid) and would anyway be a systematic shift for the entire data set (and therefore not affect any observed distribution or relative trends in the Coma cluster) *no* corrections are applied to the Hβ and [MgFe] data in this dissertation.

A comparison analysis of the velocity dispersion and other line index measurements in this dissertation shows that there are *no* highly statistically significant offsets between this and any other study of the Coma cluster. The exception is the Mg_1 index which has a mean offset of 0.0190 ± 0.0015 mag. It is uncertain why there is such a large offset for this index, however since it is not used subsequently in this study, this offset is not corrected for and will not affect any of the study conclusions.

The conclusion of the correlation analysis is that there is no highly statistically significant evidence for any correlations between the sample differences and the parameters from this study, implying that there are no underlying unknown problems or differences either in the parameters or in the measurement processes used.

If I consider again the indices Hβ and [MgFe] I see that I find an overall intrinsic rms difference after aperture corrections between this data set and the comparison data sets of 0.075Å and 0.022Å respectively. If we assume that there are indeed no systematic differences between the comparison data sets and the data set in this disseration, the presence of an intrinsic rms implies that the random errors of the data have been underestimated. In the previous chapter I calculated that the median errors for these indices in this data set were 0.106Å for Hβ and 0.085Å for [MgFe] (Table 3.7). As discussed in Section 3.8, I believe my error estimation represents the first time a completely independent and truly statistical method has been used to calculate the errors. Previous methods have relied too much on comparisons between each other to normalise their error estimations to agree with each other. My conclusion is therefore that the published errors are underestimated. In the worst case scenario, if the errors in the comparison data sets are however perfect and it is the errors in this study that are underestimated, this analysis implies that the median errors for the indices Hβ and [MgFe] should in fact be 0.130Å and 0.088Å respectively. The true situation is likely to be somewhere in between, with both errors requiring some scale factor to be applied. A scale factor is not applied to the errors in this study because of the large uncertainties of this scaling and the question of the validity of such a scaling to my independent error estimates. However it does highlight the importance of rigorous error treatments and of obtaining high-quality repeat observations to fully characterise both the random and systematic errors in a data set. Both of these approaches have been taken in this study.

In conclusion, the data from this dissertation has been compared to previous studies of the Coma cluster and is found to be of high quality, with no systematic offset corrections required for the parameters used later in analyses of the cluster. This reaffirms the merit of the approach of obtaining a large, homogeneous, high quality and high signal-to-noise data set to analyse galaxy stellar populations and cluster properties which does not have any inherent internal systematic errors clouding any results.

Chapter 5

Stellar population analysis

5.1 Introduction

One of the goals of this work is to probe the age and metallicity distribution of bright early-type galaxies within the rich Coma cluster. This is done through the analysis of the stellar populations of these early-type galaxies which act as fossil records of their formation and evolution, allowing us to better understand the star formation history of the cluster.

Section 1.6 has already introduced the theory of stellar population analysis. In this chapter I will apply this theory to the data set summarised below:

— homogeneous set of high quality 2.7″ aperture fibre (equivalent to $0.94\,h^{-1}$ kpc at Coma) line strength data;
— central velocity dispersion corrections applied;
— data corrected to Lick/IDS system;
— central absorption line strengths corrected for nebula emission using [OIII]λ5007Å;
— only data with a signal-to-noise of 35 per Å or greater included in analysis;
— 87 early-type galaxy morphological types (36 ellipticals, 51 lenticulars) matching criteria.

This data will be analysed using the Worthey (1994) models (Section 1.6.5). The main stellar population line indices used are H$\beta_{\rm G}$ and [MgFe]. These indices counter both the age–metallicity degeneracy problem (Section 1.6.3) and the non-solar abundance problem (see Sections 1.6.6, 3.7.2 and 5.3). The data analysed in this section is shown in Table 3.9

The layout of this chapter is given below:

§5.1 — *Introduction*
§5.2 — *Stellar population synthesis model*
§5.3 — *Non-solar abundance ratios*

As in Chapter 4, where a statistical p-value is quoted it should be interpreted according to:

$p < 0.05$	the null hypothesis is strongly inconsistent with the data
$0.05 < p < 0.10$	there is a marginal inconsistency with the null hypothesis
$p > 0.10$	there is little or no evidence against the null hypothesis

where the null hypothesis in question depends upon the particular statistical analysis tool being used.

5.2 Stellar population synthesis model

In this study I over-plot the age and metallicity sensitive absorption line indices corrected to the Lick/IDS system on a Worthey (1994) model generated stellar population analysis grid. The version of these models that I use has the following parameters:

— assumes a single initial star burst to form the stellar population;
— age range of star burst: 1<age<18 Gyr;
— Salpeter power law initial mass function, $x = 2.35$ (Salpeter 1955);
— a relation between fractional element abundances by weight (Y) is adopted so that the

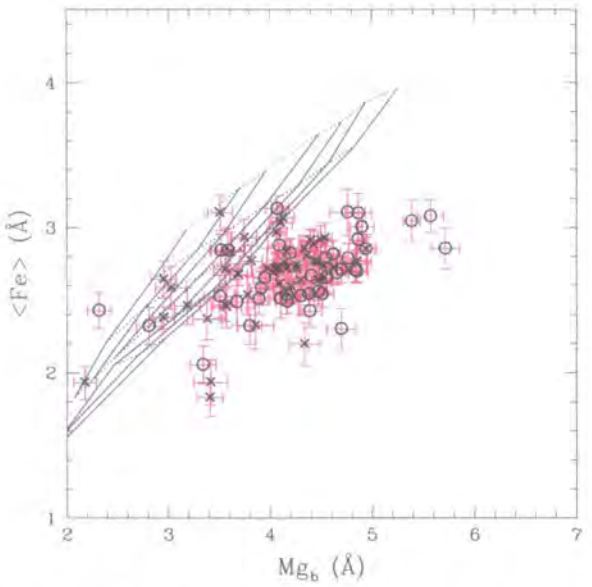

Figure 5.1: Non-solar abundance problems with indices ⟨Fe⟩ and Mg_b. The two indices are overlaid on a Worthey (1994) grid. In the figure ellipticals are represented by circles and lenticulars by crosses. The data points lay off of the grid due to the non-solar abundance problem (see text and Worthey et al. 1992, Worthey 1998 or Kuntschner et al. 2001).

primordial value is 0.228 and so that $Y_\odot = 0.274$ at $Z_\odot$ ($Y = 0.228 + 2.7Z$);

— metallicity range: $-2 < [Fe/H] < 0.5$;

— stellar population grid is derived from libraries of nearby stars with solar abundance ratios.

The version does in addition have corrections to improve the red giant branch treatment within the models (provided by Dr. Guy Worthey via private communication). See Section 1.6.7 for caveats to the application of these models.

Combinations of model parameters allow arbitrarily complex stellar populations to be modelled. The models are based on three major ingredients: isochrones and opacities; a flux library; and absorption line strengths (see Section 1.6.5).

5.3 Non-solar abundance ratios

The indices $H\beta_G$ versus [MgFe] provide the best compromise to non-solar abundance problems (see Sections 1.6.6 and 3.7.2). Figure 5.1 shows a plot of Mg_b versus ⟨Fe⟩ overlaid on a Worthey 1994 grid (after Worthey et al. 1992, Worthey 1998 and Kuntschner et al. 2001). It can be

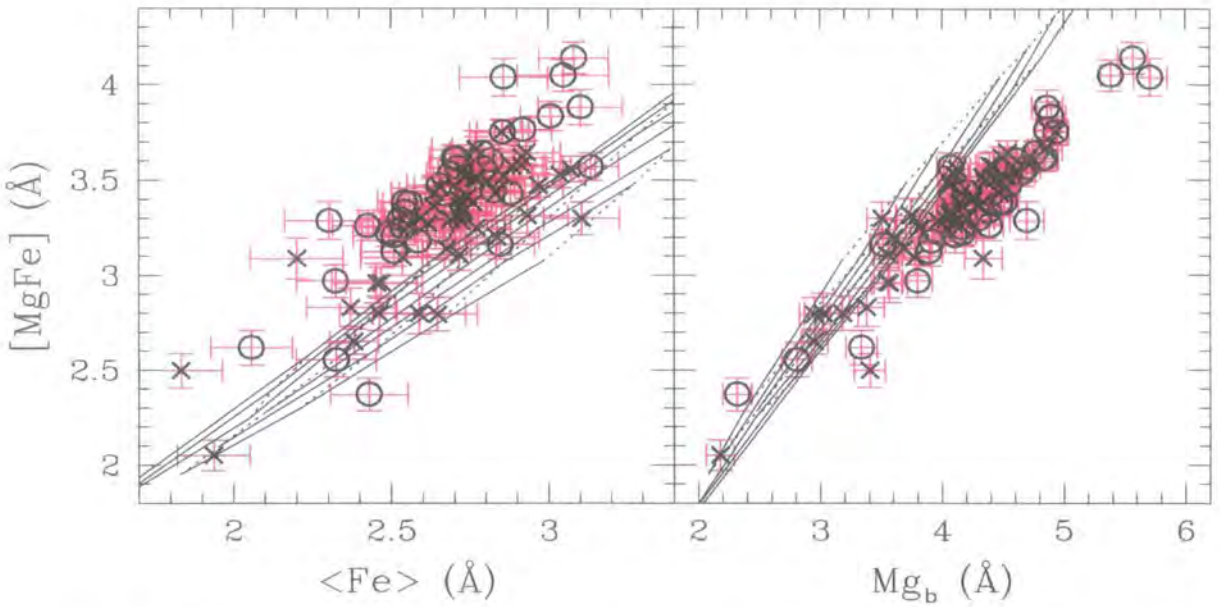

Figure 5.2: Non-solar abundance problems with indices ⟨Fe⟩ and Mg_b. The two indices are plotted against [MgFe] and are overlaid on a Worthey (1994) grid. In the figure ellipticals are represented by circles and lenticulars by crosses. The data points either lay above or below the grid, but when the indices are combined to create the [MgFe] index the non-solar abundance problem is minimised by the the deviations cancelling each other out (see text and Worthey 1998 or Kuntschner et al. 2001). Hence [MgFe] is a good tracer of the metallicity of stellar populations.

seen that the stellar population model predictions, which are based upon stellar data with solar abundance ratios, only cover a narrow band in the parameter space since the effects of age and metallicity are almost degenerate. In addition, the great majority of the galaxies plotted on this grid do not agree with the model predictions; this is due to the problem of the observed galaxies containing stellar populations with non-solar abundance ratios.

However if we consider Figure 5.2 we can see that if we combine the indices Mg_b and ⟨Fe⟩ to form the index [MgFe] (the geometric mean of the two) we can significantly reduce this problem since the non-solar abundance problem causes the indices Mg_b and ⟨Fe⟩ to deviate from the model predictions in *opposite* directions and hence the problem is minimised when the index [MgFe] is derived. Thus the indices $H\beta_G$ versus [MgFe] do indeed provide a good compromise to non-solar abundance problems, with maximal breaking of the age/metallicity degeneracy problem and are henceforth the principal probes of stellar populations used in this study (see Sections 1.6.6 and 3.7.2, Worthey 1998 or Kuntschner 2000).

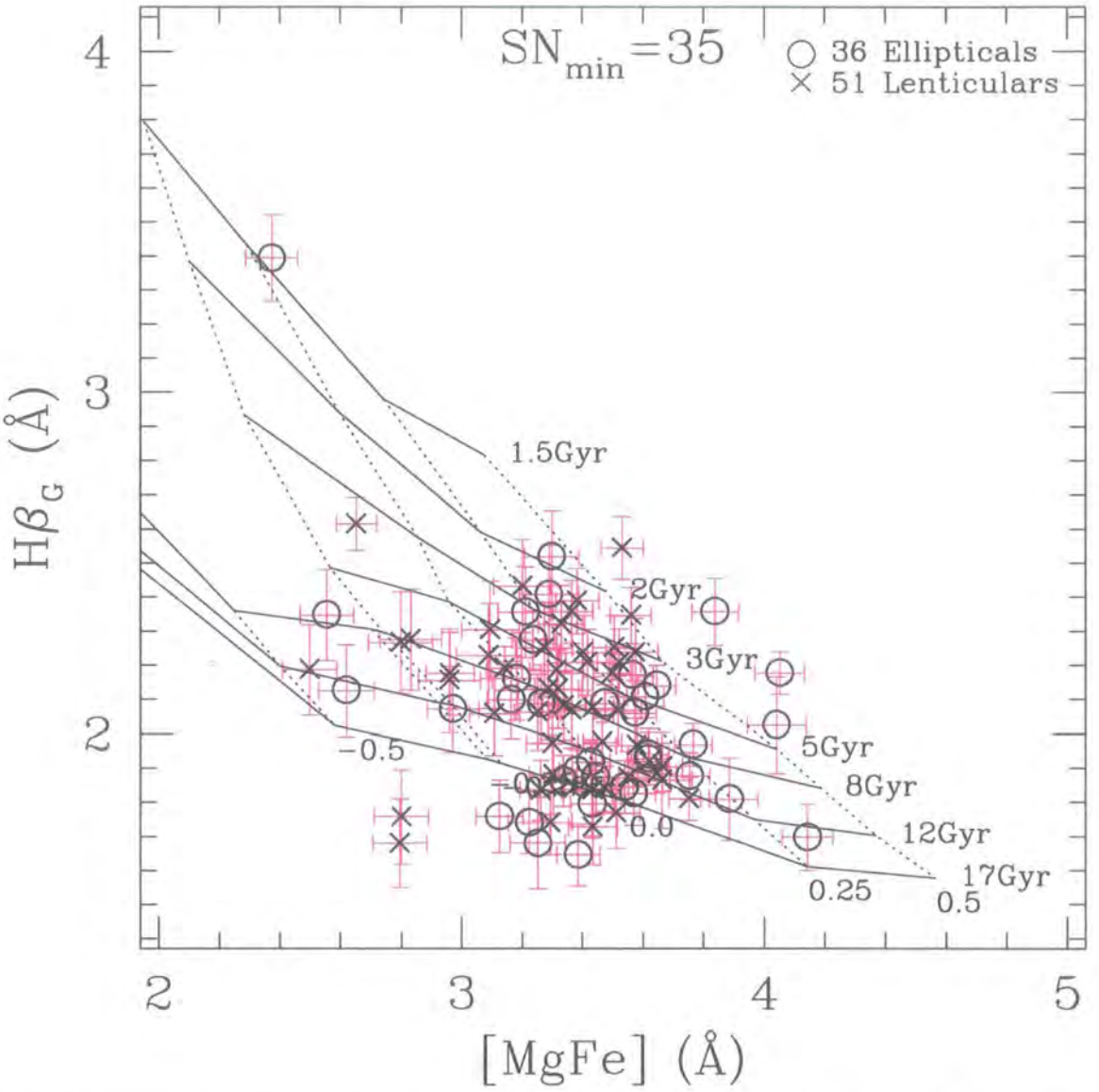

Figure 5.3: Analysis of Coma cluster galaxian stellar populations using Hβ_G vs [MgFe] indicators overlaid on a Worthey (1994) grid. Isochrones (lines of constant age) are represented by the almost horizontal solid lines (1.5<age<17 Gyr). The almost vertical dotted lines represent lines of constant metallicity (-2 < [Fe/H] < 0.5). In the top right hand corner of the plots is a key giving the different symbol for each morphological type and the number of galaxies of each type plotted. The symbol size is fixed and the errors for each data point are shown.

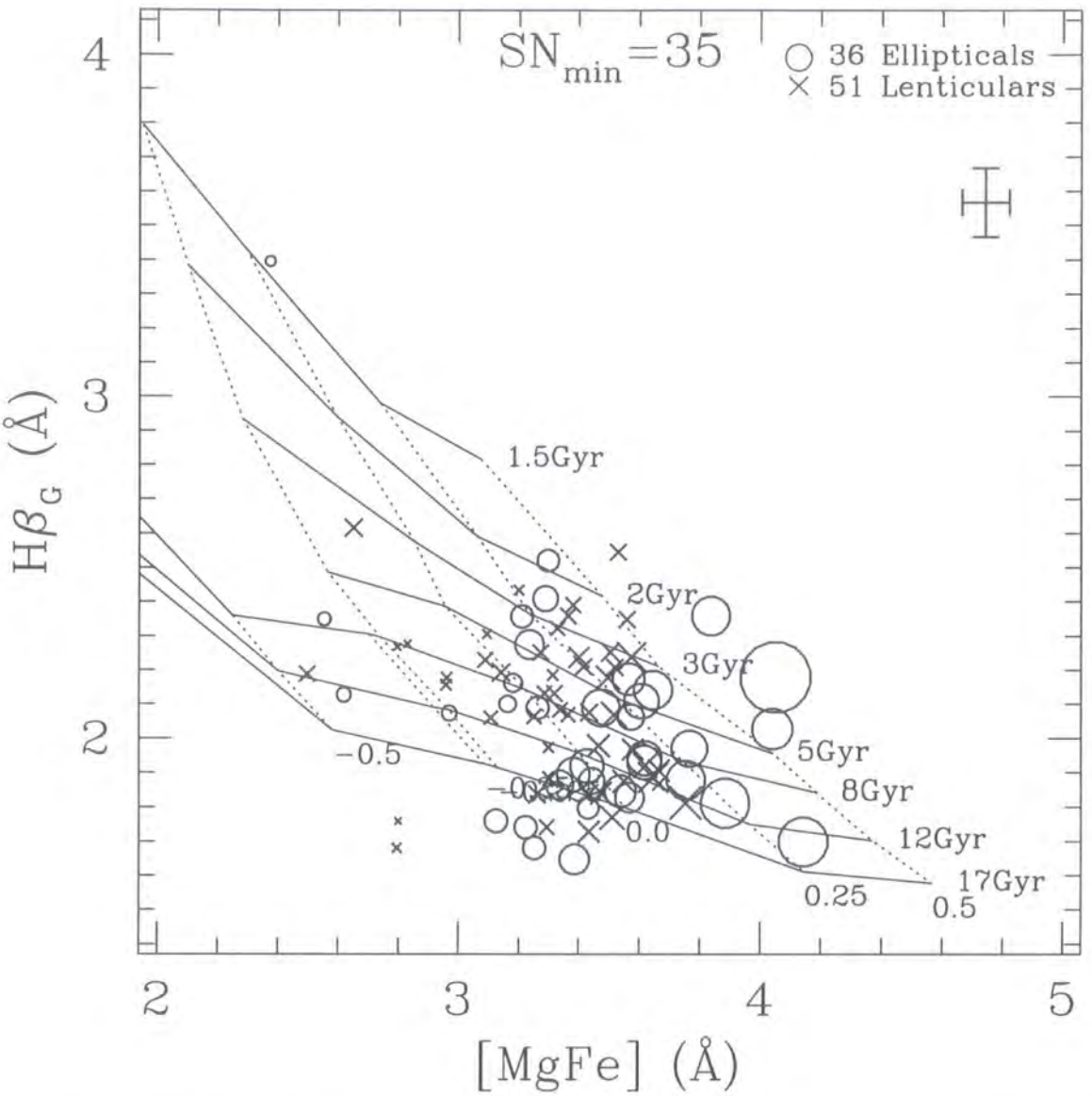

Figure 5.4: Analysis of Coma cluster galaxian stellar populations using Hβ_G vs [MgFe] indicators overlaid on a Worthey (1994) grid, points scaled by velocity dispersion. Isochrones (lines of constant age) are represented by the almost horizontal solid lines (1.5<age<17 Gyr). The almost vertical dotted lines represent lines of constant metallicity (-2 < [Fe/H] < 0.5). In the top right hand corner of the plots is a key giving the different symbol for each morphological type and the number of galaxies of each type plotted. The symbol size is scaled to the velocity dispersion of the galaxy (larger point size, larger velocity dispersion) and a median error bar is shown.

5.4 Coma cluster stellar population grids

Figures 5.3 and 5.4 show the Hβ_G and [MgFe] absorption line index data for the Coma cluster galaxies observed in this study overlaid on a Worthey (1994) grid. Figure 5.3 has a fixed symbol size and shows the errors on each data point, whereas Figure 5.4 has a symbol size scaled to the velocity dispersion of the galaxy (larger point size, larger velocity dispersion) and a median error bar. Only data with a minimum signal-to-noise of 35 per Å are included in the plot.

At a qualitative level, there are a number of points that can immediately be made about the data shown in Figures 5.3 and 5.4:

1. galaxies with a larger velocity dispersion (i.e. larger galaxies) are situated to the right of the grid at higher values of [MgFe] and hence at *higher* metallicities. Galaxies with lower velocity dispersions (i.e. smaller galaxies) are at the left of the grid at lower values of [MgFe] and consequently have *lower* metallicities. This can be seen more clearly in Figure 5.5.

2. there is an obvious distribution of galaxies across the stellar population grid. [MgFe] values vary from 2.37 to 4.14Å (a spread of 1.77Å), whilst Hβ_G varies from 1.70 to 3.40Å (a spread of 1.70Å) across the grid. If the stellar populations of Coma's early-type galaxies had either a single age of formation or a single metallicity (i.e. followed either a solid line or a dashed line of the Worthey (1994) grid shown in Figures 5.3 and 5.4) then the measurement errors would imply a smaller scatter than that observed. This implies that different hypotheses are required to explain the observed distribution and scatter of data across the Hβ_G—[MgFe] grid. This will be investigated further later in this chapter.

3. various inadequacies of the stellar population grid are evident, with a number of galaxies laying outside the defined grid. The grid is also not rectilinear, with the age sensitive index Hβ_G not being at right angles to the metal sensitive index [MgFe]. This causes investigations into the age and metallicity distributions of galaxies to be affected by the errors in both indices. The other problem with the grid is the logarithmic nature of the constant age contours (or "isochrones"); this leads to large errors in ages for old galaxies.

However this Hβ_G–[MgFe] stellar population grid represents an important tool in understanding the distribution of the age and metallicities within galaxy clusters, being the best method available at present to counter the age/metallicity degeneracy problems inherent in other systems.

The distribution of the galaxies across the Hβ_G–[MgFe] grid and their positional correlation with central velocity dispersion bears further examination. As I have said, galaxies with a larger velocity dispersion (i.e. larger galaxies) are situated to the right of the grid at higher values of [MgFe] and hence at *higher* metallicities. Galaxies with lower velocity dispersions (i.e. smaller galaxies) are at the left of the grid at lower values of [MgFe] and consequently have *lower* metallicities (as shown in Figure 5.5). If I consider the distribution of the galaxies across the same grid and partition them by magnitude I see the same result (Figure 5.6). This is easily understood because of the correlation between central velocity dispersion and magnitude (Figure 5.7): larger galaxies are brighter and have a higher central velocity dispersion, smaller galaxies are fainter and have a smaller central velocity dispersion. This relation is known as the Faber–Jackson relation (after the paper of Faber & Jackson 1976). In this case I have plotted central velocity dispersion against apparent magnitude, b_j (Figure 5.7). Apparent magnitude is a relatively crude way of showing this relation; a better correlation, with smaller scatter, would be seen if central velocity dispersion were plotted against total magnitude. This correspondence between the positional correlations across the Hβ_G–[MgFe] grid with both central velocity dispersion and apparent magnitude reinforce the power of the chosen stellar population analysis parameters (and indeed show the quality of the data).

5.5 Determination of ages and metallicities from stellar population grids

The irregularly-sampled and non-rectilinear (or non-orthogonal) nature of stellar population grids in observational space requires careful methods to derive ages and metallicities from observations.

The age and metallicity of a galaxy is calculated by superimposing a measurement of its Hβ_G and [MgFe] absorption line strength onto a Worthey (1994) grid. Intra-grid points were interpolated using the linear interpolation program of Worthey (provided via private communication). Points outside of the grid were extrapolated to using linear extrapolation. Isochrones were calculated at 0.05 Gyrs intervals and iso-metallicity contours at 0.01 [Fe/H] intervals. Other, more complicated methods were investigated including bicubic and bivariate interpolation and extrapolation to the irregularly distributed 2D grid surface. However such methods were found to be unreliable when dealing with the regions around the extremities of the grid. Linear interpolation

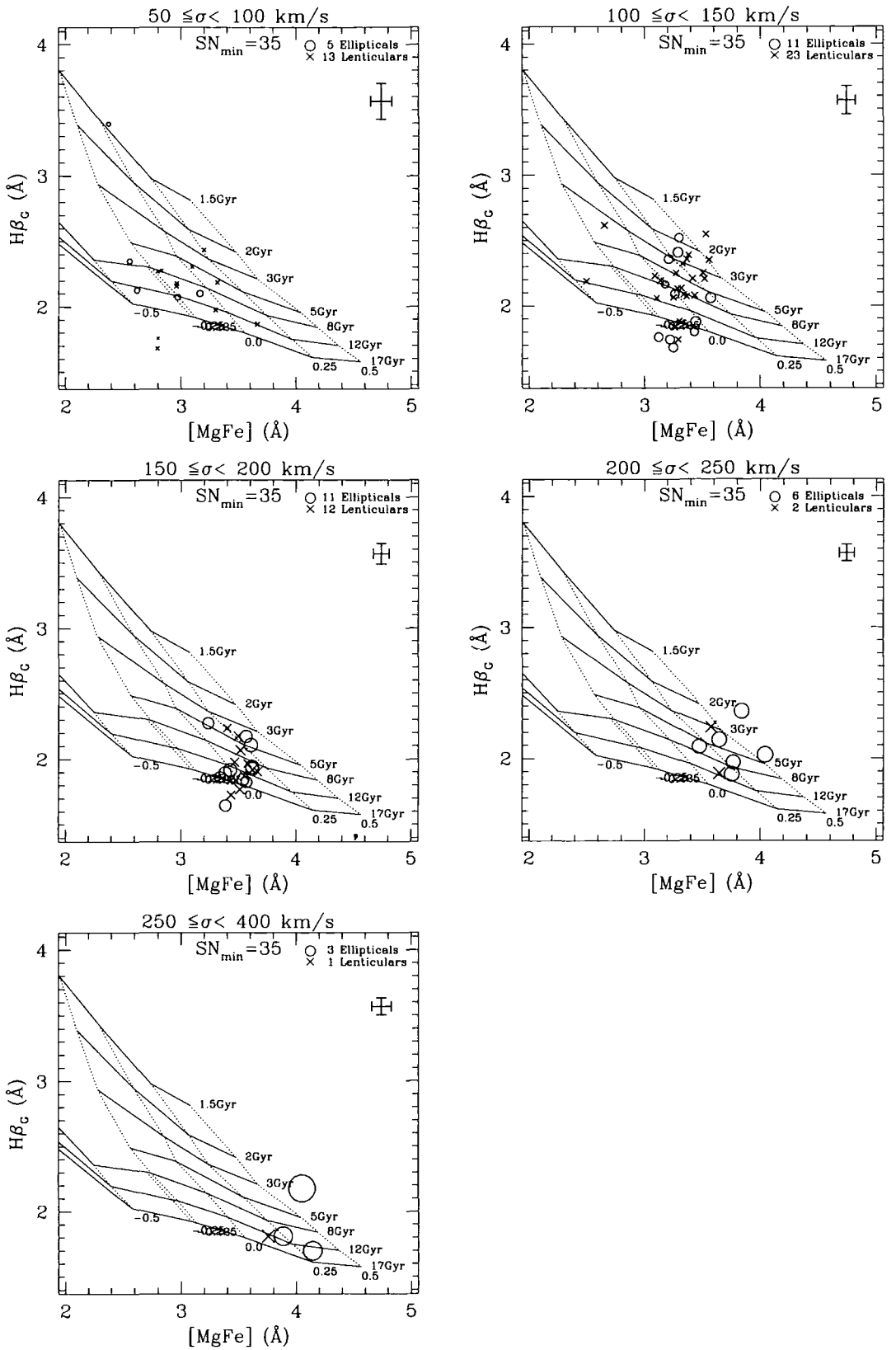

Figure 5.5: Hβ_G vs [MgFe] plots sifted by velocity dispersion. This figure clearly shows how lower velocity dispersion galaxies (i.e. smaller galaxies) have lower values of [MgFe] (and hence *lower* metallicities) and that higher velocity dispersion galaxies (i.e. larger galaxies) have higher values of [MgFe] (and hence *higher* metallicities).

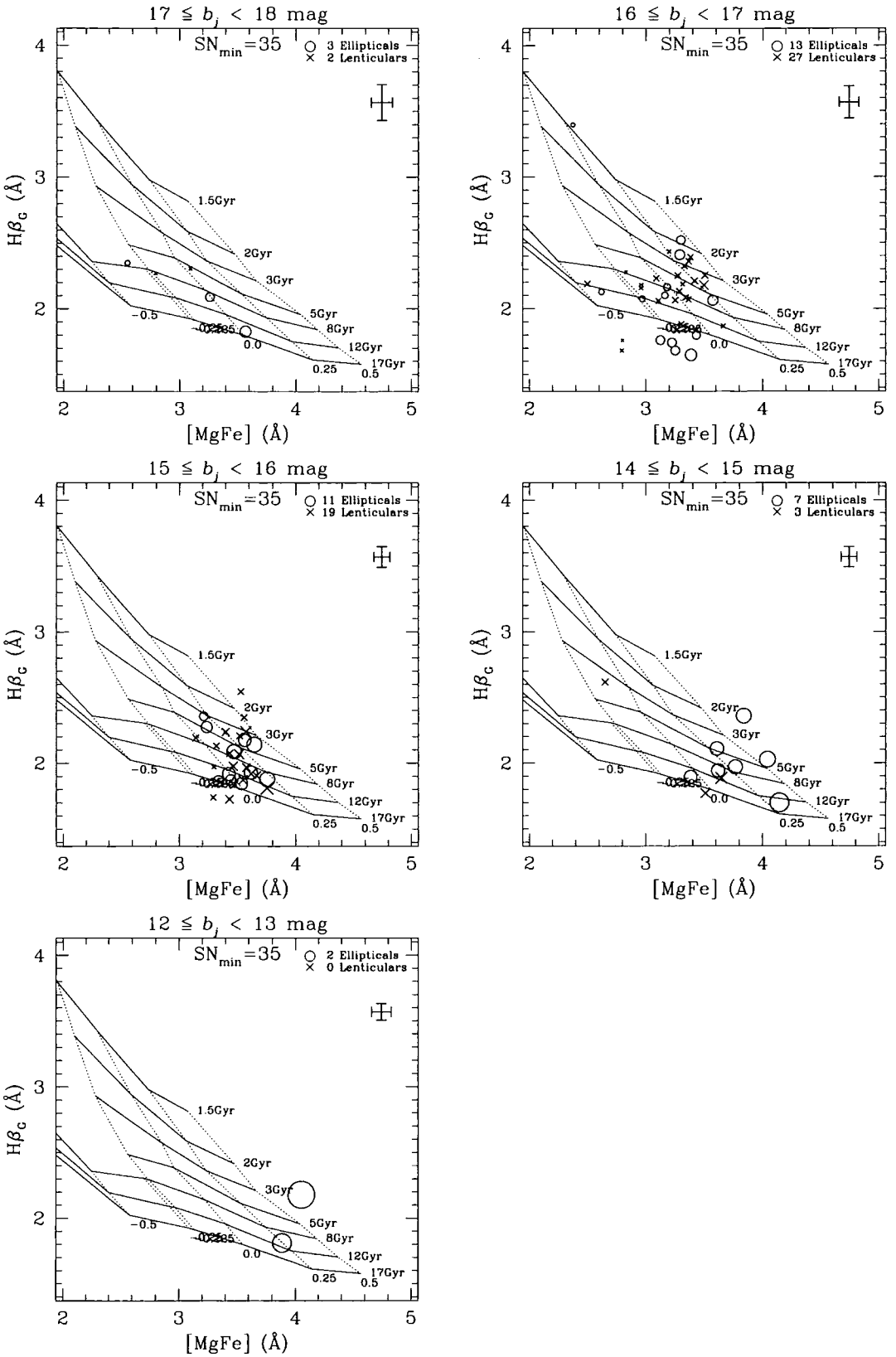

Figure 5.6: Hβ_G vs [MgFe] plots sifted by magnitude. The apparent magnitudes, b_j, are taken from Godwin, Metcalfe & Peach (1983). This figure clearly shows how fainter galaxies (i.e. smaller galaxies) have lower values of [MgFe] (and hence *lower* metallicities) and that brighter galaxies (i.e. larger galaxies) have higher values of [MgFe] (and hence *higher* metallicities).

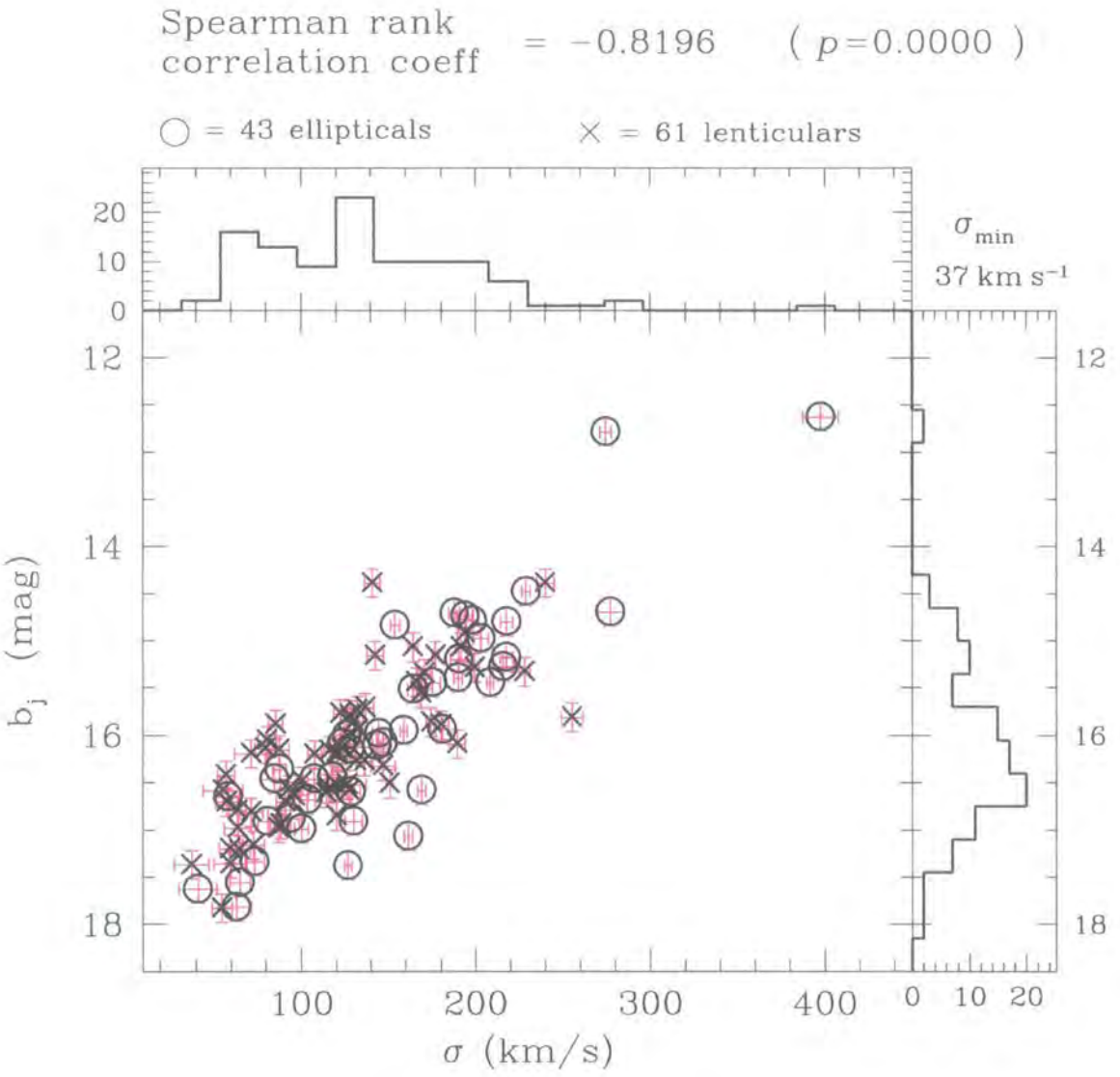

Figure 5.7: Correlation between central velocity dispersion and apparent magnitude. This figure includes all early-type galaxies (including low signal-to-noise observations). This relation is the well known Faber–Jackson relation (after the paper by Faber & Jackson 1976). The apparent magnitudes, b_j, are taken from Godwin, Metcalfe & Peach (1983). A Spearman rank correlation test confirms the presence of a correlation.

and extrapolation do not suffer from these effects and are readily repeatable.

It should be noted that the "ages" and "metallicities" that are derived using stellar population models are in fact luminosity-weighted mean ages and metallicities such that younger (brighter) populations are disproportionally important compared with their mass (see Section 1.6.7 for caveats when using stellar population models). This is because the Worthey (1994) grid has been generated from the model described in Section 5.2, which assumes that a single initial star burst formed the stellar population of a galaxy. As discussed in Section 1.6.7, a more complicated star formation history will affect the derived metallicities and ages. For example, if there has been a burst of star formation in the past 1 Gyr this will have a large effect on a galaxys' spectrum, leading to a much younger estimates of the galaxys' age and a significantly higher metallicity. Therefore if there are large amounts of recent star formation activity within the Coma cluster core then this will affect any age and metallicity distribution analysis. However Section 3.7.7 showed that there are no large scale dynamic interactions triggering excessive star formation within the core of the Coma cluster, implying that any merging event in the cluster cores' history is largely over or that any remaining gas density is insufficient to support any further starburst activity. Section 5.10 also shows that there is no correlation between nebula emission and either age or metallicity, implying that whilst there are a range of emissions across the cluster, with some galaxies having signs of active star formation whilst others are dormant, the observed small level of star formation does not effect the overall measurement of galaxy metallicities and ages. Therefore subsequent studies of the age and metallicity relative distribution within the Coma cluster core are not affected by the single star burst assumption and the luminosity-weighted caveats (though individual measurements for a particular galaxy may be affected).

5.6 Age and metallicity errors

The errors on the derived luminosity-weighted mean ages and metallicities are calculated by mapping the one standard deviation error ellipse in the index–index domain (typically in this case the Hβ_G–[MgFe] domain) and transforming it to the age–metallicity domain through a comparison with each ellipsoid point to the Worthey (1994) grid. In this way an accurate representation of the age and metallicity errors for each galaxy can be computed. It also demonstrates (see Figures 5.8 and 5.9) the variation in ellipse shape and orientation across the Worthey (1994)

grid; this variation and geometry can lead to false results of an age–metallicity trend in a cluster if the errors are not properly understood.

To simplify the presentation of these error ellipsoids in data tables I present only the maximum error (at the extremity of the ellipsoid). The "average" error will be less than this value.

5.7 Luminosity-weighted mean ages and metallicities

The luminosity-weighted mean ages and metallicities of 87 Coma cluster early-type galaxies (36 ellipticals, 51 lenticulars) with a signal-to-noise of 35 per Å or greater are presented in Table 5.1. The values have been calculated by superimposing $H\beta_G$–[MgFe] data onto a Worthey (1994) grid and comparing the two as previously described. These numbers are not intended to be absolute measurements of the age and metallicity of a galaxy, merely as a probe of the *relative* age and metallicities within the cluster.

name	type		S/N	b_j	$b-r$	$cz_\odot$	σ	Age in *Gyrs*			[Fe/H]		
d26	S0p		53.5	16.18		7396	71.5	1.00	±	0.26	−0.22	±	0.01
d28	E/S0		57.9	16.67	1.99	5974	103.5	7.85	±	3.40	−0.01	±	0.13
d39	S0/E		76.1	16.17	1.89	5897	120.4	8.40	±	3.26	0.06	±	0.11
d40	S0		47.0	17.15	1.84	5597	72.9	5.55	±	3.23	0.05	±	0.17
d42	S0		80.7	16.31	1.86	6016	147.1	3.25	±	1.19	0.39	±	0.12
d44	S0	E+A	55.7	16.57	1.77	7533	55.4	1.02	±	0.28	0.92	±	0.08
d53	E		80.2	16.59	1.87	5742	128.4	22.45	±	3.48	−0.23	±	0.07
d57	S0/a		97.4	15.15	1.78	8384	142.5	7.65	±	1.84	−0.02	±	0.08
d59	E		66.0	16.90	1.85	6947	129.9	22.75	±	4.00	−0.28	±	0.07
d62	S0		51.9	16.51	1.90	8359	126.2	11.70	±	6.29	−0.44	±	0.15
d64	E		50.5	16.90	1.79	7010	80.9	12.95	±	4.89	−0.40	±	0.12
d65	S0		65.1	16.15	1.77	6191	116.3	3.10	±	1.76	0.30	±	0.13
d67	S0		52.3	16.50	1.94	6039	150.8	16.60	±	5.61	−0.05	±	0.12
d71	S0		42.3	16.97	1.85	6919	63.9	7.75	±	3.48	−0.17	±	0.13
d73	E	E+A	49.2	17.33	1.84	5440	73.5	7.95	±	3.00	−0.30	±	0.10

Table 5.1: *continued on next page*

continued from previous page

name	type		S/N	b_j	$b-r$	$cz_\odot$	σ	Age in *Gyrs*			[Fe/H]		
d75	S0		48.2	16.13	1.91	6132	79.6	28.05	±	4.91	−0.55	±	0.37
d81	E		48.7	16.10	1.85	5928	143.3	2.60	±	1.67	0.33	±	0.17
d84	S0		46.8	16.20	1.98	6553	120.6	7.60	±	4.53	0.06	±	0.16
d87	E		63.2	16.87	1.79	7770	94.0	9.85	±	3.93	−0.06	±	0.10
d90	S0		52.0	16.93	1.88	5522	88.5	5.95	±	3.86	0.14	±	0.16
d93	S0		78.4	16.26	2.06	6063	136.3	18.65	±	3.53	−0.16	±	0.08
d98	S0/a		77.7	15.85	1.91	6868	130.0	1.60	±	0.26	0.61	±	0.09
d108	S0		66.8	16.55	1.85	6424	115.9	8.55	±	3.76	0.07	±	0.12
d110	S0/E		60.3	16.60	1.93	6948	114.4	16.55	±	4.78	−0.12	±	0.10
d112	E	E+A	50.8	16.64	1.78	7433	58.3	1.45	±	0.30	0.09	±	0.15
d116	SB0		75.7	16.13	1.90	8437	123.2	2.55	±	0.80	0.39	±	0.11
d132	S0		46.7	16.63	1.88	7698	96.2	11.75	±	6.29	0.14	±	0.14
d134	E		63.7	17.37	1.98	7009	126.7	9.50	±	3.88	−0.01	±	0.12
d136	E		82.0	16.57	1.81	5682	168.8	24.25	±	3.44	−0.17	±	0.08
d142	E		79.0	17.06	1.94	7652	161.4	15.75	±	4.42	0.03	±	0.09
d147	S0		58.9	16.19	1.85	7713	107.7	11.50	±	4.52	−0.13	±	0.11
d153	E		52.7	16.14	1.83	6684	127.9	24.50	±	5.09	−0.26	±	0.10
d154	S0		51.1	16.41	1.78	6833	57.1	25.25	±	5.18	−0.49	±	0.47
d156	E/S0		51.8	16.45		6671	84.8	12.45	±	4.49	−0.23	±	0.11
d157	S0		74.8	16.26	1.81	6107	131.5	4.25	±	2.28	0.24	±	0.13
d161	E		86.9	15.19	1.87	7146	190.3	10.40	±	3.57	0.15	±	0.09
d171	S0		81.0	16.57	1.78	6135	127.5	2.75	±	0.98	0.36	±	0.11
d181	S0		63.0	16.52	1.87	6090	120.3	10.30	±	4.06	−0.03	±	0.11
d182	S0		44.0	16.84	1.72	5702	120.2	7.30	±	3.96	−0.03	±	0.15
d191	S0		44.4	16.69	1.77	6592	90.9	10.15	±	4.80	−0.17	±	0.14
d192	S0		56.4	16.14	1.79	5435	87.5	9.45	±	3.64	−0.15	±	0.11
d193	E		72.4	16.43	1.82	7567	117.6	18.40	±	4.09	−0.07	±	0.09
d200	S0		104.0	16.08	1.82	7466	189.3	4.40	±	1.29	0.28	±	0.09

Table 5.1: *continued on next page*

continued from previous page

name	type		S/N	b_j	$b-r$	$cz_\odot$	σ	Age in *Gyrs*			[Fe/H]		
d204	E		53.1	15.99	1.75	7578	126.1	3.45	±	2.46	0.21	±	0.15
d207	E		78.1	16.07	1.80	6743	146.9	6.40	±	3.04	0.23	±	0.11
d209	S0		48.5	16.04	1.77	7182	80.7	2.70	±	1.68	0.26	±	0.15
d210	E		66.6	15.97	1.88	7252	144.6	15.05	±	4.69	−0.02	±	0.10
d224	S0		42.2	17.19	1.77	7597	59.5	8.20	±	3.66	−0.20	±	0.13
d231	S0		62.9	15.78	2.09	7878	127.8	7.35	±	3.58	0.09	±	0.13
ic3943	S0/a		97.8	15.55	1.97	6789	168.6	16.40	±	3.26	−0.03	±	0.07
ic3946	S0		73.8	15.28	1.95	5927	199.6	6.75	±	3.43	0.20	±	0.12
ic3947	E		93.6	15.94	1.91	5675	158.8	16.60	±	3.31	−0.10	±	0.07
ic3959	E		95.1	15.27	1.94	7059	215.9	10.30	±	3.38	0.21	±	0.08
ic3960	S0		95.5	15.85	1.89	6592	174.3	10.50	±	3.44	0.17	±	0.08
ic3963	S0		74.7	15.76	1.87	6839	122.4	21.75	±	3.60	−0.20	±	0.08
ic3973	S0/a		78.3	15.32	1.88	4716	228.0	3.10	±	1.23	0.44	±	0.13
ic3976	S0		105.8	15.80	1.95	6814	255.2	12.95	±	3.47	0.16	±	0.07
ic3998	SB0		75.5	15.70	1.90	9420	136.9	7.50	±	3.22	0.14	±	0.11
ic4011	E		52.5	16.08	1.82	7253	123.2	1.95	±	0.67	0.42	±	0.14
ic4012	E		90.7	15.93	1.86	7251	180.7	4.15	±	1.48	0.34	±	0.12
ic4026	SB0		86.3	15.73	1.77	8168	132.2	2.25	±	0.58	0.51	±	0.08
ic4041	S0		76.6	15.93	1.90	7088	132.5	3.80	±	1.82	0.34	±	0.14
ic4042	S0/a		67.8	15.34	1.86	6371	170.6	20.90	±	4.44	−0.11	±	0.09
ic4045	E		107.9	15.17	1.85	6992	217.6	4.20	±	1.05	0.38	±	0.10
ic4051	E		56.1	14.47	1.82	4994	228.8	3.95	±	3.25	0.57	±	0.15
ngc4850	E/S0		105.6	15.39	1.87	6027	189.8	13.65	±	2.98	−0.01	±	0.07
ngc4851	S0		50.0	16.00	1.95	7861	126.8	4.80	±	3.24	0.16	±	0.17
ngc4853	S0p	E+A	88.5	14.38	1.66	7676	140.8	3.95	±	0.85	−0.11	±	0.05
ngc4860	E		76.6	14.69	1.93	7926	277.3	13.65	±	4.20	0.33	±	0.12
ngc4864	E		103.4	14.70		6828	187.6	15.05	±	2.96	−0.05	±	0.06
ngc4867	E		117.3	15.44	1.83	4817	208.5	6.80	±	2.00	0.18	±	0.07

Table 5.1: *continued on next page*

continued from previous page

name	type	S/N	b_j	$b-r$	$cz_\odot$	σ	Age in *Gyrs*	[Fe/H]
ngc4869	E	101.9	14.97	2.06	6844	203.1	7.15 ± 2.07	0.30 ± 0.08
ngc4872	E/S0	80.1	14.79	1.78	7198	217.8	1.75 ± 0.60	0.69 ± 0.09
ngc4873	S0	100.8	15.15	1.91	5818	176.9	10.70 ± 3.18	0.07 ± 0.08
ngc4874	cD	64.4	12.78		7180	274.5	10.75 ± 5.66	0.25 ± 0.13
ngc4875	S0	88.7	15.88	1.96	8014	180.1	13.45 ± 3.72	0.06 ± 0.08
ngc4876	E	82.0	15.51	1.91	6710	164.1	4.70 ± 2.12	0.15 ± 0.12
ngc4881	E	94.7	14.73	1.87	6730	193.9	9.60 ± 3.34	0.17 ± 0.09
ngc4883	S0	85.3	15.43	1.89	8161	166.1	9.25 ± 3.27	0.16 ± 0.09
ngc4889	cD	141.6	12.62	1.91	6495	397.5	2.00 ± 1.09	0.71 ± 0.08
ngc4894	S0	55.0	15.87	1.74	4640	85.6	12.85 ± 5.31	−0.06 ± 0.12
ngc4895	S0	106.9	14.38		8458	239.8	11.40 ± 2.99	0.14 ± 0.07
ngc4896	S0	67.7	15.06	2.01	5988	164.0	3.95 ± 2.37	0.27 ± 0.14
ngc4906	E	91.4	15.44	1.98	7505	175.0	15.05 ± 3.76	0.03 ± 0.08
ngc4908	S0/E	72.5	14.91	1.87	8710	193.9	18.60 ± 4.43	−0.03 ± 0.08
ngc4919	S0	121.0	15.06	1.92	7294	191.5	10.50 ± 2.67	0.15 ± 0.06
ngc4923	E	109.0	14.78	1.93	5487	198.3	4.75 ± 1.49	0.31 ± 0.09

Table 5.1: Luminosity-weighted mean ages and metallicities of Coma cluster galaxies. Ages and metallicities have been calculated from a Worthey (1994) grid using $H\beta_G$–[MgFe] data. See the text for caveats associated with these measurements. It is primarily important that these numbers not be taken as exact measurements for a particular galaxy; they are intended only to provide a probe of the *relative* age and metallicities within the cluster. Also note that the measurement of ages older than 17 Gyrs is affected by the fact that the stellar population grid does not extend that far. The signal-to-noise (S/N) per Å given in the table is measured at the centre of the Lick/IDS index Fe5270. The apparent magnitudes, b_j and colours, $b-r$ are taken from Godwin, Metcalfe & Peach (1983).

The luminosity-weighted mean ages and metallicities can be more clearly seen in Figures 5.8 (an age–metallicity plot) and 5.9 (a log(age)–metallicity plot). The figures also show the error ellipsoids in the age–metallicity plane. A variation in shape and orientation of the error

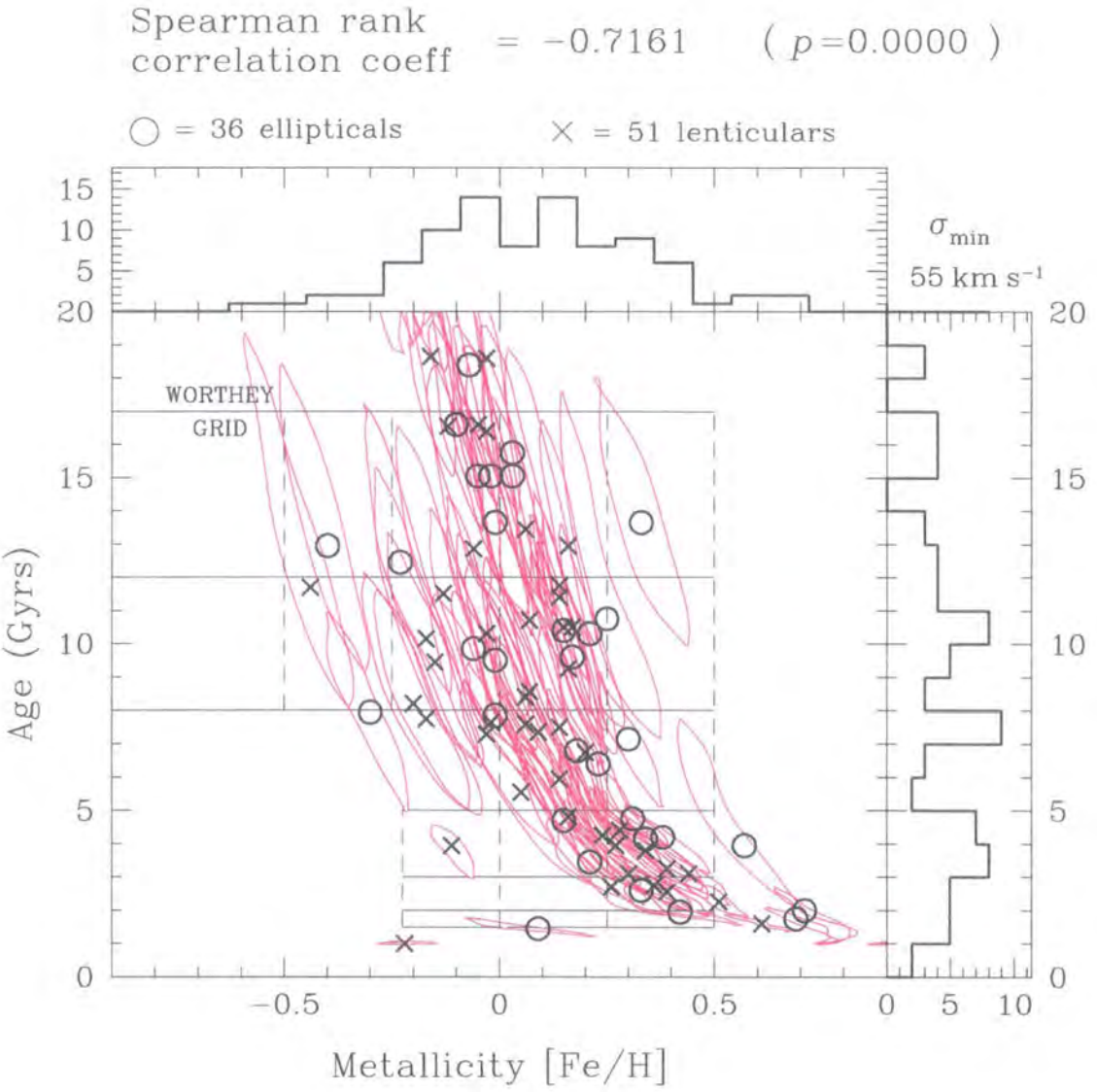

Figure 5.8: Age–metallicity plot for Coma cluster galaxies. Data is derived from Hβ_G and [MgFe] absorption line indices overlaid on a Worthey (1994) grid as described in Section 5.5. The variation in shape and orientation of the error ellipsoids across the age–metallicity plane can be seen. Errors are calculated after the method described in Section 5.6. For reference, the Worthey (1994) age and metallicity grid points are overlaid.

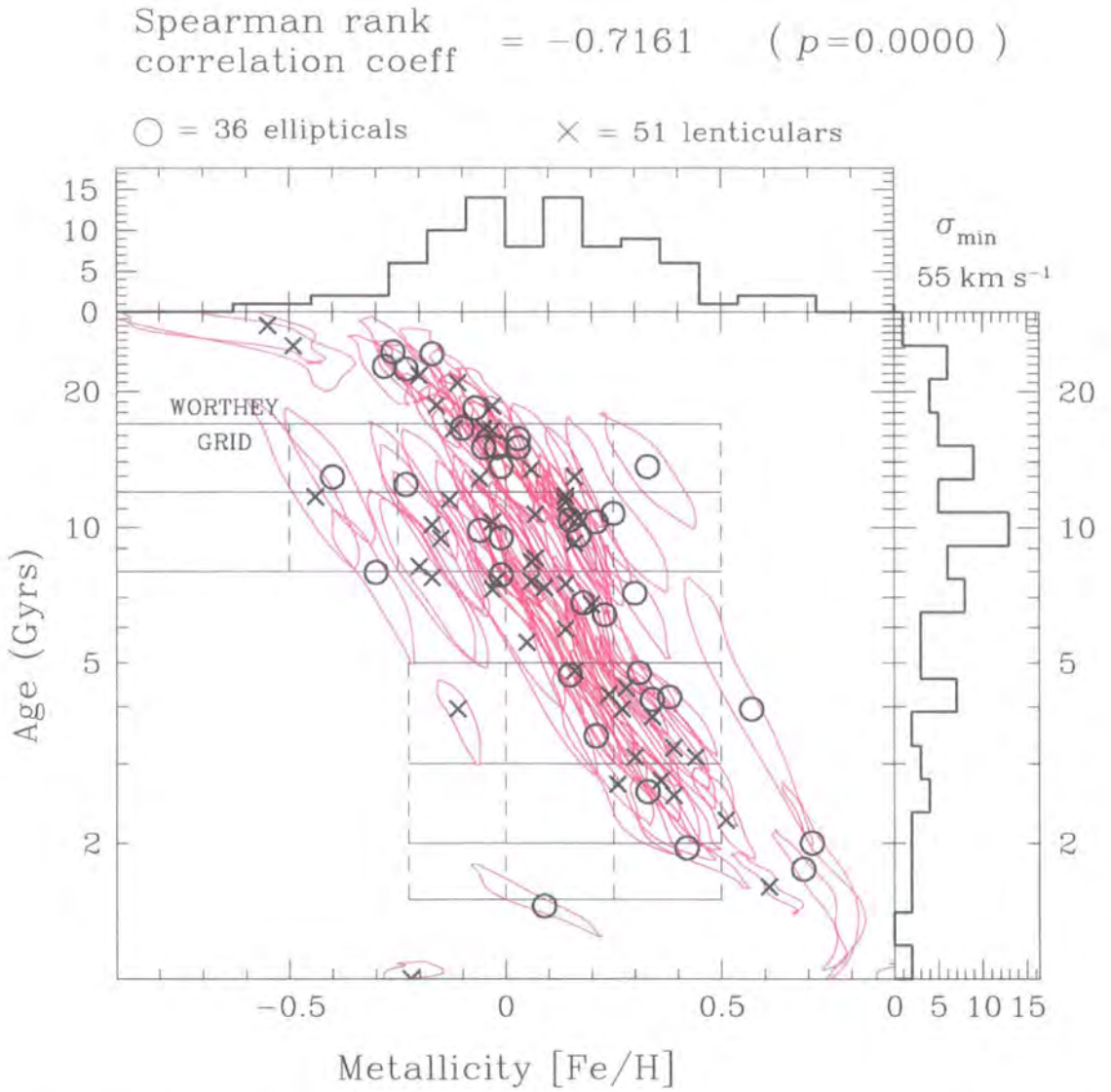

Figure 5.9: Logarithmic age–metallicity plot for Coma cluster galaxies. Data is derived from $H\beta_G$ and [MgFe] absorption line indices overlaid on a Worthey (1994) grid as described in Section 5.5. This figure is the same as Figure 5.8 except that it is plotted against logarithmic age (i.e. $\log_{10}$(age[Gyrs])). The variation in shape and orientation of the error ellipsoids across the age–metallicity plane can be seen. Errors are calculated after the method described in Section 5.6. For reference, the Worthey (1994) age and metallicity grid points are overlaid.

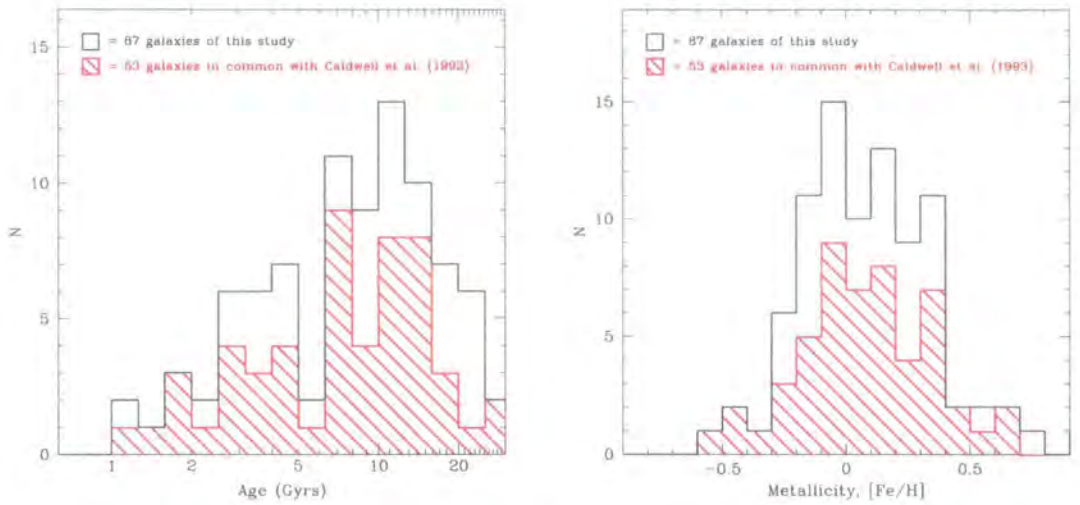

Figure 5.10: Comparison of study data with Caldwell et al. (1993) (see text).

ellipsoids across the plane is evident. It is also clear that plotting against logarithmic age (i.e. $\log_{10}$(age[Gyrs])) is more representative of the nature of the Worthey (1994) stellar population grid and gives us more power to probe the age and metallicity distributions. Qualitatively we can see that there is scatter in both the elliptical and lenticular galaxy populations across the age–metallicity plane (a distribution in logarithmic ages and in metallicity, [Fe/H] across the intervals $0 \leq \log(\text{age}) \leq 1.45$ and $-0.55 \leq [\text{Fe/H}] \leq +0.92$ is observed), though this is exacerbated by the nature of the errors which tend to exaggerate any age–metallicity relationship. A simple (i.e. ignoring the correlated nature of the errors) Spearman rank correlation coefficient test against the null hypothesis that the X and Y parameters are mutually independent is rejected ($p = 0.000$), indicating that there is indeed a correlation between luminosity-weighted mean age and metallicity.

5.8 Comparison with Caldwell et al. (1993) Coma cluster study

Caldwell et al. (1993) found that for $B < 17.2$ mag, 11 out of the 28 galaxies (39%) in the SW region of the Coma cluster are "abnormal", compared to only 3 out of 68 (4%) in the central field. They defined "abnormal" to be spectra indicative of recent star formation or nuclear activity, with CN/H8< -0.5*. This definition of "abnormal" is analogous to the "E+A" post-starburst

*a slope index which measures the depth of the H8 line ($\lambda = 3889$ Å) relative to the usually dominant CN bandhead ($\lambda = 3883$ Å)

name	type		S/N	b_j	$b-r$	$cz_\odot$	σ	Age in *Gyrs*			[Fe/H]		
d44	S0	E+A	55.7	16.57	1.77	7533	55.4	1.02	±	0.28	0.92	±	0.08
d73	E	E+A	49.2	17.33	1.84	5440	73.5	7.95	±	3.00	−0.30	±	0.10
d112	E	E+A	50.8	16.64	1.78	7433	58.3	1.45	±	0.30	0.09	±	0.15
ngc4853	S0p	E+A	88.5	14.38	1.66	7676	140.8	3.95	±	0.85	−0.11	±	0.05

Table 5.2: "E+A" galaxies in common between this study and that of Caldwell et al. (1993).

galaxies of Dressler (1987), Gunn & Dressler (1988) and MacLaren et al. (1988) which have significant star-formation ~ 1 Gyr ago for $z \simeq 0.3-0.5$†. Caldwell et al. (1993)'s results imply a small dispersion in early-type galaxy ages in the cluster core, whilst there is evidence for a wider spread in ages in the SW corner of the cluster implying that this part of the cluster (centred on NGC 4839) is possibly infalling to the main, older core of galaxies at the centre of the cluster.

Figure 5.10 contains a histogram of the early-type Coma cluster galaxy luminosity-weighted mean ages and metallicities from this dissertation. The shaded portion of the histograms indicates the galaxies in common with the Caldwell et al. (1993) study ($53/87 = 61\%$). The figure shows that the studies have similar selection functions, covering the same range in luminosity.

The Worthey (1994) grids used in this dissertation make it hard to probe directly this post-starburst population of galaxies as the youngest age supported by the grid is 1.5 Gyrs. However, it is found that in this study there are 7 out of 87 (8%) early-type galaxies with ages $\leq$2.0 Gyrs, in general agreement with Caldwell et al. (1993).

There are 4 "E+A" galaxies in common between the studies. These are: d44, d73, d112 and NGC 4853 (see Table 5.2). The two metal-rich galaxies d44 and d112 have "young" ages, possibly indicating recent star-burst activity and in agreement with Caldwell et al. (1993). The two metal-poor galaxies d73 and NGC 4853 have "intermediate" to "old" ages, indicating that any star-burst activity finished over 1 Gyr ago which is in disagreement with Caldwell et al. (1993) (see Worthey 1994 or Worthey & Ottaviani 1997 for a discussion of the effects of recent star-burst activity on galaxy spectra). This indicates that there could be an age–metallicity degeneracy for the factor CN/H8, though the sample of 4 "E+A" galaxies is too small to be conclusive about this.

†assuming a standard cosmological model with $H_0 = 50$ km s^{-1} Mpc^{-1}, $\Omega = 0.3$ and $\Lambda = 0.7$, redshifts of $z \simeq 0.3-0.5$ correspond to ages of 4.9–7.2 Gyrs

5.9 Analysis of stellar population data

Tables 5.3 and 5.4 show the results of a simplistic analysis of the Coma cluster early-type galaxy luminosity-weighted mean ages and metallicities plus the indices from which they were derived. The analysis assumes Gaussian statistics. The age parameter is analysed in the logarithmic domain, i.e. statistics for the age distribution of the cluster are calculated for $\log_{10}$(age[Gyrs]) to take into account the logarithmic nature of the age contours on the Worthey (1994) grids (see Section 5.4).

The total data set is seen to have a luminosity-weighted median age of 8.4 Gyrs with a standard deviation (SD) of 2.2 Gyrs and a luminosity-weighted median metallicity, [Fe/H] of 0.070 with a SD of 0.268 ($-0.55 \leq$ [Fe/H] $\leq +0.92$). This means that the early-type galaxies have a narrow age range, but a wide range of metallicities.

If I compare the results for the morphological sub-populations, I find an offset between the ellipticals and lenticulars in both the ([MgFe], H$\beta_{\rm G}$) and the (*metallicity, age*) plane, but a similarly small scatter in age and large scatter in metallicity. The median offset between ellipticals and lenticulars ($\Delta_{\rm E\text{-}S0}$) in the ([MgFe], H$\beta_{\rm G}$) plane is (0.098 ± 0.110 Å, -0.105 ± 0.129 Å), which is equivalent to (0.030 ± 0.073, 1.851 ± 0.593 Gyrs) in the (*metallicity, age*) plane and (0.030 ± 0.073, 0.074 ± 0.084 dex) in the (*metallicity, log(age)*) plane. It can be seen that small differences between the medians of the elliptical and lenticular H$\beta_{\rm G}$ distributions of marginal statistical significance (a 0.8 sigma detection, equivalent to a 58.4% confidence) translate to a larger differences between the medians of their *age* distributions with a higher statistical significance (a 3.1 sigma detection, equivalent to a 99.8% confidence). This increase is not seen between the medians of the elliptical and lenticular *log(age)* distributions (which has a 0.9 sigma detection of a difference, equivalent to a 62.2% confidence). This difference is due to the logarithmic nature of the age contours with respect to the H$\beta_{\rm G}$ stellar population indicator; for example, a small decrease in H$\beta_{\rm G}$ for values of H$\beta_{\rm G} \sim 1.5$ to 2.5 Å translates to a large increase in *age* but a small increase in *log(age)*. It is therefore important to analyse the age structure of a cluster in the *log(age)* domain rather than the *age* domain as the confidence levels of any results are more representative. Overall, the morphological sub-population analysis implies that the elliptical galaxy population is on average *older* than the lenticular galaxy population ($\Delta_{\rm E\text{-}S0}(log(age)) = 0.074 \pm 0.084$ dex, a 0.8 sigma detection equivalent to a 58.4% confidence). There is also marginal evidence for the elliptical galaxy population being *more metal rich* than the lenticular population ($\Delta_{\rm E\text{-}S0}(metallicity) = 0.030 \pm 0.073$, a 0.4 sigma detection equivalent

		$H\beta_G$ (Å)			Age (Gyrs)			$\log_{10}$(age[Gyrs])		
Galaxies	N	mean	median	SD	mean	median	SD	mean	median	SD
All early-types	87	2.149	2.076	0.532	7.551	8.400	2.184	0.877	0.932	0.312
		0.057	0.071		0.234	0.293		0.033	0.042	
Ellipticals	36	2.058	2.027	0.313	8.052	9.601	2.183	0.913	0.988	0.298
		0.052	0.065		0.364	0.455		0.050	0.062	
Lenticulars	51	2.213	2.132	0.636	7.216	7.750	2.178	0.851	0.914	0.322
		0.089	0.111		0.305	0.381		0.045	0.056	

Table 5.3: Stellar population data analysis: age indicator. Errors are quoted below a given statistic. This data analysis assumes Gaussian statistics.

		[MgFe] (Å)			Metallicity, [Fe/H]		
Galaxies	N	mean	median	SD	mean	median	SD
All early-types	87	3.313	3.365	0.417	0.089	0.070	0.268
		0.045	0.056		0.029	0.036	
Ellipticals	36	3.413	3.428	0.383	0.108	0.090	0.269
		0.064	0.080		0.045	0.056	
Lenticulars	51	3.243	3.330	0.426	0.076	0.060	0.266
		0.060	0.075		0.037	0.047	

Table 5.4: Stellar population data analysis: metallicity indicator. Errors are quoted below a given statistic. This data analysis assumes Gaussian statistics.

to a 31.9% confidence), though this result is uncertain due to the size of the errors in the metallicity plane. These differences are not caused by any selection effects, since the same selection function is used for ellipticals and lenticulars (see Section 2.2).

This simple analysis is illustrated in Figures 5.11 and 5.12 where the median values of the Coma cluster elliptical and lenticular galaxy populations in different planes are superimposed onto the observation distribution. It is obvious from these plots that: a small offset in the median $H\beta_G$ translates to a larger difference in the median age because of the logarithmic nature of the Worthey (1994) grid; this simplistic analysis is not a good approach to understanding the nature of the galaxies in the Coma cluster and does not take into account properly the errors of the data and their subsequent translation to the age/metallicity plane (see Section 5.7); and finally

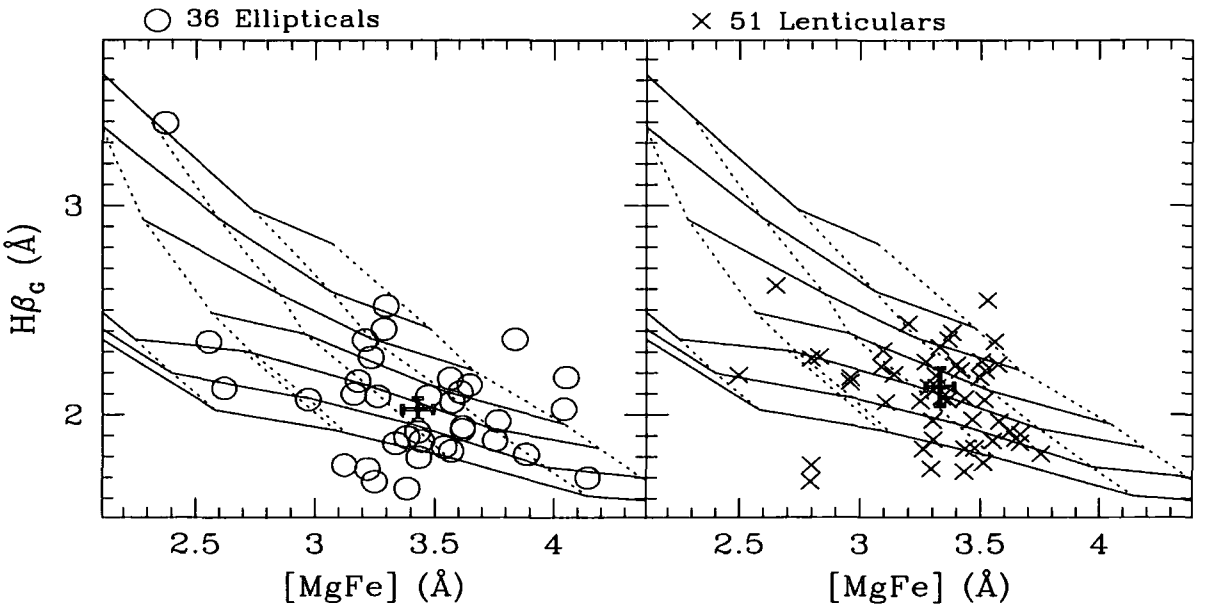

Figure 5.11: Elliptical and Lenticular galaxy population of Coma in the [MgFe] and $H\beta_G$ plane. The median value (with its errors bars) of both populations along the axes is shown. Gaussian statistics are assumed in this analysis. The data is superimposed on a Worthey (1994) grid.

that the analysis does not deal with distribution outliers well (these outliers can significantly affect any mean offset or standard deviation analysis).

Applying a two-sample Kolmogorov-Smirnov (KS) test (Smirnov 1939, Section 5.13.2) to the age and metallicity cumulative distribution functions of the elliptical and lenticular galaxy populations (Figure 5.13) gives $p_{age} = 0.6095$ and $p_{met} = 0.6601$, i.e. both the age and metallicity distributions are consistent with being drawn from the same parent distribution (since $p \gg 0.05$). This conclusion is not affected by applying a minimum velocity dispersion cutoff of $100\,\mathrm{km\,s^{-1}}$ (which gives $p_{age} = 0.4154$ and $p_{met} = 0.6010$). However this KS test analysis does not take into account any data errors.

In the following sections I will conduct a more rigorous analysis of the Coma cluster galaxy populations.

5.10 Age and metallicity correlation with galaxy parameters

Using the data in Section 5.7 combined with that from Sections 3.9, 3.10 and 6.5 I undertake a correlation analysis for the luminosity-weighted mean galaxy ages and metallicities versus various parameters. This analysis is firstly intended to demonstrate the success of the absorption line

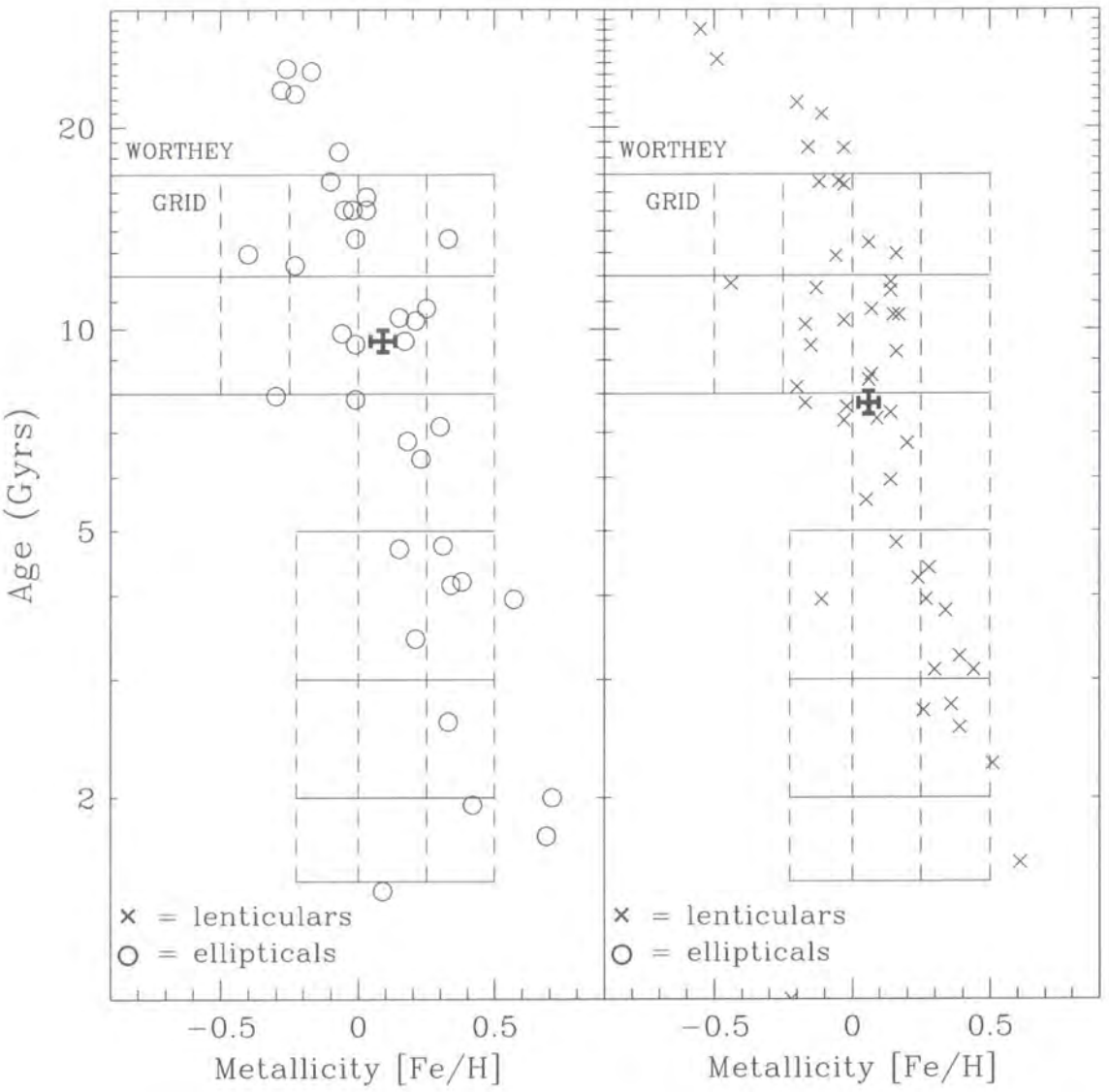

Figure 5.12: Elliptical and Lenticular galaxy population of Coma in the age/metallicity plane. The median value (with its errors bars) of both populations in the age/metallicity axes is shown. Gaussian statistics are assumed in this analysis. The data is superimposed on a Worthey (1994) grid.

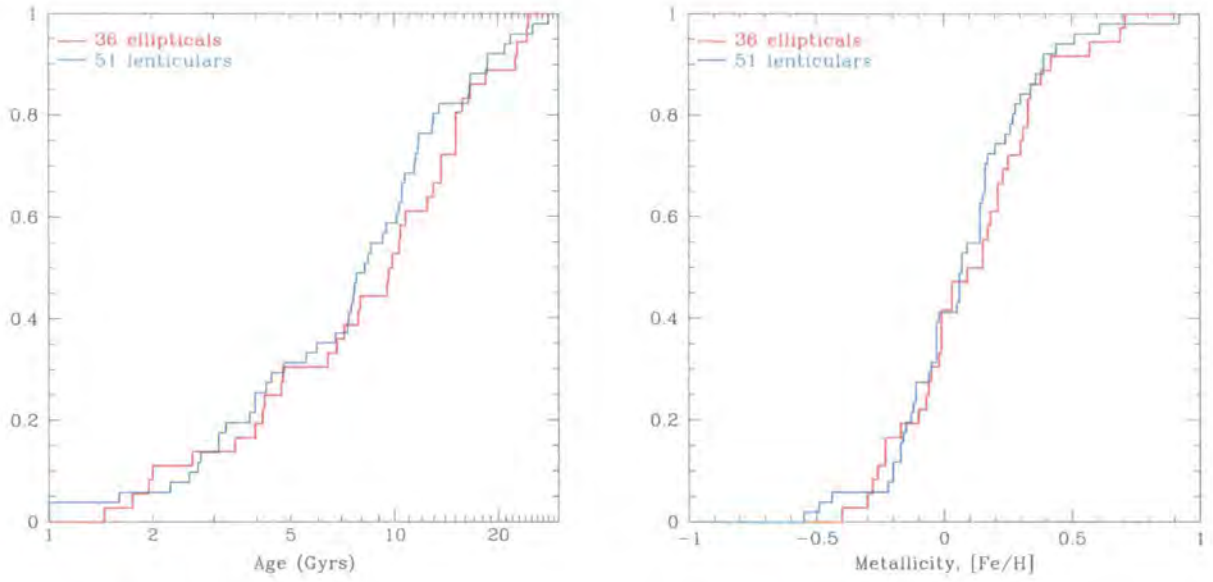

Figure 5.13: Age and metallicity cumulative distribution function analysis of the elliptical and lenticular galaxy populations of the Coma cluster core.

index strength observations plus stellar population synthesis model approach in determining galaxy ages and metallicities. The correlation analysis is also used to identify any correlations with other galaxy parameters that could affect the measurement of ages and metallicities.

Figures 5.14 to 5.17 and Table 5.5 show the results of this age and metallicity correlation analysis. Because of the logarithmic nature of the age grid in Worthey (1994)'s models, I compute correlations against log(age). A Spearman rank correlation coefficient test was used to detect any correlation. The null hypothesis was that the X and Y axes are mutually independent (i.e. un-correlated). Values of $p < 0.05$ reject this hypothesis, implying an underlying correlation between the parameters. For each two parameter family the following sub-samples were tested for correlations:

— all early-type galaxies with velocity dispersions (σ) greater than 55 and 100 $\mathrm{km\,s^{-1}}$;
— elliptical galaxies with velocity dispersions (σ) greater than 55 and 100 $\mathrm{km\,s^{-1}}$; and
— lenticular galaxies with velocity dispersions (σ) greater than 55 and 100 $\mathrm{km\,s^{-1}}$.

These sub-samples were used to examine the effect of different lower velocity dispersion cut-offs and to probe for differences between the morphological types.

I will now discuss separately the results of the age and metallicity correlation analysis.

Age correlation analysis

1. there is no trend of age with: ellipticity (ϵ_{re}), scale length ($\log r_e$), central velocity dispersion ($\log \sigma$), mass-to-light ratio ($M_{\rm dynamic}/L$), surface brightness ($\langle\mu\rangle_e$), total magnitude (Gunn $r_{\rm total}$), apparent magnitude (b_j), heliocentric redshift ($cz_\odot$), nor distance from the central cD galaxy (R (h^{-1}Mpc)). This means that the distribution of ages within the Coma cluster is not related to any of these parameters;

2. there is no correlation of age with U–V nor B–R colours. This means that these colours cannot be used to derive ages;

3. there is a clear correlation of age with H$\beta_{\rm G}$ as expected (since one is derived from the other);

4. there is a clear correlation of age with metallicity, [Fe/H] (this has already been discussed in Section 5.7);

5. there is no correlation of age with [MgFe], the metallicity dependent line index. This is actually slightly surprising, since some degree of correlation was expected because of the non-orthogonal nature of the Worthey H$\beta_{\rm G}$—[MgFe] grids. However, if the four "E+A" galaxies (see Section 5.8) d44, d73, d112 and NGC 4853 plus the young galaxy d26 (which was not observed by Caldwell et al. (1993) and which has an age of 1.00 Gyrs indicating recent starburst activity) are excluded from the correlation analysis, probabilities of $p = 0.1222$ (for $\sigma \geq 55\,{\rm km\,s^{-1}}$) and of $p = 0.1610$ (for $\sigma \geq 100\,{\rm km\,s^{-1}}$) are found. This indicates that a correlation could indeed be present;

6. there is no correlation between nebula emission (traced by [OIII]λ5007Å) and age (once the effect of outliers has been accounted for). This means that whilst there are a range of emissions across the cluster, with some galaxies having signs of active star formation whilst others are dormant, the observed small level of star formation does not effect the overall measurement of galaxy ages.

Metallicity correlation analysis

1. there is no trend of metallicity, [Fe/H] with: ellipticity (ϵ_{re}), scale length ($\log r_e$) (once the effect of outliers has been accounted for), surface brightness ($\langle\mu\rangle_e$), heliocentric redshift ($cz_\odot$), nor distance from the central cD galaxy (R (h^{-1}Mpc)). This means that the distribution of metallicities within the Coma cluster is not related to any of these parameters;

2. there is no correlation of metallicity with B–R, but there is a correlation with U–V. This implies that the U–V colour can be used to determine metallicity, though the scatter of the relationship is large. B–R cannot be used to measure metallicity. This demonstrates some of the problems inherent in using colours as indicators of stellar populations;

3. there is a clear correlation of metallicity, [Fe/H] with [MgFe] as expected (since one is derived from the other);

4. there is a clear correlation of metallicity, [Fe/H] with age (this has already been discussed in Section 5.7);

5. there is a clear correlation of metallicity, [Fe/H] with $H\beta_G$, the age dependent line index. This is due to the non-orthogonal nature of the Worthey $H\beta_G$—[MgFe] grids;

6. there is a clear trend of metallicity with central velocity dispersion (σ), total magnitude (Gunn $r_{\rm total}$) and apparent magnitude (b_j): brighter galaxies with larger central velocity dispersions are metal rich, whilst fainter galaxies with smaller central velocity dispersions are metal poor. This is a projection of a more complicated relationship, since there is a correlation between $\log\sigma$ and magnitude (the Faber–Jackson relationship) and between both Mg_2 and $\langle$Fe$\rangle$ and the central velocity dispersion (a fundamental plane relation, see Chapter 6);

7. there is a clear correlation of metallicity, [Fe/H] with mass-to-light ratio ($M_{\rm dynamic}/L$) with larger galaxies (with higher mass-to-light ratios) being metal rich whilst smaller galaxies (with lower mass-to-light ratios) are metal poor. This correlation is only seen in the elliptical galaxy population. However this could be due to the $r^{1/4}$ approximation in the derivation of the mass-to-light ratio (lenticular galaxies (and indeed fainter ellipticals) often have a more general $r^{1/n}$ relationship with $n < 4$, see Section 1.4). The observed correlation is a further result of the previously discussed correlation between metallicity

and central velocity dispersion (σ), total magnitude (Gunn $r_{\rm total}$) or apparent magnitude (b_j);

8. there is no correlation between nebula emission (traced by [OIII]λ5007Å) and metallicity. This means that whilst there are a range of emissions across the cluster, with some galaxies having signs of active star formation whilst others are dormant, the observed small level of star formation does not effect the overall measurement of galaxy metallicity.

The conclusion of this age and metallicity correlation analysis is that there are no new correlations which could affect any distribution analysis. The correlations that are observed have been found before and are readily explained.

The success of the H$\beta_{\rm G}$ and [MgFe] absorption line indices in tracing age and metallicity distributions with minimal age–metallicity degeneracy is evidenced by the small size of the correlation between H$\beta_{\rm G}$ and [Fe/H] and between [MgFe] and age. This is because the Worthey (1994) grids are approximately orthogonal in the H$\beta_{\rm G}$—[MgFe] plane. If the grids were completely orthogonal, then the age–metallicity degeneracy effect would be totally broken and no such correlations would be seen. The H$\beta_{\rm G}$ and [MgFe] line indices are currently the closest we can come to achieving this.

The lack of any correlation between the U–V and B–R colours and the age of the early-type galaxies and between B–R and their metallicities is significant. The Worthey (1994) models (see Figure 5.18) predict that for a fixed age, there is a correlation between colour and metallicity and for a fixed metallicity there is a correlation between colour and age. The simple analyses of the H$\beta_{\rm G}$ versus [MgFe] stellar population data in Sections 5.4, 5.7 and 5.9 have shown that the Coma cluster has a median age of 8.4 Gyrs with a small scatter of 2.2 Gyrs, and a median metallicity, [Fe/H] of 0.070 with a large scatter of 0.268 ($-0.55 \leq$ [Fe/H] $\leq +0.92$). This observed age and metallicity structure of the Coma cluster should be reflected in the U–V and B–R versus age plots (Figure 5.19) by the data closely following one of the vertical constant age lines (solid line). Since this is not seen, the conclusion is that the U–V and B–R colours are poor tracers of luminosity-weighted mean stellar population age. The observed age and metallicity structure should also be seen in the U–V and B–R versus metallicity plots (Figure 5.19), with the data again closely following a constant age contour (solid line at $+45°$). This is not seen

in the B–R versus metallicity plot, but is seen in the U–V versus metallicity plot. Therefore B–R is seen to be a poor tracer of both the age and metallicity structure, however whilst U–V is a poor tracer of age it is a good tracer of metallicity. To further probe the usefullness of the U–V colour, Figure 5.20 shows a closer analysis of the U–V colour versus apparant magnitude, *b*. I fit a linear relation to the colour–magnitude relation and investigate the residuals versus age and metallicity. Figure 5.20 shows that there is *no* correlation between the residuals and either age or metallicity, implying that age–metallicity degeneracy effects are indeed limiting the usefullness of the U–V colour. The next step in assessing the U–V colour is to attempt to remove the age–metallicity degeneracy effect. Figure 5.21 revists the U–V versus metallicity correlation. A linear relation is fit to the correlation and the the residuals around that fit are compared with age. A correlation is found between age and the residuals, showing that the previous lack of any correlation between U–V and age was indeed due to the masking effect of the age–metallicity degeneracy. The overall conclusion therefore is that B–R does *not* act as a good indicator of early-type galaxy stellar population ages and metallicities, probably because of the age–metallicity degeneracy effect (e.g. two galaxies with the *same* age and different metallicities will have *different* colours). However U–V does trace the metallicity sequence and the ages of the cluster early-type galaxy stellar populations, though only if the age–metallicity degeneracy is taken into account. Therefore in the absence of more detailed stellar population information (e.g. $H\beta_G$ versus [MgFe] which determine ages and metallicities to a much better precision), the U–V colour can be used to probe the age and metallicity structure of a rich clusters' early-type galaxy population.

		all early-types		ellipticals		lenticulars	
Parameter	$\sigma_{\rm min}$	N	$p_{\rm independent}$	N	$p_{\rm independent}$	N	$p_{\rm independent}$
versus log(age):							
U–V	$55\,{\rm km\,s^{-1}}$	64	0.8209	28	0.5265	36	0.9517
	$100\,{\rm km\,s^{-1}}$	52	0.5970	25	0.1626	27	0.5700
B–R	$55\,{\rm km\,s^{-1}}$	17	0.6129	15	0.8213	2	—
	$100\,{\rm km\,s^{-1}}$	16	0.8475	15	0.8213	1	—
ϵ_{re}	$55\,{\rm km\,s^{-1}}$	78	0.2382	32	0.1397	46	0.8261
	$100\,{\rm km\,s^{-1}}$	65	0.2073	29	0.1389	36	0.9024
$\log r_e$	$55\,{\rm km\,s^{-1}}$	78	0.7410	32	0.2201	46	0.5268
	$100\,{\rm km\,s^{-1}}$	65	0.3372	29	0.1428	36	0.9426
$\log \sigma$	$55\,{\rm km\,s^{-1}}$	87	0.7309	36	0.3966	51	0.4452
	$100\,{\rm km\,s^{-1}}$	69	0.9238	31	0.1373	38	0.3462
$M_{\rm dynamic}/L$	$55\,{\rm km\,s^{-1}}$	78	0.8962	32	0.3010	46	0.5613
	$100\,{\rm km\,s^{-1}}$	65	0.5178	29	0.0928	36	0.4500
$\langle\mu\rangle_e$	$55\,{\rm km\,s^{-1}}$	78	0.3237	32	0.1868	46	0.7612
	$100\,{\rm km\,s^{-1}}$	65	0.1599	29	0.2463	36	0.4819
Gunn $r_{\rm total}$	$55\,{\rm km\,s^{-1}}$	78	0.8276	32	0.2864	46	0.4884
	$100\,{\rm km\,s^{-1}}$	65	0.4503	29	0.1261	36	0.6406
b_j	$55\,{\rm km\,s^{-1}}$	87	0.3621	36	0.1206	51	0.7261
	$100\,{\rm km\,s^{-1}}$	69	0.1592	31	0.0455	38	0.8002
$cz_\odot$	$55\,{\rm km\,s^{-1}}$	87	0.7920	36	0.9648	51	0.8651
	$100\,{\rm km\,s^{-1}}$	69	0.8496	31	0.9261	38	0.6157
$H\beta_G$	$55\,{\rm km\,s^{-1}}$	87	0.0000	36	0.0000	51	0.0000
	$100\,{\rm km\,s^{-1}}$	69	0.0000	31	0.0000	38	0.0000
[Fe/H]	$55\,{\rm km\,s^{-1}}$	87	0.0000	36	0.0000	51	0.0000

Table 5.5: *continued on next page*

continued from previous page

		all early-types		ellipticals		lenticulars	
Parameter	$\sigma_{\rm min}$	N	$p_{\rm independent}$	N	$p_{\rm independent}$	N	$p_{\rm independent}$
	$100\,{\rm km\,s^{-1}}$	69	0.0000	31	0.0000	38	0.0000
[MgFe]	$55\,{\rm km\,s^{-1}}$	87	0.8147	36	0.3473	51	0.7842
	$100\,{\rm km\,s^{-1}}$	69	0.2438	31	0.1157	38	0.7108
[OIII]λ5007Å	$55\,{\rm km\,s^{-1}}$	87	0.0284	36	0.2034	51	0.0515
	$100\,{\rm km\,s^{-1}}$	69	0.0294	31	0.1187	38	0.1882
R (h^{-1}Mpc)	$55\,{\rm km\,s^{-1}}$	87	0.1878	36	0.7542	51	0.1651
	$100\,{\rm km\,s^{-1}}$	69	0.8594	31	0.8045	38	0.9692
versus [Fe/H]:							
U–V	$55\,{\rm km\,s^{-1}}$	64	0.0002	28	0.0013	36	0.0409
	$100\,{\rm km\,s^{-1}}$	52	0.0048	25	0.0065	27	0.2378
B–R	$55\,{\rm km\,s^{-1}}$	17	0.1498	15	0.3960	2	—
	$100\,{\rm km\,s^{-1}}$	16	0.3707	15	0.3960	1	—
ϵ_{re}	$55\,{\rm km\,s^{-1}}$	78	0.4996	32	0.3533	46	0.2395
	$100\,{\rm km\,s^{-1}}$	65	0.7644	29	0.4091	36	0.3263
$\log r_e$	$55\,{\rm km\,s^{-1}}$	78	0.2605	32	0.0061	46	0.3299
	$100\,{\rm km\,s^{-1}}$	65	0.1340	29	0.0179	36	0.6828
$\log \sigma$	$55\,{\rm km\,s^{-1}}$	87	0.0000	36	0.0001	51	0.0067
	$100\,{\rm km\,s^{-1}}$	69	0.0017	31	0.0015	38	0.1619
$M_{\rm dynamic}/L$	$55\,{\rm km\,s^{-1}}$	78	0.0009	32	0.0014	46	0.1040
	$100\,{\rm km\,s^{-1}}$	65	0.0154	29	0.0049	36	0.6745
$\langle\mu\rangle_e$	$55\,{\rm km\,s^{-1}}$	78	0.7210	32	0.2055	46	0.1481
	$100\,{\rm km\,s^{-1}}$	65	0.4508	29	0.1540	36	0.6368
Gunn $r_{\rm total}$	$55\,{\rm km\,s^{-1}}$	78	0.0022	32	0.0010	46	0.3494
	$100\,{\rm km\,s^{-1}}$	65	0.0130	29	0.0057	36	0.5522
b_j	$55\,{\rm km\,s^{-1}}$	87	0.0000	36	0.0001	51	0.0844
	$100\,{\rm km\,s^{-1}}$	69	0.0025	31	0.0011	38	0.4892

Table 5.5: *continued on next page*

continued from previous page

		all early-types		ellipticals		lenticulars	
Parameter	$\sigma_{\rm min}$	N	$p_{\rm independent}$	N	$p_{\rm independent}$	N	$p_{\rm independent}$
$cz_{\odot}$	$55\,{\rm km\,s^{-1}}$	87	0.5809	36	0.4608	51	0.8117
	$100\,{\rm km\,s^{-1}}$	69	0.9207	31	0.4981	38	0.6717
$H\beta_G$	$55\,{\rm km\,s^{-1}}$	87	0.0001	36	0.0190	51	0.0030
	$100\,{\rm km\,s^{-1}}$	69	0.0000	31	0.0012	38	0.0006
log(age)	$55\,{\rm km\,s^{-1}}$	87	0.0000	36	0.0000	51	0.0000
	$100\,{\rm km\,s^{-1}}$	69	0.0000	31	0.0000	38	0.0000
[MgFe]	$55\,{\rm km\,s^{-1}}$	87	0.0000	36	0.0000	51	0.0000
	$100\,{\rm km\,s^{-1}}$	69	0.0000	31	0.0003	38	0.0005
[OIII]λ5007Å	$55\,{\rm km\,s^{-1}}$	87	0.1049	36	0.5922	51	0.0875
	$100\,{\rm km\,s^{-1}}$	69	0.3114	31	0.6120	38	0.3823
R (h^{-1}Mpc)	$55\,{\rm km\,s^{-1}}$	87	0.3375	36	0.6071	51	0.3277
	$100\,{\rm km\,s^{-1}}$	69	0.1982	31	0.4877	38	0.2601

Table 5.5: Age and metallicity correlation analysis. A Spearman rank correlation coefficient test was performed against the null hypothesis that the X and Y axes were mutually independent (i.e. un-correlated). Values of $p < 0.05$ reject this hypothesis, implying an underlying correlation between the parameters.

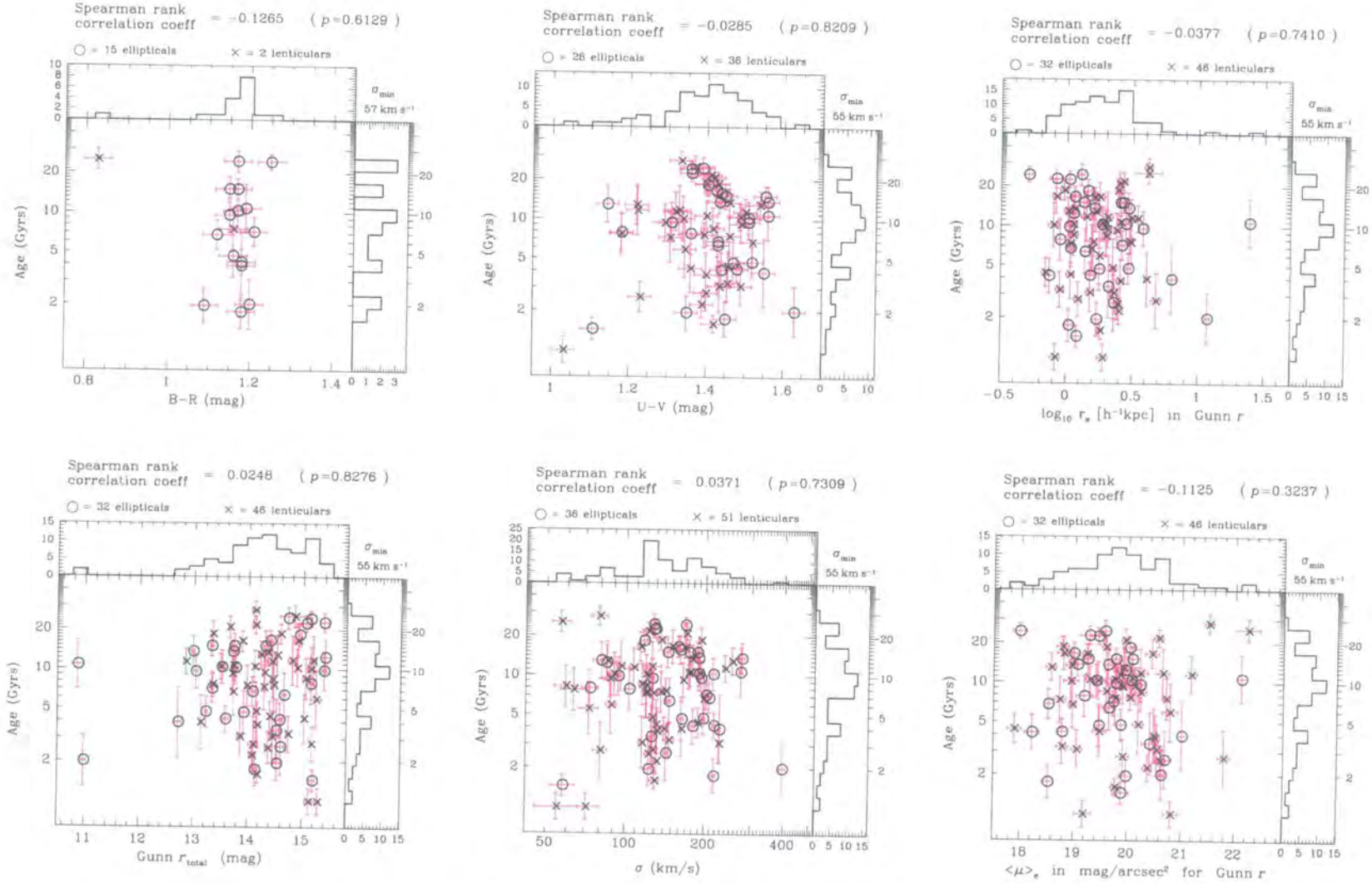

Figure 5.14: logarithmic age correlation analysis against B–R, U–V, $\log r_e$, Gunn $r_{\rm total}$, $\log \sigma$ and $\langle \mu \rangle_e$.

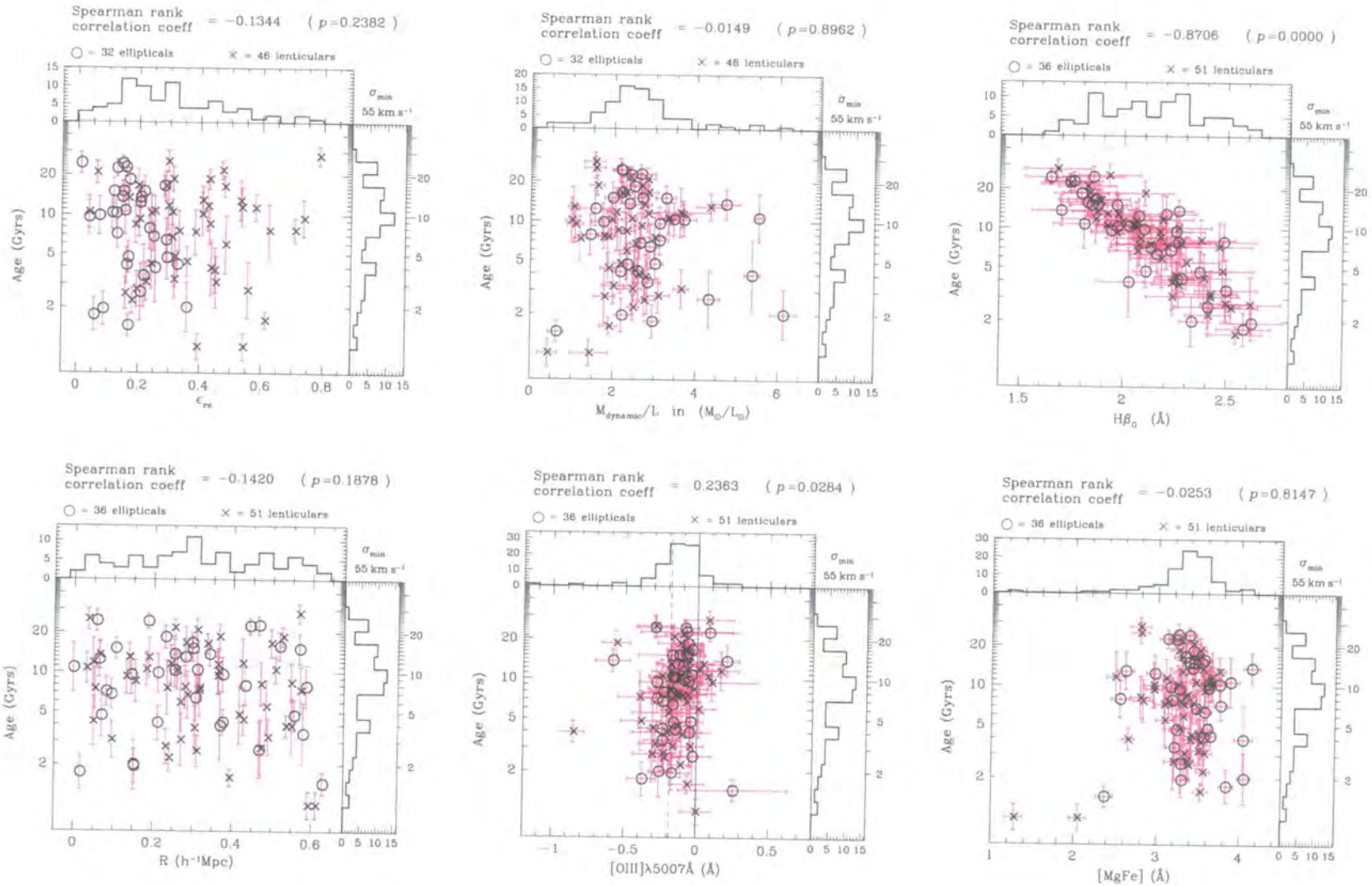

Figure 5.15: logarithmic age correlation analysis against ϵ_{re}, $M_{\rm dynamic}/L$, H$\beta_{\rm G}$, R (h^{-1}Mpc), [OIII]λ5007Å and [MgFe].

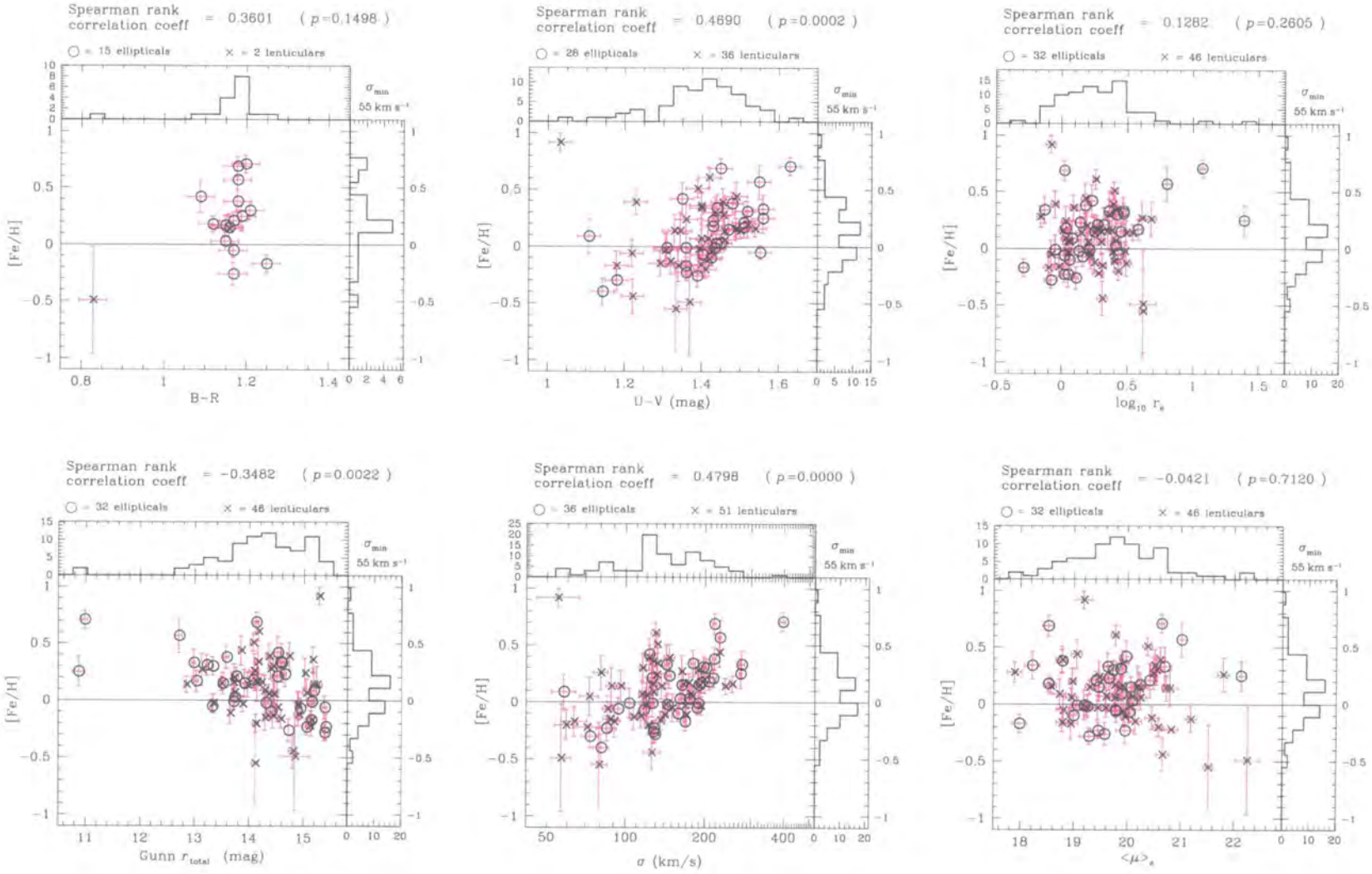

Figure 5.16: Metallicity, [Fe/H] correlation analysis against B–R, U–V, $\log r_e$, Gunn $r_{\rm total}$, $\log \sigma$ and $\langle \mu \rangle_e$.

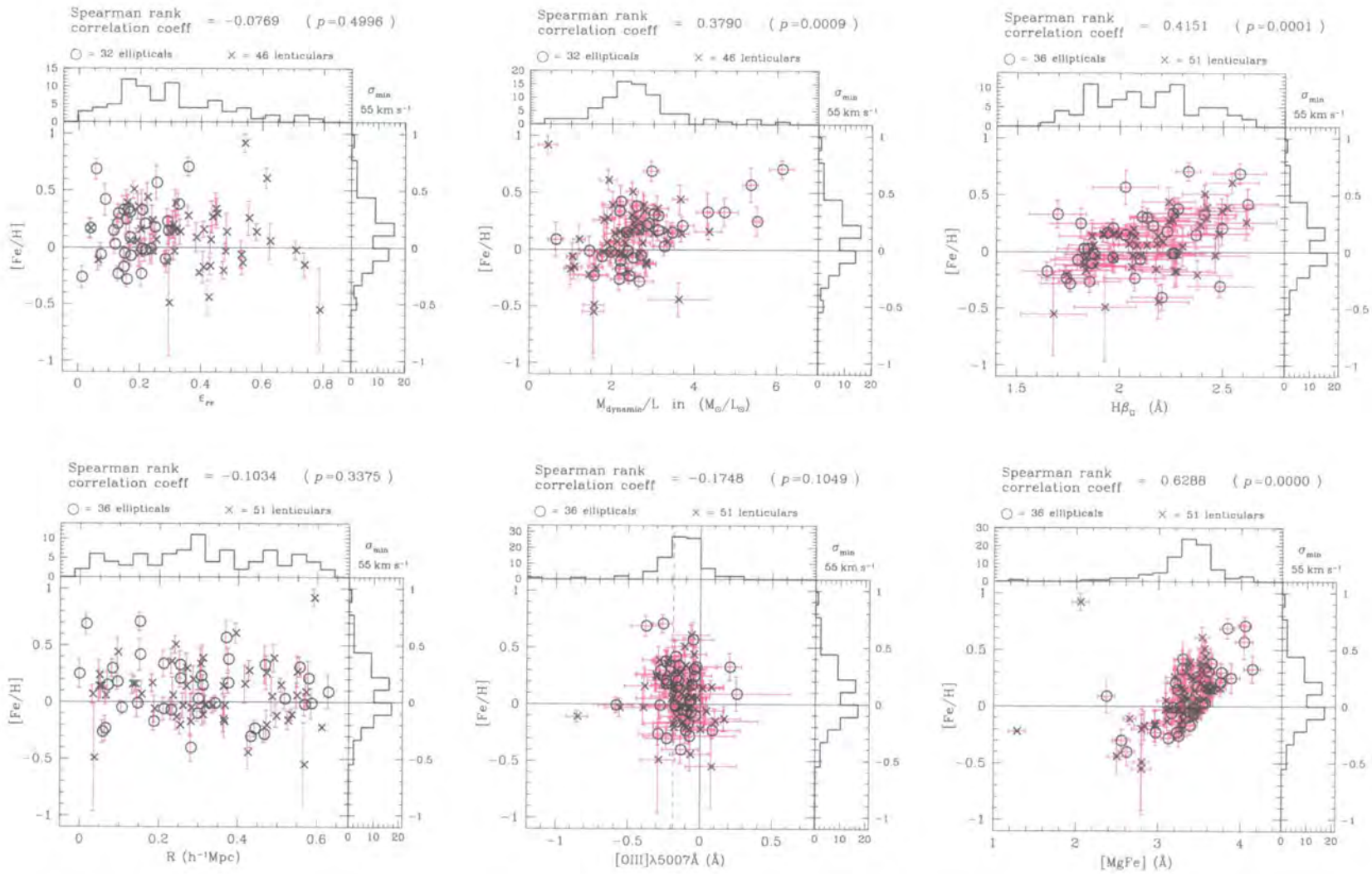

Figure 5.17: Metallicity, [Fe/H] correlation analysis against ϵ_{re}, $M_{\rm dynamic}/L$, H$\beta_{\rm G}$, R (h^{-1}Mpc), [OIII]λ5007Å and [MgFe].

5.11 Environmental dependence of galaxy ages and metallicities

Here I analyse the spatial projection of the cluster core in two dimensions. Since this study of the rich Coma cluster only contains bright early-type galaxies within the central 1 degree ($\equiv 1.26\,h^{-1}$ Mpc), the hypothesis is that there should be little environmental dependence on this relatively small scale for a virialised cluster with a common stellar population formation history within its bright early-type galaxies. Figure 5.22 shows the environmental dependence of the early-type galaxy luminosity-weighted mean stellar population ages and metallicities surrounding the central dominant galaxy NGC 4874; a plot of this dependence versus radial distance from this galaxy is also shown. The cD galaxies NGC 4874 (located at $0\,h^{-1}$Mpc in the plots) and NGC 4889 are highlighted by a large black circle surrounding their respective data points. In this figure units of h^{-1} Mpc are used for the X and Y coordinates and the radial distance. In the figures on the left (Figures 5.22(a) and 5.22(c)) the symbol size is scaled to represent either the age or metallicity value for that galaxy, with the scaling key for a figure given at its top. The figures on the right (Figures 5.22(b) and 5.22(d)) show the radial dependence of a parameter with respect to a galaxies distance from the central dominant galaxy NGC 4874. I will now discuss each of these environmental dependencies in turn.

Environmental dependence of luminosity-weighted mean galaxy age

Figures 5.22(a), 5.22(b) and Table 5.5 show that there is no radial nor environmental dependence for the mean age of the early-type galaxy stellar populations within the Coma cluster core, with galaxies with old and young stellar populations evenly distributed throughout the core of cluster. This suggests either a well-mixed cluster core, with no major merging events that trigger bursts of star formation within the past 1 Gyrs, or that any early-type galaxy stellar populations within the cluster core have followed a similar evolution history.

Environmental dependence of luminosity-weighted mean galaxy metallicity, [Fe/H]

Figure 5.22(d) and Table 5.5 show that there is no radial dependence of early-type galaxy mean stellar population metallicity with distance from the cD galaxy NGC 4874 within the Coma cluster core. However Figure 5.22(c) shows that there is instead a more complicated metallicity structure within the cluster core. In this figure it is evident that there is a concentration of

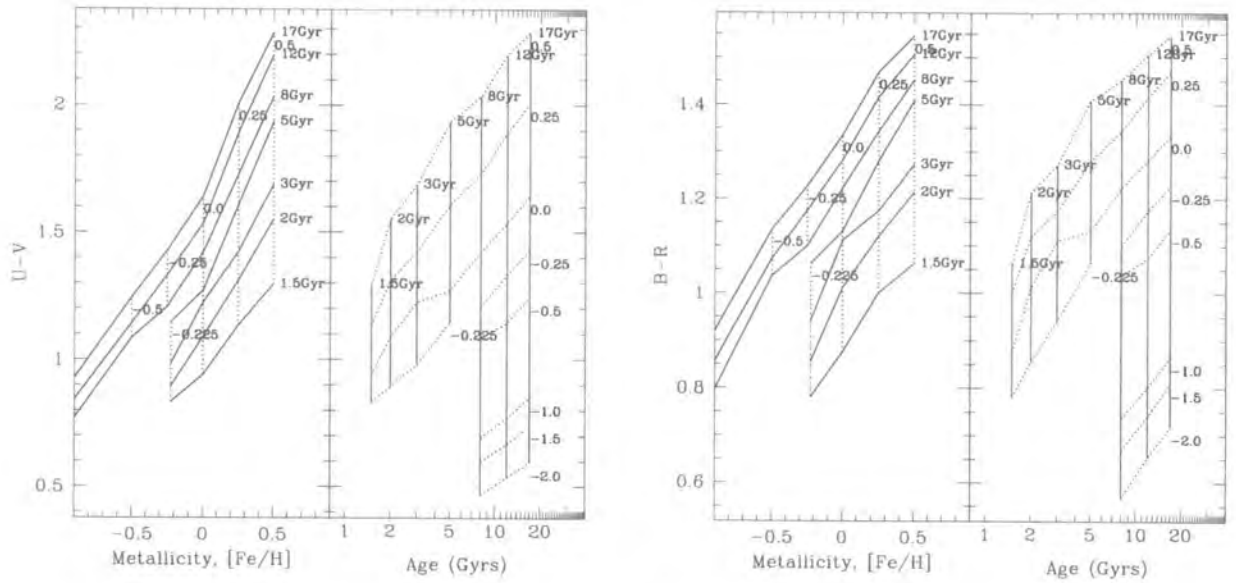

Figure 5.18: Worthey (1994) model colour grids. The Cousins R magnitudes of Worthey (1994) have been converted to Gunn r magnitudes using the transformation of Jørgensen (1994) of $r - R = 0.354$ mag. Isochrones (lines of constant age) are represented by the solid lines (1.5<age<17 Gyr). The dotted lines represent lines of constant metallicity ($-2 <$ [Fe/H] < 0.5). For a fixed age, there is a correlation between colour and metallicity and for a fixed metallicity there is a correlation between colour and age.

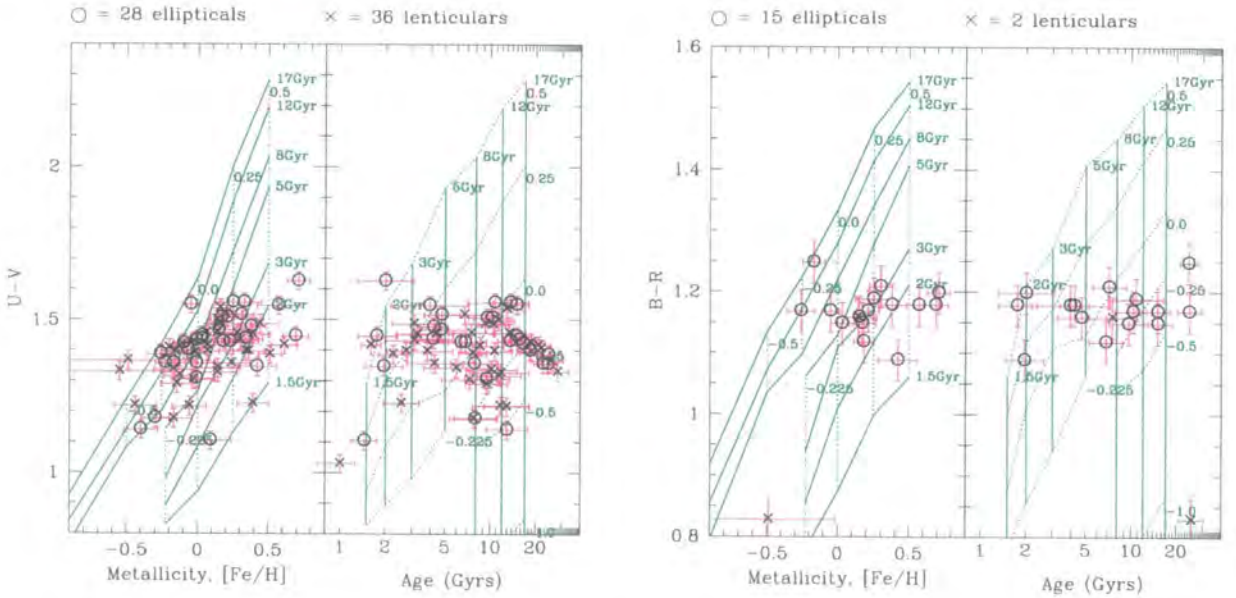

Figure 5.19: U–V and B–R colours versus age and metallicity superimposed on Worthey (1994) model grids. See text.

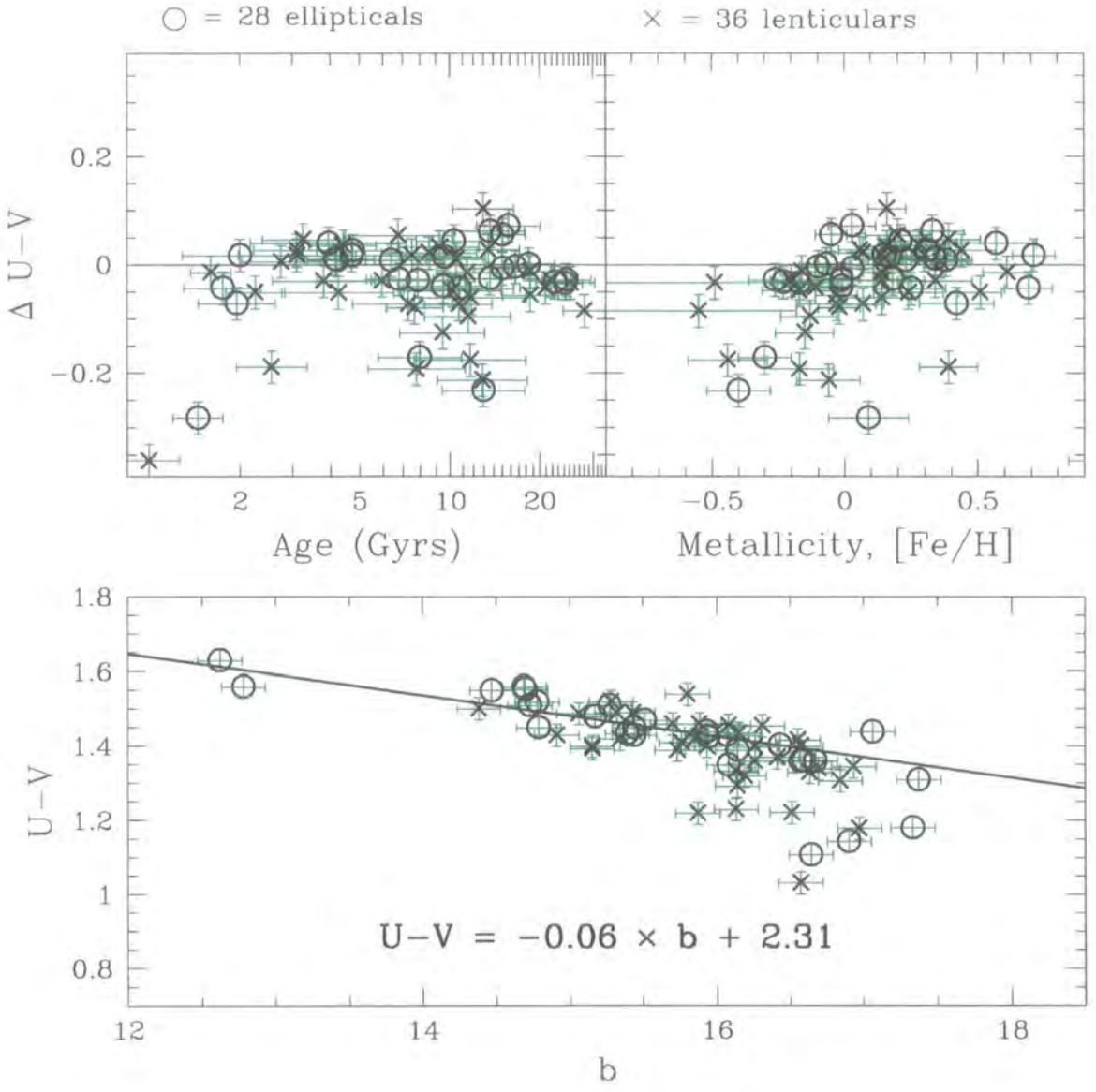

Figure 5.20: Analysis of the correlation of the colour–magnitude residuals versus age and metallicity. No correlation is found.

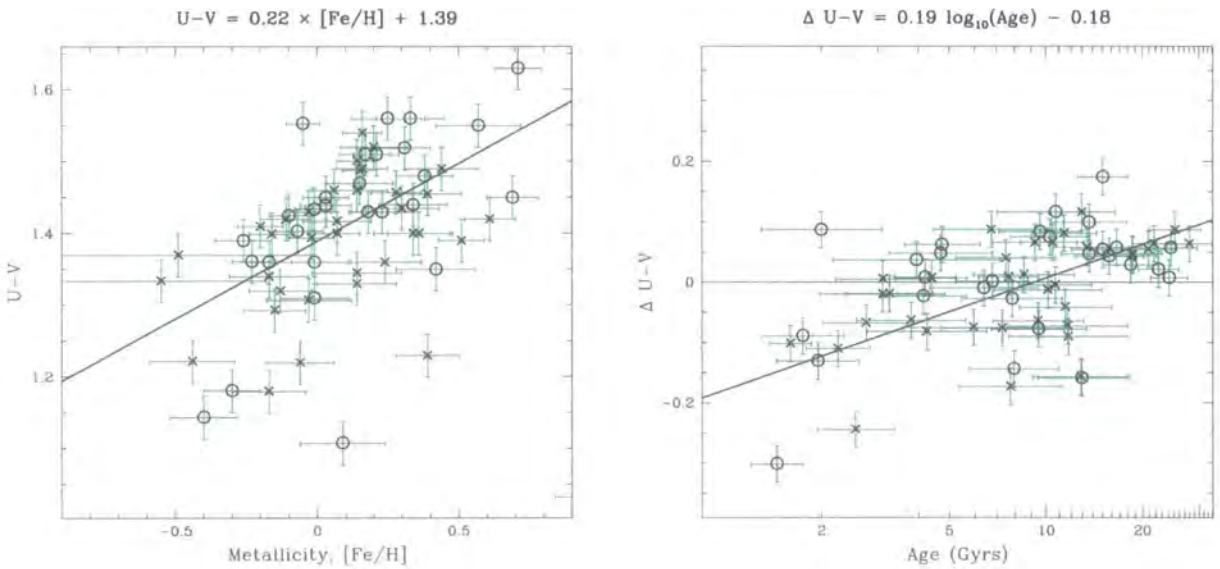

a. b.

Figure 5.21: Closer analysis of U–V versus metallicity correlation. Figure (a) shows the correlation with a linear fit superimposed. Figure (b) shows the residuals around this fit versus age. It can be seen that there is a correlation between ΔU–V and age that was previous masked by the age–metallicity degeneracy of the U–V colour.

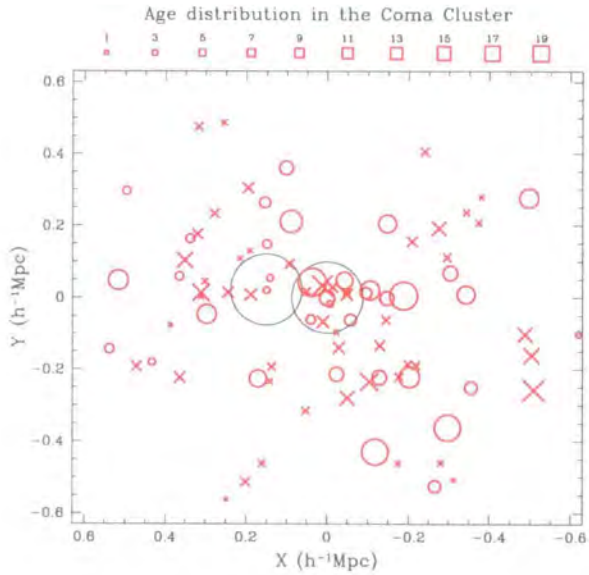

(a) age map

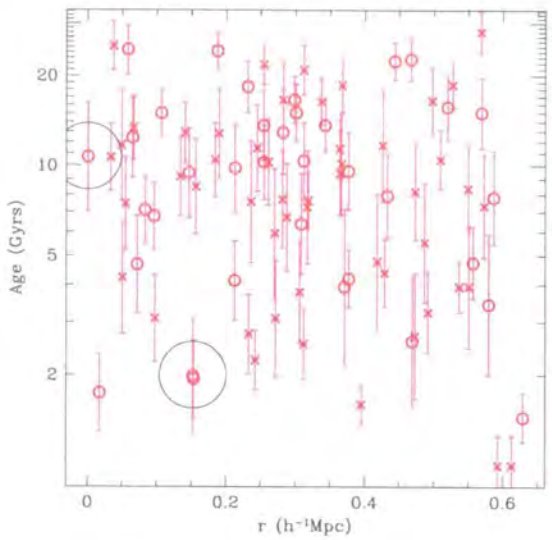

(b) age radial dependence

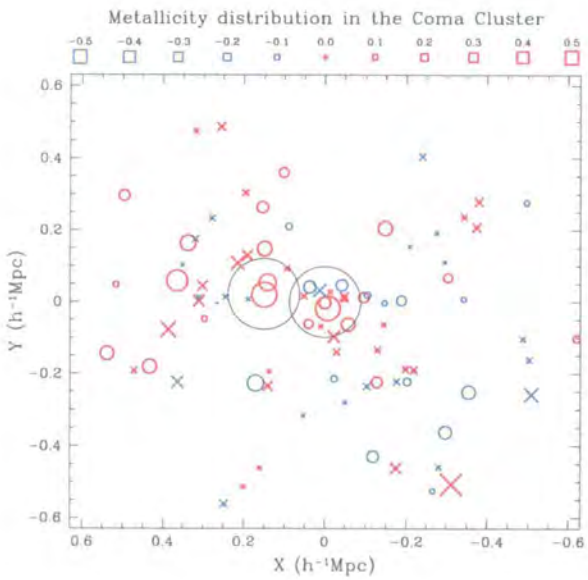

(c) metallicity map

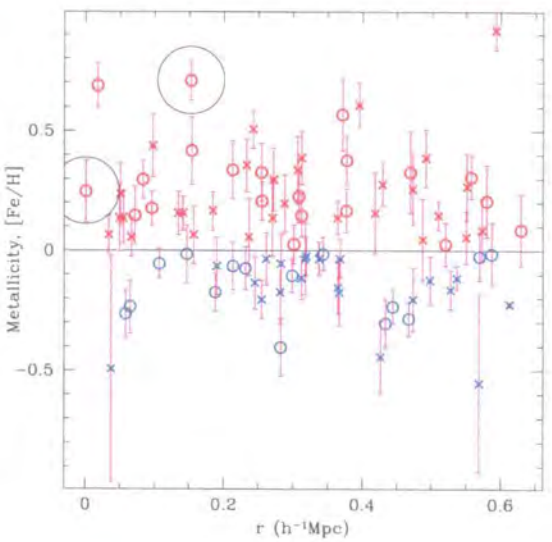

(d) metallicity radial dependence

Figure 5.22: Environmental dependence of early-type galaxy stellar population mean ages and metallicities. Ellipiticals are represented by circles, whilst lenticulars are represented by crosses. See text for a full description of this figure.

galaxies with metal rich stellar populations (red points, indicating [Fe/H]$\geq$ 0) in the north eastern part of the cluster core (top left of the figure) and a concentration of galaxies with metal poor stellar populations (blue points, indicating [Fe/H]$<$ 0) around the south western part (bottom right of the figure). This metallicity distribution structure argues against the Coma cluster core being well-mixed and relaxed. It suggests that either two large sub-groups of galaxies with different metallicities are merging to form the Coma cluster core that we see today or that the two different regions of the cluster core have undergone a different stellar population metallicity evolution history. Another possible explanation is that this is reflecting a luminosity structure within the Coma cluster core, with brighter galaxies in the north eastern part of the core and fainter galaxies in the south western part. This alternative explanation is partially supported by the presence of a marginal velocity dispersion structure within the core (Figure 1.3c), since velocity dispersion is directly related to luminosity (the Faber–Jackson relation, Figure 5.7). It is also supported by the observed correlation between metallicity and both luminosity and velocity dispersion discussed in Section 5.10 and seen in Figure 5.16. These larger, brighter galaxies are more metal rich than the smaller, fainter galaxies (see also the partition across the Worthey (1994) grid in Figures 5.5 and 5.6).

The picture that emerges from this analysis is of a rich cluster core that contains bright early-type galaxies with similar stellar population formation mean ages suggesting a common evolution history, but which contains some evidence of dynamic mergers or underlying differences between their stellar populations in the form of a metallicity "fossil record". This agrees with the conclusions from an analysis of the kinematic structure of the Coma cluster core (see Section 1.7.2) and with previous dynamical and X-ray studies of the Coma cluster (see Sections 1.7.1 and 1.7.3) that the core is not yet virialised and that structure is present.

5.12 Multiple hypothesis testing for age and metallicity distributions

Section 1.7 showed that the Coma cluster core has significant dynamical substructure (in agreement with recent studies) and is not a canonical example of a virialised rich cluster core. Section 5.11 also showed evidence that the early-type galaxies in the cluster core have differing stellar

populations, suggesting different formation/evolution histories. To investigate further the presence of any underlying distribution in the luminosity-weighted mean ages and metallicities of the stellar populations in Coma cluster bright early-type galaxies I now undertake non-parametric multiple hypothesis testing, rather than the simple Gaussian analysis discussed in Section 5.9. This multiple hypothesis testing does not assume any Gaussian distributions in the ages and metallicities and provides a much more comprehensive and powerful test for distributions, correctly taking into account the errors on the parameters. In the subsequent sections I test for the hypothesis of the presence of a *single age* of stellar population formation, for the hypothesis that the dominant stellar population in the galaxies all have the *same* metallicity and finally for the hypothesis that there is a *distribution* in ages amongst the early-type galaxy stellar populations.

5.13 Coma cluster single age of formation hypothesis

The first hypothesis to be tested is the hypothesis that there is a mean single luminosity-weighted dominant age of stellar population formation plus a distribution of metallicities within the early-type galaxies of the Coma cluster core. Section 5.13.1 details the Monte Carlo simulations that test this hypothesis, whilst Section 5.13.2 analyses the results.

5.13.1 Monte Carlo simulations testing single age of formation hypothesis

I conduct Monte Carlo simulations to test the hypothesis of a single age of stellar population formation in early-type galaxies using the following steps:

1. along the metallicity axis (cf. the [MgFe] axis) I bin the observed data in 0.1 [Fe/H] wide bins. This is done so that I preserve any distribution in metallicity whilst testing for any distribution in age.

2. I then draw N metallicity data points randomly from each bin, where N corresponds to the number of galaxies that are present in that bin in the observed data.

3. using the calculated Worthey (1994) grid points (see Section 5.5) I then match these metallicity data to the age, [MgFe] and H$\beta_{\rm G}$ values which would place it on a given isochrone. I now have coordinates in the [MgFe]–H$\beta_{\rm G}$ and age–metallicity planes for N mock galaxies per bin.

4. these ([MgFe],Hβ_G) coordinates are then compared to the observed data and the errors of the nearest observed galaxy assigned to each mock galaxy. This preserves the effect of any variation in the error ellipsoids across the [MgFe]–Hβ_G plane. The modelling has now transposed to the [MgFe]–Hβ_G plane since the errors form a well defined ellipse in this plane; this is not the case in the age–metallicity plane (see Section 5.7).

5. new ([MgFe],Hβ_G) coordinates are then sampled within the given errors, assuming a Gaussian error distribution. I now have ([MgFe],Hβ_G) coordinates for N mock galaxies per bin with the effect of random errors taken into account.

6. this new set of mock galaxies, with their randomly sampled ([MgFe],Hβ_G) coordinates, are compared to the Worthey (1994) grid and their ages and metallicities calculated.

7. this Monte Carlo simulation is repeated 1000 times to create a large database for subsequent statistical analysis through comparison with the observed data.

Using this method I test the observed data against the hypothesis that the stellar populations in the galaxies formed at a fixed age, testing a range of ages from 6.0 to 12.0 Gyrs using 1.0 Gyrs steps.

Examples of the mock data used to test the hypothesis of the presence of a single age of stellar population formation given an observed metallicity distribution are shown in Figures 5.23 (all early-type galaxies), 5.24 (elliptical galaxies) and 5.25 (lenticular galaxies). These figures show one data set from 1000 Monte Carlo randomly generated data sets, with ages ranging from 6.0 to 12.0 Gyrs (in 1.0 Gyrs steps). The data contained in these figures are compared statistically to the observed data to determine whether the hypothesis is supported.

5.13.2 Statistical analysis of single age of formation hypothesis

To statistically analyse the validity of the different hypotheses of single ages of formation against the observed data I use a two-sided two-sample Kolmogorov-Smirnov or KS test (Smirnov 1939). This test makes the following assumptions:

- the data consists of 2 mutually independent random samples, one of size n $(X_1, X_2, ..., X_n)$ and the other of size m $(Y_1, Y_2, ..., Y_m)$, where the respective unknown distribution functions are denoted by $F(x)$ and $G(x)$;

- the measurement scale is at least ordinal; and

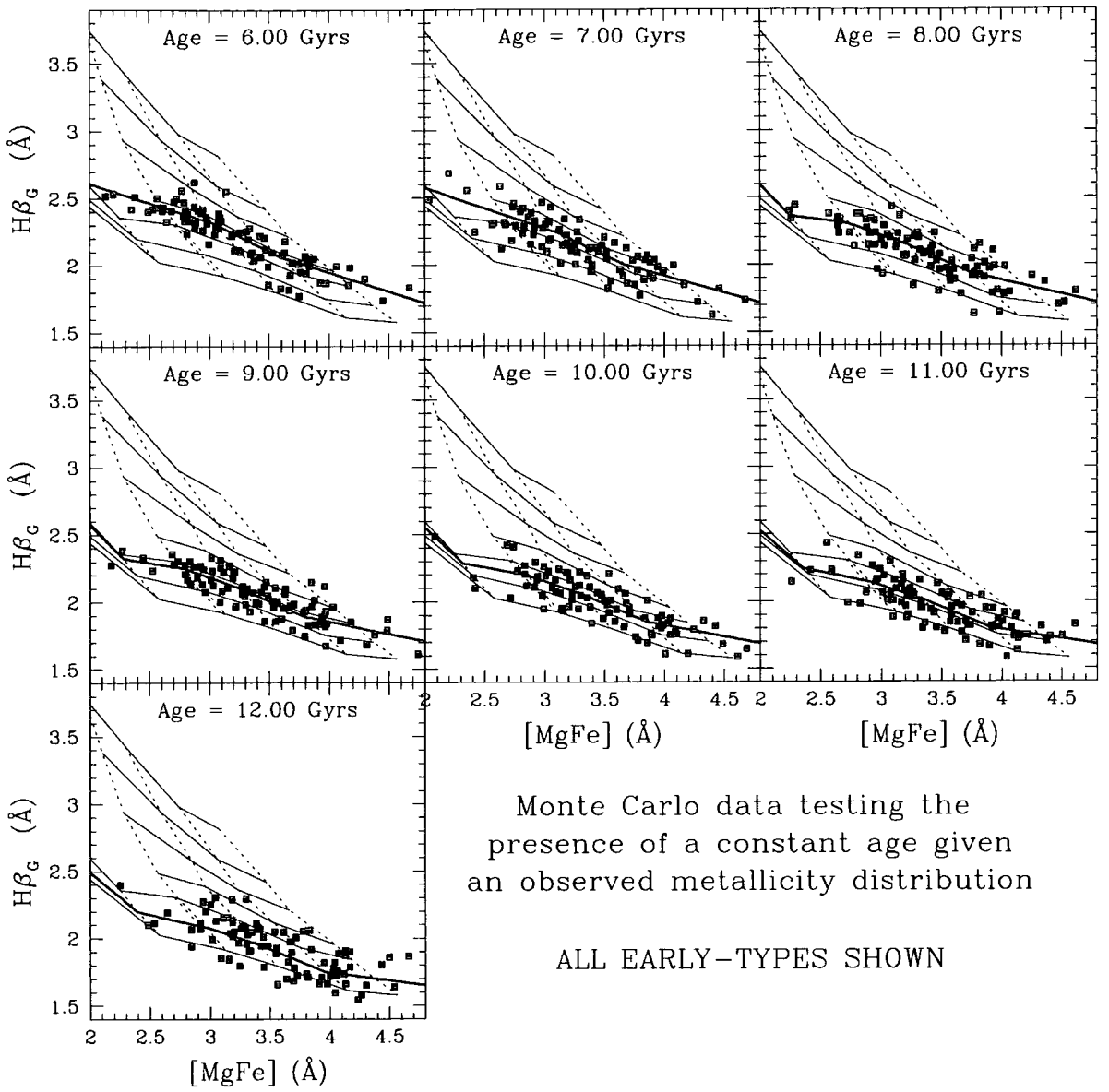

Figure 5.23: Isochrone Monte Carlo data. This figure contains Monte Carlo data in the $H\beta_G$–[MgFe] plane that is used to test the presence of a constant age given an observed metallicity distribution. One data set from the 1000 runs is shown, containing mock data to test the distribution of all the early-type galaxies in the observed sample. The solid line represents the constant age contour from which the data is drawn. The data is superimposed on a Worthey (1994) grid.

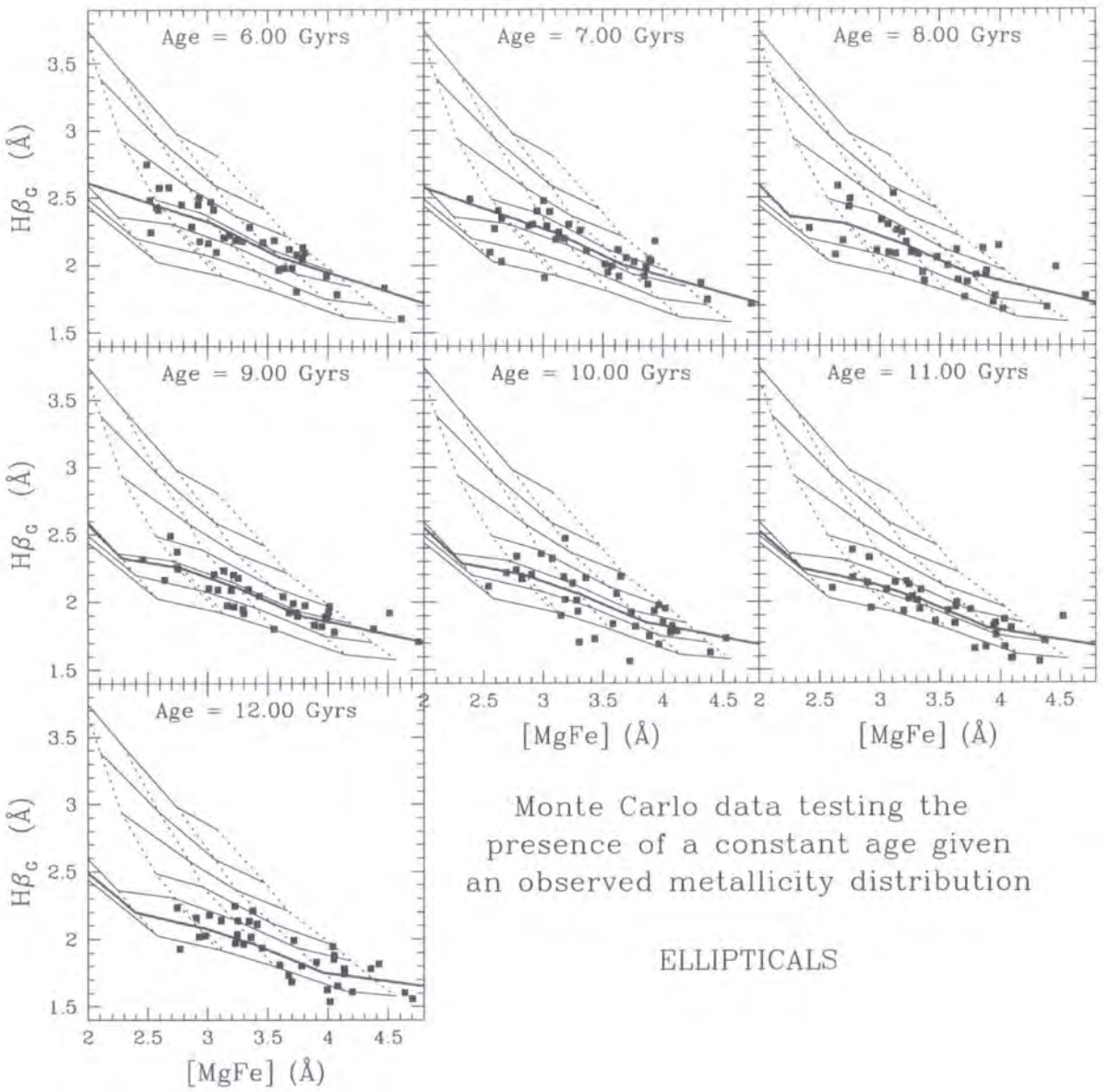

Figure 5.24: Isochrone Monte Carlo data for the Elliptical galaxy population.

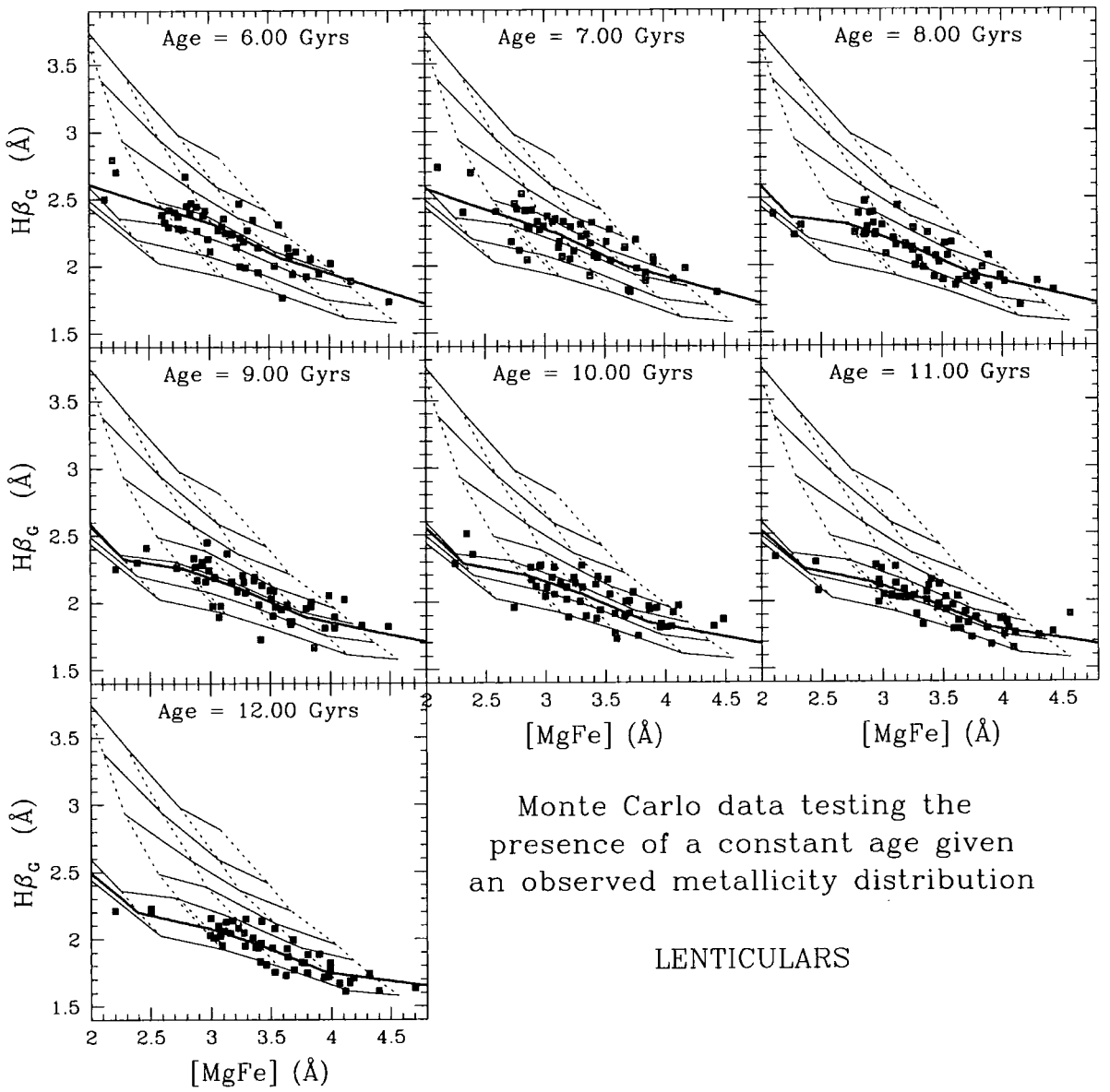

Figure 5.25: Isochrone Monte Carlo data for the Lenticular galaxy population.

- in order for the test to be exact the random variables need to be continuous, otherwise the test is likely to be conservative.

The two-sided null hypothesis that is tested for is:

$$H_o: \quad F(x) = G(x) \text{ for all } x \text{ from } -\infty \text{ to } +\infty \tag{5.1}$$

i.e. the null hypothesis is that the population distribution functions are identical. Let $S_1(x)$ be the empirical distribution function based on the random sample $X_1, X_2, ..., X_n$ and let $S_2(x)$ be the empirical distribution function based upon the other random sample $Y_1, Y_2, ..., Y_m$. The test statistic T_1 is defined as the greatest vertical distance between the two empirical distribution functions:

$$T_1 = \sup_x \| S_1(x) - S_2(x) \| \tag{5.2}$$

This test statistic is then compared to the quantiles of the two-sample Kolmogorov-Smirnov statistic and a probability, p derived. This p-value is then compared to the following criteria to decide the statistical merit of the identical population distribution function null hypothesis:

$p < 0.05$	the null hypothesis is strongly inconsistent with the data
$0.05 < p < 0.10$	there is a marginal inconsistency with the null hypothesis
$p > 0.10$	there is little or no evidence against the null hypothesis

Values of $p < 0.05$ therefore reject the hypothesis.

The test is both a two-sample KS test and a two-sided two-sample KS test since four distribution functions are compared: the observed and hypothesised (in the form of "mock data") age and metallicity distributions. This approach gives a two-dimensional statistical distribution test.

This two-sided two-sample KS test is performed on the total early-type galaxy population initially, and then on the elliptical and lenticular sub-populations to determine whether there are any differences in their population distributions.

Figure 5.26 and Table 5.6 show the results of this statistical analysis against the different hypotheses that the stellar populations in the galaxies formed at a fixed age (testing a fixed age of between 6.0 and 12.0 Gyrs using 1.0 Gyrs steps). The mean confidence value, p shown is

	E/S0 (n=87)		E (n=36)		S0 (n=51)	
Hypothesis	$p_{\rm age}$	$p_{\rm met}$	$p_{\rm age}$	$p_{\rm met}$	$p_{\rm age}$	$p_{\rm met}$
6.00 Gyrs	$0.000\ ^{+0.000}_{-0.000}$	$0.838\ ^{+0.105}_{-0.222}$	$0.007\ ^{+0.010}_{-0.006}$	$0.886\ ^{+0.096}_{-0.179}$	$0.008\ ^{+0.016}_{-0.006}$	$0.911\ ^{+0.059}_{-0.183}$
7.00 Gyrs	$0.002\ ^{+0.005}_{-0.002}$	$0.851\ ^{+0.092}_{-0.108}$	$0.045\ ^{+0.079}_{-0.037}$	$0.901\ ^{+0.081}_{-0.194}$	$0.090\ ^{+0.098}_{-0.066}$	$0.914\ ^{+0.055}_{-0.186}$
8.00 Gyrs	$0.039\ ^{+0.066}_{-0.027}$	$0.875\ ^{+0.068}_{-0.132}$	$0.203\ ^{+0.137}_{-0.134}$	$0.915\ ^{+0.067}_{-0.208}$	$0.136\ ^{+0.147}_{-0.093}$	$0.910\ ^{+0.060}_{-0.182}$
9.00 Gyrs	$0.017\ ^{+0.031}_{-0.012}$	$0.891\ ^{+0.052}_{-0.147}$	$0.311\ ^{+0.199}_{-0.187}$	$0.930\ ^{+0.052}_{-0.045}$	$0.073\ ^{+0.046}_{-0.049}$	$0.917\ ^{+0.053}_{-0.189}$
10.00 Gyrs	$0.005\ ^{+0.008}_{-0.004}$	$0.897\ ^{+0.089}_{-0.154}$	$0.254\ ^{+0.256}_{-0.129}$	$0.931\ ^{+0.051}_{-0.047}$	$0.034\ ^{+0.039}_{-0.021}$	$0.926\ ^{+0.072}_{-0.198}$
11.00 Gyrs	$0.001\ ^{+0.002}_{-0.001}$	$0.906\ ^{+0.081}_{-0.162}$	$0.133\ ^{+0.207}_{-0.064}$	$0.941\ ^{+0.042}_{-0.056}$	$0.009\ ^{+0.015}_{-0.009}$	$0.932\ ^{+0.066}_{-0.204}$
12.00 Gyrs	$0.000\ ^{+0.000}_{-0.000}$	$0.921\ ^{+0.066}_{-0.062}$	$0.053\ ^{+0.071}_{-0.036}$	$0.941\ ^{+0.042}_{-0.056}$	$0.001\ ^{+0.003}_{-0.001}$	$0.937\ ^{+0.061}_{-0.061}$

Table 5.6: Two-sample KS test results for dominant luminosity-weighted mean single age of early-type galaxy stellar population formation hypothesis (see text).

calculated from the central 68.3% of the database (i.e. 1 sigma clipping) of 1000 Monte Carlo runs for each test; this minimises the effect of any rogue outliers in the sample distribution. The upper and lower limit to this mean probability is taken as the values at the 1 sigma boundaries.

It can be seen that the metallicity distribution *always* supports the null hypothesis with a very high degree of confidence. This is in fact *by definition* since a key point in the construction of the mock data sets to test the presence of a dominant luminosity-weighted mean single age population was that they should *match* the metallicity distribution of the observed sample to maximise the power of the modelling to unlock any underlying single age population. This high confidence in the metallicity distribution comparison indicates that the modelling is working and is indeed matching the observed metallicity distribution.

The results of the two-sample KS test on the age and metallicity distributions lead to the following observations for the total early-type galaxy population and for the elliptical and lenticular sub-populations:

All early-type galaxies

I can completely rule out a dominant luminosity-weighted single aged stellar population of 6, 7, 9, 10, 11 or 12 Gyrs in the early-type galaxies within the Coma cluster given the observed metallicity distribution. I can also rule out with a high degree of confidence the presence of a 8 Gyrs single aged population, which at best is *marginally inconsistent* with the null hypothesis

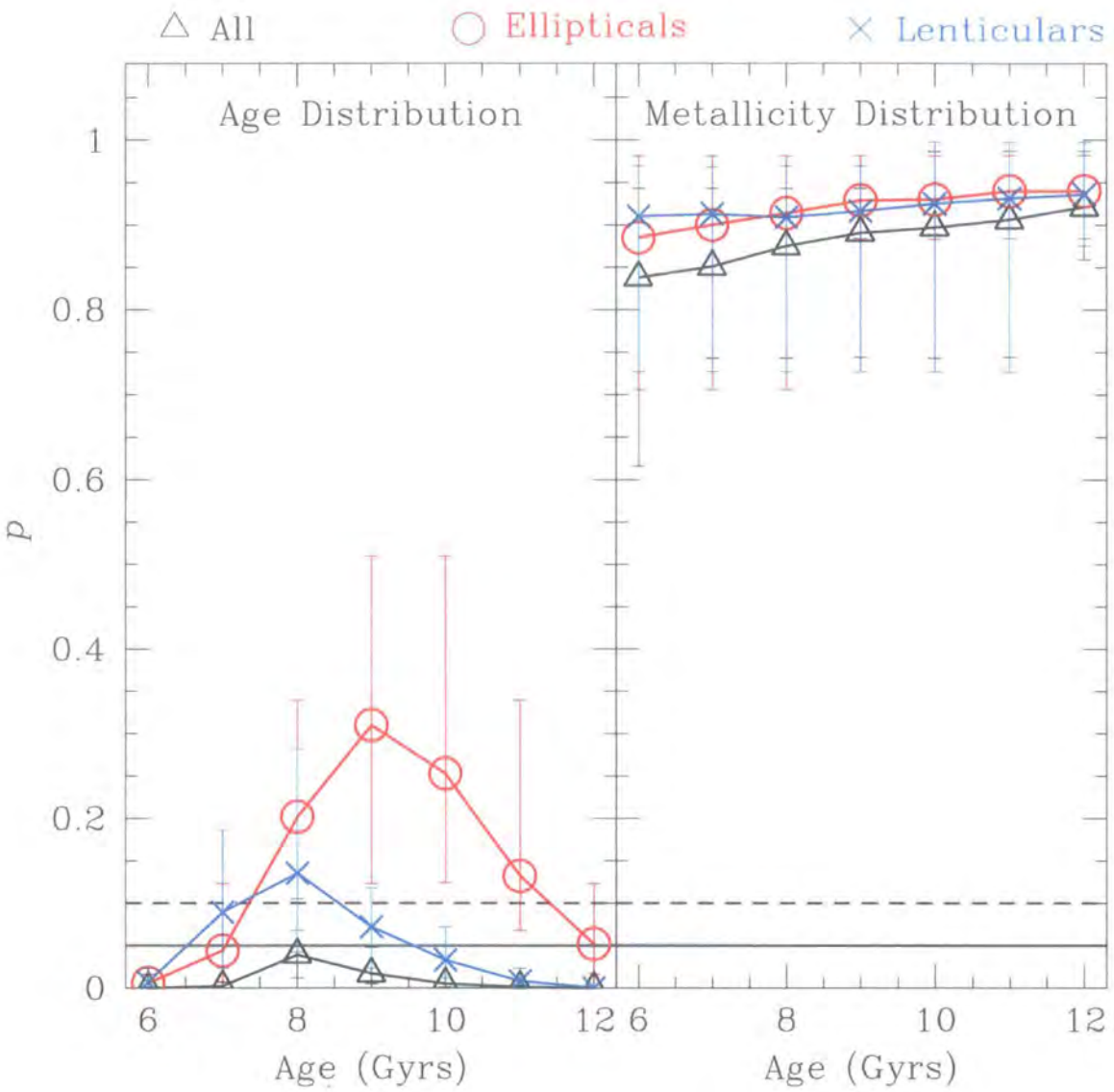

Figure 5.26: Two-sample KS test results for dominant luminosity-weighted mean single age of early-type galaxy stellar population formation hypothesis. The solid horizontal line indicates $p = 0.05$, whilst the dashed line indicates $p = 0.10$. See text.

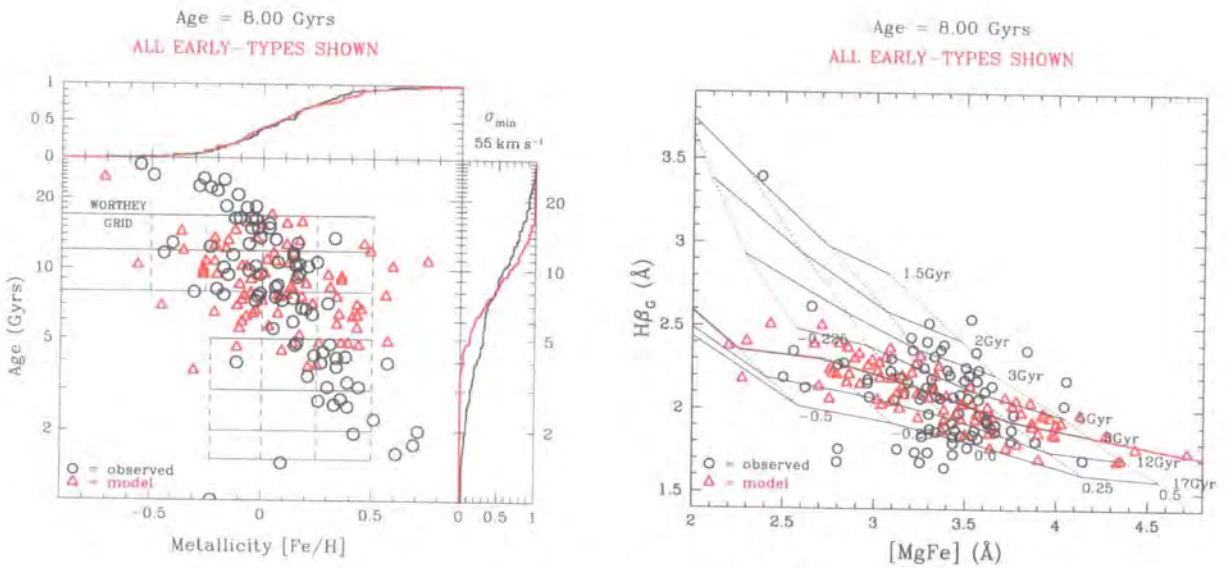

$$p = 0.039^{+0.066}_{-0.027}$$

Figure 5.27: Best matches between single age of formation hypothesis and observed data. The observed data and the model data for $p = 0.039$ are plotted on log(age)–metallicity and $H\beta_G$–[MgFe] planes, with the Worthey (1994) grid overlaid. The log(age)–metallicity plot also has the cumulative distributions of the observed and model data that are used in the statistical analysis method. See text for more details.

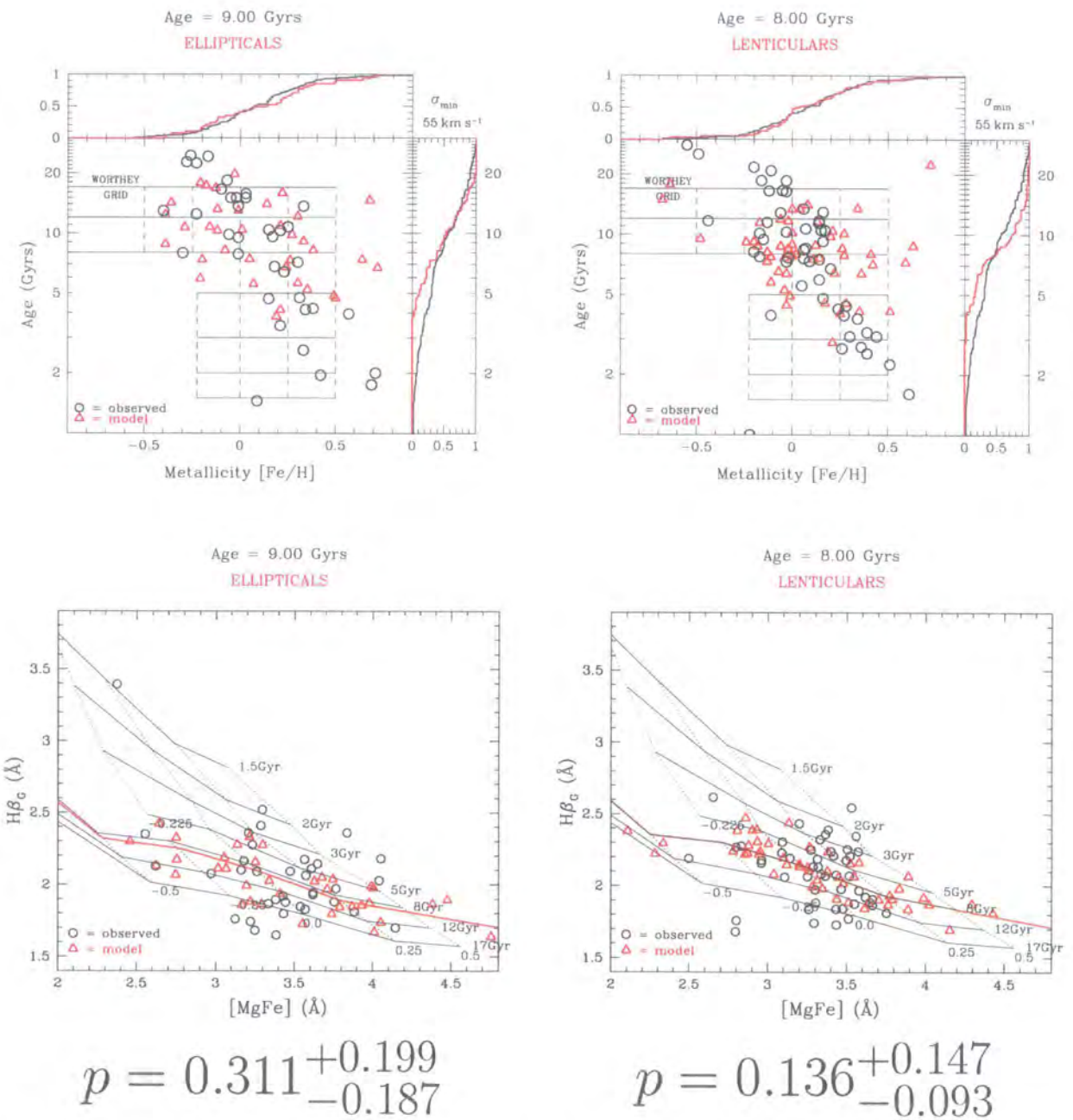

Figure 5.28: Best matches between single age of formation hypothesis and observed elliptical and lenticular data (see text).

if we consider the upper 68% confidence limit of the mean p value (see Figure 5.27).

Elliptical galaxies

I can completely support a dominant luminosity-weighted single aged stellar population of 9 or 10 Gyrs in the elliptical galaxies within the Coma cluster given the observed metallicity distribution; the most likely result being a 9 Gyrs single aged stellar population (see Figure 5.28). Also, the hypothesis of a 8 or 11 Gyrs single aged population is at worst *marginally inconsistent* with the null hypothesis if we consider the lower 68% confidence limit of the mean p value. I can completely rule out the presence of a single aged stellar population of 6 Gyrs. I can rule out with a high degree of confidence a single aged population of 7 and 12 Gyrs, since the upper 68% confidence limits of the mean p values only just increase the confidence level above the marginally inconsistent cutoff level ($p = 0.10$).

Lenticular galaxies

I can support with a reasonable degree of confidence a dominant luminosity-weighted single aged stellar population of 8 Gyrs in the lenticular galaxies within the Coma cluster given the observed metallicity distribution (see Figure 5.28) since the mean p value is greater than $p = 0.10$, however the lower 68% confidence limit of the mean p value indicates that at worst this hypothesis is *strongly inconsistent.* The next most likely result is that of a single aged population of 7 Gyrs which has a mean p value indicating that it is *marginally inconsistent* with the null hypothesis, with its' upper and lower limits either supporting or refuting the null hypothesis. It is likely that the best result should be between 7 and 8 Gyrs if the probability function is well behaved (see Figure 5.28). I can rule out completely a single aged population of 6, 11 and 12 Gyrs and can rule out with a high degree of confidence a 10 Gyrs population (the upper 68% confidence limit at best is *marginally inconsistent*). The upper limit of the mean p value shows that a single aged population of 9 Gyrs can be supported, however the mean and lower limits indicate that this result is not supported to a very high confidence level.

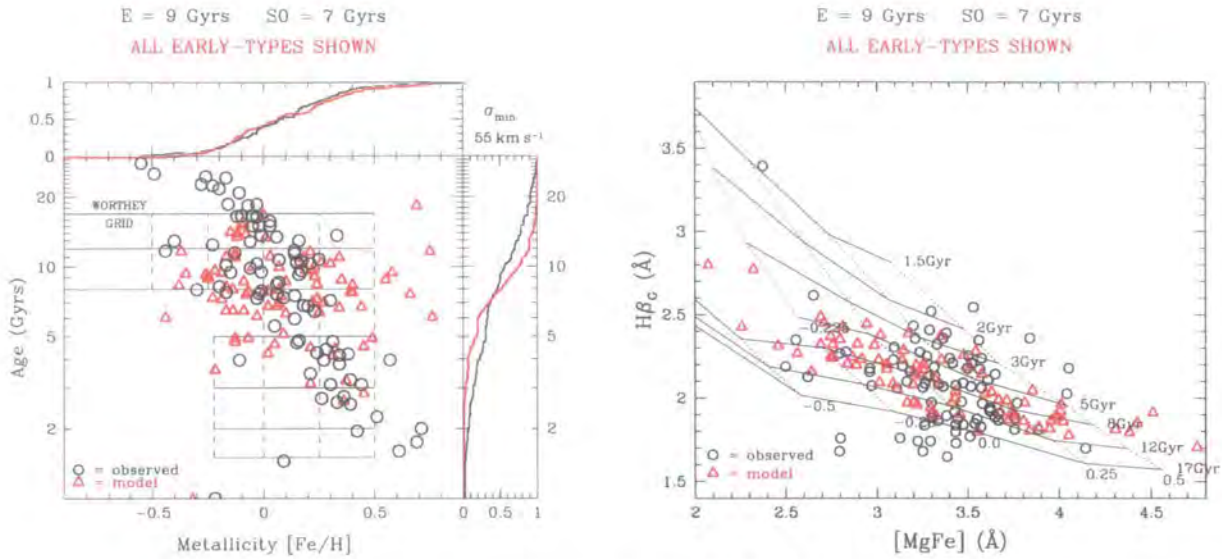

$$p = 0.071^{+0.080}_{-0.051}$$

Figure 5.29: 9 Gyrs age of stellar population formation for Ellipticals plus 7 Gyrs age of stellar population formation for Lenticulars (see text).

Key points to note from these observations are that the elliptical and lenticular populations give *different* results, indicating that they have *different* distributions in age. Also, the numbers of galaxies observed and the errors associated with these observations have a profound effect on subsequent data analysis and hypothesis testing (higher signal-to-noise means smaller errors which in turn means more power to test underlying distributions; more galaxies yield more data points to test the true distribution which is hidden by data errors).

To test the efficacy of these results I combined the most likely single age mock data for the elliptical galaxy population separately with the two most likely single age mock data for the lenticular populations. I find that a 7 Gyrs age of stellar population formation for the lenticular galaxies gives the best result when the population is combined with elliptical galaxies with a stellar population formed at 9 Gyrs (see Figure 5.29), with a confidence value of $p = 0.071^{+0.080}_{-0.051}$ (a 8 Gyrs old lenticular plus a 9 Gyrs old elliptical galaxy combination gives a confidence value of $p = 0.050^{+0.055}_{-0.031}$). Therefore the conclusion of this hypothesis is that the elliptical galaxies have a mean stellar population that is ~2 Gyrs *older* than the lenticular galaxies.

5.14 Coma cluster single metallicity hypothesis

The next hypothesis to be tested is that there is a mean single luminosity-weighted dominant metallicity within the Coma cluster early-type galaxy stellar populations but a distribution in the age the stellar populations formed. Section 5.14.1 details the Monte Carlo simulations that test this hypothesis, whilst Section 5.14.2 analyses the results.

5.14.1 Monte carlo simulations testing single metallicity hypothesis

I conduct Monte Carlo simulations to test this hypothesis using the following steps:

1. along the logarithmic age axis (cf. the logarithmic $H\beta_G$ axis, i.e. $\log_{10}(H\beta_G)$) I bin the observed data in 0.75dex wide bins. This is done so that I preserve any distribution in age whilst testing for any distribution in metallicity.

2. I then draw N age data points randomly from each bin, where N corresponds to the number of galaxies that are present in that bin in the observed data.

3. using the calculated Worthey (1994) grid points (see Section 5.5) I then match these age data to the metallicity, [MgFe] and $H\beta_G$ values which would place it on a given constant metallicity contour. I now have coordinates in the [MgFe]–$H\beta_G$ and age–metallicity planes for N mock galaxies per bin.

4. these ([MgFe],$H\beta_G$) coordinates are then compared to the observed data and the errors of the nearest observed galaxy assigned to each mock galaxy. This preserves the effect of any variation in the error ellipsoids across the [MgFe]–$H\beta_G$ plane. The modelling has now transposed to the [MgFe]–$H\beta_G$ plane since the errors form a well defined ellipse in this plane; this is not the case in the age–metallicity plane (see Section 5.7).

5. new ([MgFe],$H\beta_G$) coordinates are then sampled within the given errors, assuming a Gaussian error distribution. I now have ([MgFe],$H\beta_G$) coordinates for N mock galaxies per bin with the effect of random errors taken into account.

6. this new set of mock galaxies, with their randomly sampled ([MgFe],$H\beta_G$) coordinates, are compared to the Worthey (1994) grid and their ages and metallicities calculated.

7. this Monte Carlo simulation is repeated 1000 times to create a large database for subsequent statistical analysis through comparison with the observed data.

Using this method I test the observed data against the hypothesis that the stellar populations in the galaxies have a single metallicity, testing a range of possible metallicities from a [Fe/H] of –0.30 to 0.30 using 0.05 steps.

Examples of the mock data used to test the hypothesis of the presence of a single metallicity given an observed age distribution are shown in Figures 5.30 (all early-type galaxies), 5.31 (elliptical galaxies) and 5.32 (lenticular galaxies). These figures show one data set from 1000 Monte Carlo randomly generated data sets, with metallicities, [Fe/H] ranging from –0.30 to 0.30 (in 0.10 steps). The data contained in these figures are compared statistically to the observed data to determine whether the hypothesis is supported.

5.14.2 Statistical analysis of single metallicity hypothesis

To analyse the validity of the different hypotheses of single metallicities against the observed data I use the same two-sided two-sample Kolmogorov-Smirnov statistical testing approach described in Section 5.13.2 against the null hypothesis that the distributions of the mock data (constructed from the hypothesis that there is a mean single luminosity-weighted dominant metallicity, but a distribution in age) and the observed data are identical.

Figure 5.33 and Table 5.7 show the results of this statistical analysis against the different hypotheses that the stellar populations in the galaxies have a fixed metallicity (testing a fixed metallicities of between –0.30 and 0.30 using 0.05 steps). The mean confidence value, p shown is calculated from the central 68.3% of the database (i.e. 1 sigma clipping) of 1000 Monte Carlo runs for each test; this minimises the effect of any rogue outliers in the sample distribution. The upper and lower limit to this mean probability is taken as the values at the 1 sigma boundaries.

It can be seen that the age distribution *always* supports the null hypothesis with a very high degree of confidence. This is in fact *by definition* since a key point in the construction of a mock data set to test the presence of a dominant luminosity-weighted mean single metallicity population was that it should *match* the age distribution of the observed sample to maximise the power of the modelling to unlock any underlying single metallicity population. This high confidence in the age distribution comparison indicates that the modelling is working and is indeed matching the observed age distribution. The presence of significant structure in the age distribution analysis (cf. the lack of structure in the metallicity distribution analysis in Figure 5.26) is due to the difficulty in measuring ages outside of the Worthey (1994) grid. The means that model data points, ($H\beta_G$,[MgFe]), which are outside of the grid and have high metallicities

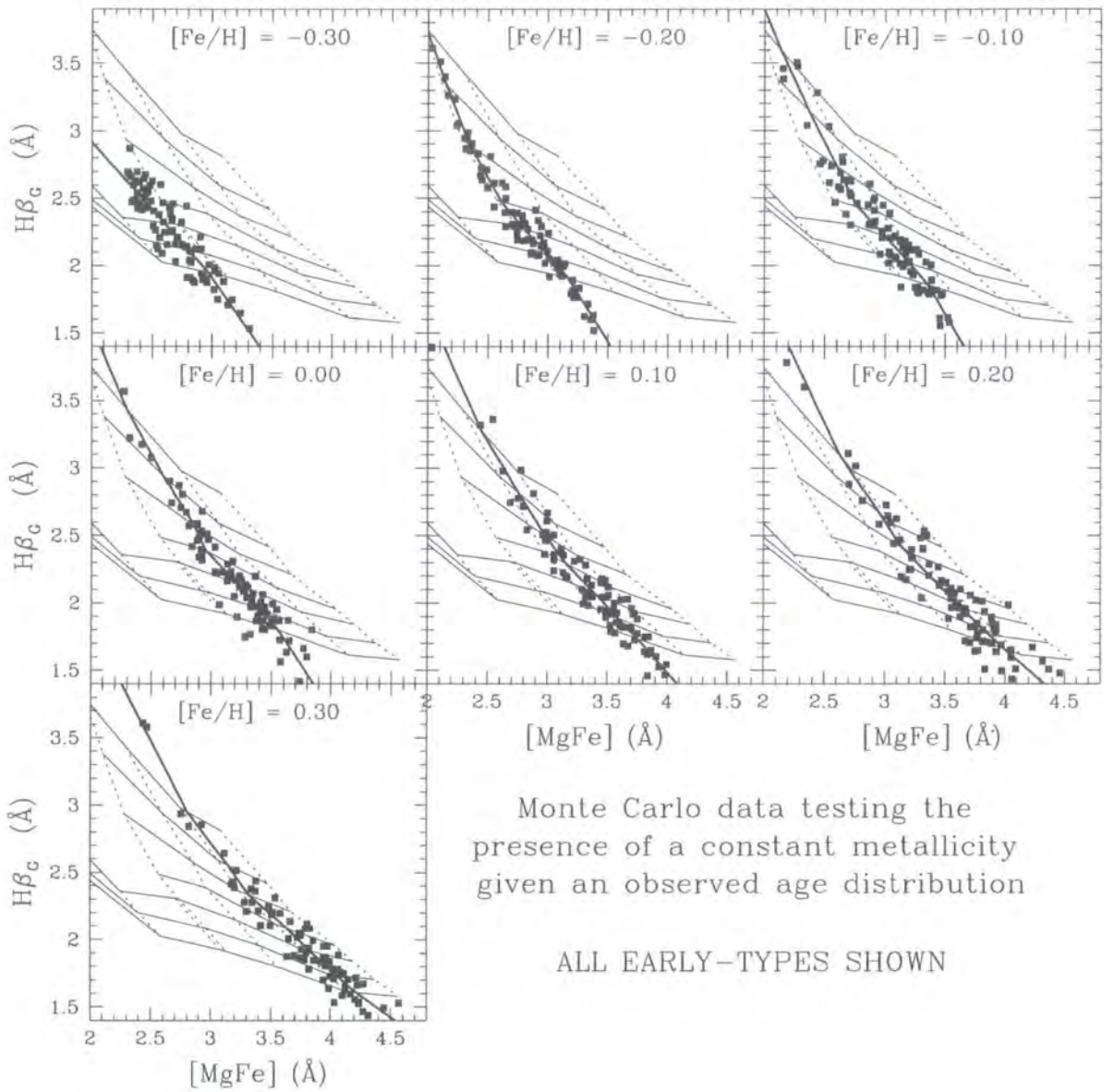

Figure 5.30: Constant metallicity Monte Carlo data. This figure contains Monte Carlo data in the $H\beta_G$–[MgFe] plane that is used to test the presence of a constant metallicity given an observed age distribution. One data set from the 1000 runs is shown, containing mock data to test the distribution of all the early-type galaxies in the observed sample. The solid line represents the constant metallicity contour from which the data is drawn. The data is superimposed on a Worthey (1994) grid.

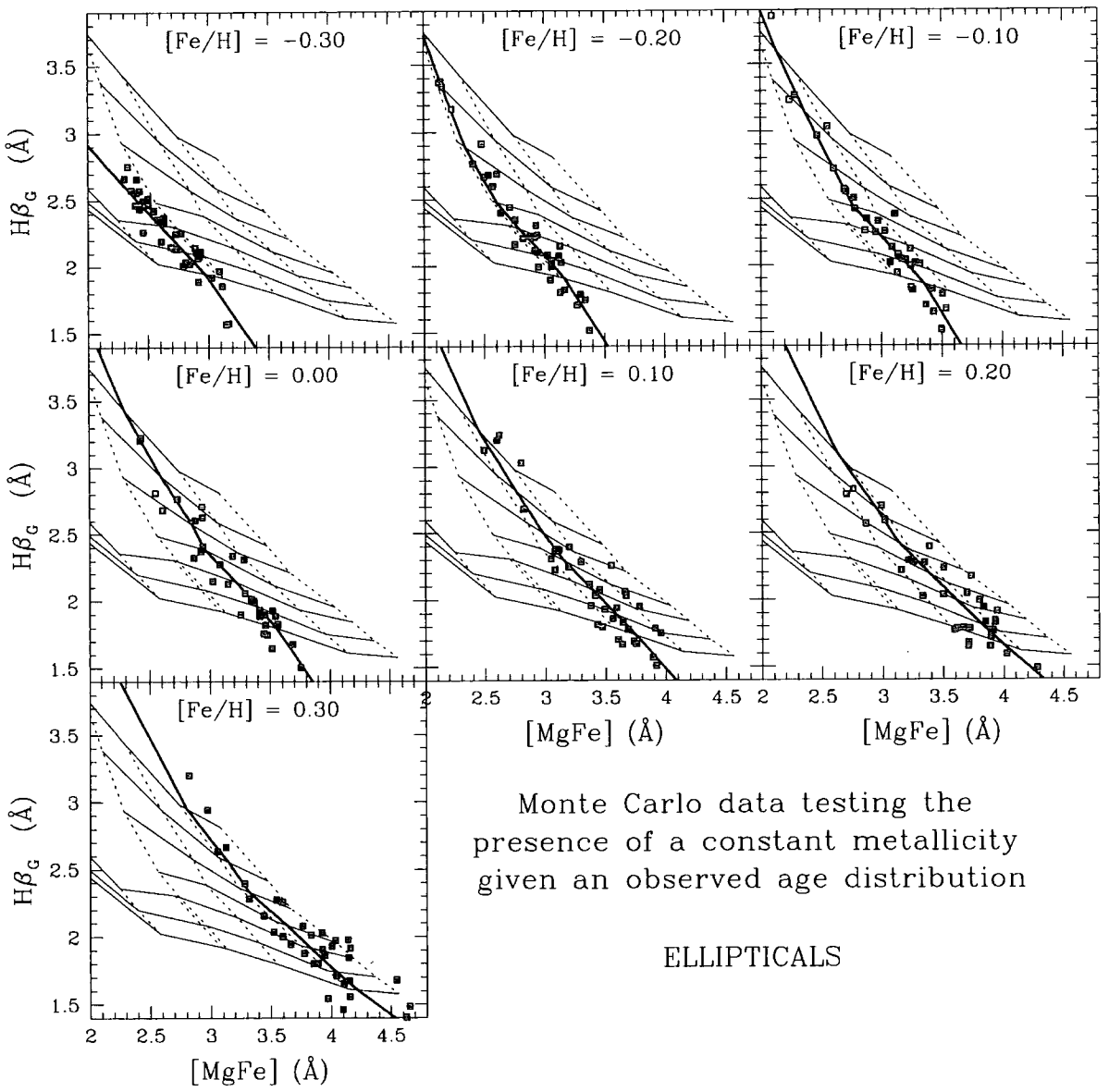

Figure 5.31: Constant metallicity Monte Carlo data for the Elliptical galaxy population.

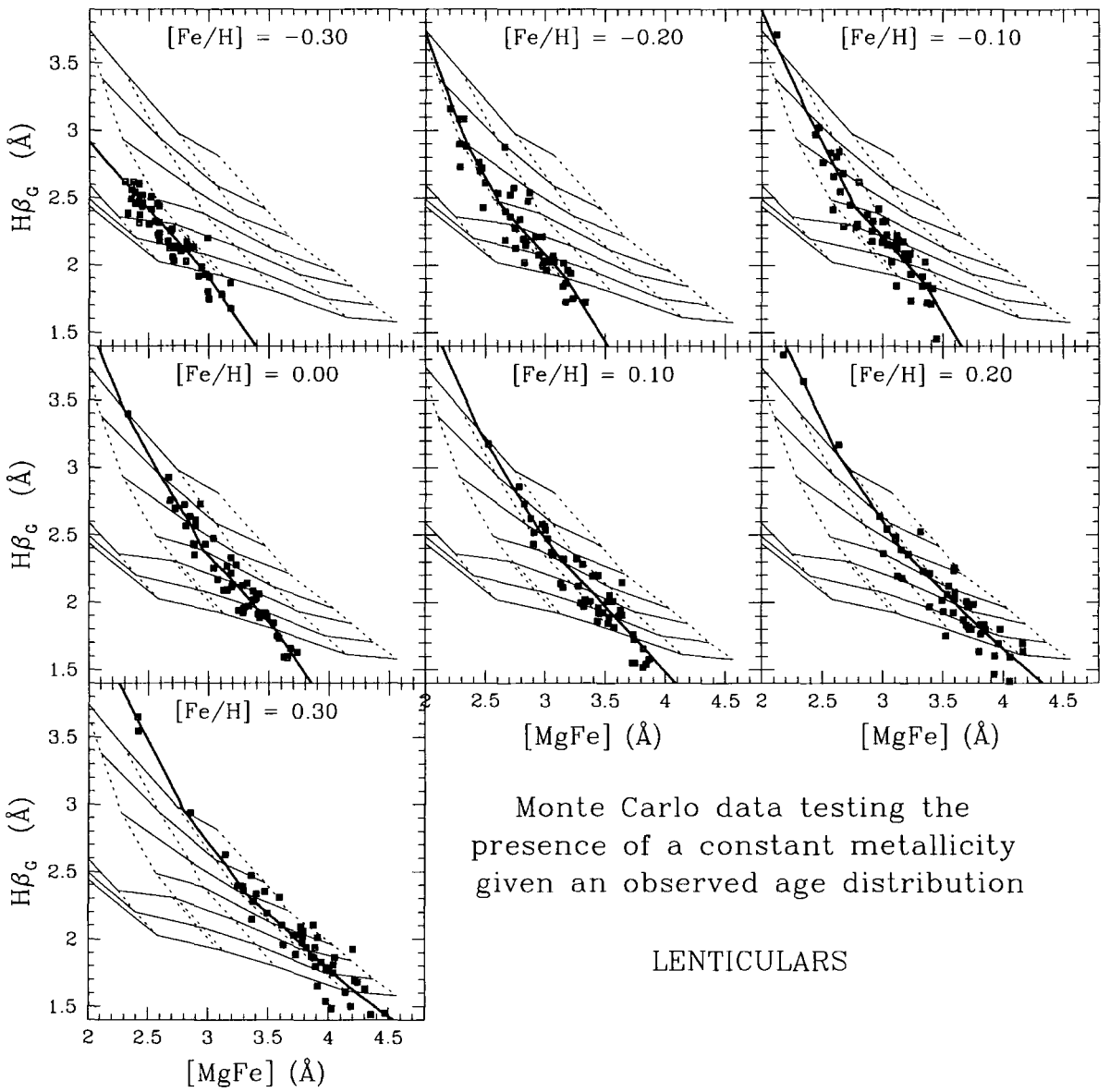

Figure 5.32: Constant metallicity Monte Carlo data for the Lenticular galaxy population.

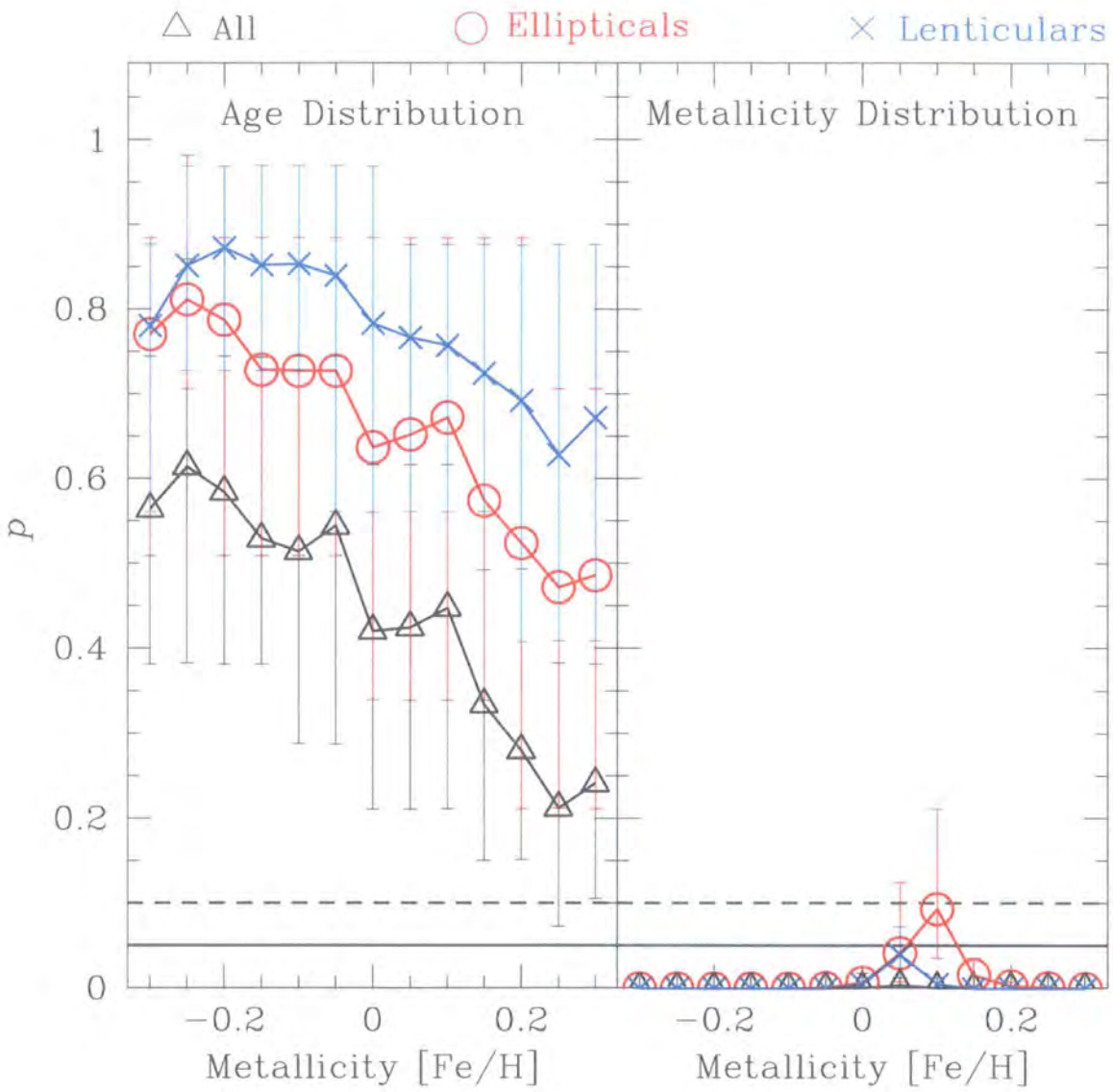

Figure 5.33: Two-sample KS test results for dominant luminosity-weighted mean single metallicity of early-type galaxy stellar population hypothesis. The solid horizontal line indicates $p = 0.05$, whilst the dashed line indicates $p = 0.10$. See text.

	E/S0 (n=87)		E (n=36)		S0 (n=51)	
Hypothesis	$p_{\rm age}$	$p_{\rm met}$	$p_{\rm age}$	$p_{\rm met}$	$p_{\rm age}$	$p_{\rm met}$
−0.30 [Fe/H]	$0.564\,^{+0.180}_{-0.183}$	$0.000\,^{+0.000}_{-0.000}$	$0.771\,^{+0.114}_{-0.261}$	$0.000\,^{+0.000}_{-0.000}$	$0.781\,^{+0.096}_{-0.219}$	$0.000\,^{+0.000}_{-0.000}$
−0.25 [Fe/H]	$0.614\,^{+0.245}_{-0.232}$	$0.000\,^{+0.000}_{-0.000}$	$0.812\,^{+0.170}_{-0.105}$	$0.000\,^{+0.000}_{-0.000}$	$0.852\,^{+0.117}_{-0.124}$	$0.000\,^{+0.000}_{-0.000}$
−0.20 [Fe/H]	$0.584\,^{+0.160}_{-0.203}$	$0.000\,^{+0.000}_{-0.000}$	$0.788\,^{+0.097}_{-0.278}$	$0.000\,^{+0.000}_{-0.000}$	$0.873\,^{+0.096}_{-0.145}$	$0.000\,^{+0.000}_{-0.000}$
−0.15 [Fe/H]	$0.529\,^{+0.214}_{-0.148}$	$0.000\,^{+0.000}_{-0.000}$	$0.729\,^{+0.156}_{-0.219}$	$0.000\,^{+0.000}_{-0.000}$	$0.853\,^{+0.117}_{-0.125}$	$0.000\,^{+0.000}_{-0.000}$
−0.10 [Fe/H]	$0.514\,^{+0.230}_{-0.226}$	$0.000\,^{+0.000}_{-0.000}$	$0.728\,^{+0.157}_{-0.218}$	$0.000\,^{+0.000}_{-0.000}$	$0.854\,^{+0.116}_{-0.126}$	$0.000\,^{+0.000}_{-0.000}$
−0.05 [Fe/H]	$0.544\,^{+0.200}_{-0.257}$	$0.000\,^{+0.000}_{-0.000}$	$0.728\,^{+0.157}_{-0.218}$	$0.001\,^{+0.001}_{-0.000}$	$0.840\,^{+0.130}_{-0.278}$	$0.000\,^{+0.000}_{-0.000}$
0.00 [Fe/H]	$0.420\,^{+0.196}_{-0.210}$	$0.000\,^{+0.000}_{-0.000}$	$0.638\,^{+0.247}_{-0.297}$	$0.007\,^{+0.011}_{-0.005}$	$0.784\,^{+0.185}_{-0.223}$	$0.005\,^{+0.008}_{-0.004}$
0.05 [Fe/H]	$0.424\,^{+0.192}_{-0.214}$	$0.003\,^{+0.009}_{-0.003}$	$0.653\,^{+0.232}_{-0.313}$	$0.042\,^{+0.083}_{-0.034}$	$0.767\,^{+0.110}_{-0.205}$	$0.040\,^{+0.033}_{-0.027}$
0.10 [Fe/H]	$0.447\,^{+0.169}_{-0.236}$	$0.000\,^{+0.001}_{-0.000}$	$0.673\,^{+0.212}_{-0.333}$	$0.094\,^{+0.118}_{-0.058}$	$0.758\,^{+0.119}_{-0.196}$	$0.005\,^{+0.008}_{-0.004}$
0.15 [Fe/H]	$0.334\,^{+0.158}_{-0.184}$	$0.000\,^{+0.000}_{-0.000}$	$0.575\,^{+0.310}_{-0.235}$	$0.016\,^{+0.020}_{-0.013}$	$0.725\,^{+0.152}_{-0.163}$	$0.000\,^{+0.001}_{-0.000}$
0.20 [Fe/H]	$0.280\,^{+0.213}_{-0.129}$	$0.000\,^{+0.000}_{-0.000}$	$0.525\,^{+0.360}_{-0.313}$	$0.003\,^{+0.005}_{-0.002}$	$0.693\,^{+0.183}_{-0.285}$	$0.000\,^{+0.000}_{-0.000}$
0.25 [Fe/H]	$0.212\,^{+0.170}_{-0.140}$	$0.000\,^{+0.000}_{-0.000}$	$0.473\,^{+0.234}_{-0.260}$	$0.001\,^{+0.001}_{-0.000}$	$0.629\,^{+0.248}_{-0.220}$	$0.000\,^{+0.000}_{-0.000}$
0.30 [Fe/H]	$0.241\,^{+0.140}_{-0.136}$	$0.000\,^{+0.000}_{-0.000}$	$0.487\,^{+0.220}_{-0.275}$	$0.000\,^{+0.000}_{-0.000}$	$0.673\,^{+0.204}_{-0.264}$	$0.000\,^{+0.000}_{-0.000}$

Table 5.7: Two-sample KS test results for dominant luminosity-weighted mean single metallicity of early-type galaxy stellar population hypothesis (see text).

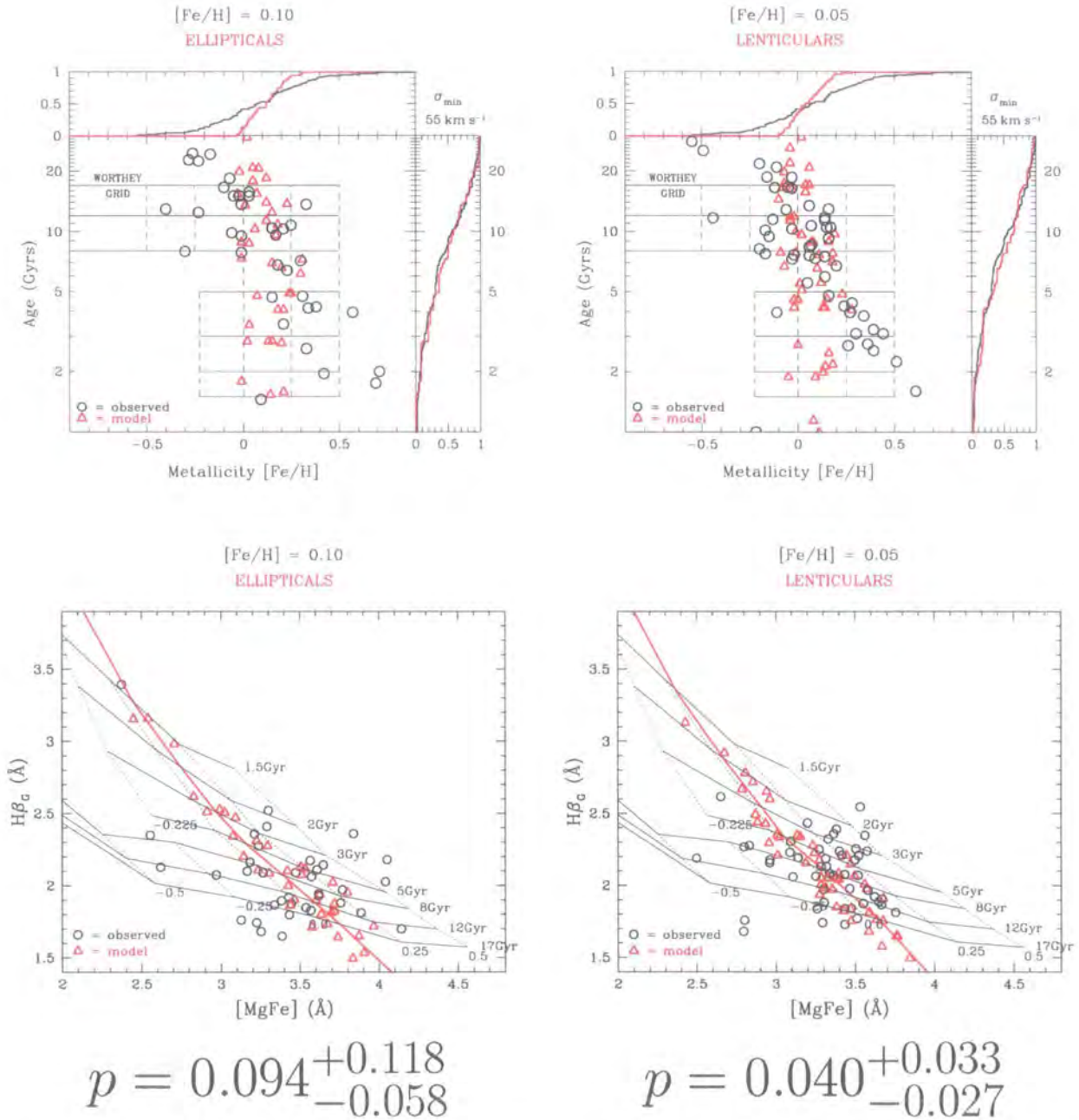

$$p = 0.094^{+0.118}_{-0.058} \qquad p = 0.040^{+0.033}_{-0.027}$$

Figure 5.34: Best matches between single metallicity hypothesis and observed elliptical and lenticular data (see text).

have uncertain age measurements (i.e. larger errors on the determined age for a given data point) leading to less than perfect matching to the observed age distribution. However, as stated previously, the age distribution is still well modelled and does match the observed distribution with a very high degree of confidence. Therefore this structure in the age distribution analysis has no effect on the final conclusions from this modelling.

The results of the two-sample KS test on the age and metallicity distributions lead to the following observations for the total early-type galaxy population and for the elliptical and lenticular sub-populations:

All early-type galaxies

I can completely rule out a dominant luminosity-weighted single stellar population metallicity in the early-type galaxies within the Coma cluster given the observed age distribution.

Elliptical galaxies

I can completely rule out a dominant luminosity-weighted single stellar population metallicity of [Fe/H] –0.30 to 0.00 and 0.15 to 0.30 in the elliptical galaxies within the Coma cluster given the observed age distribution. I can also rule out with a high degree of confidence a single metallicity of 0.05 or 0.10, since their mean p values are respectively strongly and marginally inconsistent with the null hypothesis. However both these models have upper and lower limits that either indicate that they are consistent *or* are strongly inconsistent with the null hypothesis.

Lenticular galaxies

I can completely rule out a dominant luminosity-weighted single stellar population metallicity in the lenticular galaxies within the Coma cluster given the observed age distribution. The only result that does not have $p \simeq 0$ is for [Fe/H]=0.05 and this result is at best marginally inconsistent with the null hypothesis if we consider the upper 68% confidence limit of the mean p value.

The overall result of testing this hypothesis is that there is *no supportable single stellar population metallicity* that fits the observed data, assuming a distribution in the age the stellar populations formed. This was indeed evident from the basic analysis in Section 5.9 and from the figures shown in Sections 5.4 and 5.7.

5.15 Single age of formation plus scatter in logarithmic age hypothesis

Finally I test the hypothesis that there is a mean single luminosity-weighted dominant age of stellar population formation with a logarithmic scatter in age around it plus a distribution of metallicities within the early-type galaxies of the Coma cluster core.

The Monte Carlo modelling is essentially the same as that discussed in Section 5.13. However when I draw N metallicity data points randomly from each bin (where N corresponds to the number of galaxies that are present in that bin in the observed data) I introduce a scatter in logarithmic age (i.e. $\log_{10}$(age[Gyrs])) before I match the data to the observed data to apply a scatter reflecting the observation errors. The scatter I introduce is assumed to be Gaussian and is applied in the logarithmic age plane because this more accurately reflects the logarithmic nature of the age sensitive indicator H$\beta_{\rm G}$ in the Worthey (1994) grid (see Section 5.4). I analyse herein the scatter in the elliptical, lenticular and total early-type galaxy populations using as a baseline the best fitting single age result from Section 5.13 and testing different values of logarithmic age scatter around this baseline. I use the same two-sided two-sample Kolmogorov-Smirnov statistical testing approach described in Section 5.13.2 against the null hypothesis that the distributions of the mock data (constructed from the hypothesis that there is a mean single luminosity-weighted dominant age with a logarithmic scatter around it and a distribution in metallicity) and the observed data are identical. The modelling is repeated 1000 times to increase the confidence in the final results.

The results of this modelling are shown in Table 5.8 and Figure 5.35. These results lead to the following observations for the total early-type galaxy population and for the elliptical and lenticular sub-populations:

Scatter	E/S0 (n=87) 8 Gyrs		E (n=36) 9 Gyrs		S0 (n=51) 7 Gyrs	
(dex)	$p_{\rm age}$	$p_{\rm met}$	$p_{\rm age}$	$p_{\rm met}$	$p_{\rm age}$	$p_{\rm met}$
±0.000	$0.039\ ^{+0.066}_{-0.027}$	$0.823\ ^{+0.120}_{-0.207}$	$0.300\ ^{+0.210}_{-0.176}$	$0.890\ ^{+0.092}_{-0.184}$	$0.079\ ^{+0.108}_{-0.067}$	$0.890\ ^{+0.079}_{-0.162}$
±0.025	$0.042\ ^{+0.063}_{-0.030}$	$0.835\ ^{+0.108}_{-0.219}$	$0.332\ ^{+0.178}_{-0.207}$	$0.893\ ^{+0.089}_{-0.186}$	$0.084\ ^{+0.103}_{-0.072}$	$0.886\ ^{+0.084}_{-0.158}$
±0.050	$0.051\ ^{+0.054}_{-0.039}$	$0.833\ ^{+0.110}_{-0.217}$	$0.328\ ^{+0.182}_{-0.204}$	$0.904\ ^{+0.079}_{-0.197}$	$0.101\ ^{+0.181}_{-0.078}$	$0.885\ ^{+0.084}_{-0.157}$
±0.075	$0.062\ ^{+0.089}_{-0.042}$	$0.824\ ^{+0.119}_{-0.207}$	$0.360\ ^{+0.150}_{-0.147}$	$0.898\ ^{+0.085}_{-0.191}$	$0.124\ ^{+0.159}_{-0.081}$	$0.885\ ^{+0.085}_{-0.157}$
±0.100	$0.078\ ^{+0.073}_{-0.058}$	$0.827\ ^{+0.116}_{-0.211}$	$0.393\ ^{+0.314}_{-0.180}$	$0.891\ ^{+0.091}_{-0.185}$	$0.153\ ^{+0.130}_{-0.110}$	$0.882\ ^{+0.088}_{-0.154}$
±0.125	$0.105\ ^{+0.106}_{-0.074}$	$0.829\ ^{+0.114}_{-0.213}$	$0.460\ ^{+0.247}_{-0.248}$	$0.890\ ^{+0.093}_{-0.183}$	$0.191\ ^{+0.217}_{-0.119}$	$0.892\ ^{+0.077}_{-0.164}$
±0.150	$0.154\ ^{+0.133}_{-0.082}$	$0.818\ ^{+0.125}_{-0.202}$	$0.499\ ^{+0.208}_{-0.287}$	$0.891\ ^{+0.092}_{-0.184}$	$0.232\ ^{+0.177}_{-0.159}$	$0.892\ ^{+0.078}_{-0.164}$
±0.175	$0.207\ ^{+0.175}_{-0.101}$	$0.823\ ^{+0.120}_{-0.206}$	$0.568\ ^{+0.317}_{-0.228}$	$0.887\ ^{+0.095}_{-0.180}$	$0.284\ ^{+0.278}_{-0.165}$	$0.897\ ^{+0.072}_{-0.169}$
±0.200	$0.277\ ^{+0.216}_{-0.126}$	$0.818\ ^{+0.125}_{-0.201}$	$0.625\ ^{+0.260}_{-0.285}$	$0.889\ ^{+0.093}_{-0.182}$	$0.357\ ^{+0.205}_{-0.238}$	$0.895\ ^{+0.074}_{-0.167}$
±0.225	$0.378\ ^{+0.239}_{-0.167}$	$0.829\ ^{+0.114}_{-0.086}$	$0.690\ ^{+0.195}_{-0.180}$	$0.891\ ^{+0.091}_{-0.184}$	$0.436\ ^{+0.292}_{-0.249}$	$0.898\ ^{+0.072}_{-0.170}$
±0.250	$0.507\ ^{+0.237}_{-0.220}$	$0.831\ ^{+0.112}_{-0.214}$	$0.740\ ^{+0.145}_{-0.230}$	$0.898\ ^{+0.084}_{-0.191}$	$0.498\ ^{+0.230}_{-0.311}$	$0.905\ ^{+0.064}_{-0.177}$
±0.275	$0.600\ ^{+0.258}_{-0.219}$	$0.834\ ^{+0.109}_{-0.090}$	$0.740\ ^{+0.145}_{-0.230}$	$0.902\ ^{+0.080}_{-0.195}$	$0.547\ ^{+0.330}_{-0.359}$	$0.904\ ^{+0.066}_{-0.176}$
±0.300	$0.643\ ^{+0.215}_{-0.262}$	$0.846\ ^{+0.097}_{-0.102}$	$0.723\ ^{+0.162}_{-0.213}$	$0.896\ ^{+0.086}_{-0.189}$	$0.590\ ^{+0.286}_{-0.308}$	$0.909\ ^{+0.061}_{-0.181}$
±0.325	$0.570\ ^{+0.289}_{-0.283}$	$0.850\ ^{+0.093}_{-0.107}$	$0.671\ ^{+0.214}_{-0.331}$	$0.900\ ^{+0.082}_{-0.193}$	$0.640\ ^{+0.236}_{-0.358}$	$0.916\ ^{+0.053}_{-0.188}$
±0.350	$0.444\ ^{+0.300}_{-0.234}$	$0.848\ ^{+0.095}_{-0.104}$	$0.582\ ^{+0.303}_{-0.242}$	$0.907\ ^{+0.075}_{-0.200}$	$0.625\ ^{+0.251}_{-0.343}$	$0.906\ ^{+0.063}_{-0.178}$
±0.375	$0.307\ ^{+0.185}_{-0.201}$	$0.856\ ^{+0.087}_{-0.112}$	$0.479\ ^{+0.228}_{-0.267}$	$0.907\ ^{+0.075}_{-0.200}$	$0.592\ ^{+0.285}_{-0.309}$	$0.915\ ^{+0.083}_{-0.187}$
±0.400	$0.203\ ^{+0.178}_{-0.131}$	$0.849\ ^{+0.094}_{-0.105}$	$0.412\ ^{+0.295}_{-0.287}$	$0.904\ ^{+0.078}_{-0.197}$	$0.548\ ^{+0.329}_{-0.265}$	$0.911\ ^{+0.059}_{-0.183}$
±0.425	$0.132\ ^{+0.155}_{-0.101}$	$0.852\ ^{+0.091}_{-0.108}$	$0.324\ ^{+0.186}_{-0.199}$	$0.903\ ^{+0.080}_{-0.196}$	$0.484\ ^{+0.244}_{-0.202}$	$0.908\ ^{+0.062}_{-0.180}$
±0.450	$0.079\ ^{+0.132}_{-0.059}$	$0.859\ ^{+0.084}_{-0.115}$	$0.259\ ^{+0.251}_{-0.190}$	$0.906\ ^{+0.076}_{-0.199}$	$0.404\ ^{+0.158}_{-0.216}$	$0.911\ ^{+0.058}_{-0.183}$
±0.475	$0.046\ ^{+0.060}_{-0.038}$	$0.855\ ^{+0.087}_{-0.112}$	$0.205\ ^{+0.135}_{-0.136}$	$0.923\ ^{+0.059}_{-0.217}$	$0.349\ ^{+0.213}_{-0.161}$	$0.911\ ^{+0.058}_{-0.183}$

Table 5.8: Two-sample KS test results for dominant luminosity-weighted mean single age of early-type galaxy stellar population plus scatter in logarithmic age (i.e. $\log_{10}$(age[Gyrs])) hypothesis (see text).

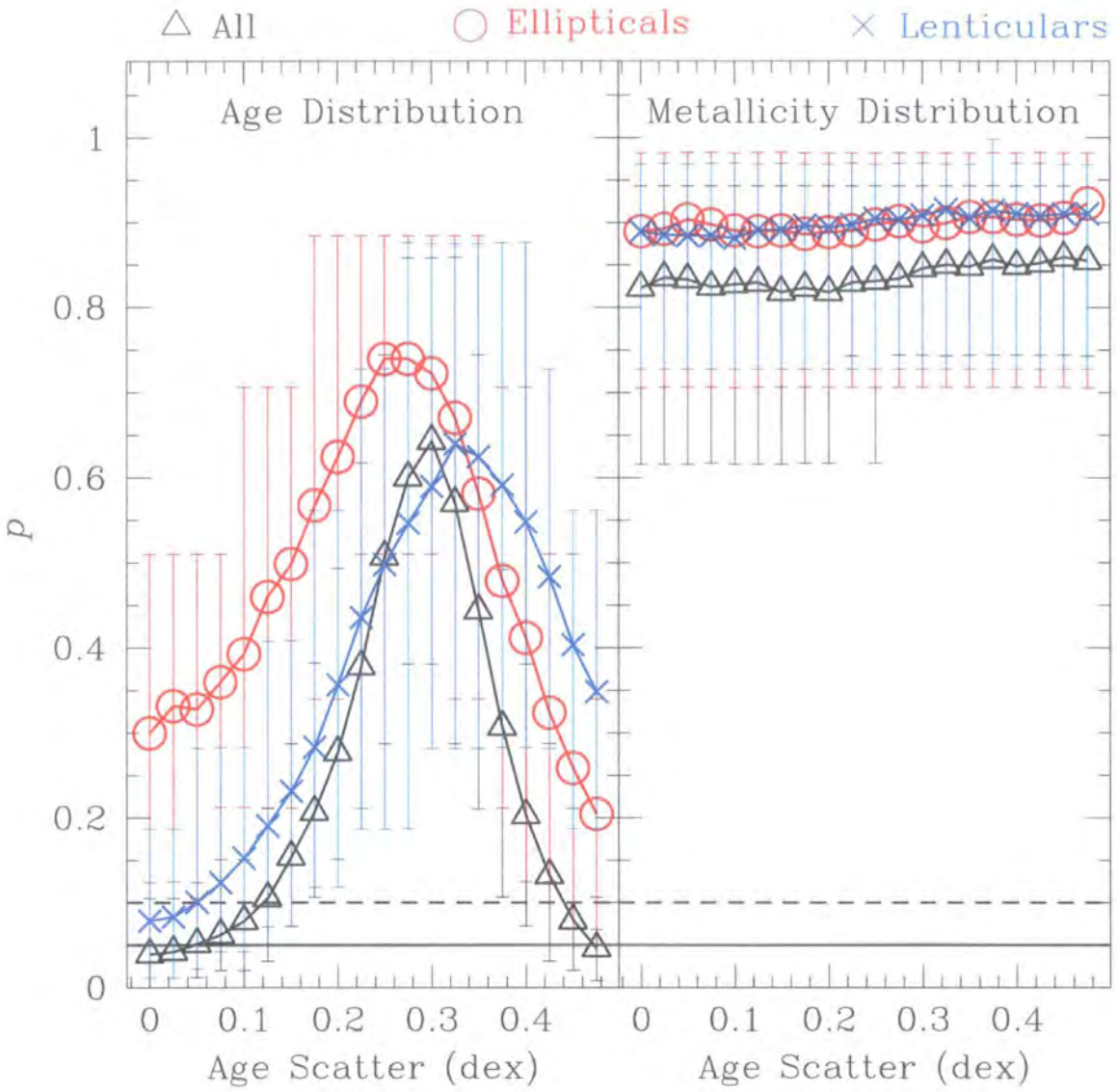

Figure 5.35: Two-sample KS test results for dominant luminosity-weighted mean single age of early-type galaxy stellar population formation plus scatter in logarithmic age (i.e. $\log_{10}$(age[Gyrs])) hypothesis (see text).

All early-type galaxies

The hypothesis of a single age of 8 Gyrs for the formation of the dominant stellar population of all the early-type galaxies in the Coma cluster, which is at best only just consistent with the null hypothesis (since $p_{upper} > 0.10$) if no scatter is included (see Section 5.13.2), is fully supported if a scatter of ± 0.175 dex or greater in logarithmic age (i.e. $\log_{10}$(age[Gyrs])) is included. A scatter of between 0.025 and 0.150 dex is supported with varying degrees of marginal inconsistency with the null hypothesis (considering both the mean p value and its upper and lower limits). A scatter of up to 0.450 dex is supported, with progressively lower confidence; a scatter of 0.475 dex is unlikely. The best fitting hypothesis is of a single age of 8 Gyrs of stellar population formation with a scatter of ± 0.300 dex around it ($p = 0.643^{+0.215}_{-0.262}$).

Elliptical galaxies

The hypothesis of a single age of 9 Gyrs for the formation of the dominant stellar population of the elliptical galaxies with no scatter (the best fitting result from Section 5.13.2 that is completely supported by the data) is supported with a higher degree of confidence when a scatter is introduced. The best fitting hypothesis is of a single age of 9 Gyrs of stellar population formation with a scatter of ± 0.250 or 0.275 dex around it ($p = 0.740^{+0.145}_{-0.230}$). If the probability function is well behaved, the best fitting result is 0.275 dex. A scatter of up to 0.475 dex is supported.

Lenticular galaxies

The hypothesis of a single age of 7 Gyrs for the formation of the dominant stellar population of the lenticular galaxies with no scatter (the best fitting result from Section 5.13.2 that is at best supported with a good degree of confidence by the data) is fully supported if a scatter of ± 0.175 dex or greater in logarithmic age (i.e. $\log_{10}$(age[Gyrs])) is included. A scatter of between 0.025 and 0.150 dex is supported with varying degrees of marginal inconsistency with the null hypothesis (considering both the mean p value and its upper and lower limits). The best fitting hypothesis is of a single age of 7 Gyrs of stellar population formation with a scatter of ± 0.325 dex around it ($p = 0.640^{+0.236}_{-0.358}$). A scatter of up to 0.475 dex is supported.

The best fitting results are shown in Figure 5.36

These results show that whilst there are acceptable fits for a single luminosity-weighted dominant age for the stellar populations of the elliptical and lenticular galaxies, if a logarithmic scatter in age is introduced the confidence level of the statistical test result is greatly increased. Therefore, even though we cannot rule out the single age hypothesis, the most likely hypothesis is that of a dominant elliptical stellar population formed 9 Gyrs ago with a scatter of ± 0.275 dex around it ($p = 0.740^{+0.145}_{-0.230}$) and of a dominant lenticular population formed 7 Gyrs ago with a scatter of ± 0.325 dex around it ($p = 0.640^{+0.236}_{-0.358}$). This assumes that the metallicity distribution is identical to that observed. The total early-type galaxy population supports a single age of 8 Gyrs plus logarithmic scatter only for a scatter of ± 0.175 dex or greater. This is unsurprising because of the previous result (Section 5.13.2) showing that the elliptical galaxies are 2 Gyrs *older* than the lenticular galaxies; this means that a larger scatter is needed in order to "mask" the problem of the initial assumption that the total early-type galaxy population is made up of stellar populations formed at 8 Gyrs ago rather than a mixed population formed at 9 Gyrs and 7 Gyrs ago. The best fitting result for the total early-type galaxy population is of a single age of 8 Gyrs of stellar population formation with a scatter of ± 0.300 dex around it ($p = 0.643^{+0.215}_{-0.262}$); though the previous caveat about the mixed nature of the total population applies, this result supports the previous conclusions that if a logarithmic scatter in age is introduced then the statistical confidence in the hypothesised model greatly increases.

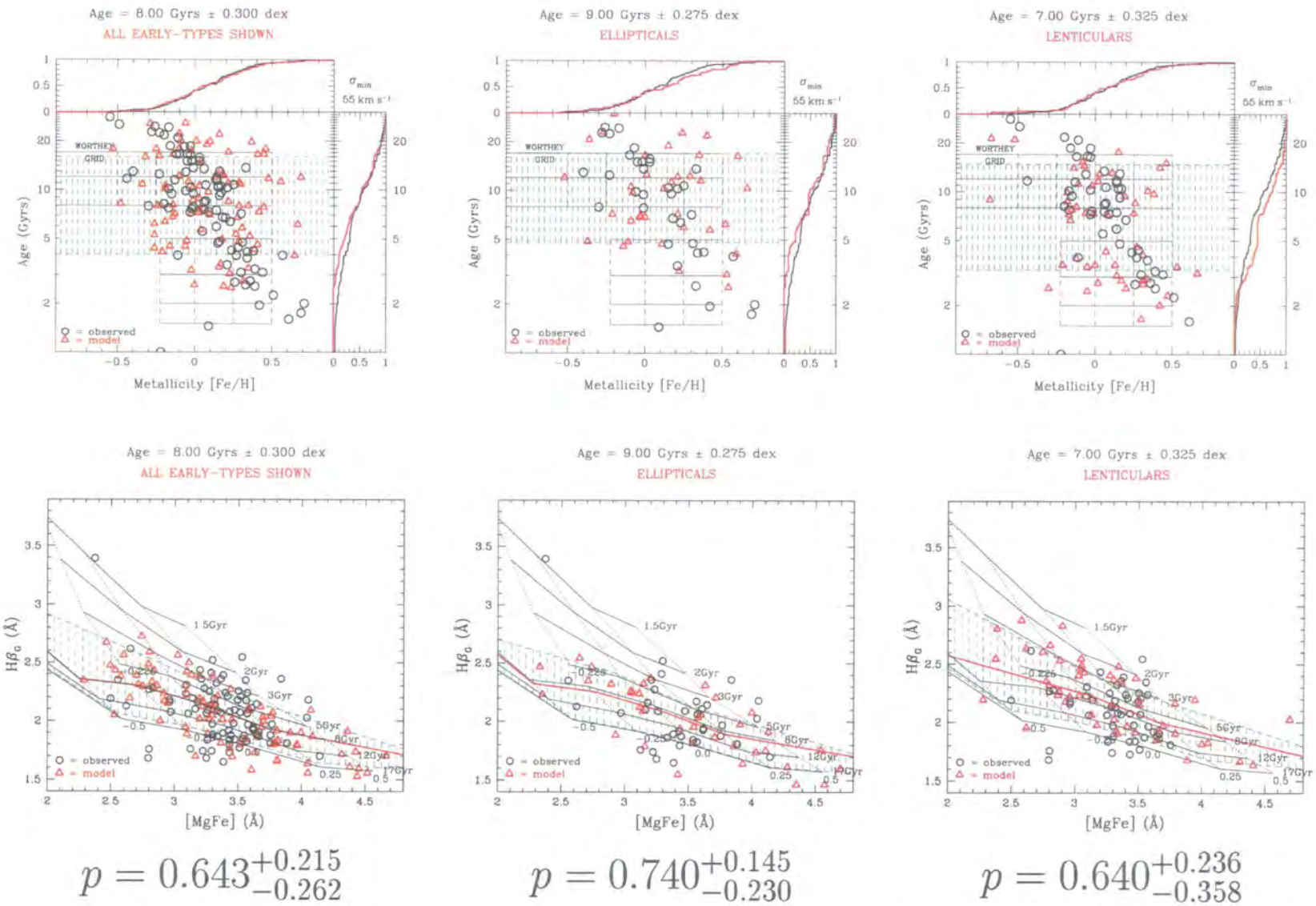

Figure 5.36: Single age of stellar formation plus scatter in logarithmic age (i.e. $\log_{10}$(age[Gyrs])) hypothesis given the observed metallicity distribution. The best matches for logarithmic age scatter around a given single age of dominant stellar population formation are shown superimposed on the observed data. The scatter is indicated in the background of the plots by the shaded area (see text).

5.16 Conclusions

In this chapter I have analysed the stellar populations (which act as fossil records of galaxy formation and evolution) of 87 bright early-type galaxies within the core of the rich Coma cluster using the high quality, homogeneous data set with well characterised errors in this dissertation. This data set has allowed a new unbiased assessment of the Coma cluster early-type galaxies' intrinsic properties, without any need to combine multiple data sets with the inherent systematic error problem that ensues. The analysis has concentrated on Lick/IDS age ($H\beta_G$) and metallicity ([MgFe]) sensitive absorption line indices over-plotted on a Worthey (1994) model generated grid based on the assumption of a single initial burst of star formation from a Salpeter power law initial mass function and a primordial fractional element abundance by weight (Y) of 0.228. These indices counter the age–metallicity degeneracy problem and are relatively unaffected by the non-solar abundance ratio problems[‡]. This use of a high-quality, large data set of such indices on a homogeneous system is a major step forward in the analysis of stellar populations over previous work, which has relied either upon colour–magnitude plots (which suffer from an age/metallicity degeneracy problem) or on line index data sets that have suffered from a number of limitations (low signal-to-noise, small numbers of galaxies, poor and uncertain characterisation of errors, systematic errors introduced through the combination of data sets to form one heterogeneous sample, and finally relatively poor age and metallicity indicators).

The main conclusions of this analysis of bright early-type galaxy stellar populations in the Coma cluster core are:

(a) The majority of the early-type galaxies within the Coma cluster core do not have solar abundance ratios (Section 5.3). This highlights both the importance of choosing the correct indicators to study stellar populations and the limitations of existing synthesis models to deal with extra-galactic objects.

(b) It is important to fully understand the nature of the errors in the age–metallicity plane (through correct mapping from the index–index plane) to forestall any simplistic assumption of an inherent age–metallicity trend in the cluster (Sections 5.6 and 5.7). Rather, the errors should

[‡]The Worthey (1994) stellar population models rely upon a library of nearby stars which have solar abundance ratios.

be included in a fully statistical analysis to probe for the presence of any underlying relationship.

(c) Early-type galaxies are segregated across the $H\beta_G$–[MgFe] grid by velocity dispersion, with galaxies with larger velocity dispersions (i.e. larger galaxies) situated to the right of the grid at higher values of [MgFe] and hence at *higher* metallicities, whilst galaxies with lower velocity dispersions (i.e. smaller galaxies) are at the left of the grid at lower values of [MgFe] and consequently with *lower* metallicities. As a consequence of the Faber–Jackson relationship (Faber & Jackson 1976), this same segregation is seen in magnitude since larger galaxies are bright and have a higher central velocity dispersion whilst smaller galaxies are fainter and have a smaller central velocity dispersion (Section 5.4).

(d) A correlation analysis of the luminosity-weighted mean galaxy ages and metallicities versus various parameters (Section 5.10) has demonstrated that there are no new correlations which could affect any distribution analysis. The correlations that are observed have been found before and are readily explained.

(e) A colour analysis (Section 5.10) has shown the B–R colour to be a poor indicator of early-type galaxy stellar population ages and metallicities. However the U–V colour does trace the metallicity sequence and the ages of the cluster early-type galaxy stellar populations, though only if the age–metallicity degeneracy is taken into account. Therefore in the absence of more detailed stellar population information, the U–V colour can be used to probe the age and metallicity structure of a rich clusters' early-type galaxy population.

(f) An environmental analysis of the cluster core using the spatial projection in two dimensions (Section 5.11) has shown that:

— there is no radial nor environmental dependence for the mean age of the early-type galaxy stellar populations within the Coma cluster core, with galaxies with old and young stellar populations evenly distributed throughout the core of cluster. This suggests either a well-mixed cluster core, with no major merging events that trigger bursts of star formation within the past 1 Gyrs, or that any early-type galaxy stellar populations within the cluster core have followed a similar evolution history.

— there is no radial dependence of early-type galaxy mean stellar population metallicity with

distance from the cD galaxy NGC 4874 within the Coma cluster core. There is, however, a more complicated metallicity structure within the cluster core. There is a concentration of galaxies with metal rich stellar populations in the north eastern part of the cluster core and a concentration of galaxies with metal poor stellar populations around the south western part. This metallicity distribution structure argues against the Coma cluster core being well-mixed and relaxed. It suggests that either two large sub-groups of galaxies with different metallicities are merging to form the Coma cluster core that we see today or that the two different regions of the cluster core have undergone a different stellar population metallicity evolution history.

(f) Both a simple Gaussian statistical analysis (Section 5.9) and advanced multiple hypothesis testing techniques using Monte Carlo simulations (Sections 5.12 to 5.15) have been used to probe the early-type galaxy stellar population luminosity-weighted mean ages and metallicities within the Coma cluster core and their distributions. They have shown that there is a metallicity distribution within the Coma cluster (with $-0.55 \leq$ [Fe/H] $\leq +0.92$ and a median [Fe/H] for the total early-type galaxy population of 0.070 and a SD of 0.268), but that whilst it is more likely that there is also a small distribution in age, a single age of stellar population formation for the dominant group of galaxies is supportable (only however separately for the elliptical and lenticular populations, not for the total early-type galaxy population). It has also been shown that the dominant elliptical and lenticular galaxy populations have significantly *different* age distributions from one another, but have the same metallicity distributions. The best fitting models shown in Figure 5.36 were:

SAMPLE	AGE MODEL	METALLICITY MODEL
all early-type galaxies	8 Gyrs $\pm$ 0.300 dex	observed distribution ($-0.55 <$ [Fe/H] $< +0.92$)
ellipticals	9 Gyrs $\pm$ 0.275 dex	observed distribution ($-0.55 <$ [Fe/H] $< +0.92$)
lenticulars	7 Gyrs $\pm$ 0.325 dex	observed distribution ($-0.55 <$ [Fe/H] $< +0.92$)

This analysis implies that for the dominant body of early-type galaxies within the Coma cluster core, the stellar populations within the elliptical galaxies are on average 2 Gyrs *older* than those within the lenticular galaxies. These differences between the ellipticals and the lenticulars plus the probable presence of a small scatter in their ages of stellar population formation all go

towards supporting a hierarchical clustering model of galaxy cluster formation. However whilst most galaxies can be well-fit by these hypotheses, it is evident that there are a few galaxies with very strong $H\beta_G$ absorption that cannot be accounted for. These are galaxies with genuinely younger stellar populations than the main body of Coma cluster early-type galaxies.

The results of the age and metallicity distribution analysis of the Coma cluster core broadly agree with the findings of Kuntschner & Davies (1998) and Kuntschner (2000) for the Fornax cluster and of Kuntschner et al. (2001) for a sample of early-type galaxies from the SMAC study (Smith et al. 2000), who all find that a single age model can be supported and who derive a mean age close to the value of 8 Gyrs that I find. They also find a similar metallicity distribution, though I find a slightly larger distribution than that found for the small sample of Fornax cluster ellipticals (Kuntschner & Davies 1998 found their 11 Fornax ellipticals had a metallicity distribution of $-0.25 \leq$ [Fe/H] $\leq +0.30$, whilst their 11 lenticulars had a distribution of $-0.50 \leq$ [Fe/H] $\leq +0.50$). These studies also support the conclusion that there are clear differences between the elliptical and lenticular galaxies.

My findings do however disagree completely with the work of González (1993), whose conclusions of a large variation in the ages of ellipticals (ages of ~ 4 to 15 Gyrs) and a small variation in their metallicities (a scatter in Z of ~ 0.3 dex) are at odds with those of this study. The González (1993) sample of 40 elliptical galaxies is however very heterogeneous in nature, containing a variety of galaxies spanning several different nearby galaxy groups with a range of richness (all though with richnesses less than that of the Coma cluster); it is therefore not surprising that there should be differences in the conclusions of the two studies, since the González (1993) sample will be affected by complicated selection effects/biases and will not anyway be representative of a rich cluster like Coma.

My findings also broadly disagree with the findings of Jørgensen (1999), who finds an early-type galaxy mean age $\sim$3 Gyrs *younger* than that found here and who finds an intrinsic scatter in age of ~ 0.166 dex (i.e. does not support the presence of a single age). However I do find a similar range in metallicity to Jørgensen (1999). This difference between the age distribution analyses of this study and that of Jørgensen (1999) can be explained by the large offset of

-0.197 ± 0.038 Å between the two studies measurements of the age sensitive index $H\beta$ (see Chapter 4); this offset translates directly to a difference in early-type galaxy mean age of $\sim$3 Gyrs in the correct direction (i.e. applying the offset to the data in this dissertation yields a *younger* mean age). This offset will also affect any conclusions about an intrinsic scatter in age. Chapter 4 discussed at length about such offsets, describing how it is often difficult to ensure that line index measurements are fully on the Lick/IDS system; a problem with this offset calculation by Jørgensen (1999) is the likely cause of this difference (since the data in this dissertation compares well with other studies).

In conclusion, this stellar populations study has shown that the bright early-type galaxies within the Coma cluster core have a large metallicity distribution (with $-0.55 \leq$ [Fe/H] $\leq +0.92$) and a small, but significant age distribution (with a best fit model of 8 Gyrs $\pm$ 0.300 dex). However the Worthey (1994) models used herein assume a single star burst formed the stellar populations, whilst in reality the situation is likely to be more complex (with for example merging events triggering new star bursts). Since this study has shown, in agreement with previous studies, that there is *no* evidence for significant large-scale star-formation occurring in the cluster core (Section 3.7.7) the conclusions about *relative* trends based upon the large numbers of early-type galaxies will not be greatly affected by this assumption. The presence of a distribution in the luminosity-weighted mean ages of the early-type galaxy stellar populations supports a hierarchical galaxy formation model. However since a single mean age is also found to be supported (implying a monolithic dissipative collapse model), this stellar population study cannot distinguish between hierarchical or monolithic dissipative collapse models on the basis of their luminosity-weighted mean ages. Real differences between the elliptical and lenticular galaxy populations are found, showing the importance of understanding the different morphologies of early-type galaxies before blindly applying analysis tools and relationships to a poorly defined early-type galaxy sample.

Chapter 6

Spectro-photometric relations

6.1 Introduction

I undertake here a detailed analysis of the fundamental plane relation and spectroscopic parameters that provide an insight into underlying trends and previously unknown factors affect this relation.

This is the first time that a large, high signal-to-noise, high resolution and homogeneous spectroscopic data set of a rich cluster has existed and it provides the opportunity to test previous conjectures about FP dependencies as well as probing for new dependencies that provide clues to the origin and evolution of the cluster galaxies. The uniqueness of the data set is that it contains no systematics that are typically introduced by combining multiple data sets from disparate sources.

In this chapter I will answer the following questions:

- are there differences between the FP relations for lenticulars and ellipticals? Any morphological dependence for the FP relation undermines its straightforward application to early-type galaxy samples.
- is there an additional factor that affects the FP relation? This is investigated through the analysis of any correlations between the residuals of the FP relation and possible factors. If there are indeed extra terms then previous applications of the FP and conclusions drawn from them are affected. The level to which they are affected depends upon the contributing size of the additional term.
- does environment affect the FP relation? This question is linked to the previous one, but goes further towards probing the universality of the FP relation to different clusters and less dense regions.
- what is the scatter around the FP relation and what does it depend upon? A small scatter is needed to reduce the errors on determining the relationship zero point which leads to

the cluster distance. If the scatter is too large or if it depends on some factor that has not previously been recognised then this will affect its use as a distance indicator and any results on cosmic bulk flows that result from its application. Quantifying the intrinsic scatter also allows probing of the "noise" of galaxy formation.

I will answer these questions by using the Coma cluster as a laboratory with which to probe the FP relation.

6.2 Fundamental plane relation

The global parameters of elliptical and lenticular galaxies have been found to follow a number of tight scaling relations. With the work on elliptical galaxies by Djorgovski & Davis (1987) and by Dressler et al. (1987) it became clear that a relation exists between the effective radius (r_e in h^{-1} kpc, the radius encompassing half the light), the mean surface brightness within this radius ($\langle\mu\rangle_e$ in mag arcsec^{-2}, $\langle I\rangle_e$ in $L_\odot/pc^2$) and the central velocity dispersion (σ in km s^{-1}). This relation is linear in logarithmic space and is known as the Fundamental Plane (FP):

$$\log_{10} r_e = \alpha \log_{10} \sigma + \beta \log_{10} \langle I\rangle_e + \gamma \tag{6.1}$$

The effective radius (r_e) is related to the effective semi-major axis (a_e), the effective semi-minor axis (b_e) and the effective ellipticity (ϵ_{re}) through $r_e = \sqrt{a_e b_e} = a_e\sqrt{1-\epsilon_{re}}$. Within the effective radius, the mean surface brightness ($\langle\mu\rangle_e$) in mag arcsec^{-2} is related to the mean surface brightness ($\langle I\rangle_e$) in $L_\odot/pc^2$ by the following equation:

$$\log_{10}\langle I\rangle_e = -0.4(\langle\mu\rangle_e - \text{constant}) \tag{6.2}$$

where the constants for different passbands are those from Jørgensen et al. (1996). This leads to the following parameterisation of the Fundamental Plane:

$$\log_{10} r_e = \alpha \log_{10} \sigma - 0.4\beta \times \langle\mu\rangle_e + \gamma + 0.4\beta \times (\text{constant}) \tag{6.3}$$

This is the form of the Fundamental Plane that is used herein.

The FP relation can be interpreted as a relation between the mass-to-light ratios and the masses of the galaxies (Faber et al. 1987; Bender, Burstein & Faber 1992). If the luminosity

profiles as well as the dynamical structure of the galaxies are similar (i.e. are homologous), then the virial theorem implies that the mass-to-light (M/L) ratio is a function of r_e, $\langle I \rangle_e$ and σ (from which the masses can be derived). If this function is unique and a power law, then a relation like the FP is to be expected (see also Faber et al. 1987; Djorgovski, de Carvalho & Han 1988). Section 6.3 describes the underlying physics of the FP relation in more detail.

The interest in relations like the FP between global parameters for galaxies is twofold. Firstly the relations provide information on the properties of the galaxies as a class, and secondly the relations may be used for distance determination. The application of the relations as distance determinators is based on the assumption that they are to a good approximation universally valid (no dependence on other factors).

The line indices Mg_2 and Hβ have also been found to be strongly correlated with the velocity dispersions of the galaxies (e.g. Burstein et al. 1988; Fisher, Franx & Illingworth 1995; Jørgensen 1997; Trager et al. 1998), whilst the $\langle$Fe$\rangle$ index has shown a rather weak correlation with the velocity dispersion (Jørgensen 1997; Trager et al. 1998). The data in this dissertation supports these findings. A simple Spearman rank correlation coefficient analysis of the line indices measured in this dissertation versus the corresponding logarithmic velocity dispersions (Table 6.1 and Figures 6.1 and 6.2) shows that all of the magnesium (Mg_1, Mg_2, Mg_b and [MgFe]) and iron (C4668, Fe5015, Fe5270, Fe5335, Fe5406, $\langle$Fe$\rangle$ and [MgFe]) dependent line indices are strongly correlated with $\log_{10}\sigma$. The exception being Fe4930, possibly due to the effect of Ba II on the index (see Table 3.5 and the work of Tripicco & Bell 1995). The Hβ_G is also correlated with $\log_{10}\sigma$; this is possibly due to the contaminating effect of magnesium on the line index (again see Table 3.5 and the work of Tripicco & Bell 1995).

		all early-types		ellipticals		lenticulars	
Parameter	σ_{min}	N	$p_{independent}$	N	$p_{independent}$	N	$p_{independent}$
C4668	55 km s^{-1}	101	0.0000	42	0.0000	59	0.0000
	100 km s^{-1}	73	0.0000	34	0.0000	39	0.0838
Fe4930	55 km s^{-1}	101	0.5619	42	0.1390	59	0.6842
	100 km s^{-1}	73	0.4835	34	0.4616	39	0.0242
Fe5015	55 km s^{-1}	101	0.0000	42	0.0002	59	0.0001

Table 5.5: *continued on next page*

continued from previous page

		all early-types		ellipticals		lenticulars	
Parameter	$\sigma_{\rm min}$	N	$p_{\rm independent}$	N	$p_{\rm independent}$	N	$p_{\rm independent}$
	$100\,{\rm km\,s^{-1}}$	73	0.0247	34	0.0080	39	0.2167
Fe5270	$55\,{\rm km\,s^{-1}}$	101	0.0000	42	0.0030	59	0.0009
	$100\,{\rm km\,s^{-1}}$	73	0.0471	34	0.0370	39	0.0901
Fe5335	$55\,{\rm km\,s^{-1}}$	100	0.0000	42	0.0031	58	0.0057
	$100\,{\rm km\,s^{-1}}$	72	0.0006	34	0.0082	38	0.0240
Fe5406	$55\,{\rm km\,s^{-1}}$	49	0.0020	20	0.0145	29	0.0688
	$100\,{\rm km\,s^{-1}}$	39	0.0657	17	0.0895	22	0.4334
$H\beta_G$	$55\,{\rm km\,s^{-1}}$	101	0.0001	42	0.0217	59	0.0032
	$100\,{\rm km\,s^{-1}}$	73	0.0054	34	0.2684	39	0.0269
Mg_1	$55\,{\rm km\,s^{-1}}$	100	0.0000	42	0.0000	58	0.0000
	$100\,{\rm km\,s^{-1}}$	72	0.0000	34	0.0000	38	0.0000
Mg_2	$55\,{\rm km\,s^{-1}}$	100	0.0000	42	0.0000	58	0.0000
	$100\,{\rm km\,s^{-1}}$	72	0.0000	34	0.0000	38	0.0001
Mg_b	$55\,{\rm km\,s^{-1}}$	101	0.0000	42	0.0000	59	0.0000
	$100\,{\rm km\,s^{-1}}$	73	0.0000	34	0.0000	39	0.0001
$\langle$Fe$\rangle$	$55\,{\rm km\,s^{-1}}$	100	0.0000	42	0.0005	58	0.0007
	$100\,{\rm km\,s^{-1}}$	72	0.0007	34	0.0071	38	0.0081
[MgFe]	$55\,{\rm km\,s^{-1}}$	100	0.0000	42	0.0000	58	0.0000
	$100\,{\rm km\,s^{-1}}$	72	0.0000	34	0.0000	38	0.0000

Table 6.1: Early-type galaxy line index correlation with velocity dispersion. No lower signal-to-noise cutoff is applied. Data with velocity dispersions greater than 55 and $100\,{\rm km\,s^{-1}}$ are analysed by morphological type. A Spearman rank correlation coefficient test was performed against the null hypothesis that the X and Y axes were mutually independent (i.e. un-correlated). Values of $p < 0.05$ reject this hypothesis, implying an underlying correlation between the parameters.

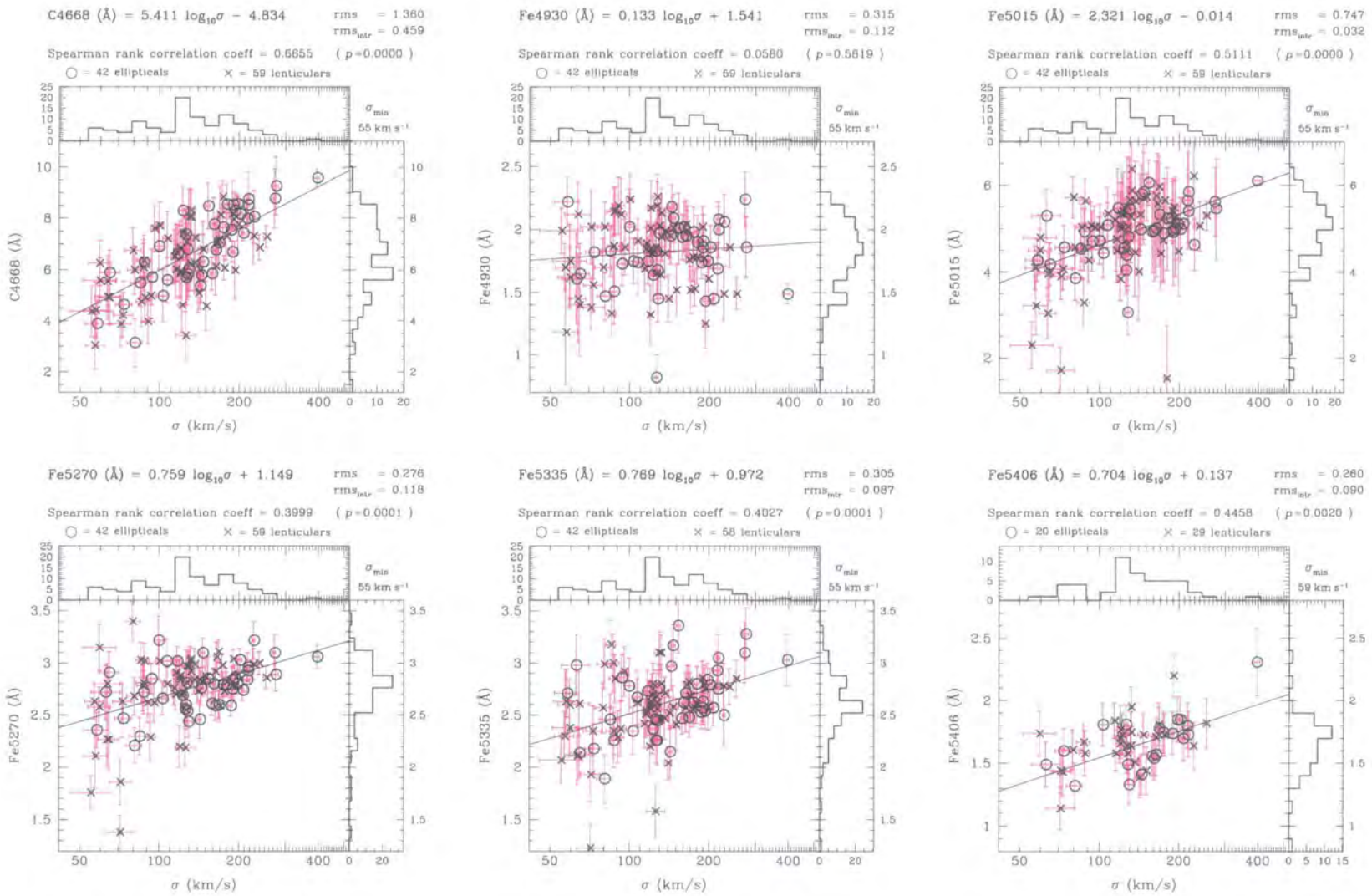

Figure 6.1: logarithmic velocity dispersion correlation analysis against C4668, Fe4930, Fe5015, Fe5270, Fe5335 and Fe5406. Early-type galaxies with velocity dispersions greater than $55\,\mathrm{km\,s^{-1}}$ are included. No lower signal-to-noise cutoff is applied.

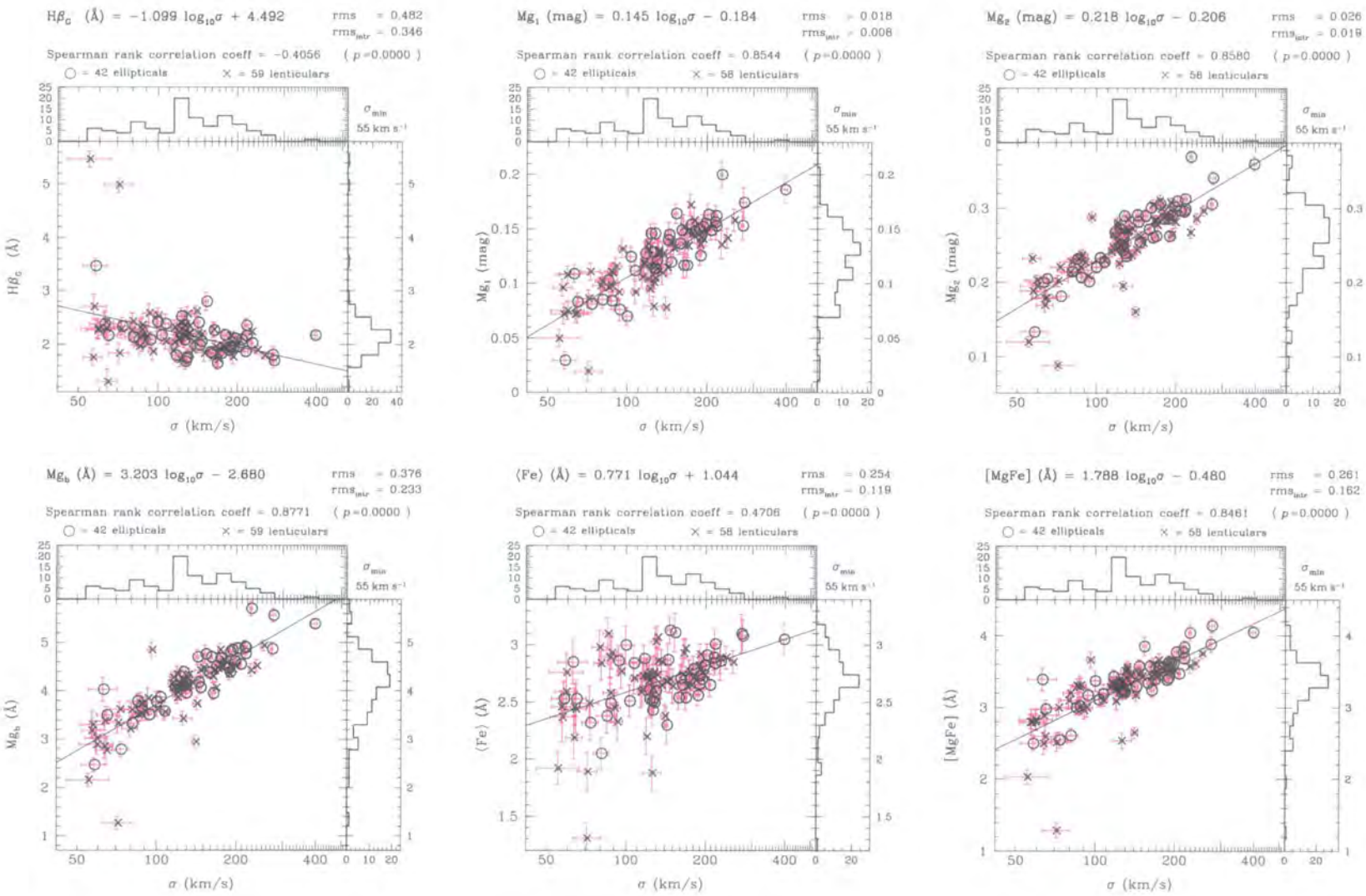

Figure 6.2: logarithmic velocity dispersion correlation analysis against $H\beta_G$, Mg_1, Mg_2, Mg_b, $\langle Fe \rangle$ and [MgFe]. Early-type galaxies with velocity dispersions greater than $55\,km\,s^{-1}$ are included. No lower signal-to-noise cutoff is applied. $H\beta_G$ has been corrected for nebula emission using [OIII]λ5007Å.

The low scatter of the FP and of the relations between the velocity dispersions and the line indices can be used to set limits on the allowed variations of ages and metallicities among ellipticals and lenticular galaxies. Worthey et al. (1994) found that the mean ages and metallicities derived from the line indices are correlated, in the sense that galaxies with lower mean ages have higher mean metallicities. The consequence of this relation may be that rather large age and metal variations are present while the low scatter of the scaling relations is maintained.

6.3 Physics underlying the fundamental plane relation

To interpret the empirically derived FP relation we need to relate the observable quantities to the physical quantities. The observable quantities are effective radius (r_e in kpc, the radius encompassing half the light), the mean surface brightness within this radius ($\langle I \rangle_e$ in $L_\odot/pc^2$) and the central velocity dispersion (σ in $km\,s^{-1}$).

The Virial Theorem states that for a bound system:

$$2T + \Omega = 0 \tag{6.4}$$

where T is the total kinetic energy (rotational plus random contributions) and Ω is the gravitational potential energy of the system. Summing over all the mass, M_i, in a galaxy we can write the gravitational potential energy as:

$$\Omega = -\frac{1}{2}\sum_{i \neq j} \frac{GM_iM_j}{\mid r_i - r_j \mid} = -\frac{GM^2}{\langle R \rangle} = -k_R\frac{GM^2}{r_e} \tag{6.5}$$

where k_R reflects the density structure. Similarly the total kinetic energy can be written as:

$$T = \frac{1}{2}\sum_i M_i v_i^2 + T_{rotational} = \frac{1}{2}M\langle v^2 \rangle = \frac{1}{2}M\frac{\sigma^2}{k_V} \tag{6.6}$$

since $T_{rotational} = 0$ for elliptical galaxies and where k_V reflects the kinematical structure of the galaxy. Note that the mass in these equations refers to the *total mass*, which includes both the luminous matter (stars) and dark matter. Substituting these equations for the kinetic and potential energy of the galaxy into the Virial Theorem yields:

$$\frac{M\sigma^2}{k_V} = k_R\frac{GM^2}{r_e} \tag{6.7}$$

therefore,

$$M = \frac{1}{Gk_Rk_V}\sigma^2 r_e \tag{6.8}$$

now since*,

$$L = 2\pi\langle I\rangle_e r_e^2 \tag{6.9}$$

then the mass-to-light ratio (M/L) for elliptical galaxies can be written as:

$$\frac{M}{L} = \frac{\frac{1}{Gk_Rk_V}\sigma^2 r_e}{2\pi\langle I\rangle_e r_e^2} \tag{6.10}$$

hence,

$$r_e = \frac{1}{2\pi Gk_Rk_V}\left(\frac{M}{L}\right)^{-1}\sigma^2\langle I\rangle_e^{-1} \tag{6.11}$$

from observations, the empirical FP relation is:

$$r_e = \text{constant} \times \sigma^\alpha \langle I\rangle_e^\beta \tag{6.12}$$

since observations typically give $\alpha \sim 1.3$ and $\beta \sim -0.8$ it follows that:

$$\frac{1}{2\pi Gk_Rk_V}\left(\frac{M}{L}\right)^{-1} \neq \text{constant} \tag{6.13}$$

rather it has to be a power law function of σ and $\langle I\rangle_e$:

$$\frac{1}{2\pi Gk_Rk_V}\left(\frac{M}{L}\right)^{-1} \propto \sigma^{\alpha-2}\langle I\rangle_e^{\beta+1} \tag{6.14}$$

therefore the structural parameters k_R and k_V and/or the mass-to-light ratio (M/L) need to vary in a systematic way to produce the observed FP slope.

*strictly there should be an additional term $10^6 \text{pc}^2/\text{kpc}^2$ in this equation since $\langle I\rangle_e$ is measured in units of $L_\odot/\text{pc}^2$ and r_e in units of kpc

Equation 6.9 implies that:

$$r_e = \sqrt{\frac{L}{2\pi\langle I\rangle_e}} \tag{6.15}$$

equating this with Equation 6.11 gives:

$$\frac{1}{2\pi G k_R k_V}\left(\frac{M}{L}\right)^{-1}\sigma^2\langle I\rangle_e^{-1} = L^{1/2}\langle I\rangle_e^{-1/2}\frac{1}{\sqrt{2\pi}} \tag{6.16}$$

i.e.,

$$\sigma = (2\pi)^{1/4}(Gk_Rk_V)^{1/2}\left(\frac{M}{L}\right)^{1/2}L^{1/4}\langle I\rangle_e^{1/4} \tag{6.17}$$

hence substituting for σ in Equation 6.14 gives:

$$\frac{1}{2\pi G k_R k_V}\left(\frac{M}{L}\right)^{-1} \propto (2\pi)^{\frac{1}{4}(\alpha-2)}(Gk_Rk_V)^{\frac{1}{2}(\alpha-2)}\left(\frac{M}{L}\right)^{\frac{1}{2}(\alpha-2)}L^{\frac{1}{4}(\alpha-2)}\langle I\rangle_e^{\frac{1}{4}(\alpha-2)+\beta+1} \tag{6.18}$$

therefore,

$$\left(\frac{M}{L}\right) \propto \underbrace{(2\pi)^{-(1/2+1/\alpha)}(Gk_Rk_V)^{-1}}_{\sim\text{constant}}L^{(1/\alpha-1/2)}\langle I\rangle_e^{-(1/\alpha+2\beta/\alpha+1/2)} \tag{6.19}$$

Bender, Burstein & Faber (1992) calculated the term k_Rk_V from Equation 6.8 using models with King profiles and isotropic velocity dispersions. Assuming $M_{\text{total}} = 10M_{\text{dynamic}}$, then for ellipticals with tidal-to-core radii ratios (r_t/r_c) of 100–300 they found that, for M_{dynamic}, $k_Rk_V = 1/5$ to $1/4$ if $G = 4.30\times10^{-6}\,(\text{km/s})^{-2}\,\text{kpc}\,M_\odot^{-1}$ — i.e. k_Rk_V is a approximately a constant for a sample of galaxies. Since typically $\alpha \sim 1.3$ and $\beta \sim -0.8$ then the exponent for the $\langle I\rangle_e$ term is -0.04 — i.e. not significant. This means that Equation 6.19 reduces to:

$$\left(\frac{M}{L}\right) \propto L^{\xi} \quad \text{where } \xi = \frac{1}{\alpha} - \frac{1}{2} \tag{6.20}$$

and with $\alpha \sim 1.3$ this implies that $\xi = 0.27$ thus,

$$\left(\frac{M}{L}\right) \propto L^{0.27} \tag{6.21}$$

This is the underlying physical relationship that leads to the observed fundamental plane relationship for elliptical galaxies.

The models of Bender, Burstein & Faber (1992) applied to Equation 6.11 also imply the following relationship for ellipticals with $r_t/r_c = 100$ and $M_{\rm total} = 10 M_{\rm dynamic}$:

$$\log(M_{\rm dynamic}/L) = 2\log\sigma - \log\langle I\rangle_e - \log r_e - 0.733 \tag{6.22}$$

with σ in km/s, $\langle I\rangle_e$ in $L_\odot/{\rm pc}^2$ and r_e in kpc.

In addition to the basic physical relationship in Equation 6.21, there are other factors that affect the FP relation which can lead to scatter around it:

- higher luminosity galaxies have higher metallicity than fainter galaxies, and because of the line-blanketing effect, brighter galaxies will emit more of their light at longer wavelengths than fainter galaxies. This is apparent in a variation in the slope of the colour–magnitude relation of early-type galaxies with wavelength (Bower, Lucey & Ellis 1992; Scodeggio et al. 1998 and Mobasher et al. 1998). Djorgovski & Santiago (1993) found the FP coefficient α to increase monotonically with the effective wavelength of the bandpass from $\alpha \approx 0.95$ at U ($\lambda_{\rm eff} \approx 365$nm) to $\alpha \approx 1.5$ at K ($\lambda_{\rm eff} \approx 2190$nm) whilst β remained constant at $\beta \approx -0.8$. The increase in α with wavelength is a sign of line blanketing since it implies a decrease in ξ, the coefficient in $(M/L) \propto L^{\xi}$. Recillas-Cruz et al. (1990) found the same trend with $\alpha = 1.36 \pm 0.11$ at B ($\lambda_{\rm eff} \approx 445$nm), $\alpha = 1.48 \pm 0.13$ at V ($\lambda_{\rm eff} \approx 551$nm) and $\alpha = 1.69 \pm 0.11$ at K ($\lambda_{\rm eff} \approx 2190$nm). Pahre & Djorgovski (1997) were the first to derive firm evidence of a wavelength dependence of the FP parameters by comparing their K-band FP relation with the V-band FP relation of Lucey, Bower & Ellis (1991). Their result was reproduced by Mobasher et al. (1998), who also used K-band photometric data, and by a study of 251 early-type galaxies in clusters and groups by Pahre, Djorgovski & de Carvalho (1998). Scodeggio et al. (1998) performed a comprehensive multi-wavelength study of the FP relation for 79 early-type galaxies within 2° of the Coma cluster centre

(a field diameter of 4°) using the B, V, r, I and K bands (the H-band data is from their study, whilst the remaining photometric data is from the literature) and found α to increase significantly with increasing wavelength from ~ 1.35 to ~ 1.70 (± 0.1) from the optical to the infrared, confirming previous results.

- the dark matter fraction ($M_{\rm dark}/M_{\rm dynamic}$) could increase with luminosity whilst $M_{\rm dynamic}/L$ remains constant. This problem has been explored by Renzini & Ciotti (1993), Guzmán et al. (1993), Ciotti, Lanzoni & Renzini (1996) and Mobasher et al. (1998).
- there could be a systematic variation of mean age along the FP (Faber et al. 1995), with the stellar populations of high luminosity galaxies having higher mean ages than for low luminosity galaxies (see also Prugniel & Simien 1996).
- imperfect fitting of surface brightness profiles and deviations from a classic $r^{1/4}$ profile to a more generic $r^{1/n}$ profile (with $n < 4$) and other deviations from homology (e.g. the presence of disks — see e.g. Jørgensen & Franx 1994) can lead to errors in both the r_e and $\langle I \rangle_e$ terms in the FP relation (see for example Caon et al. 1993).

Also there may indeed be other currently unknown factors affecting the FP relation, including the presence of an additional term reflecting stellar population or environmental dependencies.

6.4 Findings of previous spectro-photometric studies

Djorgovski & Davis (1987) found that:

- the morphological shape parameters (ellipticity, ellipticity gradient, isophotal twist rate, and slope of the surface brightness profile) did *not* correlate with the FP residuals
- the thickness of the FP was found to be given by the measurement errors and that the *intrinsic scatter* therefore had to be small

Their main sample only consisted of elliptical galaxies, but they reported preliminary results that a fundamental plane also existed for lenticular galaxies and that it might even be identical to that for elliptical galaxies.

Jørgensen et al. (1996) analysed the shape of the fundamental plane (FP) with a sample of 226 elliptical and lenticular galaxies from 9 galaxy clusters, spanning a wide range of richness

and regularity. Using Gunn r photometry and a data set of $\log\sigma$'s from a variety of sources (with a range in quality), they found that the distribution of galaxies is well-fit by a plane of the form:

$$\log_{10} r_e = \underset{\pm 0.07}{1.24} \log_{10}\sigma - \underset{\pm 0.02}{0.82} \log_{10}\langle I\rangle_e + 0.182 \qquad \text{with no } \sigma \text{ cutoff} \tag{6.23}$$

$$\log_{10} r_e = \underset{\pm 0.05}{1.35} \log_{10}\sigma - \underset{\pm 0.03}{0.82} \log_{10}\langle I\rangle_e + 0.182 \qquad \text{for galaxies with } \sigma \geq 100\,\mathrm{km\,s^{-1}} \tag{6.24}$$

They found an FP scatter of 0.073 in $\log r_e$ for galaxies with velocity dispersions larger than $100\,\mathrm{km\,s^{-1}}$ (0.084 when all galaxies are included). For galaxies with velocity dispersions less than $100\,\mathrm{km\,s^{-1}}$ the scatter is 0.125. Some of this difference is due to the larger measurement errors on the low velocity dispersion measurements, however Jørgensen et al. (1996) state that this cannot explain the whole difference. They also found that the FP does not significantly differ from cluster to cluster once selection effects and measurement errors were taken into account (they obtain coefficients in the range $1.09 \leq \alpha \leq 1.39$ and $-0.87 \leq \beta \leq -0.79$). A significant intrinsic scatter in the FP relation was found which could not be explained using structural parameters like ellipticity nor isophotal shape. When the residuals of the elliptical and lenticular galaxies with respect to a common FP fit were analysed they concluded that there are very small differences between the two populations. A median difference in ΔFP of 0.006 ± 0.011 was observed.

6.5 Coma cluster photometry

Photometry for the Coma cluster galaxies was taken from Jørgensen et al. (1995a). They present CCD surface photometry in Gunn r for 147 elliptical and lenticular galaxies (Figure 6.3(a)), with 31 of them also having Johnson B photometry (Figure 6.3(b)). Effective radii and mean surface brightnesses at these effective radii are derived by fitting a de Vaucouleurs $r^{1/4}$ growth curve. The parameter $\log r_n$ is also calculated. This parameter, corresponding to the D_n parameter introduced by Dressler et al. (1987), is the radius in arcsecs inside which $\langle\mu\rangle = 19.60\,\mathrm{mag\,arcsec^{-2}}$. Values have been corrected for seeing, galactic extinction and for cosmological dimming. After Jørgensen et al. (1995a), total magnitudes (m_T) are calculating with the following equation:

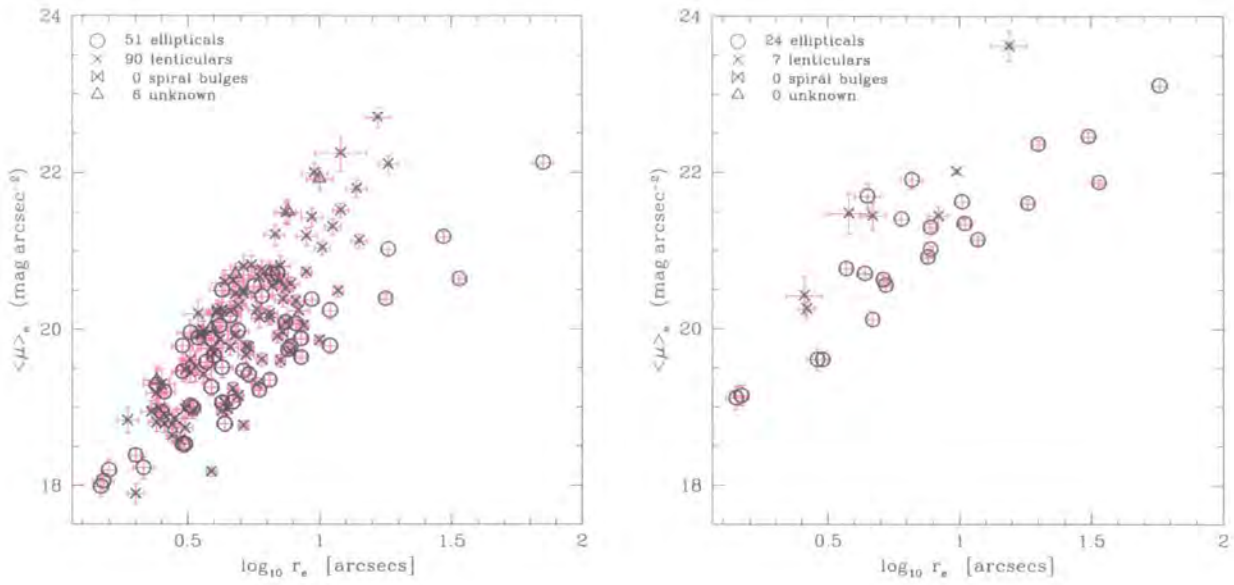

(a) Gunn r (b) Johnson B

Figure 6.3: Coma cluster surface photometry from Jørgensen et al. (1995a).

$$m_T = \langle \mu \rangle_e - 5 \log r_e - 2.5 \log 2\pi \tag{6.25}$$

Mass-to-light ratios are calculated using Equation 6.22.

In their study they match the galaxies to velocity dispersions (mostly of low signal-to-noise) both from their own observations and from a wide variety of sources (including the literature). This method of construction of a velocity dispersion data set introduces systematics which can greatly affect any conclusions about the FP relation since the error in the velocity dispersion is the dominant factor affecting it.

Herein I combine instead their high-quality photometric data with my new homogeneous, high signal-to-noise, high resolution data set. The combined data set has a total of 89 galaxies with full spectro-photometric data (Table 6.2). This is the sample that is analysed here. It allows in depth analysis of the FP and factors affecting it without the effects of systematics inherent in the construction of data sets from multiple sources by previous authors.

In Table 6.2, column (2) is the galaxy type from Dressler (1980). Columns (3) and (4) are from Godwin, Metcalfe & Peach (1983) and are accurate to ± 0.15 mag (note that $b-r \simeq B-R$). Columns (5) and (6) are from Jørgensen et al. (1995a), with $v-r$ = Gunn v − Gunn r and $B-r$ = Johnson B − Gunn r . Column (7) is from Bower et al. (1992) and Terlevich et al.

(1999) and is accurate to ± 0.03 mag. Column (8) is calculated from the velocity dispersion, σ (in $\mathrm{km\,s^{-1}}$) in this study. Columns (9) and (10) are ellipticities from Jørgensen et al. (1995a), with ϵ_{re} the ellipticity at r_e and $\epsilon_{21.85}$ the ellipticity at a local surface brightness of 21.85 mag arcsec^{-2} (both from Gunn r photometry). Columns (11) to (13) are Gunn r photometry from Jørgensen et al. (1995a): r_e is the effective equivalent radius in arcsec derived from a fit to an $\mathrm{r}^{1/4}$ growth curve; $\langle\mu\rangle_e$ is the mean surface brightness within r_e; and r_n is the equivalent radius within which the mean surface brightness in Gunn r is 19.60 mag arcsec^{-2}. Columns (14) to (16) are Johnson B photometry from Jørgensen et al. (1995a): r_e is the effective equivalent radius in arcsec derived from a fit to an $\mathrm{r}^{1/4}$ growth curve; $\langle\mu\rangle_e$ is the mean surface brightness within r_e; and r_n is the equivalent radius within which the mean surface brightness in Johnson B is 20.75 mag arcsec^{-2}. There are 89 galaxies in this table.

Previous studies have recognised that the errors in $\log \mathrm{r}_e$ and $\langle\mu\rangle_e$ are correlated in such a way that the combination that enters into the fundamental plane relation ($\log \mathrm{r}_e - 0.35\langle\mu\rangle_e$) is very stable. Jørgensen et al. (1995b) derive from their data a typical error of 0.020 for the quantity $\log \mathrm{r}_e - 0.35\langle\mu\rangle_e$; this is the value that is used herein.

										Gunn r photometry			Johnson B photometry		
gal	type	b_j	$b-r$	$B-r$	$v-r$	U–V	$\log_{10}\sigma$	ϵ_{re}	$\epsilon_{21.85}$	$\log r_e$	$\langle\mu\rangle_e$	$\log r_n$	$\log r_e$	$\langle\mu\rangle_e$	$\log r_n$
(1)	(2)	(3)	(4)	(5)	(6)	(7)	(8)	(9)	(10)	(11)	(12)	(13)	(14)	(15)	(16)
d26	S0p	16.18					1.854 ± 0.054	0.394	0.366	0.74 ± 0.04	20.82 ± 0.13	0.06			
d27	E	16.45	1.88				2.031 ± 0.014	0.164	0.147	0.66 ± 0.04	20.17 ± 0.14	0.48			
d28	E/S0	16.67	1.99			1.36	2.015 ± 0.018	0.236	0.324	0.41 ± 0.04	19.20 ± 0.15	0.47			
d39	S0/E	16.17	1.89				2.081 ± 0.012	0.191	0.186	0.76 ± 0.03	20.25 ± 0.11	0.56			
d42	S0	16.31	1.86			1.46	2.168 ± 0.020	0.318	0.427	0.41 ± 0.03	18.79 ± 0.11	0.61			
d44	S0	16.57	1.77			1.03	1.743 ± 0.082	0.544	0.635	0.38 ± 0.04	19.19 ± 0.15	0.35			
d53	E	16.59	1.87			1.36	2.109 ± 0.018	0.130	0.133	0.48 ± 0.04	19.46 ± 0.13	0.52			
d57	S0/a	15.15	1.78			1.39	2.154 ± 0.014	0.711	0.735	0.94 ± 0.02	20.05 ± 0.06	0.80			
d59	E	16.90	1.85				2.114 ± 0.016	0.159	0.150	0.38 ± 0.05	19.29 ± 0.18	0.47			
d62	S0	16.51	1.90			1.22	2.101 ± 0.036	0.427	0.428	0.77 ± 0.04	20.66 ± 0.12	0.47			
d63	S0/a	16.97	1.90				1.941 ± 0.023	0.329	0.501	0.83 ± 0.04	21.21 ± 0.13	0.37			
d65	S0	16.15	1.77			1.44	2.066 ± 0.012	0.454	0.435	0.82 ± 0.03	20.55 ± 0.11	0.51			
d67	S0	16.50	1.94				2.178 ± 0.006	0.199	0.403	0.38 ± 0.03	18.81 ± 0.12	0.58			
d75	S0	16.13	1.91			1.33	1.901 ± 0.031	0.789	0.781	1.08 ± 0.03	21.52 ± 0.09	0.28			
d81	E	16.10	1.85				2.156 ± 0.007	0.208	0.212	0.82 ± 0.04	20.70 ± 0.13	0.52			
d84	S0	16.20	1.98				2.081 ± 0.012	0.627	0.656	0.66 ± 0.03	19.77 ± 0.10	0.58			
d87	E	16.87	1.79				1.973 ± 0.021	0.074	0.074	0.48 ± 0.04	19.79 ± 0.16	0.43			
d90	S0	16.93	1.88			1.34	1.947 ± 0.020	0.485	0.460	0.71 ± 0.05	20.80 ± 0.15	0.27			
d93	S0	16.26	2.06			1.40	2.135 ± 0.015	0.431	0.677	0.44 ± 0.03	18.79 ± 0.11	0.63			
d98	S0/a	15.85	1.91			1.42	2.114 ± 0.018	0.615	0.662	0.72 ± 0.02	19.78 ± 0.08	0.63			
d107	E	16.35	1.81	1.23	0.98	1.24	1.943 ± 0.018	0.410	0.415	0.75 ± 0.04	20.55 ± 0.14	0.42	0.82 ± 0.04	21.91 ± 0.11	0.44
d108	S0	16.55	1.85			1.42	2.064 ± 0.012	0.433	0.508	0.51 ± 0.04	19.61 ± 0.13	0.49			
d110	S0/E	16.60	1.93				2.058 ± 0.012	0.289	0.289	0.71 ± 0.04	20.46 ± 0.13	0.43			
d112	E	16.64	1.78			1.11	1.766 ± 0.046	0.169	0.199	0.54 ± 0.04	19.89 ± 0.15	0.41			
d116	SB0	16.13	1.90			1.23	2.091 ± 0.014	0.159	0.210	0.85 ± 0.03	20.62 ± 0.10	0.55			
d117	S0/a	16.56	1.88			1.35	1.969 ± 0.022	0.439	0.436	0.66 ± 0.04	20.23 ± 0.13	0.43			
d123	SB0	16.47	1.93				2.003 ± 0.014	0.323	0.437	0.97 ± 0.04	21.43 ± 0.12	0.35			
d132	S0	16.63	1.88			1.33	1.983 ± 0.015	0.298	0.318	0.61 ± 0.04	20.24 ± 0.14	0.44			
d135	E	16.98	1.86	1.12	1.19	1.29	2.001 ± 0.017	0.210	0.213	0.63 ± 0.05	20.50 ± 0.15	0.37	0.65 ± 0.05	21.70 ± 0.16	0.38
d136	E	16.57	1.81	1.25	1.31	1.36	2.227 ± 0.006	0.149	0.241	0.17 ± 0.03	17.99 ± 0.13	0.57	0.15 ± 0.04	19.12 ± 0.15	0.56
d147	S0	16.19	1.85			1.32	2.032 ± 0.016	0.537	0.543	0.95 ± 0.04	21.19 ± 0.11	0.45			
d153	E	16.14	1.83	1.17		1.39	2.107 ± 0.009	0.013	0.018	0.57 ± 0.02	19.58 ± 0.10	0.56	0.57 ± 0.02	20.77 ± 0.08	0.56
d154	S0	16.41	1.78	0.83		1.37	1.756 ± 0.036	0.297	0.286	1.08 ± 0.10	22.25 ± 0.23	0.19	1.19 ± 0.07	23.63 ± 0.19	
d156	E/S0	16.45					1.929 ± 0.039	0.206	0.252	0.51 ± 0.05	19.96 ± 0.16	0.36			

Table 6.2: *continued on next page*

continued from previous page

										Gunn r photometry			Johnson B photometry		
gal	type	b_j	$b-r$	$B-r$	$v-r$	U–V	$\log_{10}\sigma$	ϵ_{re}	$\epsilon_{21.85}$	$\log r_e$	$\langle\mu\rangle_e$	$\log r_n$	$\log r_e$	$\langle\mu\rangle_e$	$\log r_n$
(1)	(2)	(3)	(4)	(5)	(6)	(7)	(8)	(9)	(10)	(11)	(12)	(13)	(14)	(15)	(16)
d157	S0	16.26	1.81			1.36	2.119 ± 0.008	0.242	0.380	0.49 ± 0.03	19.48 ± 0.12	0.51			
d161	E	15.19	1.87				2.279 ± 0.011	0.115	0.119	0.91 ± 0.03	20.07 ± 0.09	0.78			
d171	S0	16.57	1.78			1.40	2.105 ± 0.010	0.196	0.235	0.55 ± 0.03	19.92 ± 0.12	0.48			
d181	S0	16.52	1.87				2.080 ± 0.016	0.242	0.534	0.51 ± 0.03	19.45 ± 0.13	0.55			
d191	S0	16.69	1.77			1.34	1.958 ± 0.024	0.409	0.598	0.36 ± 0.04	18.95 ± 0.14	0.47			
d192	S0	16.14	1.79			1.29	1.942 ± 0.027	0.739	0.768	0.77 ± 0.03	20.15 ± 0.12	0.51			
d193	E	16.43	1.82			1.40	2.071 ± 0.012	0.171	0.151	0.62 ± 0.03	20.04 ± 0.12	0.47			
d200	S0	16.08	1.82			1.46	2.277 ± 0.010	0.359	0.512	0.30 ± 0.03	17.90 ± 0.13	0.72			
d204	E	15.99	1.75				2.101 ± 0.014	0.218	0.254	0.78 ± 0.04	20.42 ± 0.15	0.57			
d207	E	16.07	1.80			1.43	2.167 ± 0.008	0.291	0.347	0.60 ± 0.03	19.66 ± 0.12	0.56			
d209	S0	16.04	1.77				1.907 ± 0.027	0.558	0.532	1.14 ± 0.04	21.80 ± 0.11	0.38			
d210	E	15.97	1.88				2.160 ± 0.011	0.219	0.126	0.59 ± 0.03	19.26 ± 0.11	0.68			
d231	S0	15.78	2.09				2.107 ± 0.017	0.386	0.395	0.49 ± 0.03	18.74 ± 0.12	0.70			
ic3943	S0/a	15.55	1.97				2.227 ± 0.005	0.481	0.595	0.67 ± 0.02	19.24 ± 0.08	0.75			
ic3946	S0	15.28	1.95			1.52	2.300 ± 0.006	0.310	0.479	0.65 ± 0.02	18.98 ± 0.07	0.81			
ic3947	E	15.94	1.91			1.42	2.201 ± 0.006	0.284	0.322	0.52 ± 0.03	19.00 ± 0.11	0.67			
ic3959	E	15.27	1.94	1.17		1.51	2.334 ± 0.012	0.128	0.095	0.73 ± 0.03	19.42 ± 0.10	0.78	0.72 ± 0.02	20.56 ± 0.08	0.77
ic3960	S0	15.85	1.89				2.241 ± 0.007	0.040	0.058	0.73 ± 0.02	19.77 ± 0.08	0.68			
ic3963	S0	15.76	1.87			1.41	2.088 ± 0.013	0.474	0.464	0.89 ± 0.03	20.58 ± 0.09	0.60			
ic3973	S0/a	15.32	1.88			1.49	2.358 ± 0.006	0.226	0.252	0.64 ± 0.03	19.06 ± 0.10	0.78			
ic3976	S0	15.80	1.95			1.54	2.407 ± 0.011	0.410	0.532	0.47 ± 0.03	18.58 ± 0.10	0.72			
ic3998	SB0	15.70	1.90	1.16		1.46	2.136 ± 0.015	0.333	0.322	0.95 ± 0.02	20.73 ± 0.07	0.61	0.99 ± 0.00	22.02 ± 0.02	0.61
ic4011	E	16.08	1.82	1.09		1.35	2.091 ± 0.013	0.088	0.099	0.69 ± 0.04	19.98 ± 0.12	0.57	0.78 ± 0.03	21.41 ± 0.10	0.58
ic4012	E	15.93	1.86			1.44	2.257 ± 0.009	0.163	0.220	0.33 ± 0.04	18.23 ± 0.14	0.68			
ic4026	SB0	15.73	1.77			1.39	2.121 ± 0.010	0.181	0.181	0.86 ± 0.03	20.38 ± 0.09	0.63			
ic4041	S0	15.93	1.90			1.40	2.122 ± 0.007	0.450	0.442	0.87 ± 0.03	20.52 ± 0.09	0.58			
ic4042	S0/a	15.34	1.86			1.42	2.232 ± 0.008	0.065	0.063	0.86 ± 0.02	19.96 ± 0.08	0.76			
ic4045	E	15.17	1.85	1.18		1.48	2.338 ± 0.007	0.328	0.316	0.64 ± 0.03	18.79 ± 0.10	0.85	0.67 ± 0.02	20.12 ± 0.08	0.84
ic4051	E	14.47	1.82	1.18	1.24	1.55	2.359 ± 0.005	0.256	0.217	1.26 ± 0.03	21.02 ± 0.09	0.82	1.30 ± 0.02	22.37 ± 0.06	0.79
ngc4850	E/S0	15.39	1.87			1.43	2.278 ± 0.006	0.208	0.127	0.67 ± 0.03	19.07 ± 0.09	0.81			
ngc4851	S0	16.00	1.95				2.103 ± 0.011	0.320	0.313	0.81 ± 0.03	20.20 ± 0.10	0.61			
ngc4853	S0p	14.38	1.66				2.149 ± 0.013	0.176	0.137	0.59 ± 0.02	18.18 ± 0.06	0.96			
ngc4860	E	14.69	1.93			1.56	2.443 ± 0.011	0.148	0.171	0.93 ± 0.02	19.64 ± 0.07	0.91			
ngc4864	E	14.70		1.17	1.24	1.55	2.273 ± 0.007	0.151	0.141	0.89 ± 0.02	19.78 ± 0.08	0.84	0.88 ± 0.02	20.92 ± 0.06	0.83
ngc4867	E	15.44	1.83	1.12	1.13	1.43	2.319 ± 0.004	0.250	0.246	0.49 ± 0.03	18.53 ± 0.10	0.77	0.48 ± 0.02	19.61 ± 0.08	0.78
ngc4869	E	14.97	2.06	1.21	1.24		2.308 ± 0.009	0.131	0.096	0.88 ± 0.02	19.74 ± 0.08	0.84	0.89 ± 0.01	21.02 ± 0.05	0.82
ngc4872	E/S0	14.79	1.78	1.18	1.22	1.45	2.338 ± 0.007	0.058	0.232	0.48 ± 0.03	18.53 ± 0.11	0.76	0.46 ± 0.04	19.61 ± 0.14	0.75

Table 6.2: *continued on next page*

continued from previous page

										Gunn r photometry			Johnson B photometry		
gal	type	b_j	$b-r$	$B-r$	$v-r$	U-V	$\log_{10}\sigma$	ϵ_{re}	$\epsilon_{21.85}$	$\log r_e$	$\langle\mu\rangle_e$	$\log r_n$	$\log r_e$	$\langle\mu\rangle_e$	$\log r_n$
(1)	(2)	(3)	(4)	(5)	(6)	(7)	(8)	(9)	(10)	(11)	(12)	(13)	(14)	(15)	(16)
ngc4873	S0	15.15	1.91			1.40	2.248 ± 0.004	0.254	0.269	0.87 ± 0.02	20.09 ± 0.08	0.71			
ngc4874	D	12.78		1.19	1.42	1.56	2.439 ± 0.005	0.157	0.096	1.85 ± 0.04	22.13 ± 0.09	1.01	1.76 ± 0.03	23.12 ± 0.08	0.98
ngc4875	S0	15.88	1.96			1.46	2.255 ± 0.010	0.169	0.246	0.52 ± 0.03	18.96 ± 0.10	0.69			
ngc4876	E	15.51	1.91	1.16		1.47	2.215 ± 0.008	0.294	0.333	0.71 ± 0.03	19.47 ± 0.09	0.74	0.71 ± 0.02	20.63 ± 0.06	0.74
ngc4881	E	14.73	1.87	1.15		1.51	2.288 ± 0.011	0.040	0.043	1.04 ± 0.03	20.24 ± 0.11	0.85	1.02 ± 0.02	21.35 ± 0.07	0.85
ngc4883	S0	15.43	1.89			1.49	2.220 ± 0.007	0.204	0.245	0.84 ± 0.02	19.91 ± 0.08	0.74			
ngc4886	E	14.83	1.76	1.10		1.33	2.187 ± 0.008	0.024	0.024	0.97 ± 0.03	20.38 ± 0.09	0.74	1.01 ± 0.03	21.63 ± 0.08	0.75
ngc4889	D	12.62	1.91	1.20		1.63	2.599 ± 0.011	0.359	0.358	1.53 ± 0.02	20.64 ± 0.05	1.21	1.53 ± 0.02	21.88 ± 0.04	1.18
ngc4894	S0	15.87	1.74			1.22	1.932 ± 0.019	0.533	0.586	0.68 ± 0.03	19.93 ± 0.11	0.56			
ngc4895	S0	14.38				1.50	2.380 ± 0.009	0.582	0.614	1.00 ± 0.02	19.86 ± 0.06	0.91			
ngc4896	S0	15.06	2.01				2.215 ± 0.007	0.438	0.436	1.07 ± 0.02	20.49 ± 0.07	0.79			
ngc4906	E	15.44	1.98	1.15	1.17	1.45	2.243 ± 0.011	0.120	0.124	0.87 ± 0.03	20.09 ± 0.10	0.73	0.89 ± 0.02	21.30 ± 0.06	0.73
ngc4908	S0/E	14.91	1.87			1.43	2.288 ± 0.010	0.313	0.308	0.85 ± 0.02	19.60 ± 0.08	0.85			
ngc4919	S0	15.06	1.92			1.49	2.282 ± 0.007	0.311	0.431	0.76 ± 0.02	19.30 ± 0.08	0.83			
ngc4923	E	14.78	1.93			1.52	2.297 ± 0.008	0.168	0.183	0.93 ± 0.02	19.88 ± 0.08	0.85			
rb74	SA0	16.78	1.74				1.805 ± 0.031	0.440	0.397	0.88 ± 0.05	21.50 ± 0.16				
rb94	SB0/a	16.69	1.81				1.760 ± 0.046	0.205	0.413	1.00 ± 0.05	21.92 ± 0.14				
rb129	unE	16.86	1.85			1.25	1.954 ± 0.021	0.029	0.043	0.68 ± 0.05	20.70 ± 0.15	0.42			

Table 6.2: Coma cluster fundamental plane parameters. See text.

6.6 Coma cluster fundamental plane

6.6.1 Fitting fundamental plane to the Coma cluster

Using a method similar to Jørgensen et al. (1996), I fit a plane to the distribution of galaxies in $\log r_e$, $\log\langle I\rangle_e$ and $\log\sigma$. This was done as an "orthogonal fit" where I calculate the vector normal to the plane $\boldsymbol{n} = (-1, \alpha, \beta)$ that minimises the rms of the residuals perpendicular to the plane. The residual perpendicular to the plane can be written as:

$$\Delta = \frac{\log_{10} r_e - \alpha \log_{10}\sigma - \beta \log_{10}\langle I\rangle_e}{\sqrt{1+\alpha^2+\beta^2}} \tag{6.26}$$

This residual can alternatively be written as:

$$\Delta = \frac{\log_{10} r_e - \alpha \log_{10}\sigma + 0.4\beta\langle\mu\rangle_e}{\sqrt{1+\alpha^2+\beta^2}} \tag{6.27}$$

using equation 6.2 (the constant is dealt with separately in the minimisation procedure and a median cluster zero point calculated). This procedure is relatively insensitive to outliers and treats all parameters symmetrically. The uncertainties in the quantities α, β and γ were determined using standard bootstrap re-sampling with replacement techniques; this gives an estimation of the random uncertainties, but does not take into account any systematic uncertainties.

6.6.2 Fundamental plane of the Coma cluster

The results of fundamental plane (FP) fits to the total early-type galaxy populations and for the elliptical and lenticular sub-populations with lower velocity dispersion limits of $55\,\mathrm{km\,s^{-1}}$ (this is the lowest velocity dispersion of the data set, i.e. there is no lower velocity dispersion cutoff for this sample) and $100\,\mathrm{km\,s^{-1}}$ are shown in Table 6.3 and Figure 6.4. An observed rms and an intrinsic rms (taking into account the measurement errors) are given.

Galaxies	Min σ	N	α	β	γ_{cl}	rms_{obs}	rms_{intr}
all early-types	$55\,\mathrm{km\,s^{-1}}$	87	1.08 ± 0.09	-0.78 ± 0.03	-0.02 ± 0.14	0.082	0.056
	$100\,\mathrm{km\,s^{-1}}$	69	1.36 ± 0.07	-0.78 ± 0.03	-0.64 ± 0.16	0.067	0.044
ellipticals	$55\,\mathrm{km\,s^{-1}}$	36	1.18 ± 0.12	-0.81 ± 0.04	-0.15 ± 0.31	0.073	0.049
	$100\,\mathrm{km\,s^{-1}}$	32	1.38 ± 0.09	-0.78 ± 0.03	-0.71 ± 0.22	0.058	0.036
lenticulars	$55\,\mathrm{km\,s^{-1}}$	51	0.93 ± 0.16	-0.72 ± 0.06	$+0.16 \pm 0.22$	0.080	0.052
	$100\,\mathrm{km\,s^{-1}}$	37	1.41 ± 0.19	-0.79 ± 0.06	-0.71 ± 0.36	0.075	0.051

Table 6.3: Fundamental plane of the Coma cluster. An FP is fit to the total early-type galaxy population and to the elliptical and lenticular sub-populations. Two lower velocity dispersion cutoffs are used: 55 and $100\,\mathrm{km\,s^{-1}}$. Two values of the scatter around the FP are quoted: one is the observed scatter and the other one is the *intrinsic* scatter, calculated by taking into account the measurement errors of the sample.

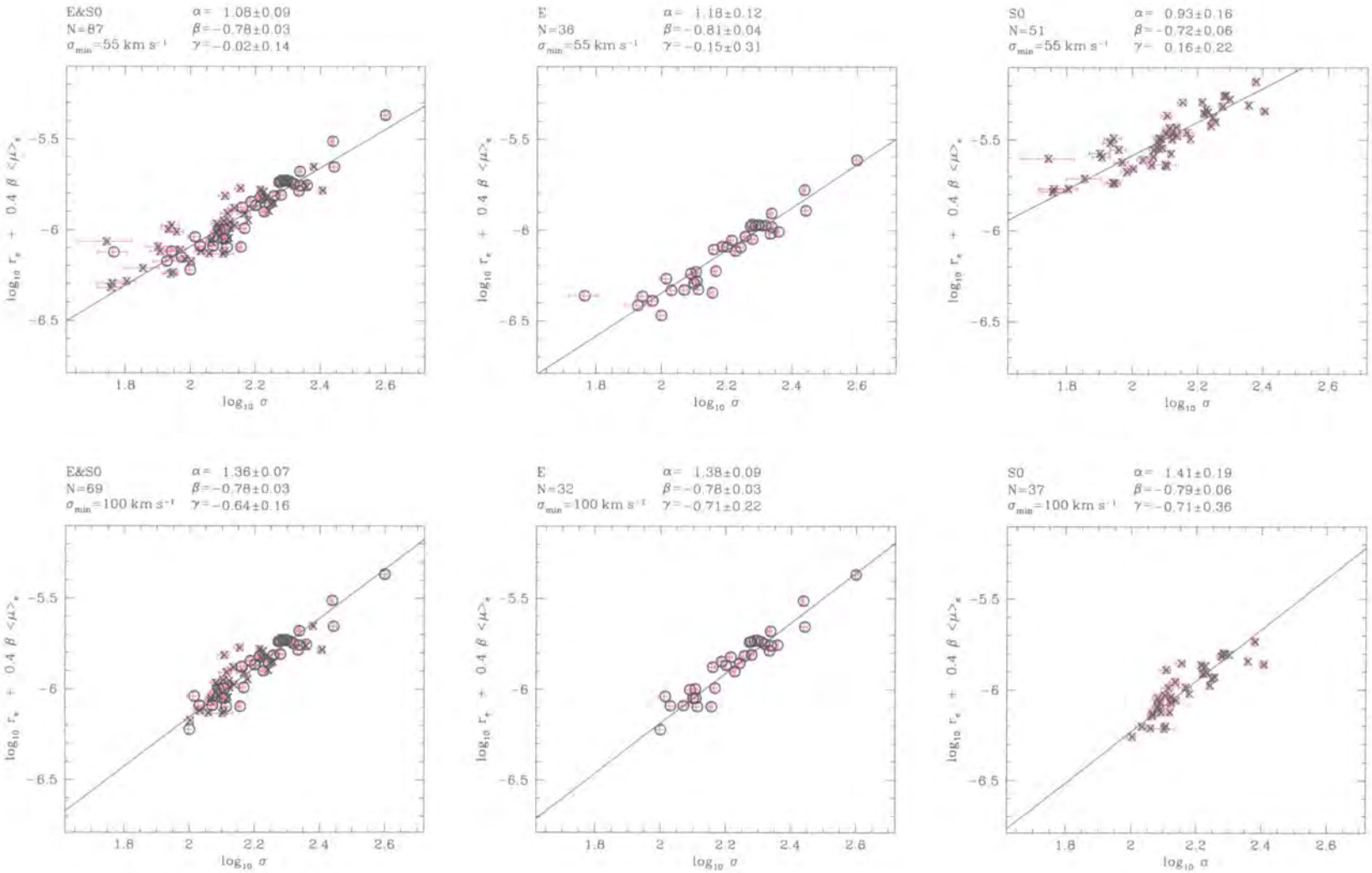

Figure 6.4: Fundamental plane of Coma cluster early-type galaxies. The top 3 figures include galaxies with $\sigma \geq 55\,\mathrm{km\,s^{-1}}$. The bottom 3 figures include galaxies with $\sigma \geq 100\,\mathrm{km\,s^{-1}}$. The figures on the left include all early-type galaxies, whilst the figures in the middle contain ellipticals and the figures on the right contain lenticulars. In each case the best-fitting FP relation for that data set is shown.

6.6.3 Testing the robustness of the FP fit

To test the robustness of the FP fitting method described in Section 6.6.1 I investigate any dependency of residuals around the FP fit on $\log\sigma$, $\log r_e$ and $\log\langle\mu\rangle_e$ (the parameters within the FP equation).

Figures 6.5 to 6.7 show these plots. The residual around the FP relation is calculated using:

$$\Delta FP = \log_{10} r_e - \alpha \log_{10}\sigma - \beta \log_{10}\langle I\rangle_e - \gamma \tag{6.28}$$

The robustness of the FP fit can be tested by determining whether there is any correlation between the residuals and the parameters from which it is derived. To test for this correlation I use the Spearman rank correlation coefficient. Since the distribution of the residuals is Gaussian (see Section 6.6.6), I use the two-tailed Spearman rank correlation coefficient test against the null hypothesis that the X and Y parameters are mutually independent. Any significance level, p less than 0.05 rejects this null hypothesis indicating the presence of a correlation. The results of this correlation analysis are included in Table 6.6. I find no evidence of any dependency of the FP residuals on the parameters $\log\sigma$, $\log r_e$ and $\log\langle\mu\rangle_e$ (with all significance levels, p greater than 0.05). The conclusion of this testing is that the FP fitting method used is robust and does not introduce any spurious correlations that could contaminate any findings.

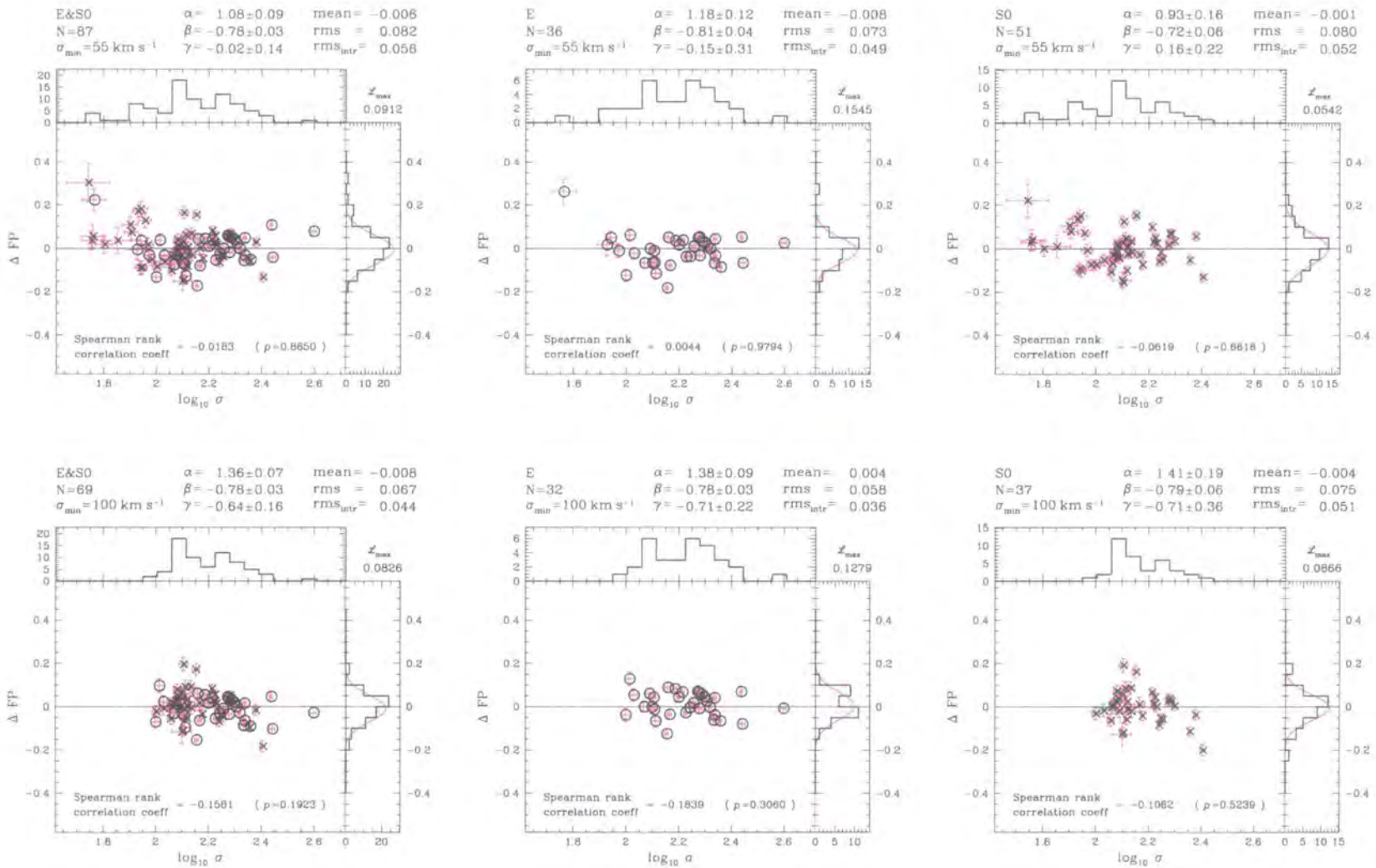

Figure 6.5: Fundamental plane residuals versus log σ. The top 3 figures include galaxies with $\sigma \geq 55\,\mathrm{km\,s^{-1}}$. The bottom 3 figures include galaxies with $\sigma \geq 100\,\mathrm{km\,s^{-1}}$. The figures on the left include all early-type galaxies, whilst the figures in the middle contain ellipticals and the figures on the right contain lenticulars. In each case the FP residuals are calculated with respect to the best-fitting FP relation for that data set using the equation: $\Delta\mathrm{FP} = \log \mathrm{r}_e - \alpha \log \sigma - \beta \log\langle \mathrm{I} \rangle_e - \gamma_{cl}$.

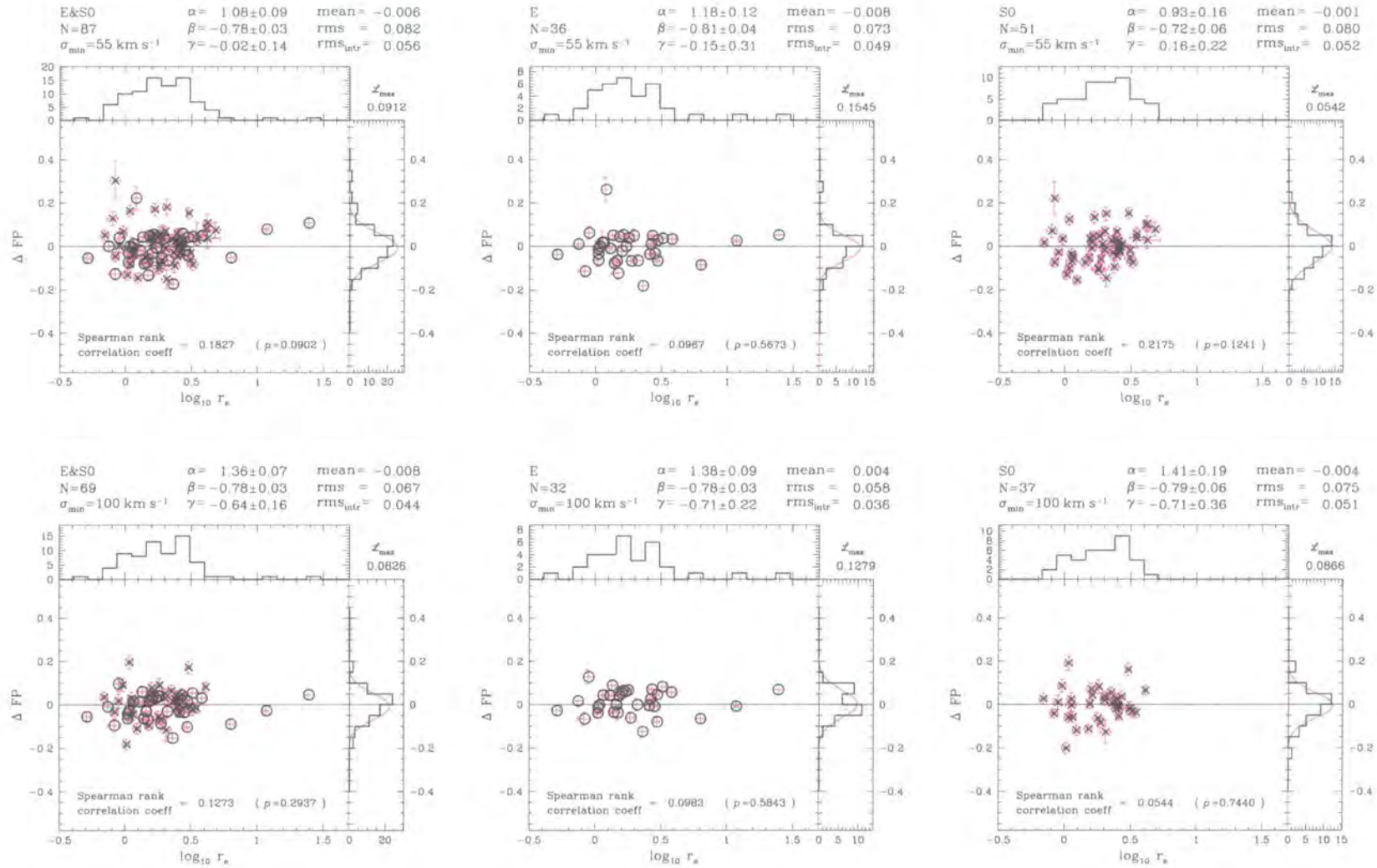

Figure 6.6: Fundamental plane residuals versus log r_e. The top 3 figures include galaxies with $\sigma \geq 55\,\mathrm{km\,s^{-1}}$. The bottom 3 figures include galaxies with $\sigma \geq 100\,\mathrm{km\,s^{-1}}$. The figures on the left include all early-type galaxies, whilst the figures in the middle contain ellipticals and the figures on the right contain lenticulars. In each case the FP residuals are calculated with respect to the best-fitting FP relation for that data set using the equation: $\Delta\mathrm{FP} = \log \mathrm{r}_e - \alpha \log \sigma - \beta \log\langle \mathrm{I} \rangle_e - \gamma_{cl}$.

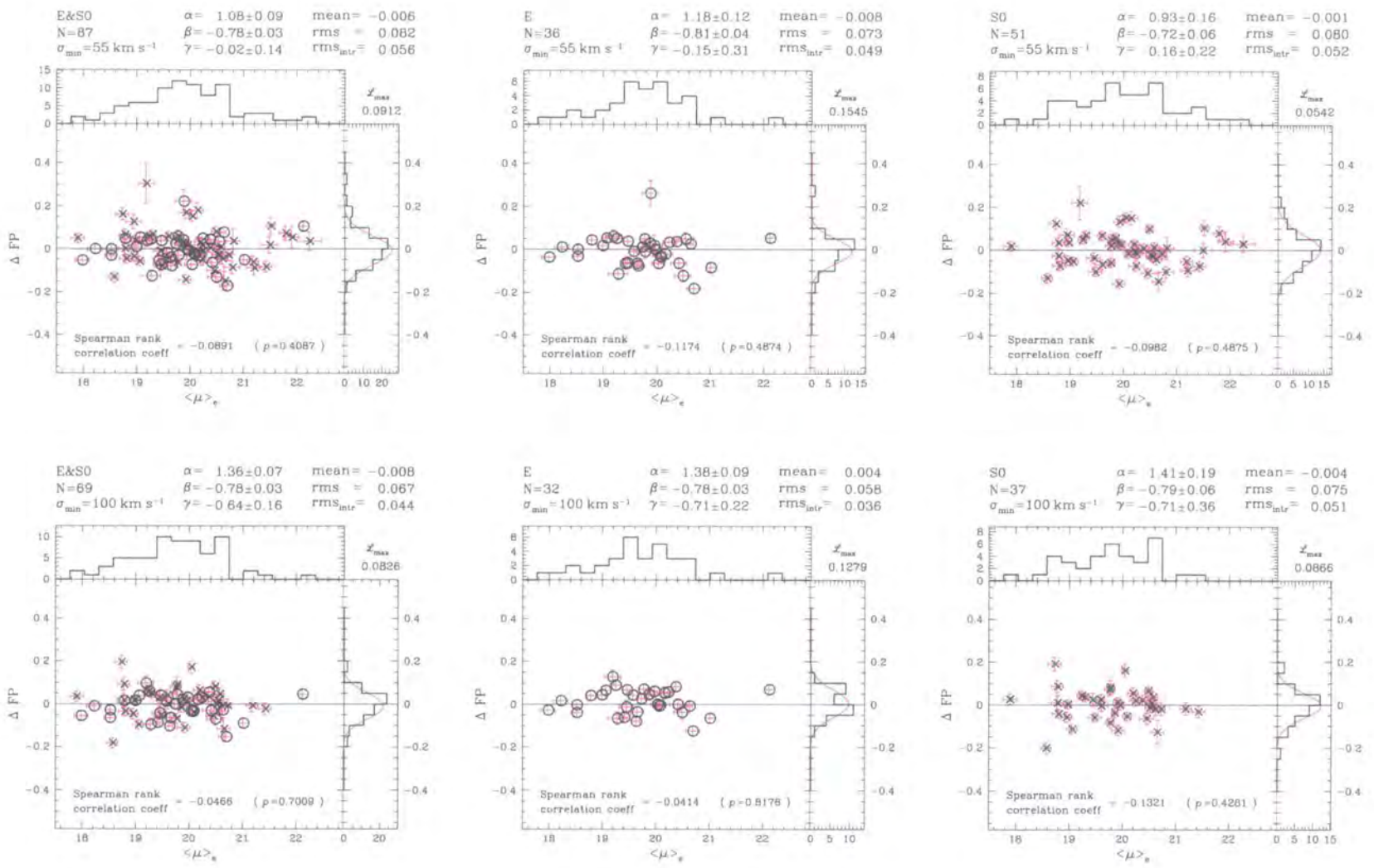

Figure 6.7: Fundamental plane residuals versus $\langle\mu\rangle_e$. The top 3 figures include galaxies with $\sigma \geq 55\,\mathrm{km\,s^{-1}}$. The bottom 3 figures include galaxies with $\sigma \geq 100\,\mathrm{km\,s^{-1}}$. The figures on the left include all early-type galaxies, whilst the figures in the middle contain ellipticals and the figures on the right contain lenticulars. In each case the FP residuals are calculated with respect to the best-fitting FP relation for that data set using the equation: $\Delta\mathrm{FP} = \log \mathrm{r}_e - \alpha \log \sigma - \beta \log\langle \mathrm{I}\rangle_e - \gamma_{cl}$.

6.6.4 Coma fundamental plane analysis

Fitting separate relations to the elliptical and lenticular sub-populations yields similar α, β and γ values for galaxies with velocity dispersions, $\sigma = 100$ to $398\,\mathrm{km\,s^{-1}}$ but different values if I include lower velocity dispersion galaxies ($\sigma = 55$ to $398\,\mathrm{km\,s^{-1}}$). The slope of the fundamental plane, β remains the same, but the α and γ values vary[†]: $\Delta\alpha_{100-55} = 0.28 \pm 0.11$ (a 2.5 sigma detection, equivalent to a 98.9% confidence) and $\Delta\gamma_{100-55} = -0.62 \pm 0.21$ (a 3.0 sigma detection, equivalent to a 99.7% confidence). Jørgensen et al. (1996) also noted the dependence of the FP coefficients on selection criteria and observed that the coefficient α rose in a systematic way if galaxies with velocity dispersions less than $100\,\mathrm{km\,s^{-1}}$ were excluded. In this study, I believe the difference between the FP fits for galaxies with $\sigma \geq 100\,\mathrm{km\,s^{-1}}$ to those for $\sigma \geq 55\,\mathrm{km\,s^{-1}}$ is partly due to incompleteness in the low dispersion, faint early-type galaxy sample causing a bias that is affecting the FP fit (this can be seen in Figure 6.4). These low dispersions galaxies have a significant effect on the FP relation in this study. The higher dispersion and brighter galaxy sample suffers no such bias. The results of this study and that of previous studies highlight the necessity to understand the selection biases of a given sample and the caution needed when applying the derived FP relation to calculate distances.

The scatter around the fundamental plane is seen to depend upon morphological type: the FP scatter of an elliptical galaxy fit ($\mathrm{rms}_{intr}\{\mathrm{E}\} = 0.036 \pm 0.006$ for $\sigma \geq 100\,\mathrm{km\,s^{-1}}$) is *smaller* than that for a lenticular galaxy fit ($\mathrm{rms}_{intr}\{\mathrm{S0}\} = 0.051 \pm 0.008$ for $\sigma \geq 100\,\mathrm{km\,s^{-1}}$), with $\Delta\mathrm{rms}_{intr}\{\mathrm{S0\text{-}E}\} = 0.015 \pm 0.010$ (a 1.5 sigma detection, equivalent to a 86.6% confidence). This agrees with the conclusions of Chapter 5 that there are important differences between ellipticals and lenticulars and that analyses should be cautious when considering an early-type galaxy data set. The scatter is also dependent upon the lower velocity dispersion cutoff, with the total early-type galaxy sample having $\mathrm{rms}_{intr}\{\mathrm{E\&S0}\} = 0.056 \pm 0.006$ for $\sigma \geq 55\,\mathrm{km\,s^{-1}}$ and $\mathrm{rms}_{intr}\{\mathrm{E\&S0}\} = 0.044 \pm 0.005$ for $\sigma \geq 100\,\mathrm{km\,s^{-1}}$ giving $\Delta\mathrm{rms}_{intr}\{55-100\} = 0.012 \pm 0.008$ (a 1.5 sigma detection, equivalent to a 86.6% confidence). This is unsurprising since the $\log\sigma$ parameter in the FP equation is the dominant source of error and is therefore the most important to determine well when trying to measure cluster distances. This dependence on minimum velocity dispersion is repeated in the elliptical and lenticular sub-samples. This once again highlights the importance of selection criteria in obtaining a tight FP relation to compute

[†]the subscript "100" refers to the $\sigma = 100$ to $398\,\mathrm{km\,s^{-1}}$ sample whilst the subscript "55" refers to the $\sigma = 55$ to $398\,\mathrm{km\,s^{-1}}$ sample

distances. The best data sample that yields the smallest thickness is the elliptical galaxy sample with $\sigma \geq 100\,\mathrm{km\,s^{-1}}$.

The values of intrinsic scatter for the total early-type galaxy sample are smaller than those found by Jørgensen et al. (1996). They found intrinsic scatters of 0.073 dex in $\log r_e$ for $\sigma \geq 100\,\mathrm{km\,s^{-1}}$ and 0.084 dex for $\sigma \geq 55\,\mathrm{km\,s^{-1}}$ for their early-type galaxies FP relation. Since this dissertation uses the same photometry as Jørgensen et al. (1996) and a similar FP fitting method, the conclusion is that the higher scatter they found is due to the fact that they had to construct a data set of $\log\sigma$'s from a variety of sources (with a range in quality) thereby introducing systematic errors or because of cluster-to-cluster differences in the fundamental plane. In contrast, the data set in this study is homogeneous, high signal-to-noise and high-quality which allows a true estimate of the underlying intrinsic scatter of the FP relation in the rich Coma cluster core.

Since a significant and non-zero intrinsic scatter is found for the FP relation, the conclusion is that there is a scatter in the FP relation that is not simply due to measurement errors. Subsequent sections will probe what else might be contributing to this scatter.

6.6.5 The nature of the residuals around the FP

The distribution of the residuals around the FP relation is important since if the distribution function is Gaussian then this simplifies any analyses. I will first consider the distribution of the residuals around the FP for the total early-type galaxy population fit and for the separate elliptical and lenticular fits, all with two separate lower velocity dispersion cutoffs ($\sigma \geq 55\,\mathrm{km\,s^{-1}}$ and $\sigma \geq 100\,\mathrm{km\,s^{-1}}$). Table 6.4 shows the results of a simple analysis of the mean of the FP residuals, the rms thickness of the FP relation (see 6.6.3) and of a Lilliefors test[‡] ($p_{gaussian}$) performed to determine whether a Gaussian is a good fit to the distribution of the residuals about the FP. Each of the separate fits have a negligible mean offset, indicating the goodness of the fit[§]. The Lilliefors test supports a Gaussian distribution of FP residuals for all samples except the early-type and elliptical galaxy samples with $\sigma \geq 55\,\mathrm{km\,s^{-1}}$. This is because of the outlying galaxy d112. When this galaxy is removed the Lilliefors test gives $p_{gaussian} = 0.146$

[‡]the Lilliefors test is similar to the Kolmogorov-Smirnov (KS) test except that it tests the goodness of fit of a model *derived* from the data, whereas the KS test tests the goodness of fit of an independently postulated model

[§]The mean of the residuals is non-zero since the FP fitting method minimises the effect of outliers. Therefore when a simple analysis of the mean of the residuals is performed using all points (including the outliers), each with equal weight, a non-zero mean is found.

Galaxies	Min σ	N	mean	rms_{obs}	rms_{intr}	$p_{gaussian}$
all early-types	$55\,\mathrm{km\,s^{-1}}$	87	−0.006	0.082	0.056	0.077
	$100\,\mathrm{km\,s^{-1}}$	69	−0.008	0.067	0.044	0.280
ellipticals	$55\,\mathrm{km\,s^{-1}}$	36	−0.008	0.073	0.049	0.028
	$100\,\mathrm{km\,s^{-1}}$	32	+0.004	0.058	0.036	0.194
lenticulars	$55\,\mathrm{km\,s^{-1}}$	51	−0.001	0.080	0.052	0.972
	$100\,\mathrm{km\,s^{-1}}$	37	−0.004	0.075	0.051	0.683

Table 6.4: Distribution of residuals around the FP. The distribution of the elliptical and lenticular sub-populations is that calculated around a separate FP fit for each data sample (sifted by morphological type and lower velocity dispersion cutoff). See text for an explanation of the non-zero mean of the residuals.

for the early-type galaxy sample and $p_{gaussian} = 0.210$ for the elliptical sample, supporting the Gaussian nature of the residuals. Therefore the conclusion of this Lilliefors analysis is that a Gaussian distribution is a good fit and that the Gaussian approximation can be used subsequently without any prejudice.

Next I consider the distribution of the elliptical and lenticular residuals around a common early-type galaxy FP fit. A different FP early-type galaxy fit is used for velocity dispersions, $\sigma \geq 55$ and $\sigma \geq 100\,\mathrm{km\,s^{-1}}$. Table 6.5 shows the results of this analysis. A Gaussian FP residual distribution is fully supported and the rms thickness are either identical or similar to the separate FP fits (see Table 6.4), but the mean offsets are now significant. Figures 6.8 and 6.9 illustrate these offsets more clearly. For $\sigma \geq 55\,\mathrm{km\,s^{-1}}$ I find a mean difference, $\Delta_{\mathrm{E\text{-}S0}}$ between the elliptical mean and the lenticular mean of −0.019±0.017 (a 1.1 sigma detection, equivalent to a 73.6% confidence); this corresponds to a 4.4±4.0% difference in distance determinations between the two samples. When I consider just galaxies with $\sigma \geq 100\,\mathrm{km\,s^{-1}}$, I find a mean difference, $\Delta_{\mathrm{E\text{-}S0}}$ of −0.024±0.016 (a 1.5 sigma detection, equivalent to a 86.6% confidence) corresponding to a 5.6±3.7% difference in distance determinations. Since this dissertation is intended to investigate the stellar populations of early-type galaxies at the bright-end of the luminosity function, galaxies with low velocity dispersions (which are generally faint galaxies) are under-sampled. This affects conclusions about the total sample of galaxies with $\sigma \geq 55\,\mathrm{km\,s^{-1}}$, but not the sample of galaxies with $\sigma \geq 100\,\mathrm{km\,s^{-1}}$. The detection of a mean difference, $\Delta_{\mathrm{E\text{-}S0}} = -0.024 \pm 0.016$ for $\sigma \geq 100\,\mathrm{km\,s^{-1}}$ *disagrees* with the work of Saglia et al. (1993), who found an offset in the Coma

Galaxies	Min σ	N	mean	rms_{obs}	rms_{intr}	$p_{gaussian}$
all early-types	$55\,\mathrm{km\,s^{-1}}$	87	−0.006	0.082	0.056	0.077
	$100\,\mathrm{km\,s^{-1}}$	69	−0.008	0.067	0.044	0.280
ellipticals	$55\,\mathrm{km\,s^{-1}}$	36	−0.005	0.073	0.049	0.375
	$100\,\mathrm{km\,s^{-1}}$	32	−0.015	0.058	0.036	0.204
lenticulars	$55\,\mathrm{km\,s^{-1}}$	51	+0.014	0.089	0.061	0.380
	$100\,\mathrm{km\,s^{-1}}$	37	+0.009	0.075	0.051	0.815

Table 6.5: Distribution of elliptical and lenticular residuals around a common FP. The distribution of the elliptical and lenticular sub-populations is calculated around a common early-type galaxy FP fit. A different FP early-type galaxy fit is used for velocity dispersions, $\sigma \geq 55$ and $\sigma \geq 100\,\mathrm{km\,s^{-1}}$. The distribution of the total early-type galaxy population residuals is given for reference.

cluster of $\Delta_{\text{E-S0}} = +0.043 \pm 0.019$ (a 2.3 sigma detection, equivalent to a 97.6% confidence) between 25 ellipticals and 31 lenticulars (all with $\sigma > 100\,\mathrm{km\,s^{-1}}$) by measuring photometry from the CCD frames of Dressler et al. (1987) and combining it with velocity dispersions from Dressler et al. (1987) and Dressler (1987). It is uncertain why there is disagreement, but possible explanations are: the heterogeneous nature of their velocity dispersions (as their ellipticals and lenticulars measurements are drawn from *different* observing runs, possibly introducing a systematic offset); the lower numbers of early-type galaxies in their sample; or because of their different fundamental plane fitting method (they determine a much smaller value of the FP parameter α, finding $\alpha = 1.07$). The result also disagrees with the result of Jørgensen et al. (1996), who found a much smaller median offset of $\Delta_{\text{E-S0}} = +0.006 \pm 0.011$ (a 0.5 sigma detection, equivalent to a 41.4% confidence) between 95 ellipticals and 131 lenticulars in a sample spanning 9 clusters of a wide range of richness. Since this FP study uses the same photometry as Jørgensen et al. (1996) and a similar FP fitting method, the differing conclusions can only be due to either the heterogeneous nature of the velocity dispersions used in the Jørgensen et al. (1996) study (who collated velocity dispersions from a variety of different sources) or due to cluster-to-cluster differences. This again shows the importance of a homogeneous data set. The result does however *agree* with the result of a recent study of the Shapley Supercluster by Smith et al. (2001), who found an offset of $\Delta_{\text{E-S0}} = -0.033 \pm 0.021$ (a 1.6 sigma detection, equivalent to a 88.4% confidence) for a sample of 122 early-type galaxies.

The conclusion of my analysis of the FP residual distributions is that there are differences between the elliptical and lenticular populations around a common early-type galaxy fundamental plane, though admittedly at a low significance level of 1.1 to 1.5 sigma. This again shows the need for careful morphological segregation when constructing a FP sample with a tight scatter for distance determination. When the FP relation is used to determine cluster distances for clusters significantly further away than Coma, the presence of a mean offset between the fundamental planes of elliptical and lenticular galaxies can lead to large errors in the cluster distance if the sample morphology is poorly understood. The offset means that a common fit to an early-type galaxy sample with similar numbers of elliptical and lenticular galaxies will also lead to the incorrect conclusion that the elliptical galaxies are systematically *further away* than the lenticular galaxies. Thus it is important to understand the detailed morphology of any galaxy sample used to determine cluster distances.

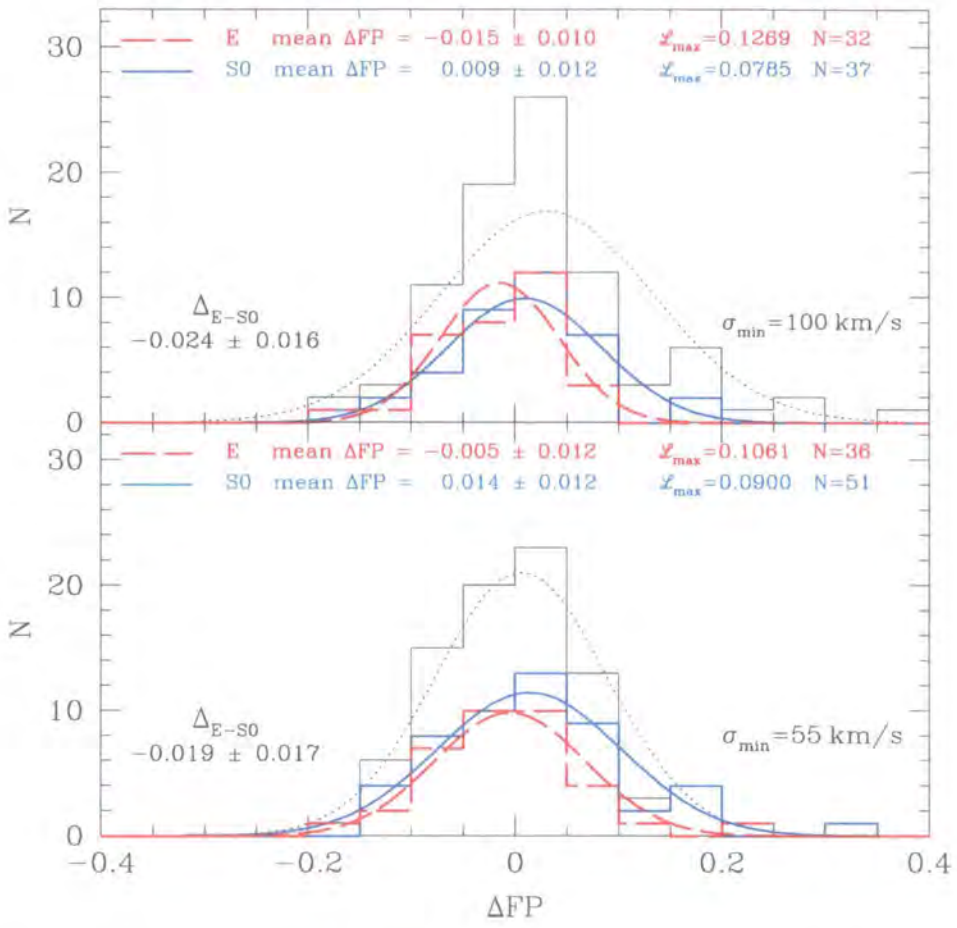

Figure 6.8: FP residual distribution split into morphological components. In each section of this figure the histogram of the FP residuals for a fit to the total early-type galaxy population is shown (black), together with a superimposed Gaussian distribution curve fit to the data (black curve). This early-type galaxy sample is then split into two separate components, ellipticals (red dashed line) and lenticulars (blue solid line), and histograms shown of their distribution (together with Gaussian curve fits) for the given FP parameters (i.e. in each section the same α, β and γ FP parameters are used to calculate the residuals for the total sample and its constituents). The top section of this figure shows the distribution for galaxies with velocity dispersions (σ) greater than $100\,\mathrm{km\,s^{-1}}$, whilst the bottom section shows the same results for galaxies with $\sigma \geq 55\,\mathrm{km\,s^{-1}}$. Gaussian statistics are assumed in the analysis of the component residual distributions since a Lilliefors test versus the null hypothesis of a Gaussian distribution gives $p >> 0.10$, thus supporting the hypothesis. In each case it can be seen that there is a small offset ($\Delta_{\mathrm{E\text{-}S0}}$) between the elliptical and lenticular components of the early-type galaxy sample.

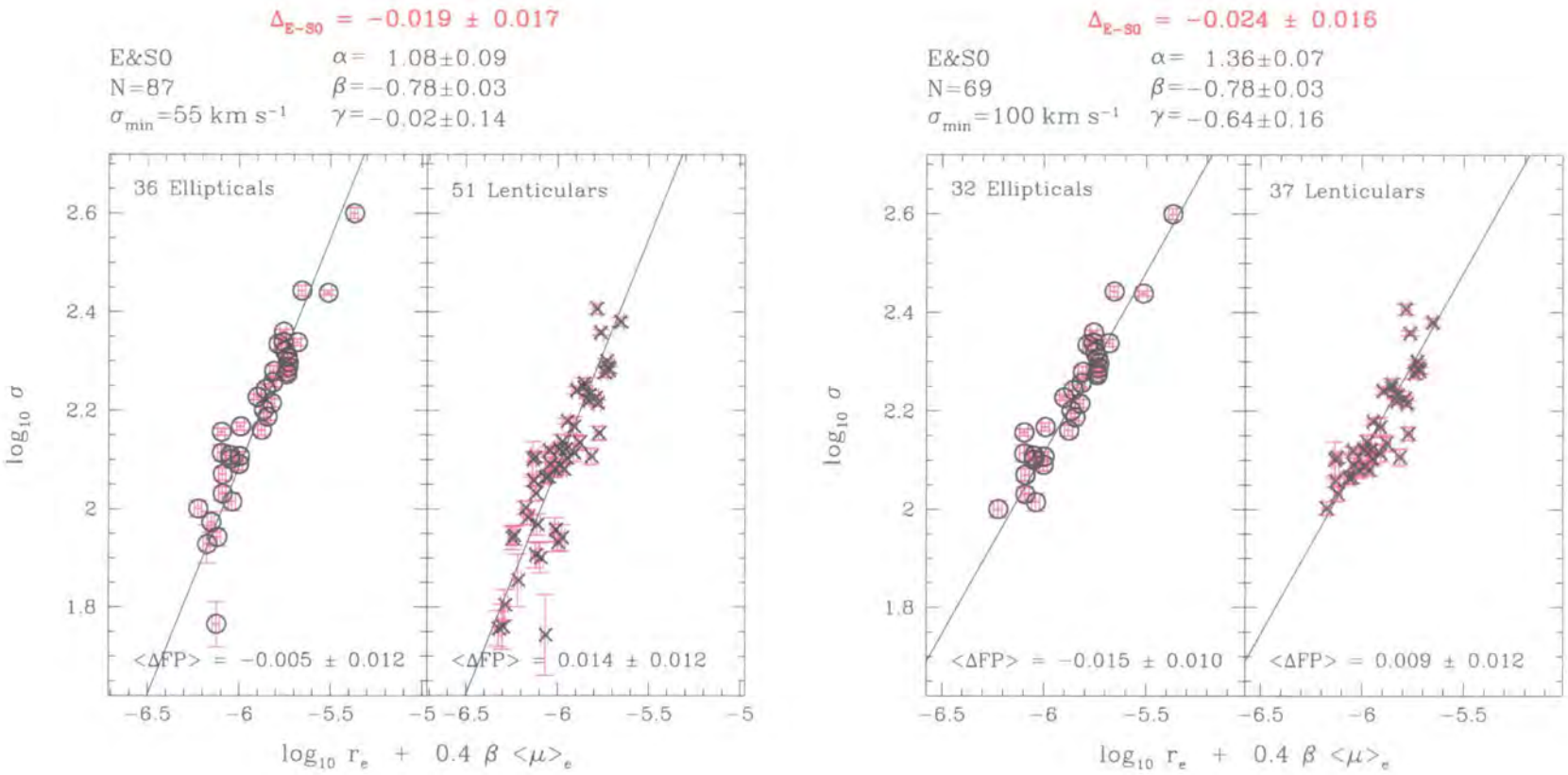

(a) $\sigma \geq 55\,\mathrm{km\,s^{-1}}$ (b) $\sigma \geq 100\,\mathrm{km\,s^{-1}}$

Figure 6.9: Differences between the FP residuals of ellipticals and lenticulars around a common early-type galaxy FP fit (solid line).

6.6.6 Dependence of FP thickness on velocity dispersion

To investigate the dependence of fundamental plane thickness on velocity dispersion (Jørgensen et al. 1996) I took the FP parameters from fits to the total early-type galaxy population with $\sigma \geq 55\,\mathrm{km\,s^{-1}}$ and then $\sigma \geq 100\,\mathrm{km\,s^{-1}}$ and analysed the effect on the intrinsic rms of removing galaxies with velocity dispersions less than $\log\sigma = 1.7$ to $\log\sigma = 2.3$ in 0.15 dex steps. This approach is taken, rather than binning the data in 0.15 dex wide bins, because of the relatively low numbers of galaxies for a binning analysis which would lead to large errors in the intrinsic rms calculation. Progressively removing galaxies with velocity dispersions lower than a given $\log\sigma$ maximises the power of this analysis for the given sample.

Figure 6.10 shows the results of this analysis. It can be seen that the FP parameters corresponding to the total early-type galaxy fit with a minimum velocity dispersion of $\sigma_{\mathrm{min}} = 55\,\mathrm{km\,s^{-1}}$ (with $\mathrm{rms}_{intr}\{\mathrm{E\&S0}\} = 0.056$ at $\sigma = 55\,\mathrm{km\,s^{-1}}$) give only a small variation in intrinsic rms with sample minimum velocity dispersion. The FP parameters derived from the total early-type galaxy population with a minimum velocity dispersion of $\sigma_{\mathrm{min}} = 100\,\mathrm{km\,s^{-1}}$ (with $\mathrm{rms}_{intr}\{\mathrm{E\&S0}\} = 0.044$ at $\sigma = 100\,\mathrm{km\,s^{-1}}$) give a much greater variation in intrinsic rms with sample minimum velocity dispersion. The differences between these two scenarios are caused by the lenticular galaxy population. The elliptical galaxies show little variation with removal of lower velocity dispersion galaxies and little difference between the two scenarios. Also, the intrinsic rms of the lenticulars is always greater than that of the ellipticals and therefore increases the intrinsic rms of a total early-type galaxy sample. These findings again illustrate the morphological complexity of the fundamental plane relation.

6.6.7 Dependence of FP residuals on stellar population indicators and other parameters

To continue to try to answer the question of whether the FP relation is truly a fundamental, tight and well understood relation with the scatter around it solely due to measurement error, discounting any other unrealised factors contributing to the FP, it is necessary to investigate the dependence of residuals around the fundamental plane on stellar population indicators and other parameters.

The existence of the FP implies that the M/L ratios of ellipticals and lenticulars are very regular. Hence the stellar populations of the galaxies must be very regular, as any differences in age or metallicity would be reflected directly in the M/L ratio through a change in the

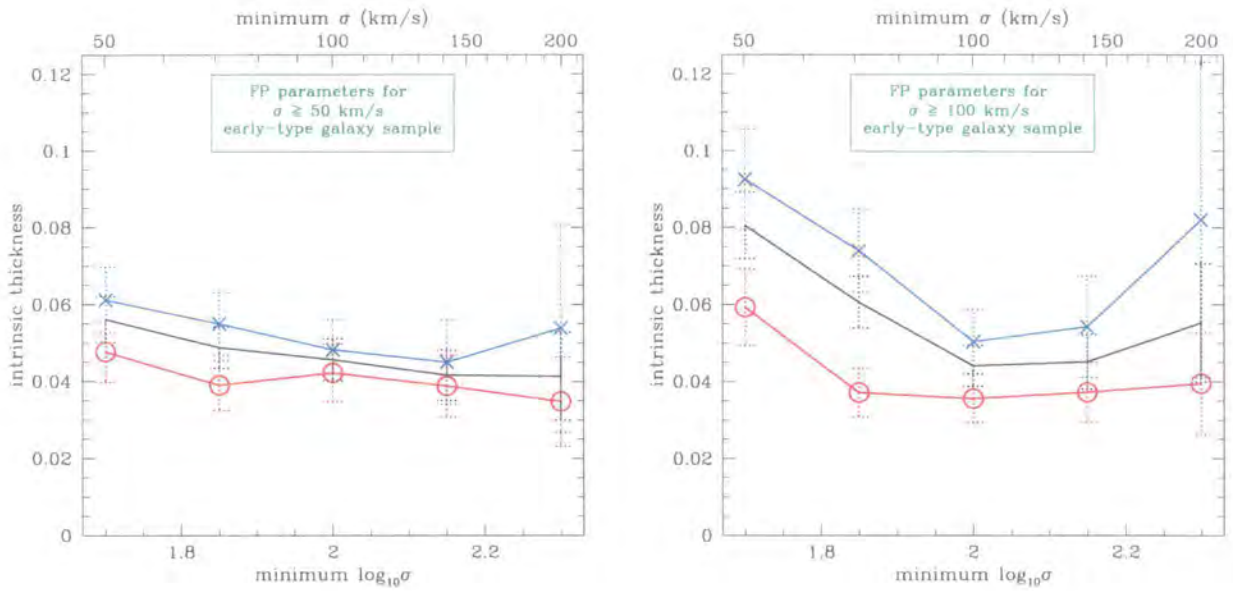

Figure 6.10: Intrinsic thickness of FP relation versus minimum velocity dispersion cutoff. The thickness is defined as the intrinsic rms of $\Delta\mathrm{FP} = \log r_e - \alpha \log \sigma - \beta \log\langle I\rangle_e - \gamma_{cl}$ and is calculated for galaxies with velocity dispersions greater than or equal to the x-axis value. Figure (a) shows the thickness versus minimum velocity dispersion cutoff for the total early-type galaxies (solid line), the ellipticals (red line and circles) and the lenticulars (blue line and crosses) for a fixed set of FP parameters corresponding to the total early-type galaxy fit with a minimum velocity dispersion of $\sigma_{\min} = 55\,\mathrm{km\,s^{-1}}$ (with $\mathrm{rms}_{intr}\{\mathrm{E\&S0}\} = 0.056$ at $\sigma = 55\,\mathrm{km\,s^{-1}}$). The same set of FP parameters is used when examining the different morphological types so that their contribution to the total relationship can be seen. Figure (b) is the same as Figure (a) except this time a fixed set of FP parameters derived from the total early-type galaxy population with a minimum velocity dispersion of $\sigma_{\min} = 100\,\mathrm{km\,s^{-1}}$ (with $\mathrm{rms}_{intr}\{\mathrm{E\&S0}\} = 0.044$ at $\sigma = 100\,\mathrm{km\,s^{-1}}$) is used.

luminosity. Here I investigate this hypothesis through the analysis of the relation between the residuals around the FP and various stellar population indicators together with out parameters.

Table 6.6 contains the results of a correlation analysis of FP residuals, calculated using the equation $\Delta FP = \log r_e - \alpha \log \sigma - \beta \log\langle I\rangle_e - \gamma_{cl}$, versus the following parameters: $\log\sigma$, $\log r_e$, $\langle\mu\rangle_e$, projected distance from the cluster centre (R [h^{-1}Mpc]), ϵ_{re}, $M_{\rm dynamic}/L$, $M_{\rm dynamic}$, Gunn $r_{\rm total}$, b_j, U–V, B–R, $H\beta_G$ (which has been corrected for nebula emission using [OIII]λ5007), $\log_{10}$(age[Gyrs]), [MgFe], [Fe/H], Mg_b, Mg_2, $\langle$Fe$\rangle$, and [OIII] λ5007. A raw or "observed" rms (rms_{obs}), an intrinsic rms (rms_{intr}) and the result of a Spearman rank correlation test[¶] ($p_{independent}$) are calculated. These parameters are calculated for FP residuals from fits to all the early-type galaxies and to the elliptical and lenticular sub-populations, all of which were sifted for two different minimum velocity dispersions, $\sigma \geq 55$ and $\sigma \geq 100\,{\rm km\,s^{-1}}$. This gives a total of 6 statistics for each FP residual versus parameter correlation analysis. This residual analysis for each data set and its' best fitting FP relation prevents any biasing from a FP fit to a single data set contaminating any trends. Figures 6.11 to 6.26 illustrate this correlation analysis. In each figure, the top 3 plots include galaxies with $\sigma \geq 55\,{\rm km\,s^{-1}}$, whilst the bottom 3 plots include galaxies with $\sigma \geq 100\,{\rm km\,s^{-1}}$. The plots on the left include all early-type galaxies, whilst the plots in the middle contain ellipticals and the plots on the right contain lenticulars.

The conclusions of this correlation analysis of the FP residuals of the early-type galaxies in the central 1 degree ($\equiv 1.26\,h^{-1}$ Mpc) of the Coma cluster are:

— no correlation of FP residuals with $\log\sigma$, $\log r_e$, $\langle\mu\rangle_e$, $M_{\rm dynamic}$, U–V, B–R, $H\beta_G$, $\log_{10}$(age[Gyrs]), [MgFe], [Fe/H], Mg_b, Mg_2, nor $\langle$Fe$\rangle$. Any marginal detection of a correlation disappears when one or two outliers are removed.

— no correlation of FP residuals with nebula emission, traced by [OIII]λ5007, is seen. This result means that in the cores of elliptical and lenticular galaxies recent starburst activity does not contribute to the FP residuals (and therefore the FP scatter).

[¶]since the distribution of the FP residuals is Gaussian (see Section 6.6.5), I use the two-tailed Spearman rank correlation coefficient test against the null hypothesis that the X and Y parameters are mutually independent. Any significance level, p less than 0.05 rejects this null hypothesis indicating the presence of a correlation.

— a small, insignificant correlation of FP residuals with projected distance from the cluster centre, R (h^{-1}Mpc) and ϵ_{re} for lenticulars.

— a clear correlation of FP residuals with Gunn $r_{\rm total}$ for lenticulars with $\sigma \geq 55\,{\rm km\,s^{-1}}$, but not for $\sigma \geq 100\,{\rm km\,s^{-1}}$ nor for the ellipticals or the total early-type galaxy sample. This is due to the relatively poor determination of the total magnitude of smaller/dwarf lenticulars due to a $r^{1/4}$ assumption rather than a more general $r^{1/n}$ model (with $n < 4$ and $n \simeq 1$ to 2 for dwarfs). A correlation is also seen between the FP residuals and b_j for the same sub-sample due to the same problem, even though the b_j are aperture magnitudes, since they are highlighting the $r^{1/4}$ assumption in the parameters that are used to calculate the FP residual. Only conclusions herein reliant upon lenticular galaxies with $55 \leq \sigma < 100\,{\rm km\,s^{-1}}$ are affected; conclusions based on other samples are unaffected by the $r^{1/4}$ assumption.

— a clear correlation of FP residuals with $M_{\rm dynamic}/L$, with bright galaxies having negative residuals and faint galaxies having positive residuals. The cD galaxies NGC 4874 and NGC 4889 do not however follow this correlation. The simplest explanation for this correlation is a variation in α for:

$$\left(\frac{M}{L}\right) \propto L^{\xi} \quad \text{where } \xi = \frac{1}{\alpha} - \frac{1}{2} \tag{6.29}$$

This variation agrees with previous findings of variations in α for different velocity dispersions (and therefore different luminosities) and for fundamental planes in different wavebands (e.g. Scodeggio et al. (1998) who performed a multi-wavelength study of the FP relation for 79 early-type galaxies within 2° of the Coma cluster centre (a field diameter of 4°) using the B, V, r, I and K bands and found α to increase significantly with increasing wavelength from $\sim$ 1.35 to $\sim$ 1.70 ($\pm$0.1) from the optical to the infrared). It could also be due to a variation in $M_{dark}/M_{dynamic}$ (since for a fixed ratio of $M_{total} = 10 M_{dynamic}$ there is no correlation of FP residuals with $M_{\rm dynamic}$ nor with Gunn $r_{\rm total}$) and/or the kinematic "constants" with size. Another explanation is that the FP relation could be *curved*. A possible explanation for why the cD galaxies do not follow this correlation is that their dark matter ratios ($M_{dark}/M_{dynamic}$) could be significantly larger than for other cluster galaxies.

— there is no variation in the scatter of the FP residuals with any of the tested parameters at a highly significant level. The principal conclusion of this is that there is no age nor metallicity trend in scatter nor the FP relation itself. These results imply that the scatter is therefore due to variations in $(\frac{M}{L}) \propto L^{\xi}$ and/or variations in dark matter fractions ($M_{dark}/M_{dynamic}$) and/or the kinematic "constants". Since the scatter is different between ellipticals and lenticulars, the conclusion is that there are differing kinematics and/or dark matter fractions between these morphologies.

In conclusion the FP relation is in general well behaved and common for ellipticals and lenticulars (since any variations are small, though significant). The correlation analysis has highlighted no additional terms for the existing FP relation. Exploration of the intrinsic scatter shows that previously suggested mechanisms are not responsible and that the real source lies in the underlying physics of the kinematics and dark matter structures. The mass-to-light ratio correlation with FP residuals supports this conclusion. Real intrinsic differences between the elliptical and lenticular galaxies have again been shown, leading to the conclusion that they have differing kinematics and/or dark matter fractions.

		$\sigma \geq 55\,\mathrm{km\,s^{-1}}$				$\sigma \geq 100\,\mathrm{km\,s^{-1}}$			
FP res vs	Types	N	rms_{obs}	rms_{intr}	$p_{independent}$	N	rms_{obs}	rms_{intr}	$p_{independent}$
$\log\sigma$	E&S0	87	0.082	0.056	0.8650	69	0.067	0.044	0.1923
	E	36	0.073	0.049	0.9794	32	0.058	0.036	0.3060
	S0	51	0.080	0.052	0.6616	37	0.075	0.051	0.5239
$\log r_e$	E&S0	87	0.082	0.056	0.0902	69	0.067	0.044	0.2937
	E	36	0.073	0.049	0.5673	32	0.058	0.036	0.5843
	S0	51	0.080	0.052	0.1241	37	0.075	0.051	0.7440
$\langle\mu\rangle_e$	E&S0	87	0.082	0.056	0.4087	69	0.067	0.044	0.7009
	E	36	0.073	0.049	0.4874	32	0.058	0.036	0.8176

Table 6.6: *continued on next page*

continued from previous page

		$\sigma \geq 55\,\mathrm{km\,s^{-1}}$				$\sigma \geq 100\,\mathrm{km\,s^{-1}}$			
FP res vs	Types	N	rms_{obs}	rms_{intr}	$\mathrm{p}_{independent}$	N	rms_{obs}	rms_{intr}	$\mathrm{p}_{independent}$
	S0	51	0.080	0.052	0.4875	37	0.075	0.051	0.4281
R (h^{-1}Mpc)	E&S0	87	0.082	0.056	0.0170	69	0.067	0.044	0.0198
	E	36	0.073	0.049	0.6100	32	0.058	0.036	0.7813
	S0	51	0.080	0.052	0.0014	37	0.075	0.051	0.0010
ϵ_{re}	E&S0	87	0.082	0.056	0.0041	69	0.067	0.044	0.0124
	E	36	0.073	0.049	0.3324	32	0.058	0.036	0.9439
	S0	51	0.080	0.052	0.0021	37	0.075	0.051	0.0079
M_{dynamic}/L	E&S0	87	0.082	0.056	0.0000	69	0.067	0.044	0.0000
	E	36	0.073	0.049	0.0156	32	0.058	0.036	0.0045
	S0	51	0.080	0.052	0.0000	37	0.075	0.051	0.0000
M_{dynamic}	E&S0	87	0.082	0.056	0.6736	69	0.067	0.044	0.8913
	E	36	0.073	0.049	0.7747	32	0.058	0.036	0.9740
	S0	51	0.080	0.052	0.8503	37	0.075	0.051	0.5540
Gunn r_{total}	E&S0	87	0.082	0.056	0.0009	69	0.067	0.044	0.0375
	E	36	0.073	0.049	0.1921	32	0.058	0.036	0.3735
	S0	51	0.080	0.052	0.0026	37	0.075	0.051	0.0942
b_j	E&S0	87	0.082	0.056	0.0022	69	0.067	0.044	0.1520
	E	36	0.073	0.049	0.2087	32	0.058	0.036	0.5893
	S0	51	0.080	0.052	0.0023	37	0.075	0.051	0.1115
U–V	E&S0	62	0.086	0.060	0.9121	51	0.063	0.040	0.7969
	E	27	0.072	0.048	0.8505	25	0.055	0.033	0.5177
	S0	35	0.085	0.058	0.6591	26	0.074	0.050	0.9332
B–R	E&S0	20	0.055	0.032	0.8255	18	0.048	0.025	0.4089
	E	18	0.050	0.027	0.4724	17	0.051	0.029	0.2085
	S0	2	—	—	—	1	—	—	—
$H\beta_G$	E&S0	76	0.074	0.049	0.9512	66	0.068	0.045	0.4535
	E	31	0.058	0.035	0.4113	29	0.058	0.035	0.6131
	S0	45	0.077	0.052	0.5127	37	0.075	0.051	0.7554

Table 6.6: *continued on next page*

continued from previous page

		$\sigma \geq 55\,\mathrm{km\,s^{-1}}$				$\sigma \geq 100\,\mathrm{km\,s^{-1}}$			
FP res vs	Types	N	rms_{obs}	rms_{intr}	$p_{independent}$	N	rms_{obs}	rms_{intr}	$p_{independent}$
$\log_{10}$(age)	E&S0	78	0.084	0.058	0.4393	65	0.068	0.045	0.9022
	E	32	0.074	0.050	0.5627	29	0.058	0.035	0.6331
	S0	46	0.082	0.055	0.9713	36	0.076	0.052	0.6336
[MgFe]	E&S0	78	0.084	0.058	0.2617	65	0.068	0.045	0.0609
	E	32	0.074	0.050	0.6388	29	0.058	0.035	0.2128
	S0	46	0.082	0.055	0.0936	36	0.076	0.052	0.1123
[Fe/H]	E&S0	78	0.084	0.058	0.8472	65	0.068	0.045	0.3295
	E	32	0.074	0.050	0.8064	29	0.058	0.035	0.2544
	S0	46	0.082	0.055	0.4657	36	0.076	0.052	0.6645
Mg_b	E&S0	83	0.082	0.057	0.1004	68	0.067	0.044	0.0043
	E	35	0.072	0.047	0.3435	31	0.059	0.036	0.0803
	S0	48	0.081	0.054	0.0390	37	0.075	0.051	0.0197
Mg_2	E&S0	82	0.082	0.057	0.4758	67	0.068	0.045	0.1602
	E	35	0.072	0.047	0.5044	31	0.059	0.036	0.2041
	S0	47	0.081	0.054	0.2471	36	0.076	0.052	0.3811
⟨Fe⟩	E&S0	84	0.083	0.057	0.6457	68	0.068	0.045	0.9834
	E	36	0.073	0.049	0.5160	32	0.058	0.036	0.8583
	S0	48	0.081	0.054	0.6701	36	0.076	0.052	0.9381
[OIII] λ5007	E&S0	84	0.077	0.052	0.9734	69	0.067	0.044	0.8349
	E	36	0.073	0.049	0.7969	32	0.058	0.036	0.4575
	S0	48	0.076	0.050	0.9469	37	0.075	0.051	0.8762

Table 6.6: A summary of the results of plotting fundamental plane residuals versus various parameters. A Spearman rank correlation coefficient test was performed against the null hypothesis that the X and Y axes were mutually independent (i.e. un-correlated). Values of $p < 0.05$ reject this hypothesis, implying an underlying correlation between the fundamental plane residuals and the parameter.

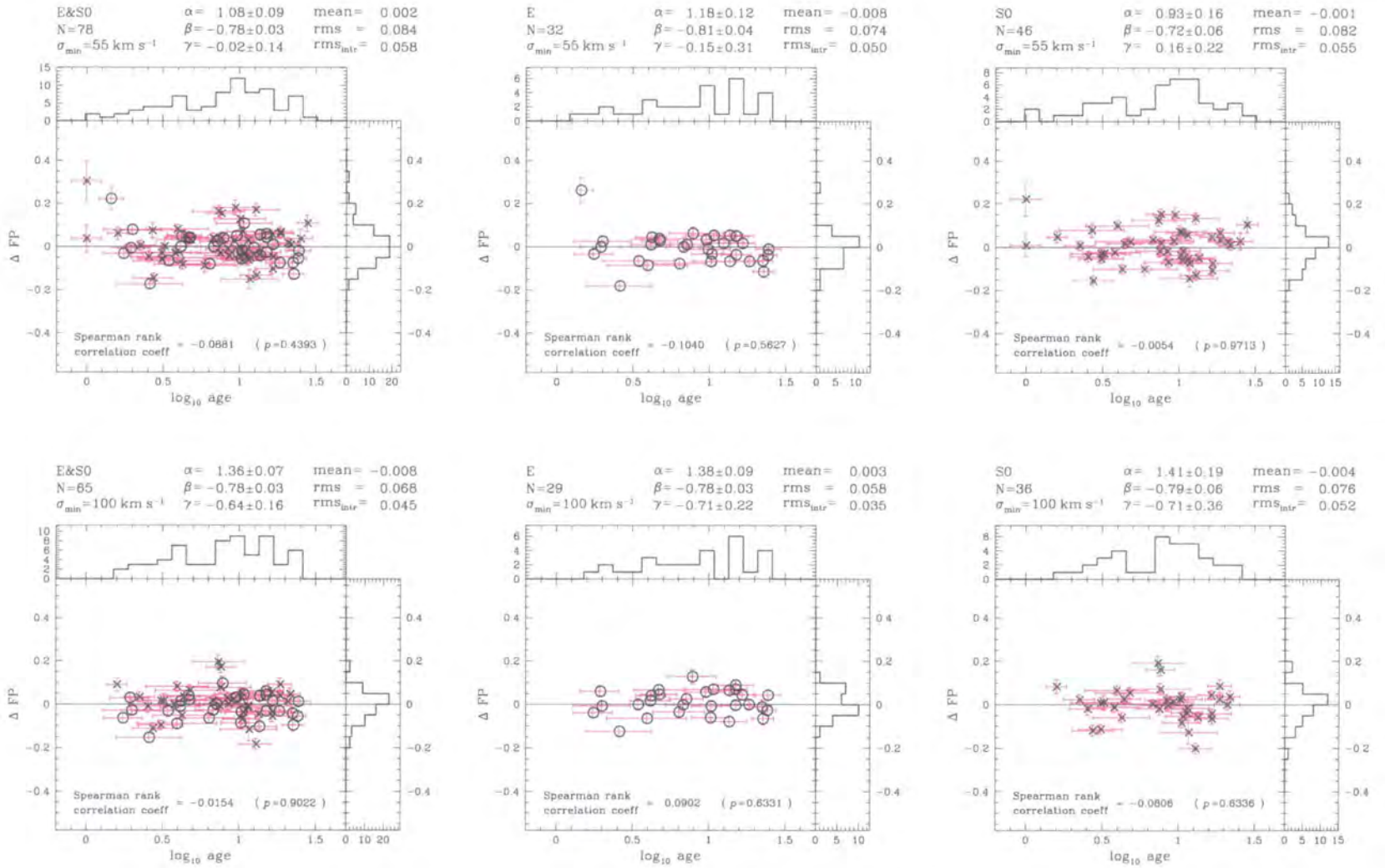

Figure 6.11: Fundamental plane residuals versus $\log_{10}$(age[Gyrs]). See text.

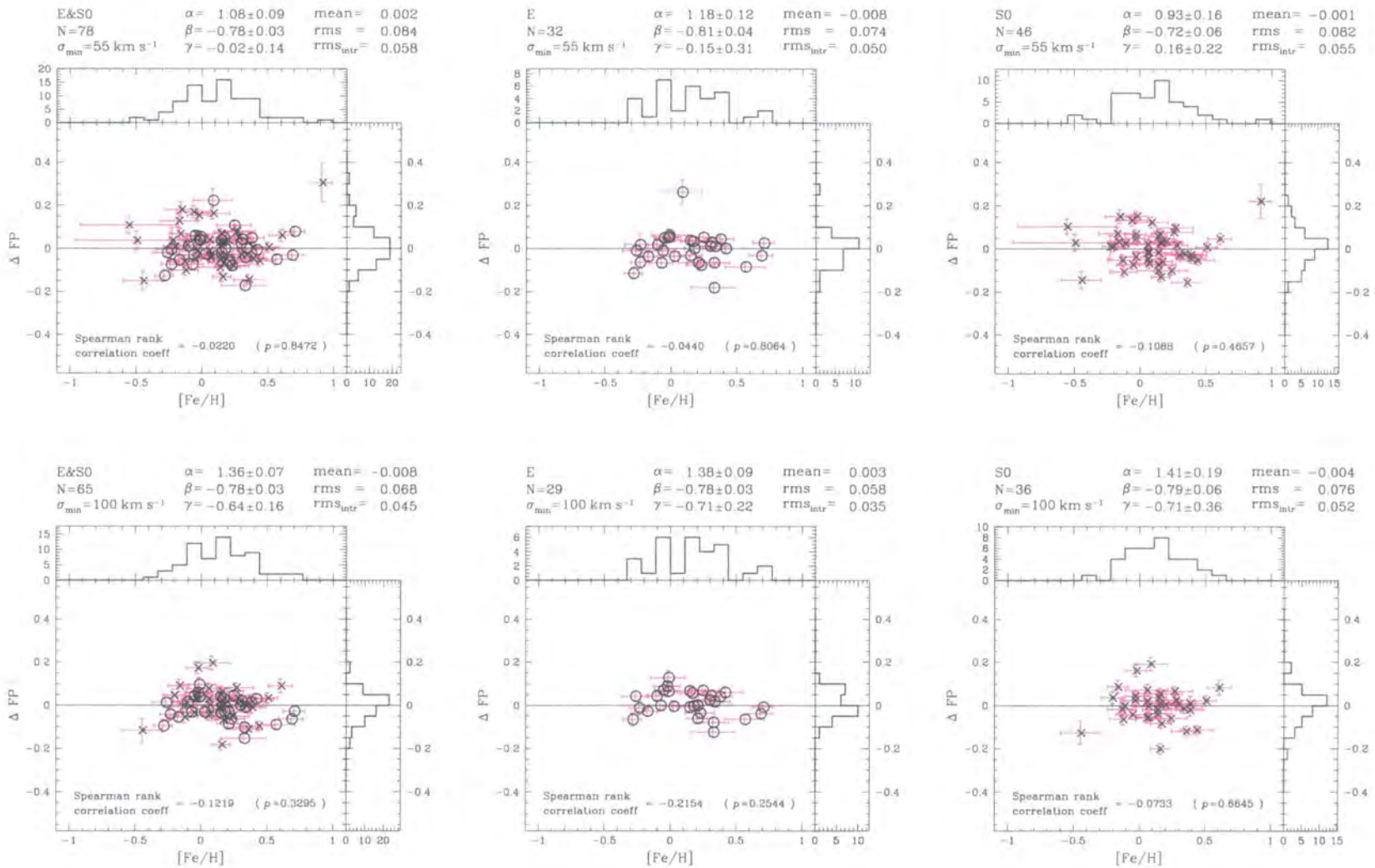

Figure 6.12: Fundamental plane residuals versus [Fe/H]. See text.

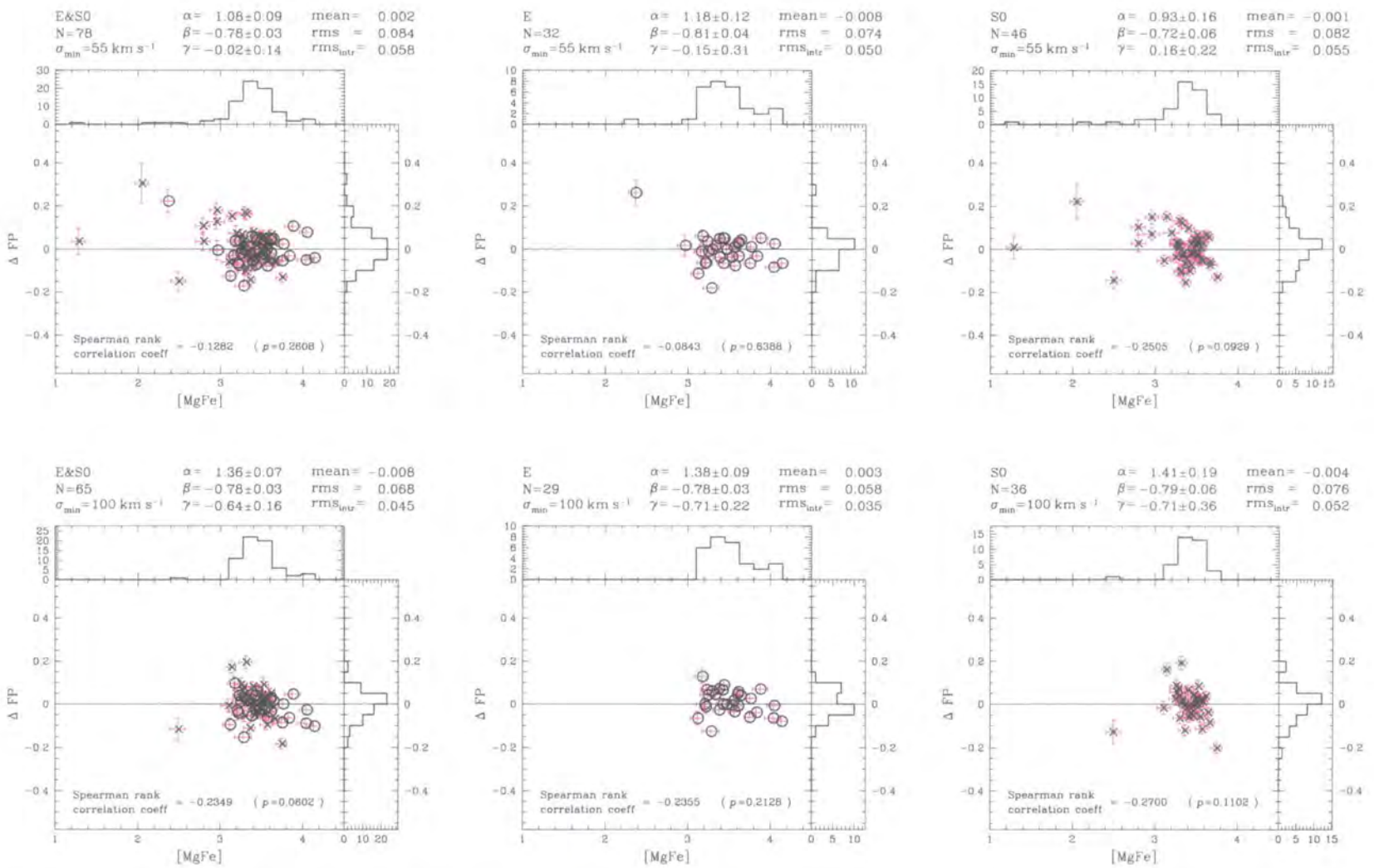

Figure 6.13: Fundamental plane residuals versus [MgFe], my primary tracer of galaxy luminosity-weighted mean metallicity. See text.

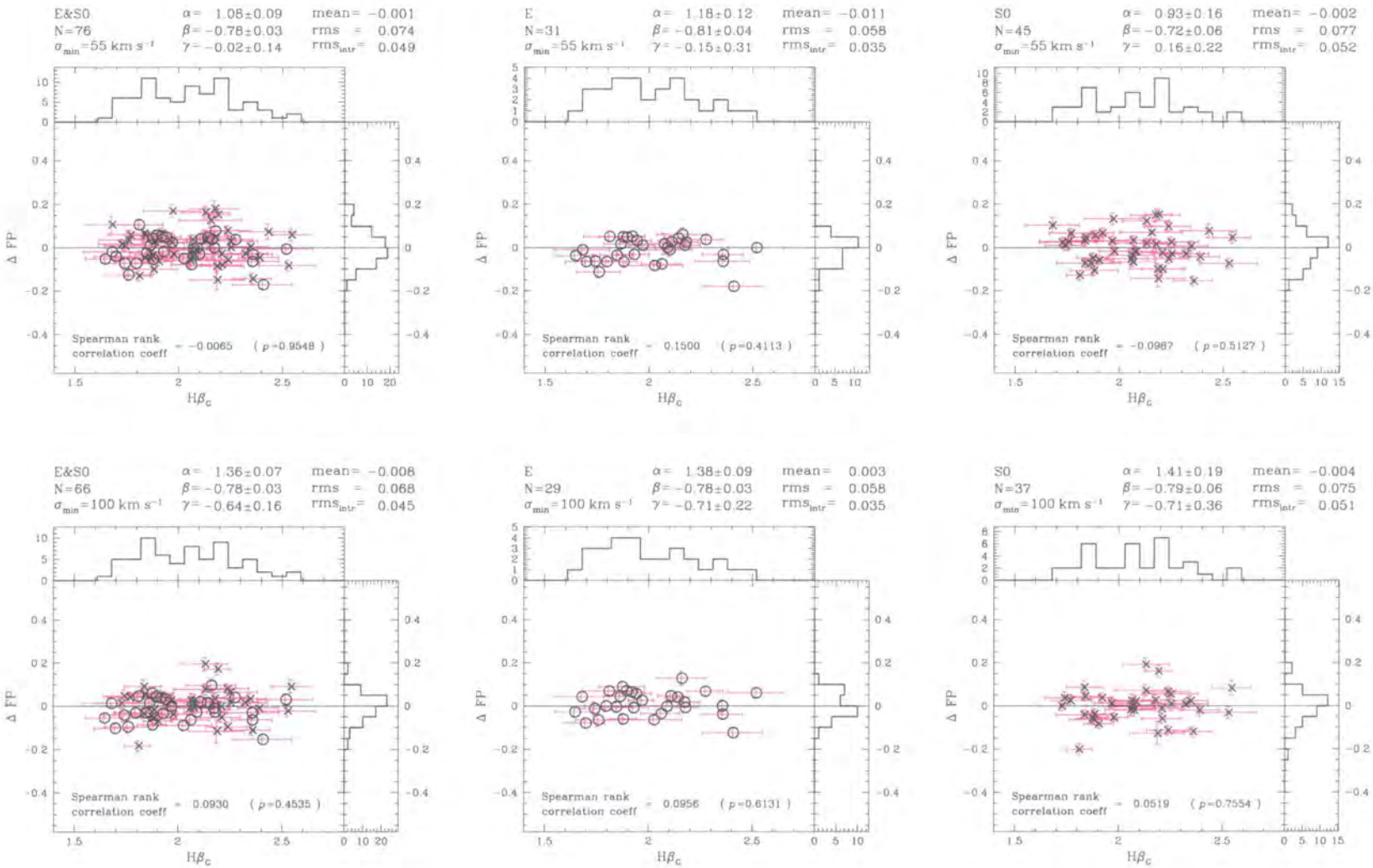

Figure 6.14: Fundamental plane residuals versus $H\beta_G$, my primary tracer of galaxy luminosity-weighted mean stellar population age (NB: $H\beta_G$ has been corrected for nebula emission using [OIII] λ5007). See text.

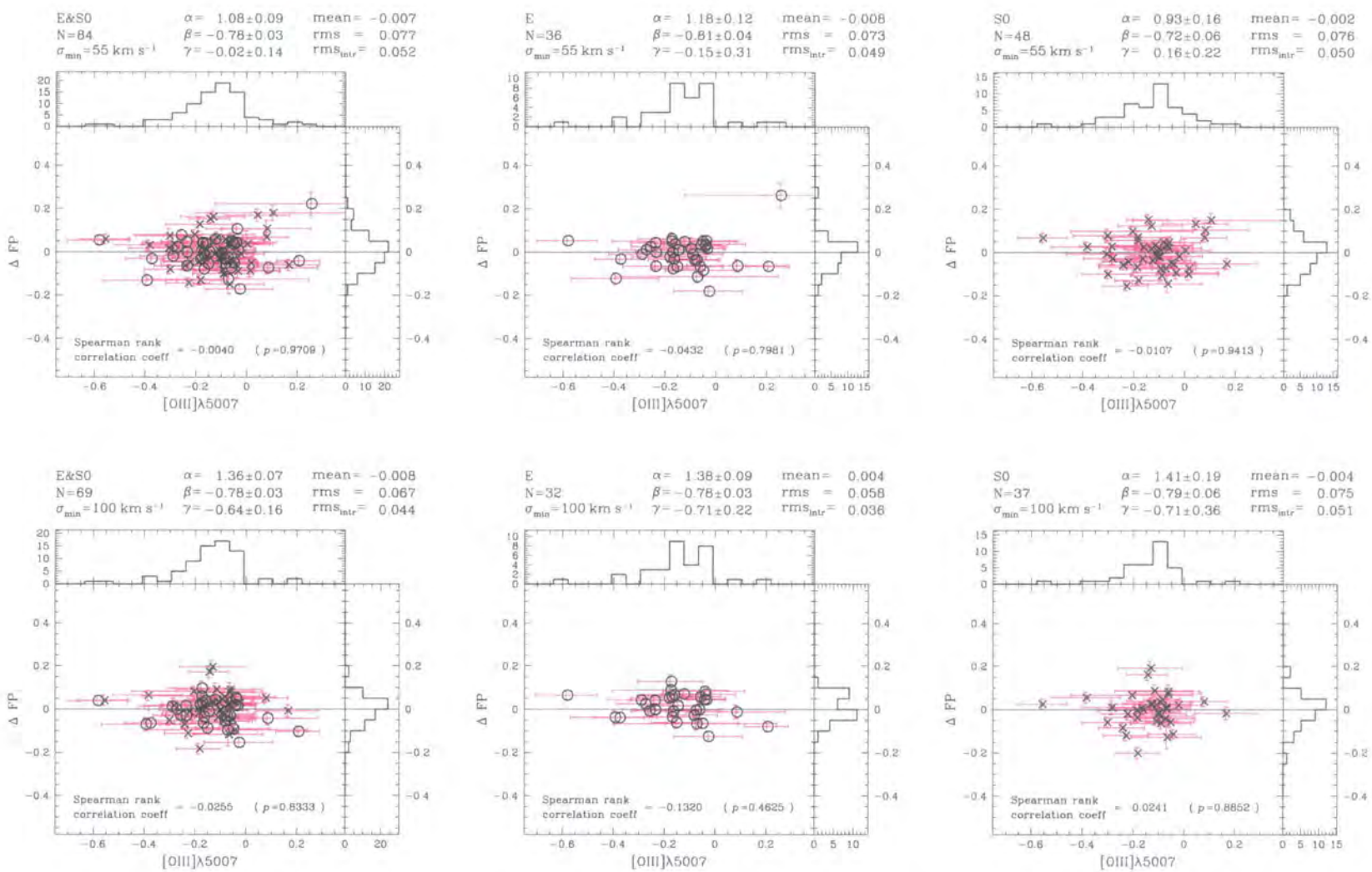

Figure 6.15: Fundamental plane residuals versus [OIII] λ5007, my primary tracer of galaxy nebula emission. See text.

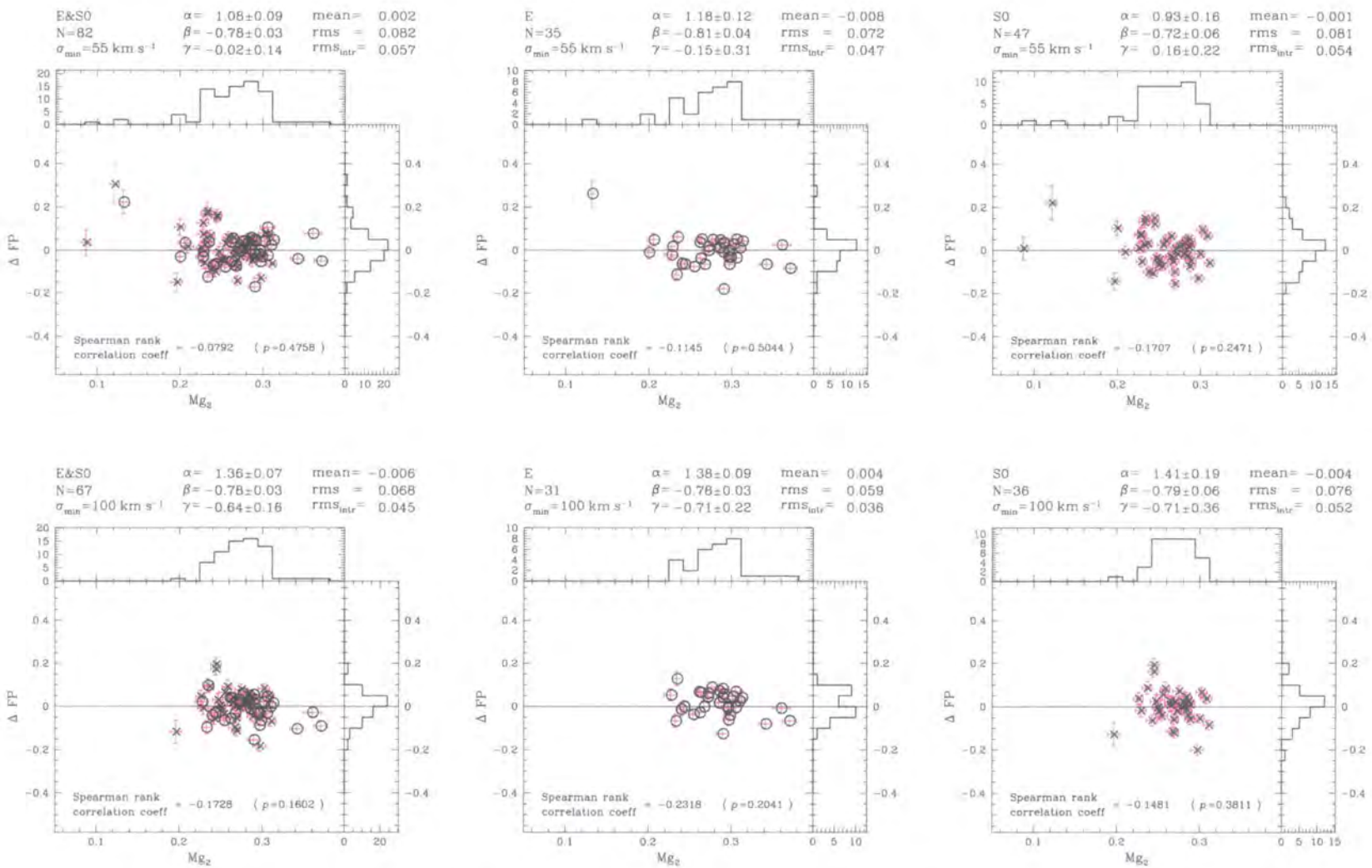

Figure 6.16: Fundamental plane residuals versus Mg_2, a tracer of galaxy luminosity-weighted mean metallicity. See text.

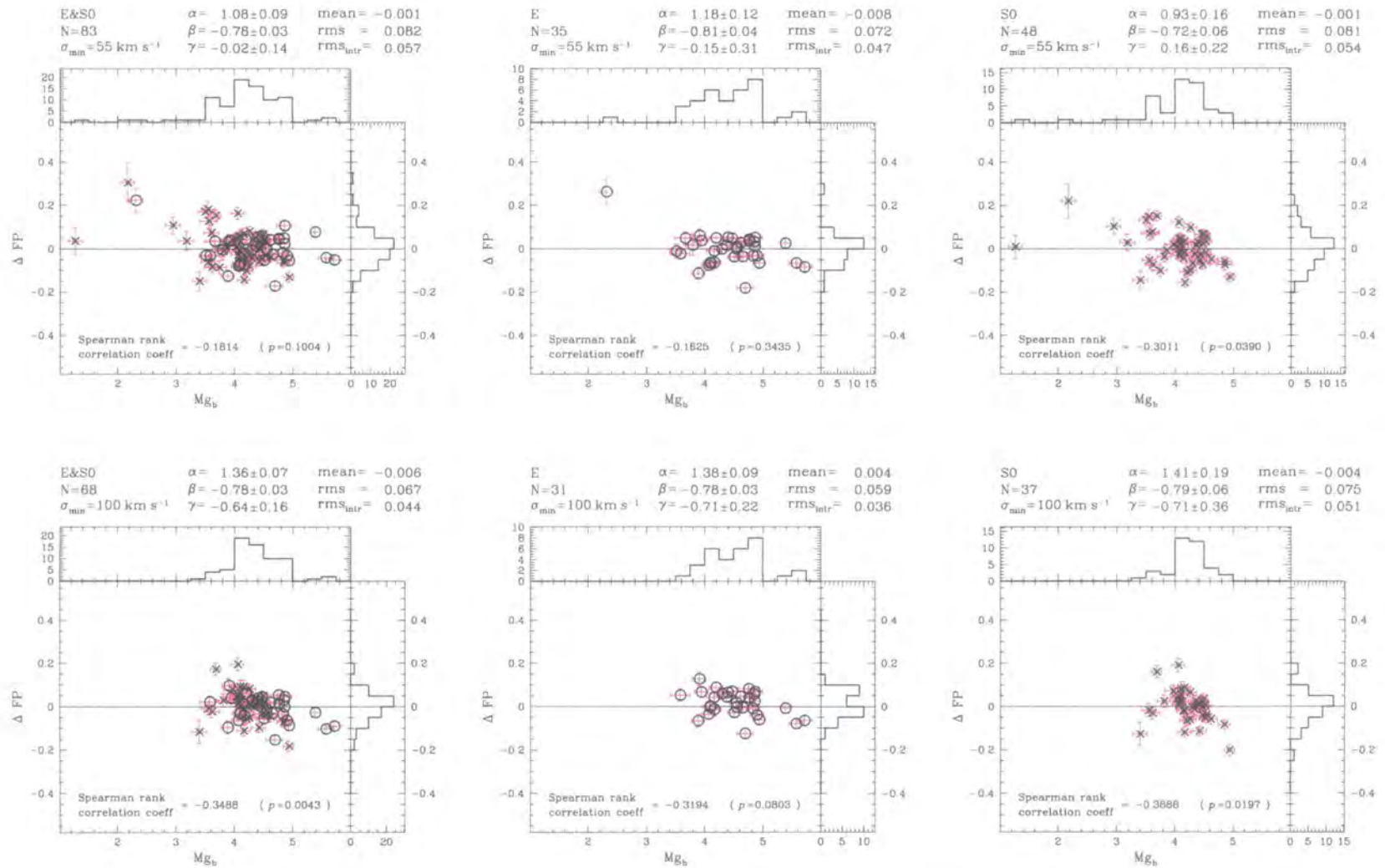

Figure 6.17: Fundamental plane residuals versus Mg_b, a tracer of galaxy luminosity-weighted mean metallicity. See text.

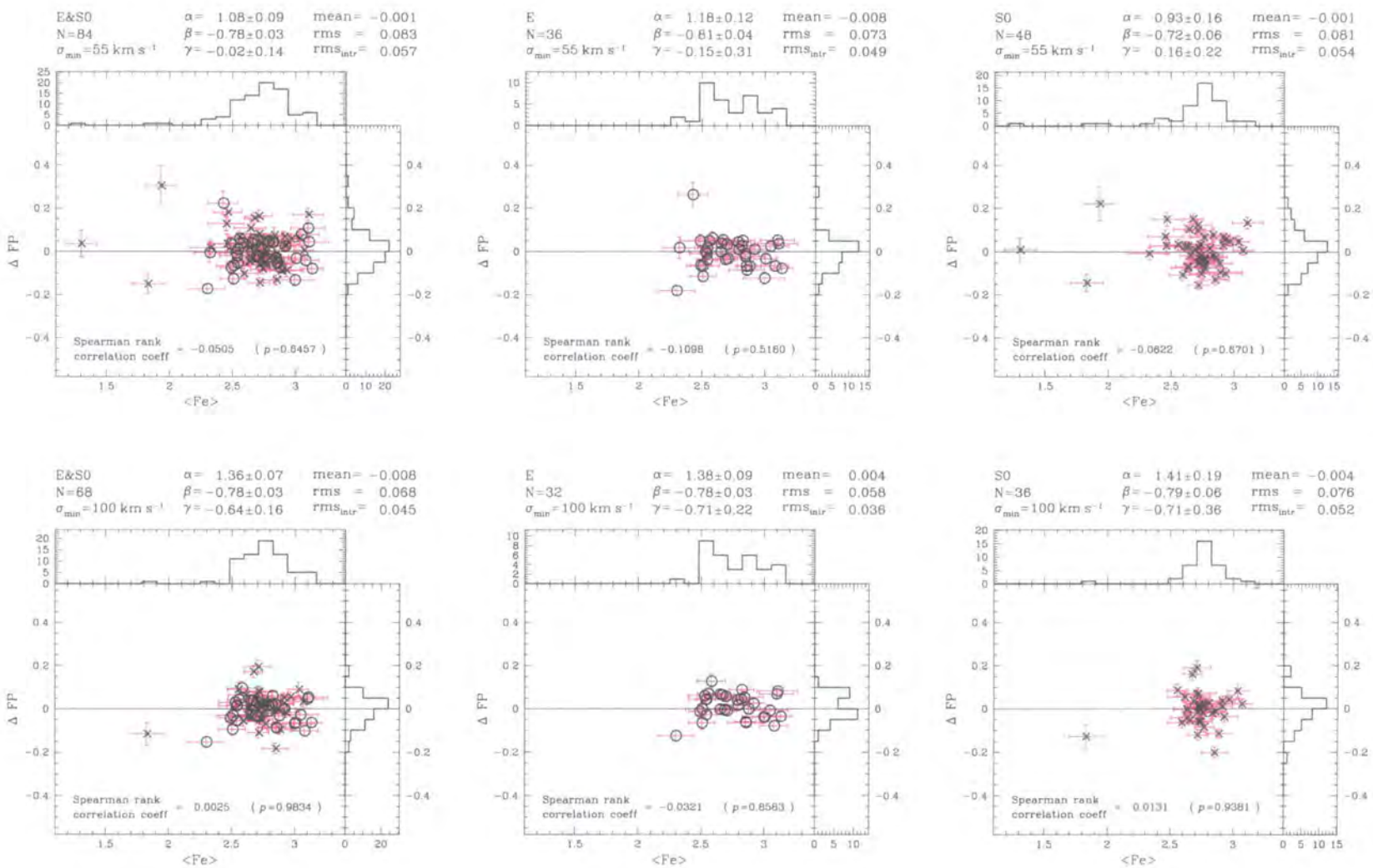

Figure 6.18: Fundamental plane residuals versus ⟨Fe⟩, a tracer of galaxy luminosity-weighted mean metallicity. See text.

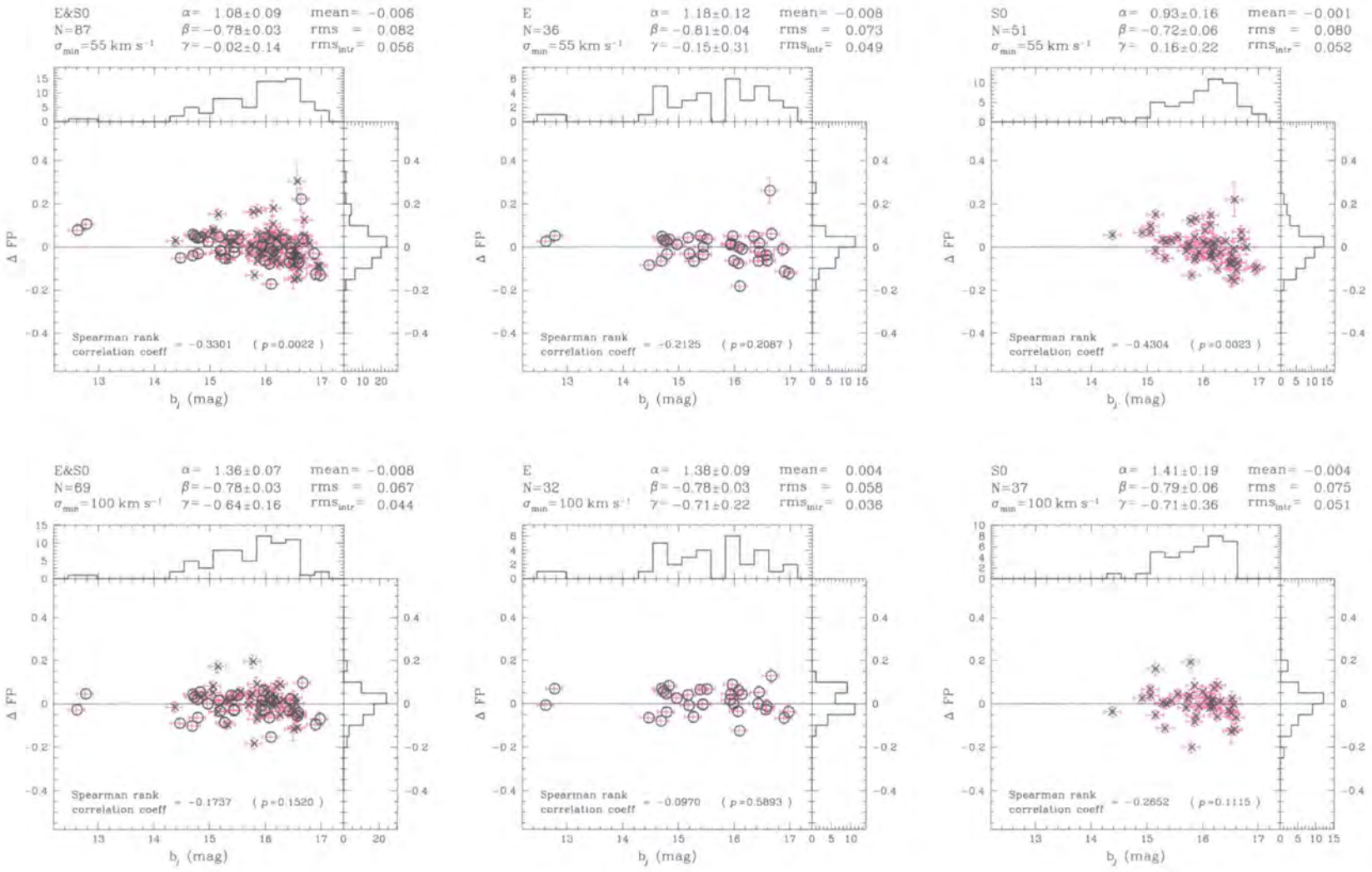

Figure 6.19: Fundamental plane residuals versus b_j from Godwin, Metcalfe & Peach (1983). See text.

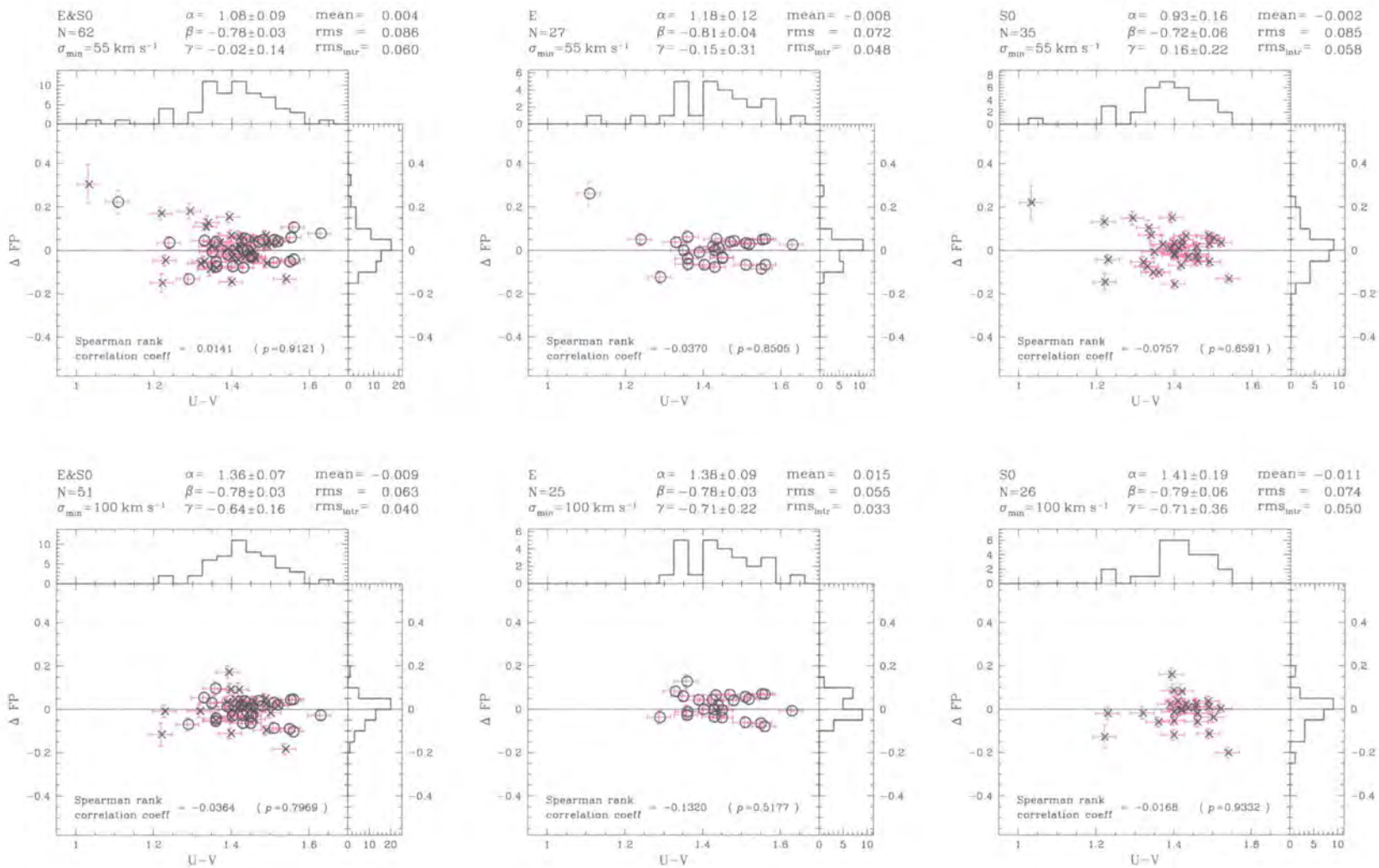

Figure 6.20: Fundamental plane residuals versus U–V from Bower et al. (1992) and Terlevich et al. (1999). See text.

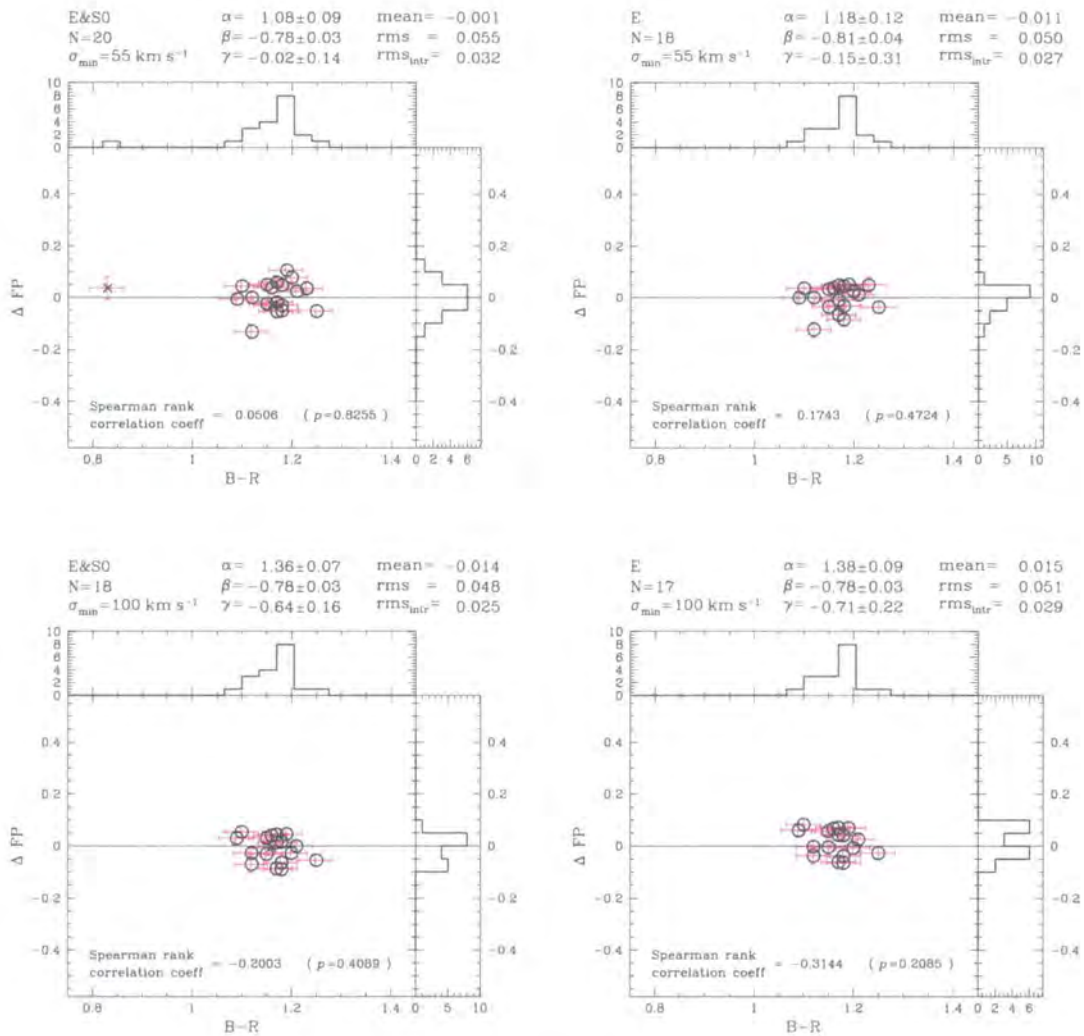

Figure 6.21: Fundamental plane residuals versus B–R from Jørgensen et al. (1995a). See text.

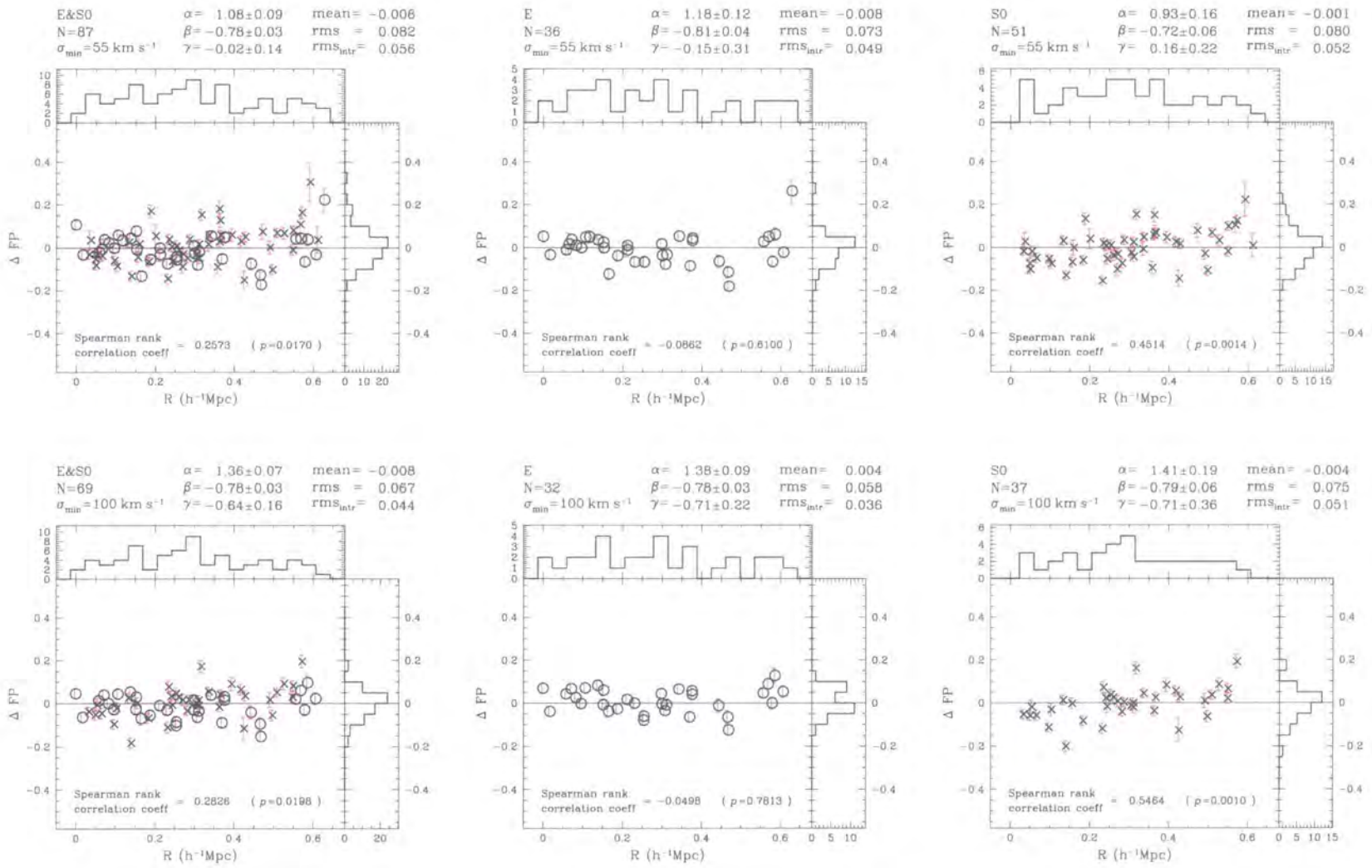

Figure 6.22: Fundamental plane residuals versus projected distance, R (in h^{-1}Mpc) from the cD galaxy NGC 4874. See text.

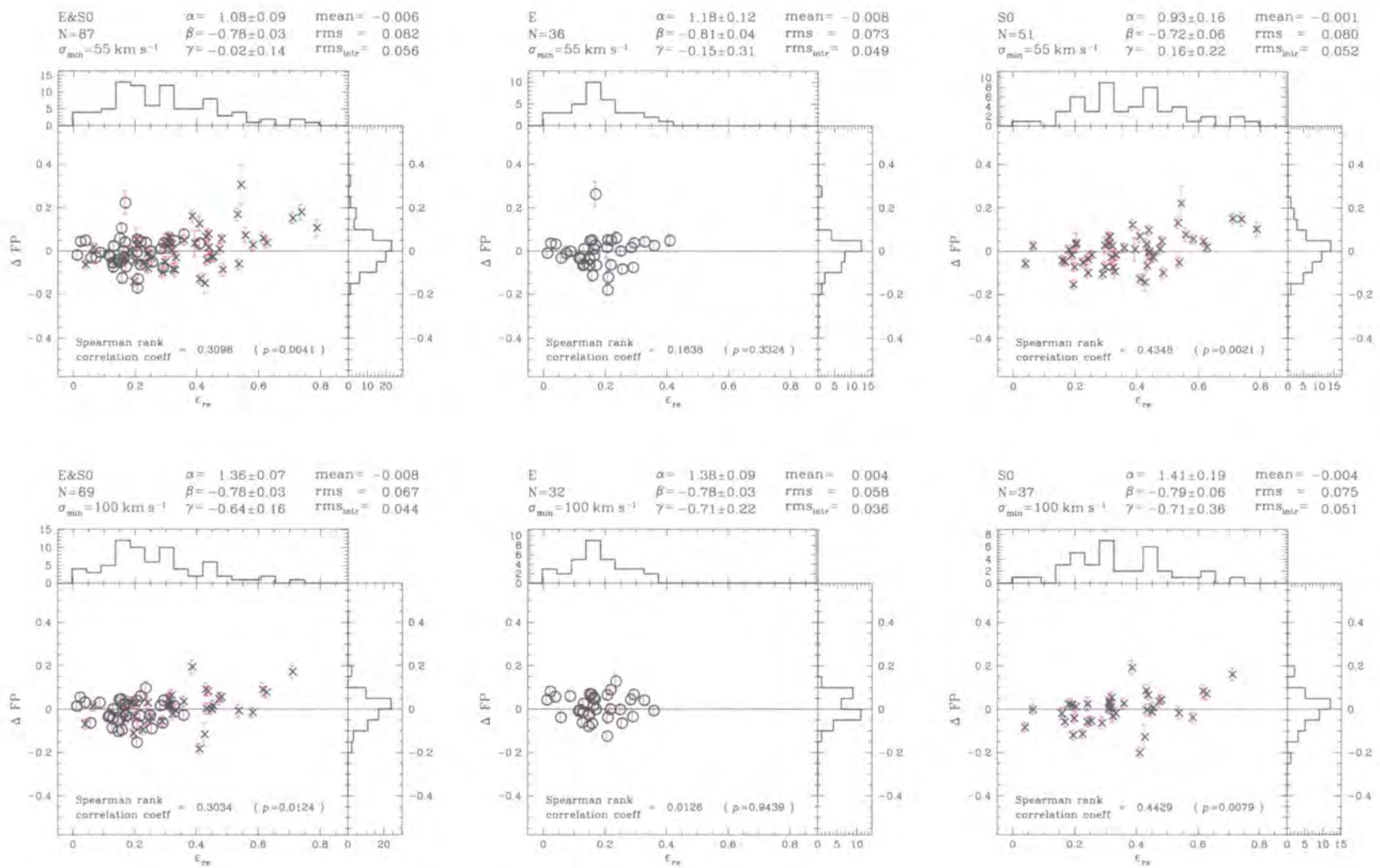

Figure 6.23: Fundamental plane residuals versus ellipticity, ϵ_{re}, at the effective radius, r_e. See text.

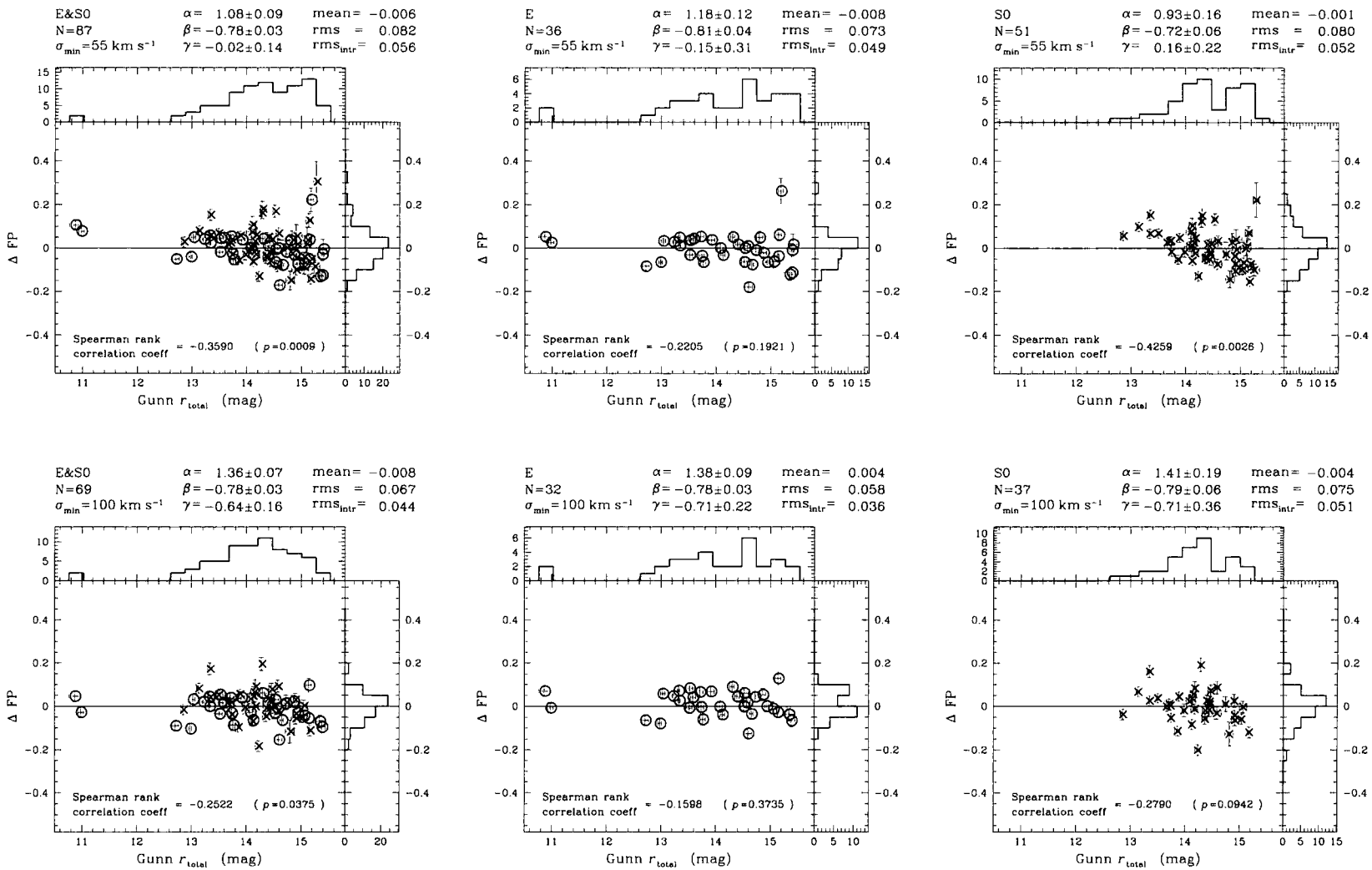

Figure 6.24: Fundamental plane residuals versus Gunn $r_{\rm total}$, calculated as $m_T = \langle\mu\rangle_e - 5\log r_e - 2.5\log 2\pi$ after Jørgensen et al. (1995a). See text.

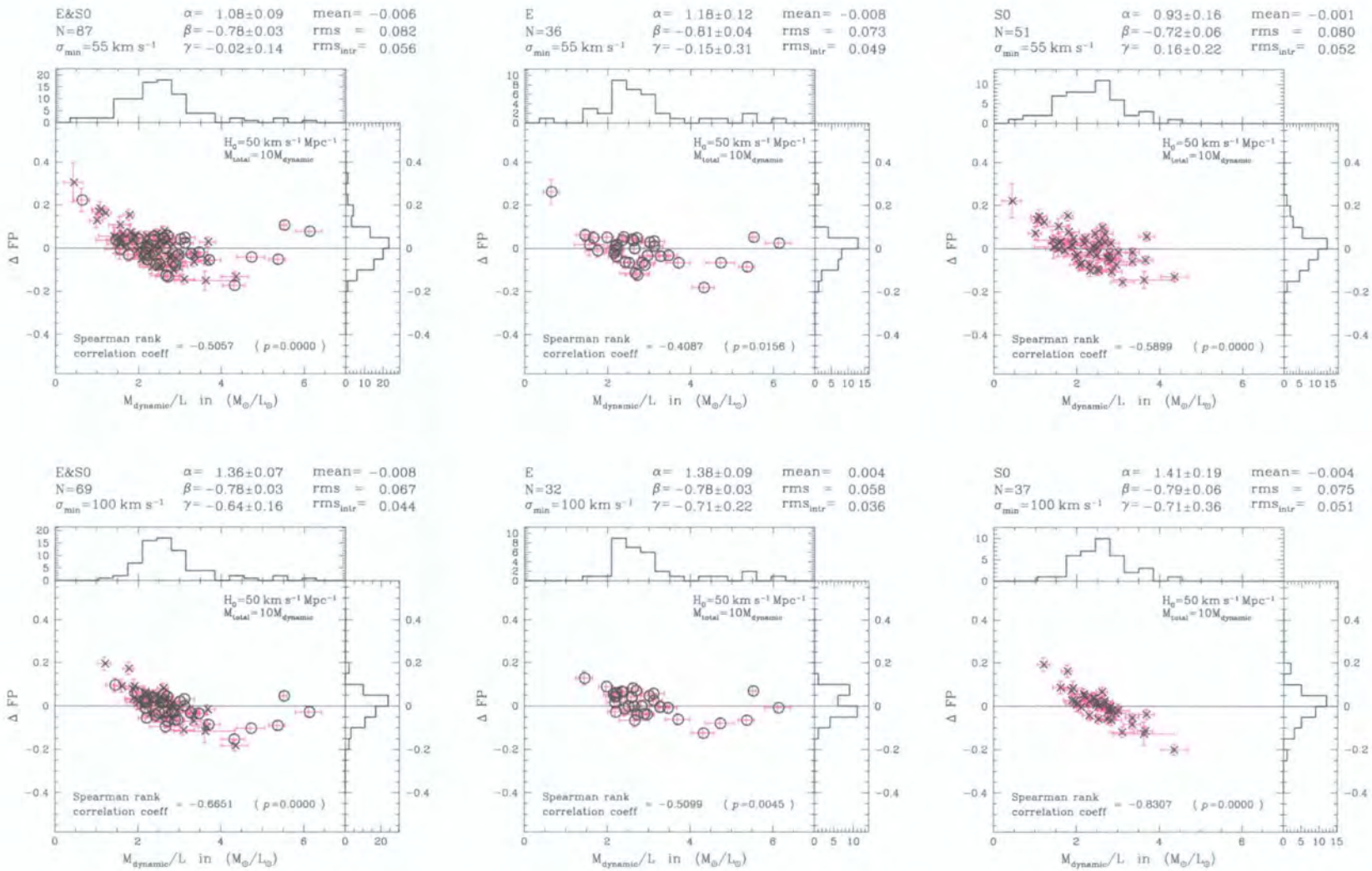

Figure 6.25: Fundamental plane residuals versus mass-to-light ratio, $M_{\rm dynamic}/L$ in units of $(M_\odot/L_\odot)$ calculated from Equation 6.22 for $H_0 = 50\,{\rm km\,s^{-1}\,Mpc^{-1}}$ and $M_{\rm total} = 10 M_{\rm dynamic}$. See text.

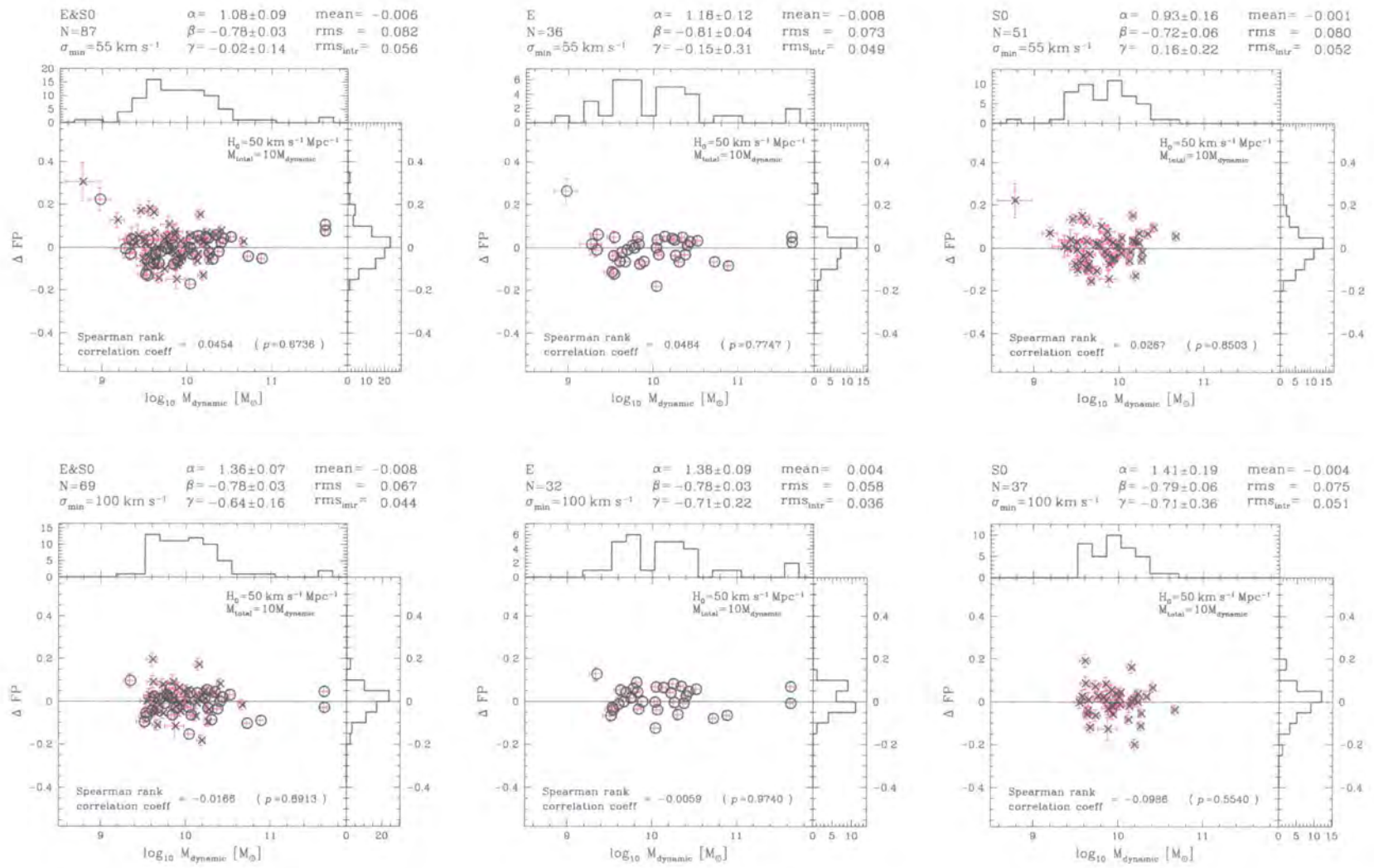

Figure 6.26: Fundamental plane residuals versus mass, $M_{\rm dynamic}$ in units of $M_\odot$ calculated from Equation 6.8 for $H_0 = 50\,{\rm km\,s^{-1}\,Mpc^{-1}}$, $M_{\rm total} = 10 M_{\rm dynamic}$ and a tidal-to-core radii ratio (r_t/r_c) of 100 (implying that $k_R k_V = 1/5$). See text.

6.6.8 2D distribution of FP residuals

Section 6.6.7 only analysed the dependence of FP residuals on stellar population indicators and other parameters in *one dimension*. Here I investigate the two dimensional distribution of FP residuals of the early-type galaxies in the central 1 degree ($\equiv 1.26\,h^{-1}\,$Mpc) of the Coma cluster across the H$\beta_{\rm G}$–[MgFe] and age–metallicity grids, as well as across the spatial projection of the cluster. FP residuals are calculated using $\Delta{\rm FP} = \log {\rm r}_e - \alpha \log \sigma - \beta \log\langle {\rm I}\rangle_e - \gamma_{cl}$.

Figure 6.27 shows the distribution of FP residuals across the spatial projection of the cluster for FP parameters from fits to the total early-type galaxy samples with $\sigma_{\rm min} = 55\,{\rm km\,s^{-1}}$ and $\sigma_{\rm min} = 100\,{\rm km\,s^{-1}}$. No correlation between the size nor the sense (i.e. positive or negative) of the FP residual is seen.

Figure 6.28 shows the distribution of FP residuals across the H$\beta_{\rm G}$–[MgFe] and age–metallicity grids, again for FP parameters from fits to the total early-type galaxy samples with $\sigma_{\rm min} = 55\,{\rm km\,s^{-1}}$ and $\sigma_{\rm min} = 100\,{\rm km\,s^{-1}}$. The conclusion is identical to that of Figure 6.27, in that no correlation between the size nor the sense (i.e. positive or negative) of the FP residual is seen.

Section 5.11 concluded that there was no radial (1D) nor any environmental (2D) dependence for early-type galaxy stellar population derived ages within the Coma cluster core. However, whilst there was no radial dependence for the galaxies' metallicities, there was an environmental dependence, with a concentration of metal rich galaxies ([Fe/H]$\geq$ 0) in the north eastern part of the cluster core and a concentration of metal poor galaxies ([Fe/H]$<$ 0) around the south western part. The lack of age structure is in agreement with the FP residual distribution across the cluster core, however the presence of a metallicity structure is not reflected in the FP residual distribution. This implies that the thickness of the FP relation is not affected by age nor metallicity (since if it was, a 2D distribution would be seen in the FP residuals *and* in the ages or metallicities) and that any observed metallicity structure in the cluster core is not related to mass-to-light ratios.

The conclusion of this 2D FP residual distribution analysis is that the FP is well behaved in 2D, in agreement with the previous 1D correlation findings.

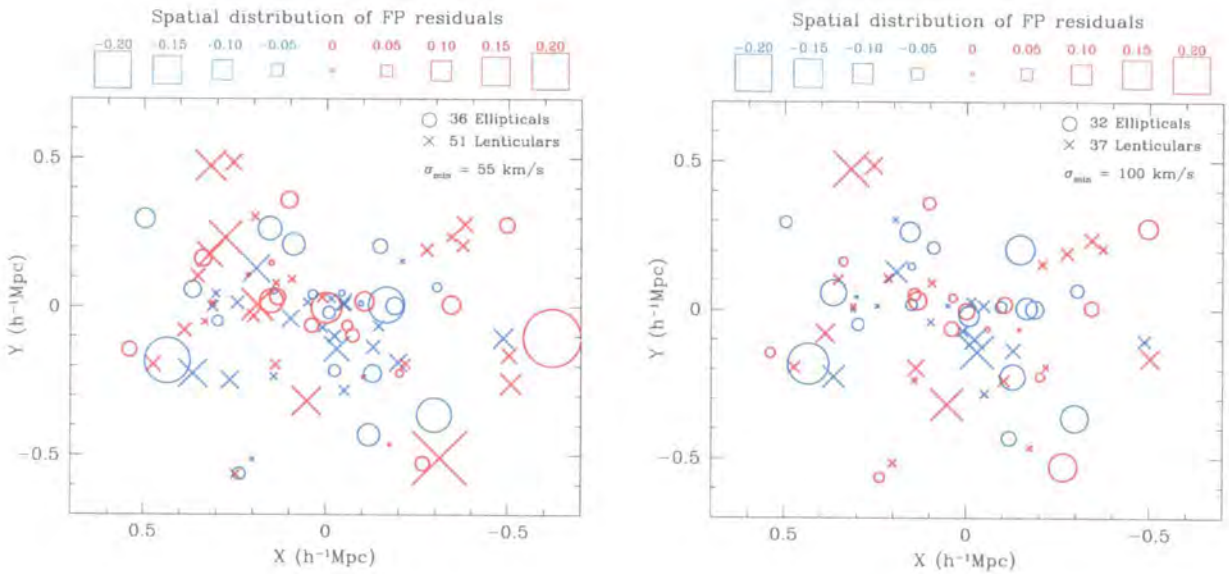

a. b.

Figure 6.27: Spatial distribution of FP residuals. The residuals are calculated using: $\Delta\mathrm{FP} = \log r_e - \alpha \log \sigma - \beta \log\langle I\rangle_e - \gamma_{cl}$. Figure (a) is for the FP parameters from a total early-type galaxy sample fit with $\sigma_{\min} = 55\,\mathrm{km\,s^{-1}}$, whilst (b) is for $\sigma_{\min} = 100\,\mathrm{km\,s^{-1}}$. The symbol size for each galaxy type is scaled to represent the absolute size of the residual and is coloured to indicate whether it is a negative residual (blue) or a positive residual (red) and a comparison scale is given at the top of the figure.

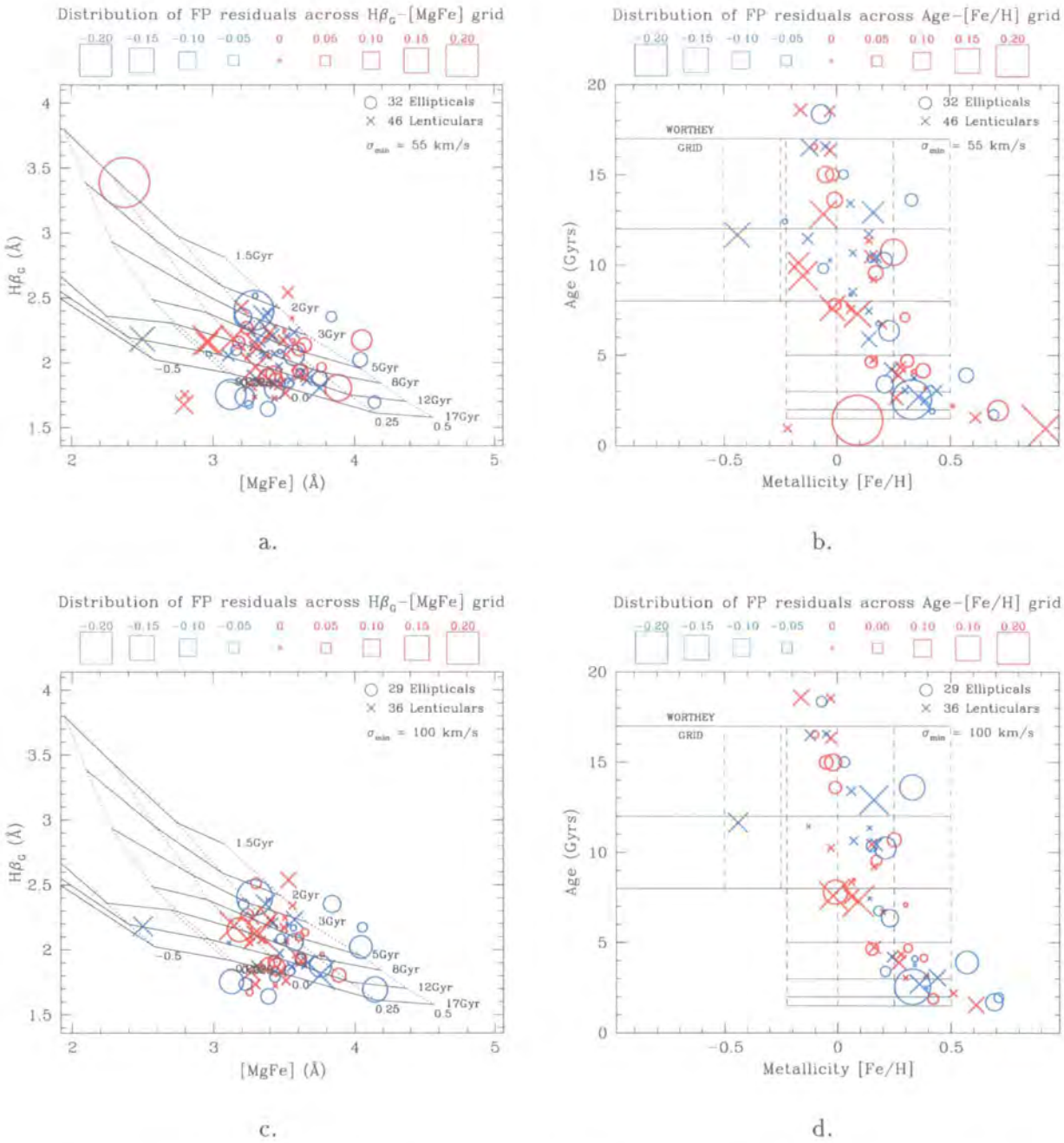

Figure 6.28: Distribution of FP residuals across H$\beta_{\rm G}$–[MgFe] and age–metallicity grids. The residuals are calculated using: $\Delta{\rm FP} = \log {\rm r}_e - \alpha \log \sigma - \beta \log \langle {\rm I} \rangle_e - \gamma_{cl}$. Figures (a) and (b) are for the FP parameters from a total early-type galaxy sample fit with $\sigma_{\rm min} = 55\,{\rm km\,s^{-1}}$, whilst (c) and (d) are for $\sigma_{\rm min} = 100\,{\rm km\,s^{-1}}$. The symbol size for each galaxy type is scaled to represent the absolute size of the residual and is coloured to indicate whether it is a negative residual (blue) or a positive residual (red) and a comparison scale is given at the top of each figure.

6.7 Conclusions

In this chapter I have analysed the spectro-photometric relations of a sample of 87 bright early-type galaxies within the central 1 degree ($\equiv 1.26\,h^{-1}$ Mpc) of the rich Coma cluster using the high quality, homogeneous data set with well characterised errors in this dissertation together Gunn r CCD surface photometry from Jørgensen et al. (1995a). This data set has allowed a new unbiased assessment of the Coma cluster intrinsic properties and factors affecting the spectro-photometric relations, without any need to combine multiple data sets with the inherent systematic error problem that ensues. I find that the early-type galaxy sample is well fit (using a robust method) by a fundamental plane of the form:

$$\log_{10} r_e = \underset{\pm 0.07}{1.36} \log_{10}\sigma - \underset{\pm 0.03}{0.78} \log_{10}\langle I\rangle_e - \underset{\pm 0.16}{0.64} \qquad \text{for galaxies with } \sigma \geq 100\,\mathrm{km\,s^{-1}} \quad (6.30)$$

This fundamental plane agrees with that determined by Jørgensen et al. (1996).

The main conclusions of this analysis of bright early-type galaxy spectro-photometric relations in the Coma cluster core are:

(a) All of the magnesium (Mg_1, Mg_2, Mg_b and [MgFe]) and iron (C4668, Fe5015, Fe5270, Fe5335, Fe5406, $\langle$Fe$\rangle$ and [MgFe]) dependent line indices are strongly correlated with $\log_{10}\sigma$. The exception being Fe4930, possibly due to the effect of Ba II on the index. The Hβ_G is also correlated with $\log_{10}\sigma$; this is possibly due to the contaminating effect of magnesium on the line index.

(b) Fitting separate relations to the elliptical and lenticular sub-populations yields similar α, β and γ values for galaxies with velocity dispersions, $\sigma = 100$ to $398\,\mathrm{km\,s^{-1}}$ but <u>different</u> values if I include lower velocity dispersion galaxies ($\sigma = 55$ to $398\,\mathrm{km\,s^{-1}}$). The slope of the fundamental plane, β remains the same, but the α and γ values vary: $\Delta\alpha_{100-55} = 0.28 \pm 0.11$ and $\Delta\gamma_{100-55} = -0.62 \pm 0.21$. This is in agreement with the study of Jørgensen et al. (1996).

(c) I find the intrinsic rms thickness of the fundamental plane to be 0.044 ± 0.005 for early-type galaxies with a velocity dispersion greater than $100\,\mathrm{km\,s^{-1}}$ (0.056 ± 0.006 for $\sigma \geq 55\,\mathrm{km\,s^{-1}}$).

Since a significant and non-zero intrinsic scatter is found for the FP relation, the conclusion is that there is a scatter in the FP relation that is not simply due to measurement errors. This intrinsic scatter is smaller than that found by Jørgensen et al. (1996), who found an intrinsic scatters of 0.073 dex in $\log r_e$ for $\sigma \geq 100\,\mathrm{km\,s^{-1}}$ (0.084 dex for $\sigma \geq 55\,\mathrm{km\,s^{-1}}$) for their early-type galaxies FP relation. Since this dissertation uses the same photometry as Jørgensen et al. (1996) and a similar FP fitting method, the conclusion is that the higher scatter they found is due to the fact that they had to construct a data set of $\log\sigma$'s from a variety of sources (with a range in quality) thereby introducing systematic errors or because of cluster-to-cluster differences in the fundamental plane.

(d) The scatter around the fundamental plane is seen to depend upon morphological type: the FP scatter of an elliptical galaxy fit ($\mathrm{rms}_{intr}\{\mathrm{E}\} = 0.036 \pm 0.006$ for $\sigma \geq 100\,\mathrm{km\,s^{-1}}$) is *smaller* than that for a lenticular galaxy fit ($\mathrm{rms}_{intr}\{\mathrm{S0}\} = 0.051 \pm 0.008$ for $\sigma \geq 100\,\mathrm{km\,s^{-1}}$), with $\Delta\mathrm{rms}_{intr}\{\mathrm{S0\text{-}E}\} = 0.015 \pm 0.010$. The scatter is also dependent upon the lower velocity dispersion cutoff, with the total early-type galaxy sample having $\mathrm{rms}_{intr}\{\mathrm{E\&S0}\} = 0.056 \pm 0.006$ for $\sigma \geq 55\,\mathrm{km\,s^{-1}}$ and $\mathrm{rms}_{intr}\{\mathrm{E\&S0}\} = 0.044 \pm 0.005$ for $\sigma \geq 100\,\mathrm{km\,s^{-1}}$ giving $\Delta\mathrm{rms}_{intr}\{55 - 100\} = 0.012 \pm 0.008$. This is unsurprising since the $\log\sigma$ parameter in the FP equation is the dominant source of error and is therefore the most important to determine well when trying to measure cluster distances. This dependence on minimum velocity dispersion is repeated in the elliptical and lenticular sub-samples. This once again highlights the importance of selection criteria in obtaining a tight FP relation to compute distances.

(d) An analysis of the distribution of the residuals around the fundamental plane showed that they are well-fit by a Gaussian distribution. If the separate distribution of the elliptical and lenticular residuals around a common early-type galaxy FP fit is analysed, the mean offsets of the sub-populations are found to be significant, with $\Delta_{\mathrm{E\text{-}S0}} = -0.024 \pm 0.016$ for $\sigma \geq 100\,\mathrm{km\,s^{-1}}$ ($\Delta_{\mathrm{E\text{-}S0}} = -0.019 \pm 0.017$ for $\sigma \geq 55\,\mathrm{km\,s^{-1}}$). The detection of a mean offset *disagrees* with the work of Saglia et al. (1993), who found an offset in the Coma cluster of $\Delta_{\mathrm{E\text{-}S0}} = +0.043 \pm 0.019$ (with however a greatly different value of α of 1.07), and with the work of Jørgensen et al. (1996), who found a much smaller median offset of $\Delta_{\mathrm{E\text{-}S0}} = +0.006 \pm 0.011$ for a sample of 9 clusters using a heterogeneous set of velocity dispersions. The result does however *agree* with the result of a recent study of the Shapley Supercluster by Smith et al. (2001), who found an

offset of $\Delta_{\text{E-S0}} = -0.033 \pm 0.021$. The presence of a mean offset shows the importance of a homogeneous data set and the need for careful morphological segregation when constructing a FP sample with a tight scatter for distance determination. When the FP relation is used to determine cluster distances for clusters significantly further away than Coma, the presence of a mean offset between the fundamental planes of elliptical and lenticular galaxies can lead to large errors in the cluster distance if the sample morphology is poorly understood. The offset means that a common fit to an early-type galaxy sample with similar numbers of elliptical and lenticular galaxies will also lead to the incorrect conclusion that the elliptical galaxies are systematically *further away* than the lenticular galaxies. Thus it is important to understand the detailed morphology of any galaxy sample used to determine cluster distances.

(e) The results of a 1D and 2D correlation analysis show that the FP relation is in general well behaved and common for ellipticals and lenticulars (since any variations are small, though significant). The correlation analysis has highlighted no additional terms for the existing FP relation. Exploration of the intrinsic scatter shows that previously suggested mechanisms are not responsible (since there is no variation in the scatter of the FP residuals with any of the tested parameters at a highly significant level) and that the real source lies in the underlying physics of the kinematics and dark matter structures. The mass-to-light ratio correlation with FP residuals supports this conclusion. A clear correlation of FP residuals with M_{dynamic}/L is seen, with bright galaxies having negative residuals and faint galaxies having positive residuals. The cD galaxies NGC4874 and NGC4889 do not however follow this correlation. The simplest explanation for this correlation is a variation in α for:

$$\left(\frac{M}{L}\right) \propto L^{\xi} \qquad \text{where } \xi = \frac{1}{\alpha} - \frac{1}{2} \tag{6.31}$$

This variation agrees with previous findings of variations in α for different velocity dispersions (and therefore different luminosities) and for fundamental planes in different wavebands. It could also be due to a variation in $M_{dark}/M_{dynamic}$ (since for a fixed ratio of $M_{total} = 10M_{dynamic}$ there is no correlation of FP residuals with M_{dynamic} nor with Gunn r_{total} — see Figure 6.29) and/or the kinematic "constants" with size. Another explanation is that the FP relation could be *curved*. A possible explanation for why the cD galaxies do not follow this correlation is that their dark matter ratios ($M_{dark}/M_{dynamic}$) could be significantly larger than for other cluster galaxies. Real intrinsic differences between the elliptical and lenticular galaxies have again been

shown (differences are seen between their: FP parameters; mean offsets around the FP; and their intrinsic scatters), leading to the conclusion that they have differing kinematics and/or dark matter fractions.

The overall conclusion from this fundamental plane analysis is that the FP relation is in general well behaved and common for ellipticals and lenticulars. However the evidence for real intrinsic differences between the elliptical and lenticular galaxies is overwhelming. Therefore when applying the FP relation to clusters to determine their distance, the morphological classification of galaxies is vitally important if high accuracy distance measurements are desired.

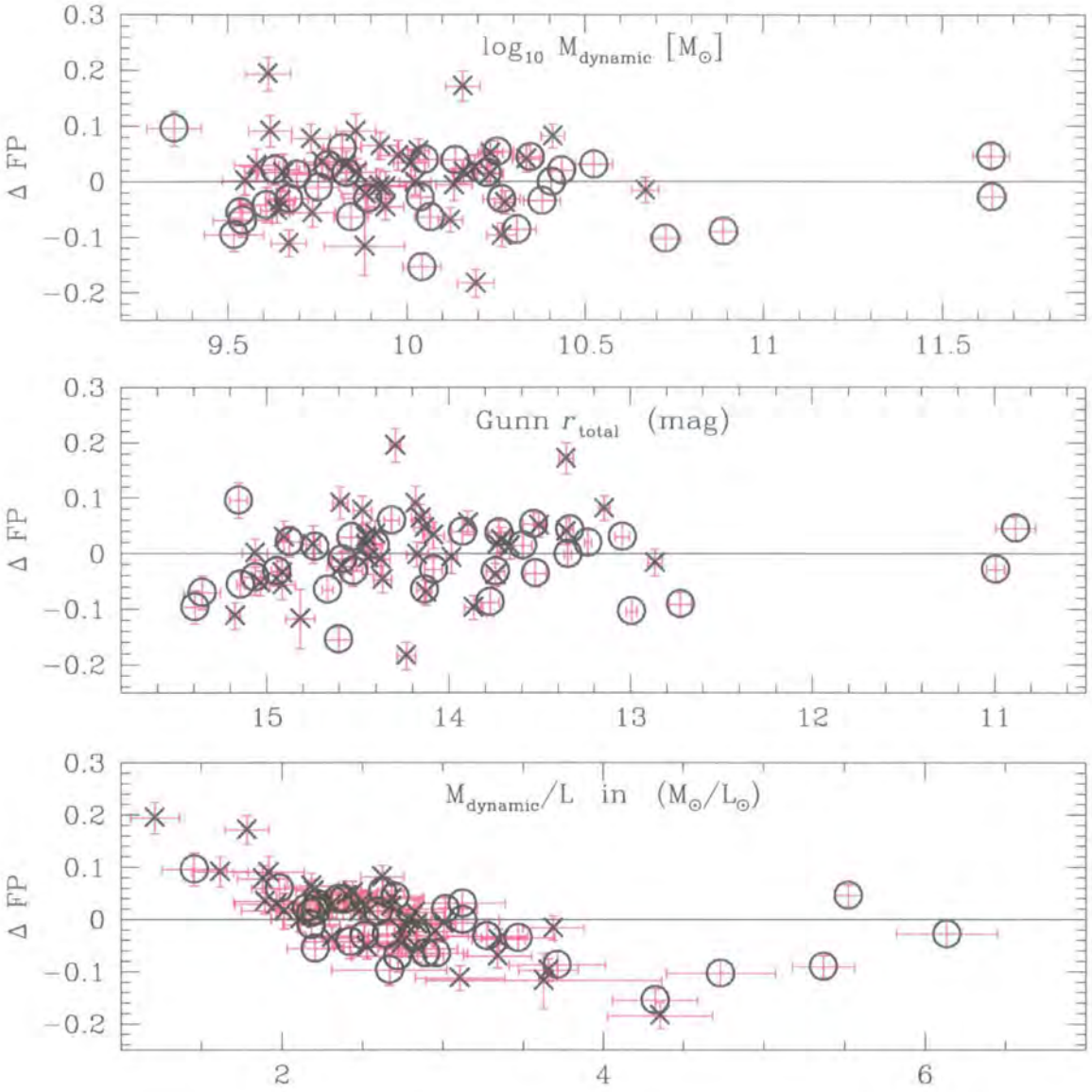

$M_{\rm dynamic} = \frac{1}{10}\frac{1}{Gk_Rk_V}\sigma^2 r_e$

Gunn $r_{\rm total} = \langle\mu\rangle_e - 5\log r_e - 2.5\log 2\pi$

$\log(M_{\rm dynamic}/L) = 2\log\sigma - \log\langle I\rangle_e - \log r_e - 0.733$

Figure 6.29: Correlation of mass-to-light ratio with the residuals of the FP. The FP parameters are from a total early-type galaxy sample fit with $\sigma_{\rm min} = 100\,{\rm km\,s^{-1}}$. Assumptions are: $H_0 = 50\,{\rm km\,s^{-1}\,Mpc^{-1}}$, $M_{\rm total} = 10 M_{\rm dynamic}$ and a tidal-to-core radii ratio (r_t/r_c) of 100 (implying that $k_R k_V = 1/5$). Only galaxies with $\sigma \geq 100\,{\rm km\,s^{-1}}$ are shown. Ellipticals are represented by circles and lenticulars by crosses. The cD galaxies NGC 4874 and NGC 4889 are furthest right on each plot. No correlation is seen between the residuals (ΔFP) and $\log_{10} M_{dynamic}$ or Gunn $r_{\rm total}$, but there is a correlation between ΔFP and the mass-to-light ratio, $M_{\rm dynamic}/L$.

Chapter 7

Conclusions

7.1 Thesis summary

In this thesis I have analysed the stellar populations (which act as fossil records of galaxy formation and evolution) and the spectro-photometric relations of a sample of 87 bright early-type galaxies within the core of the rich Coma cluster (a diameter of 1 degree $\equiv 1.26\,h^{-1}$ Mpc) using the high quality, homogeneous data set with well characterised errors in this dissertation together Gunn r CCD surface photometry from Jørgensen et al. (1995a). This data set has allowed for the first time a new unbiased assessment of the Coma cluster intrinsic properties and factors affecting the spectro-photometric relations, without any need to combine multiple data sets with the inherent systematic error problem that ensues. This work acts as an important baseline at $z \sim 0$ for studies of distant, high redshift clusters. It also expands the existing knowledge base of galaxy formation and evolution in rich clusters and provides further evidence for the usefulness of the fundamental plane as a distance indicator.

The stellar populations have shown that the bright early-type galaxies within the Coma cluster core have a large metallicity distribution (with $-0.55 \leq$ [Fe/H] $\leq +0.92$). Whilst it is more likely that there is also a small distribution in age, a single age of stellar population formation for the dominant group of galaxies is supportable. The bright early-type galaxies are found to have a luminosity-weighted mean age of 8 Gyrs. There are in addition real differences between the elliptical and lenticular galaxy populations, with the elliptical stellar populations (mean age of 9 Gyrs) on average 2 Gyrs *older* than those within the lenticulars (mean age of 7 Gyrs). Modelling of the age distributions of the early-type galaxies has shown that an age model of 8 Gyrs with a scatter of 0.300 dex is likely, with the ellipticals having a smaller age scatter of 9 Gyrs $\pm$ 0.275 dex rather than the 7 Gyrs $\pm$ 0.325 dex of the lenticulars. There are however a few galaxies with very strong H$\beta_{\rm G}$ absorption that are galaxies with genuinely younger stellar populations than the main body of Coma cluster early-type galaxies. The main caveat on these conclusions is that the Worthey (1994) models used herein assume a single star burst formed the stellar populations, whilst in reality the situation is likely to be more complex (with for example

merging events triggering new star bursts). Since this study has shown, in agreement with previous studies, that there is *no* evidence for significant large-scale star-formation occurring in the cluster core (Section 3.7.7) the conclusions about *relative* trends based upon the large numbers of early-type galaxies will not be greatly affected by this assumption. The presence of a distribution in the luminosity-weighted mean ages of the early-type galaxy stellar populations supports a hierarchical galaxy formation model. However since a single mean age is also found to be supported (implying a monolithic dissipative collapse model), this stellar population study cannot distinguish between hierarchical or monolithic dissipative collapse models on the basis of their luminosity-weighted mean ages.

The fundamental plane (FP) analysis showed that the FP relation is in general well behaved and common for ellipticals and lenticulars. The early-type galaxy sample is well fit by a fundamental plane of the form:

$$\log_{10} r_e = \underset{\pm 0.07}{1.36} \log_{10}\sigma - \underset{\pm 0.03}{0.78} \log_{10}\langle I\rangle_e - \underset{\pm 0.16}{0.64} \qquad \text{for galaxies with } \sigma \geq 100\,\mathrm{km\,s^{-1}} \quad (7.1)$$

with a significant intrinsic rms thickness of 0.044 ± 0.005, implying that the scatter in the FP relation is not simply due to measurement errors. A detailed FP residual correlation analysis concluded that there are no additional terms for the existing FP relation and that previously suggested mechanisms are *not* responsible for the presence of an intrinsic scatter, suggesting that the real source lies in the underlying physics of the kinematics and dark matter structures. A mass-to-light ratio correlation with the FP residuals supports this conclusion, with bright galaxies having negative residuals and faint galaxies having positive residuals. This correlation suggests either a variation in α for $(M/L) \propto L^{\xi}$ (where $\xi = 1/\alpha - 1/2$), or a variation in $M_{dark}/M_{dynamic}$ (since for a fixed ratio of $M_{total} = 10M_{dynamic}$ there is no correlation of FP residuals with $M_{\rm dynamic}$ nor with Gunn $r_{\rm total}$), or that the kinematic "constants" vary with size, or finally that the FP relation could be *curved.* The evidence for real intrinsic differences between the elliptical and lenticular galaxies is however overwhelming, leading to the conclusion that they have *differing* kinematics and/or dark matter fractions. There are differences between the intrinsic thicknesses of their FP fits, with $\Delta\mathrm{rms}_{intr}\{\mathrm{S0\text{-}E}\} = 0.015 \pm 0.010$ (for $\sigma \geq 100\,\mathrm{km\,s^{-1}}$). There is also a mean offset between the ellipticals and lenticulars around a common early-type galaxy fit of $\Delta_{\mathrm{E\text{-}S0}} = -0.024 \pm 0.016$ (for $\sigma \geq 100\,\mathrm{km\,s^{-1}}$) which can lead to the incorrect conclusion that the elliptical galaxies are systematically *further away* than the

lenticular galaxies. Therefore when applying the FP relation to clusters to determine their distance, the morphological classification of galaxies is vitally important if high accuracy distance measurements are desired.

This dissertation has shown, using detailed modelling and statistical techniques with a high quality data set and utilising the rich Coma cluster as a laboratory, the importance of understanding the different morphologies of early-type galaxies before blindly applying analysis tools and relationships to a poorly defined cluster early-type galaxy sample. The many differences between ellipticals and lenticulars lead to the conclusion that they have either different formation mechanisms or different evolution histories. It is therefore important to no longer analyse conglomerate samples of early-type galaxies, and instead to consider separately elliptical and lenticular galaxies in rich galaxy clusters.

7.2 Directions for future research

Possible extensions to this work to further expand the study of the stellar populations of the early-type galaxies in the Coma cluster are summarised below:

— the second wavelength range 3900–4900Å observed as part of this project can be analysed to obtain the Hγ Lick/IDS absorption line index. Hγ is also an age sensitive line index and can be used to place further constraints on the age distribution of the early-type galaxy stellar populations;

— the Worthey (1994) models provide a large number of grids other than the H$\beta_{\rm G}$ versus [MgFe] grid used herein. These grids have different degrees of age–metallicity degeneracy hampering the derivation of luminosity weighted mean ages and metallicities. They also suffer from non-solar abundance ratio problems. However if these problems are quantified in a rigorous sense, then the ages and metallicities derived from each grid can be weighted and then a weighted average age and metallicity calculated for each galaxy from all its absorption line indices. This could potentially reduce the errors on the age and metallicity measurements;

— other stellar population synthesis models (e.g. Bruzual & Charlot 1993, Vazdekis et al. 1996b, 1997, Vazdekis 1999) can be used to derive ages and metallicities. These models are all

in good, general agreement with the Worthey (1994) but offer the attraction of additional power through multiple derivations with different models to further constrain the age and metallicity measurements. In addition, more recent models (e.g. Vazdekis 1999) perform evolutionary stellar population synthesis at a higher spectral resolution (2Å in Vazdekis 1999) than the mean resolution of 9Å in the Worthey (1994) models; this higher resolution helps to break the age–metallicity degeneracy of indices by removing the effect of contaminating spectral features to concentrate on the age or metallicity dependent features;

— the stellar population synthesis modelling herein assumes a single initial burst of star formation formed the stellar population. The modelling can be extended to investigate differing star formation histories, e.g. the effect of recent small star bursts ($\leq 1.0\,\mathrm{Gyrs}$) on an overall galaxy stellar population. This allows investigation of the effect of star formation histories on the scatter of mean ages in the Coma cluster early-type galaxy stellar populations;

— higher signal-to-noise data (~ 100 per Å) can be obtained to further constrain the errors. If the errors can be reduced still further, then it will be become possible to distinguish between a single luminosity-weighted mean age of dominant stellar population formation and more complication distributions. These new observations can also be extended to include the dwarf early-type galaxy population to place further constraints on the stellar population distributions in the Coma cluster.

In addition to the above future avenues of research on the Coma cluster early-type galaxy stellar populations, I am also currently involved in a stellar population and fundamental plane peculiar velocity survey of rich galaxy clusters within $200h^{-1}\mathrm{Mpc}$. The purpose of this survey is to probe for environmental and evolutionary differences between galaxy clusters and to use their peculiar velocity field to probe the large scale ($\geq 10h^{-1}\mathrm{Mpc}$) mass distribution in the nearby Universe. The study will investigate the presence of a bulk flow of the local volume with respect to the cosmic microwave background. This deep, homogeneous, all-sky spectroscopic and photometric study contains ~ 100 X-ray selected clusters with a total of ~ 4000 early-type galaxies which will significantly reduce combined and systematic errors for each component of the bulk flow vector to $\leq 120\,\mathrm{km\,s^{-1}}$ and will provide for the first time a comprehensive sample of stellar population information to finally answer the question of the presence of any

environmental or evolutionary differences between galaxy clusters.

Appendix A

Comparison Data

A.1 Seven Samurai comparison

The Seven Samurai group (Djorgovski & Davis 1987; Dressler et al. 1987; Faber et al. 1987) observed 35 galaxies within the Coma cluster using the Lick 3m telescope with a slit of dimension $1.5'' \times 4''$ and using the Las Campanas Observatory with a $4'' \times 4''$ slit. Out of this total, there are 23 galaxies in common with this study. Table A.1 lists the matching data from the study.

A.2 Lick/IDS comparison

The Lick/IDS database (Trager et al. 1998) has absorption line strength measurements for 22 galaxies in the Coma cluster (all corrected to an equivalent long-slit of dimension $1.4'' \times 4''$), 11 of which are in common with this study. Table A.2 lists the matching data from the study.

A.3 Comparison with Jørgensen (1999)

Jørgensen (1999) measured mean ages and metal abundances for the stellar populations in a sample of 115 early-type galaxies in the central 64 arcmin $\times$ 70 arcmin of the Coma cluster. This data set became the definitive spectroscopic data set for the Coma cluster and as such represents a key test of the data presented in this study. Spectroscopic observations were made on two separate occasions. The first set of spectroscopic observations of 44 galaxies were obtained with the McDonald Observatory 2.7m telescope equipped with the Large Cassegrain Spectrograph (LCS). The second set of observations of 38 galaxies (which includes 11 galaxies in common with the first set of observations) were obtained with the McDonald Observatory equipped with the Fibre Multi-Object Spectrograph (FMOS) — a grism spectrograph with 90–100 fibres and a field of view of 66 arcmin diameter. This produced a sample of 71 galaxies with Mg_2, $\langle Fe \rangle$ and $H\beta_G$

absorption line index measurements together with mass-to-light ratios (M/L). This sample is 61 per cent complete to a total magnitude of 15.05 in Gunn r. Luminosity weighted mean age and metal abundance estimates are based upon these absorption line indices. Table A.3 summarises the observations. All her spectroscopic parameters of the galaxy centres were corrected to a circular aperture with a diameter of 3.4″, i.e. 1.19 h^{-1} kpc* (Jørgensen, Franx & Kjaergaard 1995a,b; Jørgensen 1997). Line indices are corrected for velocity dispersions using the same method I described in Section 3.7.5. Jørgensen tested her sample for the presence of nebular emission by subtracting template stellar spectra used for velocity dispersion determination and analysing the residual spectra for emission lines. With the SN of the spectra she was able to detect emission in galaxies if the equivalent width of [OIII]5007Å was larger than about 0.5Å. She detected only 3 galaxies with significant emission and excluded them from her sample. There are 36 galaxies from this sample in common with this study. These are shown in Table A.4.

*assumes $H_0 = 100\ h\ \mathrm{km\,s^{-1}Mpc^{-1}}$, where h represents the uncertainty with which we know Hubbles constant at this epoch. $h = 0.5$ would imply a Hubbles constant of $50\,\mathrm{km\,s^{-1}Mpc^{-1}}$

name	type‡	b_j†	B_T	B-V_0	$cz_\odot$	$\log\sigma$	σ	$\log A_e$	SB_e	$\log D_n$	Mg_2
		mag	mag	mag	km s^{-1}	dex	km s^{-1}				mag
ngc4860	E	14.69	14.43	1.02	7862	2.391	246.0	0.46	21.11	0.39	0.346$^\psi$
ngc4864	E	14.70	14.62	0.95	6760	2.297	198.2	0.46	21.30	0.34	0.292
ngc4869	E	14.97	14.57	1.00	6703	2.312	205.1	0.45	21.20	0.35	0.323
ngc4874	cD	12.78	12.31	0.97	7176	2.389	244.9	1.31	23.24	0.51	0.328
ngc4876	E	15.51	15.22	0.93	6629	2.260	182.0	0.30	21.10	0.23	0.252
ngc4881	E	14.73	14.43	0.95	6691	2.340	218.8	0.58	21.71	0.33	0.293
ngc4886	E	14.83	14.78	0.96	6218	2.215	164.1	0.49	21.61	0.27	0.257
ngc4889	cD	12.62	12.48	1.04	6497	2.581	381.1	1.02	21.96	0.69	0.359
ngc4906	E	15.44	14.87	0.92	7505	2.225	167.9	0.43	21.40	0.28	0.297
ic4051	E	14.47	14.01	0.97	4964	2.348	222.8	0.83	22.54	0.30	0.337
ngc4923	E	14.78	14.59	0.96	5458	2.283	191.9	0.45	21.22	0.35	0.311
d136	E	16.57	16.37	0.89	5668	2.262	182.8	−0.14	20.05	0.09	0.287
ic3959	E	15.27	15.07	0.00	7121	2.301	200.0	0.31	21.00	0.27	0.315
ngc4867	E	15.44	15.28	0.92	4818	2.346	221.8	0.15	20.41	0.28	0.314
d107	E	16.35	15.90	0.86	6518	1.845	70.0	0.40	22.28	−0.04	0.241
d87	E	16.87	16.58	0.00	7833	1.903	80.0	0.10	21.46	−0.07	0.236
ngc4872	E/S0	14.79	15.35	1.03	7145	2.326	211.8	0.09	20.18	0.28	0.307
d153	E	16.14	15.97	0.94	6640	2.130	134.9	0.16	21.15	0.08	0.287
d193	E	16.43	16.05	0.91	7544	2.079	119.9	0.21	21.48	0.04	0.271
ic4011	E	16.08	15.74	0.93	7142	2.025	105.9	0.28	21.52	0.09	0.287
ic4012	E	15.93	15.68	0.92	7218	2.253	179.1	0.07	20.41	0.20	0.299
d207	E	16.07	15.77	0.92	6764	2.167	146.9	0.21	21.20	0.12	0.273
ic4045	E	15.17	14.96	0.97	6855	2.324	210.9	0.28	20.74	0.32	0.312

† taken from Godwin, Metcalfe & Peach (1983)

‡ taken from Dressler (1980)

$^\psi$ this value differs by −0.186 mag from the value in this study. This point is excluded from the analysis

Table A.1: Data from the Seven Samurai in common with this study. There are 23 galaxies in common between the two data sets (measurements for 35 Coma cluster galaxies were reported by the Seven Samurai).

name	C4668	Fe5015	Fe5270	Fe5335	Fe5406	Hβ	$\langle$Fe$\rangle$	Mg_1	Mg_2	Mg_b	[MgFe]
	Å	Å	Å	Å	Å	Å	Å	mag	mag	Å	Å
ic4051	9.59	3.94	2.43	2.69		1.80	2.56	0.204	0.344	5.30	3.68
	1.37	1.18	0.50	0.66		0.45	0.41	0.014	0.016	0.54	0.34
ngc4860	7.74	6.03	3.42	2.51		1.37	2.96	0.162	0.322	5.20	3.92
	0.70	0.65	0.28	0.38		0.23	0.24	0.007	0.008	0.31	0.20
ngc4864	5.80	5.32	3.67			2.35		0.110	0.283	5.02	
	1.11	0.97	0.41			0.37		0.011	0.013	0.43	
ngc4869	8.41	5.76	3.25	2.68	1.71	0.79	2.96	0.137	0.265	5.16	3.91
	1.17	1.02	0.43	0.55	0.40	0.38	0.35	0.012	0.014	0.46	0.29
ngc4874	7.38	5.28	2.74	3.26		1.31	3.00	0.154	0.328	5.41	4.03
	0.61	0.57	0.24	0.39		0.20	0.23	0.006	0.007	0.29	0.19
ngc4876	5.52	4.97	2.63	2.04	2.36	2.20	2.34	0.116	0.233	4.02	3.07
	1.20	1.03	0.43	0.53	0.41	0.40	0.34	0.012	0.014	0.46	0.29
ngc4881	8.61	4.90	2.77	2.20		1.87	2.48	0.133	0.287	4.59	3.38
	1.12	0.98	0.41	0.53		0.37	0.34	0.011	0.013	0.44	0.28
ngc4886	6.24	5.27	2.96	2.25		1.25	2.60	0.093	0.240	3.92	3.19
	0.91	0.78	0.33	0.40		0.30	0.26	0.009	0.011	0.34	0.22
ngc4889	8.67	5.61	3.00	2.84	1.80	1.16	2.92	0.186	0.346	5.46	3.99
	0.68	0.64	0.28	0.45	0.31	0.21	0.26	0.007	0.007	0.34	0.22
ngc4906	6.76	6.11	2.60	2.15	1.08	1.66	2.37	0.121	0.244	4.49	3.26
	1.32	1.13	0.47	0.57	0.43	0.44	0.37	0.013	0.016	0.50	0.31
ngc4923	8.86	5.00	2.55	2.89	1.79	1.87	2.72	0.145	0.296	5.05	3.71
	1.02	0.88	0.37	0.48	0.35	0.34	0.30	0.010	0.012	0.40	0.25

Table A.2: Data from the Lick/IDS team (Trager et al. 1998) in common with this study. There are 11 galaxies in common between the two data sets (measurements for 22 Coma cluster galaxies were reported by Trager et al. 1998).

	LCS Spectra	FMOS Spectra
Dates	14–21 March 1994	21–26 April 1995
Telescope	McD. 2.7m	McD. 2.7m
Instrument	LCS	FMOS
Grating/Grism	#47, 1200 lines mm^{-1}	300 lines mm^{-1}
Wavelength range	4879–5580 Å	3810–7660 Å
Resolution	0.97Å, 56 $km\,s^{-1}$	4.25Å, 246 $km\,s^{-1}$
Slit width	2 arcsec	...
Aperture	$6.35'' \times 2'$	$2.6''$
CCD	TI1, 800×800	Tek, 1024×1024
Read-out noise	7.94 e^-	7.3 e^-
Gain	3.37 e^-/ADU	5.69 e^-/ADU
Spatial scale	$1.27''$	...
Galaxies in Coma	44	38

Table A.3: Instrumentation used by Jørgensen (1999).

name	type‡	SN	b_j†	$cz_\odot$	$\log\sigma$	σ	Hβ	Hβ_G	Mg$_1$	Mg$_2$	Mg$_b$	$\langle$Fe$\rangle$	[MgFe]
			mag	km s^{-1}	dex	km s^{-1}	Å	Å	mag	mag	Å	Å	Å
d110	S0/E	15.4	16.60	6969	2.090	123.0	1.38	1.59	0.089	0.249	4.83	2.77	3.80
					0.004	1.1	0.45	0.31	0.011	0.014	0.46	0.42	0.31
d147	S0	28.3	16.19	7728	1.993	98.4	1.85	2.18	0.084	0.223	3.58	3.23	3.41
					0.005	1.1	0.24	0.16	0.006	0.007	0.26	0.23	0.17
d161	E	27.5	15.19				2.10	2.15	0.133	0.268	4.34	2.83	3.58
							0.25	0.17	0.006	0.008	0.26	0.24	0.18
d209	S0	28.7	16.04	7202	1.968	92.9	2.25	2.40	0.072	0.215	3.67	2.54	3.10
					0.005	1.1	0.24	0.16	0.006	0.007	0.26	0.23	0.17
d231	S0	29.3	15.78	7928	2.106	127.6	2.13	2.31	0.101	0.261	4.19	2.68	3.44
					0.004	1.1	0.23	0.16	0.006	0.007	0.25	0.22	0.17
d39	S0/E	28.3	16.17	5907	2.112	129.4	2.01	2.27	0.100	0.253	4.10	3.06	3.58
					0.004	1.1	0.24	0.16	0.006	0.007	0.26	0.23	0.17
d42	S0	27.4	16.31	6031	2.136	136.8	2.10	2.29	0.117	0.260	4.11	2.96	3.54
					0.004	1.1	0.25	0.17	0.006	0.008	0.27	0.24	0.18
d57	S0/a	53.1	15.15				2.28	2.32	0.095	0.249	3.94	2.82	3.38
							0.12	0.08	0.003	0.003	0.12	0.11	0.08

Table A.4: *continued on next page*

continued from previous page

name	type‡	SN	b_j†	$cz_\odot$	$\log\sigma$	σ	Hβ	Hβ_G	Mg$_1$	Mg$_2$	Mg$_b$	$\langle$Fe$\rangle$	[MgFe]
			mag	km s^{-1}	dex	km s^{-1}	Å	Å	mag	mag	Å	Å	Å
d62	S0	24.5	16.51	8341	2.124	133.0	1.82	2.03	0.048	0.169	3.17	2.08	2.62
					0.003	1.1	0.28	0.19	0.007	0.008	0.30	0.27	0.20
d75	S0	25.3	16.13	6168	1.852	71.1	2.64	2.89	0.077	0.220	3.28	2.29	2.79
					0.007	1.1	0.27	0.18	0.007	0.008	0.29	0.26	0.19
d84	S0	24.2	16.20	6562	2.117	130.9	1.82	2.15	0.112	0.262	4.29	3.46	3.88
					0.004	1.1	0.29	0.19	0.007	0.009	0.30	0.27	0.20
d93	S0	29.0	16.26	6063	2.140	138.0	2.27	2.29	0.091	0.251	3.91	2.99	3.45
					0.003	1.1	0.24	0.16	0.006	0.007	0.25	0.22	0.17
d98	S0/a	19.2	15.85				2.36	2.44	0.102	0.246	3.87	3.39	3.63
							0.36	0.24	0.009	0.011	0.38	0.34	0.25
ic3943	S0/a	29.6	15.55	6821	2.262	182.8	1.97	2.29	0.124	0.276	4.71	3.02	3.87
					0.003	1.1	0.23	0.16	0.006	0.007	0.24	0.22	0.16
ic3946	S0	27.7	15.28	5923	2.327	212.3	1.57	1.83	0.124	0.271	4.18	2.49	3.33
					0.002	1.1	0.25	0.17	0.006	0.008	0.26	0.24	0.18
ic3959	E	25.6	15.27	7059	2.334	215.8	1.57	1.94	0.143	0.304	4.50	3.11	3.80
					0.002	1.1	0.27	0.18	0.007	0.008	0.28	0.25	0.19
ic3963	S0	46.5	15.76				2.13	1.98	0.107	0.266	4.11	2.64	3.38
							0.15	0.10	0.004	0.004	0.16	0.14	0.11

Table A.4: *continued on next page*

continued from previous page

name	type‡	SN	b_j†	$cz_\odot$	$\log\sigma$	σ	Hβ	Hβ_G	Mg$_1$	Mg$_2$	Mg$_b$	$\langle$Fe$\rangle$	[MgFe]
			mag	km s^{-1}	dex	km s^{-1}	Å	Å	mag	mag	Å	Å	Å
ic3973	S0/a	25.2	15.32				2.14	2.27	0.156	0.322	4.66	3.19	3.92
							0.27	0.19	0.007	0.008	0.29	0.26	0.19
ic3998	SB0	47.2	15.70				2.12	2.22	0.113	0.279	4.44	3.06	3.75
							0.15	0.10	0.004	0.004	0.15	0.14	0.10
ic4026	SB0	25.2	15.73				2.48	2.41	0.095	0.258	4.34	3.10	3.72
							0.27	0.19	0.007	0.008	0.29	0.26	0.19
ic4041	S0	15.0	15.93				1.72	1.62	0.103	0.261	4.15	3.20	3.68
							0.47	0.32	0.011	0.014	0.49	0.43	0.33
ic4045	E	47.3	15.17				1.67	1.78	0.120	0.298	4.81	2.75	3.78
							0.15	0.10	0.004	0.004	0.15	0.14	0.10
ic4051	E	32.8	14.47	5020	2.339	218.3	1.09	1.48	0.152	0.331	4.99	2.89	3.94
					0.002	1.1	0.21	0.15	0.005	0.007	0.22	0.20	0.15
ngc4850	E/S0	52.5	15.39				1.35	1.59	0.130	0.288	4.37	2.77	3.57
							0.13	0.09	0.003	0.004	0.14	0.12	0.09
ngc4851	S0	28.0	16.00	7895	2.128	134.3	1.80	2.17	0.095	0.249	4.29	2.80	3.54
					0.004	1.1	0.25	0.17	0.006	0.007	0.26	0.23	0.17
ngc4853	S0p	32.3	14.38	7718	2.115	130.3	1.89	2.03	0.059	0.163	2.61	1.69	2.15
					0.004	1.1	0.21	0.15	0.005	0.006	0.23	0.21	0.16

Table A.4: *continued on next page*

continued from previous page

name	type‡	SN	b_j†	$cz_\odot$	$\log\sigma$	σ	Hβ	Hβ_G	Mg$_1$	Mg$_2$	Mg$_b$	$\langle$Fe$\rangle$	[MgFe]
			mag	km s^{-1}	dex	km s^{-1}	Å	Å	mag	mag	Å	Å	Å
ngc4860	E	29.8	14.69				1.82	1.99	0.147	0.330	5.36	2.71	4.04
							0.23	0.16	0.006	0.007	0.24	0.22	0.16
ngc4867	E	18.9	15.44				1.77	1.79	0.145	0.280	4.87	2.89	3.88
							0.37	0.25	0.009	0.011	0.38	0.35	0.26
ngc4874	cD	28.0	12.78	7191	2.432	270.4	2.01	2.09	0.136	0.305	4.67	3.17	3.92
					0.002	1.1	0.25	0.17	0.006	0.008	0.26	0.23	0.17
ngc4875	S0	29.9	15.88				1.61	1.77	0.131	0.288	4.60	3.31	3.96
							0.23	0.16	0.006	0.007	0.24	0.22	0.16
ngc4876	E	58.2	15.51				2.15	2.18	0.098	0.261	3.92	2.97	3.45
							0.12	0.08	0.003	0.004	0.13	0.11	0.09
ngc4881	E	42.8	14.73				1.78	2.01	0.133	0.314	4.69	2.97	3.83
							0.16	0.11	0.004	0.005	0.17	0.15	0.11
ngc4883	S0	48.0	15.43				2.03	2.12	0.121	0.302	4.61	3.36	3.99
							0.14	0.10	0.004	0.004	0.15	0.14	0.10
ngc4886	E	84.1	14.83				2.09	2.12	0.107	0.266	4.16	2.68	3.42
							0.08	0.06	0.002	0.002	0.09	0.08	0.06
ngc4896	S0	29.3	15.06	5986	2.188	154.2	2.30	2.35	0.118	0.284	4.53	2.75	3.64
					0.003	1.1	0.23	0.16	0.006	0.007	0.25	0.22	0.17

Table A.4: *continued on next page*

continued from previous page

name	type‡	SN	b_j†	$cz_\odot$	$\log\sigma$	σ	Hβ	Hβ_G	Mg_1	Mg_2	Mg_b	$\langle Fe\rangle$	[MgFe]
			mag	$km\,s^{-1}$	dex	$km\,s^{-1}$	Å	Å	mag	mag	Å	Å	Å
ngc4908	S0/E	32.9	14.91				2.36	2.19	0.101	0.284	4.48	2.90	3.69
							0.21	0.14	0.005	0.006	0.22	0.20	0.15

† taken from Godwin, Metcalfe & Peach (1983)

‡ taken from Dressler (1980)

Table A.4: Data from Jørgensen (1999) in common with this study. There are 36 galaxies in common between the two data sets (measurements for 71 Coma cluster galaxies were reported by Jørgensen 1999).

A.4 Comparison with Mehlert et al. (2000)

Mehlert et al. (2000) measured high signal-to-noise long-slit spatially resolved spectra, giving line strength measurements as a function of radius from the galaxy centre, for a sample of 35 early-type Coma cluster galaxies (27 in the inner square degree, 8 at a distance greater than 40 arcmin). The spectra were centred on the 5170Å Mg triplet and were taken along the major axes of the galaxies. Observations were made during 6 runs at 3 different telescopes: the 2.4m Michigan-Dartmouth-MIT (MDM) telescope at Kitt Peak, the 2.7m at the McDonald observatory (McD) and the 3.5m at the German-Spanish Astronomical Centre on Calar Alto (CA). The inner sample of 27 galaxies is complete to a Kron-Cousins magnitude R = 12.63 mag and 42% complete in the range 12.63 mag $< R <$ 14.06 mag. The outer sample is complete to R = 13.21 mag. The observations are summarised in Table A.5.

Run	Date	Telescope	Detector Spectrograph	Wavelength Range (Å)	Scale (″ per pix)	Slit width	Spectral resolution (σ)
1	3/95	MDM	TI: 1024×1024	4300–6540	0.777	1.7″	2.23Å
4	3/96	2.4m	Mark III				129.4 km s^{-1}
2	4/95	McD	TI: 800×800	4850–5560	0.635	2.5″	1.17Å
5	4/96	2.7m	LCS				67.9 km s^{-1}
3	5/95	CA	TI: 1024×1024	4730–5700	0.896	3.6″	1.17Å
6	5/96	3.5m	TWIN/R				67.9 km s^{-1}

Table A.5: Observing setup of Mehlert et al. (2000). The spectral resolutions in km s^{-1} were derived at the 5170Å Mg triplet.

Following Jørgensen et al. (1995a,b) and Mehlert et al. (2000) I use equation A.1 to convert the aperture radius used in my study (r_A) to a "slit-equivalent" radius (r_L). The slit widths (b) used by Mehlert et al. (2000) are: 1.7″, 2.5″ and 3.6″. These result in slit-equivalent radii of: 2.5″, 1.7″ and 1.2″ respectively. To convert their long slit line index measurements I take

all their data within a radius of 5″ and fit a 4th order polynomial to it. I then compute the index value at the slit equivalent radii ($\pm r_L$) matched to my 2.7″ diameter fibres and average the values for a final value that can be compared to my data. An example of this is shown in Figure A.1 for the galaxy NGC 4952.

$$r_L = \left(\frac{r_A}{1.025}\right)^2 \frac{\pi}{2b} \tag{A.1}$$

There are 18 galaxies from this sample in common with this study. These are shown in Table A.6.

A.5 Comparison with Kuntschner et al. (2001)

Kuntschner et al. (2001) re-analysed a spectroscopic run from the SMAC programme (Smith et al. 2000) to measure line indices to investigate the Mg–σ and ⟨Fe⟩–σ relations from a sample of 72 early-type galaxies from a selection of cluster and group environments. They published data for 31 galaxies in the Coma cluster, all with S/N≥30 and corrected to 3.4″ diameter fibres. There are 14 galaxies from this sample in common with this study. These are shown in Table A.7.

A.6 Comparison with the SMAC programme

The SMAC or "Streaming Motions of Abell Clusters" programme constructed a catalogue of fundamental plane data within 12,000 km s^{-1} to analyse streaming motions (Hudson et al. 1999, Smith et al. 2000). They published measurements for 56 Coma cluster galaxies (Hudson et al. 1999), corrected to 3.4″ diameter fibres. There are 34 galaxies from this sample in common with this study. These are shown in Table A.8.

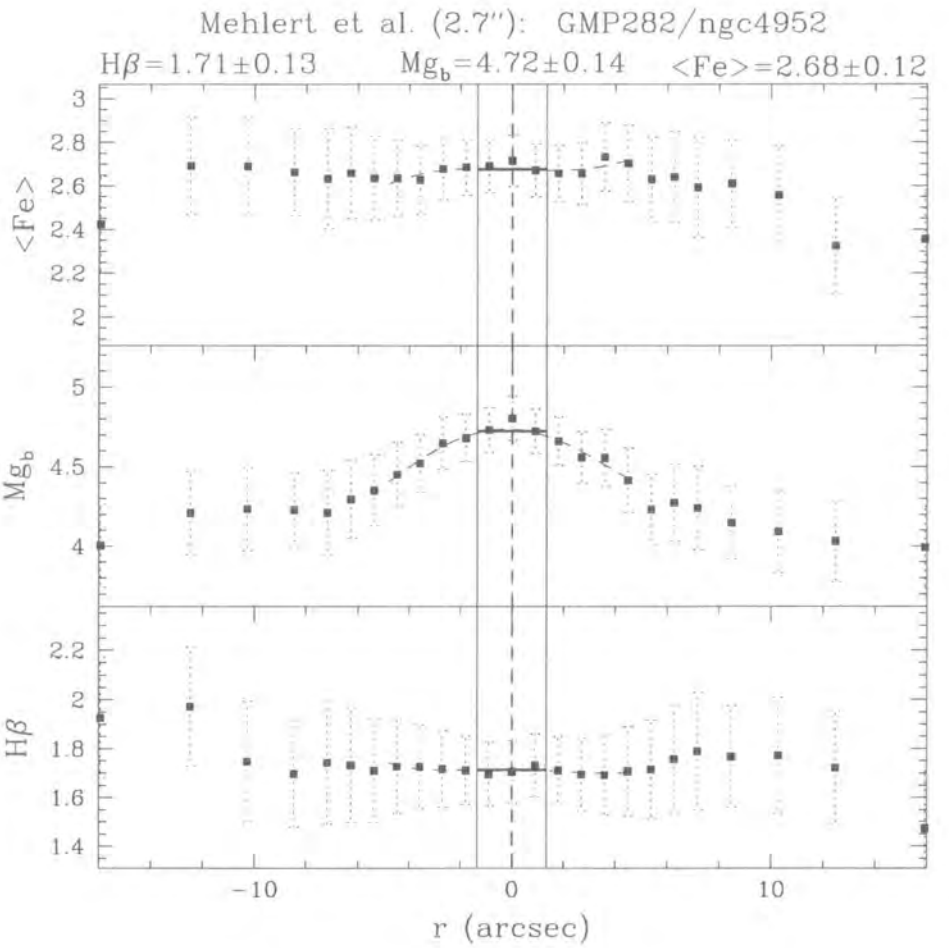

Figure A.1: Conversion of Mehlert et al. (2000)'s long slit data to aperture equivalent line strengths. The derivation of the aperture equivalent line strengths for the indices Hβ, Mg$_b$ and $\langle$Fe$\rangle$ are shown in this figure. The two vertical lines represent the size of the fibres used in this study. The final value is shown as a solid horizontal line.

name	type‡	b_j†	$cz_\odot$	$\log\sigma$	σ	$\log R_e$	$\langle\mu\rangle_e$	Mg_2
		mag	km s^{-1}	dex	km s^{-1}			mag
[ht] d27	E	16.45	7820	1.983 ± 0.021	96.2 ± 4.8	0.667	19.84	0.262
d81	E	16.10	5966	2.109 ± 0.017	128.5 ± 5.1	0.756	20.10	0.258
d107	E	16.35	6518	1.748 ± 0.031	56.0 ± 4.1	0.790	20.41	0.237
d135	E	16.98	8322	2.001 ± 0.024	100.2 ± 5.7	0.510	19.71	0.237
d136	E	16.57	5697	2.234 ± 0.016	171.4 ± 6.4	0.184	17.77	0.269
d153	E	16.14	6686	2.100 ± 0.021	125.9 ± 6.2	0.506	19.02	0.278
d156	E/S0	16.45	6706	1.987 ± 0.021	97.0 ± 4.8	0.497	19.65	0.213
d161	E	15.19	7169	2.265 ± 0.021	184.1 ± 9.1	0.847	19.52	0.300
d193	E	16.43	7575	2.056 ± 0.021	113.8 ± 5.6	0.547	19.32	0.267
d204	E	15.99	7643	2.154 ± 0.024	142.6 ± 8.1	0.773	20.04	0.249
d207	E	16.07	6779	2.182 ± 0.021	152.1 ± 7.5	0.579	19.18	0.259
d210	Ep	15.97	7243	2.166 ± 0.018	146.6 ± 6.2	0.515	18.70	0.248
ic3947	E	15.94	5676	2.174 ± 0.021	149.3 ± 7.4	0.531	18.74	0.265
ic3959	E	15.27	7079	2.306 ± 0.015	202.3 ± 7.1	0.739	19.12	0.300
ic4011	E	16.08	7263	2.030 ± 0.014	107.2 ± 3.5	0.665	19.59	0.269
ic4012	E	15.93	7266	2.266 ± 0.021	184.5 ± 9.1	0.412	18.07	0.284
ic4041	S0	15.93	7110	2.102 ± 0.024	126.5 ± 7.2	0.800	19.99	0.274
ic4045	E	15.17	6938	2.334 ± 0.021	215.8 ± 10.7	0.647	18.56	0.293
ic4051	E	14.47	5026	2.381 ± 0.016	240.4 ± 9.0	1.216	20.59	0.336
ngc4850	E/S0	15.39	6033	2.235 ± 0.021	171.8 ± 8.5	0.706	19.03	0.260
ngc4860	E	14.69	7951	2.419 ± 0.011	262.4 ± 6.7	0.865	19.16	0.337
ngc4864	E	14.70	6841	2.310 ± 0.016	204.2 ± 7.7	0.881	19.50	0.286
ngc4869	E	14.97	6856	2.308 ± 0.016	203.2 ± 7.6	0.891	19.43	0.310
ngc4872	E/S0	14.79	7222	2.298 ± 0.021	198.6 ± 9.8	0.543	18.46	0.288
ngc4874	cD	12.78	7213	2.422 ± 0.013	264.2 ± 8.0	1.804	21.66	0.318
ngc4875	S0	15.88	8041	2.252 ± 0.024	178.7 ± 10.2	0.509	18.57	0.284

Table A.8: *continued on next page*

continued from previous page

name	type‡	b_j†	$cz_\odot$	$\log\sigma$	σ	$\log R_e$	$\langle\mu\rangle_e$	Mg_2
		mag	km s^{-1}	dex	km s^{-1}			mag
ngc4876	E	15.51	6727	2.273 ± 0.013	187.5 ± 5.7	0.629	18.86	0.246
ngc4881	E	14.73	6730	2.297 ± 0.011	198.2 ± 5.1	1.026	19.91	0.295
ngc4889	cD	12.62	6519	2.600 ± 0.010	398.1 ± 9.3	1.561	20.51	0.344
ngc4895	S0	14.38	8490	2.326 ± 0.029	211.8 ± 14.6	1.014	19.52	0.279
ngc4906	E	15.44	7519	2.218 ± 0.021	165.2 ± 8.2	0.756	19.32	0.273
ngc4908	S0/E	14.91	8749	2.294 ± 0.016	196.8 ± 7.4	0.810	19.11	0.292
ngc4919	S0	15.06	7328	2.270 ± 0.024	186.2 ± 10.6	0.766	19.00	0.290
ngc4923	E	14.78	5507	2.320 ± 0.019	208.9 ± 9.3	0.881	19.39	0.300

† taken from Godwin, Metcalfe & Peach (1983)

‡ taken from Dressler (1980)

Table A.8: Data from the SMAC study (Hudson et al. 1999) in common with this study. $\log R_e$ is the effective radius, with R_e in arcsecs. $\langle\mu\rangle_e$ is the mean R-band surface brightness within the effective radius, in magnitudes per square arcsecond. There are 34 galaxies in common between the two data sets (measurements for 56 Coma cluster galaxies were reported by the SMAC study).

name	type	R (mag)	Hβ (Å)	$\langle$Fe$\rangle$ (Å)	Mg$_b$ (Å)	[MgFe] (Å)
d39	S0/E	14.06	1.98 ± 0.20	2.29 ± 0.18	4.17 ± 0.22	3.09 ± 0.14
d75	S0	13.71	2.36 ± 0.24	2.53 ± 0.21	3.46 ± 0.26	2.96 ± 0.16
ic3947	E	14.00	1.31 ± 0.20	1.93 ± 0.17	4.17 ± 0.21	2.84 ± 0.14
ic4041	S0	13.81	2.22 ± 0.12	2.89 ± 0.10	3.92 ± 0.12	3.36 ± 0.08
ic4045	E	13.24	1.52 ± 0.16	2.74 ± 0.15	4.60 ± 0.18	3.55 ± 0.11
ic4051	E	12.34	1.41 ± 0.26	2.71 ± 0.23	5.34 ± 0.28	3.80 ± 0.18
ngc4850	E/S0	13.36	1.46 ± 0.16	2.48 ± 0.15	4.33 ± 0.17	3.28 ± 0.11
ngc4860	E	12.63	1.42 ± 0.22	2.97 ± 0.19	5.27 ± 0.24	3.95 ± 0.16
ngc4869	E	12.93	1.42 ± 0.17	2.84 ± 0.16	4.80 ± 0.19	3.69 ± 0.12
ngc4872	E/S0	13.75	2.05 ± 0.18	2.79 ± 0.15	4.02 ± 0.19	3.35 ± 0.12
ngc4874	cD	10.61	2.19 ± 0.12	3.07 ± 0.11	5.01 ± 0.13	3.92 ± 0.09
ngc4876	E	13.51	1.85 ± 0.42	2.52 ± 0.37	3.95 ± 0.44	3.15 ± 0.29
ngc4883	S0	13.36	1.58 ± 0.20	2.78 ± 0.17	4.42 ± 0.21	3.50 ± 0.14
ngc4889	cD	10.64	1.94 ± 0.22	3.10 ± 0.19	5.40 ± 0.24	4.09 ± 0.15
ngc4895	S0	12.49	1.60 ± 0.17	2.64 ± 0.16	4.33 ± 0.19	3.38 ± 0.12
ngc4896	S0	12.76	1.65 ± 0.22	2.71 ± 0.15	4.28 ± 0.22	3.41 ± 0.14
ngc4908	S0/E	12.97	1.57 ± 0.27	2.55 ± 0.23	4.16 ± 0.28	3.26 ± 0.18
ngc4923	E	12.86	1.71 ± 0.18	2.68 ± 0.16	4.43 ± 0.19	3.45 ± 0.12

Table A.6: 2.7″ diameter fibre data from Mehlert et al. (2000) in common with this study. There are 18 galaxies in common between the two data sets (measurements for 35 Coma cluster galaxies were reported by Mehlert et al. 2000). The line strength data of Mehlert et al. (2000) has been converted to an equivalent line strength measurement for a 2.7″ diameter fibre the diameter of the fibres used in this dissertation).

name	type‡	b_j†	S/N	$\log\sigma$	σ	Hβ	Mg_2	Mg_b	$\langle$Fe$\rangle$
		mag	per Å	dex	km s^{-1}	Å	mag	Å	Å
ngc4860	E	14.69	41	2.436	272.9	1.53	0.330	4.98	2.81
				0.014	8.9	0.16	0.005	0.17	0.15
ngc4864	E	14.70	43	2.309	203.7	1.85	0.278	4.51	2.79
				0.014	6.7	0.17	0.005	0.17	0.15
ngc4869	E	14.97	31	2.306	202.3	1.01	0.304	4.78	2.63
				0.019	9.0	0.22	0.007	0.23	0.20
ngc4874	cD	12.78	35	2.453	283.8	1.80	0.306	4.62	2.66
				0.019	12.7	0.21	0.006	0.21	0.19
ngc4876	E	15.51	37	2.276	188.8	1.44	0.239	3.95	2.98
				0.016	7.1	0.18	0.005	0.19	0.17
ngc4881	E	14.73	37	2.293	196.3	1.62	0.293	4.83	3.06
				0.018	8.3	0.19	0.005	0.19	0.17
ngc4886	E	14.83	31	2.227	168.7	1.78	0.248	4.32	2.83
				0.019	7.5	0.21	0.006	0.23	0.20
ngc4889	cD	12.62	44	2.601	399.0	1.51	0.334	5.56	3.00
				0.017	15.9	0.16	0.005	0.17	0.15
ngc4908	E	14.91	33	2.293	196.3	1.69	0.289	4.28	2.80
				0.019	8.8	0.21	0.006	0.21	0.18
ic3973	S0/a	15.32	38	2.341	219.3	1.78	0.283	4.46	2.51
				0.016	8.2	0.17	0.005	0.19	0.17
ic4011	E	16.08	30	1.982	95.9	1.51	0.260	4.19	2.55
				0.029	6.6	0.22	0.007	0.24	0.21
ic4045	E	15.17	35	2.327	212.3	1.36	0.283	4.54	2.50
				0.016	8.0	0.20	0.006	0.20	0.18
d81	E	16.10	30	2.067	116.7	1.54	0.247	4.15	2.36
				0.021	5.8	0.22	0.007	0.24	0.22
d210	Ep	15.97	35	2.148	140.6	1.27	0.239	3.87	2.09
				0.022	7.3	0.20	0.006	0.21	0.19

† taken from Godwin, Metcalfe & Peach (1983)

‡ taken from Dressler (1980)

Table A.7: Data from Kuntschner et al. (2001) in common with this study. There are 14 galaxies in common between the two data sets (measurements for 31 Coma cluster galaxies were reported by Kuntschner et al. 2001).

Bibliography

The following abbreviations are used in this bibliography:

A&A	Astronomy and Astrophysics
AAS	American Astronomical Society Meeting
A&AS	Astronomy and Astrophysics Supplement
AJ	The Astronomical Journal
ApJ	The Astrophysical Journal
ApJS	The Astrophysical Journal Supplement
ARA&A	Annual Reviews of Astronomy and Astrophysics
IAUS	International Astronomical Union Symposium
MNRAS	Monthly Notices of the Royal Astronomical Society
PASP	Publication of the Astronomical Society of the Pacific
SPIE	Society of Photo-optical Instrumentation Engineers

Aaronson M., Bothun G. D., Cornell M. E., Dawe J. A., Dickens R. J., Hall P. J., Sheng H. M., Huchra J. P., Lucey J. R., Mould J. R., Murray J. D., Schommer R. A. & Wright A. E., 1989, ApJ, 338, 654

Anders E. & Grevesse N., 1989, Geochimica et Cosmochimica Acta, 53, 197

Arimoto N. & Yoshii Y., 1987, A&A, 173, 23

Arnaud M., Aghanim N., Gastaud R., Neumann D. M., Lumb D., Briel U., Altieri B., Ghizzardi S., Mittaz J., Sasseen T. P. & Vestrand W. T., 2001, A&A, 365, 67

Baade W., 1944, ApJ, 100, 137

Barger A. J., Aragon-Salamanca A., Ellis R. S., Couch W. J., Smail I. & Sharples R. M., 1996, MNRAS, 279, 1

Baugh C. M., Cole S. & Frenk C. S., 1996, MNRAS, 283, 1361

Bingham R. G., Gellatly D. W., Jenkins C. R. & Worswick S. P., 1994, SPIE, 2198, 56

Bender R., Burstein D. & Faber S. M., 1992, ApJ, 399, 462

Bender R., Burstein D. & Faber S. M., 1993, ApJ, 411, 153

Bessell M. S., Brett J. M., Wood P. R. & Scholz M., 1989, A&AS, 77, 1

Bessell M. S., Brett J. M., Scholz M. & Wood P. R., 1991, A&AS, 89, 335

Biviano A., Durret F., Gerbal D., Le Fevre O., Lobo C., Mazure A. & Slezak E., 1996, A&A, 311, 95

Bower R. G., Lucey J. R. & Ellis R. S., 1992, MNRAS, 254, 601

Bower R. G., Kodama T. & Terlevich A., 1998, MNRAS, 299, 1193

Bressan A., Chiosi C. & Fagotto F., 1994, ApJS, 94, 63

Briel U. G., Henry J. P. & Boehringer H., 1992, A&A, 259, 31

Briel U. G. & Henry J. P., 1998, "An X-ray temperature map of Coma", Untangling Coma Berenices: A New Vision of an Old Cluster, Proceedings of the meeting held in Marseilles (France), June 17-20, 1997, Word Scientific Publishing Co Pte Ltd, 170

Briel U. G., Henry J. P., Lumb D. H., Arnaud M., Neumann D., Aghanim N., Gastaud R., Mittaz J. P. D., Sasseen T. P. & Vestrand W. T., 2001, A&A, 365, 60

Bruzual A. G., 1983, ApJ, 273, 105

Bruzual A. G. & Charlot S., 1993, ApJ, 405, 538

Burstein D., Faber S. M., Gaskell C. M. & Krumm N., 1984, ApJ, 287, 586

Burstein D., Davies R. L., Dressler A., Faber S. M. & Lynden-Bell D., 1988, "Global stellar populations of elliptical galaxies. A - Optical properties", Towards understanding galaxies at large redshift, Proceedings of the Fifth Workshop of the Advanced School of Astronomy, Erice, Italy, June 1-10, 1987, Dordrecht, Kluwer Academic Publishers, 17

Burstein D., Faber S. M. & Dressler A., 1990, ApJ, 354, 18

Butcher H. & Oemler A., 1978, ApJ, 226, 559

Butcher H. & Oemler A., 1978, ApJ, 285, 426

Caldwell N., Rose J. A., Sharples R. M., Ellis R. S. & Bower R. G., 1993, AJ, 106, 473

Caldwell N., 1984, PASP, 96, 287

Caon N., Capaccioli M. & d'Onofrio M., 1993, MNRAS, 265, 1013

Capelato H. V., de Carvalho R. R. & Carlberg R. G., 1995, ApJ, 451 525

de Carvalho R. R. & Djorgovski S., 1992, ApJ, 389, 49

Charlot S. & Bruzual A. G., 1991, ApJ, 367, 126

Charlot S., Worthey G. & Bressan A., 1996, ApJ, 457, 625

Ciotti L., Lanzoni B. & Renzini A., 1996, MNRAS, 282, 1

Cole S., Lacey C. G., Baugh C. M. & Frenk C. S., 2000, MNRAS, 319, 168

Colless M. & Dunn A. M., 1996, ApJ, 458, 435

O'Connell R. W., 1976, ApJ, 206, 370

O'Connell R. W., 1980, ApJ, 236, 430

Couch W. J. & Sharples R. M., 1987, MNRAS, 229, 423

Davies R. L., Efstathiou G., Fall S. M., Illingworth G. & Schechter P. L., 1983, ApJ, 266, 41

Davies R. L., Sadler E. M. & Peletier R. F., 1993, MNRAS, 262, 650

Djorgovski S. & Davis M., 1987, ApJ, 313, 59

Djorgovski S., de Carvalho R. & Han M. S., 1988, "The universality(?) of distance-indicator relations", Proceedings of the ASP 100th Anniversary Symposium, Victoria, 329

Djorgovski G. & Santiago B. X., 1993, "The Meaning and the Implications of the Fundamental Plane", Structure, Dynamics and Chemical Evolution of Elliptical Galaxies: ESO Conference and Workshop Proceedings, Marciana Marina, Isola d'Elba, 25-30 May 1992, Garching: ESO, 59

van Dokkum P. G. & Franx M, 1995, AJ, 110, 2027

Donnelly R. H., Markevitch M., Forman W., Jones C., Churazov E. & Gilfanov M., 1999, ApJ, 513, 690

Dreyer J. L. E., 1888, "A New General Catalogue of Nebulae and Clusters of Stars, being the Catalogue of the late Sir John F.W. Herschel, Bart., revised, corrected, and enlarged", Mem. R. Astron. Soc., 49, 1

Dreyer J. L. E., 1908, "Index Catalogue of Nebulae and Clusters of Stars (IC 1530–5386), containing objects found in the years 1895 to 1907; with Notes and Corrections to the New General Catalogue and to the Index Catalogue for 1888-94", Mem. R. Astron. Soc., 59, 105

Dressler A., 1980, ApJS, 42, 565

Dressler A. & Gunn J. E., 1982, ApJ, 263, 533

Dressler A. & Gunn J. E., 1983, ApJ, 270, 7

Dressler A., 1987, ApJ, 317, 1

Dressler A., Lynden-Bell D., Burstein D., Davies R. L., Faber S. M., Terlevich R. & Wegner G., 1987, ApJ, 313, 42

Dressler A. & Faber S. M., 1990, ApJ, 354, 13

Dressler A. & Gunn J. E., 1992, ApJS, 78, 1

Faber S. M., 1972, A&A, 20, 361

Faber S. M. & Jackson R. E., 1976, ApJ, 204, 668

Faber S. M., Friel E. D., Burstein D. & Gaskell C. M., 1985, ApJS, 57, 711

Faber S. M., Dressler A., Davies R. L., Burstein D. & Lynden-Bell D., 1987, "Global scaling relations for elliptical galaxies and implications for formation", Proceedings of the Eighth Santa Cruz Summer Workshop in Astronomy and Astrophysics

Faber S. M., Wegner G., Burstein D., Davies R. L., Dressler A., Lynden-Bell D. & Terlevich R. J., 1989, ApJS, 69, 763

Faber S. M., Trager S. C., González J. J. & Worthey G., 1995, IAU Symp. 164, 249

Ferreras I., Benitez N. & Martinez-Gonzalez E., 1998, A&A, 333, 43

Fisher D., Franx M. & Illingworth G., 1995, ApJ, 448, 119

Fisher D., Franx M. & Illingworth G., 1996, ApJ, 459, 110

Fitchett M. & Webster R., 1987, ApJ, 317, 653

Freeman K. C., 1970, ApJ, 160, 811

Gambera M., Pagliaro A., Antonuccio-Delogu V. & Becciani U., 1997, ApJ, 488, 136

Godwin J. G., Metcalfe N. & Peach J. V., 1983, MNRAS, 202, 113

González J. J., 1993, Ph.D. Thesis, University of California, Santa Cruz

Goudfrooij P., Hansen L., Jorgensen H. E., Norgaard-Nielsen H. U., de Jong T. & van den Hoek L. B., 1994, A&AS, 104, 179

Goudfrooij P. & Emsellem E., 1996, A&A, 306, 45

Green E. M., Demarque P. & King C .R., 1987, "The revised Yale isochrones and luminosity functions", New Haven: Yale Observatory (*book*)

Gunn J. E., Stryker L. L. & Tinsley B. M., 1981, ApJ, 249, 48

Gunn J. E. & Stryker L. L., 1983, ApJS, 52, 121

Gunn J. E. & Dressler A., 1988, in "Towards an Understanding of Galaxies at High Redshift", edited by R. G. Kron and A. Renzini, Kluwer, 227

Guzmán R., Lucey J. R., Carter D. & Terlevich R. J., 1992, MNRAS, 257, 187

Guzmán R., Lucey J. R. & Bower R. G., 1993, MNRAS, 265, 731

Hayes D. S. & Latham D. W., 1975, ApJ, 197, 593

Henry R. B. C. & Worthey G., 1999, PASP, 111, 919

Ho L. C., Filippenko A. V. & Sargent W. L. W., 1997, ApJS, 112, 315

Honda H., Hirayama M., Watanabe M., Kunieda H., Tawara Y., Yamashita K., Ohashi T., Hughes J. P. & Henry J. P., 1996, ApJ, 473, 71

Horne K., 1986, PASP, 98, 609

Hudson M. J., Smith R. J., Lucey J. R., Schlegel D. J. & Davies R. L., 1999, ApJ, 512, 79

Illingworth G., 1977, ApJ, 218, 43

Jansen F., Lumb D., Altieri B., Clavel J., Ehle M., Erd C., Gabriel C., Guainazzi M., Gondoin P., Much R., Munoz R., Santos M., Schartel N., Texier D. & Vacanti G., 2001, A&A, 365, 1

Jones L. A. & Worthey G., 1995, ApJ, 446, 31

Jørgensen I., 1994, PASP, 106, 967

Jørgensen I. & Franx M., 1994, ApJ, 433, 553

Jørgensen I., Franx M. & Kjaergaard P., 1995a, MNRAS, 273, 1097

Jørgensen I., Franx M. & Kjaergaard P., 1995b, MNRAS, 276, 1341

Jørgensen I., Franx M. & Kjaergaard P., 1996, MNRAS, 280, 167

Jørgensen I., 1997, MNRAS, 288, 161

Jørgensen I., Hjorth J., Franx M. & van Dokkum P., 1997, AAS, 190, 302

Jørgensen I., 1999, MNRAS, 306, 607

Jørgensen I., Franx M., Hjorth J. & van Dokkum P., 1999, MNRAS, 308, 833

Kauffmann G., White S. D. M. & Guiderdoni B., 1993, MNRAS, 264, 201

Kauffmann G., 1996, MNRAS, 281, 487

King D. L. & Worswick S. P., 1998, SPIE, 3355, 918

Kodama T. & Arimoto N., 1997, A&A, 320, 41

Kormendy J., 1984, ApJ, 287, 577

Kormendy J. & Djorgovski S., 1989, ARA&A, 27, 235

Kuntschner H., 1998, Ph.D. Thesis, University of Durham

Kuntschner H. & Davies R. L., 1998, MNRAS, 295, 29

Kuntschner H., 2000, MNRAS, 315, 184

Kuntschner H., Lucey J. R., Smith R. J., Hudson M. J. & Davies R. L., 2001, MNRAS, 323, 615

Kurucz R. L., 1992, IAUS, 149, 225

Larson R. B., 1974a, MNRAS, 166, 585

Larson R. B., 1974b, MNRAS, 169, 229

Larson R. B. & Tinsley B. M., 1974, ApJ, 192, 293

Larson R. B., Tinsley B. M. & Caldwell C. N., 1980, ApJ, 237, 692

Lauer T. R., 1983, Ph.D. Thesis, University of California, Santa Cruz

Lauer T. R., 1985a, ApJS, 57, 473

Lauer T. R., 1985b, ApJ, 292, 104

Lauer T. R., 1985c, MNRAS, 216, 429

Leonard P. J. T., 1989, AJ, 98, 217

Longhetti M., Rampazzo R., Bressan A. & Chiosi C., 1998, A&AS, 130, 251

Lucey J. R., Bower R. G. & Ellis R. S., 1991, MNRAS, 249, 755

Lubin L. M., 1996, AJ, 112, 23

Lynden-Bell D., Faber S. M., Burstein D., Davies R. L., Dressler A., Terlevich R. J. & Wegner G., 1988, ApJ, 326, 19

MacLaren I., Ellis R. S. & Couch W. J., 1988, MNRAS, 230, 249

Massey P., Strobel K., Barnes J. V. & Anderson E., 1988, ApJ, 328, 315

Marsh T. R., 1989, PASP, 101, 1032

Mehlert D., 1998, Ph.D. Thesis, University of Munich

Mehlert D., Saglia R. P., Bender R. & Wegner G., 2000, A&AS, 141, 449

Mobasher B., Guzmán R., Aragon-Salamanca A. & Zepf S., 1998, "Near infrared study of elliptical galaxies in the Coma cluster", Untangling Coma Berenices: A New Vision of an Old Cluster, Proceedings of the meeting held in Marseilles (France), June 17-20, 1997, Word Scientific Publishing Co Pte Ltd, 83

Mobasher B., Guzmán R., Aragon-Salamanca A. & Zepf S., 1999, MNRAS, 304, 225

Mould J. R., Sheng H. M., Roth J., Staveley-Smith L., Schommer R. A., Bothun G. D., Hall P. J., Huchra J. P., Walsh W. & Wright A. E., 1991, ApJ, 383, 467

Mukai K., 1990, PASP, 102, 183

Neumann D. M., Arnaud M., Gastaud R., Aghanim N., Lumb D., Briel U. G., Vestrand W. T., Stewart G. C., Molendi S. & Mittaz J. P. D., 2001, A&A, 365, 74

d'Onofrio M., Capaccioli M. & Caon N., 1994, MNRAS, 271, 523

Osterbrock D. E., 1995, IAUS, 164, 21

Pagel B. E. J., Simonson E. A., Terlevich R. J. & Edmunds M. G., 1992, MNRAS, 255, 325

Pagliaro A., Antonuccio-Delogu V., Becciani U. & Gambera M., 1999, MNRAS, 310, 835

Pahre M. A. & Djorgovski S. G., 1997, "Observational Constraints on the Origins of the Fundamental Plane", The Nature of Elliptical Galaxies, Proceedings of the Second Stromlo Symposium, ASP Conference Series, 116, 154

Pahre M. A., Djorgovski S. G. & de Carvalho R. R., 1998, AJ, 116, 1591

Peimbert M. & Torres-Peimbert S., 1976, ApJ, 203, 581

Peletier R. F., 1989, Ph.D. Thesis, University of Groningen, The Netherlands

Peletier R. F., Vazdekis A., Arribas S., del Burgo C., Garcia-Lorenzo B., Gutierrez C., Mediavilla E. & Prada F., 1999, MNRAS, 310, 863

Phillips M. M., Jenkins C. R., Dopita M. A., Sadler E. M. & Binette L., 1986, AJ, 91, 1062

Pickles A. J., 1985, ApJ, 296, 340

Pollacco D., Bridges T. J., Rees P. C. T., Lewis J. R., Boyle B. J., Lewis I. & King D. L., 1999, "AUTOFIB2/WYFFOS User Manual", `http://www.ing.iac.es/Astronomy/instruments/af2/af2manual.ps.gz`

Prugniel P. & Simien F., 1996, A&A, 309, 749

Rakos K. D. & Schombert J. M., 1995, ApJ, 439, 47

Recillas-Cruz E., Serrano P. G. A., Cruz-Gonzalez I. & Carrasco L., 1990, A&A, 229, 64

Renzini A. & Ciotti L., 1993, ApJ, 416, 49

Roman N. G., 1995, IAUS, 164, 31

Rood H. J. & Baum W. A., 1967, AJ, 72, 398

Rose J. A., 1994, AJ, 107, 206

Saglia R. P., Bender R. & Dressler A., A&A, 279, 75

Salpeter E. E., 1955, ApJ, 121, 161

Sandage A. & Visvanathan N., 1978, ApJ, 225, 742

Sargent W. L. W., Schechter P. L., Boksenberg A. & Shortridge K., 1977, ApJ, 212, 326

Scodeggio M., Gavazzi G., Belsole E., Pierini D. & Boselli A., 1998, MNRAS, 301, 1001

Sérsic J. L., 1968, Bulletin of the Astronomical Institute of Czechoslovakia, 19, 105

Smith R. J., Lucey J. R., Hudson M. J., Schlegel D. J. & Davies R. L., 2000, MNRAS, 313, 469

Smith R. J., Lucey J. R., Moore S. A. W., Colless M. M., Kaldare R. & Sharples R. M., 2001, *in preparation*

Smirnov N. V., 1939, "Estimate of deviation between emprical distribution functions in two independent samples", Bulletin Moscow University, 2(2), 3

Spinrad H. & Taylor B. J., 1971, ApJS, 22, 445

Steel J., 1998, Ph.D. Thesis, University of Durham

Tantalo R., Chiosi C. & Bressan A., 1998, A&A, 333, 419

Terlevich A., 1998, Ph.D. Thesis, University of Durham

Terlevich A., Kuntschner H., Bower R. G., Caldwell N. & Sharples R. M., 1999, MNRAS, 310, 445

Tinsley B. M. & Gunn J. E., 1976, ApJ, 203, 52

Tody D., 1986, SPIE, 627, 733

Tody D., 1993, "IRAF in the Nineties", Astronomical Data Analysis Software and Systems II, A.S.P. Conference Series, 52, 173

Trager S. C., 1997, Ph.D. Thesis, University of California, Santa Cruz

Trager S. C., Worthey G., Faber S. M., Burstein D. & González J. J., 1998, ApJS, 116, 1

Trager S. C., Faber S. M., Worthey G. & González J. J., 2000a, AJ, 119, 1645

Trager S. C., Faber S. M., Worthey G. & González J. J., 2000b, AJ, 120, 165

Tripicco M. J. & Bell R. A., 1995, AJ, 110, 3035

Turner M. J. L. et al., 2001, A&A, 365, 27

Vandenberg D. A., 1985, ApJS, 58, 711

Vandenberg D. A. & Bell R. A., 1985, ApJS, 58, 561

Vandenberg D. A. & Laskarides P. G., 1987, ApJS, 64, 103

de Vaucouleurs G., 1948, Annales d'Astrophysique, 11, 247

Vazdekis A., 1996a, IAUS, 171, 460

Vazdekis A., Casuso E., Peletier R. F. & Beckman J. E., 1996b, ApJS, 106, 307

Vazdekis A., Peletier R. F., Beckman J. E. & Casuso E., 1997, ApJS, 111, 203

Vazdekis A., 1999, ApJ, 513, 224

Vikhlinin A., Forman W. & Jones C., 1994, ApJ, 435, 162